

User's Short Reports

You can jump to the top of the section by clicking titles.

USER'S SHORT REPORTS

CONTENTS OF USER'S PROGRESS REPORTS

Title	First Author	Proposal No.	Page
A : EXAFS			
Temperature Dependence of EXAFS in CeO ₂ and ReO ₃	Miyanaaga, T.	89-004	15
Structural Studies of Copper(II)-Aminocarboxylato Complexes in Aqueous Solution by EXAFS	Miyata, Y.	89-014	16
EXAFS and XANES Analysis of Selenium Compounds (III)	Kawashima, T.	87-008	17
EXAFS Studies on the Local Structure of TiO ₂ Super-thin Layer on SiO ₂	Asakura, K.	87-013	18
An EXAFS Study of Highly Dispersed Vanadium Oxide Catalysts Prepared by a CVD Method	Kanai, H.	87-116	19
Xanes Estimation of Ce Valence in L-Pd ₅ Ce and H-Pd ₅ Ce	Kuwano, N.	87-129	20
Characterization of Zeolite-Encapsulated Metal Phthalocyanine Catalysts	Fukuoka, A.	87-131	21
EXAFS Studies on the Local Structures of Calcium Catalyst for Coal Gasification	Yamashita, H.	87-139	22
Structural Studies on Precipitation Reactions in Qualitative Analysis by EXAFS and XANES Technique (II)	Nomachi, I.	87-141	23
Local Structures around Fe ³⁺ and Mn ²⁺ Ions in Silicate Glasses	Tabira, Y.	88-001	24
XAFS Study of Ti-Zr Binary Oxide on Silica	Tanaka, T.	88-011	25
EXAFS Studies on the Reversible Enhancement Phenomenon for C ₂ H ₄ Hydrogenation Activity on Pt/one-atomic Layer TiO ₂ /SiO ₂	Asakura, K.	88-022	26
EXAFS and XANES Studies on Dynamic Behavior of Two-site Promotion of CO Catalyzed by Bimetal Clusters	Fukuoka, A.	88-027	27
EXAFS Study of Relaxation of Cu ⁺ Impurities in Alkali Halides	Murata, T.	88-115	28
Studies on the EXAFS Intensities for 3d Transition Metal Complexes	Sakane, H.	88-116	29
EXAFS Studies on Local Structure of Amorphous LANI _{5,0} Films	Sakaguchi, H.	88-117	30
EXAFS and XANES Studies on the Coordination of Copper Ion in Zeolites	Kagawa, S.	88-118	31

XAFS Study on Nickel Thiolate Complexes in Terms of the Nickel in Hydrogenases	Yamamura, T.	88-120	32
EXAFS and XANES Studies on Characterization of Electron Donor-Acceptor Metal Phthalocyanine Complexes Entrapped in Zeolite Supercages	Fukuoka, A.	88-124	33
Experimental Examination of "Phase Shift Transferability" on EXAFS Analysis	Hida, M.	88-138	34
Local Structure of the Pb Substituted Bi-Sr-Ca-Cu-O High- T_c Superconductors	Miura, Y.	88-139	35
EXAFS and XANES Studies on the Crystallization of Pentasil Zeolite I. Local Structure around Iron of Ferrisilicate	Matsubayashi, N.	88-143	36
EXAFS and XANES Analyses of V_2O_5 Thin Film Catalysts Prepared by CVD - The Effects of Supports-	Inumaru, K.	89-003	37
XANES Study on the Density of d-State of SMSI-Platinum and Related Catalysts	Yoshitake, H.	89-007	38
Photo-Modulated EXAFS	Emura, S.	89-009	39
An EXAFS Study of Cr(III, IV, V)-edta Complexes in Aqueous Solution	Ozutsumi, K.	89-015	40
EXAFS Studies of Nickel(II) and Manganese(II) Complexes of Some 2-(Polyhydroxy-Alkyl) Thiazolidine-4-Carboxylic Acids	Nagy, L.	89-028	41
Structure Studies on Cr/ ZrO_2 Catalyst by XAFS	Ushikubo, T.	88-Y009	42
EXAFS Studies of SiO_2 and Mg_2SiO_4	Ogata, K.		43
Structure Studies of Amorphous Silicon Nitrides by Si-K-edge EXAFS	Nakano, A.		44
EXAFS Studies on the Reaction Mechanism of Rh Dimer Species	Asakura, K.	87-011	45
The Structure Analysis of Ag_3AsS_3 Glass by EXAFS Measurement	Okuno, M.	87-020	46
EXAFS as a Probe to the Crystallization of Aluminosilicate Gels	Parise, J. B.	87-025	47
Relation between Superconducting Transition and Thermal Vibrations in $YBa_2Cu_3O_{7-\delta}$ Compounds	Yamazaki, H.	87-123	48
Chemical Short Range Order in Liquid Rb-Se Alloys	Endo, H.	87-124	49
Structure of Liquid State of Bi_2O_3 by EXAFS	Koto, K.	87-130	50
Cu K-edge Absorption Spectra of a Novel Superconducting Oxide : $Nd_{2-x}Ce_xCuO_{4-y}$ I. Unreduced Samples	Kosugi, N.	87-132 88-U004	51
XANES of Low-dimensional Complexes with Highly Oxidized Ni and Cu I. Cu Valence of Different Sites in $YBa_2Cu_3O_y$	Kuroda, H.	87-132 88-128	52
XANES of Low-dimensional Complexes with Highly Oxidized Ni and Cu II. Local Structures of Different Cu Sites in $YBa_2Cu_3O_y$	Kuroda, H.	87-132 88-128	53

Temperature-dependent EXAFS Study on Supported Pd and Ag Small Metal Clusters	Yokoyama, T.	87-135	54
EXAFS Study on Ni-Nb Amorphous Alloy Prepared by Mechanical Alloying	Nasu, T.	87-145	55
The Structure of Intercalated CdS Particles in Layered $K_4Nb_6O_{17}$	Yoshimura, J.	88-003	56
EXAFS Analysis of ZrF_4 - BaF_2 -CsF Glasses and Related Compounds	Kawamoto, Y.	88-004	57
EXAFS Study on the Active Intermediates of Chemical Models for Cytochrome P-450	Hirobe, M.	88-005	58
XAFS Studies on Martensitic Transformation in Fe-Ni Alloys	Yamazaki, H.	88-017	59
EXAFS Studies on the Structure of Silica Attached Nb-Dimer Catalyst	Ichikuni, N.	88-020	60
The structural Studies on the Al_2O_3 Attached Cobalt Catalyst in the No-Co Reaction	Takahara, S.	88-021	61
Elucidation of Structure of Catecholdioxygenase-model Complexes and Mechanism of Oxygenation of Aromatic Ring	Funabiki, T.	88-023	62
EXAFS Study on Amorphization Process of Pd-Si Alloy by Mechanical Alloying	Nasu, T.	88-024	63
Temperature Dependence of XANES in CeO_2 - $Tb_2O_{3.5}$ Mixed Conductor	Arashi, H.	88-125	64
EXAFS Studies on the Local Structures of Strontium and Iron Catalysts for Coal Gasification	Yamashita, H.	88-126	65
EXAFS Studies of $Cu(I,II)$ - NH_3 , py, phen, bpy Complexes in Aqueous Solution	Ozutsumi, K.	88-127	66
Oxidative Disruption of Rhodium Particle Supported on Silica by O_2 and CO	Fukushima, T.	88-132	67
EXAFS Study on Amorphous Fe-Ti-H Alloys Produced by Vapor Quenching	Sumiyama, K.	88-134	68
EXAFS Study on Anharmonic Vibration in CuBr	Maeda, H.	88-137	69
Br K-edge XANES and EXAFS Studies on Bromine-adsorbed Small Pd Clusters Supported on Silica	Yokoyama, T.	88-140	70
Anharmonic Interatomic Potentials Determined by Temperature-dependent EXAFS Spectra of AgBr and CuBr	Yokoyama, T.	88-140	71
Characterization of Cu-Ta Alloy System Synthesized by Mechanical Alloying	Sakurai, K.	88-144	72
EXAFS Measurement of Niobium Acid Thin Layer on SiO_2 Catalyst	Shirai, M.	88-006	73
Reduction Process of Binary Oxides Containing Fe	Tanaka, T.	89-012	74
EXAFS Studies on the Photocatalysis of Mo Dimer	Asakura, K.	89-018	75

EXAFS Study of Zeolite NaY Supported Cu-Pt Bimetallic Catalyst	Tzou, M-S	89-019	76
Studies on the Structure of Bimetallic Colloidal Catalysts	Toshima, N.	89-020	77
The EXAFS and XANES Spectra of $\text{M}\text{CaSi}_2\text{O}_6$ (M=Co, Ni, Sr) Glasses	Okuno, M.	89-022	78
EXAFS and XANES Studies on Intercalation Compounds M_xTiS_2 (M=Mn, Fe, Co, Ni)	Negishi, H.	89-025	79
EXAFS Studies of $\text{MoO}_3/\text{TiO}_2$ Catalysts Prepared by an Equilibrium Adsorption Method	Soeya, T.	89-027	80
Local Structure of Diorganotin(IV) Complexes with Carbohydrate	Nagy, L.	89-028	81
EXAFS and XANES Studies of Copper(II) Complexes Formed with Adenosine and Uridine at Different pH	Yamaguchi, T.	89-028	82
Structural Analysis of Hopeite Crystal by Curve Fitting of EXAFS	Sato, N.	88-Y005	83
EXAFS Studies on Pd-M/C Catalyst	Akai, T.	89-Y006	84
XAFS Studies on Silica-supported Tantalum Oxides	Yanai, H.	88-Y009	85
EXAFS Study on the Structure of Amorphous $\text{Se}_{1-x}\text{Te}_x$ Alloy-films	Tani, K.		86
Simple Performance Test of EXAFS Facilities	Nomura, M.		87
Cl K-edge EXAFS Study on $\text{AgBr}_x\text{Cl}_{1-x}$ Solid Solutions	Yokoyama, T.	89-032	88
Copper K-edge X-ray Absorption Near-edge Structure of High-Tc Superconductor $\text{Ba}_2\text{Y}_{1-x}\text{Pr}_x\text{Cu}_3\text{O}_y$	Maeyama, S.	89-Y008	89
Copper K-edge Polarized X-ray Absorption Near-edge Structure of High-Tc Superconducting Single-crystal $\text{YBa}_2\text{Cu}_3\text{O}_y$	Maeyama, S.	89-Y011	90

B : Biology

Induction of Chromosome Aberrations by Synchrotron-produced Monochromatic X-rays with Resonance Energy of Phosphorus K-shell Absorption Edge	Saigusa, S.	88-036	91
Molecular Changes of an Amino Acid Including Sulfur with Irradiation of Monochromatic Soft X-rays at the Resonance Absorption Peak of Sulfur	Yokoya, A.	88-040	92
Inactivation Action Spectra of <u>Bacillus Subtilis</u> Spores with Monochromatic Soft X rays (1-6A)	Munakata, N.	88-042	93
Repair Susceptibility of DNA Lesions Produced by K-shell Resonance Absorption of Phosphorus in Wild Type and rad54 Mutant of Yeast	Usami, N.	88-052	94

Irradiation Effect on Deoxyuridine- monophosphate Induced by Soft-X-rays with Resonance Energy of Phosphorus K-absorption Edge	Takakura, K.	88-153	95
Further Analysis of the Soft X-ray Micro- images of Unstained Human Chromosome Fibers Dried with No Fixative	Shinohara, K.	88-033	96
Nondestructive X-ray Fluorescence Spectroscopic Imaging of Trace Elements in Animal Tissues (II)	Nakai, I.	88-034	97
Detection of Damaged DNA Irradiated with Mono- X-ray in the Presence of BrdU; Part II: Effect of Hematoporphyrin Oligomer	Miyoshi, N.	88-037	98
Mutagenic and Transforming Effects of Soft- X-rays with Resonance Energy of Phosphorus K-absorption Edge	Watanabe, M.	88-038	99
Radiosensitization of 5-Iododeoxyuridine in the Soft X-ray region	Shinohara, K.	88-041	100
X-ray Crystal Structural Analysis of Tobacco Necrosis Virus	Tsukihara, T.	89-039	101
Crystal Structure of Myoglobin Reconstituted with Synthesized Hemes	Takenaka, A.	88-043	102
Polymorphism of Ribonuclease Rh Crystals Which Is Enhanced Through Exposure to Synchrotron Beam and Its Remedy	Kurihara, H.	88-047	103
On the Local Heterogeneity in a Crystal of Hydrogenase	Higuchi, Y.	88-049	104
Crystal Structure Determination of Cytochrome c553 by the Multi-wavelength Anomalous Dispersion Method	Nakagawa, A.	88-050	105
High Resolution Data Collection of GAPDH and Its Derivatives with Weissenberg Camera System	Zhang, F.	88-148	106
Diffraction Studies of the Heat-Labile Enterotoxin B Subunit Produced by Entero- toxicogenic <i>Escherichia Coli</i>	Fukuyama, K.	89-036	107
High Resolution Structure Analysis of Taka Amylase A at 1.8 Å	Kusunoki, M.	89-037	108
High Resolution Data Collection of Glutathione Synthetase from <i>Escherichia Coli</i> B	Yamaguchi, H.	89-038	109
Crystal Structure Analysis of L-lactate Dehydrogenase from <i>Bifidobacterium Longum</i>	Iwata, S.	89-042	110
Structure of a Multienzyme Complex from Spinach Chloroplasts	Sainis, J. K.	89-046	111
Structure Function-drug Interaction of Carbonic Anhydrase High Resolution Data Collection of Human Carbonic Anhydrase I and inhibitor Complexes and Buffalo Carbonic Anhydrase II	Kannan, K. K.	89-046	112
X-ray Analysis of Recombinant Human Renin	Einspahr, H. M.	89-150	114

Structural Characteristics of Cation K-Carrageenate in Sol and Gel States as Observed by Small-angle X-ray Scattering	Kajiwara, K.	87-146	116
Complexation of Low Molecular Weight Amylose with Iodine	Hirai, M.	87-149	117
Conformational Change of Poly-N ⁵ -(2-Hydroxyethyl)-L-glutamine in Solution with Solvent and Temperature Studied by Small Angle X-ray Scattering	Muroga, Y.	88-149	118
Structure of Thermally Denatured Ribonuclease A by Means of Small-angle X-ray Scattering	Hiragi, Y.	88-150	119
Structural Analysis of Oligomeric Protein in Solution	Nitani, S.	89-049	120
Small-angle X-ray Scattering Studies of Isolated Linker and Core Histones	Inoko, Y.	89-050	121
X-ray Diffraction Study on the Structure of M-intermediate in the Photoreaction Cycle of Bacteriorhodopsin	Nakasako, M.	87-036	122
Measurement of the Intensity of the First Actin Layer-line during Contraction of Frog Skeletal Muscle	Yagi, N.	87-038	123
Effects of BDM(2,3-butanedione-2-monoxime) on the Axial X-ray Diffraction Pattern from Frog Skeletal Muscle during Contraction	Yagi, N.	87-045	124
Folding Mechanism of Bacteriorhodopsin Peptide Chain by X-ray Diffraction	Tokunaga, F.	88-055	125
Stable Lamellar Phase of 1,2-Q-di-tetradecyl-3-Q-β-D-glucopyranosyl-sn-glycerol	Akiyama, M.	88-059	126
Stopped-flow X-ray Scattering Study on Allosteric Transition of Aspartate Transcarbamylase at Subzero Temperature	Tsuruta, H.	88-060	127
Oligomerization of Actin Monomer at the Early Stage of Actin Polymerization Measured by Stopped-flow X-ray Small Angle Scattering	Kuroda, M.	88-060	128
A Dynamic X-ray Diffraction Study on Slow Skeletal Muscle of the Chick at the Beginning of Contraction	Matsubara, I.	89-058	129
Studies of Phase Transition in Phosphatidylcholine-water Systems by Time-resolved X-ray Diffraction at Low Temperature Scan Rates	Matuoka, S.	89-060	130
X-ray Diffraction of the Live Squid Retina in the Dark and Light	Hamanaka, T.	87-040	131
X-ray Diffraction from Insect Flight Muscle in a Partially Relaxed Condition	Tregeear, R. T.	87-041	132
Frequency and Temperature Dependence of the Intensity Changes in the 14.3 NM Meridional and the Equatorial 1,0 and 1,1 Reflections from a Tetanized Frog Muscle during Sinusoidal Length Changes	Wakabayashi, K.	88-056	133

X-ray Diffraction Studies of the Modified Purple Membrane during Its Photocycle	Uruga, T.	88-057	134
Studies of the Medium Angle X-ray Pattern from a Tonically Contracting Molluscan Smooth Muscle	Tajima, Y.	88-058	135
X-ray Small Angle Scattering of Alpha-2-macroglobulin after Treatment with 2,4-dinitrophenyl Thiocyanate	Ikai, A.	88-060	136
Solution X-ray Scattering Study on Dissociation of <i>Eisenia foetida</i> (Earthworm) Hemoglobin at Acidic and Alkaline pH	Igarashi, Y.	88-060	137
X-ray Diffraction Studies on the Chemically-modified Glycerinated Fibers of Rabbit Skeletal Muscle	Tanaka, H.	89-064	138
Real Time K-edge Subtraction X-ray Imaging - Animal Experiment	Fukagawa, H.	89-067	139
Optimum Energy Separation in K-edge Energy Subtraction Angiography	Nishimura, K.	89-068	140

C : X-ray Experiments

Soft X-ray Standing Wave Measurements of Clean and Oxygen Adsorbed GaAs(111) Surfaces	Izumi, K.	87-190	141
Soft X-ray Standing Wave Measurements of NiSi _x /Si(111) at the Bragg Angle of $\pi/2$	Izumi, K.	87-190	142
Structure-refinement of Orthorhombic Superstructure of Tridymite : An Application of the Powder Diffraction Method	Motoyama, T.	87-154	143
X-ray Fluorescence Analysis Using a Crystal Spectrometer with a Position Sensitive Proportional Counter	Iida, A.	87-054	144
X-ray Fluorescence Imaging by Image Reconstruction Technique	Takahashi, M.	87-155	145
Determination of Trace Ruthenium in Meteoritic Minerals by Microbeam X-ray Fluorescence Spectrometer	Saito, J.	88-061	146
X-ray Microbeam by Multilayer Zone Plate	Saitoh, K.	88-063	147
Analysis of Ultra Trace Elements in Marine Ecological Samples by SR Monochromatized X-ray	Ishikawa, M.	88-064	148
X-ray Absorption near Edge Structure (XANES) of CuInSe ₂ by Photoacoustic Method	Toyoda, T.	88-089	149
X-ray Photoacoustic Absorption Spectra of Brass and Phosphor Bronze	Toyoda, T.	88-089	150
Photoacoustic EXAFS of Brass (Cu-Zn Alloy)	Toyoda, T.	88-089	151
EXAFS in Photoacoustic Phase Spectrum	Masujima, T.	88-089	152
Chemical State Imaging and Trace Element Analysis of Meteorites by X-ray Fluorescence Spectroscopy	Nakai, I.	89-070	153

Micro Fluorescence EXAFS/XANES from Rock Sample	Hayakawa, S.	89-071	154
Near-surface Chemical Characterization Using Grazing Incidence X-ray Fluorescence	Sakurai, K.	89-072	155
X-ray Diffraction Analysis on Local Structure Changes of Amorphous Alloy	Nasu, T.	86-110	156
Pressure Induced Amorphization of Ca(OH)_2	Yamanaka, T.	87-062	157
The Structure Study of $\text{GeO}_2\text{-P}_2\text{O}_5$ Glasses with the Anomalous X-ray Scattering (II)	Shimizugawa, Y.	88-065	158
A Synchrotron Radiation Beam Following System of the X-ray Powder Diffractometer for the Photon Factory	Ozawa, H.	88-159	159
Evaluation of Dimensional and Orientational Distribution of Crystallites in Powder Specimen	Ozawa, H.	89-075	160
Texture Analysis of Silver Halide Photographic Grain	Yagi, T.	89-C020	161
Local Structure and Valence States of Tl-Ba-Ca-Cu-O Superconductors	Yamaguchi, H.	87-065	162
Ge/Si Monolayer Superlattices on Si(100) Studied by Surface-sensitive EXAFS	Oyanagi, H.	87-065	163
Single-crystal Diffractometry with Poly- crystalline Samples	Stevenson, A. W.	88-071	164
X-ray Diffraction from GaAs/AlAs/GaAs Grown on GaAs(001) by MBE	Kashihara, Y.	88-071	165
Diffraction Patterns of Third-order Fibonacci Series	Terauchi, H.	88-072	166
Study on the Precursive Phenomena of Phase Transition from Layered Compounds	Ohshima, K.	88-161	167
Determination of the Low Temperature Phase Diagram of the Fe-Ni Alloy System	Hashimoto, S.	89-080	168
Appearance of Superstructure in Ferroelectrics at Low Temperature below the Incommensurate- commensurate Transition	Mashiyama, H.	89-083	169
AB Initio Structure Analysis of 5-Aminovaleric Acid by X-ray Powder Diffraction	Kurahashi, M.	88-067	170
New Technique for the Observation of X-ray CTR Scattering Using Imaging Plate Detector	Harada, J.	88-071	171
Structural Instability of PbSe/SnSe Superlattices under Pressure	Ohishi, Y.	88-070	172
Determination of the Environmental Structure around a Specific Atom in Disordered Materials by the Anomalous X-ray Scattering	Waseda, Y.	88-074	173
Pressure-induced Molecular Dissociation in Iodine at Low Temperatures	Fujihisa, H.	87-157	174
Alternate Abstraction of Rotatory Polarized SR X-rays with Different Helicity and Its Utilization	Nakajima, T.	88-076	175

Low-temperature and High-pressure X-ray Study on the Pressure-induced Phase Transition of Amorphous Semiconductors	Imai, M.	88-164	176
Research Study of Cooling down to mK Region by He-3 Dilution Refrigerator Used for SR X-ray Diffraction Experiments	Nakajima, T.	89-179	177
Kinetics of Phase Transition in Graphite Intercalation Compounds --First Order Transition in a One-dimensional System --	Metoki, N.	88-062	178
A Cine K-edge Subtraction Coronary Angiography in the Rabbit Experiment	Takeda, T.	87-189	179
Observation of Fibers in Long Fiber Reinforced Metal Matrix Composites by X-ray Computed Tomography Using Synchrotron Radiation	Masuda, C.	88-175	180
Observation of Meteorites by Monochromatic X-ray CT Based on Synchrotron Radiation	Funaki, M.	88-U033	181
Three-dimensional Monochromatic X-ray CT Based on Synchrotron Radiation	Hirano, T.	88-U003	182
X-ray Microprobe with a Pair of Elliptical Mirrors	Suzuki, Y.	89-Y015	183
Structural Study on SiO ₂ /Si Interface	Hirosawa, I.		184
Analysis of Diffuse X-ray Scattering from the Omega Phase in Titanium Alloys	Morinaga, M.	87-160	185
Observation of Critical Scattering from NaNO ₃ Single Crystal under High Pressure on Synchrotron Radiation Source	Okazaki, A.	87-161	186
Studies on the Process of Reaction in Crystals by SR --Dehydration of Alpha-FeOOH--	Ohmasa, M.	89-089	187
Cu K-edge Absorption Spectra of a Novel Superconducting Oxide : Nd _{2-x} Ce _x CuO _{4-y} II. Reduced Samples	Kosugi, N.	88-U004	188
Tertiary Structure of Calmodulin Fragments in Solution	Izumi, Y.	87-082	189
X-ray Photoacoustic Spectroscopy for Determination of Iron in Powdered Samples	Kato, K.	87-188	190
Composition Fluctuation with Small Wave Length in Early Stage Spinodal Decomposition of Polystyrene/Poly(2-chlorostyrene) Blend Systems	Takahashi, M.	88-082	191
Imaging by Semi-pulse X-ray Photoacoustic Method		88-089	192
Subtraction Imaging by X-ray Photoacoustic Method		88-089	193
Surface Structure Analysis of Si(111) $\sqrt{3} \times \sqrt{3}$ -Ag by Transmission X-ray Diffraction	Takahashi, T.	89-090	194
Anisotropic Effects in X-ray Raman Scattering	Udagawa, Y.	89-091	195
Small-angle X-ray Scattering Study of Reconstitution Process of Tobacco Mosaic Virus Particles	Sano, Y.	88-Y152	196

X-ray Detection Characteristics of Microchannel Plates in the Energy Range from 0.06 to 0.6 keV	Yamaguchi, N.	87-164	197
The Energy Response of a Silicon Surface Barrier Detector (0.06-0.9 keV)	Cho, T.	87-164	198
Time-resolved Two-dimensional Observation of the Change in X-ray Diffuse Scattering Using an Imaging Plate on Synchrotron Radiation Source	Iwasaki, H.	88-162	199
X-ray Standing Wave Analysis of GaAs/Si(111) Interface	Kawamura, T.	87-190	200
X-ray Reflectivity and Fluorescence Yield from a Perfect Germanium Crystal at Grazing-incidence Bragg Condition	Hashizume, H.	88-085	201
Study of Lattice Distortion of Porous Silicon Layers by Means of X-ray Diffractometry	Nittono, O.	88-167	202
Structure of Liquid Selenium under Pressure	Tsuji, K.	85-081	203
Section Topography Using a High-order Reflection and Its Application	Sugita, Y.	88-169	204
High Resolution Pair Distribution Function of $\text{Al}_{68}\text{Mn}_{20}\text{Ru}_8\text{Si}_4$ Icosahedral Phase	Sakurai, Y.	88-170	205
Development of Synchrotron Radiation Dosimetry Techniques	Nakashima, H.	88-172	206
Two-stage Temper Embrittlement of Amorphous Fe-B-Si Alloys and Structural Changes Examined by SR-small Angle X-ray Scattering	Yamasaki, T.	87-099	207
X-ray Photoacoustic Imaging of Subsurface Layer and Correlation Spectra	Sugitani, Y.	87-188	208
Diffusion of Self-interstitials in Ice under Hydrostatic Pressure	Hondoh, T.	87-095	209
Dislocation Motion in Ice under Stress	Pimienta, P.	89-095	210
X-ray Magnetic Scattering Studies on the $\text{R}_2\text{Fe}_{14}\text{B}$ Intermetallic Compounds	Yamazaki, H.	89-100	211
Study of Crystal Moiré	Yoshimura, J.	88-086	212
Lattice Spacing Measurement around Dislocations in Undoped GaAs Crystal	Kitano, T.	89-C002	213
Contrast Formation Mechanism around the Cell Walls in Equi-lattice-spacing Mapping X-ray Topographs for Undoped GaAs Crystal	Kitano, T.	89-C002	214
Time-resolved X-ray Diffraction from a Germanium Crystal Irradiated by a Visual Pulsed-laser	Kojima, S.	89-C008	215
High-resolution Diffraction Profiles of Silicon Single Crystals Measured by Highly Collimated X-ray Beams	Kawado, S.	89-C008	216
Grazing Incidence Diffraction from Monolayers of Arachidic Acid on Water Surfaces and Glass Substrates	Matsushita, T.	89-086	217
A New Drickamer-type Cell for In-situ X Ray Studies at High Pressure and Temperature	Leinenweber, K.	88-178	218

Accurate Determination of Phase Boundary of Rutile- α PbO ₂ Transition in TiO ₂ at High Pressures and High Temperatures	Akaogi, M.	88-091	219
Investigation of the Phase Transformations in Au-Ge and Au-Si Alloys by In-situ High-pressure X-ray Diffraction	Fujinaga, Y.	88-176	220
Compton-profile Observation of Negative Spin Polarization of Conduction Electrons in Ferromagnetic Ni Metal	Sakai, N.	88-168	221
Improved Measurement of Magnetic-electron Compton Profiles of Ferromagnetic Fe	Sakai, N.	88-168	222
High Resolution Compton Spectromator at AR-NEL	Sakurai, Y.	88-168	223
Structure of Liquid Gallium under Pressure	Tsuji, K.	87-094	224
Structure of Liquid Bismuth under Pressure	Tsuji, K.	87-167	225
Structure of Liquid Cesium under Pressure	TSuji, K.	88-182	226
Picosecond Synchrotron Radiation Pulse Radiolysis	Tagawa, S.	88-183	227

D : VUV & Soft X-ray Experiments

Photoelectron Spectroscopy of RbF- and LiF-covered GaAs(100) Surfaces	Klauser, R.	87-191	228
Dynamical X-ray Diffraction in Backreflection Geometries and Its Application to the Registry of Overlayer Atoms	Hashizume, H.	88-197	229
Photoelectron Emission Study on (NH ₄) ₂ S _x -treated GaAs	Nannichi, Y.	89-106	230
Photoemission Analysis for (NH ₄) ₂ S _x -treated GaAs with a Photon Energy of 80 eV	Sugahara, H.	89-Y106	231
Initial Stage of Au Schottky Barrier Formation on (NH ₄) ₂ S _x -treated n-GaAs	Sugahara, H.	89-Y106	232
Synchrotron Radiation Photoelectron Spectroscopy of Nd _{1.80} Ce _{0.20} CuO _{4-y} Single Crystals	Maeda, F.		233
Initial Oxidation of Metal/Si(100) Surfaces by Ultra Clean Oxygen Gas	Oshima, M.		234
Synchrotron Radiation Photoionization of Sputtered Neutrals	Oshima, M.		235
Initial Oxidation of Si(100) Surfaces by Ultra-clean Oxygen	Kawamura, N.		236
Angle Scanning X-ray Standing Wave Analysis in High Vacuum	Kawamura, T.		237
Photoionization Cross Sections of Xenon in the L Edge Region	Koizumi, T.	88-186	238
Multiple-photoionization of Neon in the K-edge Region	Koizumi, T.	89-108	239
Measurement of the Mass of the Electron Neutrino Using Electron Capture in ¹⁶³ Ho	Yasumi, S.	87-175	240

Two-dimensional Pattern Demagnification by Asymmetric Bragg Reflection	Morigami, M.	89-C007	241
p.A Scattering of Soft X-ray by Solids of Light Element	Tanokura, A.	88-110	242
Image Formation in a Zone Plate Microscope Using Undulator Radiation	Kagoshima, Y.	89-107	243
Determination of CO Orientation on a Ni(7 9 11) Stepped Surface by NEXAFS	Okawa, Y.		244
Two Electron Excitation Process of H ⁺ Desorption from H ₂ O Adsorbed on Ge(100)	Namba, H.		245
Higher-Harmonics Suppression System for Soft X-rays	Waki, I.	87-Y002	246
Evaluation of Thickness and Its Uniformity in Langmuir-Blodgett (LB) Films Using Soft X-ray Reflection	Momose, A.	87-Y002	247
Soft X-ray Analysis System: Performance Test of a Reflectometer	Hirai, Y.	87-Y002	248
Investigations of Si Oxidation Process by XPS and XANES Using Synchrotron Radiation	Sekiyama, H.		249
The Effects of Secondary Electrons from a Silicon Substrate on SR X-ray Lithography	Ogawa, T.		250
A Mask Alignment System for SR X-ray Lithography	Tanaka, Y.		251
X-ray Absorption Spectra of Poly-p-phenylenes: Localization of π^* Orbitals	Yokoyama, T.	87-178	252
UV Photopolymerization of Long-chain Diacetylene Compounds Studied by Polarized XANES Spectroscopy	Seki, K.	88-105	253
Threshold Photoionization of N ₂ K Shell	Hayaishi, T.	88-106	254
X-ray Absorption Spectroscopy of Nd _{2-x} Ce _x CuO ₄	Matsuyama, H.	88-187	255
Polarized X-ray Absorption Spectroscopy of Bi ₂ Sr ₂ CaCu ₂ O ₈	Matsuyama, H.	88-187	256
XANES Study of Diamond Films Synthesized by Hot Filament CVD	Takata, Y.	89-111	257
Surface EXAFS Studies of Sulphur Adsorbed on Stepped Surface; S/Ni(7 9 11)	Ishii, H.	88-188	258
Surface Relaxation in c(2 × 2)Cl/Ni(100) Determined by the Soft X-ray Standing-wave Method Combined with SEXAFS Spectroscopy	Yokoyama, T.	88-189	259
The Use of a Si(Li) Solid State Detector for the X-ray Standing-wave Method	Takata, Y.	88-189	260
Surface EXAFS Study of ($\sqrt{7} \times \sqrt{7}$)R19.1° S/Cu(111)	Kitajima, Y.	88-189	261
Study of S KLL Auger Electron Spectra by X-ray Excitation near S K-edge I. Dependence of Auger Electron Spectra of Na ₂ SO ₄ and Na ₂ S ₂ O ₃ on Incident X-ray Energy	Matsubayashi, N.	88-190	262

Measurement of the Soft X-ray Absorption by Al, Cr, and Ni	Fujisaki, H.	89-C017	263
Optical Study of the Stoichiometry-dependent Electronic Structure of TiCx, VCx and NbCx	Koide, T.	86-144	264
Development of a VUV Magneto-optical Apparatus and Magnetic Circular Dichroism of Excitons in Alkali Halides	Koide, T.	87-111	265
Adsorption Kinetics of SiH ₄ and Si ₂ H ₆ on Si(100) 0° off and 4° off Surfaces	Takakuwa, Y.	87-180	266
Kinetics of Photon-induced Si-H Bond Breaking Reaction on SiH ₄ -adsorbed Si(100) Surface	Takakuwa, Y.	87-180	267
Piezorefectivity of BaF ₂ in the Core Excitation Region	Sato, S.	87-181	268
The Optical Spectra of α -Al ₂ O ₃ Single Crystals in the VUV Region III	Tomiki, T.	88-191	269
Angle-resolved Photoemission Study of the Bulk Magnetic Phase Transition in Cr	Komeda, T.	86-150	270
Angle-resolved Photoemission of Xe Physisorbed on Cr(110)	Komeda, T.	86-150	271
Angle-resolved Photoemission Study of Ag(111)	Edamoto, K.	86-151	272
Photoemission from SmPd ₃ B _x	Sugawara, H.	87-184	273
Angle-resolved Photoemission Study of NbC(111) Surface	Edamoto, K.	88-194	274
Photoelectron Spectra of Molybdenum during Ion Bombardment	Kitajima, M.	88-195	275
Angle-resolved Photoemission Study of Relativistic Effects in the Electronic Structure of Fe	Sakisaka, Y.	89-115	276
Absolute Calibration of a Normal Incidence Vacuum Spectrometer for Fusion Plasma Diagnostics	Kubo, H.	87-185	277
An Attempt of Fluorescence Lifetime Measurements Using the Pulse Structure of Photon Factory	Ukai, M.	88-100	278
Absolute Measurements of Photoabsorption Cross Section and Ionization Quantum Yield of SiH ₄	Kameta, K.	89-117	279
Synchrotron Radiation-assisted Etching of Si	Terakado, S.	89-C007	280
Photoabsorption Cross Sections of Rare Gases in Their Autoionization Regions	Maeda, K.	88-102	281
High-resolution VUV Absorption Coefficients for Molecules of Interest to Astrophysics	Yoshino, K.	89-118	272
Measurement of Gas-phase Ions Generated from Silane by Synchrotron Radiation Excitation	Nara, Y.	89-C004	283

Photon Energy Dependence of the Film Quality Prepared by Adsorbed SiH ₄ on Low-temperature Surfaces	Sugita, Y.	89-C004	284
Radiation Damage of a Mo/C Multilayer Film due to Synchrotron Radiation	Komano, H.	89-C012	285
Performance of a Double Crystal Monochromator at BL-17A	Tanida, Y.		286
Pattern Replication Accuracy for Soft X-ray Lithography	Yamashita, Y.		287
Measurement of Synchrotron Radiation Spectra in Soft X-ray Region	Gotoh, S.		288

.....

A : EXAFS

EXAFS Study on Vanadium in Blood Cells (Vanadocytes) of Ascidians	Sakurai, H.	88-007	289
---	-------------	--------	-----

C : X-ray Experiments

High Pressure X-ray Study Using Diamond Anvils	Shimomura, O.	89-097	290
--	---------------	--------	-----

D : VUV & Soft X-ray Experiments

BL-16 VUV/Soft X-ray Monochromator for Undulator Radiation (1) Special Distribution of Undulator Radiation Using Thermally Resistant Optical Elements	Muramatsu, Y.	89-C010	291
--	---------------	---------	-----

TEMPERATURE DEPENDENCE OF EXAFS IN CeO_2 and ReO_3

Takafumi MIYANAGA, Tsutomu SATO, Iwao WATANABE*, and Shigero IKEDA**

Department of Physics, Faculty of Science, Hirosaki University, Hirosaki 036

* Department of Chemistry, Faculty of Science, Osaka University, Toyonaka 560

** Institute of Science and Technology, Ryukoku University, Kyoto 612

Introduction

The lattice vibrations contribute a Debye-Waller-type factor $\exp(-2\sigma_j^2 k^2)$ to the EXAFS interference function. The term σ_j^2 in the exponent is the second cumulant of the interatomic distance distribution. In a harmonic crystalline material, cumulants beyond the second are zero and the effects of thermal vibrations on the EXAFS amplitude are fully characterized by σ_j^2 . However, when phonon-phonon interactions are important, higher cumulants must be included in the EXAFS formula. EXAFS spectroscopy is sensitive to anharmonic effects and from it unique information about anharmonic interaction can be obtained.¹⁾ On the other hand, the temperature dependence of the Raman linewidth and frequency reflects the anharmonic effects and that of some ionic crystals have been discussed with consideration of the cubic and quartic anharmonic terms in the crystal potential energy.²⁾ In this report, the applications of the EXAFS technique to the anharmonic vibrations are tried in CeO_2 and ReO_3 comparing with the Raman results.

Experimental and Data Analysis

Powder samples of CeO_2 and ReO_3 were purchased from Wako Pure Chemical Industries, LTD. and Soekawa Chemicals, LTD., respectively. After grinding, they were dusted uniformly onto Scotch Magic tape. A sample 8 tape layers thick was attached to a stainless steel holder and mounted on the cold finger in a cryostat for the measurements at the temperature of 20-300 K. On the other hand, a sample was mixed with boron nitride and pressed to 1 mm thick disk for the measurements at the temperature of 300-600 K using the electric furnace.

The X-ray absorption measurements were performed at BL 7C. S(111) double crystal was used to monochromatize X-ray from the positron source ring.

Once the single-shell amplitude of EXAFS function are isolated, the cumulants can be extracted using the ratio method. If we multiply the amplitude $A(T)$ by the square of the distance and call the product $P(T)$, it is found that

$$\ln[P(T_1)/P(T_2)] = -2\Delta\sigma^2 k^2 + \frac{2}{3}\Delta C_4 k^4 + \dots, \quad (1)$$

where T is the temperature, k is the photoelectron wave number and C_4 is the fourth order cumulant. The higher cumulants are neglected in eq.(1).

Fig.1. Single-shell amplitude data plotted in the form $\ln[P(T)/P(20K)]$ for CeO_2 L_{III}-edge EXAFS at various temperature T . □:100K, ■:200K, △:296K, ▲:372K, ○:472K, ●:572K.

Fig.2. Single-shell amplitude data for ReO_3 L_{III}-edge EXAFS. The notations for the temperature are same as that in Fig.1.

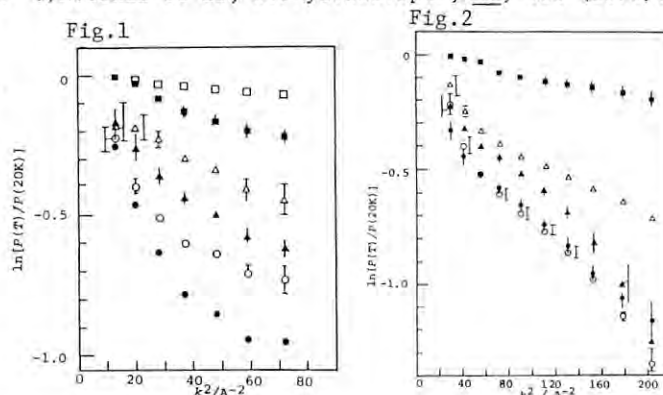
Results and Discussion

Figure 1 shows the plots of $\ln[P(T)/P(20K)]$ versus k^2 for the first-shell amplitude of EXAFS for CeO_2 . The anharmonic effect of the crystalline CeO_2 has been studied by one of the present authors and it was concluded that the temperature dependence of the linewidth of Raman spectra could be explained with only the cubic anharmonic term of the crystal potential energy.²⁾ In the EXAFS analysis, the anharmonic effect appears as a deviation of the plot of $\ln[P(T)/P(20K)]$ vs. k^2 from the straight line. The deviations come from the second term in the right hand side of eq.(1). Figure 1 shows that the fourth cumulant is not trivial in the amplitude of EXAFS in CeO_2 . Further, the contribution of not only $\Delta\sigma^2$ but also ΔC_4 increase with the temperature. Quantitative analyses for C_4 are currently under way. The result of Fig. 1 seems to be consistent with that of Raman study for CeO_2 , qualitatively.

Figure 2 shows the same plot for ReO_3 . It should be noted that the scale of abscissa is different from that of Fig. 1. It is found that the result for ReO_3 shows some different properties from that for CeO_2 . (1) No change between the amplitudes of EXAFS at 472 and 572 K are observed. (2) The amplitude of EXAFS function at 200 K is very small in comparison with that at more than 296 K. (3) The contribution of C_4 term is smaller than that in CeO_2 . The temperature dependence of the linewidth of the Raman spectra for ReO_3 is difficult to be obtained, since the first order Raman scatterings are forbidden for ReO_3 structure which belongs to the space group O_h^1 ($pm3m$).³⁾ In CeO_2 , each oxygen atom is coordinated by four cerium atoms tetrahedrally. On the other hand, rhenium and oxygen atoms are aligned linearly in cubic ReO_3 . From such fact, it is expected that the anharmonic effect in CeO_2 is more significant than that in ReO_3 and this expectation agree with the present EXAFS result (3). Further investigation would make EXAFS be a strong technique to study the anharmonicity of the vibration complementarily to the Raman technique.

References

- 1) J.M. Tranquada and R. Ingalls, Phys.Rev.B **28**, 3520 (1983).
- 2) T.Sato and S.Tateyama, Phys.Rev.B **26**, 2257 (1982).
- 3) M.Ishii et al, J.Phys.Soc.Jpn., **41**, 908 (1976).



STRUCTURAL STUDIES OF COPPER(II)-AMINOCARBOXYLATO COMPLEXES IN AQUEOUS SOLUTION BY EXAFS

Yayoi MIYATA, Kazuhiko OZUTSUMI, Izumi NAKAI, and Takuji KAWASHIMA

Laboratory of Analytical Chemistry, Department of Chemistry,
The University of Tsukuba, Tsukuba 305Introduction

Aminocarboxylic acids and pyridine derivatives well accelerate the formation reaction of porphyrin complexes with transition metal ions such as manganese(II), cobalt(II), nickel(II), copper(II), and zinc(II) in aqueous solution. The catalytic behaviour is suggested to be originated from more labile water molecules within the aminocarboxylato and pyridine complexes than the hexaquaametal(II) ion or the hydrophobic interactions between the ligands and porphyrins. In the present study we determined the structure of the mono- and bis-(aminocarboxylato)copper(II) complexes in aqueous solution in order to obtain more information on the origin of the catalytic action of complexes.

Experimental

Sample solutions were prepared by dissolving copper(II) nitrate and bis(aminocarboxylato)-copper(II) at suitable mole ratios in water. Aminocarboxylic acids examined were glycine (gly), α -alanine (α ala), β -alanine (β ala), valine (val), serine (ser), threonine (thr), proline (pro), and hydroxyproline (pOH). X-Ray absorption spectra were measured around the Cu K-edge at the BL6B of the Photon Factory, KEK.

Results and Discussion

Figure 1 depicts the Fourier transforms of sample solutions containing the mono(aminocarboxylato)copper(II) complexes as a main species. The first intense peaks around 155 pm are due to the Cu-O and Cu-N bonds within the complexes. The positions and intensities of the peaks are very similar among the test solutions examined, indicating that the structures of the complexes in solutions are very similar. Structure parameters of the complexes were finally determined by least-squares calculations applied to the Fourier filtered $k^3 \cdot \chi(k)$ values. In the fitting procedure, the contribution of the hexaquaacopper(II) ion and bis-complex existing with the mono-complex in solutions to the $k^3 \cdot \chi(k)$ values were taken into accounts. The amounts of complexes existing in solutions were evaluated on the basis of the individual electronic spectra of complex species and thus the structure parameters obtained (Table 1) are the ones for mono-complex species. All the mono-complexes have an axially elongated octahedral structure. The Cu-O_{eq}, Cu-N_{eq}, and Cu-O_{ax} bond distances are practically the same among the complexes.

In Table 2 the structure parameters of bis-complexes are given. It is also shown that the structure of the bis-complexes is axially elongated octahedral and the Cu-O and Cu-N bond lengths are indifferent among the bis-complexes.

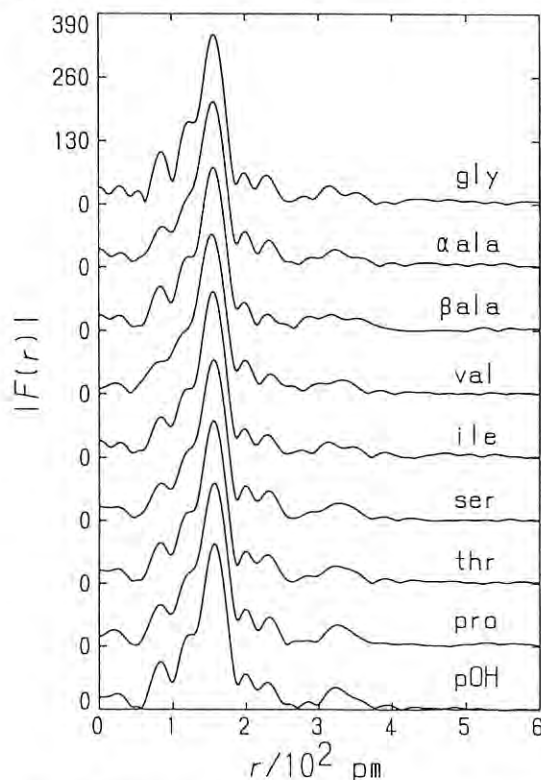


Fig. 1. Fourier transforms of sample solutions.

Table 1. Structure parameters of mono-complexes.

	gly	α ala	β ala	val	ile	ser	thr	pro	pOH
Cu-O _{eq}									
r/pm	197	197	197	196	197	198	197	197	197
σ /pm	6.0*	6.0*	6.0*	6.0*	6.0*	6.0*	6.0*	6.0*	6.0*
n	3*	3*	3*	3*	3*	3*	3*	3*	3*
Cu-N _{eq}									
r/pm	199	199	199	200	198	194	200	199	199
σ /pm	6.0*	6.0*	6.0*	6.0*	6.0*	6.0*	6.0*	6.0*	6.0*
n	1*	1*	1*	1*	1*	1*	1*	1*	1*
Cu-O _{ax}									
r/pm	228	228	227	228	227	235	227	229	228
σ /pm	11.1	10.2	12.0	10.7	10.9	17.4	11.6	10.1	10.6
n	2*	2*	2*	2*	2*	2*	2*	2*	2*

*Fixed.

Table 2. Structure parameters of bis-complexes.

	β ala	ser	thr	pro	pOH
Cu-O _{eq}					
r/pm	197	197	197	197	197
σ /pm	6.0*	6.0*	6.0*	6.0*	6.0*
n	2*	2*	2*	2*	2*
Cu-N _{eq}					
r/pm	199	199	199	199	199
σ /pm	6.0*	6.0*	6.0*	6.0*	6.0*
n	2*	2*	2*	2*	2*
Cu-O _{ax}					
r/pm	232	230	230	230	231
σ /pm	12.4	8.9	9.9	10.7	10.9
n	2*	2*	2*	2*	2*

*Fixed.

EXAFS AND XANES ANALYSIS OF SELENIUM COMPOUNDS (III)

Takuji KAWASHIMA, Ichiro NOMACHI, Kazuhiko OZUTSUMI and Izumi NAKAI
Department of Chemistry, The University of Tsukuba, Tsukuba, Ibaraki 305

Introduction

The authors have studied the structures of piaselelenols, and the electronic effect of substituents and solvent effect of various organic solvents on the structures of piaselelenols by using EXAFS/XANES technique.^{1,2)} However, the electronic and solvent effects can not be observed definitely. Therefore, in this work to study effects of organic solvents further, organic solvents are chosen in view of the acceptor property which is opposite to the property of solvents used in the previous work.

In our previous report we qualitatively showed the variation of oxidation states of selenium in the course of the reaction of selenious acid with methyl-substituted o-phenylenediamine by XANES spectra.²⁾ Therefore, in this study we tried to elucidate the variation of a local structure around selenium quantitatively by using the EXAFS technique.

Experimental

Piaselelenol ($C_6H_4N_2Se$) and its 5-substituted derivatives were prepared as described previously.³⁾ Hexamethylphosphoric triamide(HMPA), pyridine(Py), formamide(FA), acetic acid(Ac) and trifluoroacetic acid(TFAc) were chosen as organic solvents and their 0.1 mol dm⁻³ solutions of piaselelenols were prepared.

A water-ethanol (1:1) solution of 0.5 mol dm⁻³ selenious acid and 0.75 mol dm⁻³ methyl-substituted o-phenylenediamine was prepared to study the reaction process. Five cm³ of each solution were mixed with 15cm³ of 1.5 mol dm⁻³ sodium acetate water-ethanol(1:1) solution to slow down the reaction. These solutions were frozen with liq. N₂ to stop the reaction and EXAFS spectra were measured at a certain time interval.

The K-edge absorption spectra were measured by using a Si(311) channel-cut crystal monochromator on the EXAFS facilities installed at BL-10B at PF.

Results and Discussion

The results of the curve fitting method using Fourier-filtered $k^3 \cdot \chi(k)$ values were summarized in Table 1, where Δ denotes the difference between the Se-N bond lengths in solid state and in solution. As shown in Table 1, the Se-N bond distances of piaselelenols in solution are generally longer than those in solid state and no correlation between the Se-N bond lengths and the properties of solvents is observed. A similar tendency was also found in previous study.²⁾ It is thought that solvent molecules may not specifically interact with the Se or N atoms of piaselelenols. Therefore, no correlation between the Se-N bond length and the properties of solvents could be seen.

The Fourier-transforms for samples frozen several minutes after the beginning of the reactions are given in Fig. 1, together with those of selenious acid and methyl-substituted piaselelenol solution. With a progress of the reaction it is observed that the first intense peak shifts from 1.24Å to 1.34Å and the second peak around 2.1Å gradually increased. Therefore, it is thought that the local structures around selenium gradually vary in the course of the reaction. In order to examine the presence of reaction intermediates, we tried to reproduce the Fourier filtered $k^3 \cdot \chi(k)$ of samples frozen 2 or 5 minutes after the beginning of the reaction by those of the Fourier-filtered $k^3 \cdot \chi(k)$ of selenious acid and of methyl-substituted piaselelenol. However, it was not possible to reproduce the curve by any combination of $k^3 \cdot \chi(k)$ values of the two components. Hence, some reaction intermediate would exist during the reaction process. Further analysis of the reaction mechanism may require time resolved EXAFS measurement utilizing stopped flow technique.

References

- 1) T. Kawashima, I. Nomachi, T. Hirano & I. Nakai, PF Activity Report, #5, 223 (1987)
- 2) T. Kawashima, I. Nomachi, T. Hirano, K. Ozutsumi & I. Nakai, PF Activity Report #6, 37 (1988)
- 3) M. Tanaka & T. Kawashima, Talanta, 12, 211 (1964)

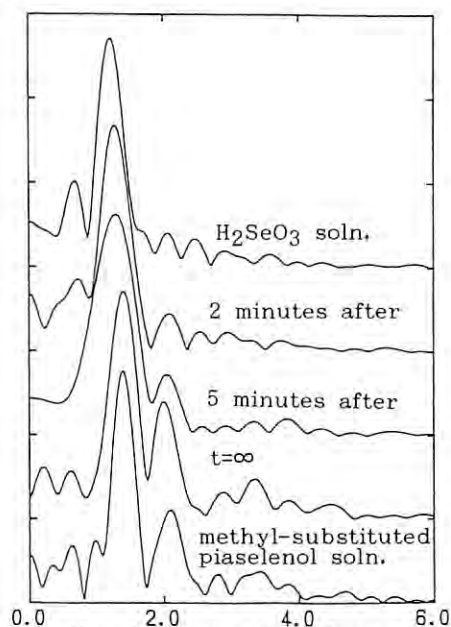


Fig. 1 Fourier transforms for Se compounds

Table 1. Solvent effects on the Se-N bond distance.

Solvent	Acceptor Number	Donor Number	Piaselelenol		Methyl substituted		Nitro substituted	
			Se-N (Å)	Δ (Å)	Se-N (Å)	Δ (Å)	Se-N (Å)	Δ (Å)
Solidstate			1.83		1.83		1.83	
HMPA	10.6	38.8	1.86	0.03	1.84	0.01	1.85	0.02
Py	14.2	33.1	1.84	0.01	1.84	0.01	1.83	0.00
FA	39.8		1.84	0.01	1.85	0.02		
Ac	52.9	10.5	1.85	0.02	1.85	0.02		
TFAc	129.1		1.83	0.00	1.85	0.02	1.81	-0.02

EXAFS STUDIES ON THE LOCAL STRUCTURE OF TiO₂ SUPER-THIN LAYER ON SiO₂

Kiyotaka ASAKURA, Junji INUKAI, and Yasuhiro IWASAWA
Department of Chemistry, Faculty of Science, the University of Tokyo,
Hongo, Bunkyo-ku, Tokyo 113.

TiO₂ is one of the interesting support materials for the supported metal catalysts. Pt and Rh particles on TiO₂ lose its chemisorption ability after high temperature reduction due to the some kind of metal-support interaction¹⁾. It is practically and scientifically interesting to modify the support surface of the supported metal in order to control the nature of the support.

In this context we have prepared TiO₂ super-thin layer supported on the SiO₂ with high surface area. In this paper we will report the structure of the Ti in the TiO₂ super-thin layers with and without Pt particles on it. In the following paper we will report the unique properties and structures of Pt particle on the TiO₂ layer/SiO₂.

Experimental

Ti super-thin layer was prepared by impregnation of SiO₂ with Ti(OC₃H₇)₄ hexane solution under reflux conditions. Unreacted Ti(OC₃H₇)₄ was washed with hexane followed by calcination at 773 K for 2 hours. XRF studies showed that the Ti content is corresponding to that of the half of the full coverage calculated from the surface area of SiO₂ and the lattice parameters of TiO₂. Thus this procedure was conducted twice and we deposited the TiO₂ on the surface of SiO₂ with the Ti loading corresponding to the full coverage which was confirmed by the XRF measurement. EXAFS measurements were carried out at BL 7C using Si(111) double crystal monochromator.

Results and Discussion

Table 1 showed that the curve fitting analyses. Comparing the Ti-Ti distances of the super-thin layer TiO₂ is similar to that of anatase. The ratio of two Ti-Ti coordination numbers were almost equal to 3:2, which is well corresponding to (110) face of anatase. We also found Ti-Si

distances at 0.376 nm, indicating Ti one-atomic layer structure. Table 1 also showed the curve fitting results of Ti K-edge EXAFS of Pt/TiO₂/SiO₂ after the reaction at 773 K. This structure parameters are almost the same as those of TiO₂/SiO₂. Thus the one-atomic layer structure is maintained after the high temperature reduction. Fig.1 showed the Ti K-edge spectra of TiO₂ standards, TiO₂ super-thin layer with and without Pt particle. Ti K-edge of super-thin layer is quite similar to that of Ti K-edge of anatase, indicating the local structure is similar to that of anatase. Also Ti is in the state of 4+ even after the reduction at 773 K in the presence of Pt. This is quite different property from that of conventional TiO₂-supported Pt, where the surface Ti is reduced to Ti³⁺. The stability of the TiO₂ super-thin layer might arise from the direct Ti-O-Si bonding formed in the attaching reaction.

1) S.J. Tauster et al., J.Catal., 55, 29(1978)

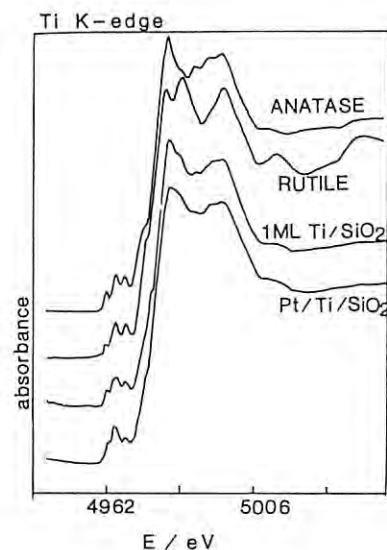


Fig.1 X-ray Near edge spectra of TiO₂ (anatase, rutile) and Super thin layer of TiO₂ on SiO₂ (1ML Ti/SiO₂) together with Pt deposited on it (Pt/Ti/SiO₂)

Table 1 Curve Fitting results

	Ti-O		Ti-Ti		Ti-Ti		Ti-Si	
	N	r/nm	N	r/nm	N	r/nm	N	r/nm
TiO ₂ super-thin layer/SiO ₂	3.7	0.195	2.7	0.305	1.7	0.369	1.0	0.364
Pt/TiO ₂ super-thin layer/SiO ₂	3.9	0.196	3.2	0.303	1.8	0.367	0.9	0.360
TiO ₂ anatase	(6)	0.197	(4)	0.305	(4)	0.366		
rutile	5.8	0.197	4.1	0.298	6.8	0.335		

AN EXAFS STUDY OF HIGHLY DISPERSED VANADIUM OXIDE CATALYSTS PREPARED BY A CVD METHOD

Hiroyoshi KANAI, Tadahide SONE, Yasuo NISHIMURA, Tsunehiro TANAKA*, and Satoshi YOSHIDA

* Department of Molecular Engineering, Faculty of Engineering, Kyoto University, Sakyo-ku, Kyoto 606

* Department of Chemistry, Faculty of Science, Hokkaido University, Kita-ku, Sapporo 060

Catalytic active species of supported vanadium oxide catalysts are influenced structurally and electronically by supports. EXAFS/XANES spectroscopy was applied for highly dispersed supported V_2O_5 species which were prepared by a CVD method to elucidate relationship between their structures and photocatalytic activities.¹⁾

Experimental

V_2O_5/SiO_2 (VSCVD) or Al_2O_3 (VACVD) was prepared by the following method; vaporized $VO(OPr^i)_3$ was reacted and fixed with OH groups of SiO_2 or Al_2O_3 which had been evacuated at 673 K for 2 h, and then alkoxyvanadyl-fixed SiO_2 or Al_2O_3 was evacuated at 373 K for 1 h followed by heating in O_2 at 673 K for 2 h. V_2O_5/SiO_2 (VSIMP) or V_2O_5/Al_2O_3 (VAIMP) was prepared by impregnating SiO_2 or Al_2O_3 into an NH_4VO_3 aqueous solution. After drying at 383 K the impregnated sample was heated in air at 773 K for 3 h. X-ray absorption spectroscopy was run at r. t. at the BL-7C.

Results and discussion

The XANES spectrum of VSCVD is very similar to that of tetrahedral $VO(OPr^i)_3$, a CVD source and quite different from V_2O_5 which is distorted square pyramidal. (Fig. 1) The XANES spectrum of VSIMP looks almost like that of VSCVD. However, XANES spectra of alumina-supported V_2O_5 are different from those of silica-supported one. The initial product of $AlO-VO(OPr^i)_n$ has almost the same structure as the reactant, $VO(OPr^i)_3$. (Fig. 2) On being heated at 373 K, it released alkoxy group and the XANES spectrum changes into the one very similar to that of V_2O_5/Al_2O_3 .

The FT of VSCVD shows a somewhat broad peak attributed to V=O and V-O bonds and small peaks around nearest V-V bonds which appear around 2.5 Å in V_2O_5 . (Fig. 3) VSIMP has a similar peak for V=O and V-O bonds and a small peak due to nearest V-V bonds. Al_2O_3 -supported V_2O_5 reveals peaks shorter than SiO_2 -supported one. Curve-fitting for these catalysts reveals that SiO_2 -supported V_2O_5 is tetrahedral having one V=O and three V-O bonds, while Al_2O_3 -supported V_2O_5 is also tetrahedral having two V=O and two V-O bonds. (Table 1)

When water was adsorbed on both catalysts, drastic change in XANES and FT spectra was seen for SiO_2 -supported V_2O_5 , and no change appeared for Al_2O_3 -supported one. (Fig. 3) Water makes bridges between adjacent V atoms which are located in the range of 2.5-3 Å a little shorter than V-V in V_2O_5 .

The XANES/EXAFS study shows that tetrahedral V(V) species having a single V=O bond is responsible for photocatalysis of olefins.¹⁾

1) H. Kanai et al., Intern. Symp. Photoinduced Surface Reactions, (Kyoto) p. 67 (1989).

2) T. Tanaka et al., J. Chem. Soc., Faraday Trans. 84, 2987 (1988).

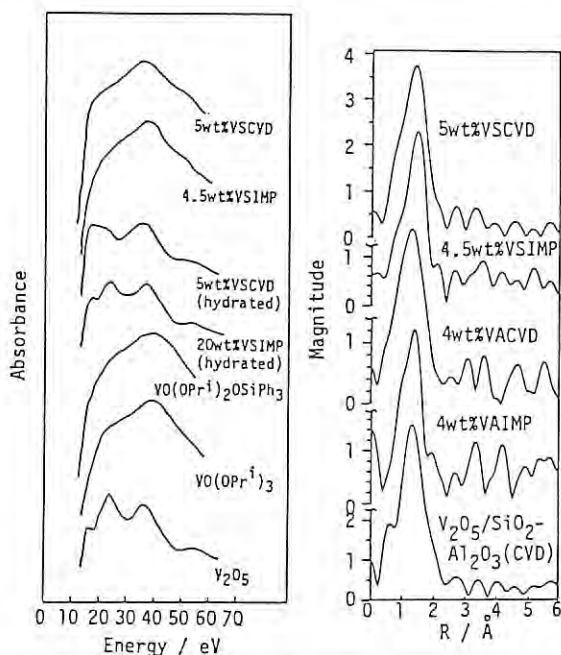


Fig. 1 Spectra of XANES and Fourier transforms of supported V_2O_5

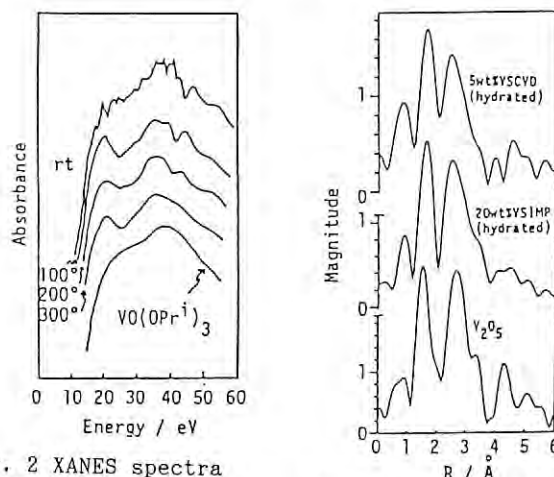


Fig. 2 XANES spectra of heat-treated $Al_2O_3-VO(OPr^i)_n$

Fig. 3 Fourier transforms of hydrated VSCVD

Table 1, Curve-fitting for V-O shells^{a)} of supported V_2O_5 catalysts

Catalyst	R	CN	$\Delta\sigma^2$ Å ²
5wt%VSCVD	1.59	1.22	0.00341
	1.78	3.09	0.00555
4.5wt%VSIMP	1.61	1.05	0.00694
	1.79	3.08	0.00870
4wt%VACVD	1.62	2.02	0.00747
	1.80	2.05	0.00592
5wt%VAIMP	1.61	2.02	0.00414
	1.78	2.00	0.00344

a) See Reference 2).

XANES ESTIMATION OF Ce VALENCE IN L-Pd₅Ce AND H-Pd₅Ce

Noriyuki KUWANO, Yasutoshi SAITO, Kazunori UMEO, Masaru ITAKURA, Kensuke OKI

Department of Materials Science and Technology, Graduate School of Engineering Sciences,
Kyushu University-39, Kasuga, Fukuoka 816

Seiichi YAMASHITA, Toshio YAMAGUCHI, Hisanobu WAKITA

Department of Chemistry, Faculty of Science, Fukuoka University,
Nanakuma, Jonan-ku, Fukuoka 814-01

In Ce alloys and compounds, 4f electrons give rise to various kinds of interesting physical anomalies, such as a negative temperature coefficient of electrical resistivity. We reported in a previous paper⁽¹⁾ that H-Pd₅Ce and L-Pd₅Ce, which have almost the same composition as each other, exhibit a significant difference in electrical resistivity change from each other. In this study, Ce valences in H-Pd₅Ce, L-Pd₅Ce and other Pd-Ce alloys were estimated from the X-ray absorption near edge structure (XANES) to clarify the origin of the difference in resistivity.

Ingots of Pd-Ce alloys with 12.5, 16.7, 17.2, 25.0, 37.5 and 50 at%Ce were prepared by arc melting under an atmosphere of extra pure argon. The alloy ingots were homogenized by annealing at proper temperatures. Pd-12.5 at%Ce, or Pd₇Ce⁽²⁾, has an order structure of Pt₇Cu type, Pd-16.7 at%Ce (L-Pd₅Ce⁽³⁾) a long period antiphase superstructure derived from Ll₂, Pd-17.2 at%Ce (H-Pd₅Ce⁽⁴⁾) a stacking structure related to Ni₃Ce⁽⁵⁾ and Ni₇Ce₂⁽⁶⁾. It was also reported that Pd-37.5 at%Ce (Pd₅Ce₃⁽⁷⁾) has a hexagonal structure, and Pd-50 at%Ce (PdCe⁽⁷⁾) a CrB structure. Powder specimens made from the ingots were sealed in evacuated quartz capsules and annealed at temperatures so that the alloys had their equilibrium phases.

XANES spectra were taken, using the facility of BL-7C, at energy intervals of about 0.45 eV with a double crystal monochromator of Si(111). The spectra were analyzed by the method⁽⁸⁾, which is similar to Röhler's⁽⁹⁾, where two major white lines were conventionally assigned to Ce³⁺ and Ce⁴⁺. Ce-valence was evaluated from the ratio in area of the Ce³⁺- and Ce⁴⁺ components.

Figure 1 shows the change of Ce-valence with the alloy composition. One can see that the valence increases monotonously with decreasing Ce content and reaches a saturated value of about 3.3, except that the Ce-valence of H-phase deviates from the smooth variation. The deviation can be explained as follows. In L-Pd₅Ce which has a basic structure of Ll₂, there are few Ce-Ce nearest neighbors (nn), provided that the phase is well ordered. H-Pd₅Ce, in contrast, has Kagomé networks which include many Ce-Ce nn. Thus, the local Ce concentration becomes high, compared with the mean value over the bulk, so that Ce atoms have a property as in a higher concentration alloy such as Pd₃Ce. The present authors⁽¹⁾ reported that below room temperature the resistivities of H-Pd₅Ce and Pd₃Ce exhibit negative temperature coefficients,

while Pd₇Ce, L-Pd₅Ce, Pd₅Ce₃ and PdCe have positive ones, as shown in Fig. 2^(1,10). These results suggest that the "dense Kondo effect" is most remarkable in Pd-Ce alloys with Ce valence of about 3.2.

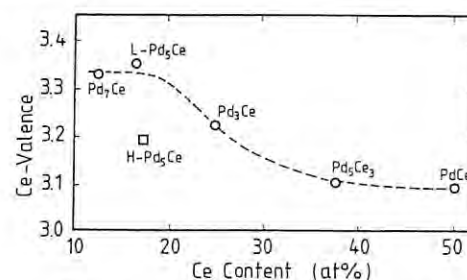


Fig. 1 The change in Ce valence with Ce concentration in Pd-Ce alloys

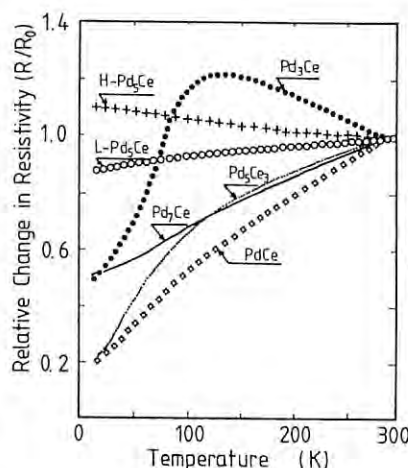


Fig. 2 The relative changes in electrical resistivity with temperature for various Pd-Ce alloys

References

- (1) M. Itakura, Y. Hisatsune, H. Sato, N. Kuwano and K. Oki: Jpn. J. Appl. Phys., 27(1988), 684.
- (2) N. Kuwano, T. Shiwa, Y. Tomokiyo and T. Eguchi: Jpn. J. Appl. Phys., 20(1981), 1603.
- (3) N. Kuwano, S. Higo, K. Yamamoto, K. Oki and T. Eguchi: Jpn. J. Appl. Phys., 24(1985), L807.
- (4) N. Kuwano, I. Hiroshige, Y. Tomokiyo and T. Eguchi: Proc. 7th Int. Conf. HVEM, Berkeley, (1983) p.291
- (5) D. T. Cromer and C. E. Olsen: Acta Cryst., 12(1959), 689.
- (6) D. T. Cromer and A. A. Larson: Acta Cryst., 12(1959), 855.
- (7) J. P. Kappler, M. J. Besnus, P. Lehmann and A. Meyer: J. Less-Common Met., 111(1985), 261.
- (8) N. Kuwano, Y. Saito, K. Umeo, M. Itakura and K. Oki: Eng. Sci. Rep. Kyushu Univ., 11(1989), 195. (in Japanese)
- (9) J. Röhler: J. Magn. & Magn. Mater., 47/48(1985), 175.
- (10) N. Kuwano et al.: unpublished

CHARACTERIZATION OF ZEOLITE-ENCAPSULATED METAL PHTHALOCYANINE CATALYSTS

Atsushi FUKUOKA, Takuma KIMURA, Toshiyuki FUJIMOTO,
Nobuhiro KOSUGI*, Haruo KURODA*, and Masaru ICHIKAWA*

Catalysis Research Center, Hokkaido University, Sapporo 060

*Department of Chemistry, Faculty of Science, The University of Tokyo, Hongo, Tokyo 113

Introduction

"Ship-in-a-bottle" synthesis of metal complexes inside zeolite cages has gained growing attention for the purpose of obtaining the catalytically active precursors surrounded with configurationally constrained circumstances.¹⁾ The zeolite framework impose shape selectivity in metal-catalyzed reactions due to the limitation of size against in-coming reactant molecules.²⁾ Metallophthalocyanine complexes and their electron donor-acceptor complexes have been extensively studied as biological analogs such as chlorophylls and hemoglobins.³⁾

We synthesized iron phthalocyanine (FePc) inside NaY zeolite from the precursor of Fe carbonyl cluster, and the structural properties of FePc in NaY were studied by Fe K-edge XANES and EXAFS, ⁵⁷Fe Mössbauer, FTIR, and UV-VIS. We have found by EXAFS that FePc highly dispersed within the NaY supercage is distorted from its original planar structure.⁴⁾

Experimental

Iron phthalocyanine in NaY supercage (FePc/NaY) was synthesized from [HFe₃(CO)₁₁]⁻/NaY and 1,2-C₆H₄(CN)₂. FePc on the NaY surface (FePc+NaY) was prepared by impregnation of NaY with pyridine solution of FePc. Fe K-edge XANES and EXAFS measurements were carried out at room temperature at BL 10B and 7C in KEK-PF.

Results and Discussion

XANES spectra for FePc/NaY, FePc+NaY, and FePc crystalline have the sharp peak at about 7110 eV, arising from 1s-4p π^* transition characteristic of FePc. On the other hand, FePc(Pyridine)₂ complex gave no absorption at 7110 eV, because two pyridine molecules coordinate to Fe perpendicularly with respect to FePc plane of FePc(Py)₂. These results support the formation of FePc in NaY in the similar electronic states to those of FePc crystalline. ⁵⁷Fe Mössbauer study also shows that the electronic states of Fe in FePc/NaY is almost the same as in FePc.

Figure 2 shows the Fourier transforms of $k^3\chi(k)$ for FePc/NaY, FePc+NaY, and FePc crystalline. The major peak at 1.8 Å is attributed to the first neighbor Fe-N of an FePc molecule by the curve-fitting analysis. As summarized in Table 1, FePc/NaY gave a smaller coordination number (C.N.) and a longer interatomic distance (R) for the Fe-N compared with those for FePc+NaY and FePc crystalline. The results suggest that an iron atom in FePc/NaY is slightly out of the phthalocyanine ring. This

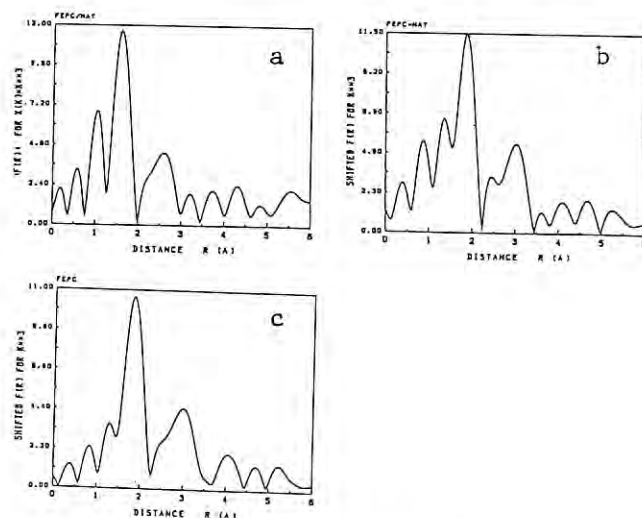


Figure 1. Fourier transforms of $k^3\chi(k)$ at Fe K-edge for FePc/NaY (a), FePc+NaY (b), and FePc crystalline (c).

Table 1. Results of curve-fitting analysis for FePc/NaY, FePc+NaY, and FePc.

Sample	C.N.	R(Å)	$\Delta\sigma^2$
FePc/NaY	3.6	1.84	-1.20×10^{-3}
FePc+NaY	4.0	1.83	-0.47×10^{-3}
FePc	4.0	1.83	0.00

is reflected in the difference of Debye-Waller type factor ($\Delta\sigma^2$) for FePc/NaY, which was larger than for FePc+NaY, possibly due to the distortion of a phthalocyanine ring caused by the encapsulation of an FePc molecule (13 Å diameter) inside a NaY supercage (13 Å diameter).

FTIR and UV-visible study also suggest the distortion of the FePc ring. Electron donor-acceptor complex (Na⁺₄(FePc⁴⁻)/NaY derived from FePc/NaY gave high trans/cis ratio of 2-butene in the catalytic butadiene hydrogenation.⁴⁾

References

- 1) P.A. Jacobs, in: *Metal Clusters in Catalysis*, Eds. B.C. Gates, L. Guzzi, and H. Knözinger (Elsevier, Amsterdam, 1986) Ch. 8.
- 2) T.-N. Huang and J. Schwartz, *J. Am. Chem. Soc.*, **104**, 5245(1982).
- 3) K. Tamaru and M. Ichikawa, *Catalysis by Electron Donor-Acceptor Complexes* (Kodansha-Halsted, Tokyo, 1975); N. Herron, G. D. Stucky, and C. A. Tolman, *J. Chem. Soc., Chem. Commun.*, 1521(1986).
- 4) T. Kimura, A. Fukuoka, and M. Ichikawa, submitted to *Catal. Lett.*

EXAFS STUDIES ON THE LOCAL STRUCTURES OF CALCIUM CATALYST FOR COAL GASIFICATION

Hiromi YAMASHITA, Satohiro YOSHIDA* and Akira TOMITA

Chemical Research Institute of Non-Aqueous Solutions, Tohoku University, Katahira, Sendai 980, Japan.

*Department of Hydrocarbon Chemistry, Faculty of Engineering, Kyoto University, Kyoto 606, Japan.

Introduction

Calcium compounds are very useful catalysts for the gasification of coal. Many studies have been carried out to know the state of calcium catalyst. Huffman et al. have been carried out EXAFS examination of Ca-rich lignite¹ and found out that the dispersion of calcium in char much depended on method of devolatilization of coal. In the present study, the dependence of the structure of calcium in the devolatilized coal (char) on method of addition of calcium compounds to coal has been investigated by EXAFS.

Experimental

Loy Yang brown coal from Victoria, Australia, was used. Several coal samples with different calcium salts, $\text{Ca}(\text{NO}_3)_2$, CaCl_2 , CaCO_3 and etc., were prepared by physical-mixing, impregnation and ion-exchanging methods. The Ca-loaded coals (5 wt% as Ca) were devolatilized in N_2 at atmospheric pressure in a small fluidized bed reactor. EXAFS and XANES spectra at Ca K-edge were recorded in a transmission mode on a beam line BL-7C at KEK-PF at room temperature using a Si(111) double crystal monochromator. Mirror was used to remove higher harmonics.

Results and Discussion

Devolatilization of coals were carried out at 650°C for 20 min. Figure 1 shows XANES spectra of standard compound, CaO, and Ca-loaded chars. XANES spectrum of CaO (a) exhibited main peak at 4051 eV (uncorrected) with a sharp sub-peak at 4043 eV, indicating the characteristic of the NaCl structure. Ca-loaded char prepared by the physical-mixing with CaCO_3 [PCO] (b) exhibited main peak at 4048 eV with a sharp sub-peak at 4059 eV and a obvious shoulder at 4043 eV. This spectrum was very similar to that of CaCO_3 indicating the presence of bulk CaCO_3 crystalline. The Ca-loaded chars which were prepared by impregnation with $\text{Ca}(\text{NO}_3)_2$ [INO] (c) and CaCl_2 [ICL] (d) and by ion-exchanging with CaCl_2 [ECL] (e), exhibited a broad main peak at 4050 eV with a small pre-edge peak at 4039 eV and no remarkable difference was observed between them. These spectra were very similar to that of calcium in lignite which was demonstrated previously², suggesting that calcium is bonded to functional groups and atomically dispersed on surface of char.

Figure 2 shows Fourier transforms (F.T.s) of the k^3 -weighted EXAFS spectra. CaO (a) shows the peak due to neighboring oxygen atoms (Ca-O) at 2.0 Å (phase shift uncorrected) and the peaks due to neighboring calcium atoms (Ca-Ca) at 2.9 Å, 4.2 Å and 5.3 Å. PCO char (b) exhibited

strong Ca-O peak at 2.0 Å and Ca-Ca peak at 3.4 Å indicating the presence of CaCO_3 . INO char (c) exhibited strong Ca-O peak but no Ca-Ca peak. ECL char (e) exhibited very weak Ca-Ca peak. On the other hand, ICL char (d) exhibited obvious Ca-Ca peak at 3.2 Å. These results indicated that the highly dispersion of calcium atoms was kept in INO and ECL chars and the partial aggregation of calcium atoms occurred in ICL char. The Cl^- anion might accelerate the aggregation of calcium atoms. However, the effect of Cl^- anion on the dispersion of calcium atoms was not so clear as that observed in the case of iron compounds previously².

References

- 1) G. P. Huffman et al., *Fuel*, **65** 1339 (1986).
- 2) H. Yamashita et al., 58th Meeting of Jpn. Chem. Soc., 2I103 (1989).

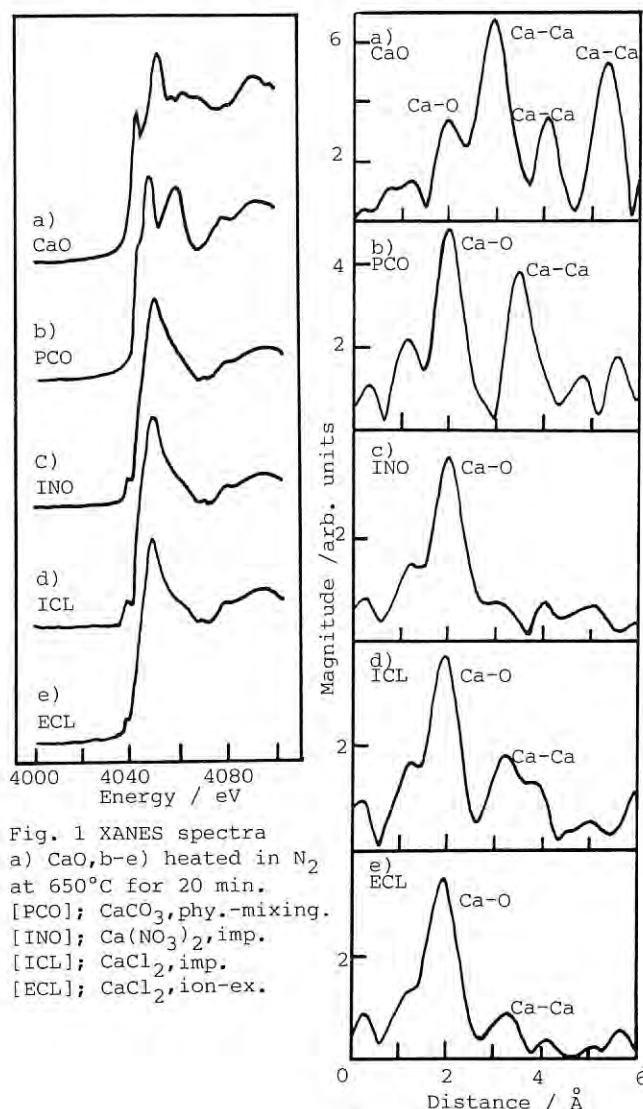


Fig. 1 XANES spectra
a) CaO, b-e) heated in N_2
at 650°C for 20 min.
[PCO]; CaCO_3 , phy.-mixing.
[INO]; $\text{Ca}(\text{NO}_3)_2$, imp.
[ICL]; CaCl_2 , imp.
[ECL]; CaCl_2 , ion-ex.

Fig. 2 F.T.s of EXAFS

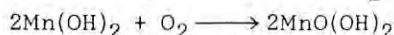
STRUCTURAL STUDIES ON PRECIPITATION REACTIONS IN QUALITATIVE ANALYSIS BY EXAFS AND XANES TECHNIQUE (II)

Ichiro NOMACHI, Izumi NAKAI, Kazuhiko OZUTSUMI and Takuji KAWASHIMA
Department of Chemistry, The University of Tsukuba, Tsukuba, Ibaraki 305

INTRODUCTION

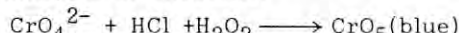
The precipitation and coloration reactions are widely used in qualitative and/or quantitative analyses of metal ions. However the mechanism of these reactions and structural properties of the products are not fully understood. Therefore, the authors have been studying structure of precipitates by using EXAFS technique.¹⁾ In this work, we studied reactions involving manganese and chromium.

1) Usually, Winkler method has been used for the determinations of dissolved oxygen in water. The mechanism is tentatively expressed by the following reactions.



$2\text{MnO}(\text{OH})_2 + 2\text{I}^- + 4\text{H}^+ \longrightarrow \text{Mn}^{2+} + \text{I}_2 + 3\text{H}_2\text{O}$
The dissolved oxygen can be determined by titrating the free iodine by thiosulfate. However, the structure, chemical forms of the products and oxidation number of manganese in these reactions are not well understood.

2) The following reaction is used as qualitative analysis of chromate.



CrO_5 can be extracted with diethyl ether and is stable at low temperature. However, the structure and oxidation number of CrO_5 in ether solution are not well characterized.

The purpose of this work is to elucidate these reactions from structural point of view. We have utilized EXAFS/XANES technique to examine the reaction products.

EXPERIMENTAL

The samples were prepared by a conventional method generally used in qualitative analysis. The Mn K-edge and Cr K-edge absorption spectra were measured by a Si(111) channel-cut crystal monochromator on the EXAFS facilities installed at BL-7C and 6B at PF. In order to eliminate evaporation of ether and decomposition of sample, the measurement of CrO_5 spectrum was made under liq. N_2 temperature.

RESULTS AND DISCUSSION

As shown in Fig. 1, the positions and the shapes of the Mn K-edge XANES spectra of $\text{Mn}(\text{NO}_3)_2$ solutions (Fig. 1 a) do not change by even in the presence of O_2 (Fig. 1 b) or H_2O_2 (c). The shape of the spectra of manganese hydroxide precipitate with passing O_2 or H_2O_2 resemble to that of Mn_2O_3 , which is a mixture of Mn(II) and Mn(III). On the other hand, the spectra of HCl solution (e) of manganese hydroxide precipitate treated with O_2 is similar to that of MnCl_2 solution (d).

Structure parameters were obtained by a curve fitting method using the Fourier-filtered $k^3 \cdot \chi(k)$ values and the results are summarized in Table 1. A comparison of Mn-O distances and coordination numbers between a), b) and c) indicate that the structures of Mn in solutions do not change in the presence of O_2 or H_2O_2 . $\text{Mn}(\text{OH})_2$ precipitates treated with O_2 or H_2O_2 have four shorter Mn-O bonds (1.91 Å) and two further Mn-O bond (av. 2.26 Å), which is similar to that of Mn_2O_3 . Moreover, Mn in the solution (j) has four Mn=O bonds (2.15 Å) and two Mn-Cl bonds (2.43 Å) and this structure is similar to that of $\text{MnCl}_2 \cdot 4\text{H}_2\text{O}$ crystal.

From these results, the Mn^{2+} seems to be oxidized to Mn^{3+} but not to Mn^{4+} by dissolved oxygen. On the other hand, the Mn^{3+} is tend to be reduced by Cl ion. Consequently, it is concluded that $\text{Mn}(\text{OH})_2$ is oxidized to trivalent state by dissolved oxygen and then reduced to divalent state by iodide ion.

As shown in Fig. 2, a sharp peak before the Cr K-edge is observed in the spectra of CrO_3 , K_2CrO_4 , CrO_5 in solution and $\text{CrO}_5(\text{bpy})$ crystal. This sharp pre-edge peak is characteristic of the spectra of Cr(VI) compounds. Therefore, it is thought that the oxidation state of Cr in the CrO_5

solution is hexavalent. The Fourier transform of $\text{CrO}_5(\text{bpy})$ crystal is similar to that of CrO_5 in ether solution (Fig. 3). Structure parameters obtained by the curve fits are summarized in Table 2. the Cr-O bond of CrO_5 in ether solution has three different values. From a comparison between these values and those of $\text{CrO}_5(\text{bpy})$, it is found that Cr in CrO_5 ether solution is coordinated by four oxygen atoms of two peroxide ions at 1.83 Å, with an oxide ion at 1.52 Å, and with an oxygen atom of diethylether at 2.24 Å. Therefore, it is concluded that the Cr atom in the ether solution of CrO_5 is six-coordinated to form a distorted octahedron.

Table 1. Structure parameters of Mn compounds

	n	r/Å	σ
$\text{Mn}(\text{NO}_3)_2$ soln. (a)			
Mn-O	6.0	2.20	0.088
$\text{Mn}(\text{NO}_3)_2$ soln. + O_2 (b)			
Mn-O	6.0	2.18	0.087
$\text{Mn}(\text{NO}_3)_2$ soln. + H_2O_2 (c)			
Mn-O	6.0	2.15	0.072
$\text{Mn}(\text{OH})_2$ ppt. + O_2 (f)			
Mn-O	4.0	1.91	0.000
Mn-O	2.0	2.29	0.036
$\text{Mn}(\text{OH})_2$ ppt. + H_2O_2 (g)			
Mn-O	4.0	1.91	0.035
Mn-O	2.0	2.23	0.036
Mn_2O_3 crystal (h)			
Mn-O	4.0	1.91	0.047
Mn-O	2.0	2.30	0.119
MnO_2 crystal (i)			
Mn-O	6.0	1.88	0.021
$\text{MnCl}_2 \cdot 4\text{H}_2\text{O}$ crystal			
Mn-O	4.0	2.17	0.075
Mn-Cl	2.0	2.47	0.072
MnCl_2 solution (d)			
Mn-O	5.0	2.16	0.065
Mn-Cl	1.0	2.39	0.100
$\text{Mn}(\text{OH})_2$ + HCl (e)			
Mn-O	4.0	2.15	0.089
Mn-Cl	2.0	2.43	0.134

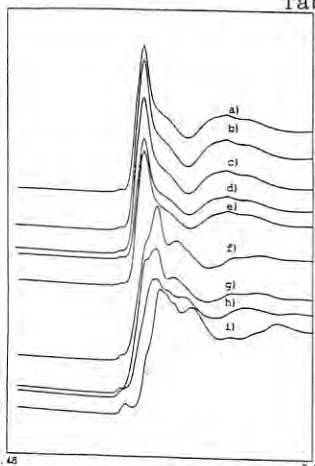


Fig. 1 Mn K-edge spectra of Mn compounds
a) $\text{Mn}(\text{NO}_3)_2$ soln.
b) $\text{Mn}(\text{NO}_3)_2 + \text{O}_2$ soln.
c) $\text{Mn}(\text{NO}_3)_2 + \text{H}_2\text{O}_2$ soln.
d) MnCl_2 soln.
e) $\text{Mn}(\text{OH})_2$ ppt. + HCl soln.
f) $\text{Mn}(\text{OH})_2$ ppt. + O_2
g) $\text{Mn}(\text{OH})_2$ ppt. + H_2O_2
h) Mn_2O_3 cryst.
i) MnO_2 cryst.

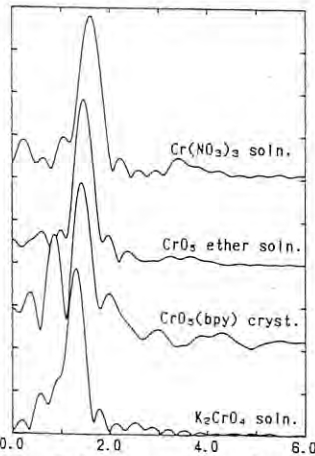


Fig. 3 Fourier transforms for Cr compounds

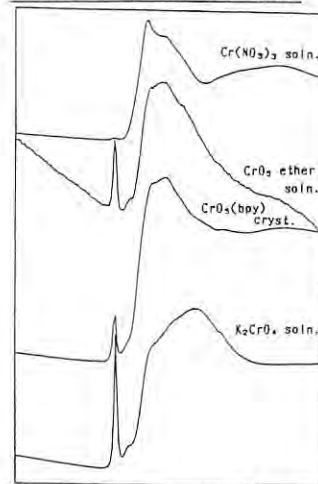


Fig. 2 Cr K-edge spectra of Cr compounds

Table 2. Structure parameters of Cr compounds

	n	r/Å	σ
$\text{CrO}_5(\text{bpy})$ crystal			
Cr-O (O_2^{2-})	4.0	1.85	0.032
Cr-O (O^{2-})	1.0	1.57	0.032
Cr-N (bpy)	2.0	2.17	0.116
K_2CrO_4 solution			
Cr-O	4.0	1.67	0.021
CrO_5 ether solution			
Cr-O (O_2^{2-})	4.0	1.83	0.001
Cr-O (O^{2-})	1.0	1.52	0.055
Cr-O (Et ₂ O)	1.0	2.24	0.062
$\text{Cr}(\text{NO}_3)_3$ solution			
Cr-O	6.0	1.98	0.034

References

- 1) I. Nakai, I. Nomachi, T. Hirano, K. Ozutsumi & T. Kawashima, PF Activity Report, #6, 60 (1988)

LOCAL STRUCTURES AROUND Fe^{3+} AND Mn^{2+} IONS IN SILICATE GLASSES

Yasunori TABIRA, Hideki MORIKAWA and Fumiyuki MARUMO

Research Laboratory of Engineering Materials, Tokyo Institute of Technology, Nagatsuta 4259, Midori-ku, Yokohama 227

Introduction

Extensive studies have been carried out on phase relations in the forsterite(Fo)-anorthite(An)-diopside(Di) system which is important as a compositional model of basaltic magma. It is known that a small amount of Cr^{3+} ion changes mineral assemblages, giving a wide primary field of spinel(MgCr_2O_4)¹⁾. On the other hand, diopside solid solution has wide primary fields in the Di-CaFeTs(CaFeAlSiO_6) and the Di-Mnpx($\text{CaMnSi}_2\text{O}_6$) systems containing a considerable amount of Fe^{3+} and Mn^{2+} ions. This report describes the relationship between the local structures around the transition metals in quenched glasses and the phase relations mentioned above on the basis of the results obtained by EXAFS analyses.

Experimental

Homogeneous glasses with the compositions Mnpx10, 20, 30, 40, 50, 60 and 70wt%, and CaFeTs20, 40, 60 and 70wt% were obtained by quenching the melts of appropriate mixtures of CaCO_3 , MgO, MnO and SiO_2 in the Di-Mnpx system, and of CaCO_3 , MgO, $\alpha\text{-Fe}_2\text{O}_3$, Al_2O_3 and SiO_2 in the Di-CaFeTs system by putting the melts into ice water. The temperatures of melts were set at just above the respective melting points, and the melts were kept at those temperatures for 1 - 2h before quenching.

EXAFS spectra of the glasses were measured, using a Si(111) monochromator for MnK-edge and Si(311) for FeK-edge on the EXAFS spectrometer at the BL7C and 10B, respectively. MnO, Mn_2O_3 , $\beta\text{-MnO}_2$ and $\alpha\text{-Fe}_2\text{O}_3$ crystals were used as reference materials.

Results and discussion

Figs.1(a) and (b) show the Fourier transforms of $k^3\chi(k)$ of MnK- and FeK-edge EXAFS spectra, respectively. The first peaks at about 2 Å in Fig.1(a) are due to the nearest Mn-O pairs and those at about 1.5 Å in (b) are due to the nearest Fe-O pairs. Oxidation or reduction of Mn^{2+} and Fe^{3+} ions in the glasses is not expected to have occurred, since the threshold energy of each spectrum is similar to that of MnO or $\alpha\text{-Fe}_2\text{O}_3$.

In Figs.2(a) and (b), the atomic distances of the nearest Mn-O and Fe-O pairs are plotted against the compositions. The distances were evaluated by curve-fitting analyses, using the theoretical phase shifts and back-scattering amplitudes²⁾ for MnK-edge data and the experimentally determined values for FeK-edge data. All the distances are significantly short compared with the sums of ionic radii³⁾ of Mn^{2+} or Fe^{3+} and O^{2-} ions in sixfold coordinations. It is of interest that Mn^{2+} ions seem to have mostly fourfold coordinations over all compositions of these glasses, whereas average coordination of Fe^{3+} is close to sixfold in spite of its small ionic radius (0.645 Å for sixfold coordination) than that of Mn^{2+} (0.83 Å for sixfold coordina-

tion). This fact implies that large Mn^{2+} ions act as network-formers rather than modifiers to form a continuous solid solution. As for Fe^{3+} , magnetite solid solution crystallizes from melts containing the CaFeTs components more than 45 wt%⁴⁾, which shows that Fe^{3+} ions partly act as network-modifiers. This fact is consistent with the evidence obtained in the present study, that the average Fe^{3+} -O distances in the glasses are larger than that expected for Fe^{3+} in a fourfold coordination.

References

- 1) K. Onuma and T. Tohara: Contrib. Mineral. Petrol., **84**, 174-181 (1983)
- 2) A. G. Mckale, B. W. Veal, A. P. Paulikas, S. K. Chan and G. S. Knapp: J. Am. Chem. Soc., **110**, 3763-3768 (1988)
- 3) R. D. Shannon: Acta Cryst., **A32**, 751-767 (1976)
- 4) K. Hijikata and K. Onuma: J. Japan Assoc. Min. Petr. Econ. Geol., **62**, 209-217 (1969)

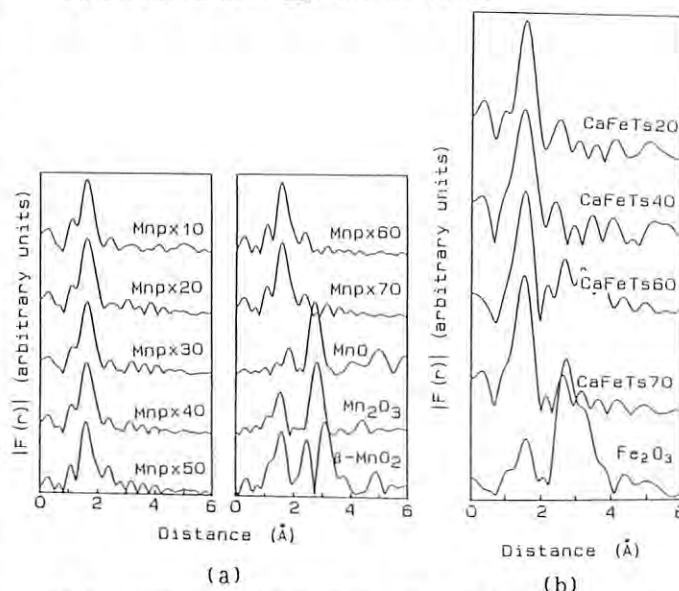


Fig.1 Fourier transforms of (a) MnK-edge and (b) FeK-edge EXAFS data.

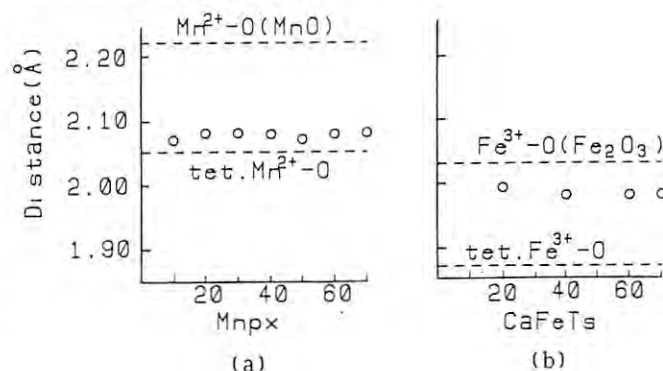


Fig.2 Evaluated atomic distances of the nearest (a) Mn-O and (b) Fe-O pairs by curve-fitting analyses.

XAFS STUDY OF Ti-Zr BINARY OXIDE ON SILICA.

Tsunehiro TANAKA, Tarek M. SALAMA, Tsutomu YAMAGUCHI
And Kozo TANABE

Department of Chemistry, Faculty of Science, Hokkaido University,
Sapporo 060, Japan.

A composite oxide of TiO_2 - ZrO_2 is known as a more effective catalyst for acid- and base-catalyzed reactions than each of TiO_2 and ZrO_2 . The reason is thought to be that new active sites are generated by the composition of these metal oxides. To discuss the genesis of the active sites, more information on surface structure of the metal oxide is needed. In this regard, we have prepared Ti-Zr binary oxide deposited on silica surface as a model compound for the surface species of TiO_2 - ZrO_2 and the structure of this binary oxide compound has been clarified by EXAFS/XANES spectroscopy.

Experimental

The catalyst samples were prepared by the impregnation of silica with the toluene solution dissolving alkoxides of Zr and Ti, followed by calcination at 773 K. The deposition procedure in this way was repeated several times. The samples having been evacuated at 773 K were mixed with polyethylene powder and pressed into discs under atmospheric nitrogen. X-Ray absorption spectra were collected on EXAFS facilities installed at BL10B and BL7C in KEK-PF.

Results and Discussion

Zr K-edge XAFS. Fig. 1 shows the Fourier Transforms (FTs) of k^3 -weighted EXAFS spectra of the sample which is obtained by three times deposition of Ti and Zr cations and relating compounds. The phase-shift correction has not been performed. The FT of bulk zirconium oxide (monoclinic) shows two kinds of peaks which are due to scatterings by adjacent oxygen and zirconium atoms. On the other hand, the FT of TiO_2 - ZrO_2 binary oxide shows a high peak due to scattering by oxygens at 1.6 Å and an unclear peak at 2.8 Å. The FT of the sample is similar to that of TiO_2 - ZrO_2 , suggesting strongly that environmental structure around Zr cations of the sample is close to that for TiO_2 - ZrO_2 although no X-ray diffraction patterns for TiZrO_4 as well as other probable compounds have been observed.

Ti K-edge XAFS. Fig. 2 shows the Ti K-edge XANES spectra of the sample and relating compounds. Spectra are normalized to the height of edge jump. The XANES spectra of octahedrally coordinated Ti cations like rutile and anatase have plural peaks in the pre-edge region which are assigned to 1s-3d transitions. The great distortion of a TiO_x structure from octahedral one causes the great enhancement of 1s-3d transition as found for TiO_2 - ZrO_2 XANES. The total feature of the XANES spectrum of the sample shows that TiO_x of the sample is closer to that of TiO_2 - ZrO_2 than those of rutile and anatase. This is consistent with the results obtained from the Zr K-edge EXAFS. However, the height and sharpness of the pre-edge peaks for the sample XANES should be noticed. The clear pre-edge

absorption indicate that Ti cations in the sample are predominantly located at the center of a highly distorted field from octahedral symmetry. It is very likely that the coordination of Ti ions of the sample are unsaturated, i.e., Ti may be surrounded by five or four oxygen atoms.

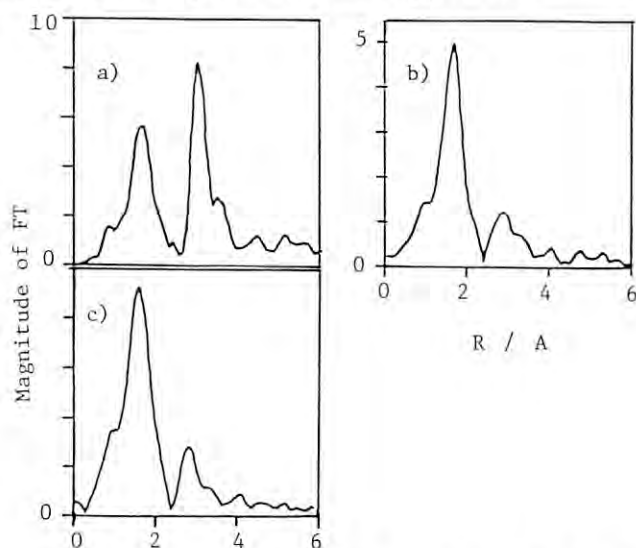


Figure 1 Fourier transforms of Zr K-edge EXAFS of (a) monoclinic ZrO_2 , (b) bulk TiO_2 - ZrO_2 and the catalyst sample.

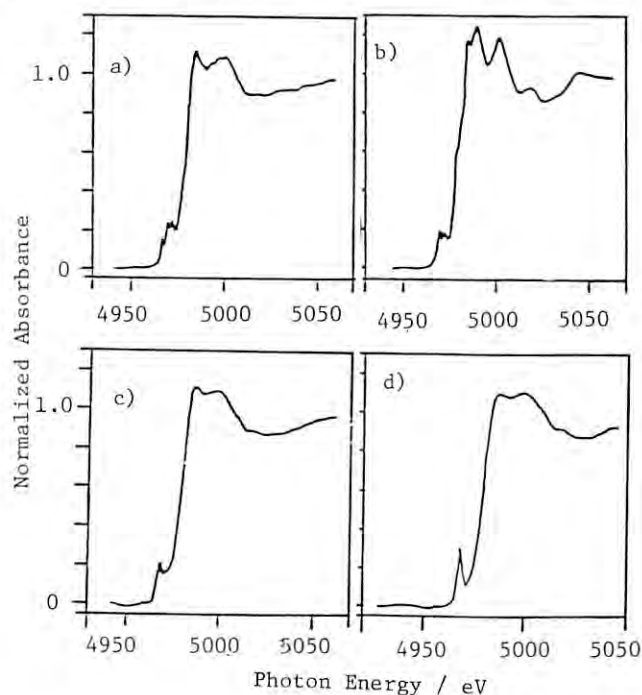


Figure 2 Ti K-edge XANES spectra of (a) anatase, (b) rutile, (c) bulk TiO_2 - ZrO_2 and (d) the catalyst sample.

EXAFS STUDIES ON THE REVERSIBLE ENHANCEMENT PHENOMENON FOR C_2H_4 HYDROGENATION ACTIVITY ON PT/ONE-ATOMIC LAYER TiO_2/SiO_2

Kiyotaka ASAKURA, Junji INUKAI, and Yasuhiro IWASAWA

Department of Chemistry, Faculty of Science, the University of Tokyo,
Hongo, Bunkyo-ku, Tokyo 113, Japan

It is important to modify the surface structure in order to control the catalytic properties of the surface. We have found an interesting phenomenon in the SiO_2 -supported metal particles.¹⁾ When Rh/SiO_2 and Pt/SiO_2 are treated at 773 K and are cooled to room temperature in a second, their activities for C_2H_4 hydrogenation reaction are one to two order higher than those treated at 473 K. This enhancement phenomenon is reversible in the sense that the high active state is lost when treated at 473 K for 10 min. Moreover the activity abruptly increases when treated at the temperature more than 673 K like a phase transition. Our previous EXAFS data of Rh/SiO_2 with the particle size of 2 nm showed that the Debye-Waller factor abruptly increased at the same temperature where the activity abruptly increases.²⁾ However, in the case of Pt/SiO_2 with Pt particle size of 10 nm we could not find such abrupt change in Debye-Waller factor probably because this reversible enhancement phenomenon is related to some kind of surface structure change of the small particle on SiO_2 and the low dispersion of the Pt particle on SiO_2 hinders the change of the Debye-Waller factor on the surface. Therefore the experiment should be done for the smaller Pt particles on SiO_2 . However, the reversible enhancement phenomenon occurs only for the Pt with the particle size 10 nm in the case of Pt/SiO_2 . It seems to be difficult to confirm the relation between the reversible enhancement phenomenon and Debye-Waller factor in the case of Pt/SiO_2 . We have prepared Pt/one-atomic layer TiO_2/SiO_2 , where we found similar enhancement phenomenon. However in this case rapid cooling is not necessary to obtain the high active state. Moreover the Pt particle size is as small as 2 nm. In this paper we will report the results of temperature-dependence EXAFS on the Pt/one-atomic layer TiO_2/SiO_2 .

Experimental

Pt/one-atomic layer TiO_2/SiO_2 is prepared in the previously reported way. EXAFS spectra were measured using in-situ EXAFS cell, varying the temperatures from 273 K-823 K. EXAFS analysis is carried out by the ratio method.

Results and Discussion

Fig.1 showed the temperature dependence of Debye-Waller factor. The Debye-Waller factor abruptly changes at 673 K. At this temperature the activity for C_2H_4 hydrogenation activity increases. Thus the

relation between the structure change and the activity is reconfirmed by this experiment.

The enhancement phenomenon must be related to the surface structure change because no abrupt increase is found in the large Pt particle in Pt/SiO_2 . We are now planning a further study to confirm directly that the phenomenon is related to the surface structure change.

1) J. Inukai et al., in preparation.

2) K. Asakura, PF activity report 1988.

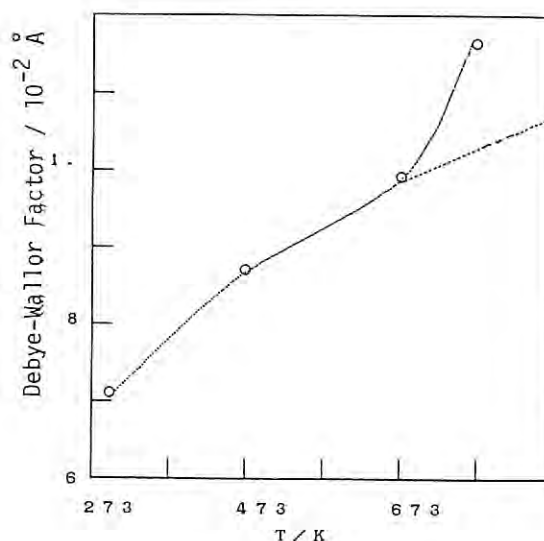


Fig.1 Temperature dependence of Debye-Waller factor derived from EXAFS oscillations using ratio method. The coordination number remained almost the same value. The real curve interpolates the observed values. The dotted curve indicates the extrapolation.

EXAFS AND XANES STUDIES ON DYNAMIC BEHAVIOR OF TWO-SITE PROMOTION
OF CO CATALYZED BY BIMETAL CLUSTERSAtsushi FUKUOKA, Toshiyuki FUJIMOTO, Takuma KIMURA,
Nobuhiro KOSUGI,⁺ Haruo KURODA⁺, and Masaru ICHIKAWA^{*}

Catalysis Research Center, Hokkaido University, Sapporo 060

⁺Department of Chemistry, Faculty of Science, The University of Tokyo, Hongo, Tokyo 113Introduction

The use of bimetallic carbonyl clusters as catalyst precursors is an important aspect of homogeneous and heterogeneous bimetallic catalysis.¹⁾ The bimetallic clusters offer prospects of synergistic effect for the two metal components in many useful catalytic reactions. Particularly, bimetallic clusters grafted on solid surfaces have attracted much attention, because they may provide the advantage of obtaining highly dispersed bimetallic particles which are managed at the molecular-level.²⁾

SiO₂-supported PdFe catalyst derived from [NMe₃Bz]₃[Fe₆Pd₆(CO)₂₄H] showed a high activity for producing methanol.³⁾ The structural properties of the catalyst have been studied by EXAFS.

Experimental

Fe₆Pd₆/SiO₂ was prepared from [NMe₃Bz]₃[Fe₆Pd₆(CO)₂₄H]. This cluster was deposited on SiO₂ from THF solution under N₂. After drying in vacuo and mild oxidation by air, the catalysts were reduced with H₂ at 673 K for 2 h. EXAFS measurements were performed at room temperature at BL 10B in KEK-PF.

Results and Discussion

Figure 1 shows the Fourier transforms of $k^3\chi(k)$ at Fe K- and Pd K-edges for [NMe₃Bz]₂[Fe₄Pd(CO)₁₆] and Fe₆Pd₆/SiO₂. Two strong peaks were observed at 2.1-2.8 Å and 1.0-2.1 Å in Figure 1c. From the curve-fitting analysis (Table 1), the former peak is assigned to the overlap of Fe-Fe and Fe-Pd, and the latter to Fe-O. The large contribution of Fe-O is consistent with the preferential existence of Fe³⁺ and Fe²⁺ in the Mössbauer results. In the Fourier transform of $k^3\chi(k)$ at Pd K-edge (Figure 1d), a strong peak was obtained at 1.9-2.8 Å, which was assigned to Pd-Pd. The contribution of Pd-Fe and Pd-O was negligible. Although Fe-Pd was found in the Fe K-edge EXAFS, the contribution of Pd-Fe was not detectable in the Pd K-edge EXAFS.

Combining with ⁵⁷Fe Mössbauer study, we suggest that Fe³⁺ ions are highly dispersed and located at the Pd-SiO₂ interface to anchor Pd atoms, where Pd-Fe³⁺ sites are generated to promote MeOH production.⁵⁾

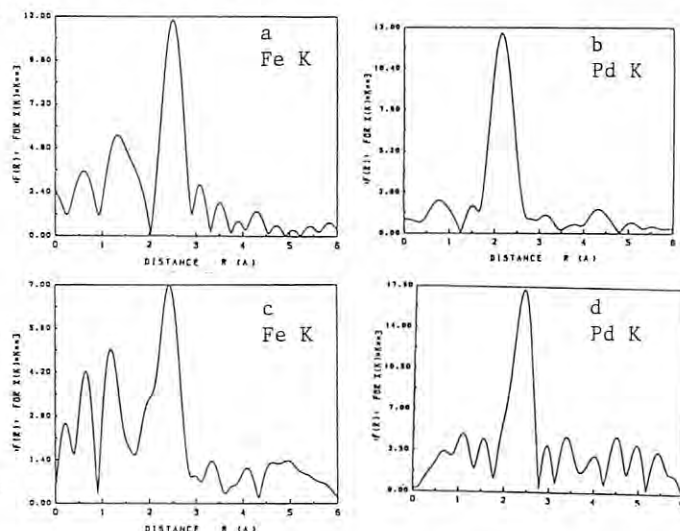


Figure 1. Fourier transforms of $k^3\chi(k)$ at Fe K- and Pd K- edges for [NMe₃Bz]₂[Fe₄Pd(CO)₁₆] (a,b) and Fe₆Pd₆/SiO₂ (c,d).

References

- 1) B. C. Gates et al. ed., "Metal Clusters in Catalysis", Elsevier(1986).
- 2) M. Ichikawa, Polyhedron, **3**, 2351(1988).
- 3) T. Kimura, A. Fukuoka, A. Fumagalli, and M. Ichikawa, Catal. Lett., **2**, 227(1989).
- 4) H. Kuroda, T. Yokoyama, N. Kosugi, M. Ichikawa, and T. Fukushima, J. de Phys., **47**, C8-301(1986).
- 5) A. Fukuoka, M. Ichikawa et al., J. Catal., submitted.

Table 1. Results of the curve-fitting analysis of $k^3\chi(k)$ of H₂-reduced PdFe Bimetallic Cluster-derived Catalysts.^a

precursor/SiO ₂	at ratio Fe/Pd	Fe K-edge EXAFS						Pd K-edge EXAFS			
		Fe-O		Fe-Fe		Fe-Pd		Pd-Fe		Pd-Pd	
		C.N.	R(Å)	C.N.	R(Å)	C.N.	R(Å)	C.N.	R(Å)	C.N.	R(Å)
[NMe ₃ Bz] ₃ [Fe ₆ Pd ₆ (CO) ₂₄ H]	1	3.8	1.93	0.4	2.50	0.9	2.62	—	—	6.5	2.75
PdCl ₂ + FeCl ₃ ⁴⁾	0.45	—	—	0.9	2.46	9.0	2.62	4.6	2.63	7.7	2.76

EXAFS Study of Relaxation of Cu^+ Impurities in Alkali Halides

Takatoshi MURATA, Shuichi EMURA*, Hiroyuki ITO*, Hironobu MAEDA**, and Masaharu NOMURA

Department of Physics, Kyoto University of Education, Kyoto 612

*Institute of Scientific and Industrial Research, Osaka University, Ibaraki 565

**Department of Chemistry, Faculty of Science, Okayama University, Okayama 700

***Photon Factory, National Laboratory for High Energy Physics, Tsukuba, Ibaraki 305

Introduction

Copper impurities in several alkali halides are known to relax at an off-center position in the host lattice. Several experimental¹⁻³⁾ and theoretical⁴⁾ studies have been done in order to determine the amount and the direction of the displacement of the impurity ion from the on-center position in the lattice. However, no definite results have been obtained so far. EXAFS is the most suitable method for observing the ionic relaxation in the lattice. We have been studying on systems of Cu^+ impurity in several alkali halides such as NaCl and NaBr. We report here recent results on NaBr: Cu^+ .

Experimental

Method of sample preparation was described previously⁵⁾. Cu K-edge EXAFS spectra have been measured at BL-7C in the Photon Factory. Measurements were carried out in a fluorescence mode at various temperatures by using fluorescence detector developed by Lytle et al.⁶⁾. X-ray beam was focused on the sample by means of sagittal focusing of the monochromator crystal. CuBr was used for the reference material. The signal to noise ratio has been considerably improved from previous measurements. As a result the data obtained in the present measurements were quite reproducible and reliable.

Results and Discussion

In Figs. 1 and 2 are shown the Fourier transforms of the EXAFS spectra of CuBr and NaBr: Cu^+ at 10 K. The results show that both spectra are practically identical with each other for the first shell distance. Curve fitting

calculations were performed for the first shells, and the distance between Cu^+ and Br^- in both cases are in fact identical, i.e. 2.48 Å. The value is very different from the interionic distance of the host matrix of NaBr (2.985 Å at room temperature). The result means that the local lattice structure around a cuprous ion is very much deformed in the host matrix. Consequently, we can reasonably speculate that the Cu^+ ion in the host does not relax at the on center position by the substitution with the sodium ion of NaBr. This fact may rather be interpreted as the introduction of micro-crystallite clusters of CuBr into NaBr even when the concentration of impurities is very low. If this is the case, the direction of the shift of cuprous ion from the substitutional on-center position can be regarded as [111] direction from the viewpoint of the off-center relaxation, since cuprous bromide crystallizes into zinc blende structure and copper ion is located at the position along [111] axis in the cubic lattice. Further investigation including calculations of simulation is in progress.

References

- 1) S. Kapphan and F. Luty, Phys. Rev. **B6**, 1537 (1972).
- 2) M. S. Li et al., Phys. Rev. **B7**, 4677 (1973).
- 3) S. Emura and M. Ishiguro, J. Phys. Soc. Jpn. **45**, 1425 (1978).
- 4) S. Nagasaka, J. Phys. Soc. Jpn. **51**, 898 (1981).
- 5) T. Murata and S. Emura, J. Phys. (Paris) **47**, C8-795 (1986).
- 6) F. W. Lytle et al., Nucl. Instr. Meth. **226**, 542 (1982).

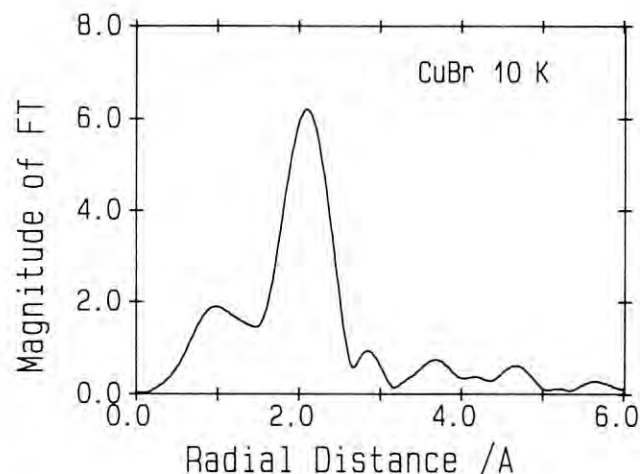


Fig. 1 Magnitude of Fourier transform of k^3 weighted Cu K-EXAFS of CuBr at 10K.

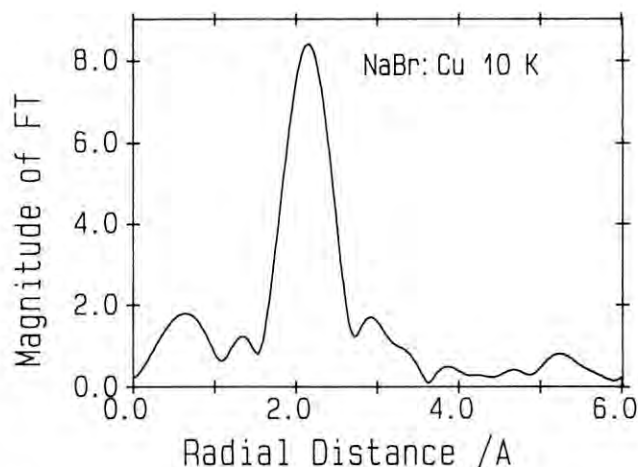


Fig. 2 Magnitude of Fourier transform of k^3 weighted Cu K-EXAFS of NaBr: Cu^+ at 10 K.

STUDIES ON THE EXAFS INTENSITIES FOR 3d TRANSITION METAL COMPLEXES

Hideto SAKANE, Iwao WATANABE, and Yu YOKOYAMA

Department of Chemistry, Faculty of Science, Osaka University, Toyonaka, Osaka 560

Introduction

By EXAFS method, one can obtain the distances r of coordinating atoms from central metal M in complexes reasonably. On the other hand, in many cases, it is hard to determine coordination number N because of the involvement of the disorders σ in bond distances (Debye-Waller factor) in the calculation. Both N and σ contribute to the EXAFS oscillation intensity. In this study, X-ray absorption spectra of many simple 3d transition metal complexes with monodentate ligands in solids (s) and aqueous solutions (aq) are measured in order to study the relation between the kind of central metals or ligands and their EXAFS intensities.

Experimental

Samples are six- or four-coordinate complexes of Cr(III), Mn(II), Fe(II)·(III), Co(II)·(III), Ni(II), Cu(II), and Zn(II) with H_2O , NH_3 , NO_2^- , Cl^- , and Br^- as ligands. The concentrations of metal ions in aqueous solutions were 0.2–1.0 mol/dm³. X-Ray absorption spectra of central metal K-edge were measured at BL10B using a Si(311) channel-cut or BL7C using a Si(111) double crystal monochromator. Fourier transform calculations of EXAFS were performed by using the phase shift and scattering amplitude parameters tabulated by Teo and Lee. Transformations were performed over k -range of 3.50–12.50 Å⁻¹ for six-coordinate complexes or 3.15–17.15 Å⁻¹ for four-coordinate ones.

Results

EXAFS intensity will be discussed in terms of hr^2 where r is the Fourier transform peak position (metal-ligand bond length) and h is the height. It was found¹⁾ that there is an almost linear correlation between hr^2 of H_2O complexes and logarithm of the rate constants for ligand water exchange reactions in solutions. Figure 1 shows the EXAFS intensities for six-coordinate H_2O and NH_3 complexes in solids and solutions. The hr^2 values in Figs. are in common and in relative unit. EXAFS intensities of H_2O and NH_3 complexes obviously correlate each other.

In Fig. 2 are shown hr^2 of six-coordinate NH_3 and NO_2^- complexes. The intensities of NO_2^- complexes correlate less with those of NH_3 complexes than those of H_2O complexes do. This means that the $M-NO_2$ bonds are somewhat different in character from those of $M-OH_2$ and $M-NH_3$.

The intensities for four-coordinate Cl^- and Br^- complexes in solids are shown in Fig. 3. The Cl^- and Br^- complexes give a good linear correlation with respect to hr^2 . It should be noted that the sequence of hr^2 values in magnitudes for four-coordinate metal complexes is different from that for six-coordinate ones.

Reference

- 1) T. Miyanaga, I. Watanabe, and S. Ikeda, *Chem. Lett.*, 1073 (1988).

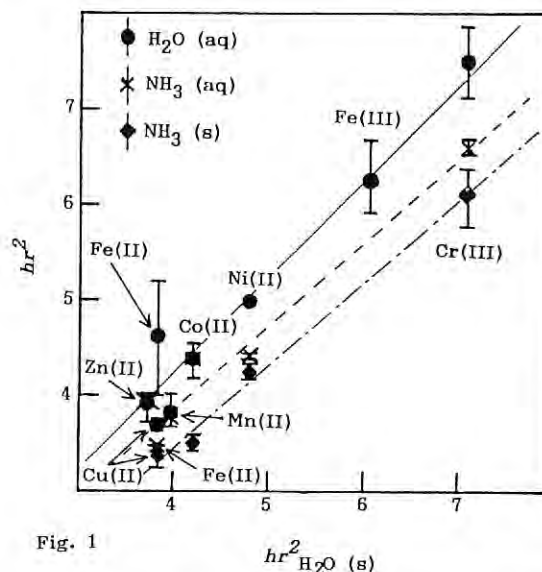


Fig. 1

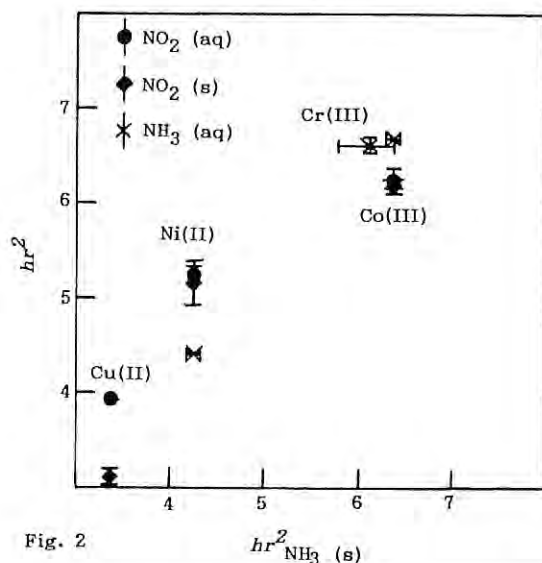


Fig. 2

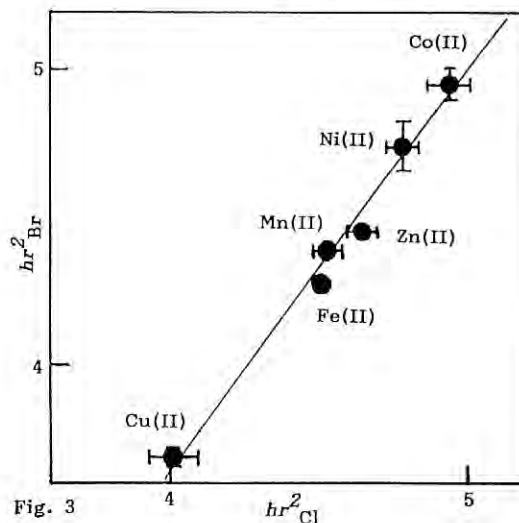


Fig. 3

EXAFS STUDIES ON LOCAL STRUCTURE OF AMORPHOUS $\text{LaNi}_{5.0}$ FILMS

Hiroki SAKAGUCHI, Hajime SERI, Takaharu TSUJI, Gin-ya ADACHI*,
Hirotooshi KANAI and Satoshi YOSHIDA**

* Department of Applied Chemistry, Faculty of Engineering, Osaka
University, Yamadaoka 2-1, Suita, Osaka 565, Japan

** Department of Hydrocarbon Chemistry and Division of Molecular
Engineering, Kyoto University, Kyoto 606, Japan

Introduction

Amorphous hydrogen storage alloys have attracted considerable technological and scientific interest, such as hydrogen purification, catalysis and batteries. In order to understand their chemical and physical properties, it is necessary to obtain detailed structural information at an atomic level by EXAFS. Numerous EXAFS studies have been carried out for the amorphous alloys consisted of the transition metals, but less is known about the rare-earth hydrogen storage alloys.

The local structure around La and Ni atoms in amorphous $\text{LaNi}_{5.0}$ films prepared by an evaporation method was investigated, and the results were compared with those of the crystalline sample. The relationship between the structure and the properties of hydrogen absorption was discussed.

Experimental

The La-Ni amorphous alloy films were deposited on a polyimide membrane by using a flash-evaporation method under a pressure of ca. 6.6×10^{-3} Pa¹⁾. Their homogeneity, stoichiometry and structure were checked by means of X-ray fluorescent spectroscopy, X-ray photoelectron spectroscopy and X-ray powder diffraction. The compositions of alloy powders used for the film preparation were $\text{LaNi}_{3.0}$ and $\text{LaNi}_{5.0}$ (Santoku Metal Industries). Commercially available Ni metals (The Japan Lamp Industries), La_2O_3 (Shinetsu Chemical Company) were used as reference materials. The La metal standard was prepared by sputtering methods.

X-ray absorption spectral measurements (XAS) were performed by means of synchrotron radiation employing the EXAFS facilities of BL-7C of the Photon Factory in the National Laboratory for High-Energy Physics, Tsukuba, Japan. A Si(111) double crystal was used to monochromatize X-rays from a 2.5-GeV electron storage ring. EXAFS spectra were collected at Ni K-edge and La L-edge. All XAS data were obtained at room temperature. Analyses of EXAFS data were performed with a "KABO" program in the FACOM M382 computer system at the Data Processing Center of Kyoto University²⁾.

Results and Discussion

Figure 1(a) shows the radial distribution function (RDF) obtained by a Fourier analysis of the EXAFS data after the nickel K-edge both in the crystalline powder and the amorphous $\text{LaNi}_{5.0}$ film. The damping of the higher order peaks associated to higher shell was observed for the amorphous

film. A large peak appeared in both two samples at about 0.2 nm (2 Å) mainly corresponding to the Ni-Ni distance.

The Fourier transforms (FT) of the lanthanum L_{III}-edge are shown in Fig. 1(b). The magnitude of peaks was much smaller for the amorphous film than for the crystalline $\text{LaNi}_{5.0}$ samples. The peaks appearing in the region of 0.25-0.35 nm (2.5-3.5 Å) in the RDF seem to be due to the La-Ni and La-La pairs.

The main peak in the RDF has been Fourier filtered and backtransformed in k space. The results of the curve fitting analysis are presented in Table 1.

LaNi_5 crystallizes with the hexagonal CaCu_5 -type structure (P6/mmm space group). The structure consists of two alternating types of plane: the basal plane with lanthanum and nickel atoms which occupy the 1a and 2c sites respectively; the z=1/2 plane with only nickel atoms on the 3g site. Consequently, there are two types of nickel atoms. The metal-metal distances estimated from the X-ray diffraction method are also shown in Table 1.

It seems that the local environmental structure of nickel and lanthanum atoms in the amorphous films is almost identical to that in the crystalline bulk except for the longer Ni-Ni pair.

It is known that the amount of hydrogen absorption taken up by the amorphous LaNi_5 films is much smaller than that by the crystalline bulk³⁾. This appears to be due to the decrease of concentration in the sites which are occupied by hydrogen atoms and not due to the difference of the short range order between the two samples.

References

- 1) G. Adachi et al., Bull. Chem. Soc. Jpn., **58**, 885 (1985).
- 2) B. J. Tan et al., J. Am. Chem. Soc., **110**, 5951 (1988).
- 3) H. Sakaguchi et al., J. Phys. Chem., **89**, 5550 (1985).

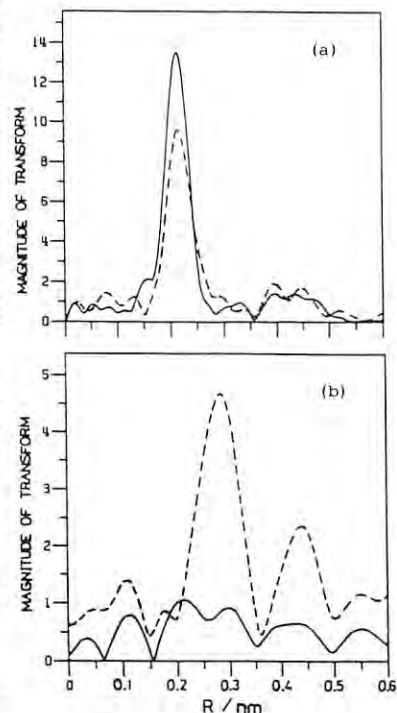


Fig. 1 Fourier transforms for $\text{LaNi}_{5.0}$
(a) on the Ni edge (b) on the La edge.
— amorphous film --- crystalline bulk

Table 1. Structural parameter for $\text{LaNi}_{5.0}$

Central atom	B	EXAFS				XRD			
		Crystalline bulk			Amorphous film	Crystalline bulk			
		L(nm)	$\sigma^2(\text{nm}^2 \times 10^{-5})$	R	B	Nc	L(nm)		
Ni	0.986Ni	0.239	3.04	4.50×10^{-4}	2.60Ni	0.241	5.14	5Ni	0.246
	1.26Ni	0.251	7.90		2.39Ni	0.259	10.0	4Ni	0.251
	0.744La	0.254	5.00		1.28La	0.255	5.46	3La	0.290
La	2.16Ni	0.279	19.5	1.30×10^{-3}	0.084Ni	0.278	0.860	6Ni	0.290
	3.35Ni	0.302	8.84		0.664Ni	0.304	5.27	12Ni	0.320
	2.39La	0.357	8.84		0.770La	0.358	14.1	2La	0.398

L, interatomic distance; B, apparent coordination number; $B = S \times N / S$, damping factor; N, real coordination number; σ^2 , Debye-Waller factor; R, index of the agreement between observed and calculated $\chi(k)$ s.

EXAFS AND XANES STUDIES ON THE COORDINATION OF COPPER ION IN ZEOLITES

Shuichi KAGAWA, Yasutake TERAOKA, Hiroshi FURUKAWA, Chitoshi TAI,
Kiyotaka ASAKURA* and Yasuhiro IWASAWA*

Department of Industrial Chemistry, Faculty of Engineering, Nagasaki University, Nagasaki 852

*Department of Chemistry, Faculty of Science, The University of Tokyo, Tokyo 113

Introduction

Recently, Cu(II)-exchanged ZSM-5 zeolite (Cu-ZSM-5) has attracted great attention because of its high and stable activity for the catalytic decomposition of nitrogen monoxide (NO)¹⁾. It has been suggested that Cu(I) species which are generated by heating and stabilized in a zeolite pore are the active centers and the redox cycle between Cu(I) and Cu(II) is responsible for the steady-state activity for NO decomposition¹⁾. For further understanding of the catalytic nature of Cu ions in ZSM-5, it is indispensable to elucidate the redox property and the existing state of Cu ions in zeolites. This study aims to clarify the local environment and the electronic state of Cu ions in various zeolites by means of X-ray absorption (EXAFS and XANES) measurements.

Experimental

Cu-zeolite(m)-n (m: SiO₂/Al₂O₃ molar ratio, n: exchange level (%) of Cu(II) ions) was prepared by the ion exchange of Na-zeolites in an aqueous solution of Cu(II) acetate¹⁾. Na-zeolites used were Na-ZSM-5(23.3, 40.1), Na-Y(5.2) and Na-mordenite(10.0) which were supplied from Tosoh Corporation. Cu K-edge EXAFS and XANES spectra were recorded at 77 K in a transmission mode at BL-7C station. Before X-ray absorption measurements, most disk-form samples were subjected to the pretreatment at 773 K which consisted of evacuation (0.5 h), exposure to 13 kPa of oxygen (0.5 h) and re-evacuation (0.5 h).

Results and Discussion

From the results of Cu K-edge EXAFS and XANES measurements, we have been trying to elucidate the existing state of Cu ions in Cu-zeolites and its dependence on oxygen adsorption-desorption treatment, exchange level of Cu ions, structure and SiO₂/Al₂O₃ ratio of zeolites and so on. For example, the Cu K-edge XANES spectra of Cu-ZSM-5(23.3)-75 and standard materials (CuO, Cu₂O) are shown in Fig. 1. Five structures (A, B, C, D and E) can be discerned in the spectra, among which the structure E is already in the EXAFS region. On reference to the literatures²⁻⁴⁾, structures A-D can be assigned to the following transition; weak pre-edge peak A is due to the 1s-3d transition characteristic to Cu(II) ions, B due to the shake-down accompanying the 1s-4p out-of-plane transition, C due to the 1s-4p in-plane transition and D due to the multiple scattering. The most distinct difference between Cu-ZSM-5 and standard materials is the disappearance of the structure D in the spectra of Cu-ZSM-5. It was reported that K-edge XANES spectrum of Cu(II) ions in an aqueous solution of CuCl₂ had no structure corresponding to D³⁾. This may mean that the existing state of Cu ions introduced into ZSM-5 zeolite by an ion-exchange method is different from that in crystalline oxides but similar to that of nearly isolated metal cation. Comparison between the spectra of pretreated (1) and oxygen-adsorbed (2) Cu-ZSM-5 clearly shows that the oxygen adsorption on a pretreated Cu-

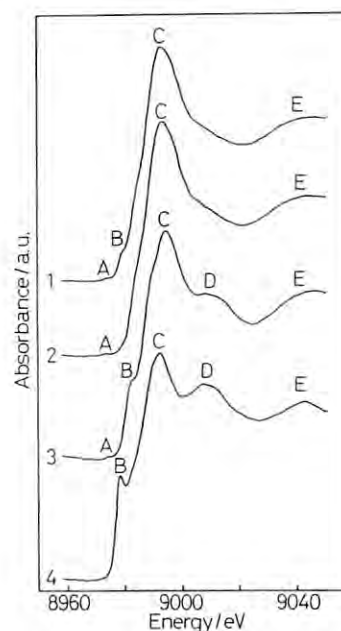


Fig. 1 Cu K-edge XANES spectra of Cu-ZSM-5(23.3)-75 pretreated at 773 K (1) and oxygen-adsorbed from 773 K to RT (2), CuO (3) and Cu₂O (4).

ZSM-5 brings about the extinction of the structure B. This implies that oxygen adsorption on a pretreated Cu-ZSM-5 in which some of Cu ions are probably reduced to a univalent state occurs in a manner to reduce the probability of the 1s-4p out-of-plane transition. The XANES spectra of Cu-ZSM-5 were hardly affected by the exchange level of Cu ions.

In EXAFS Fourier transforms of Cu-ZSM-5 subjected to evacuation or oxygen-adsorption treatment, only a single peak assigned to Cu-O bond was observed. The curve-fitting analysis showed that the coordination number increased with increasing the exchange level of Cu ions (n). This result is well consistent with the fact that the amount of adsorbed oxygen per a Cu ion increases with increasing n. EXAFS results also showed that the reducibility of Cu ions in Cu-ZSM-5 depended on the sort of reductants; the formation of metallic copper was clearly observed in the reduction by H₂ at 673 K while hardly observed in the reduction by CO even at 773 K.

The analysis of XANES and EXAFS data of Cu-zeolites are now in progress, and the comprehensive and reasonable interpretation will give useful informations on the existing state and catalytic property of Cu ions in Cu-zeolites.

References

- 1) M. Iwamoto et al., "New Developemnt in Zeolite Science Technology," eds. Y. Murakami et al., Elsevier, Amsterdam (1986), p. 943.
- 2) N. Kosugi et al., Chem. Phys., **91**, 249(1984).
- 3) J.M. Tranquada et al., Phys. Rev. B, **35**, 7187 (1987).
- 4) E.E. Alp et al., Phys. Rev. B, **35**, 7199(1987).

XAFS STUDY ON NICKEL THIOLATE COMPLEXES IN TERMS OF THE NICKEL IN HYDROGENASES

Takeshi YAMAMURA, Nobuhumi NAKAMURA, Kiyotaka ASAKURA*

Department of Chemistry, Faculty of Science, Science University of Tokyo, Kagurazaka, Shinjuku-ku, Tokyo 162

* Department of Chemistry, Faculty of Science, The University of Tokyo, Hongo, Bunkyo-ku, Tokyo 113

Introduction

XAFS and EPR studies on the H_2 -ases in arcaic bacteria have clarified that their Ni ($Ni^{3+,2+,1+}$) is immersed in a rhombic or square planar coordination sphere of 3 ~ 4 sulfur atoms. In this study we examined to accumulate XAFS knowledge on the Ni k-edges of Ni-S bonds under various circumstances in order to obtain more accurate informations on the coordination sphere of the active site of H_2 -ases.

Experimental

The nickel k-edge X-ray absorptions of the following compounds were observed in transmission mode on polyethylene pellets at room temperature by using the BL-7C facility of PF-KEK for XAFS measurements. Among the compounds listed below, 1 ~ 10 involve Ni-S bonds. 1 ~ 6 are newly prepared by us and structurally resolved by X-ray diffraction method. All the compounds are structurally known. 1 is tetrahedral (Td). 9, 10, 13 are octahedral (Oh). 2 ~ 8, 11 and 12 are square planar (Sp). Others are authentic for Td and Oh.

The compounds are as follows: [Ni(SPh)₄]²⁻; 1, [Ni(SET)₂]₆; 2, (N,N'-ethylenebis(o-mercaptobenzylidenaminato)nickel(II)); 3, (N,N'-ethylenebis(o-mercaptobenzylaminato)nickel(II)); 4, (N,N'-ethylenebis(o-mercaptobenzamidato)nickel(II)); 5, [Ni(SCH₂CH₂S)₂]²⁻; 6, [Ni₃(tetrathiaundecane)₂]²⁺; 7, [Ni₂(SCH₂CH₂S)₃]²⁻; 8, [Ni(cyclo-hexathiaoctadecan)]²⁺; 9, Ni(thiourea)₄Cl₂; 10, Ni(TPP); 11, Ni(salen); 12, [Ni(H₂O)₆]²⁺; 13, and others.

Results and Discussion

Figure 1a and 1b (solid lines) show the XANES and the Fourier transform of the EXAFS component, respectively, of 6. 6 adopts square planar geometry of NiS₄ central unit (X-ray analysis). The radial distribution function of 6 is similar to that reported for the H_2 -ase of *M. thermoautotrophicum*, which exhibits in the Fourier transform a simple major peak assigned to Ni-S₄. Whereas 3 ~ 5, which are square planar NiS₂N₂ compounds, show shoulders originating from the nitrogen atoms in the shorter radial region of the Ni-S main peaks. This resembles well the feature of the Fourier transform of *D. gigas* hydrogenase.

In this study, we also examined to classify the XANES spectra of 1 ~ 10 and others according to their local geometries (Td, Oh, Sp). Thus, the distribution map for the "shape resonance" peaks of the normalized XANES spectra of these compounds was drawn with the peak heights in ordinate and the energies in abscissa. The XANES spectrum of *D. gigas* hydrogenase was found to belong in this distribution map to square planar (Sp) geometry, and neither to Oh nor Td. The correlation between the mean ionicity of sulfur and the energy of "1s + 4p + shake down", which relates to LMCT, was also discussed for alkanethiolate compounds. In this correlation diagram, Ni in *D. gigas* H_2 -ase was found to situate in a circle, where Ni is surrounded by four RS⁻. It is proposable that nickel in *D. gigas* H_2 -ase is placed in a square planar cavity formed of four cysteinates.

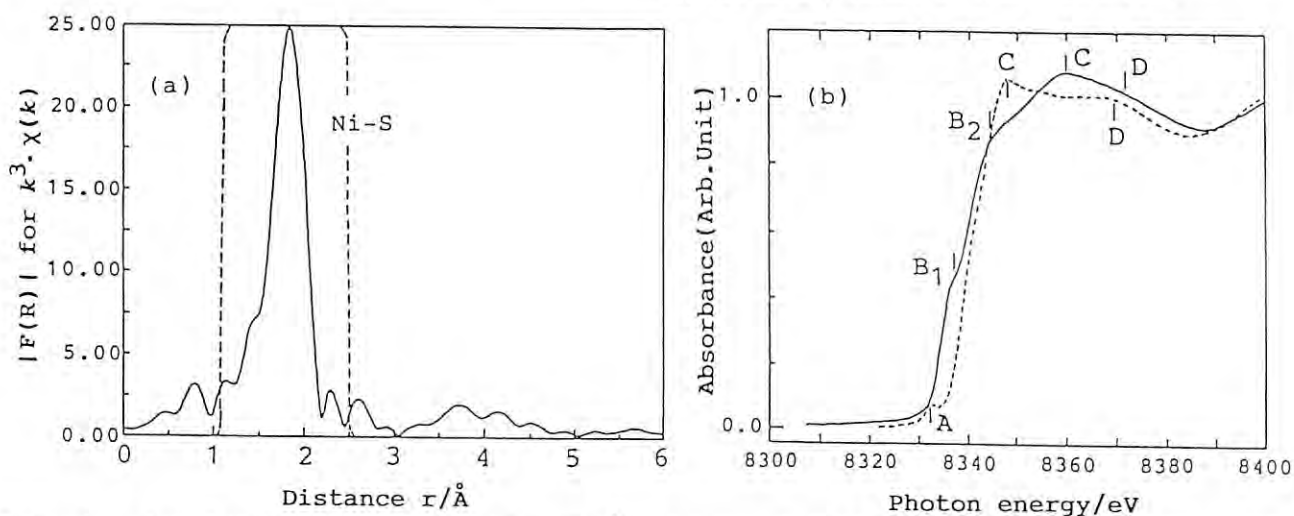


Fig. 1. (a) Fourier transform of the $k^3 \cdot \chi(k)$ vs. k EXAFS spectrum, (b) normalized XANES spectra of $(Ph_3MeP)_2[Ni(edt)_2]$ (—) and $(NEt_4)_2[Ni(PhS)_4]$ (---).

EXAFS AND XANES STUDIES ON CHARACTERIZATION OF ELECTRON DONOR-ACCEPTOR METAL PHTHALOCYANINE COMPLEXES ENTRAPPED IN ZEOLITE SUPERCAGES

Atsushi FUKUOKA, Takuma KIMURA, Toshiyuki FUJIMOTO,
Nobuhiro KOSUGI*, Haruo KURODA*, and Masaru ICHIKAWA*

Catalysis Research Center, Hokkaido University, Sapporo 060

*Department of Chemistry, Faculty of Science, The University of Tokyo, Hongo, Tokyo 113

Introduction

Metallophthalocyanine complexes encapsulated inside the zeolite framework are one of the models of natural monooxygenase enzymes such as cytochrome P 450, which exhibits a high selectivity in the partial oxidation of inactive alkanes.¹⁾ The complexes are applied to catalytic reactions such as sulfur oxidation, hydrocarbon oxidation, and hydrogenation of olefins and CO.²⁾ The cage structure of zeolite has the prospect to impose the shape selectivity in metal-catalyzed reactions.³⁾

Recently, we synthesized Fe phthalocyanine (FePc, 13 Å diameter) in NaY from $[\text{HFe}_3(\text{CO})_{11}]^-/\text{NaY}$.⁴⁾ The diameter of the NaY supercage is 13 Å. The spectroscopies such as EXAFS, XANES, Mössbauer, FTIR, UV-vis suggest that NaY-encapsulated FePc is slightly distorted from the original planar structure of a phthalocyanine molecule due to the intrazeolitic constraint.

In this study, tetra t-butyl phthalocyaninato iron ($\text{FePc}(\text{t-Bu})_4$, 18 Å diameter) was prepared in NaY by "ship-in-a-bottle" synthesis from the highly dispersed iron particles in NaY and 4-t-butyl-1,2-dicyanobenzene. The structural properties of $\text{FePc}(\text{t-Bu})_4/\text{NaY}$ were studied by EXAFS.

Experimental

NaY-entrapped $\text{FePc}(\text{t-Bu})_4/\text{NaY}$ was synthesized from $[\text{HFe}_3(\text{CO})_{11}]^-/\text{NaY}$ and 4-t-Bu-1,2- $\text{C}_6\text{H}_4(\text{CN})_2$. Fe K-edge XANES and EXAFS measurements were carried out at room temperature at BL 7C and 10B in KEK-PF.

Results and Discussion

Figure 1 shows the Fourier transforms of $k^3\chi(k)$ for $\text{FePc}(\text{t-Bu})_4/\text{NaY}$ and FePc crystalline which was used as a standard material. The major peaks at 1.7 Å may be assigned to the first neighbor Fe-N by the curve-fitting analysis. The coordination number and the interatomic distance of the Fe-N for $\text{FePc}(\text{t-Bu})_4/\text{NaY}$ were 2.0 and 1.98 Å, respectively. On the other hand, FePc gave the coordination number of 1.6 and the interatomic distance of 1.94 Å. These results suggest that an iron atom in $\text{FePc}(\text{t-Bu})_4/\text{NaY}$ is out of the phthalocyanine plane. This is reflected in the Debye-Waller type factors: $\sigma = 0.091$ for $\text{FePc}(\text{t-Bu})_4/\text{NaY}$, $\sigma = 0.025$ for FePc. The distortion of a phthalocyanine ring was caused by the encapsulation of an $\text{FePc}(\text{t-Bu})_4$ molecule inside a NaY supercage.

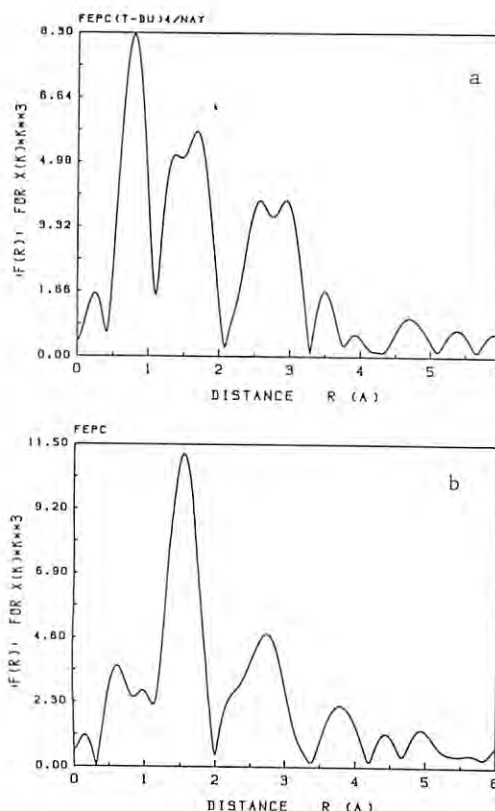


Fig. 1. Fourier transforms of $k^3\chi(k)$ at Fe K-edge for $\text{FePc}(\text{t-Bu})_4/\text{NaY}$ (a) and FePc crystalline (b).

^{57}Fe Mössbauer, FTIR, and UV-vis studies suggested that the electronic states of phthalocyanine of $\text{FePc}(\text{t-Bu})_4/\text{NaY}$ were shifted compared to $\text{FePc}(\text{t-Bu})_4$ crystalline.

Zeolite-entrapped $\text{FePc}(\text{t-Bu})_4/\text{NaY}$ showed high activity and selectivity toward 1-hexanol in the hydroxylation of n-hexane in the presence of PhIO .

References

- 1) N. Herron, G. D. Stucky, and C. A. Tolman, *J. Chem. Soc., Chem. Commun.*, 1521(1986).
- 2) A.B.P. Lever, *Adv. Inorg. Radiochem.*, **7**, 27(1965); F.H. Moser and A.L. Thomas, *The Phthalocyanines*, CRC Press, 1983.
- 3) A. Fukuoka, M. Ichikawa et al., *Appl. Catal.*, **50**, 295(1989).
- 4) T. Kimura, A. Fukuoka, and M. Ichikawa, *Catal. Lett.*, submitted.

EXPERIMENTAL EXAMINATION OF "PHASE SHIFT TRANSFERABILITY" ON EXAFS ANALYSIS

Moritaka HIDA, Hironobu MAEDA*, Woo-Yeong LIM, Yoshito TAKEMOTO, Akira SAKAKIBARA

Department of Mechanics, Faculty of Engineering, Okayama University, Okayama 700

* Department of Chemistry, Faculty of Science, Okayama University, Okayama 700

Introduction

From data analysis of EXAFS, we have obtained some structural informations based on the following assumptions. (1) EXAFS is composed of a simple sum of waves due to chemically different neighbouring atoms. (2) The phase function is transferable for each type of pair atoms. (3) The amplitude function is also transferable for each neighbour. Especially the chemical effect on the phase transferability has been applied to a large extent of EXAFS spectroscopy, but any experimental support for the transferability has not been done yet. In order to verify the transferability, the experimental attempts were carried out by using covalent and metallic bond tin (grey and white Sn, respectively; 286K of phase transformation temperature). Another aim of this work was to compare the structural informations obtained from Sn K-edge with the ones from Sn L-edge EXAFS.

Experimental and Data Analysis

Very fine powder samples of grey tin are prepared by milling brittle granular grey tin (99.9999% Sn) at about dry ice temperature. The white tin samples were obtained by heating up grey tin powder samples to ~320K. The white samples showed strong supercooled phenomenon and therefore never changed to grey tin at 283K for long time. EXAFS measurement (BL-10B & BL-7C used above the K-edge and L_{III}-edge, respectively) was carried out at 283K. A conventional mirror was used for the measurement at BL-7C to eliminate the harmonic radiations. On the EXAFS data analysis, the same Fourier transformation was carried out as used in previous reports¹⁾. To determine the struc-

tural parameter (R , N , σ) and the compatible factor ($\eta(=k/\lambda)$ or λ , ΔE) we used the nonlinear least-squares method.

Results and Discussion

Figure 1(a) and (b) show the Fourier transform of EXAFS, $k^3\chi(k)$ above Sn K-edge. The ranges of 1.89~3.71Å for white tin and of 1.99~2.92Å for grey tin were transformed back to the k-space, and then the resultant EXAFS spectrum was fitted in the k-space ranges of 3.480~13.680(1/Å) for white and grey tin²⁾.

From X-ray diffraction results³⁾, crystal structures of white and grey tin are as follows: (1) tetragonal, $a=5.820\text{\AA}$, $c=3.175\text{\AA}$, $r_1=3.02\text{\AA}$ ($N_1=4$), $r_2=3.18\text{\AA}$ ($N_2=2$), $r_3=3.77\text{\AA}$ ($N_3=4$), $r_4=4.41\text{\AA}$ ($N_4=8$); (2) diamond, $a=6.491\text{\AA}$, $r_1=2.80\text{\AA}$ ($N_1=4$), $r_2=4.59\text{\AA}$ ($N_2=12$). As the preliminary analysis three shell model for white tin was applied to the Fourier-transformed EXAFS spectrum in k-space in order to obtain the compatible factors η and ΔE . The factors obtained for white tin was transferred to the compatible factors of grey tin (one shell model used). It is noticed that the phase transferability is fairly good in conservative as shown in Table 1. Data analysis of EXAFS for Sn L-edge is now in progress.

References

- 1) H. Maeda, J. Phys. Soc. Japan, 56, 2777(1987)
- 2) A. G. McKale, B. W. Veal, A. P. Paulikas, S. K. Chan and G. S. Knapp, J. Am. Chem. Soc., 110, 3763(1988).
- 3) A. F. Wells, Structural Inorganic Chemistry(Clarendon Press, Oxford, 1975).

Table 1 Best Fitting Results

White Sn	N	R	σ	$\eta(=k/\lambda)$	ΔE
1st shell	(4.00)	(3.02)	0.093±0.0017(0)	1.139±0.056	-0.0062±0.0003
2nd shell	(2.00)	(3.18)	0.096±0.0038(0)	1.139±0.056	-0.0062±0.0003
3rd shell	(4.00)	(3.77)	0.161±0.0169(0)	1.139±0.056	-0.0062±0.0003
Grey Sn	N	R	σ	$\eta(=k/\lambda)$	ΔE
1st shell	3.09±0.13	2.813±0.0005	0.0698±0.0011	(1.139)	(-0.0062)

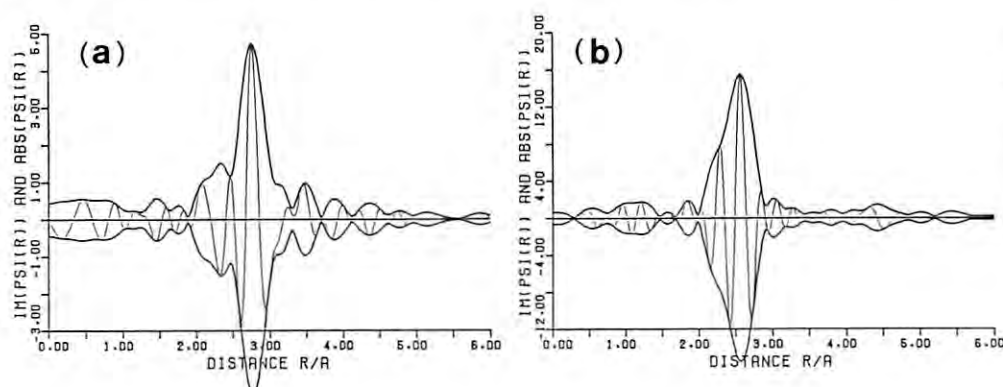


Fig.1

Fourier transformation of $k^3\chi(k)$ obtained at 283K.
(a) white Sn
(b) grey Sn

LOCAL STRUCTURE OF THE Pb SUBSTITUTED Bi-Sr-Ca-Cu-O HIGH- T_c SUPERCONDUCTORS

Yoshinari MIURA, Hiroyuki ITO**, Toshio EGI, Jun TAKADA, Kiichi ODA, Hitoshi KITAGUCHI, Akiyoshi OSAKA, Hironobu MAEDA*, Yasunori IKEDA**, Zenji HIROI**, and Mikio TAKANO**

Department of Applied Chemistry, Faculty of Engineering, Okayama University, Okayama 700

*Department of Chemistry, Faculty of Science, Okayama University, Okayama 700

**Institute for Chemical Research, Kyoto University, Uji, Kyoto 611

Introduction

The discovery of the superconductors with T_c 's above the liquid nitrogen temperature was followed by a great number of experiments aiming at identification and isolation of their monophasic materials. We have reported the substitution of Pb for Bi facilitates the formation of the so-called 2223 phase^{(1),(2)}. And also the Pb substitution has been found to induce a new mode of structure modulation with a long wave length⁽³⁾. In this study, we intend to clarify local structures around the Bi and Pb in the Bi_2O_2 layers by using EXAFS.

Experimental

The sample with a nominal composition $\text{Bi:Pb:Sr:Ca:Cu}=0.9:0.2:1:1:1.6$ was synthesized (all being $\geq 99.9\%$ pure) by usual ceramic method. XRD measurements confirmed the sample quality of the 2223 phase. Samples for EXAFS studies were prepared by dusting the powder uniformly onto both side of cellophane tape. Several layers of the tape were used to make the sample body for the measurements. X-ray absorption measurements near Bi-L_{III}, Pb-L_{III}, and Cu-K edges were made at room temperature and 77K, in transmission with synchrotron radiation on the BL-10B and BL-7C at the Photon Factory. Fitted by using a best fitting analysis of EXAFS. The structure parameters were least squares. The Debye-Waller factor, the electron mean-free path and change in energy threshold were determined from $\alpha\text{-Bi}_2\text{O}_3$ for Bi, red PbO for Pb and CuO for Cu.

Results and Discussion

The average structure model of the 2223 phase was used as a starting model, assuming that Pb substituted for Bi. Table 1 shows the obtained coordination numbers and the distances between metal and oxygen for Bi, Pb, and Cu. Bi has four oxygens with a bond length of 2.10 Å, while Pb has four oxygens with a slightly longer bond of 2.24 Å with an additional oxygen ion much far away. This result for Bi is in good accordance with the structural model of the 2212 phase recently proposed by Yamamoto et al. using Rietveld analysis⁽⁴⁾, where the Bi atom has four short bonds, three within the BiO layer and one within the SrO layer in the so-called Bi condensed region. Another oxygen within the BiO layer expected from the average structure lies far away from Bi, but in the case of Pb, the long distance may be shorthand

because of the large ionic radius of Pb^{2+} . The cause for the characteristic elongation of modulation period by introducing Pb is considered to be the relaxation of the lattice mismatch between (Bi, Pb)O layer and the perovskite block as discussed in ref. 5.

Table 1 Coordination number and atomic distances of M-O (M=Bi, Pb and Cu) refined by the best-fit method. Coordination number is fixed for Cu as determined from the ideal 2223 structure.

M	Coordination number	r(M-O) (Å)
Bi	3.8(3)	2.10(1)
Pb	3.9(5)	2.24(1)
	1.2(7)	2.54(5)
Cu	4	1.94(1)
	1	2.30(2)

Discussion with and encouragements by Emeritus Prof. T. Takada and Prof. Y. Bando are appreciated. Thanks are also to Drs. S. Nomura and K. Koyama, KEK for their help and useful advices in the experiments.

References

- 1) M. Takano, J. Takada, K. Oda, H. Kitaguchi, Y. Miura, Y. Ikeda, Y. Tomii, and H. Mazaki, Jpn. J. Appl. Phys. **27** (1988) L1041.
- 2) Y. Ikeda, H. Ito, Z. Hiroi, M. Takano, H. Kitaguchi, J. Takada, K. Oda, Y. Miura, Y. Takeda and H. Mazaki, J. Jpn. Soc. Powder & Powder Met. **35** (1988) 965.
- 3) Y. Ikeda, M. Takano, Z. Hiroi, K. Oda, H. Kitaguchi, J. Takada, Y. Miura, Y. Takeda, O. Yamamoto, and H. Mazaki, Jpn. J. Appl. Phys. **27** (1988) L2067.
- 4) A. Yamamoto, M. Onoda, E. Takayama-muromachi, F. Izumi, T. Ishigaki, and H. Asano, preprint.
- 5) Y. Ikeda, Z. Hiroi, H. Ito, S. Shimomura, and Y. Bando, to be submitted in Physica C.

EXAFS AND XANES STUDIES ON THE CRYSTALLIZATION OF PENTASIL ZEOLITE
I. LOCAL STRUCTURE AROUND IRON OF FERRISILICATENobuyuki MATSUBAYASHI, Kiyomi OKABE, Hiromichi SHIMADA, Yuji YOSHIMURA, Toshio SATO,
Hiroyuki HAGIHARA, and Akio NISHIJIMA

National Chemical Laboratory for Industry, Tsukuba, Ibaraki 305

Introduction

Hydrothermally synthesized ferrisilicate of ZSM-5 structure shows high selectivity for light olefins in methanol conversion and the Fischer-Tropsch reaction. Iron in the silicate is atomically dispersed, because iron can be substituted for silicon in the lattice of zeolite crystal. Such an ultra-high dispersion of Fe-based catalyst could not be obtained by conventional impregnation technique. It is of great importance to elucidate the crystallization process of ferrisilicate from a view point of design for high-dispersion catalysts at atomic level.

Experimental

Colloidal silica, ferric nitrate, tetra-n-propylammonium bromide (TPABr), sodium hydroxide, and distilled water were mixed together to ferrisilicate gel having the following compositions; $\text{SiO}_2/\text{Fe}_2\text{O}_3=60$, $\text{SiO}_2/\text{TPABr}=10$, $\text{SiO}_2/\text{OH}=10$. The gel was autoclaved at 433 K. The Fe K-edge EXAFS spectra were measured at BL-7C on the crystallization of ferrisilicate.

Results and Discussion

Figure 1 shows the Fourier transforms of Fe K-edge EXAFS in various steps of the crystallization of ferrisilicate. The spectrum of the gel mixture (0h) showed two peaks at 2.0 Å and 3.2 Å, similar to those of $\alpha\text{-FeO}(\text{OH})$, assigned to Fe-O and Fe-O-Fe, respectively. By hydrothermal reaction of 2h, the former peak shifted to 1.9 Å, and the other was split into 2 peaks at 3.1 Å and 3.5 Å, suggesting that the second neighbor of Fe atom was turned into Si, instead of Fe, and that Fe-silicate was formed in an early stage. The peak position at 1.9 Å did not change, but the height of the peak drastically increased between 16 h and 16.5 h of hydrothermal reaction time. The height of the peak reflects regularity of local structure surrounding Fe. The height of the peak at 3.1 Å decreased with further hydrothermal reaction, while the height of the peak at 3.5 Å increased.

Figure 2 shows the Fe K-edge XANES spectra for the crystallization of ferrisilicate. The profile of the XANES spectra varied discontinuously between 16 h and 16.5 h of hydrothermal reaction time.

In conclusion, it is suggested from these results that the micro-structure of ferrisilicate precursor containing TPA was formed in an early stage, before instantaneous crystallization of the bulk, and that the regularity of the local structure increased with the reaction time.

Further study is now progressing for Ga substituted zeolite and Si K-edge XANES in zeolite.

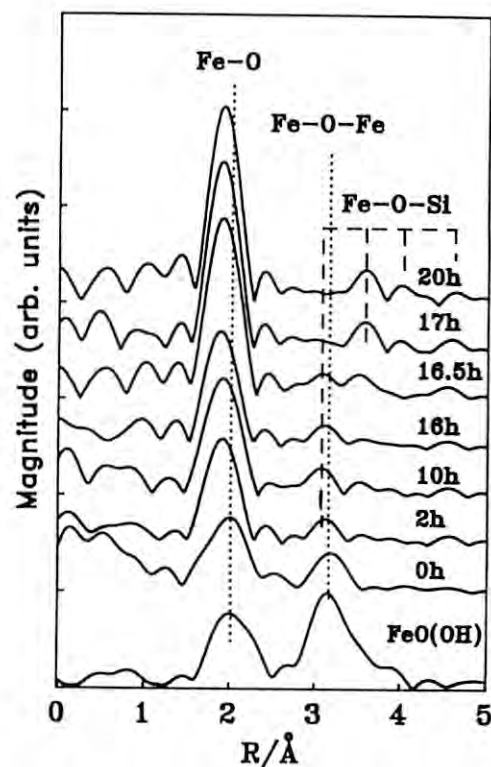


Fig. 1 The Fourier transforms of Fe K-edge EXAFS in various steps of the crystallization of ferrisilicate.

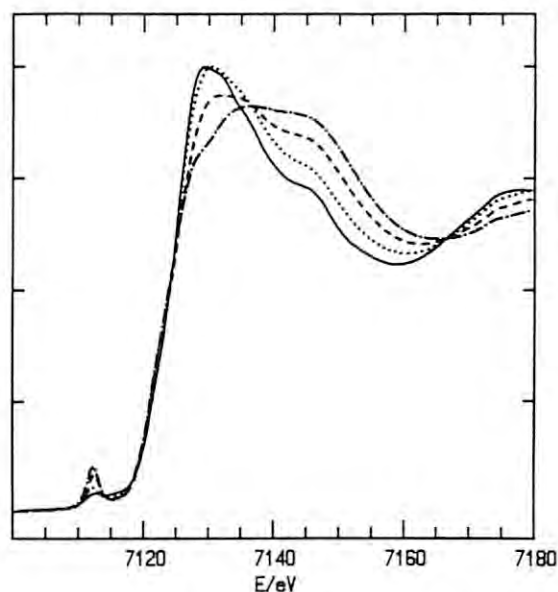


Fig.2 The Fe K-edge XANES spectra for the process of crystallization of ferrisilicate zeolite.
—: $\text{FeO}(\text{OH})$,: 0 h, ----: 2 h, - · - · -: 16.5 h

EXAFS AND XANES ANALYSES OF V_2O_5 THIN FILM CATALYSTS PREPARED BY CVD
- THE EFFECTS OF SUPPORTS -

Kei INUMARU, Toshio OKUHARA, Makoto MISONO, Nobuyuki MATSUBAYASHI,* Hiromichi SHIMADA, * and Akio NISHIJIMA *

Department of Synthetic Chemistry, Faculty of Engineering, The University of Tokyo, Bunkyo-ku, Tokyo 113

*National Chemical Laboratory for Industry, Tsukuba, Ibaraki 305

INTRODUCTION

Thin films of oxides and mixed oxides have attracted much attention as a new type of catalysts. In catalytic oxidation of hydrocarbons over supported vanadium oxide catalysts, selectivities have been affected by the kinds of supports and the microstructure of V_2O_5 ^{1,2)}. In order to control the microstructure of V_2O_5 on various oxides, the CVD (Chemical Vapor Deposition) method using $VO(OC_2H_5)_3$ were applied³⁾.

EXPERIMENTAL

Two different types of V_2O_5 catalysts were prepared. By the CVD method, V_2O_5/SiO_2 (CVD) was obtained as follows. After SiO_2 (Aerosil 200, $203\text{ m}^2\text{g}^{-1}$) was evacuated at 773 K, $VO(OC_2H_5)_3$ vapor was introduced to the sample at 423 K to react selectively with OH groups on SiO_2 . Then the sample was heated up to 723 K at heating rate of 10 degmin^{-1} . By repeating this adsorption-decomposition cycle, V_2O_5 overlayers were grown.

The others were prepared by impregnation of SiO_2 , Al_2O_3 and MgO with an aqueous oxalic acid solution of NH_4VO_3 . After all samples were calcined in dry air at 623K for 1 h, they were mixed with a cellulose powder as a binder, and pressed into disks in a N_2 atmosphere. EXAFS and XANES were measured at the Photon Factory (BL-7C) at about 15 K.

RESULTS AND DISCUSSION

Figure 1 shows the Fourier transform of V K-edge EXAFS data of the samples and V_2O_5 as a reference compound. For bulk V_2O_5 (Fig. 1a), the peaks appeared around 1.55, 1.89, 3.13, and 3.60 Å, which correspond to V=O, V-O, V-V, and another V-V, respectively. It should be noted that the peaks of V=O and V-O has been well resolved. For 9.1% V_2O_5/SiO_2 (Imp) (Fig. 1c), the positions and relative intensities of the peaks were very similar to those of the bulk V_2O_5 , showing that the V_2O_5 overlayer on this sample has the same structure as the bulk V_2O_5 . XRD measurement supported this result.

On the other hand, in the case of 9.1% V_2O_5/SiO_2 (CVD)(Fig. 1b), the peaks due to V-V (3.13 and 3.60 Å) were small, indicating that the growth of V_2O_5 crystallites was suppressed. XRD revealed that a plate-like crystallite of V_2O_5 , of which length in the [101] direction is about 150 Å, was formed. This is attributable to the preferential formation of V-O-Si bond in the CVD process.

Figure 1d and e show the difference in the structure of V_2O_5 depending on the supports. A sharp peak appeared at 1.67 Å (V=O) on V_2O_5/Al_2O_3 (Imp), together with a small peak (V-V; 3.1 Å). Probably, isolated vanadium clusters was formed on Al_2O_3 . Only one peak at 1.78 Å was observed for V_2O_5/MgO (Fig. 1e). A similar spectra were obtained when the loading amount of V_2O_5 was varied from 6.8 to 19.4 %.

In this case, it is likely that V_2O_5 reacted with the surface of MgO to form a mixed oxide layer like $Mg_2V_2O_7$.

In conclusion, EXAFS gave the direct evidence that the microstructure of V_2O_5 was greatly influenced by the nature of supports and the preparation method.

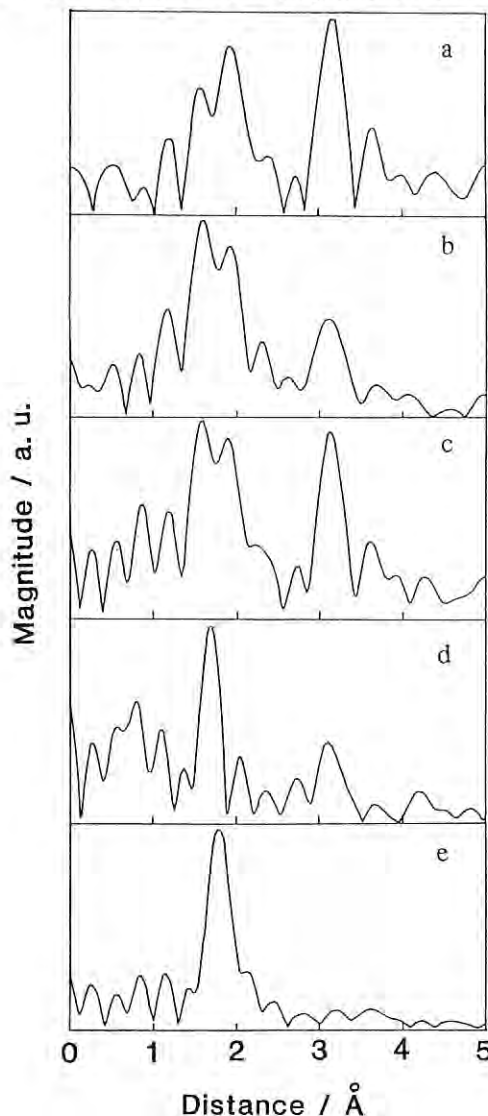


Figure 1. Fourier transforms of V K-edge EXAFS of (a) V_2O_5 , (b) 9.1% V_2O_5/SiO_2 (CVD), (c) 9.1% V_2O_5/SiO_2 (Imp), (d) 6.8% V_2O_5/Al_2O_3 (Imp), (e) 9.1% V_2O_5/MgO (Imp).

- 1) K. Mori, M. Inomata, A. Miyamoto, Y. Murakami, J. Chem. Soc., Faraday Trans. I, 80, 2666 (1984).
- 2) G. C. Bond, K. Bruckman, Faraday Disc. Chem. Soc., 72, 235 (1981).
- 3) K. Inumaru, T. Okuhara, M. Misono, Proc. of the 1989 International Chemical Congr. of Pacific Basin Societies, 9I264, Honolulu, 1989.

XANES STUDY ON THE DENSITY OF d-STATE OF SMSI-PLATINUM AND RELATED CATALYSTS.

Hideaki YOSHITAKE, Kiyotaka ASAKURA and Yasuhiro IWASAWA

Department of Chemistry, Faculty of Science, the University of Tokyo
Hongo, Bunkyo-ku, Tokyo 113.Introduction

The SMSI effect of Pt/Nb₂O₅ catalyst shows the singular behavior in hydrogenation reactions among the other group VIII metals. In the hydrogenation of acrolein (CH₂=CHCHO) it produces propanal (CH₃CH₂CHO) selectively after 393 K reduction (LTR, normal state) whereas produces 2-propene-1-ol (CH₂=CHCH₂OH) after 773 K reduction (HTR, SMSI state).¹⁾ Charge transfer from the suboxide such as NbO_x or TiO_x to d-state of the metal through a chemical bond has been proposed to cause the significant change on the catalysis in SMSI state.²⁾ This is thought to be important for the hydrogenation of unsaturated

compounds because the Pt- $\begin{array}{c} \text{C} \\ | \\ \text{C} \end{array}$ bond is known to be

controlled by the electron donation from d-orbital to π -bond. It is interesting, therefore, to estimate the density of d-state in platinum of SMSI-Pt/Nb₂O₅ and compare with the other charge transferred platinum catalyst such as Na/Pt/SiO₂ which has 100 % selectivity for propanal through $0 < \text{Na}/(\text{Pt}+\text{Na}) < 0.86$. The method developed by Mansour et al.³⁾ is adequate for this kind of study which can determine the number of unoccupied d-electron state quantitatively.

Experimental

All the catalysts were prepared by conventional impregnation method. XANES spectra of Pt were recorded in BL-7C and analyzed with the procedure in the literature³⁾. The white lines appeared at L₃ and L₂ edges (, which are related with the total density of unoccupied d-states, h, by the formula:

$$h = (1.0 + \frac{\Delta A_3 + 1.11\Delta A_2}{A_{3r} + 1.11A_{2r}})h_r, \quad \Delta A_j = A_j - A_{jr}$$

where A_j is the intensity of p-d transition in the L_j edge and r means the reference) were integrated and normalized by those of the reference, i.e. Pt foil.

Results and Discussion

h/h_r for Pt/Nb₂O₅ reduced at various temperatures and Pt/Na/SiO₂ with various loading of sodium are illustrated in Fig. 1. and Fig. 2, respectively. The electron transfer from NbO_x to d-state of Pt increases as the reduction temperature increases. As for Na, however, the number of the electron in d-orbital is constant till the amount of Na reaches that of Pt. Then it is filled with electron gradually. In contrast, the binding energy of Pt4f_{7/2} decreases monotonously. Thus, the shift of Pt4f_{7/2} in the low Na loading region is not suggested to be due to the charge transfer to unoccupied d-state of platinum.

The activation energy of CH₂=CH₂ hydrogenation is well correlated with h/h_r . For example, 8 kJ·mol⁻¹ for 373 K-Pt/Nb₂O₅ (A), 18 kJ·mol⁻¹ for 773 K-Pt/Nb₂O₅ (B), 40 kJ·mol⁻¹ for 0.16-Pt/Na/SiO₂ (C) and 43 kJ·mol⁻¹ for 0.70-Pt/Na/SiO₂ (D).¹⁾ It is strongly suggested that the density of d-state controls the kinetic parameter of C=C hydrogenation.

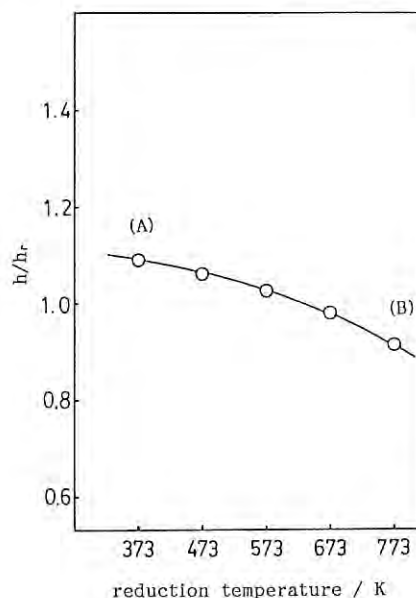


Fig. 1. The number of unoccupied d-state as a function of reduction temperature for Pt/Nb₂O₅.

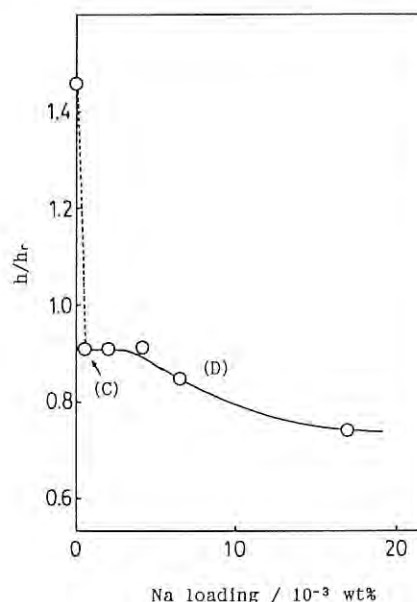


Fig. 2. The number of unoccupied d-state as a function of the amount of Na loading for Pt/Na/SiO₂.

Reference

- [1] H.Yoshitake and Y.Iwasawa, *J.Catal.*, submitted.
- [2] D.E.Resasco and G.L.Haller, *Adv.Catal.*, 1989, 36,173
- [3] A.N.Mansour, J.W.Cook, Jr. and D.E.Sayers, *J. Phys. Chem.*, 1984, 88, 2330.

PHOTO-MODULATED EXAFS

Shuichi EMURA,^{*} Hironobu MAEDA,⁺ Masaru KIMURA,⁺ Setsuo KASHINO,⁺Takatoshi MURATA,[#] and Masaharu NOMURA^{##}^{*}Institute of Scientific and Industrial Research, Osaka Univ., Ibaraki Osaka⁺Faculty of Science, Okayama Univ., Tsushima-naka, Okayama[#]Department of Physics, Kyoto Univ. of Education, Kyoto^{##}Photon Factory, National Laboratory for High Energy Physics, Oho, TsukubaIntroduction

Since recent EXAFS has been initiated by Sayers, Stern, and Lytle and SR light is available, the investigation by EXAFS of condensed matters, liquids, and others is vigorously growing. In recent year, new EXAFS techniques have been tried to exploit the new regions using EXAFS method by a few developers. One of those is an application of a modulation technique to EXAFS measurement, which was successfully used to observe the outer-perturbation response such as the electric and magnetic field, stress (piezo effect) and light irradiation in an ultraviolet, visible, and infrared region in condensed matters. Here, we will present a preliminary report on a photo-modulated EXAFS technique, which will be applied to the structural analysis of the photo-excited state of the condensed matters, liquid, gaseous state of molecule, and is only direct method in observation of it. As the first stage, the excitation behaviors of mercury in a mercury lamp will be shown, and it will be presented that the photo-modulated technique is successfully achieved to examine the photo-excited state in this simple case.

Experimental Methods

The measurements were carried out using the EXAFS facilities at Beam Line 7C. X-ray beam was focused on the specimen by means of sagittal focusing of the monochromator crystal. Figure 1 shows a block diagram for the photo-modulated EXAFS observation. A high pressure mercury lamp (L1) as the sample in this work normally lay between I₀ and I ion chambers. To evaporate the liquid mercury, the lamp was heated. The same mercury lamp (L2) was used as an excitation light-source. The light from the L2 was chopped and focused on the specimen L1. The signals from the I ion chambers were current-amplified and fed to a conventional lock-in amplifier. The intensity of the incident x-rays was monitored by the I₀ ion chamber.

Results and Discussion

We have observed the absorption spectra of x-rays at the four different con-

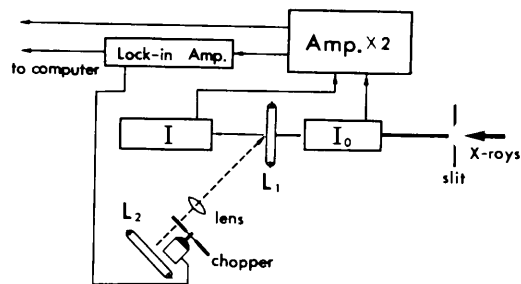


Fig.1. Block diagram of the photo-modulated EXAFS measurement.

ditions of the mercury lamp; 1. in heated state, 2. in discharge at heated state, 3. in discharge only, and 4. in irradiation in the heated state by the mercury lamp. An absorption spectrum in the heated state(1) results from isolated mercury atoms, and the spectrum on the conditions (2),(3), and (4) will contain the absorption from the excimer and other excited states of mercury. This spectrum may involve the EXAFS oscillation due to the excimers. Figure 2 shows the difference of the absorption constant at the conditions (1) and (2). Some oscillations are recognized. Figure 3 shows a photo-modulated spectrum on the condition (4). We can see some structures which coincide with the oscillation of the difference spectrum as indicated with the arrows. We can say that the photo-modulation technique is available to reveal the atomic distances in the photo-excited state.

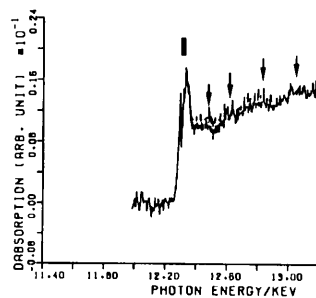


Fig.2. Difference spectrum between the condition (1) and (2).

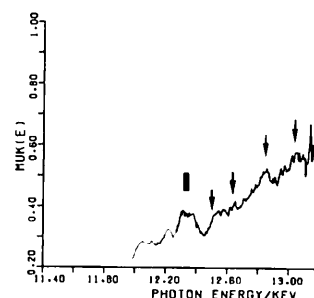


Fig.3. Photo-modulated spectrum on the condition (4).

Reference

- 1) C.G.Olson, D.W.Lynch, D.M.Wieliczka, F.S.Khumalo, and R.J.Bartlett, J.Phys. C. 16 (1983) 3813.

AN EXAFS STUDY OF Cr(III,IV,V)-edta COMPLEXES IN AQUEOUS SOLUTION

Kazuhiko OZUTSUMI, Izumi NAKAI, and Takuji KAWASHIMA

Laboratory of Analytical Chemistry, Department of Chemistry,
The University of Tsukuba, Tsukuba 305Introduction

An oxidative coupling reaction of 3-methyl-2-benzothiazolinone hydrazone (MBTH) with *N,N*-dimethylaniline (DMA) is catalyzed by metal ions and has been applied to the determination of trace amounts of metal ions. The catalytic effect on redox reactions of most metal ions is hindered when ethylenediaminetetraacetic acid ($H_4\text{edta}$) is present in the reaction system. On the other hand, the catalytic action of chromium ion is more pronounced by the presence of edta^{4-} in the system. Thus the catalytic behavior of chromium-edta complexes is different from that of edta complexes with most metal ions. The different action of chromium-edta complexes may be reflected in their structure in solution. In the present study we aimed at determining the structure of chromium(III,IV,V)-edta complexes in aqueous solution.

Experimental

Sample solution 1 was prepared by mixing equivalent of 1.2 mol dm^{-3} $[\text{Co}^{\text{II}}(\text{edta})]^{2-}$ and 0.75 mol dm^{-3} $\text{Cr}_2\text{O}_7^{2-}$ solutions. Sample solutions 2 and 3 were similarly prepared but contained a large excess of $\text{Li}_2\text{H}_2\text{edta}$ and $\text{Na}_2\text{H}_2\text{edta}$, respectively. X-Ray absorption spectra were measured around both the Co and Cr *K*-edges at the BL7C of the Photon Factory, KEK.

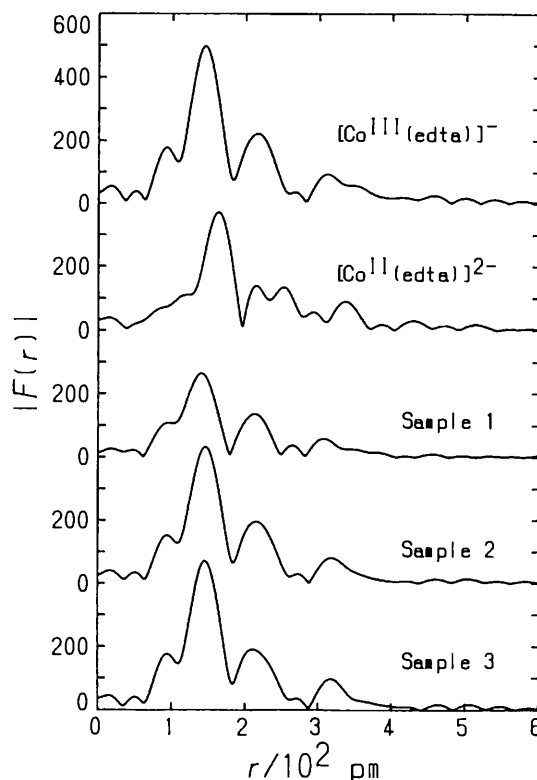
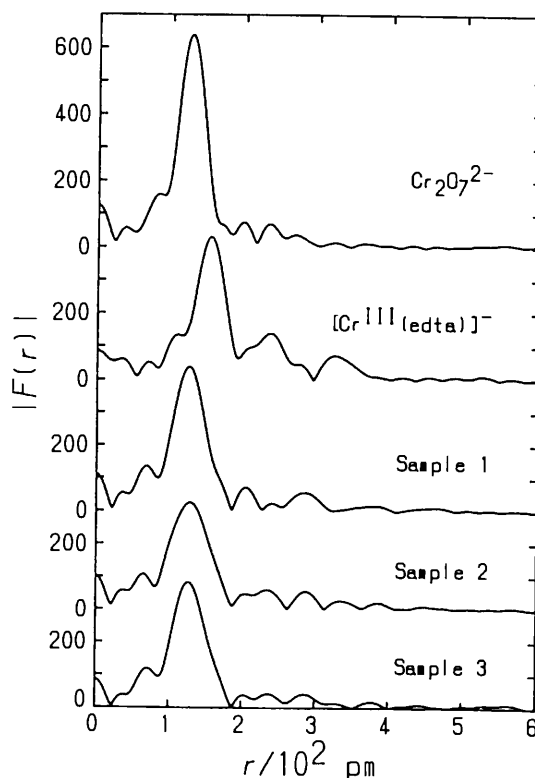
Results and Discussion

In Figs. 1 and 2 are depicted the Fourier transforms of Co and Cr *K*-edge spectra of sample solutions, respectively. The first intense peaks are due to the bonds between cobalt or chromium and ligand atoms in the first coordination sphere.

The Fourier transforms of sample solutions 2 and 3 measured at the Co *K*-edge (Fig. 1) are very similar in shape to that of an aqueous $[\text{Co}^{\text{III}}(\text{edta})]^-$ solution but are completely different from that of an aqueous $[\text{Co}^{\text{II}}(\text{edta})]^{2-}$ solution, while the curve of sample solution 1 differs from that of other solutions examined. Hence, the $[\text{Co}^{\text{II}}(\text{edta})]^{2-}$ complex in sample solutions 2 and 3 is completely oxidized to the $[\text{Co}^{\text{III}}(\text{edta})]^-$ complex by mixing with a Cr_2O_7 solution in the presence of a large excess of $\text{Li}_2\text{H}_2\text{edta}$ or $\text{Na}_2\text{H}_2\text{edta}$.

In the Cr *K*-edge spectra (Fig. 2), the peak maxima of the Fourier transforms appear at 126 and 156 pm for aqueous $\text{Cr}_2\text{O}_7^{2-}$ and $[\text{Cr}^{\text{III}}(\text{edta})]^-$ solutions, respectively. The peaks are observed around 130 pm for all sample solutions and the peak shapes are significantly different from those of aqueous $[\text{Cr}^{\text{III}}(\text{edta})]^-$ and $\text{Cr}_2\text{O}_7^{2-}$ solutions. Thus, the Cr(IV)- or Cr(V)-edta complexes may evidently be formed in sample solutions 1, 2, and 3.

Detailed curve fit analyses for the chromium-edta complexes are now doing.

Fig. 1. Fourier transforms of Co *K*-edge spectra.Fig. 2. Fourier transforms of Cr *K*-edge spectra.

EXAFS STUDIES OF NICKEL(II) AND MANGANESE(II) COMPLEXES OF SOME 2-(POLYHYDROXY-ALKYL) THIAZOLIDINE-4-CARBOXYLIC ACIDS

László NAGY, Seiichi YAMASHITA†, Toshio Yamaguchi†, Hisanobu WAKITA†, and Masaharu NOMURA†

Department of Inorganic and Analytical Chemistry, A. József University, H-6701 Szeged, P.O. Box 440, Hungary

†Department of Chemistry, Faculty of Science, Fukuoka University, Nanakuma, Jonan-ku, Fukuoka 814-01, Japan

‡Photon Factory, National Laboratory for High Energy Physics, Oho-machi, Tsukuba 305, Japan

The reaction of carbonyl compounds with β -amino-thiols, particularly cysteine form of thiazolidine, has been a subject of numerous previous studies because of its relevance to the binding of carbonyl compounds to protein containing sulphhydryl and amino group in close proximity. For this reason equilibrium constants have been measured by pH titration for protonation, zinc(II), nickel(II), manganese(II), iron(III), and silver(I) coordination of some 2-(polyhydroxyalkyl) thiazolidine-4-carboxylic acids (PHTac) in the pH range 1.5-10. It was found that the value of the protonation and formation constants depend on the structure of polyhydroxy-chains. In case of the protonation constants this may be due to the rearrangement of intramolecular hydrogen bonding network, while the formation constants probably depend on the conformation of OH-groups in the first carbon atom of the polyol chains.¹⁾ The above metal complexes formed with PHTac ligands have appeared little suitable for X-ray diffraction experiments because of the difficulties in crystallization. Our aim was therefore to determine the local structure of some of the

complexes. EXAFS spectra at the Ni and Mn K-edges were measured at BL-10B and BL-7C, KEK respectively for the sample given in Tables 1 and 2.

All of the Fourier transforms of nickel(II) complexes have a peak about 170 pm (not corrected for the phase shift), due to Ni-O and Ni-N interactions in the first shell. In addition, there are two well developed peaks, located at 240 and 340 pm. We assumed that these peaks are ascribed to the carbon (second shell) and oxygen, carbon and sulphur (third shell) backscattering atoms. On the basis of the above consideration for the Fourier transform, a multishell curve fitting was performed. The final results of the curve fitting analysis are summarized in Table 1. The proposed structure of manganese(II) and nickel(II) complexes formed with 2-(polyhydroxy-alkyl) thiazolidine-4-carboxylic acid ligands are depicted in Figure 1.

Reference

- 1) T. Gajda, L. Nagy and K. Burger, to be published in Inorg. Chim. Acta.

Table 1. Results of the curve fitting for nickel(II) complexes

Ligand	Interaction	N	r/pm	$\sigma \cdot 10^2/\text{pm}$
NO_3^-	Ni-O	6*	204.5*	7.44
2-phenyl-4-thiazolidine carboxylic acid pH = 6.0	Ni-O,N	6	202.7	8.74
	Ni...C	6*	284.3	11.14
	Ni...O,C,S	8*	395.4	15.06
L-cysteine-D-galacturonic acid	Ni-O,N	6.1	202.7	7.78
	Ni...C	6*	288.3	6.90
	Ni...O,C,S	8*	390.9	12.8
L-cysteine-L-rhamnose	Ni-O,N	5.9	199.4	8.58
	Ni...C	6*	287.8	9.62
	Ni...O,C,S	8*	370.6	13.8
L-cysteine-L-arabinose	Ni-O,N	6.2	202.0	8.11
	Ni...C	6*	288.3	7.27
	Ni...O,C,S	8*	395.1	13.4
L-cysteine-D-arabinose	Ni-O,N	6	202.0	9.06
	Ni...C	6*	284.7	9.47
	Ni...O,C,S	8*	399.6	16.69

* fixed

Table 2. Results of the curve fitting analysis for manganese(II) complexes

Ligand	Interaction	N	r/pm	$\sigma \cdot 10^2/\text{pm}$
Acetylacetonate	Mn-O	6*	211.9	8.84
Acetate	Mn-O	6*	215.5	7.87
2-phenyl-4-thiazolidine carboxylic acid	Mn-O,N	6	213.0	8.39
	Mn...C	6*	305.7	11.41
	Mn...O,C,S	8*	375.6	14.46
L-cystein-D-galacturonic acid	Mn-O,N	4.5	214.0	7.81
	Mn...C	6*	309.2	14.06
	Mn...O,C,S	8*	368.7	18.23
L-cystein-D-rhamnose	Mn-O,N	6.3	215.0	9.64
	Mn...C	6*	305.6	9.76
	Mn...O,C,S	8*	369.3	18.86
L-cystein-L-arabinose	Mn-O,N	6.6	220.0	10.12
	Mn...C	6*	325.6	10.13
	Mn...O,C,S	8*	397.0	20.62
L-cystein-D-arabinose	Mn-O,N	5.7	216.0	9.44
	Mn...C	6*	302.6	10.94
	Mn...O,C,S	8*	373.1	18.55

* fixed

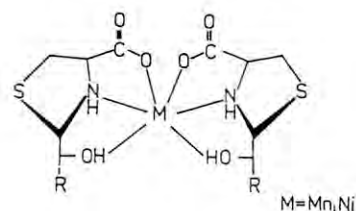


Figure 1

STRUCTURE STUDIES ON Cr/ZrO₂ CATALYST BY XAFS

Takashi USHIKUBO, Naoko MATSUYAMA, Toshiharu YOKOYAMA, Takao MAKI,
Toshio AKAI, Yasuo KOIKE, Konoe MIURA and Keisuke WADA

Research Center, Mitsubishi Kasei Corporation,
1000 Kamoshida-chou, Midori-ku, Yokohama 227

Introduction

Recently, zirconium oxide has been attracted much attention as catalysts for various kinds of reactions. Not only hydrogenation of olefins, carbon monoxide, and carboxylic acids, but also the acid-promoted reactions, such as isomerization of olefins and acylation of aromatic compounds, were extensively studied in the presence of zirconium oxide. In order to improve the catalytic performance, several studies have been carried out on the modification of zirconium oxide.

It was found that chromium was one of the effective additives for ZrO₂ catalyst. In order to investigate the effect of Cr on the catalysis, we attempted to reveal the local structure and the electronic environment around Cr atoms on ZrO₂ by using XAFS.

Experimental

The catalysts studied in this report were (a) Cr/ZrO₂ (Cr 2 wt%; via impregnation of chromium nitrate aq. solution on ZrO(OH)₂, dried and calcined), (b) (a) treated by hydrogen at 350 °C. Furthermore, (c) Cr (metal), (d) Cr₂O₃, (e) CrO₂ and (f) CrO₃ were analyzed as standard samples. The Cr K-edge XAFS data of these catalysts were obtained at EXAFS apparatus (BL-7C).

Results and Discussion

Figure 1 shows the Cr K-edge XANES for the samples. In the samples (a) and (f), Cr 1s→3d transition was clearly observed. On the other hand, the transition in the samples (b), (d) and (e) was not so clear. These results suggest that Cr⁶⁺ (highly oxidized) species existed in the sample (a) and Cr³⁺ species existed in the sample (b), that was confirmed by XPS analysis.

Figure 2 shows the results of Fourier transform of the EXAFS data for the samples. For the catalyst (a) (before hydrogen treatment), a CrO₃ like structure existed on ZrO₂. On the other hand, in the catalyst (b) (after hydrogen treatment of (a)), the pattern of the Fourier transform was similar to that of Cr₂O₃, the atomic distances of Cr-O and Cr-Cr were smaller than those in Cr₂O₃, however. Furthermore, in the catalyst (b) the coordination number of Cr-Cr was smaller than that in Cr₂O₃, that was ascertained by the results of curve-fitting analyses. These results imply that a Cr₂O₃ like structure appeared by the hydrogen treatment, and the Cr species were highly dispersed on ZrO₂. The more detailed investigations about the structure and physicochemical properties are in progress.

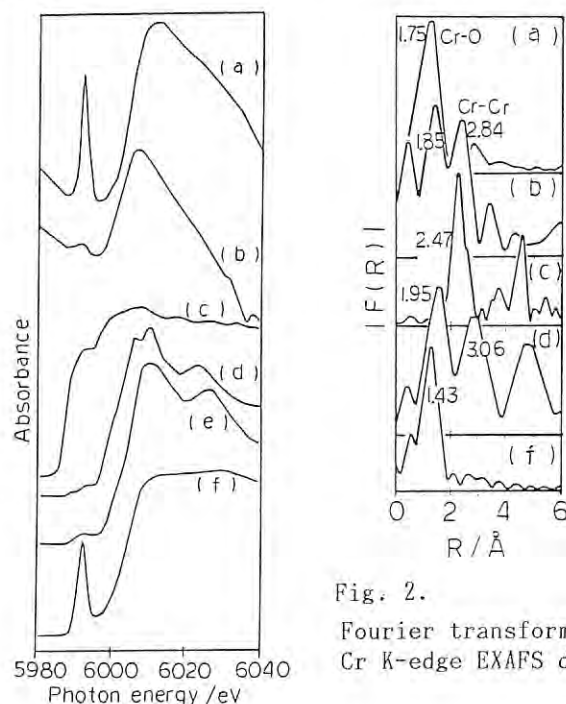


Fig. 1. XANES spectra.
Fig. 2. Fourier transform of Cr K-edge EXAFS data.

- | | |
|--|------------------------------------|
| (a) Cr/ZrO ₂
(before hydrogen treatment) | (c) Cr (metal) |
| (b) Cr/ZrO ₂
(after hydrogen treatment) | (d) Cr ₂ O ₃ |
| | (e) CrO ₂ |
| | (f) CrO ₃ |

Kiyoshi Ogata, Akira Tsuchiyama*, Asao Nakano and Kichiro Koto**

Production Engineering Research Laboratory, Hitachi, Ltd., Totsuka-ku, Yokohama 244

* Dep. of Geology and Mineralogy, Faculty of Science, Kyoto Univ., Sakyo-ku, Kyoto 606

** Dep. of Materials Science, Faculty of Integrated Arts and Sciences, Tokushima Univ., Minami-Josanjima, Tokushima 770

Introduction

Silicon k-edge XAS of some silicates were measured by using X-ray (1.7–14 keV) beam line for EXAFS at BL-8B. Structural studies of amorphous silicates are significant for both semiconductor technology and earth and planetary sciences. Very thin films of silicon oxides are used as insulator in LSI and silicates are the most common materials on a surface of the earth.

Meanwhile there are few reported XAS spectra of silicates because there is no beam line which is continually available for Si k-edge XAS except BL-8B, so it is necessary to measure many Si containing materials for references.

Experimental

Instrument Using a double crystal (InSb(111)) monochromator, XAS spectra from 1780 to 2800 eV were measured with an energy resolution of about 0.3 eV. Intensities of incident beam were detected by an ionization chamber and fluorescent yields were measured by Si(Li) detector which is set in the direction horizontally normal to the incident beam. The SSD has three semiconductor elements in a same chamber and each detector (80 mm²) has independent detection system to decrease a dead-time at higher count rate.

Sample α -quartz (SiO_2), SiO_2 glass, forsterite (Mg_2SiO_4) and the amorphous silicate were prepared for XAS measurements. The amorphous silicate was synthesized from gas with Mg-rich olivine ($(\text{Mg}_{0.9}\text{Fe}_{0.1})_2\text{SiO}_4$) composition at low pressures ($\sim 10^{-5}$ Torr)¹⁾ as an analogue for cosmic dusts.

The adequate film thickness for Si XAS measurement is about 2 μm , so the bulk samples of the silicates were grinded to powders and applied on a sample holder which is made of a diamond single crystal (about 80 mm²).

Results

Differential XAS spectra of the silicates are shown in Fig. (left). The energy at the maximum differential value (the absorption edge) of the α -quartz (a) is about 1848 eV. A silicon atom in α -quartz is coordinated to four oxygen atoms, so the peak is assigned to Si(IV)-O. The peak is 8 eV above the peak of Si-Si in pure silicon. In the case of forsterite (c), the SiO_4 tetrahedra are isolated and bound to each other only by ionic bonds from interstitial magnesium and the observed peak energy is about the same as α -quartz.

The peak value of the amorphous silicate (d) is similar to that of forsterite. However, there is no complex structure in (d).

The KL-edge absorption reported by Filipponi et al.²⁾ was subtracted from the observed EXAFS spectra and the Fourier transforms of the spectra are shown in Fig. (right). The first peaks of the transforms are assigned to Si-O bonds.

Precision of fluorescent XAS measurement is less than transmission mode because counting errors of SSD are larger than that of the ionization chamber and an inhomogeneity of the applied powders causes large statistical errors.

References

- 1) Koike, C. & Tsuchiyama, A., Grain Formation Workshop, X, 54 (1989)
- 2) Filipponi, A. et al., Phys Rev B38, 3298 (1988)

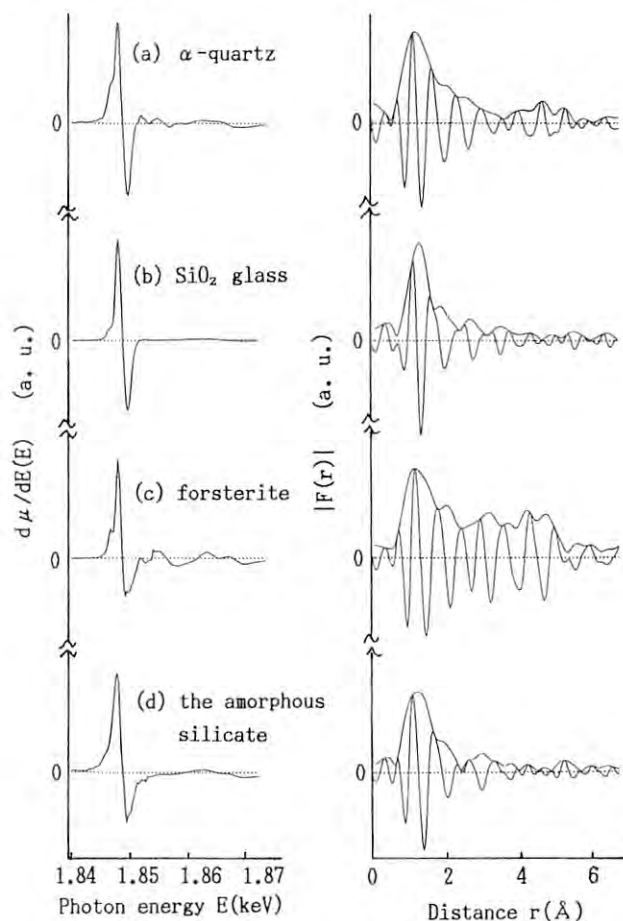


Fig. Differential XAS spectra (left) and the Fourier transforms (right) of the samples

Structure Studies of Amorphous Silicon Nitrides by Si-K-edge EXAFS

Asao Nakano, Kiyoshi Ogata and Masahiro Tanaka

Production Engineering Research Laboratory, Hitachi, Ltd.,
Totsuka-ku, Yokohama 244, Japan.

1. INTRODUCTION

The structure studies of amorphous thin films of the silicon compounds are indispensable for research works on the semiconductor devices¹⁾. We have carried out this work on the thin films of silicon nitrides using BL-8B.

2. Experiments and Results

The lattice constant of the monochromator crystal and the angle of diffraction are calibrated by the Si, P and S-K absorption edges using a disk of the mixture. Calculated energy resolution of BL-8B is 0.34eV at the Si-K-absorption edge (1.84keV).

Powders of the standard β - Si_3N_4 crystalline samples are ground and mounted on a diamond plate to measure fluorescent yields. Silicon nitride thin films are prepared by Low Pressure-CVD method on the silicon wafer and Electron Cyclotron Resonance-CVD method on the Kapton film with thickness of 7.5 μm . The thickness of the thin film sample is adjusted about 1 μm . Measured EXAFS spectra of the thin films prepared by LP- and ECR-CVD methods are shown in Fig.1. The differential profiles, $d\mu(E)/dE$, shown in Fig.2, are different between the thin films prepared by LP-CVD and ECR-CVD. The profile of ECR-CVD thin film is almost same as the standard β - Si_3N_4 sample.

The measured EXAFS spectra are analyzed through the conventional method. The radial structure functions are calculated and the results are shown in Fig.3. There are slight differences in the atomic distance of the second shell between the thin films formed by LP-CVD and ECR-CVD. The atomic distance of second shell of the ECR-CVD is slightly longer than that of LP-CVD.

3. SUMMARY

The differences of the $d\mu(E)/dE$ spectra between LP-CVD and β - Si_3N_4 might indicate the difference of composition, because the existence of the lower energy of absorption edge caused by Si-Si bond (1.84keV). The profile of ECR-CVD is almost same as those of the stoichiometric standard samples of β - Si_3N_4 crystalline. But it is well known that thin films formed by ECR-CVD involves hydrogen and Si- bonds are terminated H or N.²⁾

The difference between the atomic distance of the second shell indicates the difference of

the short range structure. The second nearest neighbour of crystalline phase is Si-Si. The average length of the Si-Si is 2.92 \AA for α - Si_3N_4 and 3.00 \AA for β - Si_3N_4 . Short range structures of the amorphous silicon nitride films formed by LP-CVD and ECR-CVD resemble to α - and β - Si_3N_4 phases, respectively.

4. REFERENCE

- 1) A.Nakano, K.Ogata and M.Tanaka: Extended Abstracts of the 21st Conference on Solid State Devices and Materials, Tokyo, 1989, pp.513-516.
- 2) W.A.Lanford and M.J.Rand: Journal of Applied Physics 49(4) 1978, 2473

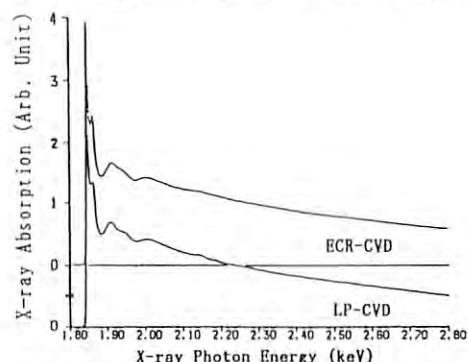


Fig.1 EXAFS of Silicon Nitride Thin Films

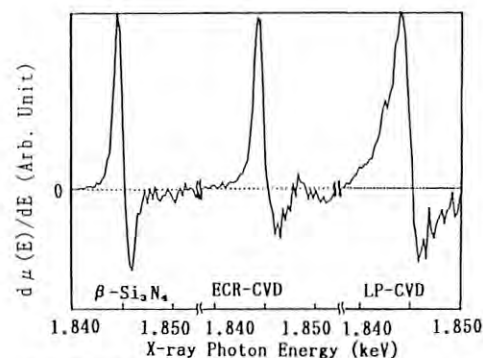


Fig.2 Differential Profiles of Si-K Edge

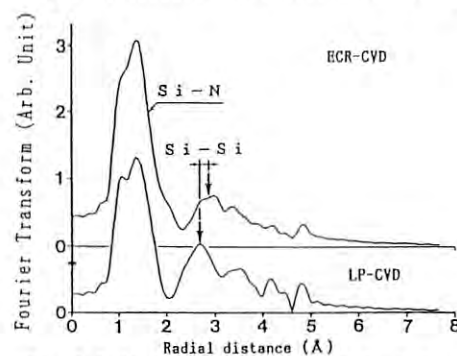


Fig.3 Radial Distributions of Si-N Films

EXAFS STUDIES ON THE REACTION MECHANISM OF Rh DIMER SPECIES.

Kiyotaka ASAKURA, Kyoko KITAMURA-BANDO, and Yasuhiro IWASAWA
Department of Chemistry, Faculty of Science, the University of Tokyo,
Hongo, Bunkyo-ku, Tokyo 113, Japan.

In order to understand the catalysis of the surface on a molecular level, it is important to accumulate the knowledge about the dynamic structure of surface in a working state. EXAFS spectra offers potential for probing the surface structure of the catalysts in the working conditions.

A reversible CO insertion reaction into C_2H_5 ligand to form acyl group was found on the SiO_2 -attached Rh dimer 1 catalyst derived from the organometallic complex $Rh_2(CH_3)_2(C_5(CH_3)_5)_2(\mu-CH_2)_2$ 0 using the reaction with the surface OH of SiO_2 . Our previous IR spectra showed that the SiO_2 -attached Rh dimer 1 adsorbed twin type CO. At this time two CO adsorbed on one Rh dimer. Thus the one Rh of Rh dimer adsorbed two CO. After the evacuation, IR spectrum showed the formation of acyl group, indicating the occurrence of the CO insertion reaction. When the sample was exposed to CO atmosphere, the acyl group was decomposed to C_2H_5 and CO. The CO insertion reversibly occurs after another evacuation of the sample.

The CO insertion reaction proceeds under a quite unusual condition. Usually the CO insertion reaction favorably occurs in high pressure of CO. We examined local structure of Rh dimer in a working state to get the clue to this question.

Experimental

Rh dimer catalyst 1 is prepared using the reaction between the complex 0 and surface OH groups of SiO_2 (Aerosil 300) pretreated at 673 K. The sample was treated and reacted in the glass-made in-situ EXAFS measurement cell. EXAFS analysis was carried out using the EXAFS analysis program "EXAFS2"¹⁾.

Results and Discussion

Fig.1 showed the Fourier transform of the Rh dimer after the exposure to CO atmosphere. Two peaks appeared in the range of 0.1-0.3 nm. The second peak might arise from the Rh-Rh distance or Rh---O(carbonyl). We carried out the curve fitting analysis assuming both model structure. We obtained a good fitting results when we assumed the bonding is due to Rh---O as shown in Fig.2. Fig.3 showed the Fourier transform of the Rh dimer subsequently after the evacuation of the sample at 473 K. Similarly two peaks appeared. However, the second peak arise from the Rh-Rh interaction as a result of curve fitting analysis as shown in Fig.4. Thus the Rh-Rh interaction was regenerated after the evacuation. This

Rh-Rh distance was cleaved after another introduction of CO and was reversibly regenerated after the subsequent evacuation. Thus the CO insertion and Rh-Rh bond formation concurred. The CO insertion reaction generally occurs when the ligand occupies the vacant site left after the CO insertion. In this case one Rh acts as a ligand for the other Rh and thus it can be said the CO insertion reaction occurs in the assistance of the Rh-Rh bond formation.

1) N. Kosugi and H. Kuroda, EXAFS analysis program "EXAFS 2".

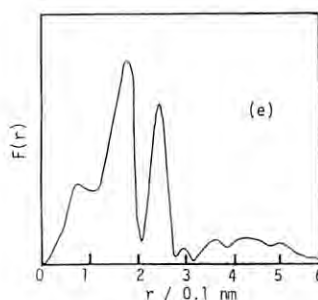


Fig.1 Fourier transform of Rh dimer attached on SiO_2 with CO adsorbed on it.

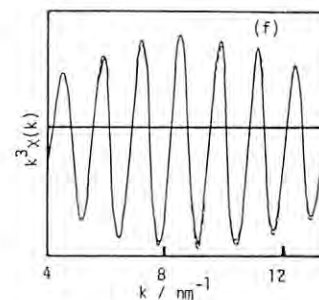


Fig.2 Curve fitting for the second shell. (○) observed; (—) calculated based on Rh---O

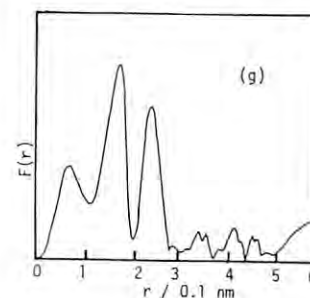


Fig.3 Fourier transform of Rh dimer attached on SiO_2 after evacuation of the CO pre-adsorbed Rh dimer.

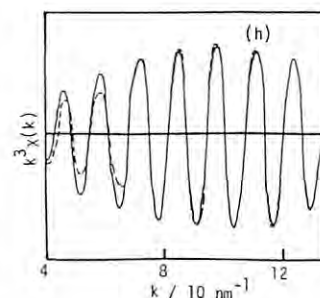


Fig.4 Curve fitting analysis for the second shell of the Fig.3. (—) observed; (---) calculated based on Rh-Rh

The structure analysis of Ag_3AsS_3 glass by EXAFS measurement

Masayuki OKUNO, Hideyuki SUGAYA, Takeo MATSUMOTO, Kuniaki KIHARA, Tsuyoshi MOTOYAMA
Hiroki OKUDERA and Hiroto ANDO

Department of Earth Sciences, Faculty of Science, Kanazawa University, Kanazawa 920, Japan

Introduction

Ag_3AsS_3 crystal (proustite) is an important ore mineral of the silver. The crystal structure consists of AsS_3 trigonal pyramid groups and Ag atoms link the groups. Recently, Yoshiasa (1989) measured the ionic conductivity of this crystal and showed the high ionic conductivity is sufficient as superionic conductor. Therefore, the glass phase of this crystal also arouse interested in its ionic conductivity. We measured EXAFS spectra on the As K and Ag K absorption edges for a Ag_3AsS_3 glass and Ag_3AsS_3 crystal, and compared the spectra to analyse the structure of the glass in details. Further, we measured the spectra for Ag edge at 300K and 80K to examine the temperature dependence of the disorder parameter of the glass.

Results and Discussion

The detailed experimental conditions were reported in the previous work (Okuno et al., 1989). Fig.1 presents the $|F(r)|$ curves for As and Ag atoms of Ag_3AsS_3 glass and the crystal. The prominent peaks of the $|F(r)|$ curves correspond to the As-S atomic pairs within AsS_3 groups and Ag-S atomic pairs. The peaks of As-S atomic pairs in the glass and the crystal have similar features. The Ag-S in the both phases have similar atomic distances, however, the peak height of the glass is about only 40% of that of the crystal. These facts suggest that the glass has rather random distribution of Ag atoms around AsS_3 groups.

We studied the glass and crystal structures in detail by the parameter fitting method. The As-S and Ag-S atomic distances, and Debye-Waller type factors ($\delta^2_{\text{As-S}}$ and $\delta^2_{\text{Ag-S}}$) were determined (table 1). The As-S atomic distance and $\delta^2_{\text{As-S}}$ of the glass are similar to those of the crystal. However, Ag-S atomic distance of the glass at 80K is larger a little than the others. And the $\delta^2_{\text{Ag-S}}$ of the glass is much larger than that of the crystal and its thermal change is also large. Because of the small difference between the $\delta^2_{\text{As-S}}$ in the glass and crystal, it is supposed that this large difference of $\delta^2_{\text{Ag-S}}$ results from the random distribution and large thermal vibration of Ag atoms in the glass.

The square of the total Debye-Waller type factor (δ^2_{total}) is expressed by the sum of the square of the static part (δ^2_{static}) and the thermal part ($\delta^2_{\text{thermal}}$). By extrapolation of δ^2 's at 80K and 300K to 0K, we can estimate the values of δ^2_{static} and $\delta^2_{\text{thermal}}$. Table 2 lists the results. The δ^2_{static} and $\delta^2_{\text{thermal}}$ of Ag-S pairs in the glass are larger than those of the crystal. This large $\delta^2_{\text{thermal}}$ of the glass suggests the possibility of high ionic conductivity by Ag atoms, though the distribution of Ag atoms is rather random.

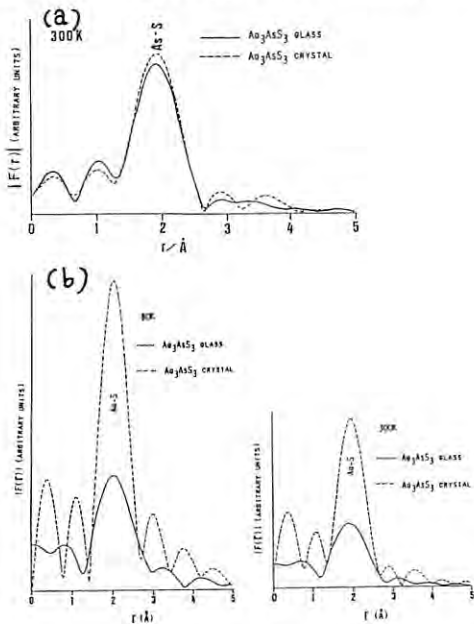


Fig.1 The $F(r)$ curves for (a) As and (b) Ag atoms in the Ag_3AsS_3 glass and the crystal at 80K and 300K.

Table 1 Parameters of Ag_3AsS_3 crystal and glass at 80K and 300K obtained by parameter fitting method.

specimen		$r_{\text{As-S}}(\text{\AA})$	$r_{\text{Ag-S}}(\text{\AA})$	$\delta^2_{\text{As-S}}(\text{\AA}^2)$	$\delta^2_{\text{Ag-S}}(\text{\AA}^2)$
Ag_3AsS_3 crystal	80 K	-----	2.450(1)	-----	0.0132
	300 K	2.254*	2.446*	0.0165	0.0166
Ag_3AsS_3 glass	80 K	-----	2.488(2)	-----	0.0191
	300K	2.254(1)	2.449(1)	0.0173	0.0237

* Engel and Nowacki(1965)

Table 2 The estimated static and thermal parts of $\delta^2_{\text{Ag-S}}$ parameters.

Specimen	Static part $\delta^2_{\text{static}}(\text{\AA}^2)$	Thermal part $\delta^2_{\text{thermal}}(\text{\AA}^2)$
Ag_3AsS_3 crystal	0.0120	80 K 0.0012
		300 K 0.0046
Ag_3AsS_3 glass	0.0174	80 K 0.0017
		300 K 0.0063

References

- 1) A.Yoshiasa, Mineral. J. 14, 293 (1989)
- 2) M. Okuno, H. Sugaya, T. Matsumoto, T.Motoyama, H. Okudera and H. Ando, PF Activity Report 1988 #6, 44 (1989)

EXAFS AS A PROBE TO THE CRYSTALLIZATION OF ALUMINOSILICATE GELS

John B. PARISE*, David R. CORBIN** and Izumi NAKAI***

* Department of E.S.S., State University of New York, Stony Brook, NY 11794 USA

** E.I. DuPont, Wilmington, DE 19880 - 0356, USA

*** Department of Chemistry, University of Tsukuba, Ibaraki, 305

Introduction

Zeolites, crystalline aluminosilicate framework structures, contain cavities into which water and cations may be exchanged. They are traditionally synthesized[1] by heating an alkaline aluminosilicate gel. More recently, quaternary ammonium salts and ternary amines have been included in preparations[2]. The role of the alkali metals in the starting gels for aluminosilicate systems from which the zeolitic framework crystallizes is primarily one of providing charge compensation. Observations of the final crystal structures[3] have suggested a structure directing or templating role for the added amines or alkali metals. For example, without the amines, only dense phases form in the open-framework aluminophosphate system where charge compensation is not required. Further, shape effects are observed with the pore and channel system bearing some resemblance to the original molecular template. Direct observation of a templating mechanism requires the development of techniques to study crystallizing gels in order to determine if some organization occurs around the alkali metal or amine prior to the establishment of long range order (crystallization).

We have followed the formation of a zeolite from a Rb/Na aluminosilicate gel using X-ray diffractometry and Extended X-ray Absorption Fine Structure (EXAFS) at the Rb edge. Since EXAFS is sensitive to short range order, this technique allows us to follow changes occurring in the vicinity of the rubidium ion prior to the onset of long range order where traditional X-ray diffractometry allows the ready identification of the zeolite structure formed.

Experimental

The gel mixture was prepared as follows: Colloidal silica (360 cc Ludox LS-30) was added to a mixture of 4 M sodium aluminate (100 cc), NaOH (16g), and 50% RbOH (25.5 cc) and shaken thoroughly. The resulting gel was placed in an oven at 100°C and sampled periodically. Part of each sample was frozen at about -5°C and sampled periodically. Part of each sample was frozen at about -5°C and transported in dry ice for EXAFS data collection. The remainder was used for X-ray diffractometry (Figure 1a). The resulting fully crystalline zeolite was identified as zeolite T[4]. EXAFS data were collected at room temperature at the photon factory at BL-10B.

Results and Discussion

The data were corrected for background[5] and the Fourier transform (FT) were taken (Figure 1b). The FT represents a radial distribution (RDF) of atomic environments around the absorbing atom. Although there is no evidence of crystallinity after 5 days in the X-ray diffraction pattern (Figure 1a), a second shell feature is evident in the RDF. This feature is more prominent in the fully crystallized material and judging from the height of this peak (at around 3Å in the RDF shown in Figure 1b) represents the silicon coordination shell around rubidium in the fully crystallized zeolite. It should be born in mind that positions of peaks in the RDF are shifted towards lower radial distance due to the neglect of the effects of phase shift due to backscattering and absorbing atoms. The deviation of absolute values of radial distance requires the employment of well characterized standard materials[6]. However insight into the mechanism of sol-sol transformation in zeolitic materials[7] has been gained by comparing the shifts in peaks in the RDF in crystalline and X-ray amorphous materials.

Similar comparison here shows that organization is occurring around rubidium prior to the full crystallization of the gel, as evidenced by the presence of peaks in the RDF attributable to a second shell composed of silicon and aluminum atoms. This shell, present in the crystalline zeolite, is also present in the amorphous zeolite after only two days of hydrothermal treatment.

In these experiments rubidium was chosen

primarily for the relative ease with which data close to its X-ray absorption edge could be collected. It is planned to extend these studies to other systems; in particular, to systems in which gel aging at room temperature has a dramatic effect on the phases formed after hydrothermal treatment. This is certainly the case for the Cs/Na/Al/Si/O system, zeolite Rho[8]. Obviously, the study would benefit from the ability to perform experiments in situ on heated gels.

Conclusion

Analysis of EXAFS data collected on a series of crystallizing rubidium/sodium alkali aluminosilicate gels has supported the intuitive notion that hydrated ions organize secondary coordination shells about them prior to the assembly of these units, into zeolitic frameworks.

R.W. Nickle is acknowledged for technical assistance.

References

- 1) D.W. Breck "Zeolite Molecular Sieves", J. Wiley & Sons, New York (1974).
- 2) R.T. Argauer et al., US Patent 3, 702, 886 (1972); M.K. Rubin, et al., US Patent 4 151 189 (1979).
- 3) For example: G.D. Price, et al., Nature 1981, 292, 818; J.M. Bennet, In "Intrazeolite Chemistry", G.D. Stucky and F.G. Dwyer, Eds.; American Chemical Society: Washington, D.C.; p. 110; J.B. Parise, J. Chem. Soc., Chem. Commun., 1985, 606; J.B. Parise, Inorg. Chem. 24, 4312 (1985).
- 4) D.W. Breck et al., US Patent 2 950 952 (1960).
- 5) J.W. Cook, Jr. et al., J. Appl. Phys. 52, 5024 (1981).
- 6) P.A. Lee, et al., Rev. Mod. Phys. 53, 769 (1981).
- 7) J.B. Parise et al., Mat. Res. Bull. 1989, 24, 303.
- 8) H.E. Robson, US Patent 3, 904, 738 (1975).

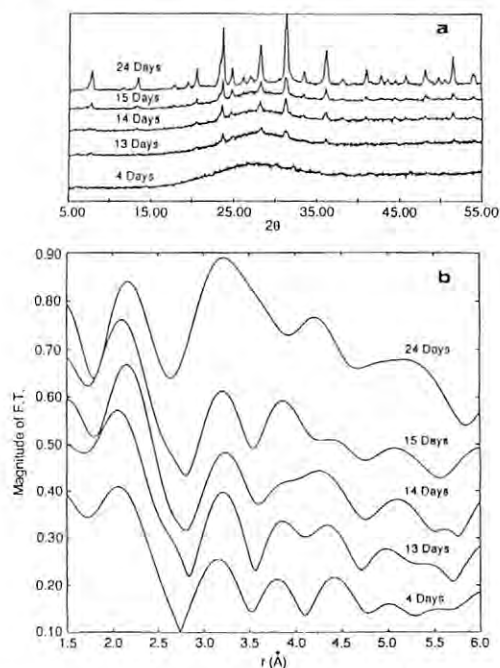


Figure 1. (a) X-ray diffraction patterns taken of Rb/Na-aluminosilicate gel after hydrothermal treatment for the number of days given. (b) The Fourier transform of the EXAFS. The peaks near 2.2Å and 3.2Å correspond to Rb-O and Rb-Si nearest neighbors, respectively. Those features present in the crystalline material (Figure 1a) are also present in the amorphous gels.

RELATION BETWEEN SUPERCONDUCTING TRANSITION AND THERMAL VIBRATIONS IN $\text{YBa}_2\text{Cu}_3\text{O}_{7-\delta}$ COMPOUNDS

Hitoshi YAMAZAKI, Kokichi OSHIMA, Hironobu MAEDA,* Hiroshi MARUYAMA, Michinobu MINO, Akihisa KOIZUMI, Hisashi KOSAKA, Hidekazu KIMURA, Manabu FUJITA and Seitaro MITSUDO.

Department of Physics, Faculty of Science, Okayama University,

* Department of Chemistry, Faculty of Science, Okayama University,
3-1-1 Tsushima-Naka, Okayama 700.

INTRODUCTION

It is very interesting to examine the relation between superconducting transition and thermal vibrations in the oxide superconductors. The thermal vibrational contribution to the EXAFS is usually characterized by mean square relative displacement (MSRD) σ^2 . If there exists any anomalous softening of the longitudinal phonons concerned with Cu-O bonds, it should be observable in the temperature dependence of the Cu-O MSRD. Although several groups tried the temperature dependent EXAFS measurements, they have reached conflicting conclusions; some groups^(1,2) found no significant anomaly at T_c , other ones^(3,4) observed an anomalous increase of σ^2 in the vicinity of T_c . In order to clear up this discrepancy, we have carried out in detail the temperature dependent EXAFS measurements and analyzed the MSRD due to local vibrations of the nearest neighbor Cu-O pairs.

EXPERIMENTAL

The $\text{YBa}_2\text{Cu}_3\text{O}_{7-\delta}$ compounds of two orthorhombic phases (ORTHO-I, ORTHO-II) and tetragonal phase (TETRA) were synthesized by the conventional procedures. La_2CuO_4 and CuO were also prepared as reference material. The transition temperature was determined by resistance or magnetic susceptibility measurements. The ORTHO-I and ORTHO-II samples have an onset T_c of 91.7 and 58K, respectively. The TETRA and La_2CuO_4 samples are non-superconducting.

X-ray absorption measurements were performed using the facility of BL-10B. Energy scanning was carried out around the Cu K-edge in the temperature range from 20 up to 300K. According to the crystal structure of the ORTHO-I phase, the Cu-O bonds consists of five kinds of interatomic distances concerning two inequivalent Cu atoms. Since three distances of Cu(1)-O(1), Cu(2)-O(2) and Cu(2)-O(3) with the a-b plane are very close, we treat the averaged distance of them as the equatorial bond length Cu-O_e. Consequently, the following parameters are determined by three-shell fitting; Cu(1)-O(4), Cu(2)-O(4) and Cu-O_e distances, and σ_a^2 of Cu-O_e bond and σ_b^2 averaged value of MSRD of Cu(1)-O(4) and Cu(2)-O(4) bonds.

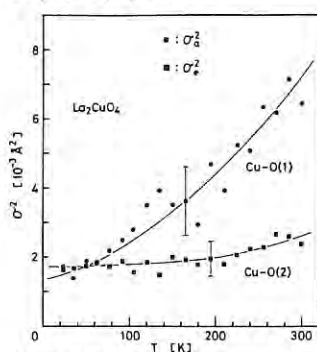


(Fig.1)

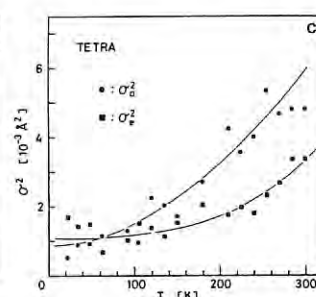
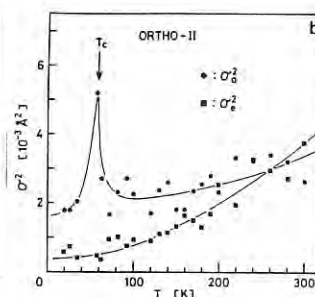
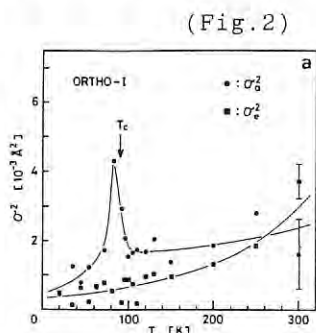


(Fig.2)

RESULTS AND DISCUSSION

The temperature dependence of MSRD σ^2 obtained on the assumption that the coordination number of Cu atoms does not change with temperature is shown in Figs. 1 and 2(a)-(c). For the reference sample La_2CuO_4 , both σ_a^2 and σ_b^2 gradually decrease with decreasing temperature (Fig.1). The temperature dependence of σ^2 for the three phases of $\text{YBa}_2\text{Cu}_3\text{O}_{7-\delta}$ is shown in Fig.2(a)-(c). The axial component σ_a^2 of the Cu-O bonds in ORTHO-I phase indicates a remarkable anomaly in contrast with the result of La_2CuO_4 . This anomalous behavior of σ_a^2 (hereafter referred to as σ -anomaly) is observable only in the temperature region of about 30 degrees around T_c . On the other hand, the equatorial component σ_e^2 shows a normal behavior without any significant anomaly. Similarly in ORTHO-II phase, the σ -anomaly occurs in σ_a^2 at temperature around $T_c \sim 58\text{K}$, but the equatorial component σ_e^2 varies normally with temperature. The σ_a^2 and σ_e^2 of TETRA phase decrease monotonically with decreasing temperature down to 20K, which is just similar to those of La_2CuO_4 . This σ -anomaly is considered to result from some softening of the vibrations of Cu-O bonds, accompanied with the superconducting transition. The important thing is that the σ -anomaly is observed only in the axial component of the MSRD σ_a^2 , related to the Cu(1)-O(4) and Cu(2)-O(4) pairs. Details have been published in Ref.(5).

REFERENCES

- (1) C.Y. Yang, S.M. Heald, J.M. Tranquada, A.R. Moodenbaugh and Y. Xu: Phys. Rev. B38 (1988) 6568.
- (2) J.B. Boyce, F. Bridges, T. Claeson and M. Nygren: Phys. Rev. B39 (1989) 6555.
- (3) H. Maeda, N. Bamba, A. Koizumi, Y. Yoshikawa, T. Ishii, H. Maruyama, M. Hida, Y. Kuroda, H. Yamazaki and T. Morimoto: Jpn. J. Phys. Soc. Jpn. 56 (1987) 3413.
- (4) E.D. Crozier, N. Alberding, K.R. Bauchspiess, A.J. Seary and S. Gyax: Phys. Rev. B36 (1987) 8288.
- (5) H. Maruyama, T. Ishii, N. Bamba, H. Maeda, A. Koizumi, Y. Yoshikawa and H. Yamazaki: Physica C160 (1989) 524.

CHEMICAL SHORT RANGE ORDER IN LIQUID Rb-Se ALLOYS

Hirohisa ENDO, Makoto YAO, Masanori INUI*, Yoshinori KATAYAMA, and Kenji MARUYAMA

Department of Physics, Faculty of Science, Kyoto University, Kyoto 606

Kozaburo TAMURA, Shinya HOSOKAWA, and Tadashi MATSUOKA

Faculty of Integrated Arts and Sciences, Hiroshima University, Hiroshima 730

Hideoki HOSHINO

Faculty of Education, Hirosaki University, Hirosaki 036

INTRODUCTION

The structure of liquid Se is mainly determined by long polymeric chain molecules with two-fold coordination. The viscosity of liquid Se is reduced drastically by the addition of alkali metals because of the scission of the polymeric chains. It is interesting to study the modification of the polymeric chain molecules by the addition of Rb. In this paper we report the results of EXAFS experiments for liquid Se-Rb mixtures.

EXPERIMENTAL

Rb-Se alloys were prepared by exposing liquid Se to Rb vapor at 400 °C in a pyrex tube. The EXAFS cell for liquid samples was made of polycrystalline sapphire with X-ray windows 250 μm thick. The optimum values of the sample thickness were from 30 to 50 μm . EXAFS measurements were carried out on both Se and Rb K-edges with spectrometer installed at BL10B.

RESULTS and DISCUSSION

Figure 1 shows the radial distribution functions around a central Se atom, $|F(r)|$, for

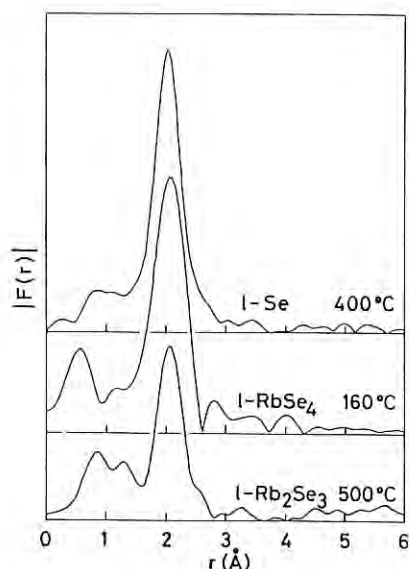


Fig.1 Radial distribution functions around a central Se atom, $|F(r)|$, for l-Se at 400°C, l-RbSe₄ at 160°C, and l-Rb₂Se₃ at 500°C deduced from Fourier transform of k times EXAFS function.

liquid (l-) Se, l-RbSe₃, and l-Rb₂Se₃ deduced from Fourier transform of k times EXAFS function. The sharp first peak in the $|F(r)|$ remains in higher Rb concentration range, which suggests the existence of the two-fold coordinated Se chains.

Figure 2 shows concentration variation of the Se-Se and Rb-Se nearest neighbor distances obtained from curve fit analysis. The Se-Se distance is estimated to be 2.34 Å for l-Se at 400 °C and changes little with increasing Rb concentration. On the other hand, the Rb-Se nearest neighbor distance decreases with Rb concentration.

It is known¹⁾ that polyselenide (Se)_n²⁻ ions in the solid Rb₂Se_n consist of two to eight Se atoms. The EXAFS results for the Rb-Se mixtures suggest that Se chains exist in liquid state as well as in solid state. The increase of Rb concentration introduces more ionic character to Rb-Se bonds. This is clearly indicated by the decrease in the Rb-Se distance shown in Fig.2.

1) P.Böttcher, Z.Kristallgr. **150** (1979) 65.

* Present address: College of General Education, Kyushu University, Fukuoka 810

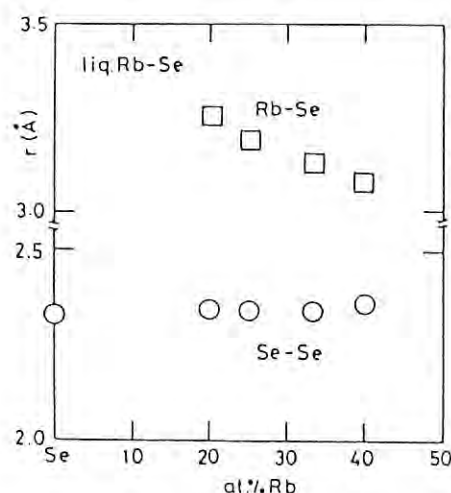


Fig.2 Concentration variations of the Se-Se and Se-Rb nearest neighbor distances, obtained from the EXAFS spectra for liquid Rb-Se mixtures.

STRUCTURE OF LIQUID STATE OF Bi_2O_3 BY EXAFS

Kichiro KOTO, Shuichi EMURA* and Akira YOSHIASA**

Department of Materials Science, Faculty of Integrated Arts and Sciences, Tokushima Univ., Minami-josanjima, Tokushima 770

*Institute of Scientific and Industrial Research, Osaka Univ., Ibaraki-Osaka 567

**Faculty of Science, Hiroshima Univ., Naka-ku, Hiroshima 730

Introduction

A high temperature form of Bi_2O_3 which is the best known oxide ion conductor with the fluorite-type structure was studied by EXAFS at high temperatures and above the melting point of 824°C .

Experimental and Results

Sample preparations and experimental procedures were described in the previous report¹⁾. The XANES spectra near the Bi-L3 edge are compared using the primary differential of XANES by energy (Fig. 1). The main difference in the features is the peak (-7 eV) before the main peak (absorption edge), but no change of the position of the absorption edge was observed. This suggests that there exists a slight change in valency and/or symmetry of coordinating atoms between in the δ -form and the melt.

The Bi-L3 edge EXAFS oscillations are shown in Fig. 2. The amplitude of the oscillations for the melt is almost one half for those of the δ -form, indicating decrease of the coordination number of Bi ions and/or increase of temperature factors.

Interatomic distances were obtained by the curve-fitting program written by Dr. H. Maeda, Okayama Univ. (Fig. 3). The Bi-O distances are almost constant (or decrease very slightly) with increasing temperature. A slight abrupt decrease was observed when it melted. The shortest

three Bi-O distances in the BiO_4 tetrahedron by neutron diffraction²⁾ were used as reference. $R(\text{M-O})$ in Fig. 3 is the average Bi-O distance calculated from the lattice constant assuming that Bi and O ions occupy the ideal site in the fluorite structure.

The authors thank to Drs. S. Nomura and A. Koyama, KEK, for useful advices and help in the experiment.

- 1) K. Koto, S. Emura and A. Yoshiasa, PF Activity Report No. 6, 81 (1988).
- 2) H. A. Harwig, Z. anorg. allg. Chem. 444, 151 (1978).

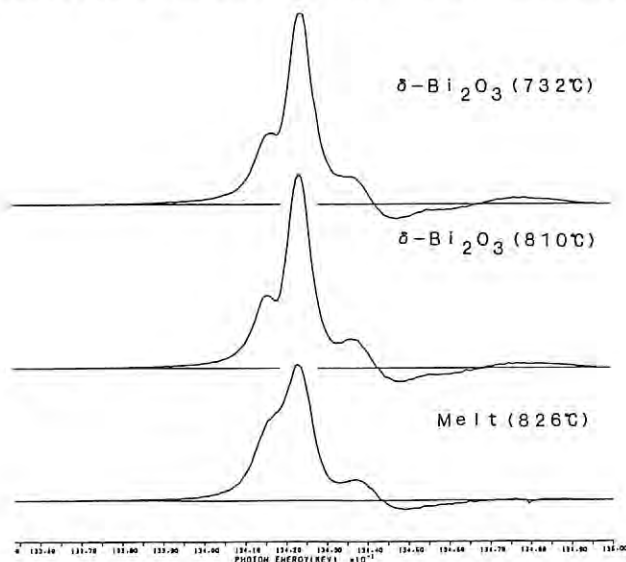


Fig. 1. Primary differential of XANES of Bi-L3 edge for δ - Bi_2O_3 and melt.

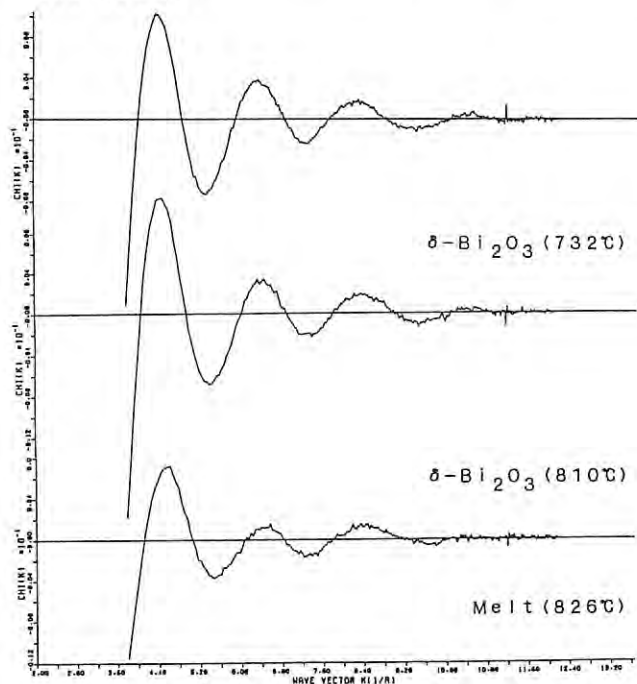


Fig. 2. The Bi-L3 edge EXAFS oscillations of δ - Bi_2O_3 and melt.

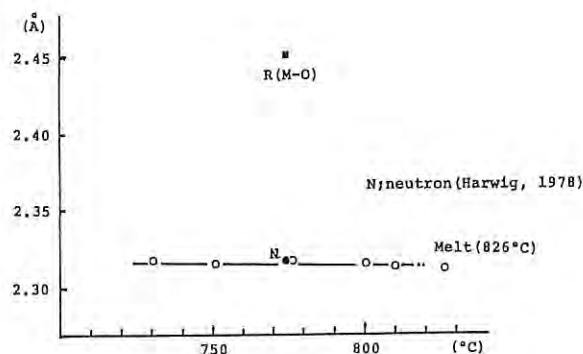


Fig. 3. Bi-O distances of δ - Bi_2O_3 at high temperatures from EXAFS.

Cu K-EDGE ABSORPTION SPECTRA OF A NOVEL SUPERCONDUCTING OXIDE :
 $\text{Nd}_{2-x}\text{Ce}_x\text{CuO}_{4-y}$ I. UNREDUCED SAMPLES

Nobuhiro KOSUGI¹, Yoshinori TOKURA², Hidenori TAKAGI³ and Shinichi UCHIDA³

1.Division of Molecular Engineering, Kyoto University, Yoshida, Kyoto 606 (JAPAN)
2.Department of Physics, The University of Tokyo, Hongo, Tokyo 113 (JAPAN)
3.Engineering Research Institute, The University of Tokyo, Hongo, Tokyo 113 (JAPAN)

Recent studies on high- T_c superconducting Cu-based oxides show that the two-dimensional (2D) sheet structure of $[\text{CuO}_4]$ squares is indispensable to superconductivity, irrespective of the types of doped carriers, electrons or holes. In $\text{Nd}_{2-x}\text{Ce}_x\text{CuO}_{4-y}$ (NCCO, $x=0.15$), electron doping to the $2\text{D } [\text{CuO}_4]$ sheet is achieved with Ce^{4+} substitution for Nd^{3+} in Nd_2CuO_4 and subsequent reduction.¹⁾ In $\text{La}_{2-x}\text{Sr}_x\text{CuO}_4$ (LSCO, $x=0.12-0.22$), hole doping to the $2\text{D } [\text{CuO}_4]$ sheet is achieved with Sr^{2+} substitution for La^{3+} in La_2CuO_4 . In the present work,²⁾ we have studied how the substitution induce changes in the electronic and geometrical structures in NCCO and LSCO by means of X-ray absorption spectroscopy (XANES) at the Cu K-edge.

Fig.1.1 shows Cu K-edge XANES spectra of the substituted compounds ($x=0.15$) with dashed lines, which are normalized relative to those of the parent (unsubstituted) compounds ($x=0$) shown with solid lines. The pre-edge structure A is assigned to the $1s-3d$ transition. The structures D and E are assigned to $1s-4p\sigma$ transitions to well-screened and poorly-screened core-hole states and the shoulder structures B and C half-way up the absorption maximum D are assigned to $1s-4p\pi$ transitions to well-screened and poorly-screened core-hole states. The splittings of the shoulder ($1s-4p\pi$) structure and of the main ($1s-4p\sigma$) structure are characteristic of divalent Cu compounds^{3,4)} with the planar coordination around Cu.^{3,4)}

The change of the spectra from $x=0$ to $x=0.15$ in NCCO is much larger than that in LSCO. This means that the substitution affects local electronic and geometrical structures around Cu drastically in Nd_2CuO_4 but not so much in La_2CuO_4 . This is consistent with the widely-accepted thoughts that the electron and hole doping occur mainly at Cu of $[\text{CuO}_2]$ in NCCO and at O in LSCO, respectively.

We have found isosbetic points in the $[x \neq 0]$ and $[x=0]$ spectra for the electron-doped and hole-doped Cu-based oxides with several Ce/Sr substitution rates, $\text{Nd}_{2-x}\text{Ce}_x\text{CuO}_4$ and $\text{La}_{2-x}\text{Sr}_x\text{CuO}_4$. This indicates that the spectra for the substituted systems consist of two components, parent and additional ones, and the former decreases and the latter increases with the substitution. Furthermore, the uniformity of the substituted samples indicates that the additional components introduced with the substitution are not segregated impurity phases but uniformly or randomly distributed "impurity states". We have tried to extract XANES spectra for the "impurity state" from the spectra of the parent (unsubstituted) and substituted compounds as follows:

$$([x \neq 0 \text{ (substituted)}] - b[x=0 \text{ (parent)}]) / a, \\ (a = 1 - b = kx).$$

When $k = 2-2.5$, the extracted spectra give reasonable features compared with known spectra for several Cu-based oxides. This means that each $\text{Ce}^{4+}/\text{Sr}^{2+}$ ion substituting $\text{Nd}^{3+}/\text{La}^{3+}$ changes 4-5 Cu sites and that an additional electron/hole supplied with the substitution is distributed mainly to 4-5 $[\text{CuO}_2]$ units, yielding "impurity (localized) states". When $x=0.15$, the "impurity states" amount to 60-75 % of the whole $[\text{CuO}_2]$ units; the interaction and superposition among the localized states are caused to produce bands like Fermi-liquid states.

In the extracted XANES spectra in NCCO the well-screened peaks B and D are considerably strong but the poorly-screened peaks C and E are remaining. This means that Cu atoms in the "impurity state" have more $3d^{10}$ contribution than in the parent compound but are still divalent. The present conclusion disagrees with that by Tranquada.⁵⁾ On the other hand, in LSCO we observe that the $1s-4p\sigma$ transition to the well-screened state D in the extracted spectra is a little weakened compared with that for the parent compound. This means that Cu atoms in the "impurity state" in LSCO have a little more $3d^9$ contribution than in the parent compound and that the substitution of Sr for La causes the hole doping mainly in oxygen atoms but also a little in Cu atoms.

- 1) Y.Tokura, H.Takagi and S.Uchida, Nature 337 (1989) 345
- 2) N.Kosugi, Y.Tokura, H.Takagi and S.Uchida, Phys.Rev.B 41 (1990) in press
- 3) N.Kosugi et al., Chem.Phys. 91 (1984) 249; 103 (1986) 101; 135 (1989) 149
- 4) N.Kosugi, in Core-level Spectroscopy in Condensed Systems, Springer Series in Solid-State Sciences Vol.81 (Springer, Berlin, 1988)
- 5) J.M.Tranquada, S.M.Heald, A.R.Moodenbaugh, G.Liang, and M.Croft, Nature 337 (1989) 720

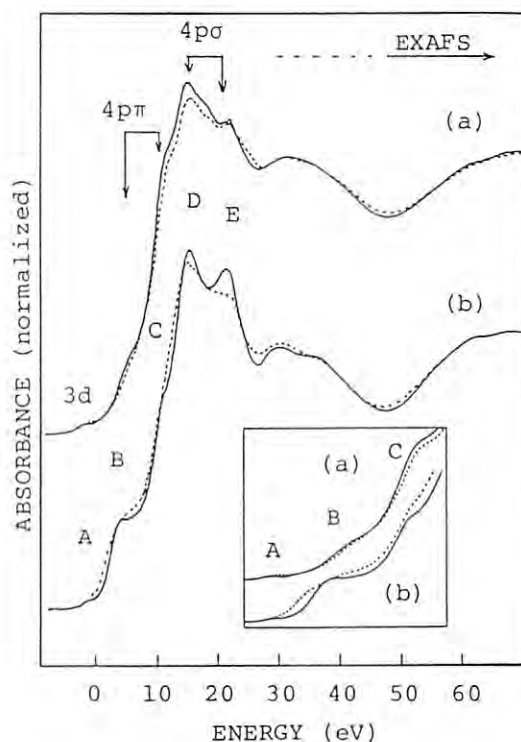


Fig.1.1. Cu K-edge XANES spectra of (a) La_2CuO_4 (solid line) and $\text{La}_{1.85}\text{Sr}_{0.15}\text{CuO}_4$ (dashed line) (b) Nd_2CuO_4 (solid line) and $\text{Nd}_{1.85}\text{Ce}_{0.15}\text{CuO}_4$ (dashed line). The $1s-3d$ and $4p\pi$ regions are inserted on a magnified scale. The excitation energy is relative to the first inflection point at the K edge of Cu foil.

XANES OF LOW-DIMENSIONAL COMPLEXES WITH HIGHLY OXIDIZED Ni AND Cu

1. Cu VALENCE OF DIFFERENT SITES IN $\text{YBa}_2\text{Cu}_3\text{O}_y$

Haruo KURODA¹, Nobuhiro KOSUGI², Hiroshi KONDOH¹,
Koichi AKEYAMA¹, Masafumi TAMURA¹ and Hiroyuki TAJIMA¹

1. Department of Chemistry, The University of Tokyo, Hongo, Tokyo 113 (JAPAN)

2. Division of Molecular Engineering, Kyoto University, Yoshida, Kyoto 606 (JAPAN)

The Cu K-edge XANES spectra of high-Tc superconductors and related oxides, $\text{YBa}_2\text{Cu}_3\text{O}_y$ (YBCO, $y=6.9, 6.85, 6.75, 6.5$ and 6.1), $\text{YBa}_2(\text{Cu}_{1-x}\text{Co}_x)_3\text{O}_y$ ($x=0.33, y\sim 7.2$) and single-crystal $\text{ErBa}_2\text{Cu}_3\text{O}_y$ ($y\sim 7, \sim 6$), have been measured. In the present study, we concentrate on interpretation of the main features of XANES of YBCO in terms of $1s-4p\pi$ and $1s-4p\sigma$ transitions.

Fig.1.1 shows Cu K-edge XANES spectra of YBCO. The main peaks and the ~ 7 eV higher-energy peaks are assigned to the $1s-4p\sigma_1$ (well-screened core hole through $L\rightarrow 3d$ LMCT, $3d^{10}L^{-1}$) and $4p\sigma_2$ (poorly-screened core hole, $3d^9$) transitions, respectively. This means that the valence states of Cu are more or less divalent in the superconductors and related oxides, even in oxygen-deficient YBCO. Other valence states of Cu would not be derived from the $1s-4p\sigma$ regions.

On the other hand, in the $1s-4p\pi$ energy region, the onset and shoulder structures, A (2.6 eV relative to the first inflection point at the K edge of Cu foil), B (4.2 eV), C (6.7 eV), D (9.7 eV), E (10.9 eV), F (13.8 eV), are observed for the superconductors and related oxides. Fig.1.2 indicates that the structures B and E are observed in the E//ab polarized XANES for the oxygen-rich ($y\sim 7$) $\text{ErBa}_2\text{Cu}_3\text{O}_y$ single crystal and the structures A and D for the oxygen-deficient ($y\sim 6$) one, and that the structures B and E are suppressed in the Co-substituted oxygen-rich YBCO for the Cu(1) site ($\text{YBa}_2\text{Cu}_2\text{CoO}_y, y\sim 7$). These observations demonstrate that the structures A and D and B and E arise from $1s-4p\pi$ at the Cu(1) site. The energy difference between A and D is a typical value, ~ 7 eV, and the structures A and D are assigned to $1s-4p\pi_1$ ($3d^{10}L^{-1}$) and $1s-4p\pi_2$ ($3d^9$) of the $[\text{CuO}_2]$ ions, respectively. This shows that Cu is not completely reduced to monovalence even in the linearly-coordinated $[\text{CuO}_2]$ ions at the Cu(1) site of oxygen-deficient YBCO. The structures B and E correspond to $1s-4p\pi_1$ and $4p\pi_2$ transitions in the 1D Cu-O chain at the Cu(1) site of oxygen-rich YBCO.

The structures C and F are distinctly observed in the Co-substituted YBCO as shown in Fig.1.2. The structures C and F correspond to $1s-4p\pi_1$ and $4p\pi_2$ transitions in the 2D Cu-O sheets with pyramidally-coordinated $[\text{CuO}_5]$ at the Cu(2) site of YBCO (π_z , parallel to the c axis). This assignment is supported with the fact that these are not observed in the E//ab polarized XANES of the $\text{ErBa}_2\text{Cu}_3\text{O}_y$ single crystals irrespective of the oxygen content as shown in Fig.1.2.

The present results show that all the Cu ions in YBCO have more or less divalent d^9 electron configurations and that the electronic structure at the Cu(1) site in YBCO is between $d^9(L^{-1})$ and $d^{10}(L^{-2})$ at $y\sim 7$ and nearly d^{10} at $y\sim 6$. It is probable that the oxygen atoms take an important part in the balance of holes in the systems and in the hole conductivity on the 2D Cu-O sheet and that the Cu(1)-O sites give small parts of holes and of electrons to the 2D Cu(2)-O sheets through the O $2p\sigma_z$ orbitals in the BaO layer at $y\sim 7$ and $y\sim 6$, respectively; the O $2p\sigma_z$ orbital serves for the 2D Cu-O sheet as electron/hole reservoir.

1) N.Kosugi, H.Kondoh, H.Tajima and H.Kuroda, Chem.Phys. 135 (1989) 149; Physica B 158 (1989) 450

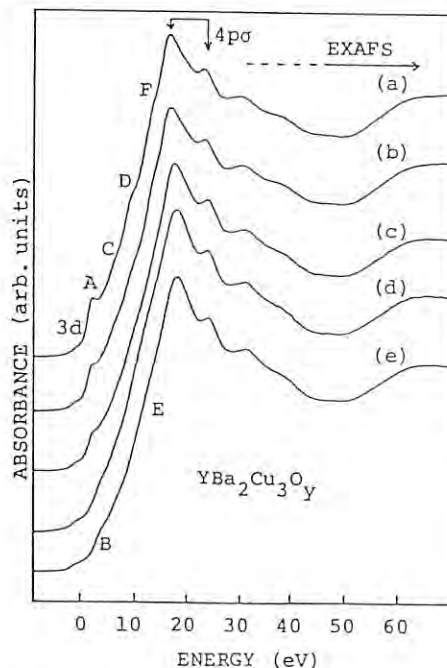


Fig.1.1. Cu K-edge XANES of $\text{YBa}_2\text{Cu}_3\text{O}_y$ (a) $y=6.1$, (b) $y=6.5$, (c) $y=6.75$, (d) $y=6.85$, (e) $y=6.90$

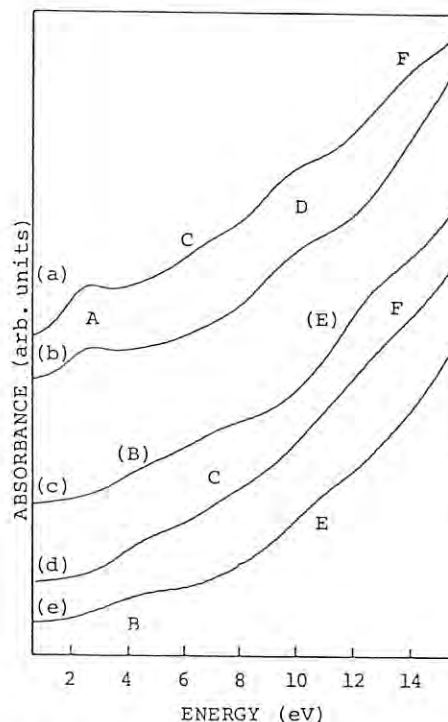


Fig.1.2. Cu $1s-4p\pi$ XANES (a) powdered YBCO ($y\sim 6$) (b) single-crystal YBCO ($\text{Y}=\text{Er}, y\sim 6, E//ab$), (c) powdered YBCO ($\text{C}=\text{Cu}_2\text{Co}, y\sim 7$), (d) powdered YBCO ($y\sim 7$), (e) single-crystal YBCO ($\text{Y}=\text{Er}, y\sim 7, E//ab$)

XANES OF LOW-DIMENSIONAL COMPLEXES WITH HIGHLY OXIDIZED Ni AND Cu II. LOCAL STRUCTURES OF DIFFERENT Cu SITES IN $\text{YBa}_2\text{Cu}_3\text{O}_y$

Haruo KURODA¹, Nobuhiro KOSUGI², Hiroshi KONDOH¹,
Koichi AKEYAMA¹, Masafumi TAMURA¹ and Hiroyuki TAJIMA¹

1.Department of Chemistry, The University of Tokyo, Hongo, Tokyo 113 (JAPAN)
2.Division of Molecular Engineering, Kyoto University, Yoshida, Kyoto 606 (JAPAN)

The Cu K-edge XANES spectra of high-Tc superconductors and related oxides, $\text{YBa}_2\text{Cu}_3\text{O}_y$ (YBCO, $y=6.95, 6.90, 6.85, 6.75, 6.60, 6.55, 6.45, 6.4, 6.3, 6.2, 6.1$) have been measured. Ortho-I phase (Tc~90K, $y>6.7$) and insulating tetragonal phase ($y<6.3$) samples were prepared by annealing under various atmosphere of different ratios of O_2/N_2 pressure. Ortho II (Tc~60K) and low Tc (<60K) phases were obtained under various quenching temperature and rate. In the present study, we concentrate on investigation of the relation between a local geometrical change and a non-monotonous Tc behavior as a function of y .

Our previous study¹⁾ showed that $1s-4p\pi$ transitions are sensitive to local geometrical structures. To determine changes of the coordination (fourfold, threefold, twofold) of oxygen ions at the Cu(1) site for different oxygen contents, we have tried to extract only $1s-4p\pi$ spectral components by subtracting a smoothed shoulder background of the $1s-4p\sigma$ transition ($E=0-20\text{eV}$) from the spectra normalized to the oxygen-rich ($y=6.95$) spectrum around the preedge ($E<0$) and post-edge regions ($E>40\text{eV}$) with the least-square fitting.

Fig.2.1 shows the "extracted" $1s-4p\pi$ spectra. The twin-peak structures A and D, which arise from the linear $[\text{Cu}(1)\text{O}_2]$ ions at the Cu(1) site, are not observed in the ortho-I phase but are observed gradually strongly as the oxygen content y decreases.

This indicates that twofold-coordinated $[\text{Cu}(1)\text{O}_2]$ ions do not exist in ortho-I phase (Tc~90K, $y>6.7$) but are produced on going from ortho-I phase to ortho-II phase and when Tc falls down to ~60K. Furthermore, the structure B, which is a well-screened $1s-4p\pi$ transition of the fourfold-coordinated $-\text{O}[\text{Cu}(1)\text{O}_2]-\text{O}-$ chain, becomes broader as the oxygen content y decreases. The broadening probably arises from threefold-coordinated $-\text{O}[\text{Cu}(1)\text{O}_2]-*[\text{Cu}(1)\text{O}_2]-\text{O}-$ structures (* denotes an O vacancy) along the chain. These observations indicate that in ortho-I phase the oxygen vacancies are distributed randomly along the $\text{O}[\text{Cu}(1)\text{O}_2]-\text{O}$ chains, and that on the phase transition from ortho-I (Tc~90K) to ortho-II (Tc~60K) the oxygen vacancies gather one another like $-*[\text{Cu}(1)\text{O}_2]-*[\text{Cu}(1)\text{O}_2]-*[\text{Cu}(1)\text{O}_2]-*$. This local oxygen vacancy model in the ortho-I and ortho-II phases is consistent with the finite-range oxygen vacancy ordering in the ortho-II phase demonstrated with the scattering experiments.

Integrated intensities of the peaks A and D correspond to the number of the twofold-coordinated $[\text{Cu}(1)\text{O}_2]$ ions. The intensity of A and D are plotted as a function of the oxygen content in Fig.2.2. The number of the twofold-coordinated $[\text{Cu}(1)\text{O}_2]$ increases with the oxygen deficiency as a whole. Furthermore, we note a flat region between $y=6.5$ and $y=6.3$. Such a peculiar change²⁾ is similarly observed by Tranquada et al.²⁾ In the $y=6.5$ sample, empty chain (twofold coordination) : filled chain (fourfold coordination) = 1:1, and the oxygen vacancies are ordered on every other chain, resulting in doubling of the unit cell along the a axis. This is a fairly stable phase; therefore, even if oxygen vacancies are further introduced into this phase, they are introduced only into the filled chains and produce threefold-coordinated sites with maintaining the

empty/filled-chain ordering structure before the orthorhombic-to-tetragonal phase transition ($y\sim 6.3$). After the phase transition, the empty/filled-chain ordering structure is destroyed, and twofold-coordinated sites begin to increase again.

- 1) N.Kosugi, H.Kondoh, H.Tajima and H.Kuroda, Chem.Phys. 135 (1989) 149
- 2) J.M.Tranquada, S.M.Heald, A.R.Moodenbaugh and Y.Xu, Phys.Rev. B 38 (1988) 8893

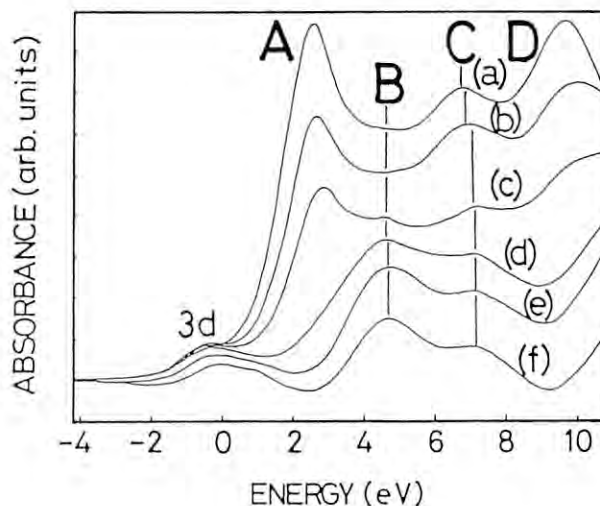


Fig.2.1. Extracted $1s-4p\pi$ structures A, B, C and D from the raw XANES spectra for $\text{YBa}_2\text{Cu}_3\text{O}_y$ (Fig.1.1). (a) $y=6.1$, (b) $y=6.5$, (c) $y=6.75$, (d) $y=6.85$, (e) $y=6.90$, (f) $y=6.95$.

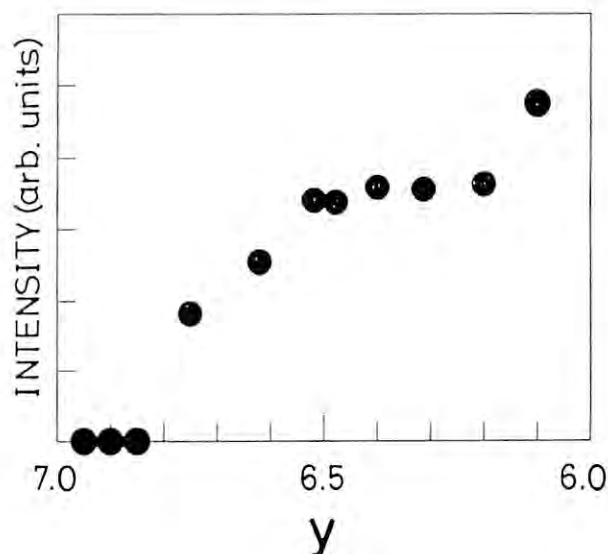


Fig.2.2. Dependence of integrated intensities of the peaks A and D on y .

Temperature-dependent EXAFS study on supported Pd and Ag small metal clusters

Toshihiko YOKOYAMA and Toshiaki OHTA

Department of Materials Science, Faculty of Science, Hiroshima University, Naka-ku, Hiroshima 730

Understanding of physical and chemical properties of small metal clusters is a very important subject for various fields such as solid state physics, surface science and heterogeneous catalysis. Our previous report [1] on the temperature-dependent EXAFS study confirmed that the metal-metal bond distance contracts and the Debye temperature decreases, and revealed for the first time that the thermal expansion coefficient becomes significantly greater.

The present report shows the subsequent results which describe the anharmonic interatomic potentials of the small metal clusters by use of the newly-developed technique shown in a separated paper[2].

Supported Pd and Ag clusters were prepared by the standard ion-exchange method. Precursor supported metal ammine species were reduced with hydrogen at 673 K (Pd) or 473 K (Ag), and then evacuated at the same temperature to give hydrogen-free clusters. Pd and Ag K-edge EXAFS spectra were measured at several temperatures under inert atmosphere at BL 10B.

EXAFS data were analyzed by means of the 4-th order cumulant expansion technique in order to account for anharmonicity. Determination of the interatomic potentials was carried out with the assumption of the Morse potential.

Table 1 shows the Debye temperatures and thermal expansion coefficients of the bulk metals and the small metal clusters. As exemplified previously[1], the Debye temperature of the clusters decreases and the thermal expansion coefficient drastically increases compared with those of the corresponding bulk metals.

Figure 1 shows the determined interatomic potentials in Ag bulk metal and Ag small metal clusters. Compared with the bulk metal, the metal cluster has a wider and shallower potential and the degree of asymmetry is more significant.

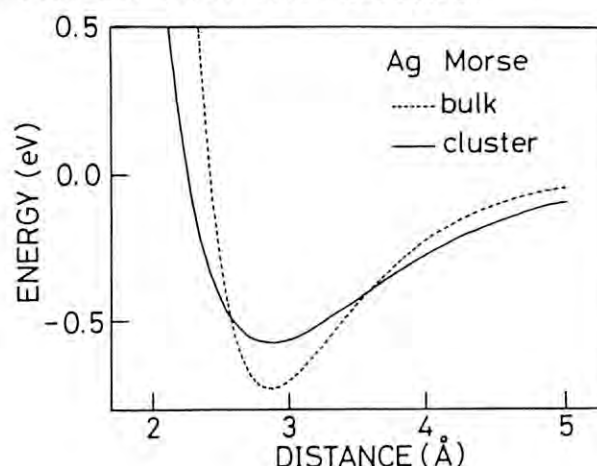
These results, which are in excellent agreement with the sophisticated theoretical predictions, support the concept that small metal particles with many surface atoms have weaker metal-metal bondings due to the decrease in the coordination numbers of surface atoms.

- [1] T.Yokoyama, S.Kimoto and T.Ohta, Photon Factory Activity Report 6 57 (1988); Jpn.J.Appl.Phys. 28 L851 (1989).
[2] T.Yokoyama, T.Satsukawa and T.Ohta, Photon Factory Activity Report this volume; Jpn.J.Appl.Phys. 28 (1989).

Table 1. Debye temperatures and thermal expansion coefficients of Pd and Ag bulk metals and small metal clusters. Values in parentheses refer to the thermodynamical data.

sample	θ_D (K)	α (K ⁻¹)
Pd bulk	281 (275)	0.9 (1.13)
cluster	236	6.4
Ag bulk	232 (228)	1.6 (1.57)
cluster	160	10.4

Fig.1. Interatomic potentials of Ag bulk metal and small metal clusters.



EXAFS STUDY ON NI-NB AMORPHOUS ALLOY PREPARED BY MECHANICAL ALLOYING

Toshio NASU, Kunio NAGAOKA, Tetsuro SEKIUCHI*, Masaki SAKURAI*, Toshiharu FUKUNAGA*, Fumitake ITOH* and Kenji SUZUKI*

Faculty of Education, Yamagata University, 1-4-12 Kojirakawa, Yamagata 990 Japan

*Institute for Materials Research, Tohoku University, 2-1-1 Katahira, Sendai 980 Japan

Introduction

A clear understanding on the mechanism of crystalline to amorphous phase transition through solid state reaction is not obtained up to now. In this report, the structural change of Ni-Nb mixture powder through solid state amorphization was studied by means of EXAFS(1).

Experimental

Ni-Nb amorphous alloy powder was prepared by mechanical alloying using a laboratory ball mill. Sample preparation was made by stopping the ball milling $0, 1.8 \times 10^5, 2.52 \times 10^5, 3.6 \times 10^5, 7.2 \times 10^5$ and 10.8×10^5 after its commencement. EXAFS measurements were carried out at the beam line 10B of Photon Factory. Energy scanning were carried out around the K-edges of nickel and niobium.

Results and Discussion

Fig.1(A) and (B) show the radial distribution function (RDF) around a Ni and Nb atom of alloy at the various stages of amorphization. The arrows indicate the first, second, third and fourth nearest neighbours around a Ni and Nb atom in the crystals. The height of the peaks corresponding to the long range orders of the crystal phases reduced as the mechanical alloying time proceeded and vanished. Only the first peak remained and shifted to the value of the amorphous

alloy prepared by rapid quenching method. From these EXAFS results combined with SEM observation and DTA measurement(2), we propose the model as

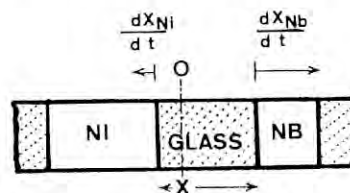


Fig.2 Illustration of amorphous phase growth in the thin layers of lamella structure consisting of crystalline Ni and Nb.

illustrated in Fig.2. The growth speed of amorphous phase in the Nb crystal layers of lamella structure, dX_{Nb}/dt , seems to be larger than that in Ni crystal layers, dX_{Ni}/dt .

The authors wish to thank Dr.N.Kosugi for offering us the computer program of EXAFS data analysis.

References

- 1) T.Nasu et al., in Proceedings of International Conference on Liquid and Amorphous Metals, Suppl. J.Non-Cryst.Solids (to be published).
- 2) T.Nasu et al., Mater.Trans.JIM, 30,620(1989).

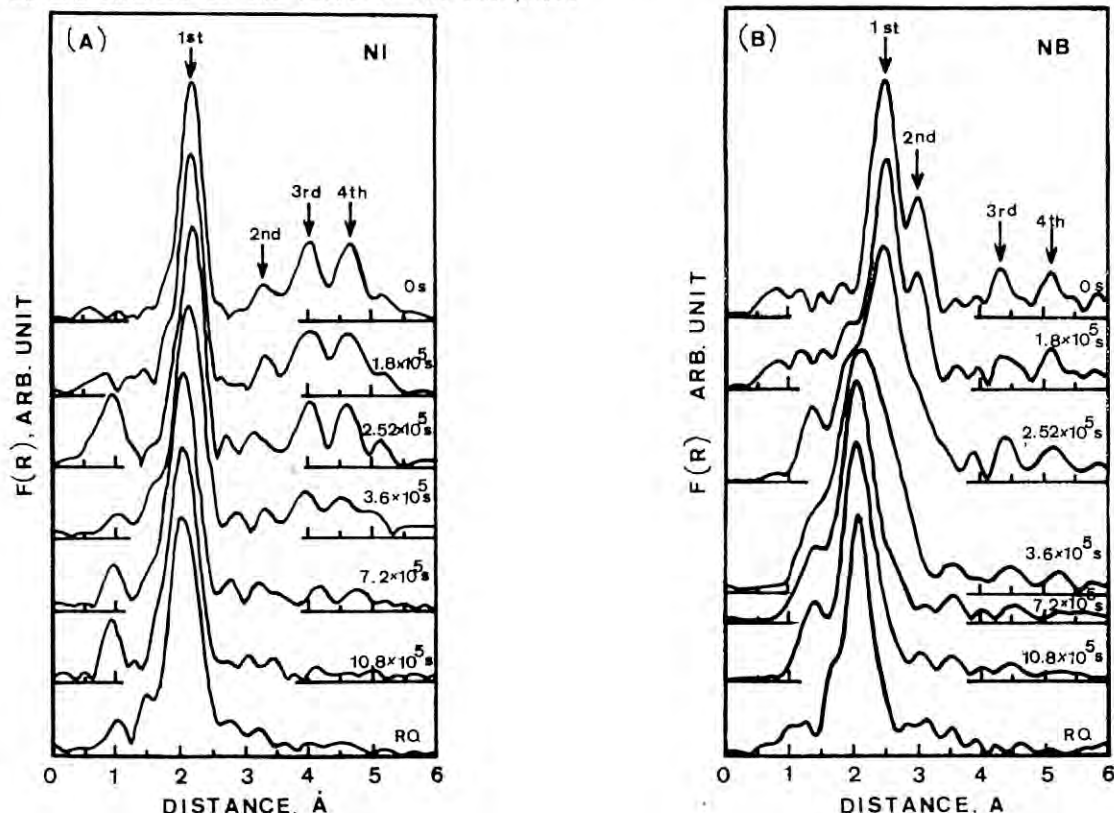


Fig.1 Fourier transform of EXAFS of Ni₆₀Nb₄₀ alloy produced by mechanical alloying as a function of milling time and the amorphous alloy prepared by rapid quenching method : (A) Ni K-edge and (B) Nb K-edge.

THE STRUCTURE OF INTERCALATED CdS PARTICLES IN LAYERED $K_4Nb_6O_{17}$

Joji YOSHIMURA, Satoko HOSHI, Tokihisa HIKITA, Kiyotaka ASAKURA*, Kazunari DOMEN and Takaharu ONISHI

Research Laboratory of Resources Utilization, Tokyo Institute of Technology,
4259 Nagatsuma, Midori-ku, Yokohama 227

*Faculty of Science, The University of Tokyo, Hongo, Bunkyo-ku, Tokyo 113

Introduction

We have studied on the photocatalytic activity of $K_4Nb_6O_{17}$. It has a mica-like layered structure, and K^+ ions which located at the interlayer of niobate sheets are ion-exchangeable. This catalyst is able to reduce H^+ to H_2 without any other metallic catalyst such as Pt. On the other hand CdS absorbs visible light, but the rate of H_2 evolution on the CdS was very slow due to a high overpotential for recombination of hydrogen. In a combined system of $K_4Nb_6O_{17}$ and CdS, H_2 evolution was observed by the electron transfer from CdS to $K_4Nb_6O_{17}$ under visible light irradiation. The activity of this system strongly depended on the method of catalyst preparation.

Therefore, CdS/ $K_4Nb_6O_{17}$ catalyst was prepared and was investigated the structure of CdS particle by method of EXAFS spectroscopy.

Experimental

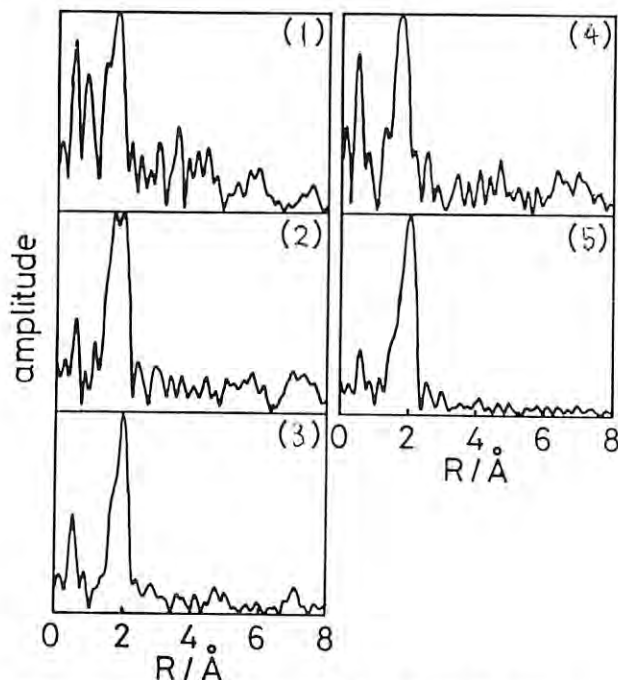
The catalysts were prepared by the method described elsewhere. Six samples were measured, (1) $Cd^{2+}/K_4Nb_6O_{17}$: untreated, (2) CdS/ $K_4Nb_6O_{17}$: sulfurized for 1 day at room temperature; low activity, (3) CdS/ $K_4Nb_6O_{17}$: sulfurized for 7 days at room temperature; high activity, (4) CdS/ $K_4Nb_6O_{17}$: H_2SO_4 treated after (3), (5) CdS. Sample (5) was used as reference.

Results and Discussion

In the figure the Fourier transforms of $K^3X(K)$ of Cd K-edge EXAFS data of those samples are shown. In these spectra, the peak at $R=2.16$ corresponds to Cd-O of untreated $Cd^{2+}/K_4Nb_6O_{17}$ sample and the peak at $R=2.42$ is attributed to Cd-S of CdS particle. In a high activity sample (3), only Cd-S bond was observed and its coordination number is ca. 3.6. On the other hand, in a low activity catalyst (2), Cd-S bond was observed with the coordination number of ca. 2.9 and Cd-O bond still remained. In H_2SO_4

while Cd-S bond disappeared although the color of the catalyst was light yellow.

These results lead us to conclude as follows; (1) the low activity of short time-sulfurized catalyst is considered to be attributed to the existence of Cd^{2+} ions which work as recombination centers for photoexcited electrons and holes. (2) the difficulty of intercalation of anions (S^{2-}) into the catalyst during the sulfurization, demanded a long time (7 days) to sulfurize the Cd^{2+} located at interlayer of catalyst. (3) Almost all the produced CdS particles were observed to exist on the outside of the catalyst.



Fourier transforms of $K^3X(K)$ of Cd K-edge EXAFS data

EXAFS ANALYSIS OF $\text{ZrF}_4\text{-BaF}_2\text{-CsF}$ GLASSES AND RELATED COMPOUNDS

Yoji KAWAMOTO, Yukihiro UMETANI, Hideki MORIKAWA* and Fumiyuki MARUMO*

Faculty of Science, Kobe University, Rokkodai, Nada, Kobe 657

*Research Laboratory of Engineering Materials, Tokyo Institute of Technology, Nagatuta, Yokohama 227

Introduction

Zirconium tetrafluoride-based glasses are known to be a vitreous solid electrolyte of F^- ions. The ionic conductivities, however, are the order of 10^{-6}Scm^{-1} at 200°C . Thus the enhancement of conductivity is necessiated for practical use of these glasses. For the improvement of conductivity, the elucidation of F^- conduction-governing factors is inquired. The compositional dependence of the conductivities of $\text{ZrF}_4\text{-BaF}_2\text{-CsF}$ glasses suggested that the activation energy for conduction is largely influenced by the Zr-F bond length and/or by the F coordination of Zr.¹⁾ The present EXAFS study is undertaken in order to confirm the validity of this suggestion.

Experimental and Results

The compositions of $\text{ZrF}_4\text{-BaF}_2\text{-CsF}$ glasses chosen for EXAFS measurement are $55\text{ZrF}_4\cdot(45-x)\text{BaF}_2\cdot x\text{CsF}$ ($x=0, 7, 14, 20, 27, 34$ and 40). The glasses annealed at the respective glass-transition temperatures were subjected to the EXAFS measurements. On the other hand, the Li_2ZrF_6 , Cs_2ZrF_6 , $\alpha\text{-BaZrF}_6$, $\beta\text{-BaZrF}_6$, and $\beta\text{-ZrF}_4$ crystals were synthesized and utilized as reference specimens in the EXAFS analysis of $\text{ZrF}_4\text{-BaF}_2\text{-CsF}$ glasses. For the EXAFS measurements, all the samples were finely powdered and pressed into discs with polyethylene powder. The measurements of Zr-K EXAFS spectra were carried out using the EXAFS facilities at BL-10B.

Figure 1 shows the Fourier transform magnitude curves, $|F(r)|$, which were obtained using EXAFS data from 3.5 to 13.5\AA^{-1} in k . The first peaks at around 1.5\AA in $|F(r)|$ correspond to the Zr-F distances. Next, the inverse Fourier transformation and curve fitting were carried out on these peaks. The amplitude and the phase shift which are required in the curve fitting calculation were obtained by employing Li_2ZrF_6 as reference. The result (Zr-F interatomic distance, r , F coordination number of Zr, N , and Debye-Waller factor, σ) is shown in Table 1.

As seen from Fig. 1, the Zr-F peaks of the 27CsF , 34CsF and 40CsF glasses exhibit appreciable shoulders at the right-hand sides of the peaks. On these three glasses, therefore, the curve fitting calculation was also performed using "two shell model". The structure parameters in this case are shown in round brackets in Table 1.

Table 2 summarized the EXAFS analysis result of reference specimens. In the table the values in round brackets are those obtained by X-ray diffraction analysis.

A detailed discussion of the present experimental result will be made elsewhere.

Reference

1) Y. Kawamoto and I. Nohara, Solid State Ionics,

22, 207 (1987).

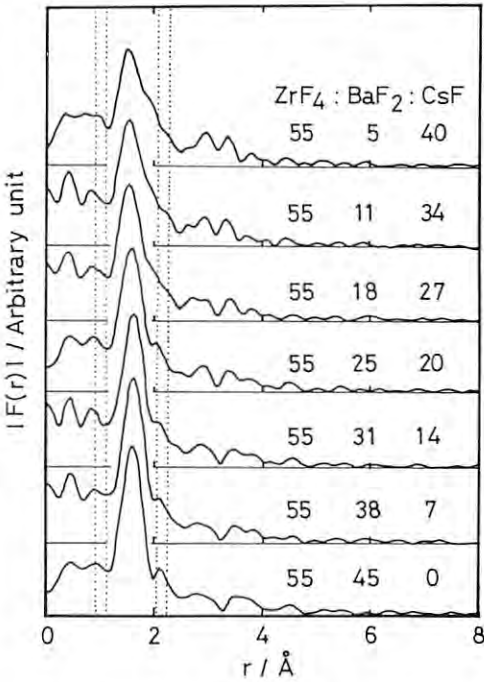


Fig. 1 Fourier transform magnitude curves of $\text{ZrF}_4\text{-BaF}_2\text{-CsF}$ glasses

Table 1 Structure parameters of $\text{ZrF}_4\text{-BaF}_2\text{-CsF}$ glasses

$\text{ZrF}_4\text{-BaF}_2\text{-CsF}$	$r/\text{\AA}$	N	σ
55 45 0	2.07	6.5	0.104
55 38 7	2.07	6.7	0.109
55 31 14	2.06	6.7	0.114
55 25 20	2.07	7.1	0.118
55 18 27	2.07	7.5	0.126
	(2.06	6.4	0.108)
	(2.27	0.6	0.002)
55 11 34	2.07	7.9	0.132
	(2.06	6.5	0.112)
	(2.27	0.6	0.006)
55 5 40	2.08	8.3	0.138
	(2.05	5.1	0.096)
	(2.23	1.9	0.063)

Table 2 Structure parameters of reference crystals

crystal	$r/\text{\AA}$	N	σ
Cs_2ZrF_6	2.02(2.04)	5.6(6)	0.075
$\alpha\text{-BaZrF}_6$	2.05(2.08)	5.4(7)	0.090
$\beta\text{-BaZrF}_6$	2.06(2.13)	5.5(8)	0.104
$\beta\text{-ZrF}_4$	2.10(2.12)	7.5(8)	0.090

XAFS STUDIES ON MARTENSITIC TRANSFORMATION IN Fe-Ni ALLOYS

Hitoshi YAMAZAKI, Hironobu MAEDA*, Hiroshi MARUYAMA, Michinobu MINO, Akihisa KOIZUMI, Hisashi KOSAKA, Hidekazu KIMURA, Manabu FUJITA and Seitaro MITSUDO.

Department of Physics, Faculty of Science, Okayama University,
 *Department of Chemistry, Faculty of Science, Okayama University,
 3-1-1 Tsushima-Naka, Okayama 700.

Introduction

The Fe-Ni alloys in Fe rich side undergo $\text{fcc}(\gamma) \rightarrow \text{bcc}(\alpha)$ martensitic transformation with decreasing temperature. It has been well-known as a typical first-order phase transition. Local structural change around Fe or Ni-atom accompanied with the transformation is far from clear understanding. The temperature dependent XAFS measurement is an effective method to study the local environment around an absorbing atom. We have carried out XAFS measurements in the temperature range from 300K to 20K.

Experimental

For 35.4 and 26.4at%Ni-Fe alloys, after gliding the ingots, the powdered samples were annealed for 24 hours at 700°C under vacuum and quenched into ice water to obtain disordered samples. For 30.4at%Ni-Fe, after slicing off from the ingot, it was mechanically polished into a foil in optimum thickness, and the same thermal treatment was given. In order to determine the lattice parameter and M_s temperature, X-ray diffraction measurements were carried out. XAFS measurements were done near Fe and Ni K-edges by using of the EXAFS facility installed at the beam line 10-B in KEK-PF. Data analysis was made by the conventional procedure. In the least-square curve fitting, it was assumed that the nature of backscattering atoms was indistinguishable to each other because of closeness in the atomic number of the

components.

Results and Discussion

XANES spectrum is clearly transformed from double peak in fcc into single peak in bcc in the vicinity of M_s temperature. Radial structure function obtained by the Fourier transform of the EXAFS is also changed the pattern $\text{fcc} \rightarrow \text{bcc}$ near M_s .

Fig.1 shows the temperature variation of the nearest neighbor distance R determined by the curve fitting. For 35.4at%Ni-Fe, R increases monotonically with decreasing temperature, which corresponds to the Invar effect. For 30.4 and 26.4at%Ni-Fe, R changes from 2.52Å to 2.48Å with decreasing temperature. These values are good agreement with the interatomic distances in the fcc and bcc structure, respectively. The nearest neighbor is composed of the 1st shell of the fcc and that of the bcc, whose interatomic distance differ only 4/100Å with each other, being unlikely to be distinguishable by the EXAFS analysis. Therefore, R should be considered to be a mean value of the distance.

Fig.2 shows the temperature variation of the 2nd neighbor distance which can be significantly separated from the others. This shows the temperature dependence of the local structure in the α phase. The following results are reached from the analysis; local structural change from fcc to bcc occurs at a higher temperature than M_s , the temperature is higher around Fe-atom than Ni-atom, and the local bcc structure is more stable around Fe-atom than Ni-atom.

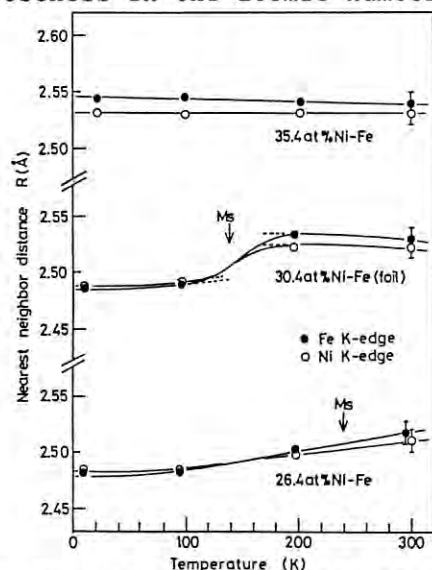


Fig.1. Temperature variation of nearest neighbor distance.

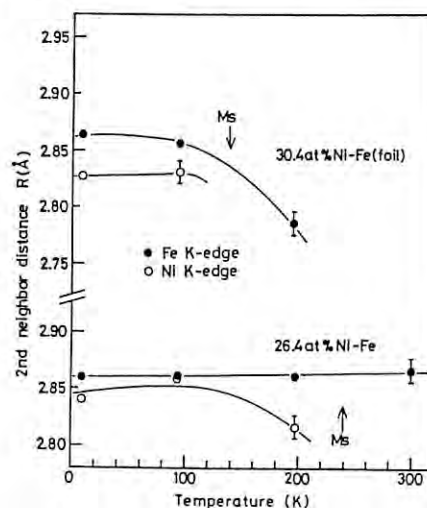


Fig.2. Temperature variation of 2nd neighbor distance.

EXAFS STUDIES ON THE STRUCTURE OF SILICA ATTACHED Nb-DIMER CATALYST.

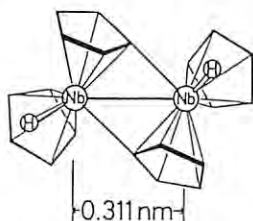
Nobuyuki ICHIKUNI, Kiyotaka ASAKURA, and Yasuhiro IWASAWA

Department of Chemistry, Faculty of Science, The University of Tokyo,
7-3-1 Hongo, Bunkyo-ku, Tokyo 113.Introduction

Chemical reactions between organometallic complex and surface OH groups give well-defined surface structure with novel catalytic activities. We have already investigated the structures and the reactivities of the attached Nb monomer catalysts, the one atomic layer Nb oxide and acid catalysts. In this study, we prepared the new SiO₂-attached Nb dimer catalysts, and defined the structures of the catalysts by means of EXAFS.

Experimental

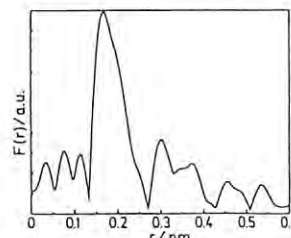
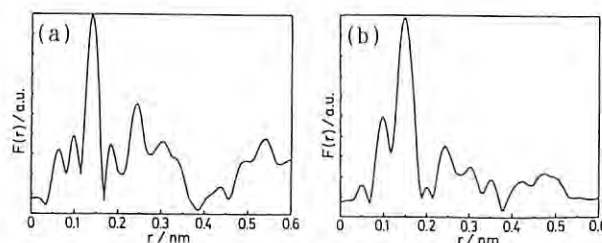
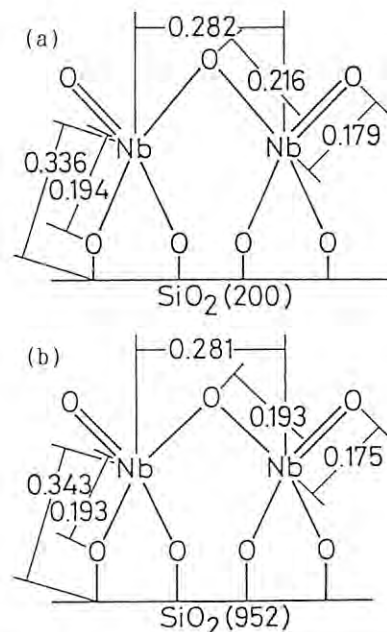
The dimeric niobium complex [Nb(C₅H₅)H(C₅H₄)]₂



was prepared by the procedures in the literature (1). Then it was attached with the surface OH groups on SiO₂ (AEROSIL #200 **1a**, FUJI DAVISON #952 **1b**) at 293 K under Ar gas to produce attached Nb₂ catalysts (**2a**, **2b**). The dimer catalysts (**2a**, **2b**) were reduced with H₂ at 823 K for 1 h, followed by oxidation with O₂ at 773 K for 1 h to be oxidized catalysts (**3a**, **3b**). EXAFS spectra of these catalysts were measured at BL-10B of Photon Factory, and analyzed with the PROGRAM EXAFS4.

Results and Discussion

Fig. 1 shows the Fourier transform of the catalyst **1a**, in which the first large shell was assigned to be Nb-O bond and Nb-C bond, and the second shell (0.3 nm) was to be Nb-Nb bond. The bond distance of Nb-Nb in catalyst **1a** was determined to be 0.33 nm (coordination number : 1) by curve-fitting analysis, which is longer by ca. 0.02 nm than original complex. Fig. 2 illustrates the Fourier transform of the oxidized catalyst **2a** and **2b**. Both **2a** and **2b** have peak near 0.25 nm, which was attributed to Nb-Nb bond with 0.28 nm length (coordination number : 1). This value is abnormally short for Nb-Nb distance in oxides. By TPD and UV-DRS together with EXAFS analysis, the structure of these catalysts were proposed as shown in Fig. 3.

Fig. 1. Fourier transform of the catalyst **1a**.Fig. 2. Fourier transform of the oxidized catalysts (a) **2a**, (b) **2b**.Fig. 3. Proposed structure of the oxidized catalysts (a) **3a**, (b) **3b**.Reference

- (1) D.A.Lemenovskii, I.F.Urazowski, I.E.Nifant'ev, and E.G.Perevalova, *J. Organomet. Chem.*, **292**, 217(1985).

THE STRUCTURAL STUDIES ON THE Al_2O_3 ATTACHED COBALT CATALYST IN THE NO-CO REACTION

Shintaro TAKAHARA, Kiyotaka ASAKURA, Yasuhiro IWASAWA

Department of Chemistry, Faculty of Science, The University of Tokyo, Hongo, Tokyo 113

Introduction

The alumina-attached $[\text{Co(II)}]_4$ catalyst derived from $\text{Co}_2(\text{CO})_8$ shows high activity toward CO oxidation reaction with O_2 at room temperature. The reaction mechanism has been determined by in-situ EXAFS spectroscopy⁽¹⁾. This catalyst is also active toward NO-CO reaction at above 353 K. According to in-situ IR measurement, NO is adsorbed on $[\text{Co(II)}]_4$ in twin type which is reactive to CO oxidation. We will argue in this report the mechanism of NO-CO reaction by means of EXAFS measurement in comparison with that of CO oxidation reaction with O_2 .

Experimental

The catalyst was prepared by the dry mixing method of $\text{Co}_2(\text{CO})_8$, which was then exposed to O_2 at 273 K, followed by evacuation at 513 K. The sample was then transferred to the EXAFS measurement cell. The preparation scheme was shown in Fig.1.

Results and Discussion

Fig.2 shows the Fourier transform of the $[\text{Co(II)}]_4$ catalyst. The sample prepared above shows only one peak around 0.17 nm. This is attributed to Co-O bond. The sample exposed to NO at 513 K for 1 h was cooled down to room temperature and submitted to EXAFS measurement. Under this condition, N_2O forms in the earlier stage, but activity decreases soon due to the accumulation of the oxygen atom on the catalyst. The Fourier transform also shows one peak, which is ascribed to Co-O bonding. This result forms striking contrast to the Fourier transform in the case of CO oxidation reaction with O_2 . $[\text{Co(II)}]_4$ catalyst under O_2 atmosphere shows two peaks. One peak around 0.17 nm is assigned to Co-O bond. The other peak appearing around 0.28 nm can be ascribed to Co-Co bonding. Even when $[\text{Co(II)}]_4$ catalyst was cooled to 80 K, no Co-Co bond was observed. This Co-Co bond became visible due to the bridged oxygen adsorbed on the neighboring Co atoms. The fact no Co-Co bond is observed in the NO-CO reaction suggests that the mechanism is different from that in the CO oxidation reaction with O_2 .

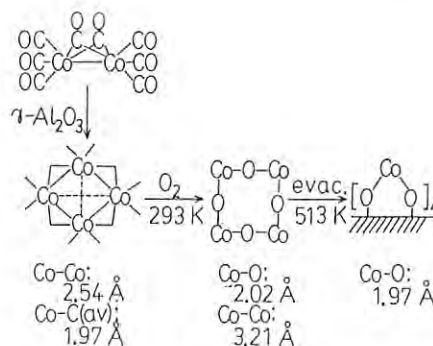


Fig.1. The preparation of the Al_2O_3 -attached $[\text{Co(II)}]_4$ catalyst.

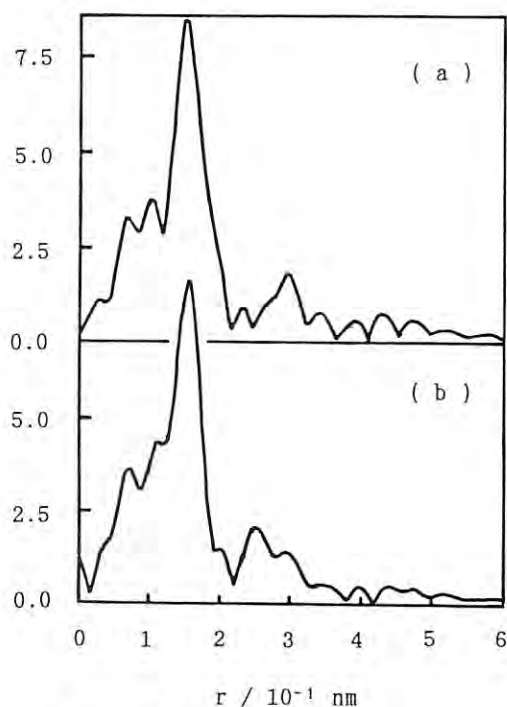


Fig.2. Fourier transform of;
(a) attached- $[\text{Co(II)}]_4$ catalyst
(b) exposure to NO at 513 K for 1 h

Reference

- (1) K.Asakura and Y.Iwasawa, *J.Phys.Chem.*, 1989, **93**, 4213.

Elucidation of Structure of Catecholdioxygenase-model Complexes and Mechanism of Oxygenation of Aromatic Ring

Takuzo FUNABIKI, Hiroyuki KOJIMA, Tunehiro TANAKA and Satohiro YOSHIDA

Department of Hydrocarbon Chemistry and Division of Molecular Engineering
Faculty of Engineering, Kyoto University, Sakyo-ku, Kyoto 606.

Introduction

In the previous study on the model chemistry of catecholdioxygenase, we observed the XANES spectra of the iron complexes prepared in situ. Here we isolated some intermediate complexes and compared spectra of these solid complexes with those in solution prepared in situ or from the isolated complexes.

Experimental

Catecholiron complexes were isolated from the solution of substituted catechols, FeCl_3 , pyridine in THF under argon atmosphere. From the elemental analysis, isolated complexes obtained from 3,5-di-*t*-butylcatechol (DTBC) or 3-Methylcatechol were identified as $[\text{Fe}(\text{cat})(\text{Py})\text{Cl}]$ and that from pyrocatechol or 4-Methylcatechol as $[\text{Fe}(\text{cat})\text{Cl}_2]$, indicating formation of 4 coordinate complexes. The THF or pyridine solution of these complexes was packed into polyethylene-nylon-polychlorovinylidene films under argon atmosphere. X-ray absorption spectra were recorded with the facilities at BL10B of KEK-PF. Concentrations of saturated solution of some complexes were not sufficiently high for observation of the edge jump in the EXAFS measurements.

Results and Discussion

Figure 1 shows the Fe K-edge XANES spectra of the solutions of 3-Methylcatecholiron complexes. All spectra show a pre-edge peak which is attributed to the $1s\text{-}3d$ transition. The pre-edge peak area of the complex in THF is approximately same as that of the isolated complex and larger than that of the complex in pyridine. Since peak area reflects the coordination number, the result indicates that a tetrahedral complex is formed in THF and an octahedral complex in pyridine. This result is consistent with the result of elemental analysis of the isolated complex. As shown in Table 1, the same results are obtained with other catechols. The probable structural change is that from $[\text{Fe}(\text{cat})\text{Cl}_2]$ in THF to $[\text{Fe}(\text{Cat})(\text{Py})_4]$ in pyridine.

Figure 2 shows the Fourier transforms of k^3 -weighted EXAFS spectra of DTBC-Fe complexes. The spectrum of the complex in solid is similar to that of the solid complex in THF and the spectrum of the solid complex in pyridine is also similar to that of the complex prepared in situ in pyridine. This indicates that the solution of the complex prepared in situ involves a single species. Detail analysis about proposed structure by curve fitting is in progress.

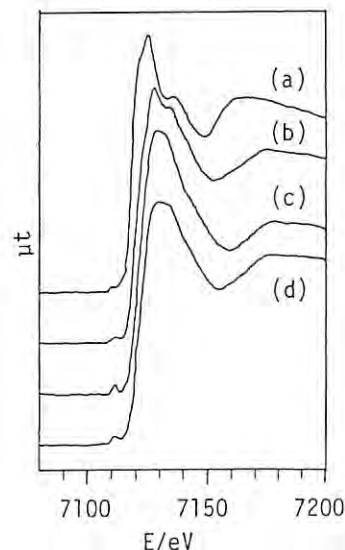


Fig. 1. XANES spectra of 3-MeCat-Fe complex
(a):3-MeCat, FeCl_3 in pyridine
(b-d):Isolated 3-MeCat complex
(b)in Py, (c)in THF, (d)powder

Table 1. Peak area of isolated complex

Catechol in Cat-Fe ^{a)}	peak area / units ^{b)}		
	powder	in THF	in Py
Pyro-Cat	15.27	15.52	5.54
3-MeCat	9.97	15.66	6.01
4-MeCat	15.22	18.90	6.11
DTBC	10.73	11.96	3.15

a)Catecholatoiron Complex. b)1 unit= 10^{-2} eV

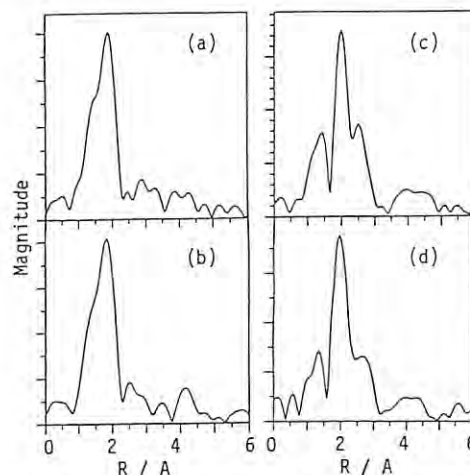


Fig. 2. FT of EXAFS of DTBC-Fe complex
(a-c):Isolated DTBC complex
(a)powder, (b)in THF, (c)in Py
(d):DTBC + FeCl_3 in Py

EXAFS STUDY ON AMORPHIZATION PROCESS OF PD-SI ALLOY BY MECHANICAL ALLOYING

Toshio NASU, Kunio NAGAOKA, Masaki SAKURAI*, Toshiharu FUKUNAGA**, Fumitake ITOH* and Kenji SUZUKI*

Faculty of Education, Yamagata University, 1-4-12 Kojirakawa, Yamagata 990 Japan

*Institute for Materials Research, Tohoku University, 2-1-1 Katahira, Sendai 980 Japan

**Faculty of Engineering, Nagoya University, Furoh-cho, Chikusa-ku, Nagoya 464 Japan

Introduction

Pd-Si amorphous alloy, prepared by rapid quenching method (RQ), is well known, and widely researched on structural properties(1). We produced the Pd-Si amorphous alloy by mechanical alloying (MA)(2). The purpose of this report is to investigate the structural changes during the solid state amorphization process of the Pd-Si alloy by means of EXAFS.

Experimental

Pd₈₃Si₁₇ alloy powder was prepared in a laboratory ball mill using stainless steel vials filled with high purity argon and hardened balls. Starting material was a mixture of Pd and Si powders. Sample preparation were performed to stop the ball milling at 0, 1.8x10⁵, 3.6x10⁵, 7.2x10⁵, 10.8x10⁵ and 14.4x10⁵s after milling commencement. EXAFS measurement were carried out at the beam line 10B. Energy scanning were carried out around the Pd K-edge.

Results and Discussion

Fig.1 shows the X-ray diffraction patterns of Pd-Si alloy prepared by MA as a function of milling time. Around 7.2x10⁵s of milling time, the Bragg peaks due to Pd and Si crystals almost disappeared and were replaced by a halo pattern, which shows that amorphous phase formed. Fig.2 shows the radial distribution function (RDF)

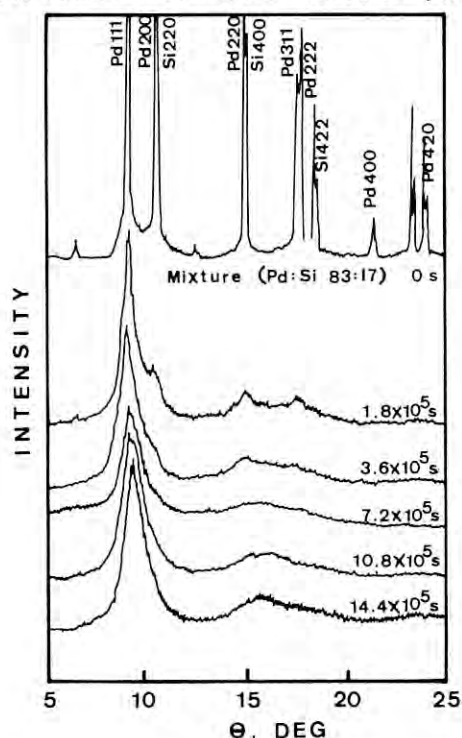


Fig.1 X-ray diffraction patterns of Pd-Si alloy produced by mechanical alloying as a function of milling time.

around a Pd atom of the alloy at the various stages of amorphization. At 3.6x10⁵s after the milling commencement, the peaks with arrows corresponding to the long range orders vanished, and appeared a new shoulder indicating the alloying of Si atom to Pd crystal. In the RDF of the amorphous alloy by RQ method, the main peak (Pd-Pd correlation) and sub peak (Pd-Si correlation) were observed separately. In contrast with this, the Pd-Si correlation was observed overlappingly to the Pd-Pd correlation as a shoulder in the case of MA. The Pd-Pd distance in the amorphous alloy produced by MA was shorter than that by RQ. The coordination number of Si atom around a Pd atom of the alloy by MA is smaller than that by RQ.

The authors wish to thank Dr.N.Kosugi for offering us the computer program of EXAFS data analysis.

References

- (1)T.Nasu et al., Materials Science and Engineering, 98, 553(1988).
- (2)T.Nasu et al., Materials Transactions,JIM., 30, 146(1989).

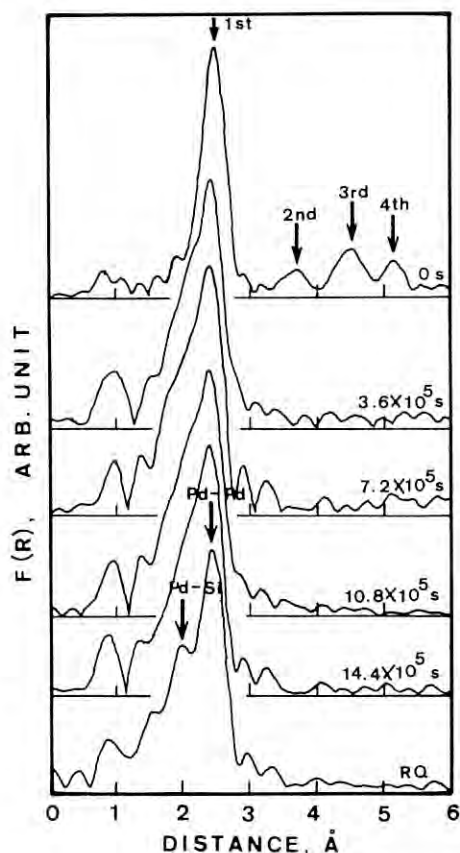


Fig.2 Fourier transform of EXAFS of Pd-Si alloy produced by mechanical alloying as a function of milling time and amorphous alloy prepared by rapid quenching method.

TEMPERATURE DEPENDENCE OF XANES IN $\text{CeO}_2\text{-Tb}_2\text{O}_{3.5}$ MIXED CONDUCTOR

Haruo ARASHI, Hitoshi NAITOH, Atsushi KAIMAI and Mareo ISHIGAME
Research Institute for Scientific Measurements, Tohoku University,
Katahira, Sendai 980, Japan

1. Introduction

Mixed electronic-ionic conductors have a wide field of application such as electrodes, electrocatalytic reactors and for gas separation. $\text{CeO}_2\text{-Tb}_2\text{O}_{3.5}$ system shows mixed conduction. Compounds containing Tb ions exhibit an electronic conduction given by the presence of Tb in either trivalent or tetravalent state. As the valence state of Tb ion changes with temperature, the electrical conductivity shows a complicated temperature dependence. In order to clarify the mechanism for electronic conduction in $\text{CeO}_2\text{-Tb}_2\text{O}_{3.5}$ system, the fraction of Tb ions in tetravalent state has to be determined over a wide temperature range.

For rare-earth ions, the XANES measurements in the L_3 absorption edge is the most direct method for determining the valence change and has been successfully applied to Ce, Eu and Tb compounds.

In this paper, results of investigations of the temperature dependence of valence state of Tb ions in $\text{CeO}_2\text{-Tb}_2\text{O}_{3.5}$ system determined by XANES measurements at various temperature are reported.

2. Experimental

The solid solutions were prepared by means of a solid-state reaction between CeO_2 and Tb_2O_3 . The mixed powders were isostatically pressed into rods under a pressure of 2 ton/cm² and sintered for 5 hrs at 1750°C in air.

XANES spectra were measured using the BL-10 beam line. XANES spectra were measured near the L_3 absorption edge of Tb ion.

3. Results and Discussions

The temperature dependence of XANES spectra of $\text{CeO}_2\text{-Tb}_2\text{O}_{3.5}$ system was measured in the temperature range from room temperature to 1000°C. The result is

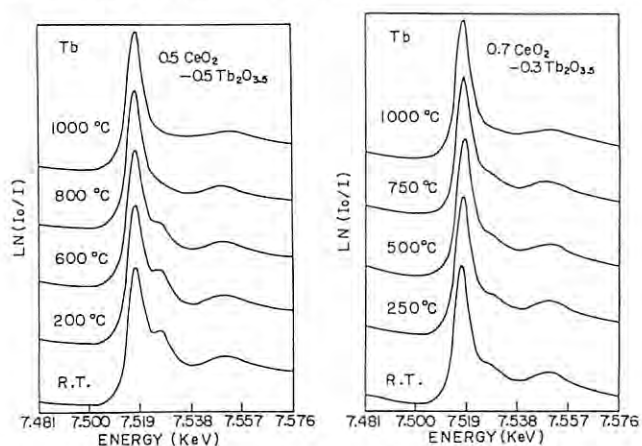


Fig. 1 Temperature dependence of XANES spectra

shown in Fig. 1. XANES spectra measured at room temperature have two absorption peaks near the L_3 edge of Tb ion. The energy difference between the two absorption peaks is about 8.4 eV. These absorption peaks correspond to the transition from the 2p to the 5d level in Tb ion. The Tb^{3+} ion changes its valence into tetravalent losing one 4f electron. The binding energy of the 2p electrons differs by 8-10 eV from the trivalent to the tetravalent state in rare-earth elements because of the difference in number of 4f electrons. In XANES spectra, this difference is observed as an energy shift of the absorption peak. Therefore, the two absorption peaks observed in XANES spectra are assigned to tetravalent and trivalent state respectively. The absorption peak observed at the higher energy side always corresponds to tetravalent state.

In the observed XANES spectra, the intensity of the shoulder $^{4+}$ which corresponds to the amount of Tb^{4+} ions decreases with increasing temperature. From these experimental results, it is concluded that Tb^{4+} ions in $\text{CeO}_2\text{-Tb}_2\text{O}_{3.5}$ solid solution change its valence state from tetravalent to trivalent with increasing temperature.

The determination of the ratio of Tb^{4+} to Tb^{3+} ions was made by using a least square fitting method. The analyzed result of temperature dependence of the $\text{Tb}^{4+}/\text{Tb}^{3+}$ ratio is shown in Fig. 2. The amount of Tb^{4+} ions decreases slightly with increasing temperature up to 500°C. Above 500°C, Tb ions in tetravalent state changes rapidly their valence to trivalent state with increasing temperature. On the basis that electronic conduction is governed by the concentration of Tb ions in tetravalent state, this observed decrease in Tb^{4+} content explains the decrease in electronic conduction with increasing temperature.

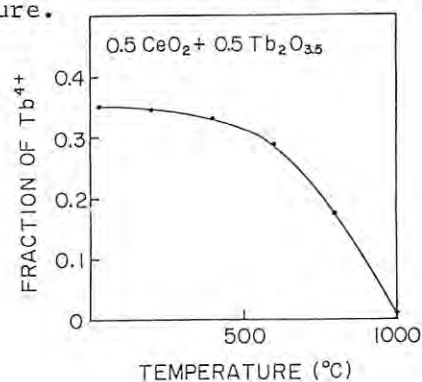


Fig. 2 Temperature dependence of the fraction of Tb^{4+}

EXAFS STUDIES ON THE LOCAL STRUCTURES OF STRONTIUM AND IRON CATALYSTS FOR COAL GASIFICATION

Hiromi YAMASHITA and Akira TOMITA

Chemical Research Institute of Non-Aqueous Solutions, Tohoku University, Katahira, Sendai 980, Japan.

Introduction

Previously, change of local structure of iron catalyst during the devolatilization or gasification process has been investigated by EXAFS¹. The structure of iron much depend on the catalyst loading, coal rank and precursor salt. Although Cl^- contamination promotes the aggregation of catalyst, the utilization of cheap iron chloride which are obtained as acid wastes from steel-making is promising process. In the present study, ion-exchanging method has been applied to remove Cl^- during preparation of Fe-loaded and Sr-loaded coals. The dependence of structure of catalysts on the condition of catalyst-addition was investigated by EXAFS.

Experimental

Loy Yang brown coal from Victoria, Australia, was used. FeCl_3 , $\text{Fe}(\text{NO}_3)_3$, SrCl_2 and $\text{Sr}(\text{NO}_3)_2$ were used as precursor salts. Several Fe-loaded coals and Sr-loaded coals (2-10 wt% as metal) were prepared by ion-exchanging under different pH 1-12 or impregnation. The coal samples were dried and devolatilized in N_2 in a fluidized bed reactor. EXAFS spectra at Fe K-edge and Sr K-edge were recorded in a transmission mode on a beam line BL-10B at KEK-PF at room temperature using Si(311) channel cut monochrometer.

Results and Discussion

On the preparation of Fe-loaded coal by ion-exchanging, structure of iron catalyst much depends on pH value of solution. Although Fe^{3+} precipitates easily in the solution of high pH value, the observation of precipitate by XRD method is very difficult, because precipitate highly dispersed on coal. Figure 1 shows Fourier transforms (F.T.s) of the k^3 -weighted EXAFS spectra of dried Fe-loaded coal prepared by ion-exchanging method with different pH solutions. The samples with pH 1-3 (a,b) exhibited a only peak due to neighboring oxygen atoms (Fe-O) at 1.5 Å. The samples with pH 4-11 (c,d) exhibited a obvious peak due to neighboring iron atoms (Fe-Fe) at 2.8 Å as well as Fe-O peak, suggesting the formation of FeOOH -like fine particles¹. The intense of Fe-Fe increased with pH values, indicating the crystallization of FeOOH -like fine particle proceeded significantly. The ion-exchanging must be carried out in the solutions with pH ~3 to realize highly dispersion of iron catalyst.

Figure 2 shows F.T.s of EXAFS spectra of standard SrO , SrCO_3 , SrCl_2 and $\text{Sr}(\text{OH})_2$ (a-d) and several Sr-loaded chars devolatilized at 950°C (e-h). The peaks due to neighboring oxygen, chlorine and strontium atoms were observed at 1.9 Å (Sr-O), 2.4 Å (Sr-Cl) and 3.4, 3.8, 4.7 Å (Sr-Sr), respectively. The Sr-loaded char (g)

prepared by impregnation of SrCl_2 [ICL] exhibited Sr-O and Sr-Cl peaks. The Sr-loaded chars prepared by impregnation of $\text{Fe}(\text{NO}_3)_2$ (e,f) and by ion-exchanging of SrCl_2 [ECL] (h) exhibited Sr-O and small Sr-Sr peaks. These results indicated that SrCl_2 crystalline and SrCO_3 fine particle formed in ICL and ECL chars, respectively.

References

- 1) H.Yamashita Y.Ohtsuka, S.Yoshida and A.Tomita, Shokubai, **31**, 88 (1989).

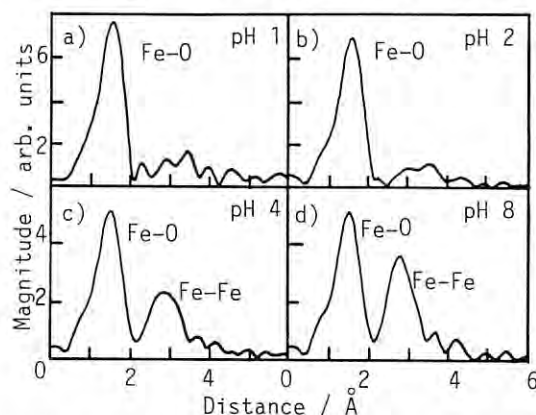


Fig. 1 F.T.s of Fe K-edge EXAFS spectra of dried Fe-loaded coals prepared by ion-exchanging in FeCl_3 solution.

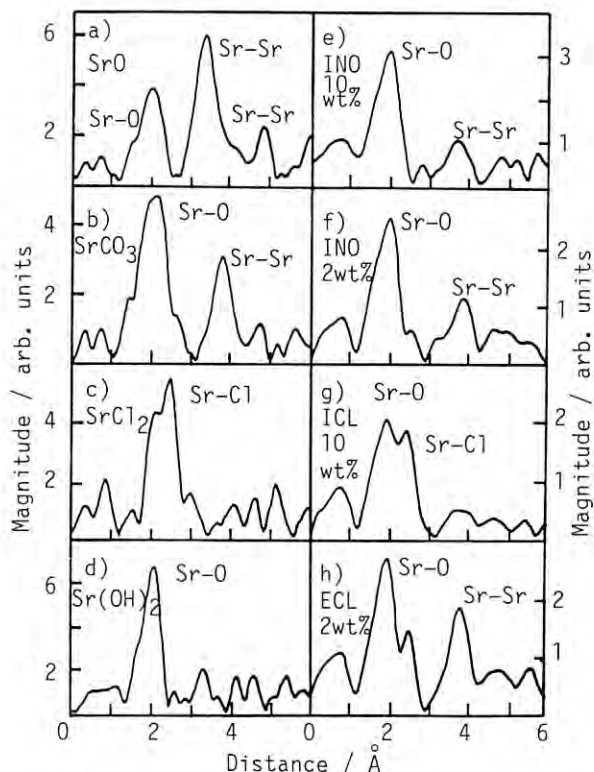


Fig. 2 F.T.s of Sr K-edge EXAFS spectra. INO; impregnation of $\text{Sr}(\text{NO}_3)_2$. ICL; impregnation of SrCl_2 . ECL; ion-exchange of SrCl_2 .

EXAFS STUDIES OF Cu(I,II)-NH₃, py, phen, bpy COMPLEXES IN AQUEOUS SOLUTION

Kazuhiko OZUTSUMI, Izumi NAKAI, and Takuji KAWASHIMA

Laboratory of Analytical Chemistry, Department of Chemistry,
The University of Tsukuba, Tsukuba 305Introduction

Kinetic methods for the determination of metal ions based on their catalytic effect on redox reactions are more sensitive than those based on stoichiometric reactions. Activators have been known as reagents which increase the sensitivity and selectivity of quantitative analysis in the presence of certain metal ions. Ammonia, pyridine, 2,2'-bipyridine, 1,10-phenanthroline are often used as an activator in the catalytic determination of copper ion. It is essential, therefore, to obtain structural data of these complexes in order to elucidate the effect of activators on catalytic reactions. In the following we report the structure of copper(I,II)-pyridine complexes in aqueous solution.

Experimental

Sample solutions were prepared by dissolving copper(II) nitrate and pyridine at suitable C_{py}/C_{Cu} mole ratios in water. A copper(I)-pyridine solution was prepared by dissolving copper(II) sulfate and pyridine in water and contained a large excess of hydroxyammonium sulfate. X-Ray absorption spectra of sample solutions were measured around the Cu K-edge at the BL10B of the Photon Factory, KEK.

Results and Discussion

Figure 1 shows the Fourier transforms of sample solutions. The first intense peaks at 155 pm found in all solutions are ascribed to the Cu-O and Cu-N bonds within the pyridine complexes. Structure parameters were finally obtained by curve fitting procedure to the Fourier-filtered $k^3 \cdot \chi(k)$ values and the results are summarized in Table 1.

For copper(II) complexes, no higher pyridine complex than the tetrakis(pyridine)copper(II) one is formed under the experimental conditions examined in the present study. It is also found that all pyridine complexes have an axially elongated octahedral structure. In solutions with C_{py}/C_{Cu} ratios of one, two, and three, some complex species are coexisting, and thus the Cu-O and Cu-N bond distances obtained by the curve fit analysis are averaged ones. As seen in Table 1, both Cu-O(eq) and Cu-N(eq) bond lengths are slightly lengthened with increasing the number of pyridine molecules bound to copper(II) ion and the Cu-O(ax) distances are also appreciably lengthened. The equatorial and axial distances within many copper(II) complexes have been found to correlate asymptotically in crystal,¹⁾ and therefore, the present observation is interesting since the distances proportionally correlate.

In a copper(I) solution containing a large excess of pyridine, the tris(pyridine)copper(I) complex is formed. No water molecule hydrates copper(I) ion and the complex has a three-

coordination structure. The Cu-O bond length is 202 pm and practically the same as that within the tetrakis(pyridine)copper(II) complex.

References

- 1) J. Gazo, I. B. Bersuker, J. Garaj, M. Kabesova, J. Kohout, H. Langfelderova, M. Serator, and F. Valach, *Coord. Chem. Rev.*, **19**, 253 (1976).

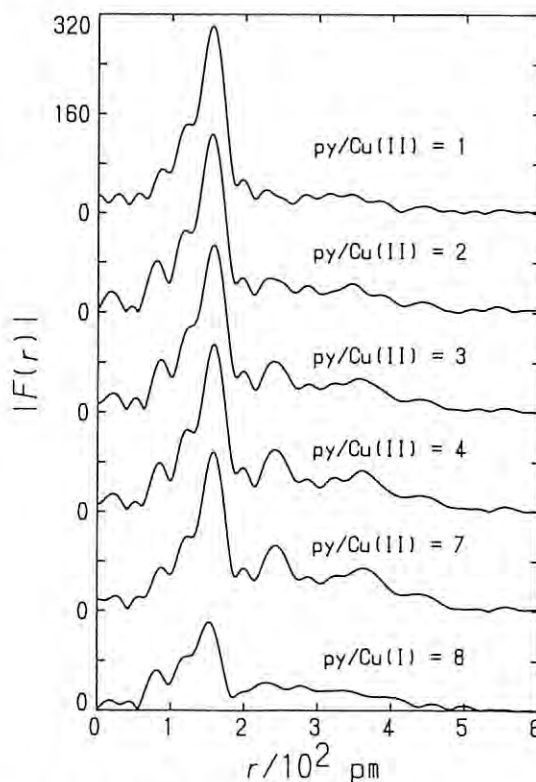


Fig. 1. Fourier transforms of sample solutions.

Table 1. Structure parameters of complexes.

		py/Cu(II)					py/Cu(I)
		1	2	3	4	6	8
Cu-O	r/pm	198	198	200	-	-	-
	(eq) σ /pm	6.3 [*]	6.3 [*]	6.3 [*]	-	-	-
	n	3 [*]	2 [*]	1 [*]	-	-	-
Cu-N	r/pm	197	200	201	202	202	202
	(eq) σ /pm	6.3 [*]	6.3 [*]	6.3 [*]	5.9	6.2	8.4
	n	1 [*]	2 [*]	3 [*]	4 [*]	4 [*]	3.1
Cu-O	r/pm	229	227	234	242	240	-
	(ax) σ /pm	12.4	14.5	16.0	19.1	18.2	-
	n	2 [*]	2 [*]	2 [*]	2 [*]	2 [*]	-
Cu...C	r/pm	295	297	298	298	299	299
	σ /pm	6.5	6.8	7.4	7.8	7.5	9.5
	n	2 [*]	4 [*]	6 [*]	8 [*]	8 [*]	6.6

* Fixed.

OXIDATIVE DISRUPTION OF RHODIUM PARTICLE SUPPORTED ON SILICA BY O₂ AND CO

Takakazu FUKUSHIMA

Department of Materials Science and Chemical Engineering, Faculty of Engineering,
Yokohama National University, 156 Tokiwadai, Hodogaya-ku, Yokohama 240

Introduction

It has been indicated using EXAFS technique¹⁾ that ultra-fine particles of Rh are disrupted by the addition of CO, and we have confirmed this using IR and EXAFS techniques²⁾. We also have shown that oxygen adsorption even at room temperature can disrupt a small Rh crystal to atomic oxides. In this report we try to show the oxidative disruption of Rh/SiO₂ by CO and O₂ and discuss the difference in IR spectra of adsorbed CO species between alumina- and silica-supported Rh catalysts on the basis of EXAFS study.

Experimental

The catalysts were prepared and reduced by the method described elsewhere³⁾. The sample powder was pressed into wafer and mounted in a glass cell. The EXAFS measurements were carried out in appropriate gas atmospheres at r.t. by use of the EXAFS spectrometer at the Beam Line 10B.

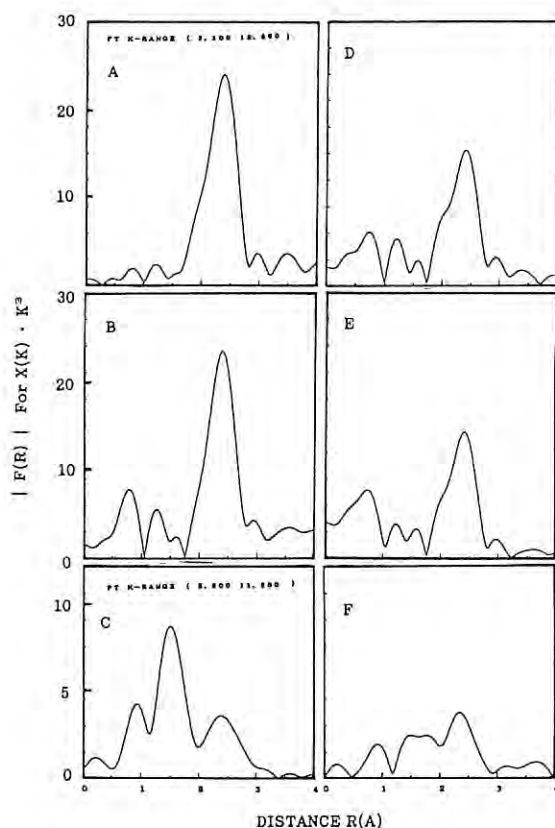


Fig. 1. Fourier transforms of the Rh K-edge EXAFS of 0.5wt% Rh/SiO₂ catalysts.

A:re-reduction at 400 C; B:re-reduction at r.t.
C:passivation only; D:CO after re-reduction at 400 C; E:CO after re-reduction at r.t.; F:CO after passivation

Results and Discussion

Fourier transforms of the Rh K-edge EXAFS of 0.5 wt% Rh/SiO₂ catalysts are shown in Fig. 1 and EXAFS parameters obtained by curvefitting analyses are tabulated in Table 1. By the re-reduction of the passivated sample at 400 C for 1 hr by H₂(Fig. 1A), the coordination number(N) of 6.9 is obtained and this is a little bigger than that of 6.3 obtained on alumina sample. It can be seen that Rh particle is disrupted to atomic oxides by the adsorption of oxygen during the passivation procedure at r.t.(Fig.1C). These atomically dispersed oxides can agglomerate easily by the contact of H₂ at r.t.(Fig. 1B) and these results coincide with that measured on alumina. Figs. 1D and 1E show that relatively smaller Rh-Rh peaks than on reduced sample and indicate that Rh particle on SiO₂ can be disrupted by CO adsorption as on alumina. Coordination value of Rh-Rh around 4.5 in Table 1 is much larger than that of 1.5 obtained on Rh/Al₂O₃ and these results agree with the difference in the IR spectra of adsorbed CO between Rh/SiO₂ and Rh/Al₂O₃. The amount of gem-species, which indicate the presence of atomically dispersed Rh, is less on SiO₂ than on Al₂O₃. It is observable that there are two peaks in the Rh-O region, and the average coordination number and the distance are 2.5 and 2.15 Å, respectively. This distance is longer than that of passivated sample 2.05 Å, which is exactly the same as Rh-O distance in Rh₂O₃. These results agree with the IR study where there are two kinds of gem-species. It is concluded that an atomic oxide with four oxygen coordination reacts with two CO molecules and gives gem-dicarbonyl attached to three oxygen of silica with a distance of 2.15 Å.

References

- 1) H.F.J.Van't Blik *et al.*, J. Am.Chem.Soc., **107**,3139(1985).
- 2) T.Fukushima *et al.*, Photon Factory Activity Report 39(1988).
- 3) T.Fukushima *et al.*, Photon Factory Activity Report 233(1987).

Table 1. Curvefitting results for 0.5wt% Rh/SiO₂

Fig.1	Rh-Rh		Rh-O	
	(N)	R(A)	(N)	R(A)
A	6.9	2.68	-	-
B	7.0	2.70	-	-
C	-	-	3.9	2.05
D	3.9	2.69	-	-
E	5.4	2.71	-	-
F	-	-	2.5	2.15

EXAFS STUDY ON AMORPHOUS Fe-Ti-H ALLOYS PRODUCED BY VAPOR QUENCHING

Kenji SUMIYAMA, Ken-ichi NISHI, Munehiro SHIMA and Hideyuki YASUDA
Department of Metal Science and Technology, Kyoto University, Kyoto 606
and

Masaaki YAMADA and Kazuhide TANAKA
Department of Materials Science and Engineering, Nagoya Institute of Technology, Nagoya 466

Introduction

Vapor quenching methods such as thermal evaporation and sputter-deposition are quite powerful to produce several nonequilibrium alloys. Amorphous $\text{Fe}_{1-x}\text{Ti}_x$ alloys, which have not been obtained by liquid quenching, can be produced by sputter-deposition for $x=0.2-0.75$. X-ray diffraction and EXAFS measurements of these alloys reveal that Fe and Ti atoms randomly mix and form a poly-tetrahedral stacking.¹⁾²⁾

Amorphous Fe-Ti alloy films show good hydrogen absorption and desorption characteristics and a candidate material of hydrogen filter. In this project, we study the local structure change of amorphous Fe-Ti alloys by hydrogenation.

Experimental

A few micron thick $\text{Fe}_{1-x}\text{Ti}_x$ alloy films were prepared by a facing target type DC sputtering equipment. Samples with high H contents were prepared by electrolytic charging in 0.1N HClO_4 solution. EXAFS measurements at 290 K were carried out at BL-10B station.

Results and Discussion

X-ray absorption spectra at the pre-edge of $\text{Fe-K}\alpha$ for amorphous $\text{Fe}_{0.29}\text{Ti}_{0.71}$ and $(\text{Fe}_{0.29}\text{Ti}_{0.711})\text{H}_{1.13}$ alloys are shown in

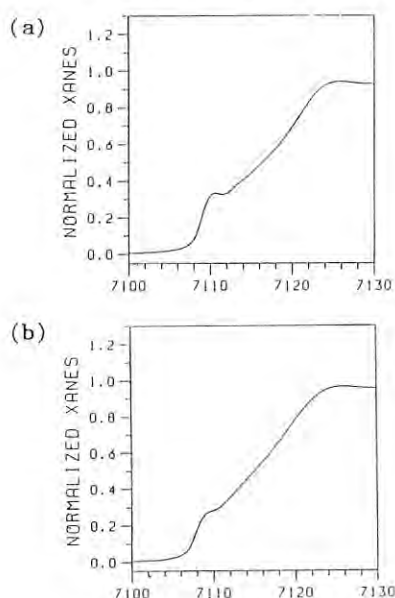


Fig.1 X-ray absorption spectra at the pre-edge of $\text{Fe-K}\alpha$ for (a) amorphous $\text{Fe}_{0.29}\text{Ti}_{0.71}$ alloy and (b) amorphous $(\text{Fe}_{0.29}\text{Ti}_{0.711})\text{H}_{1.13}$ alloy.

Figs.1(a) and (b). In the amorphous $\text{Fe}_{0.29}\text{Ti}_{0.71}$ alloys, a clear hump is ascribed to an s-p band structure of Fe just above the Fermi level, originating in the Fe-Ti mixing. In the amorphous $(\text{Fe}_{0.29}\text{Ti}_{0.711})\text{H}_{1.13}$ alloy, on the other hand, it becomes obscure, resembling to that of pure Fe. This aspect indicates that H atoms preferably bind with Ti atoms and the electronic structure of Fe atoms becomes similar to that of pure Fe.

Figures 2 shows the Fourier transform of EXAFS oscillation, $k^3\chi(k)$, at the $\text{Fe-K}\alpha$ edge for the amorphous $\text{Fe}_{0.29}\text{Ti}_{0.71}$ and $(\text{Fe}_{0.29}\text{Ti}_{0.711})\text{H}_{1.13}$ alloys. There is no qualitative difference in these spectra. However, the interatomic distances between Fe-Ti and Fe-Fe estimated from the best fitting are 2.653 and 2.476 Å for the amorphous $\text{Fe}_{0.29}\text{Ti}_{0.71}$ alloy and 2.698 and 2.499 Å for the $(\text{Fe}_{0.29}\text{Ti}_{0.711})\text{H}_{1.13}$ alloy, respectively. These results indicate that H atoms locate the interstitial sites of metal atoms and expand the interatomic distances between the metal atoms.

References

- 1) H.Yasuda, K.Sumiyama and Y.Nakamura: submitted to J.Phys. Condensed Matters.
- 2) H.Yasuda, K.Sumiyama, Y.Nakamura, S.Tanaka H.Mizutani and S.Yoshida: in preparation.

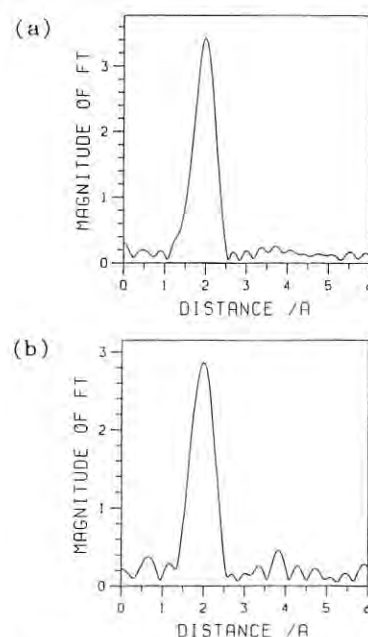


Fig.2 Fourier transform of EXAFS oscillations at $\text{Fe-K}\alpha$ edge for (a) amorphous $\text{Fe}_{0.29}\text{Ti}_{0.71}$ and (b) $(\text{Fe}_{0.29}\text{Ti}_{0.711})\text{H}_{1.13}$ alloys.

EXAFS STUDY ON ANHARMONIC VIBRATION IN CuBr

Hironobu MAEDA, Akira YOSHIASA*, Kichiro KOTO**, Tadashi ISHII*** and Sestsuo KASHINO

Faculty of Science, Okayama University, Okayama 700

*Faculty of Science, Hiroshima University, Hiroshima 730

**Faculty of Integrated Arts and Science, Tokushima University, Tokushima 770

***Faculty of Engineering, Okayama University, Okayama 700

Introduction

The EXAFS studies on CuBr of α , β and γ -phases are made on the basis of the anharmonic vibration model, which is physically clear. Thus the EXAFS data will be analyzed by the help of the EXAFS formula, given in terms of the cumulant expansion[1], to obtain the temperature dependence of the interatomic distances and cumulants.

In order to extract the temperature dependence of Br-Cu distance and cumulants, we have increased temperatures from 20 up to 753 K, which include the transition temperatures of 658 K ($\gamma \rightarrow \beta$) and 743 K ($\beta \rightarrow \alpha$). The space groups are $Im\bar{3}m$, $P6_3mc$ and $F\bar{4}3m$ for α , β and γ -phases, respectively.

Experiments

The fine powder samples of CuBr were pressed with powder of boron nitride into pellets of 0.5 mm in thickness and 13.0 mm in diameter. X-ray absorption measurements near Cu and Br K-edges were made using the EXAFS facilities installed at BL-10B. The data reduction and curve-fitting were performed as detailed elsewhere [1,2].

Results and Discussion

The cumulants of third and fourth-order play quite important role in the EXAFS contribution, where the cumulants and interatomic distance are temperature dependent (Fig. 1).

One prominent and significant result is a negative thermal expansion of the Cu-Br distance (Fig. 2(2)). The data X between 20 and 300 K in Fig. 2(a) are the X-ray diffraction data quoted from Pendl and Mansur [3], which agree with the present data. They have also observed over 10-50 K a negative thermal expansion which is quite concerned with the anharmonic lattice vibrations. On the other hand, from the other X-ray diffraction data[4], the Cu-Br distances R_{C-B} are 2.46 Å at 299 K (γ -phase), 2.49 Å at β -phase and 2.54 Å at 753 K (α -phase). Hence the temperature dependence of R_{C-B} is apparently in contradiction to that of the EXAFS. This implies that the negative thermal expansion of Cu-Br distance in the α -phase is originated in the volume contraction of the Cu occupying tetrahedrons with increasing in temperature. The Cu unoccupying tetrahedrons should enlarge, and totally the crystal volume expands with temperature. Detailed analysis is now in progress.

[1] T. Ishii: "Principles of the Theory of EXAFS Debye-Waller Type of Factors". (Okayama, Jan., 1988), unpublished.

[2] H. Maeda: J. Phys. Soc. Jpn. 56(1987)2777.

[3] J. N. Pendl et al.: Appl. Opt. 11(1972)1194.

[4] V. J. Krug et al.: Z. Natur. Forschg. 7A(1952) 369.

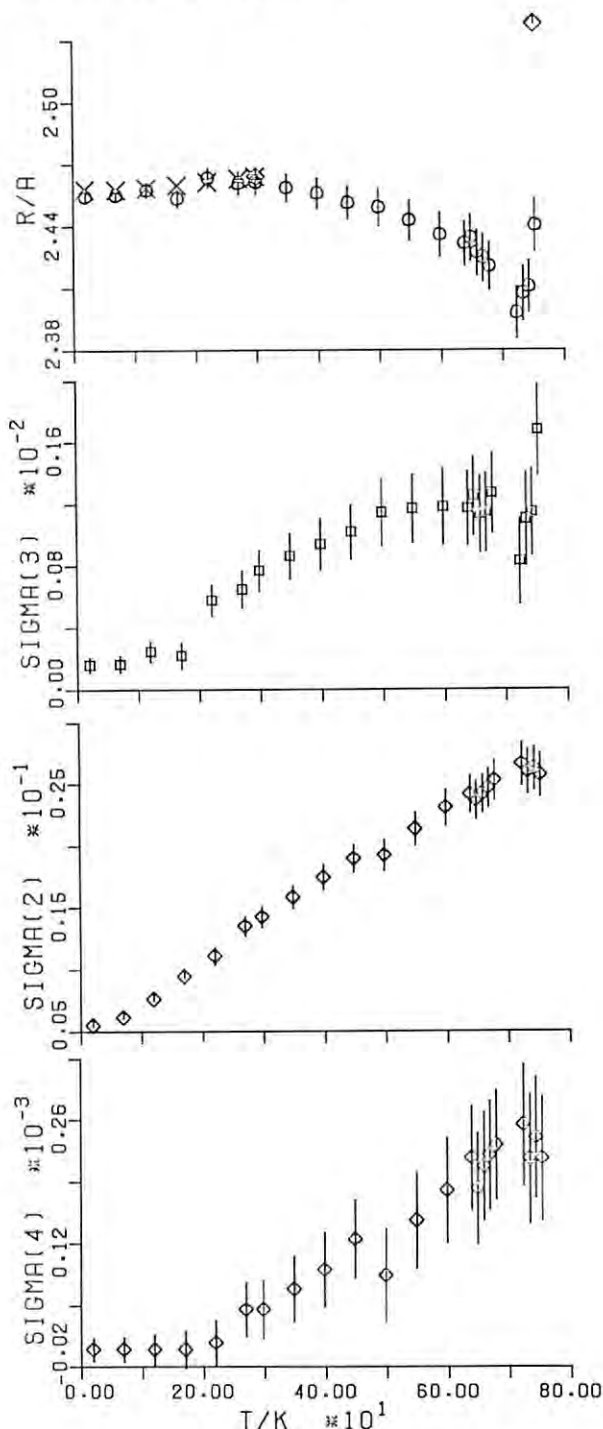


Fig.1 Temperature dependences of (a) Cu-Br distance together with X-ray diffraction data, (b) third-order cumulant $\sigma^{(3)}$, (c) second-order cumulant $\sigma^{(2)}$ and (d) fourth-order cumulant $\sigma^{(4)}$.

Br K-edge XANES and EXAFS studies on bromine-adsorbed small Pd clusters supported on silica

Toshihiko YOKOYAMA, Akiko IMADA, Fumiko TAKAMATSU, Masahiko YOSHIKI
and Toshiaki OHTA

Department of Materials Science, Faculty of Science, Hiroshima
University, Naka-ku, Hiroshima 730

It is important to characterize adsorbate-substrate interaction in order to understand the initial stage of chemical reaction process. Small metal particles have tremendously large surface area, and the adsorption experiment on them makes possible to study the adsorbate-substrate interaction. Advantages of this method are to be able to employ the conventional transmission EXAFS technique and to discuss more detailed structures owing to the acquisition of more reliable data. In this study, we have studied Br-adsorbed Pd clusters to characterize Br-Pd interaction.

The small Pd clusters (Pd 2wt% loading) supported on silica were prepared by the ion-exchange method. Supported Pd ammine complexes were reduced with hydrogen at 673 K and subsequently evacuated at the same temperature to result in bare Pd clusters. The amount of hydrogen uptake, H/Pd was 0.55. The clusters were dosed with either Br₂ (Br/Pd=0.63) or BBr₃ (saturated amounts) at ambient temperature. Br K-edge XANES and EXAFS spectra were measured at several temperatures at the EXAFS facility of BL 10B in an inert atmosphere.

Figure 1 shows the Br K-edge XANES spectra of Br₂- or BBr₃-adsorbed Pd clusters. In the spectrum of Br₂-adsorbed one, the peak due to the Br1s→Pd4d transition (indicated by an arrow) is so strong as those of typical divalent metal bromides, while the spectrum of BBr₃-adsorbed one has only a shoulder around that region.

Both of the EXAFS spectra indicate the formation of Br-Pd chemical bondings, and the lack of BrBr and BrB coordinations. Only in the Fourier transform of Br₂-adsorbed one, an additional contribution which can be ascribed to Br-Br is found. Table 1 gives the results of EXAFS analysis for the first nearest neighbor Br-Pd coordination. It is noted that the bond distance of Br₂-adsorbed one is significantly shorter and the mean square relative displacement (Debye-Waller factor) is greater than that of BBr₃-adsorbed one.

We can deduce the local structures in both Br-adsorbed systems. In the Br₂-adsorbed one, bromine adsorbs on the Pd clusters dissociatively, and is further embedded into the clusters to form PdBr₂ bulk bromide. On the contrary, BBr₃ adsorbs on the surface of the clusters dissociatively, and forms a weak chemical bond. Boron atoms might react

with hydroxyl groups of the support and form borate anions. It can be remarked that the Br-Pd bonding in the Br₂-adsorbed system is much stronger than in the BBr₃-adsorbed one, taking account of the difference of the interatomic distances and the mean square relative displacements. The dissimilarity in the XANES spectra indicates the difference of the valence state of Pd atoms; Pd atoms in the Br₂-adsorbed one is essentially divalent, while those in the BBr₃-adsorbed one may be only slightly cationic. Such a definite difference originates from the dissimilar chemical reactivities between Br₂ and BBr₃.

Table 1. Results of Br K-edge EXAFS analysis for the first nearest neighbor Br-Pd coordinations.

Sample	Temp.	N	R(A)	$\Delta\sigma(\text{\AA}^2)$
Br ₂ /Pd	106 K	2.0	2.469	0.00x10 ⁻³
	295 K	(2.0)	2.465	1.12x10 ⁻³
BBr ₃ /Pd	118 K	2.0	2.522	4.02x10 ⁻³
	209 K	(2.0)	2.527	4.82x10 ⁻³
	295 K	(2.0)	2.527	5.13x10 ⁻³

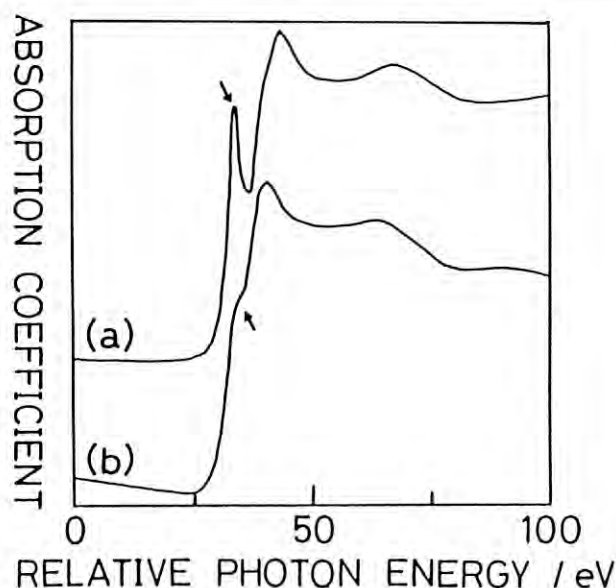


Fig.1. Br K-edge XANES of Br₂- (a) and BBr₃-adsorbed (b) Pd clusters. The Br1s→Pd4d transitions are indicated by arrows.

Anharmonic interatomic potentials determined by temperature-dependent EXAFS spectra of AgBr and CuBr

Toshihiko YOKOYAMA, Tomiaki Satsukawa and Toshiaki OHTA

Department of Materials Science, Faculty of Science, Hiroshima University, Naka-ku, Hiroshima 730

It is well recognized that EXAFS spectroscopy can give information about coordination numbers, interatomic distances and thermal vibrations around an X-ray absorbing atom. Recently, a more general EXAFS formalism has been developed, which is based on the cumulant expansion method[1]. The analysis of temperature-dependent EXAFS spectra with this method can yield detailed information such as thermal expansion coefficients[2].

In this report, we explore the possibility that the EXAFS analysis with this formalism gives a reliable anharmonic interatomic potential.

CuBr and AgBr were chosen as samples since they exhibit large anharmonicity around room temperature. Spectroscopic measurements were performed at BL 10B. Both metal and Br K-edge spectra were taken in order to enhance the reliability.

The EXAFS analyses were performed by means of the 4th-order cumulant expansion technique. The determination of interatomic potentials was subsequently carried out by use of the obtained cumulant expansion coefficients such as interatomic distances, mean square relative displacements and mean cubic relative displacements. The details of this method are described elsewhere[3]. We assumed analytical potential functions (Madelung potential) and classical Boltzmann distribution. The potential parameters are summarized in Table 1, and Fig.1 shows the Madelung potential curves derived from Ag-K and Br-K edge EXAFS data, together with the one obtained by the empirical estimation using its dissociation energy and ionic radii as parameters. Excellent agreement is achieved among these three potential curves estimated independently; it is noted that even the dissociation energies determined agree well with the thermodynamical data. This indicates that the Madelung function is appropriate enough to describe interatomic potentials of ionic crystals. Correspondingly, the Madelung constants estimated are consistent with the values given by the simple estimations.

It is revealed that reliable interatomic potentials can be determined by the analysis of temperature-dependent EXAFS spectra. The simulation analysis by means of Madelung potentials makes it possible to estimate not only the thermal expansion coefficients but also the dissociation energies and the Madelung constants quite appropriately.

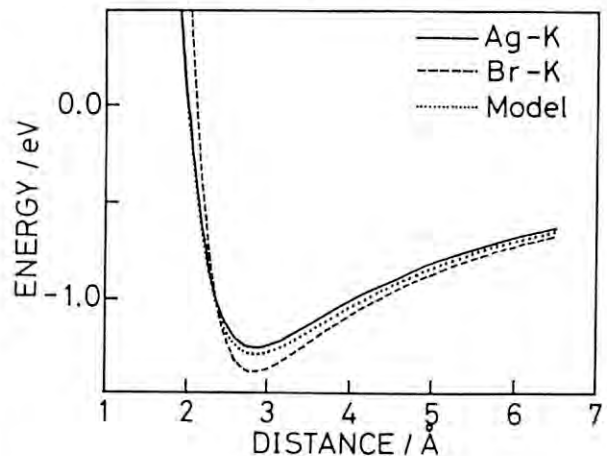
This method should be a powerful tool for the estimation of interatomic potentials of complicated materials such as supported ultrafine particles[3] which cannot be investigated by the usual thermal measurements.

- [1] G.Banker, Nucl.Instrum.Methods 207 (1983) 437.
- [2] T.Yokoyama, S.Kimoto and T.Ohta, Photon Factory Activity Report 6 57 (1988); Jpn.J.Appl.Phys. 28 (1989) L851.
- [3] T.Yokoyama and T.Ohta, Photon Factory Activity Report in this volume.

Table 1 Simulated thermal expansion coefficients α , dissociation energies D and Madelung constants κ .

Sample	$\alpha (10^{-5} K^{-1})$	D(eV)	κ
AgBr			
Ag-K	3.31(3.31)	1.26(1.56)	1.70(1.75)
Br-K	3.31(3.31)	1.38(1.56)	1.82(1.75)
CuBr			
Cu-K	1.72(1.28)	1.99(2.53)	1.56(1.64)
Br-K	1.29(1.28)	2.39(2.53)	1.92(1.64)

Fig.1. Interatomic potentials of AgBr determined by the EXAFS data.



CHARACTERIZATION OF Cu-Ta ALLOY SYSTEM SYNTHESIZED BY MECHANICAL ALLOYING

Kenji SAKURAI, Masahisa ITO*, Yuh YAMADA and Uichiro MIZUTANI**

*National Research Institute for Metals, Sengen, Tsukuba, Ibaraki 305

**Institute of Physical and Chemical Research, Hirosawa, Wako, Saitama 351-01

Department of Applied Physics, Nagoya University, Furo-cho, Chikusa-ku, Nagoya 464-01

Introduction

The mechanical alloying (MA) is a new technique for the formation of amorphous alloys by means of solid state reaction between the elemental, crystalline powders.¹⁾ Recently it has been suggested that MA might facilitate the synthesis of amorphous Cu-Ta alloy system, which is immiscible and is never amorphized by conventional liquid quenching method.²⁾ In this report, preliminary results of EXAFS study on Cu-Ta alloy prepared by MA are shown.

Experimental and Results

Pure metallic powders of copper and tantalum were mixed with a ratio of 3 to 7, and were milled for 76 hours with the Cu-Be vial and balls in an argon atmosphere. A broad X-ray diffraction halo pattern, which is usually obtained for amorphous materials, was observed for this sample.²⁾ Trace element analysis by XRF using SR shows that contamination of this sample is in extremely low level. EXAFS measurements for Cu-K and Ta-LIII absorption edges were performed at room temperature with a Si(311) channel-cut crystal monochromator on beam line 10B.

Figures 1 and 2 show the magnitude of Fourier transform of $k\chi(k)$ for Cu-K and Ta-LIII EXAFS respectively. For the starting material (a), i.e., the mixture of Cu and Ta metallic powders (MA 0h), typical fcc (Cu-K) and bcc (Ta-LIII) crystalline distribution patterns were observed. On the contrary, for the sample after 76h MA (b), higher order shells were not observed for both Cu-K and Ta-LIII EXAFS

distribution patterns, and these data are clearly distinguished from (a). This indicates that an amorphous-like alloy, which does not have long range order, is synthesized by the MA in immiscible Cu-Ta system. For further analysis of this system, the sample prepared under the different composition ratio (Cu:Ta=1:1) was also measured, and the results are shown in Figs.1, 2 (c). Basic natures of the data are quite similar to (a), though the magnitude of higher order shells is slightly weak. Complete amorphization under this condition was not expected, because the milling time dependence was not observed for EXAFS distribution patterns. There might be optimum composition range for the formation of amorphous Cu-Ta alloy.

The present results are preliminary but definitely sustain the possibility of amorphization of $\text{Cu}_{30}\text{Ta}_{70}$ alloy by the MA technique. More detailed analyses are now under way. In order to study the mechanism of MA for a system with positive heat of mixing like Cu-Ta, it is very important to investigate a relationship between atomic-scale structure of an alloy and its MA condition.

The authors would like to thank Dr. Nakai of the Univ. of Tsukuba for his help during the experiments and useful discussion.

References

- 1) R.B.Schwarz and W.L.Johnson: Phys. Rev. Lett. 51(1983)415.
- 2) T.Fukunaga, K.Nakamura, K.Suzuki, U.Mizutani: Proceedings of 7th International Conference on Liquid and Amorphous Metals (Kyoto, 1989.9)

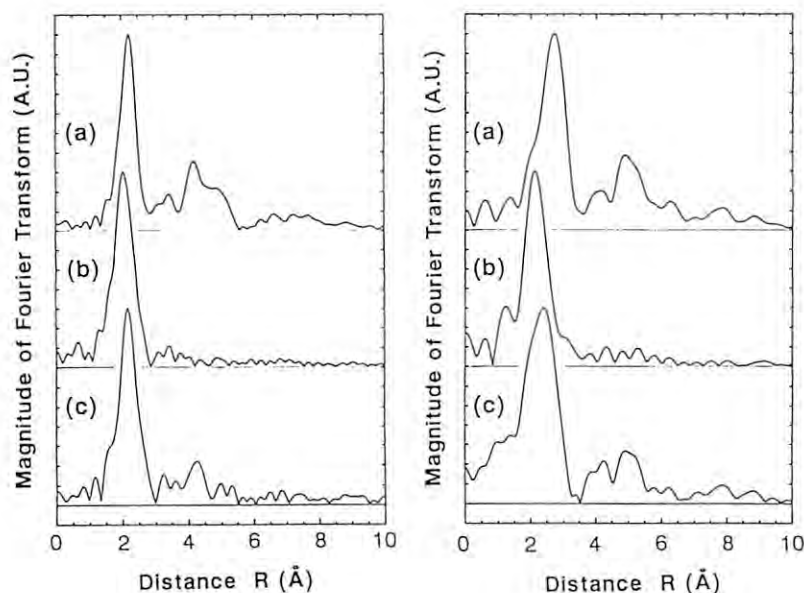


Figure 1 (Left)
Fourier transforms of Cu-K EXAFS.

Figure 2 (Right)
Fourier transforms of Ta-LIII EXAFS.

- (a) MA 0h
(b) MA 76h
(c) Cu:Ta=1:1, SUS vial/ball,
MA 30h

EXAFS MEASUREMENT ON NIOBIUM ACID THIN LAYER ON SiO₂ CATALYST
Masayuki SHIRAI, Kiyotaka ASAKURA and Yasuhiro IWASAWA
Department of Chemistry, Faculty of Science, University of
Tokyo, Hongo, Bunkyo-ku, Tokyo 113

Introduction

Nb(OC₂H₅)₅ reacts with the hydroxyl group on SiO₂ to make thin niobium acid layer on SiO₂. On niobium acid on SiO₂ catalyst, ethanol reacts with acetic acid to ethyl acetate with high activity. As increasing the contents of niobium in the catalyst up to 7 wt%, the activity of the esterification between acetic acid and ethanol increases linerly. We tried to investigate that the structure change of niobium acid layer with increasing the contents of niobium in the catalyst.

Experimental

Niobium acid thin layer on SiO₂ are made by the reaction between Nb(OC₂H₅)₅ and hydroxyl group on SiO₂. The EXAFS spectra were measured at BL-10B of Photon Factory.

Result and Discussion

Niobium acid thinlayer on SiO₂ reveals high activity for esterification between acetic acid and ethanol. Fourier Transforms of catalysts of various contents of niobium are given in Fig.1. The main peaks about 0.15nm correspond to Nb-O bondings and peaks about 0.35nm to Nb-Nb bondings. The peak height of Nb-Nb bondings are smaller than that of Nb-O bondings. No significant increasing of the Nb-Nb intensity was observed, which demonstrates on SiO₂ of two dimension. Table 1 shows the result of curve-fitting analysis. Two Nb-Nb bondings are found in niobium acid layer catalyst, it suggests niobium acid layer on SiO₂ are in amorphous state. In addition to Nb-O and Nb-Nb bondings, niobium acid layers of various contents of niobium includes Nb-Si bonding shown by curve-fitting analysis. It reveal that niobium acid are prepared to be homogeneous thin layer on SiO₂ at various contents of niobium.

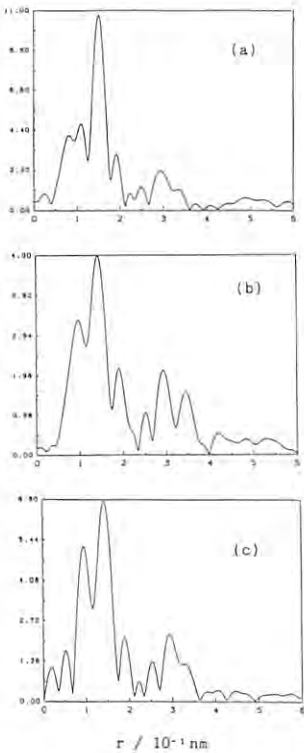


Fig.1. Fourier Transform of;
(a) 2wt% of Nb/SiO₂
(b) 4.6wt% of Nb/SiO₂
(c) 7wt% of Nb/SiO₂

Table 1. Result of Curve-Fitting Analysis of EXAFS Data for Niobium Acid Layer on SiO₂

contents of niobium/wt%	bond length / nm				
	Nb-O	Nb-O	Nb-Nb	Nb-Nb	Nb-Si
2	0.212	0.194	0.335	0.392	0.324
4.6	0.211	0.190	0.336	0.387	0.340
7	0.209	0.191	0.334	0.396	0.331

REDUCTION PROCESS OF BINARY OXIDES CONTAINING Fe

Tsunehiro TANAKA, Takashi UMEKI and Hideshi HATTORI

Department of Chemistry, Faculty of Science, Hokkaido University,
Sapporo 060, Japan.

Reducibility of Fe^{3+} in oxide form varies greatly with the second ingredient cations, examined by temperature programmed reduction, Mössbauer spectra and X-ray diffraction. However, these techniques have limitations and another type of information is needed. In the present work, we applied Fe K-edge XAFS spectra to these systems.

Experimental

The samples are Fe-Si, Fe-Mg, and Fe-Zr binary oxides. The atomic ratio of Fe to ingredient is 1:1. The samples were prepared by coprecipitation method from solutions of $\text{Fe}(\text{NO}_3)_3$, and $\text{Si}(\text{OC}_2\text{H}_5)_4$, $\text{Zr}(\text{NO}_3)_4$, or $\text{Mg}(\text{NO}_3)_2$, followed by calcination at 773 K in air. The binary oxides of Fe-Si, Fe-Mg, and Fe-Zr are denoted as FS, FM and FZ. Reduction of the samples was carried out under on atmospheric hydrogenstream at 743 K. XAFS spectra were taken on the EXAFS facility installed at BL10B of KEK-PF with an Si(311) channel-cut monochromator. XANES spectra were normalized to each edge jump.

Results and Discussion

Figure 1 shows Fe K-edge XANES spectra of FZ, FM, FS and relating compounds, hematite, FeO, Fe foil. The XANES spectra of the samples in reduced state are shown in Fig. 2. The positions of main absorption edges vary with the samples, especially the valence states while the pre-edge positions do not change greatly.

In the case of FZ, the positions of peaks in the post edge region agree with those for hematite. In fact, XRD patterns of FZ exhibit the presence of both ZrO_2 and Fe_2O_3 crystals, i.e., phase separation of Fe-Zr oxides occurs in the FZ sample. Therefore, it is easily understood that Fe cations in FZ is almost perfectly reduced to Fe^0 as shown in Fig. 2 (a).

The feature of FM is exactly the same as that of Fe_2MgO_4 , an inverse-spinell compound although XRD pattern exhibits no crystal phase in FZ suggesting ill growth of the crystal. Fe cations in FZ are also reduced to Fe^0 state.

The species in FS is ambiguous because no sample exhibiting similar XANES to that for FS. No crystal phase was detected by XRD and no characteristic absorption except Fe cations in FS are trivalent was observed in the Mössbauer spectrum. The high pre-edge peak may be indicative of the presence of tetrahedrally coordinated Fe^{3+} due to the influence of silicon atoms. We propose that Fe and Si are linked at random in FS.

This may prevent the segregation of Fe ions to form Fe metal. As shown in Fig. 2 (c), iron is reduced to divalent one judging from the position of the main absorption edge but the absorption peak in the post edge region is broader than that for FeO and pre-edge peak is still clear, suggesting that the Fe-O-Si bonds having been formed by the calcination are still remaining after reduction. The formation of iron silicate is probable. However, because iron silicate is very unstable at low pressure and it contains FeO in itself, the formation of iron silicate is unlikely.

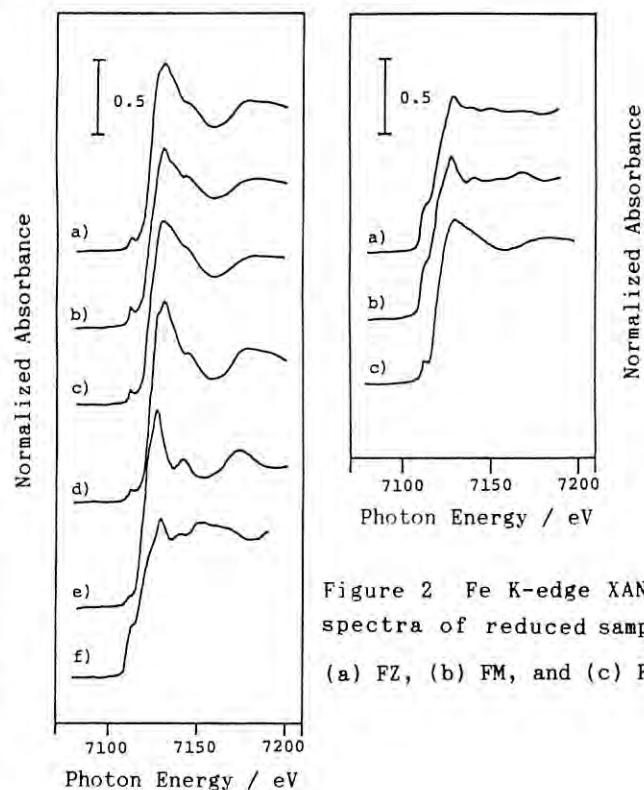


Figure 2 Fe K-edge XANES spectra of reduced samples. (a) FZ, (b) FM, and (c) FS.

Figure 1 Fe K-edge XANES spectra of (a) FZ, (b) FM, (c) FS, (d) hematite, (e) FeO and (f) Fe foil. FZ, FM and FS, see text.

EXAFS STUDIES ON THE PHOTOCATALYSIS OF MO DIMER

Kiyotaka ASAKURA and Yasuhiro IWASAWA
 Department of Chemistry, Faculty of Science, the University of Tokyo,
 Hongo, Bunkyo-ku, Tokyo 113, Japan.

Mo showed an interesting photocatalytic activity for CH_3OH oxidation reaction. To elucidate the mechanism for the photocatalysis, it is important to obtain the information about the local structure around the active site under reaction conditions. For this purpose we have prepared the Mo dimer with a well-defined surface structure using the reaction between $\text{Mo}_2(\text{C}_3\text{H}_5)_4$ and the surface OH groups of SiO_2 . We carried out the X-ray absorption spectroscopy measurement on the attached Mo dimer catalyst.

Experimental

Mo dimer is prepared using the reaction between the $\text{Mo}_2(\text{C}_3\text{H}_5)_4$ and surface OH groups of SiO_2 (Fuji Davison 952, The surface area $300 \text{ m}^2/\text{g}$). The Mo loading is 8 wt %. The sample was pressed into disks. They were put onto the specially made in-situ EXAFS cell as shown in Fig.1. The sample was pretreated in the flow of O_2/He gas at 773 K in the cell. Then the sample was placed at the X-ray path. The sample was irradiated from the bottom through the quartz window.

Results and Discussion

Fig.2 showed the Mo K-edge spectra before and after the irradiation of the Mo dimer. The difference spectrum is structureless, indicating that the Mo local structure and electronic state are little affected only by the irradiation. Fig.3 showed the Mo K-edge spectrum after the adsorption of CH_3OH . A shoulder structure appeared at 20040 eV. Difference spectrum between before and after adsorption of CH_3OH clearly showed the change accompanied with the adsorption process of CH_3OH . However, the position of peak A and the inflection point of the edge do not shifted, indicating the valence state is unchanged. After the CH_3OH -adsorbed sample was irradiated, the spectrum gradually changed. Fig.4 showed the Mo dimer adsorbed CH_3OH after the subsequent irradiation for 50 min. The difference spectrum between the 50 min irradiated Mo dimer and Mo dimer before adsorption of CH_3OH showed the loss of peak F. The analysis of EXAFS oscillation are now in progress which will show the local structure of Mo more clearly.

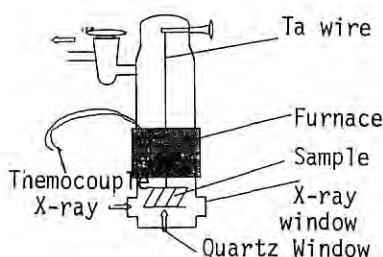


Fig.1 in-situ Photoreaction EXAFS cell.

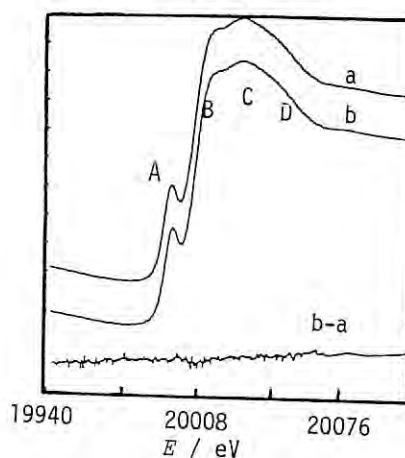


Fig.2 Mo K-edge X-ray absorption of Mo dimer before (a) and after (b) the irradiation. and difference spectrum of b-a.

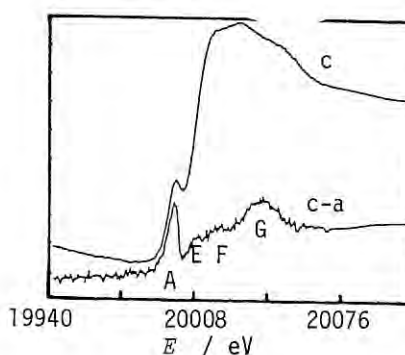


Fig.3 Mo K-edge X-ray absorption of Mo dimer after the adsorption of CH_3OH (c) and the difference spectrum (c-a)

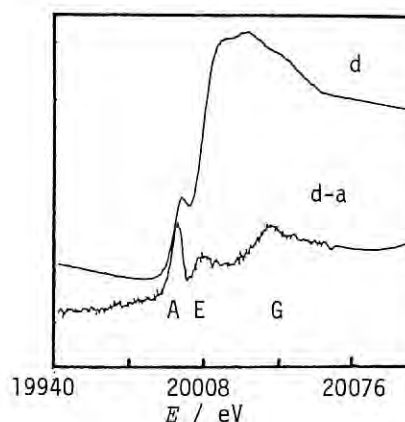


Fig.4 Mo K-edge X-ray absorption of Mo dimer pre-adsorbed with CH_3OH after irradiation (d) and the difference spectrum (d-a)

EXAFS Study of Zeolite NaY Supported Cu-Pt Bimetallic Catalyst

Ming-Shin TZOU(1), Kiyotaka ASAKURA(2),
Nobuhiro KOSUGI(3), and Haruo KURODA(1,2)

- (1) Research Development Corp. of Japan, Tokodai, Tsukuba, Ibaraki 300-26.
(2) Dept. of Chemistry, Fac. Science, Univ. Tokyo, Hongo, Tokyo 113.
(3) Division of Molecular Engineering, Kyoto University, Kyoto 606

INTRODUCTION

It has been demonstrated that the addition of second metal into a supported metal catalysts to form surface decorated or alloy particles may increase the catalytic selectivity. Based on the formation of Pt particles in NaY, it is expected that bimetallic particles could be made within the zeolite cavities(1). First of all, we study the structure of Cu-Pt in NaY since the hydrogenation(2) and hydroconversion(3) activities of Pt/NaY are strongly influenced by the presence of copper.

EXPERIMENTAL

The bimetallic Cu-Pt/NaY was prepared by successive ion exchange with copper nitrate and tetraammineplatinum (II) chloride in aqueous solution. The loading of Cu and Pt metals are 0.8 wt% and 2.4 wt%, respectively, which gave Cu/Pt atomic ratio equivalent to 1/1. It was calcined at 300 °C, reduced at 500 °C and sealed in a glass cell with capton films as windows for X-ray absorption at room temperature at the beam line 10B in the Photon Factory.

RESULTS AND DISCUSSIONS:

Figure 1 shows the results of Fourier transformations of the EXAFS data of Cu-Pt/NaY catalyst at Cu K-edge. It indicates that (1) some copper are in ionic state, and (2) other copper are in metallic state and have Cu and Pt atoms as their first coordinative shell neighbors. The coordinative distances after curve fittings are indicated in Fig. 1.

The X-ray absorption at Pt L3-edge of Cu-Pt/NaY(I) and two reference samples, Pt/NaY(II) and few micron Pt particles physically mixed with NaY, were also measured. The Fourier transformations of the EXAFS data of the first two samples are shown in Fig 2. The analysis results, the coordinative distances and available coordination numbers of samples (I) and (II), are included in Fig. 2. The C.N.(Pt-Pt) in Pt/NaY is only 6.4, indicating small Pt particles, which is

expected in Pt/NaY calcined and reduced at 300 °C. For Cu-Pt/NaY, both Cu and Pt atoms have to be included as the first shell coordinative atoms of Pt atoms in the curve-fitting analysis. The primary fitting results indicate that the C.N.(Pt-Pt) in Cu-Pt/NaY is much less than that in Pt/NaY. Obviously, CuPt alloy particles are formed in NaY after reduction.

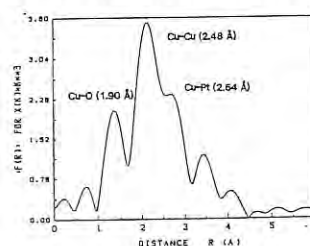


Fig. 1. Fourier transform of Cu k-edge EXAFS of Cu-Pt/NaY.

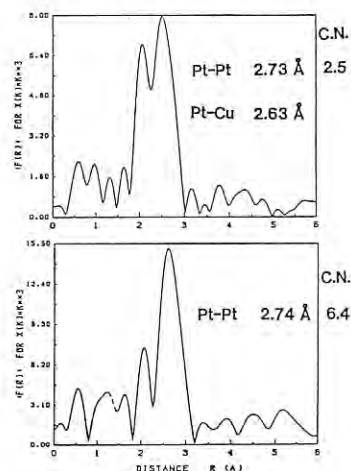


Fig. 2. Fourier transforms of Pt L3-edge EXAFS of (a) Cu-Pt/NaY and (b) Pt/NaY.

REFERENCES:

- (a) P. Gallezot, A. Alarcon-Diaz, J.A. Dalmon, Renouprez, B. Imelik, *J. Catal.* 39 (1975) 334.
(b) M.S. Tzou, B.K. Teo, W.M.H. Sachtler, *J. Catal.* 113 (1988) 220.
- L. Tebassi, a. Sayari, a. Ghorbel, M. Dufaux, C. Naccache, *J. Mol. Catal.* 25 (1984) 397.
- M. Dufaux, M. Lokolo, P. Meriaudeau, C. Naccache, and C. Naccache, *Stud. Surf. Sci. Catal.* 28 (1986) 929.

STUDIES ON THE STRUCTURE OF BIMETALLIC COLLOIDAL CATALYSTS

Naoki TOSHIMA, Masafumi HARADA,
*Kiyotaka ASAKURA, and *Yasuhiro IWASAWA

Department of Industrial Chemistry, Faculty of Engineering, and

*Department of Chemistry, Faculty of Science,
The University of Tokyo, Hongo Bunkyo-ku, Tokyo 113

Introduction

We have reported that the colloidal dispersions of noble metals protected by polymers can be prepared by reducing the noble metal salts by refluxing the solution of alcohol or alcohol/water containing water-soluble polymers such as polyvinylalcohol and poly(N-vinyl-2-pyrrolidone). The colloidal dispersions thus obtained are stable and composed of the fine metal particles with uniform size, and work as catalysts with high activity and selectivity for the hydrogenation of olefins and dienes,^{1,2)} the light-induced hydrogen generation from water, and so on. Bimetallic colloidal dispersions are interesting from a viewpoint of a model for a heterogeneous catalyst of multi-components. However, few have been reported on the bimetallic colloids.³⁾ Here we would like to report the structure of Pd-Au bimetallic colloids which can work as the catalysts for the selective partial hydrogenation of 1,3-cyclooctadiene to cyclooctene. The extended x-ray absorption fine structure (EXAFS) associated with the K-edge of palladium and the L₃-edge of gold is an useful tool for the structure determination.

Experimental

The bimetallic colloids at the various ratios of gold and palladium were prepared by refluxing the mixed solution of the corresponding ions in water-ethanol under nitrogen. These bimetallic colloids were concentrated by evaporating the solvent under reduced pressure, and the concentrated solutions were sealed in the 50 mm (for palladium) and 10 mm (for gold) cells under nitrogen. The EXAFS data of this measurement were analyzed by a program EXAFS4 (Research Center for Spectrochemistry, the University of Tokyo).^{4,5)}

Results and Discussion

Colloidal palladium is an active catalyst for hydrogenation of 1,3-cyclooctadiene, while colloidal gold is inactive for the hydrogenation. When palladium-gold bimetallic colloids at different molar ratio were examined as the hydrogenation catalysts, it has been found that the activity varies with the ratio of Pd to Au and the catalyst at Pd/Au=4 has the highest activity.⁶⁾ The EXAFS data of this bimetallic colloid can provide information on the structure of the palladium-gold bimetallic colloids. The EXAFS data shown in Table 1 indicate that the gold atoms coordinate predominantly to other gold atoms and only to a minor extent to palladium atom.⁶⁾ This fact suggests the model structures shown in Fig.1, in which the palladium atoms surround the gold atoms at the core. The coordination number around gold in this model well corresponds to the observed one. The change in the structure with the variation in the Pd/Au ratio is under investigation. The present results are expected to provide a new concept on the activity of a bimetallic catalyst.

Reference

- 1)H. Hirai, H. Chawanya and N. Toshima, *Reactive Polymers*, **3**, 127 (1985).
- 2)H. Hirai, H. Chawanya and N. Toshima, *Bull. Chem. Soc. Jpn.*, **58**(2), 682 (1985).
- 3)N. Toshima, K. Kushihashi, T. Yonezawa and H. Hirai, *Chem.Lett.*, **1769**, 1989.
- 4)K. Asakura and Y. Iwasawa, *Petrotech*, **8**(12), 41 (1985).
- 5)K. Asakura, N. Kosugi, H. Kuroda and Y. Iwasawa, *Shokubai(catalyst)*, **26**(5), 390 (1984).
- 6)N. Toshima and M. Harada, *Preprints of 58th Spring Meeting of the Chemical Society of Japan*, 2IF08 (1989) : M. Harada and N. Toshima, *Polymer Preprints, Japan*, **38**(7), p.1835 (1989).

Table 1. Coordination number of the Pd/Au (4/1) bimetallic particles

Atom	Coordination Number				
	Observed (Pd 80%)	Random Model (Pd 80%)	Model(A) (Pd 67%)	Model(B) (Pd 75%)	Model(C) (Pd 84%)
(around Pd)					
Pd	2.99	8.28	8.33	8.58	9.46
Au	5.20	2.07	1.19	1.22	0.57
(around Au)					
Au	11.33	2.07	9.63	8.34	8.98
Pd	2.80	8.28	2.37	3.66	3.02

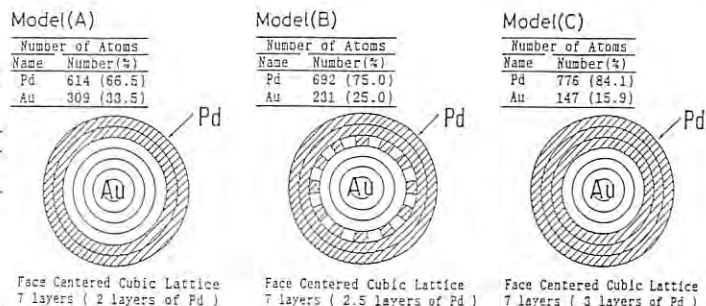


Fig. 1 Au core models of the Pd/Au(4/1) bimetallic particle composed of 923 atoms

The EXAFS and XANES spectra of MCaSi_2O_6 ($\text{M} = \text{Co}, \text{Ni}, \text{Sr}$) glasses

Masayuki OKUNO, Taketoshi TANIGUCHI and Takeo MATSUMOTO

Department of Earth Sciences, Faculty of Science, Kanazawa University,

Kanazawa 920, Japan

Introduction

The informations of the properties of magma is very important for the understanding the magmatic process in the crust and the upper mantle of the earth. The system anorthite-diopside has been studied as a model for basaltic silicate melts. Therefore, the structural study of diopside melt will give very useful informations for the study of magma properties. In this work, we study the structures of MCaSi_2O_6 ($\text{M} = \text{Co}, \text{Ni}, \text{Sr}$) glasses by EXAFS measurements to compare with their crystal structures.

Experimental

MCaSi_2O_6 ($\text{M} = \text{Co}, \text{Ni}, \text{Sr}$) glasses were prepared from Co_2O_3 , NiO , SrCO_3 , CaCO_3 and SiO_2 by melt quenching method. EXAFS measurements were carried out over the ranges of 7.4-8.9 keV (Co K absorption edge = 7.70954 keV), 8.0-9.5 keV (Ni K $\text{K}_{\text{abs}} = 8.33165$ keV) and 15.6-17.3 keV (Sr K $\text{K}_{\text{abs}} = 16.107$ keV) at 300K by a transmission mode with a channel-cut Si(311) monochromator. MCaSi_2O_6 ($\text{M} = \text{Co}, \text{Ni}$) and SrCO_3 crystals were used for reference samples.

Results and Discussion

The EXAFS and XANES spectra were shown in Fig.1-3 with the spectra of $\text{CoCaSi}_2\text{O}_6$, $\text{NiCaSi}_2\text{O}_6$ and SrCO_3 crystals. The first peaks of $\text{CoCaSi}_2\text{O}_6$ and $\text{NiCaSi}_2\text{O}_6$ crystal have two maxima, but, their glasses have only one. The pre-edge peaks of $\text{CoCaSi}_2\text{O}_6$ and $\text{NiCaSi}_2\text{O}_6$ glasses are larger a little than those of the crystals. Nevertheless, the EXAFS and XANES spectra of $\text{CoCaSi}_2\text{O}_6$ and $\text{NiCaSi}_2\text{O}_6$ glasses are similar to those of the crystals as a whole, respectively. These facts suggest that the short-range environment of Co^{2+} and Ni^{2+} ions in the glasses are similar to those of the crystals. On the other hand, the spectra of $\text{SrCaSi}_2\text{O}_6$ glass are very similar to those of SrCO_3 crystal. It is also supposed that the short-range structure of Sr^{2+} ion in the glass is very similar to that in the SrCO_3 crystal. Probably, by comparing the structures of the glasses with the crystals, we will be able to obtain the detail structural informations of the

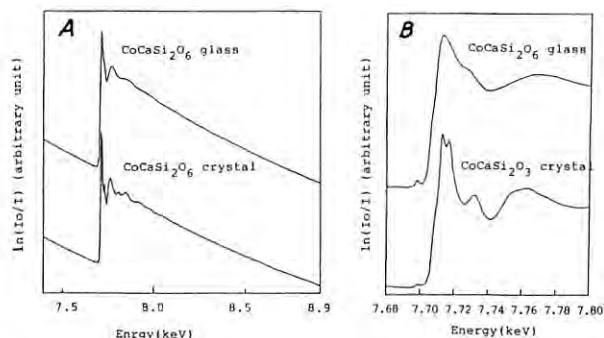


Fig.1 The EXAFS(A) and XANES(B) spectra of the $\text{CoCaSi}_2\text{O}_6$ glass and the crystal.

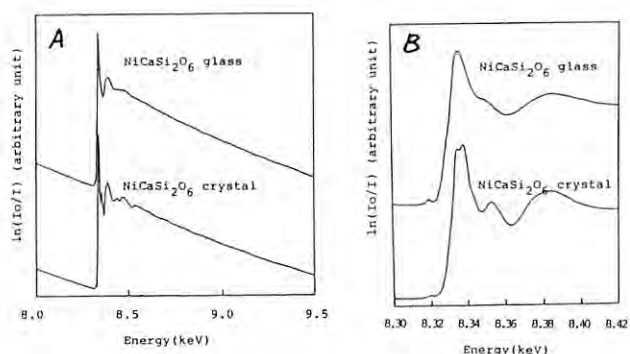


Fig.2 The EXAFS(A) and XANES(B) spectra of the $\text{NiCaSi}_2\text{O}_6$ glass and the crystal.

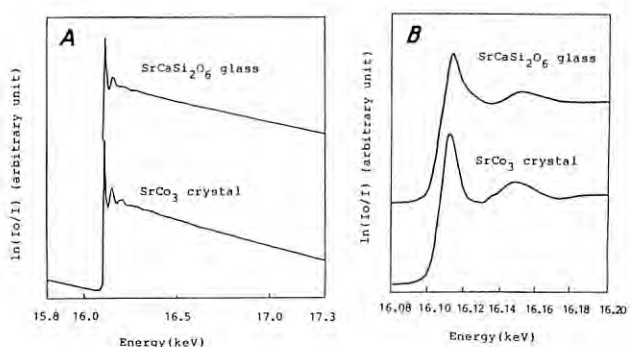


Fig.3 The EXAFS(A) and XANES(B) spectra of the $\text{SrCaSi}_2\text{O}_6$ glass and the SrCO_3 crystal.

EXAFS AND XANES STUDIES ON INTERCALATION COMPOUNDS $M_x\text{TiS}_2$ ($M=\text{Mn, Fe, Co, Ni}$)

Hiroshi NEGISHI, Shigeo OHARA, Yasutaka TAKADA, Toshihiko YOKOYAMA,
Masaki TANIGUCHI and Masasi INOUE

Department of Materials Science, Faculty of Science, Hiroshima University, Hiroshima 730

Introduction

Characteristic of transition metal dichalcogenides TX_2 ($T=\text{IV, V, VI Groups}$; $X=\text{S, Se, Te}$) with layered structures is the presence of weakly coupled van der Waals gaps, into which various guest atoms M can be inserted, forming new material systems of "intercalation compounds or intercalates", expressed as $M_x\text{TX}_2$, which show many interesting physical properties different from those of the host crystals. As guest atoms, 3d transition metals in TX_2 have been extensively studied. In particular, electronic and magnetic properties of 3d metals in the Group V dichalcogenides, such as NbS_2 and TaS_2 , are generally understood in terms of a localized electron or rigid band model, according to which the guest 3d atoms donate electrons to the partially filled d_z^2 band of the host material, becoming divalent or trivalent ions.²⁾

Similar studies have been made on materials in which one of the Group IV dichalcogenides, TiS_2 , acts as a host. These have a simple 1T-CdI_2 -type structure, and the guest 3d metals occupy the octahedrally coordinated sites between the TiS_2 layers. The formation of the in-plane superlattices of $2a \times 2a$ and $\sqrt{3}a \times \sqrt{3}a$ is known to appear at the particular guest concentrations $x=1/4$ and $1/3$, respectively, but intercalant staging does not occur in these systems, except for alkali metals and silver. In contrast to the intercalates of the Group V dichalcogenides, a characteristic of the $M_x\text{TiS}_2$ family is strong hybridization between the guest atom M 3d orbitals, and the host Ti 3d and S 3p orbitals, leading to changes in the Fermi energy E_F , and various types of magnetic orderings, as evidenced from the electron spin resonance (ESR), structural, thermal, magnetic, transport, and photoemission spectroscopic measurements; the comprehensive review will be reported elsewhere.²⁾ These properties are well elucidated by an itinerant electron or band picture predicted by self-consistent augmented-plane-wave (APW) band calculations,³⁻⁴⁾ rather than a rigid band model.

In order to get an insight into the atomic configurations in these material systems, we have attempted to carry out the EXAFS and/or XANES measurements around the K-edges of the guest 3d atoms.

Experimental

Single crystals of $M_x\text{TiS}_2$ ($M=\text{Mn, Fe, Co, and Ni}$; $x < 0.33$) were grown by a chemical vapor transport technique using iodine as a carrier gas; the details of sample preparation and structural analysis have been reported elsewhere.⁵⁾ The EXAFS and XANES spectra were taken at room temperature and ~ 30 K, using the beam line BL-10B at the Photon Factory.

Results and Discussion

Figure 1 shows the typical Fourier transformed EXAFS data of $k^3\chi(k)$ of Fe and Co K-edges at ~ 30 K for $\text{Fe}_{0.20}\text{TiS}_2$ and $\text{Co}_{0.20}\text{TiS}_2$, respectively. The strong peaks around 2.0 and 3.9 Å correspond, respectively, to the nearest-neighbor between the guest atom M and the host atom S, $M\text{-S}(1)$, and the third neighbor one $M\text{-S}(2)$; the peak corresponding to the second nearest-neighbor distance $M\text{-Ti}$ is not clearly observed. The analysis by a least-square fit to the Fourier-filtered spectra for the $M\text{-S}(1)$ has revealed that the respective interatomic distances are $R(\text{Fe-S})=2.40$ and $R(\text{Co-S})=2.37$ Å with the coordination number $N=5-7$, indicating that the guest 3d atoms M occupy the octahedral sites in the van der Waals gaps, in good agreement with the results obtained from X-ray powder diffraction.⁵⁾ We also note that these interatomic distances $R(M\text{-S})$ are smaller than that between the vacant octahedral site and S atom (~ 2.43 Å) in the unintercalated host TiS_2 , which supports that the intercalated M 3d orbitals are strongly hybridized with the host atoms S and Ti orbitals. Detailed analyses and measurements for other intercalates with various guest concentrations are now in progress.

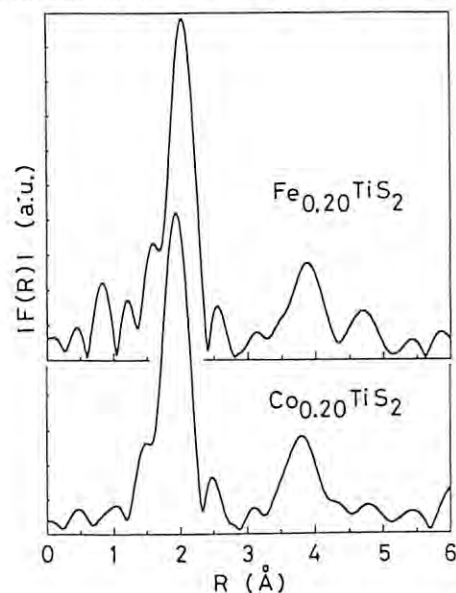


Fig. 1. Fourier transforms of $k^3\chi(k)$ of Fe and Co K-edges EXAFS for Fe and Co intercalates.

References

- 1) R.H. Friend and A.D. Yoffe, *Adv. Phys.*, **36**, 1 (1987).
- 2) M. Inoue, H.P. Hughes and A.D. Yoffe, *Adv. Phys.*, (in press).
- 3) T. Yamasaki, N. Suzuki, and K. Motizuki, *J. Phys.*, **C20**, 395 (1987).
- 4) N. Suzuki, T. Yamasaki, and K. Motizuki, *J. Magn. Magn. Mat.*, **70**, 64 (1987).
- 5) M. Inoue and H. Negishi, *J. Phys. Chem.*, **90**, 235 (1986).

EXAFS STUDIES OF $\text{MoO}_3/\text{TiO}_2$ CATALYSTS PREPARED BY AN EQUILIBRIUM ADSORPTION METHOD

SOEYA, T., KIM, D.S., MATSUBAYASHI, N.*, SHIMADA, H.*, NISHIJIMA, A.*, and SEGAWA, K.

Department of Chemistry Faculty of Science and Technology,
Sophia University, Chiyoda-ku, Tokyo 102, JAPAN

*National Chemical Laboratory for Industry, Tsukuba Ibaraki, 305 JAPAN

INTRODUCTION

Supported molybdenum catalysts are widely used for hydrodesulfurization and hydrocracking of heavy fractions of crude oil or metathesis of alkenes in the petroleum industry. Recently, an equilibrium adsorption method was devised to improve the dispersion of molybdenum species on the support.¹⁾ In this method, molybdate anions adsorb onto the positively charged titania via electrostatic attraction by controlling the pH of the impregnating solution. Therefore, the pH of the impregnating solution and the isoelectric point (IEP) of a support are very essential parameters to regulate the surface properties of catalysts. The aim of this study is to elucidate the adsorption phenomena of molybdena species onto titania surfaces.

EXPERIMENTAL

Titania supported molybdena catalysts were prepared by an equilibrium adsorption method.²⁾ Titania was impregnated at 323 K for 100 h with 0.007 M aqueous solution of ammonium heptamolybdate. After adsorption, the solids were separated from the solution by filtration. The wet catalysts were dried and then calcined in air at 773 K for 2 h. In order to determine the adsorption phenomena of molybdena species onto titania surface, ^{95}Mo NMR of impregnating solution, XANES and EXAFS (BL-10B) of the wet and calcined catalysts were carried out.

RESULTS AND DISCUSSION

^{95}Mo NMR spectroscopic studies show that the aqueous molybdena species vary as a function of the pH of the impregnating solution (Fig.1). For acidic pH values, polymeric species, $\text{Mo}_7\text{O}_{24}^{6-}$ ions are present, while in the basic solutions it was rather the monomeric MoO_4^{2-} ions are present.

The radial distribution function derived from the EXAFS of catalysts shows two large peaks, which are attributed to Mo-O (0.17 nm) and Mo-O-Mo (0.36 nm)³⁾. Up to monolayer coverage (A and B in Fig.2), no difference is observed between the wet

and the calcined catalysts. The results of EXAFS together with the results of XANES show that only octahedrally coordinated molybdena species exist on the wet and the calcined catalysts. However, beyond monolayer coverage (C in Fig.2), the intensity of Mo-O-Mo peak increased by calcination. This means that some aggregation or rearrangement of molybdena species occurred during calcination.

REFERENCES

- 1) Segawa, K., Kim, D.S., Kurusu, Y., and Wachs, I.E., in "Proc., 9th Intern. Congress on Catalysis, Calgary, 1988", p.1960.
- 2) Kim, D.S., Kurusu, Y., Wachs, I.E., Hardcastle, F.D., and Segawa, K., J.Catal., in Press.
- 3) Chiu, N.S., Bauer, S.H., and Johnson, M.F.L., J.Catal., **89**, 226(1984).

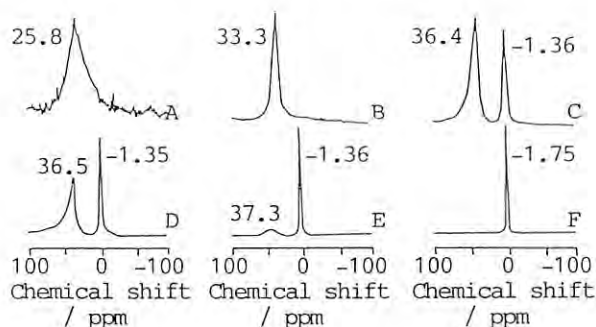


Fig.1 ^{95}Mo -NMR spectra of impregnating solution as a function of pH: (A) 3.43, (B) 5.26, (C) 5.73, (D) 5.86, (E) 6.45, (F) 9.31.

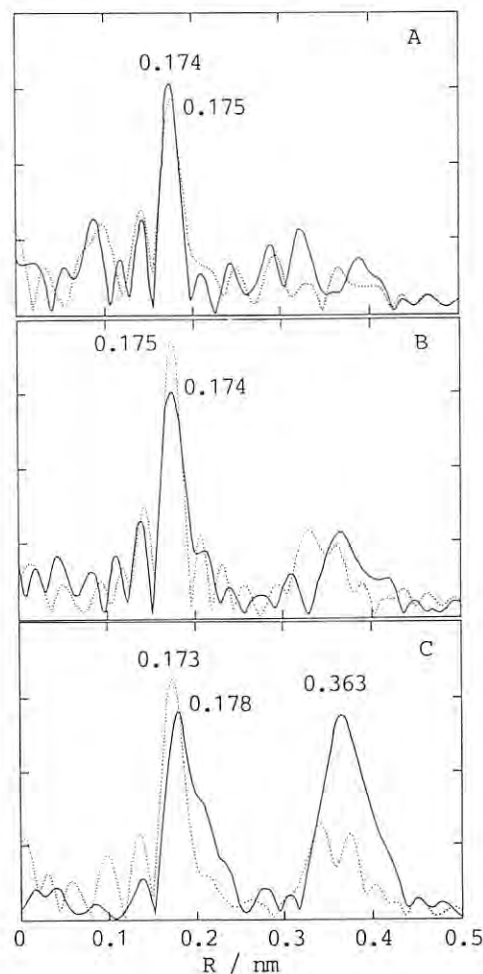


Fig.2 Radial distribution functions for $\text{MoO}_3/\text{TiO}_2$ catalysts: (A) pH=8.86(27.2 wt%), (B) pH=3.88(7.6 wt%), (C) pH=1.48(2.6wt%). (.....) wet sample, (—) calcined sample.

LOCAL STRUCTURE OF DIORGANOTIN(IV) COMPLEXES WITH CARBOHYDRATE

László NAGY, Seiichi YAMASHITA†, Toshio Yamaguchi‡,
Hisanobu WAKITA†, and Masaharu NOMURA‡

Department of Inorganic and Analytical Chemistry, A. József University,
H-6701 Szeged, P.O. Box 440, Hungary

†Department of Chemistry, Faculty of Science, Fukuoka University,
Nanakuma, Jonan-ku, Fukuoka 814-01, Japan

‡Photon Factory, National Laboratory for High Energy Physics,
Oho-machi, Tsukuba 305, Japan

Introduction

The interactions of organotin(IV) compounds with carbohydrates have attracted considerable interest because the presence of carbohydrate ligands modifies the biological properties of the organotin group. In spite of this, the chemical and electronic structures of the reaction products remain largely unexplored. The present study was undertaken to reveal structures of organotin(IV) complexes with carbohydrate ligands.

Experimental

A series of diethyltin(IV) complexes with carbohydrate ligands (aldoses, polyalcohols, sugar acids, sugar amines, and di- and trisaccharides) were prepared.¹⁾ The standard chemical analysis of compounds showed that the complexes are formed containing the diethyl moiety and the carbohydrate ligand in 1:1 ratio. The IR spectra are consistent with the presence of tin-carbohydrate oxygen vibration in the compounds. The partial quadrupole splitting values revealed that the compounds are of three types; complexes with the central tin(IV) atoms present in purely trigonal bipyramidal surrounding, in purely octahedral surroundings, or in both octahedral and trigonal bipyramidal arrangements in approximately 1:1 ratio.¹⁾ XANES and EXAFS spectra of compounds were measured at room temperature around Sn K-edge at BL-10B of

KEK.

Results and Discussion

The Sn K-edge XANES spectra of the complexes were very similar to each other. Figure 1 shows the Fourier transforms $\phi(r)$ of the $k^3\chi(k)$ values of solid sample containing the diethyltin(IV)-lactobionic acid complex. All Fourier transforms have a very similar feature and have a peak at about 170 pm (not corrected for the phase shift). This peak corresponds to Sn-O and Sn-C interactions in the first shell. The peak observed at about 265 pm arises from the second nearest neighbour atoms in the complexes.

The least squares fits for Fourier filtered spectra revealed that all complexes have the coordination number close to values estimated from Mössbauer measurements and that average Sn-O and Sn-C distances are those expected for an octahedral or trigonal bipyramidal coordination of tin(IV) atom. As to the second neighbour atom we concluded that only carbon atoms are present. The final results of the fits are summarized in Table 1.

Reference

- 1) L. Nagy, L. Korecz, I. Kiricsi, L. Zsikla and K. Burger, Accepted for publication in Struct. Chem.

Table 1. Results of the curve-fitting analysis for the diethyltin(IV)-carbohydrate complexes

Ligand	Sn-O/pm/	CN	σ /pm/10 ²	Sn...C/pm/	CN	σ /pm/10 ²	Structure
Lactobionic acid	198.5	6*	6.9	278.2	6*	12.0	Octahedral och
D-galacturonic acid	200	5.8	6.8	275.0	6*	9.6	och
Mannitol	199.9	5.1	5.2	278.2	5*	11.6	tbp
Saccharose	199.2	5.3	5.2	278.2	5*	12.0	tbp
D-glucos-amine	198.8	5.6	6.1	278.5	5.5*	12.4	och : tbp = 1:1
Maltitol	199.4	5.3	6.0	278.4	5.5*	11.6	och : tbp = 1:1
L-xylose	199.5	5.90	6.5	274.8	6*	9.2	och
L-galactose	199.5	5.88	6.5	274.8	6*	9.2	och

*fixed

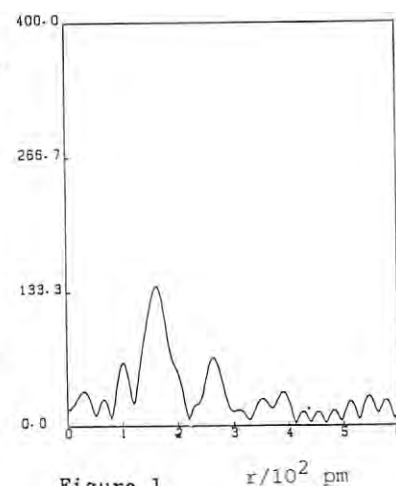


Figure 1 $r/10^2$ pm

EXAFS AND XANES STUDIES OF COPPER(II) COMPLEXES FORMED WITH ADENOSINE AND URIDINE AT DIFFERENT PH

Toshio YAMAGUCHI, László NAGY†, Masaharu NOMURA‡, and Hitoshi OHTAKI†

Department of Chemistry, Faculty of Science, Fukuoka University,
Nanakuma, Jonan-ku, Fukuoka 814-01, Japan†Department of Inorganic and Analytical Chemistry, A. József University,
H-6701 Szeged, P.O. Box 440, Hungary

‡Photon Factory, National Laboratory for High Energy Physics, Oho-machi, Tsukuba 305, Japan

§Coordination Laboratories, Institute for Molecular Science, Myodaiji, Okazaki 404, Japan

Introduction

A variety of different experimental techniques have been used to investigate the interaction of copper(II) with nucleosides, nucleotides and polynucleotides. Several studies have shown that the interactions between a metal ion and the ribose hydroxyl groups are promoted by a basic medium. Chao and Kearns¹⁾ have done a more detailed work about complexation of copper(II) with various nucleosides over the pH 3.4-12 range using ESR and NMR techniques. Instead of water as a solvent for the system, they used a H₂O-Me₂SO glass, which effectively prevents the rotational motion of the complexes, thus avoiding some spectral complication. The results indicated that para- and diamagnetic complexes are formed with variation of pH. The complexes formed between transition metal ions with ribo- and deoxyribonucleosides have appeared little suitable for X-ray diffraction experiments because of the difficulties in crystallization. Our aim was therefore, to determine the local structure of adenosine and uridine complexes of copper(II). XANES and EXAFS spectra of the Cu-K edge were measured at BL-10B, KEK for the samples given in Table 1.

copper(II)-uridine and adenosine complexes. All spectra have a small peak around 8976 eV due to the 1s-3d electron transition, showing that the oxidation state of the copper atom is 2+. A feature of the principal absorption maximum shows different patterns, indicating that the coordination symmetry are different within a species formed. For spectra A and C the peak is very sharp, while the others are broader. The broader peak may reflect asymmetrical metal-o bonds due to a splitting of the degenerate energy levels of the copper(II) ion.

All Fourier transforms for the Cu(II) complexes showed a peak at about 160 pm (not corrected for the phase shift), corresponding to Cu-O interactions. The peak located at about 220 pm will be due to the carbon (in case of diamagnetic complexes, both copper and carbon because of a dimer structure) backscattering atoms. The curve fitting analysis was carried out for the Fourier filtered spectra obtained over the *r* range of 1.1 - 3.1 pm. The final results for the curve fitting analysis are collected in Table 1.

Reference

- 1) Y. H. Chao and D. R. Kearns, J. Am. Chem. Soc., **99**, 6425 (1977).

Results and discussion

Figure 1 shows XANES spectra of the

Table 1. Samples for EXAFS measurements and the results of the curve fitting analysis

Ligand	pH	magnetic property	Cu-O interaction			Cu...C interaction		
			N	r/pm	$\sigma \cdot 10^2$ /pm	N	r/pm	$\sigma \cdot 10^2$ /pm
Adenosine	6.0	paramagnetic	3.7	191.7	6.2	2*	274.5	8.40
Adenosine	10.7	diamagnetic	3.8	190.3	5.7	4*	285.1	13.1
Adenosine	12.0	paramagnetic	4.0	190.4	5.6	4*	281.3	13.1
Adenosine	13.0	paramagnetic	3.9	190.9	5.2	4*	284.1	11.9
Uridine	6.0	paramagnetic	3.6	190.4	7.7	2*	284.8	9.8
Uridine	10.5	diamagnetic	3.7	190.9	7.0	4*	278.5	12.7
Uridine	12.0	paramagnetic	4.4	189.9	6.0	4*	280.7	16.3

* fixed

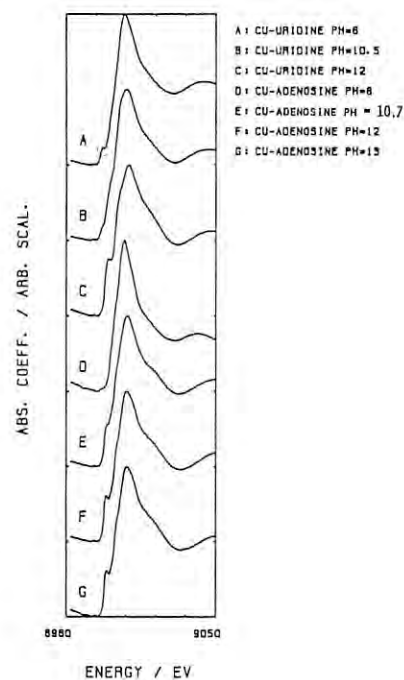


Figure 1

STRUCTURAL ANALYSIS OF HOPEITE CRYSTAL BY CURVE FITTING OF EXAFS

Noboru SATO

Materials Engineering, HONDA Motor Co., Ltd. Suzuka 513

Introduction

Chemical properties such as dehydration process or anti-corrosive property of hopeite crystal depend on the metal component incorporated in the crystal structure¹⁻³). The action of the heavy metal components in zinc phosphating solution was studied for zinc coated steels. Nickel and manganese ions in the solution entered into the crystal and modified the properties of hopeite crystal. Especially, the action of manganese ion was remarkable⁴).

Two types of hopeite crystal with and without manganese component were investigated to analyze the local structure by means of EXAFS. The purpose is to clarify the mechanism of chemical improvement of hopeite crystal by revealing the structure. In previous report⁵), these basic data and analysis were reported. Here, further detailed analysis by curve fitting method was tried and reported.

Experimental

Powder samples of hopeite-A and hopeite-B were prepared by forming on galvanized steels from each phosphate solution and used in the subsequent structure analysis. The metal component composition in the crystal was determined by atomic absorption spectroscopy.

hopeite-A : $\text{Zn}_3(\text{PO}_4)_2 \cdot 4\text{H}_2\text{O}$, Zn:42.6wt%

hopeite-B :

$\text{Zn}_{3-x}\text{Mn}_x(\text{PO}_4)_2 \cdot 4\text{H}_2\text{O}$, Zn:38.0wt%, Mn:4.8wt%

The measurement was performed at BL-10B station by using EXAFS. The samples were mounted on adhesive tapes. The wavelength of the radiation was adjusted by Si(311) dual crystal monochromator with fixed exit beam position and was determined as 1.63747Å. Data analysis was performed by Fourier transform of EXAFS, reverse operation of Fourier transform and curve fitting method. And then, chemical structure of hopeite crystal doped with manganese component was drawn by coordination number and bond distance.

Results and Discussion

Fourier transform of EXAFS related to zinc components in hopeite-A and hopeite-B were carried out and are shown in Fig.1. The radial distributions of first neighboring atoms appeared at a distance of 1.46Å for the former and 1.44Å for the latter. Both bond distances corresponded to Zn-O bond. The peaks of hopeite-B were smaller than those of hopeite-A. The reason is that the local structure of zinc component was

disordered by manganese component in hopeite-B. It was thought that the local structure of zinc component became complicated by manganese coordination in the crystal.

However, since Fourier transform contains deviation $\phi(K)$ of phase shift, these bond distances obtained by this procedure do not indicate real ones. Therefore, it is necessary to correct the $\phi(K)$ to determine the real distances by using reverse operation of Fourier transform. This procedure was performed for each peak and curve fitting method which enables to explain the best coordination number and bond distance was carried out. As a result, Zn-O bond distance of 1.94Å for hopeite-A and that of 1.96Å for hopeite-B were gotten. Further, coordination number of 4.0 for the former and that of 3.1 for the latter were acquired. 2nd peak to 4th peak corresponded to Zn-P positions.

Fourier transform of EXAFS for Mn-K absorption edge in hopeite-B was also tried. The first peak which implies Mn-O bond appeared at 1.68Å distance. Then, reverse operation of Fourier transform and curve fitting were carried out. Real bond distance of Mn-O appeared at 2.15Å and coordination number of manganese component showed 6.8. This summary is shown in Table 1. 2nd to 4th peaks corresponded to Mn-P positions.

Zinc components in hopeite crystal are consisted of ZnO , tetrahedron structure and $\text{ZnO}(\text{H}_2\text{O})$, octahedron structure. It was found that the bond relation of Zn-O in both hopeite crystals corresponded to zinc component in ZnO structure and that the bond relation of Mn-O in hopeite-B corresponded to $\text{MnO}(\text{H}_2\text{O})$, as coordination numbers show. That structure is formed by substitution of manganese component for zinc component in octahedron structure as shown in Fig.2. These data provided a conclusion that the mechanism of chemical improvement of hopeite crystal was brought by doping with manganese component in octahedron structure of hopeite crystal.

References

- 1) N.Sato, Surf. Coat. Technol., 30, 171 (1987).
- 2) N.Sato, Surf. Coat. Technol., 34, 331 (1988).
- 3) N.Sato, Proceedings of 20th ISATA International Conference on Automotive Technology and Automation, (Firenze, Italy), 1785 (1989).
- 4) N.Sato, Kinzoku Hyomen Gijutsu, 37, 758 (1986).
- 5) N.Sato, PF Activity Report, No.7, 84 (1988).

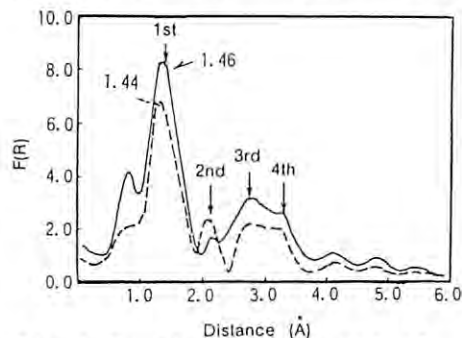


Fig.1 Fourier transforms of EXAFS showing Zn-K absorption edges of hopeite-A and B
—: hopeite-A without Mn
---: hopeite-B with Mn

Table 1 Bond distances: R and coordination numbers: N determined by means of curve fitting method for hopeite-A and B

Bond type	hopeite crystal	R/Å	N
Zn-O	A	1.94	4.0
	B	1.96	3.1
Mn-O	A	—	—
	B	2.15	6.8

*Resolving power of R and N (number of oxygen) is 0.05Å and 1 respectively.

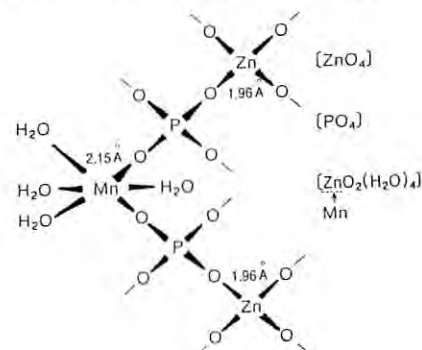


Fig.2 Crystal structure of hopeite doped with Mn

EXAFS STUDIES ON Pd-M/C CATALYST

Toshio AKAI, Takashi USHIKUBO, Yasuo KOIKE, Keisuke WADA, and Konoe MIURA

Research Center, Mitsubishi Kasei Corporation,
1000 Kamoshida-chou, Midori-ku, Yokohama 227Introduction

Pd-M (M:additive metal) supported on active carbon is an important catalyst for many kinds of chemical reactions in chemical industries. Several studies have been carried out on these catalysts. In developing it, it is useful to know its structural change before and after reactions. However, it is not easy to analyze the structure of highly dispersive catalysts with X-ray diffraction, hence we have tried to apply EXAFS to the studies on Pd-M/C catalyst.

In the first step, we measured Pd K-edge EXAFS spectra of Pd-M/C in order to clarify the local structure around Pd.

Experimental

The samples studied in this report were Pd-M/C fresh catalyst and used catalyst(after reactions). Furthermore, Pd metal foil, and PdO powder were analyzed as standard samples.

The Pd K-edge EXAFS and XANES spectra have been measured in transmission mode at BL10B. The catalyst samples were filled into glass tubes (10 mm diameter, 30 mm length). PdO powder, which was a reference sample, was mixed with polystyrene powder, and pressed into a disk (20mm ϕ). Samples were prepared in such a way that the $\Delta \mu t$ was in the range of 1 to 2.

The curve-fitting analysis was performed with theoretical parameters, which were obtained from the plane wave approximation.

Results and Discussion

Figure 1 shows the XANES spectra. The XANES spectrum of the used catalyst is different from that of the fresh catalyst, but similar to that of palladium metal. On the other hand, the K-edge energy positions of both fresh and used catalyst are about 10eV smaller than that of palladium metal.

The results of Fourier transforms are shown in Figure 2. The Pd-Pd peak at 2.5Å is found in palladium metal, the used, and the fresh catalyst. In addition, Pd-O peak exists in the fresh catalyst. However, the Fourier transform of the fresh catalyst is different from that of PdO, having two Pd-Pd peaks, and a Pd-O peak. The used catalyst has a similar Fourier transform to palladium metal that has only one Pd-Pd peak at 2.5Å.

The results of curve-fitting are shown in Table 1. The fresh catalyst showed the smallest coordination number of Pd-Pd. It indicates that the palladium particles of the fresh catalyst are more highly dispersed on active carbon, and have larger surface area. Therefore, Pd-O can be seen in Fourier

transform of the fresh catalyst. In the used catalyst, the Pd-Pd coordination number increases compared with that in the fresh one. It implies that the high dispersive palladium particles grew into larger ones during the reaction.

More detailed structure analyses of these catalysts are under way.

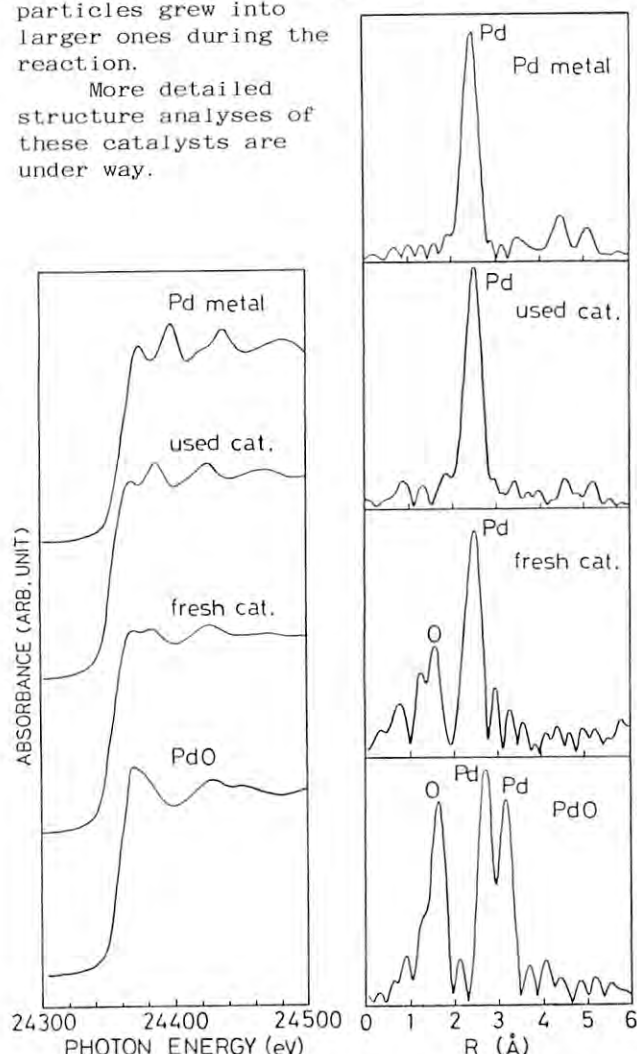
Fig.1 XANES spectra
of Pd K-edgeFig.2 Fourier transforms
of Pd K-edge EXAFS

Table 1. The structural parameters from curve-fitting analyses of EXAFS

Sample	Pd-O		Pd-Pd	
	R/Å	N	R/Å	N
Pd (metal foil)	—	—	2.72	5.54
Pd-M/C				
fresh catalyst	1.99	0.42	2.73	1.21
used catalyst	—	—	2.76	2.80
PdO (powder)	2.03	1.76	3.00	1.35
			3.44	1.35

R:interatomic distance N:coordination number
(relative value)

XAFS STUDIES ON SILICA-SUPPORTED TANTALUM OXIDES

Hisako YANAI, Takashi USHIKUBO, Keisuke WADA, Toshio AKAI, Yasuo KOIKE and Konoe MIURA

Research Center, Mitsubishi Kasei Corporation,
1000 Kamoshida-chou, Midori-ku, Yokohama 227Introduction

The hydrated tantalum oxide shows strong acid properties in its amorphous form.¹⁾ The acid property is thought to be controlled by the preparation of metal oxides - supported Ta oxide with well - defined structure. In this study, we attempted to prepare Ta oxide thin film by reaction of tantalum alkoxide (e.g. Ta n-butoxide) with the surface OH groups of silica (Ta oxide/SiO₂ (ALK)). In order to clarify the local structure and the electronic environment around Ta atoms of Ta oxide/SiO₂ (ALK), we tried to study by XAFS. And the results were compared with those of Ta oxide /SiO₂ (IMP) and Ta-Si mixed oxide (CPR) , which were prepared by impregnating acidic aqueous TaCl₅ solution on SiO₂ and hydrolysis of Si and Ta mixed alkoxides, respectively.

Experimental and Results

The Ta LIII - edge XAFS data of these silica-supported tantalum oxides were obtained at EXAFS apparatus(BL-10B).

Figure 1 shows XANES spectra for (a)~(c) ALK, (d) CPR, (e) IMP and (f) Ta₂O₅ (crystal). In the samples (a), (b) and (c), Ta oxide contents were different. There were clear differences in the shapes of the absorption curves, especially peak tops. This result implies that the symmetry around Ta in Ta oxide / SiO₂ (ALK,IMP,CPR) was different from that in the bulk Ta₂O₅.

Figure 2 shows the results of Fourier transformation of the EXAFS data. In Ta oxide/SiO₂ (ALK), especially the sample (a) (Ta oxide 4.3 wt %), highly dispersed Ta oxide species are

expected to exit on the surface. The Ta oxide (a) did not crystallize even at the high temprature (~1200°C), that was confirmed by XRD method. More detailed investigations about the structure and physicochemical properties are in progress.

We are indepted to Prof. H. Hattori, Dr. S. Hasegawa and Dr. T. Tanaka for their valuable suggestions.

Reference

- 1) T. Ushikubo, K. Wada, 4th Japan- China- U.S.A. Symp. on Catal., p-45 (1989).

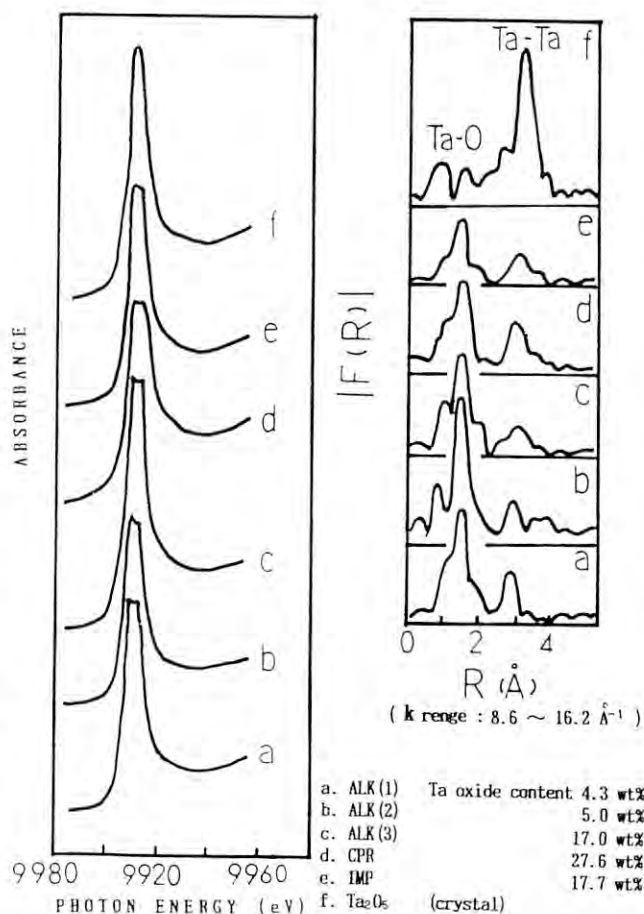


Fig. 1

Fig. 2

EXAFS STUDY ON THE STRUCTURE OF AMORPHOUS $\text{Se}_{1-x}\text{Te}_x$ ALLOY-FILMS

Katsuhiko TANI, Tadao KATSURAGAWA and Eriko CHIBA

R&D Center, RICOH Company, LTD.
16-1, Shin'ei-cho, Kouhoku-ku, Yokohama 223

Introduction

Amorphous $\text{Se}_{1-x}\text{Te}_x$ alloy-films with an atomic content of $x=0.05$ can be prepared by vacuum evaporation. The radial distribution function of this sample obtained from X-ray diffraction showed that the Se-Se bond length corresponding to the radius of the first coordination shell was 2.35Å (with fluctuation ± 0.25 Å) and the Se-Se-Se length corresponding to that of the second coordination shell was 3.75Å (fluctuation ± 0.25 Å). The coordination number calculated on the first shell was nearly 2. This amorphous alloy film has a structure which mainly consists of the "-Se-Se- -Se-" chains and the "Se_n" rings. The result agrees with the reported amorphous structure model¹⁾. The dihedral angles (Se-Se-Se) were distributed around 107.8°. This value suggests that the chain in this amorphous film is flatter than that in crystalline Se. We have supposed that the Te atoms in this alloy film not only substitute in some Se atoms but also dominate the topology of the structure. For this reason, we have determined local structures around both Se and Te atoms by means of EXAFS on this sample.

Experimental

Samples about 8 μm and 26 μm thick were prepared by vacuum evaporation. EXAFS for Se-K edge ($\sim 12.6\text{KeV}$) were

measured on two stacked 8 μm films; for Te-K edge ($\sim 31.8\text{KeV}$) 26 μm films were stacked 20 deep. Measurements were carried out at room temperature on the Beam Line 10-B of the Photon Factory. Ar(15%)+N₂ mixed gas and Ar were used in the front and rear ion chambers respectively for the Se-K edge; for the Te-K edge, Ar and Kr were used. Figures 1a and 1b show the EXAFS spectra of the Te-K edge and Se-K edge. Figures 2a and 2b show the magnitude of Fourier transforms of k^3 times $\chi(k)$ for both atoms with their imaginary parts.

Results and Discussion

By means of curve fitting calculations we have determined the following structural parameters. The Se-Se bond length was 2.38Å (with fluctuation ± 0.23 Å) and the Te-Se bond length 2.57Å (fluctuation ± 0.23 Å). These fluctuations are essential in amorphous structure. We have also found that the Se atoms in the $\text{Se}_{1-x}\text{Te}_x$ films were twofold-coordinated but the average coordination number of the Te atoms was 2.8. Hence, it is concluded that the majority of the Te atoms are threefold-coordinated and the chain is split at these Te atom positions.

Reference

1) R. Zallen; "The Physics of Amorphous Solids", John Wiley & Sons (1983)

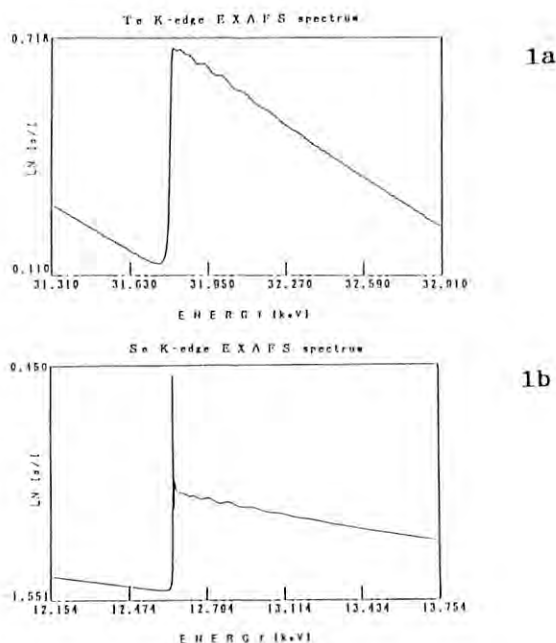


Fig.1 EXAFS spectra of Te (a), Se (b)

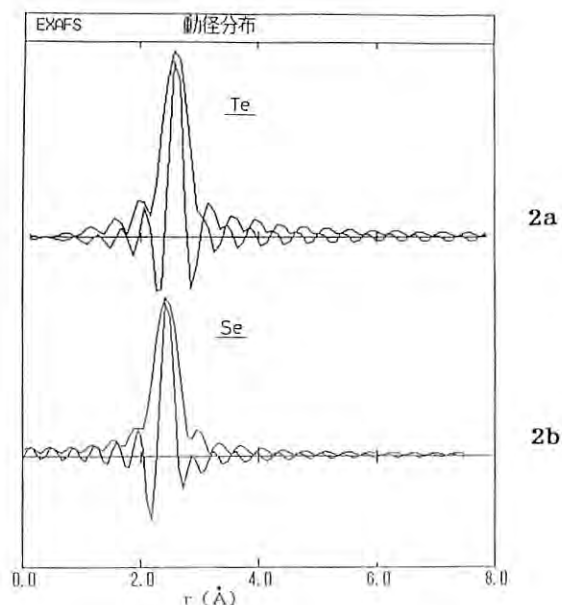


Fig.2 Fourier transforms of Te (a), Se (b)

SIMPLE PERFORMANCE TEST OF EXAFS FACILITIES

Masaharu NOMURA and Atsushi KOYAMA

Photon Factory, National Laboratory for High Energy Physics, 305

Performance of the experimental station BL10B has been studied intensively and has been published: ca. 10^9 photons/s with $\Delta E=1$ eV at 9 keV when the stored current is 300 mA and the higher order content is ca. 7.1×10^{-4} at this energy.¹⁻³⁾ Of course it is desirable to check the performance of the experimental station just before the EXAFS measurement itself, however, it is not so easy to do such test frequently because such tests need high precision equipments and are rather time-consuming. Here we propose a simple method to test the performance of the experimental station qualitatively: higher order content, adjustment of electronics etc.^{3,4)}

Experimental

The setup of the experiment is shown in Fig.1, which is similar to the normal setup for EXAFS measurements except the position of the sample. We have used copper foils of various thickness as the test sample. X-Ray absorption spectra were measured at BL10B using a Si(311) channel-cut monochromator. Nitrogen and mixture of nitrogen (50%) and argon is filled in the I_0 and I ionization chamber, respectively.

Results and Discussion

Spectra obtained with this setup, normal EXAFS one and extracted EXAFS wiggle ($k^3\chi(k)$) are shown in Fig.2. Spectra with this setup show no discontinuity at the edge position when the sample is thin and uniform, however, negative edge appears when the sample becomes thicker: the apparent edge jump is -0.015, -0.08 and -0.23 for 18, 24 and 30 μm thick foils, respectively.

There are four possibilities to explain the above described phenomena: (1) higher order harmonics, (2) non-linearity of the detector

and/or electronics, (3) incorrect offset of electronics and (4) fluorescence and/or scattering from the sample. Among them the contribution of higher order harmonics is expressed as

$$\frac{i}{i_0} = \frac{I_f \cdot \exp(-\mu_f t) \cdot (1 - \epsilon_{0f}) \cdot \epsilon_{1f} + 3I_3 \cdot \exp(-\mu_3 t) \cdot (1 - \epsilon_{03}) \cdot \epsilon_{13}}{I_f \cdot \exp(-\mu_f t) \epsilon_{0f} + 3I_3 \cdot \exp(-\mu_3 t) \epsilon_{03}}$$

where I , ϵ , μ and t means the incident photon flux, detection efficiency by an ionization chamber, the linear absorption coefficient of copper and the thickness of the copper foil, respectively. Suffix f, 3, 0, 1 indicates the fundamental X-ray, third order X-ray, front and rear ionization chambers, respectively. By using the measured I_3/I_f at 9 keV, 7.1×10^{-4} , and the mass absorption coefficient of copper metal, the apparent edge jump, $\Delta(\ln(i_0/i))$, is calculated as -0.0006, -0.003, -0.013, -0.055 and -0.20 for 6, 12, 18, 24 and 30 μm thick foils, respectively. These values fit well with the experimental ones in case of rather thin foils. The slight difference in thick samples is explained by the misadjustment of the offset in the electronics. Details will be explained in ref. 3.

References

- 1) H.Oyanagi, T.Matsushita, M.Ito and H.Kuroda, *KEK Report*, 83-30 (1984).
- 2) M.Nomura, *KEK Report*, 85-7 (1985).
- 3) M.Nomura and A.Koyama, *KEK Report*, to be published.
- 4) This experiment is proposed by Dr. J. Goulon of Université de Nancy I, however, he ascribed it to the nonlinearity of the ionization chambers. This is only one of the reason of this phenomenon as described in this report.

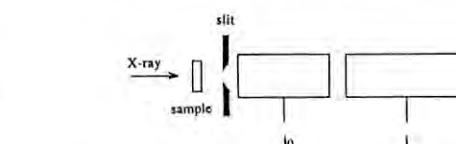
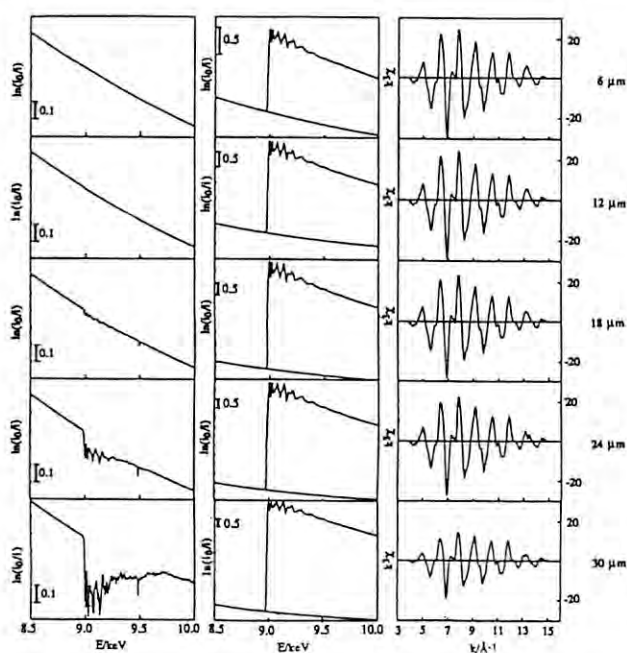


Fig.1 The setup for simple performance test. Sample is put before the i_0 -monitor.

Fig.2 $\ln(i_0/i)$ obtained from the setup shown in Fig.1, EXAFS spectrum obtained with normal setup (the sample is put between i_0 and i monitors) and extracted EXAFS wiggle ($k^3\chi$) for various thickness of copper foil (6, 12, 18, 24 and 30 μm). Vertical scale of the left and the right column is the same within each column.

Cl K-edge EXAFS study on $\text{AgBr}_x\text{Cl}_{1-x}$ solid solutions

Toshihiko YOKOYAMA, Yasutaka TAKATA, Fumiko TAKAMATSU,
Masahiko YOSHIKI, Kazuhiko SEKI and Toshiaki OHTA,

Department of Materials Science, Faculty of Science, Hiroshima
University, Naka-ku, Hiroshima 730

Tadaaki TANI and Kiyoteru MIYAKE

Fuji Photo Film Co., Ashigara Research Laboratories, Nakanuma,
Minamiashigara, Kanagawa 250-01

Introduction

It is an interesting subject to investigate the local structure of solid solutions. A number of EXAFS studies have been published on solid solutions and the breakdown of the Vegard's law has been emphasized from the microscopic points of view. However, most of the works have been the EXAFS analysis of one component atom. We can obtain more reliable information if we analyze EXAFS spectra of all component atoms of a solid solution and combine all the data. $\text{AgBr}_x\text{Cl}_{1-x}$ is a typical solid solution which is practically used as a photographic material. A preliminary EXAFS study on this material [1] has been already carried out for Br K-edge, but never for Cl K-edge spectra because Cl K-edge is in the region of soft X-rays. In this work, we have investigated Cl, Br and Ag K-edge EXAFS to reveal the whole local structure. Here we present the results of Cl K-edge data.

law. Such tendency is also observed in other solid solutions such as $\text{AgBr}_x\text{I}_{1-x}$ [2], ZnMnSe_{1-x} and HgMnTe_{1-x} [3]. At present, we cannot conclude whether the bond distance retains same or increases slightly, as the mixing ratio of Br, x increases. Lushington et al. [1] reported the results of Br K-edge EXAFS data and remarked that the Br-Ag bond distance is shortened with the decrease in x . This result is consistent with our present observation that the Cl-Ag bond distance increases slightly.

The measurements and analysis for Br and Ag K-edge EXAFS data are now in progress.

[1] K.J.Lushington and Y.T.Tan, EAST-WEST SPSE Meeting, Hawaii, 1988.

[2] A.Yoshiasa, F.Kanamaru and K.Koto, Solid state ionics 27 275 (1988)

[3] W.-F.Pong, R.A.Mayanovic and B.A.Bunker, Physica B 158 617 (1989).

Experimental

$\text{AgBr}_x\text{Cl}_{1-x}$ ($x = 0.2, 0.4, 0.6, 0.8$) were prepared by the coprecipitation of appropriate amounts of AgBr and AgCl and a subsequent annealing in an Ar atmosphere at 343 K for 25 days. Cl K-edge EXAFS spectra were taken with the total electron yield mode at 150 K and 295 K at the soft X-ray double-crystal monochromator station (BL 11B). Reliable EXAFS spectrum was not obtained for the sample of $x=0.8$.

Results and Discussion

The Cl-Ag interatomic distances determined are shown in Fig.1. They are roughly on straight lines within the experimental errors. The bond distance expected from the Vegard's law is also indicated as the straight lines in the figure, whose slopes are significantly larger than those obtained by the EXAFS measurement. This means that the Cl-Ag bond distance is definitely different from that expected from the Vegard's

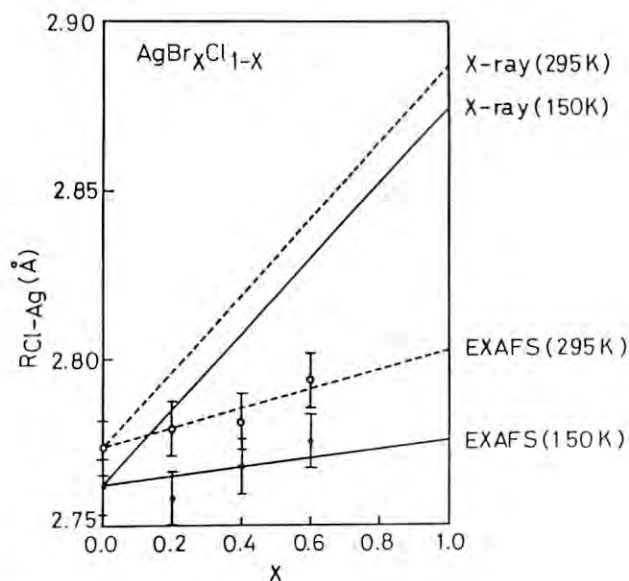


Fig.1. Nearest neighbor Cl-Ag distances derived from the Cl K-edge EXAFS data and from the X-ray diffraction data by use of the Vegard's law.

**COPPER K-EDGE X-RAY ABSORPTION NEAR-EDGE STRUCTURE OF
HIGH-T_c SUPERCONDUCTOR Ba₂Y_{1-x}Pr_xCu₃O_y**

Satoshi MAEYAMA, Azusa MATSUDA*, Masaharu OSHIMA and Yoshinori SATOW**

NTT Applied Electronics Laboratories, Musashino-shi, Tokyo 180

*NTT Basic Research Laboratories, Musashino-shi, Tokyo 180

**Faculty of Pharmaceutical Sciences, the University of Tokyo,
Hongo, Bunkyo-ku, Tokyo 113

Introduction

Ba₂Y_{1-x}Pr_xCu₃O_y (x=0 - 1) which is the substitution of Pr^Y for Y in YBa₂Cu₃O_y is an interesting system for investigating the mechanism of high-T_c superconductivity. T_c in this system gradually decreases with increasing Pr content and superconductivity disappears at around x=0.6¹⁾. However, the orthorhombic crystal structure remains unchanged²⁾. Cu K-edge XANES of this system have been measured to get the information about the suppression mechanism of superconductivity by substitution of Pr.

Experimental

A series of Ba₂Y_{1-x}Pr_xCu₃O_y samples was synthesized from BaCO₃, Y₂O₃, Pr₆O₁₁, and CuO powders¹⁾. The x-ray diffraction patterns confirmed that all the samples had single-phase oxygen-deficient perovskite structure. The samples were powdered just before each measurement, dusted onto the Scotch tape. The absorption measurements in transmission mode were carried out at room temperature using a Si(111) double-crystal monochromator installed at beam line 14A of the Photon Factory.

Results

Figure 1(a) shows Cu K-edge XANES spectra of the Ba₂Y_{1-x}Pr_xCu₃O_y samples with Pr contents (x) of 0, 0.2, 0.4, 0.6, 0.8, and 1. T_c of the samples used for the measurements are about 90K, 85K, and 43K for Pr contents of 0, 0.2, and 0.4, respectively. Significant modifications of the XANES features can be seen with increasing Pr content. In the higher energy region than the main peak B above the edge the peaks of C and D become weaker and less pronounced. A well defined shoulder A in the pre-edge region is observed for the XANES of the Ba₂PrCu₃O_y (x=1) sample. Figure 1(b) shows the corresponding derivative spectra for analyzing the changes in the XANES spectra as a function of Pr content. There are significant differences of the derivative spectra in regions of the shoulder A and peak C between Pr contents of greater and less than 0.5. These differences seem to be related with the suppression of superconductivity by the substitution of Pr.

References

- 1) A. Matsuda et al., Phys. Rev., **B38**, 2910 (1988)
- 2) K. Kinoshita et al., Jpn. J. Appl. Phys., **27**, L1642 (1988)

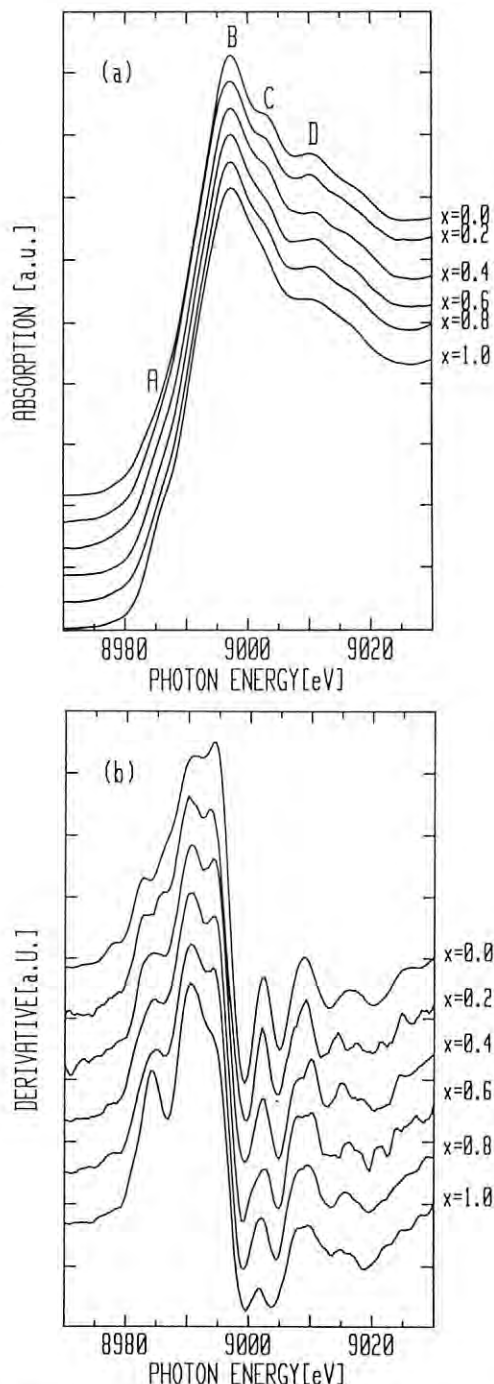


Fig.1. Cu K-edge XANES spectra(a) and their first derivatives(b) for Ba₂Y_{1-x}Pr_xCu₃O_y (x=0, 0.2, 0.4, 0.6, 0.8, and 1).

COPPER K-EDGE POLARIZED X-RAY ABSORPTION NEAR-EDGE STRUCTURE OF HIGH-T_c SUPERCONDUCTING SINGLE-CRYSTAL YBa₂Cu₃O_y

Satoshi MAEYAMA, Akinori KATSUI*, Masaharu OSHIMA and Yoshinori SATOW**

NTT Applied Electronics Laboratories, Musashino-shi, Tokyo 180

*NTT Opto-Electronics Laboratories, Tokai, Ibaraki 319-11

**Faculty of Pharmaceutical Sciences, the University of Tokyo,
Hongo, Bunkyo-ku, Tokyo 113

Introduction

Several measurements on Cu K-edge X-ray absorption near-edge structure (XANES) of YBa₂Cu₃O_y (YBCO) have been carried out to probe the valence states of Cu. However, there is only one report¹⁾ concerning the measurement on polarized XANES which can provide clarified information about the assignment of near-edge features. In this reference a YBCO sample oriented by a strong magnetic field was used. Thus Cu K-edge polarized XANES of YBCO have been measured using a single-crystal sample.

Experimental

The polarized XANES measurements were made on the Cu K-edge in a small orthorhombic single-crystal sample of YBCO²⁾ using a Si(111) double-crystal monochromator with a four-circle diffractometer installed at beam line 14A of the Photon Factory. The spectra under the conditions of the X-ray polarization vector *E* parallel to the *ab* axes (*E*//*ab*) and the *c* axis (*E*//*c*) were measured in the transmission and fluorescence mode, respectively. Temperature dependent data were collected from 60K to 298K by cooling the sample with a cryostat.

Results

Figure 1 shows Cu K-edge XANES spectra of the single-crystal YBCO measured at the temperatures of 60K to 298K under the conditions of *E*//*ab* and *E*//*c*. The polarization dependence of the Cu K-edge XANES can be seen by comparing the spectra in Figs. 1(a) and 1(b). Different features in the spectra observed between the conditions of *E*//*ab* and *E*//*c* are attributed to the bonding states of Cu in the *ab* plane and along the *c* axis. The reported XANES for powder or polycrystalline samples of YBCO are similar to the XANES with the *E*//*ab* condition. The polarized XANES spectra obtained by this measurements almost agree with the data measured for the YBCO sample oriented by magnetic field¹⁾. Temperature dependence of XANES with both conditions of *E*//*ab* and *E*//*c* was not observed; there is only a little change in the spectra measured above and below the superconducting transition temperature (90K). These results suggest that no abrupt change of the electronic structure occurs at the transition temperature.

References

- 1) S.M. Heald et al., Phys. Rev., **B38**, 761 (1988)
- 2) Y. Hidaka et al., Jpn. J. Appl. Phys., **26**, L726 (1987)

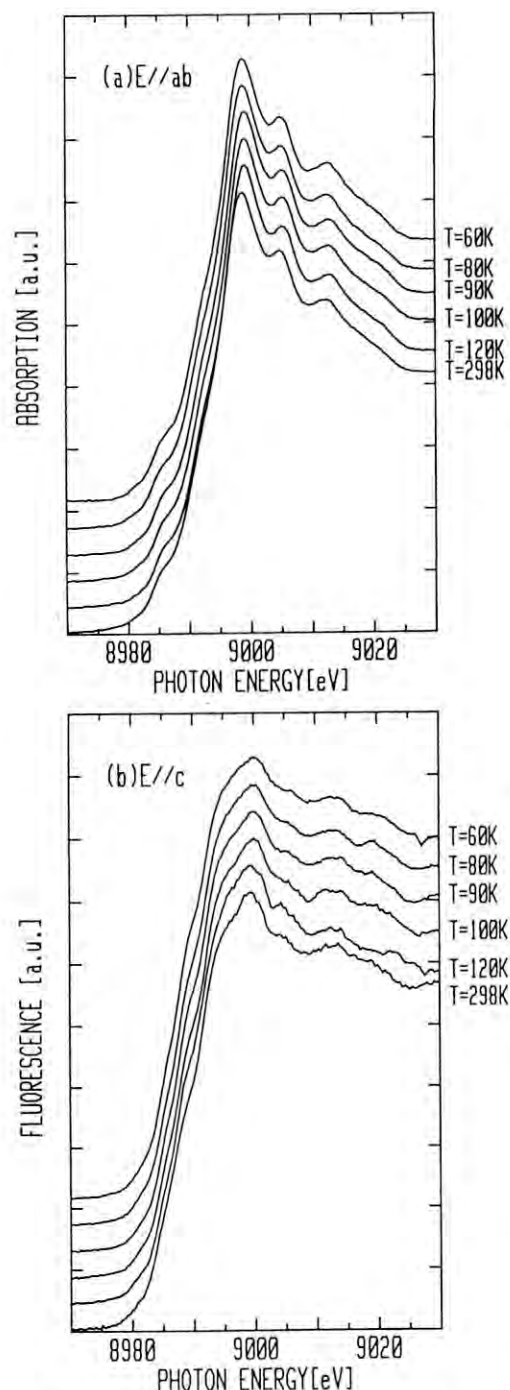


Fig.1. Cu K-edge XANES spectra of single-crystal YBa₂Cu₃O_y with the polarized conditions of (a) *E*//*ab* and (b) *E*//*c*.

INDUCTION OF CHROMOSOME ABERRATIONS BY SYNCHROTRON-PRODUCED MONOCHROMATIC X-RAYS
WITH RESONANCE ENERGY OF PHOSPHORUS K-SHELL ABSORPTION EDGE

¹Shin SAIGUSA, ¹Yosuke EJIMA, ¹Masao S. SASAKI,
²Katsumi KOBAYASHI and ³Hiroshi MAEZAWA

¹Radiation Biology Center, Kyoto University, Sakyo-ku, Kyoto
²Photon Factory, National Laboratory for High Energy Physics, Tsukuba-shi, Ibaraki
³Tokai University Medical School, Isehara-shi, Kanagawa

Introduction

Phosphorus (P) atom is one of the major constituent of DNA molecules. Monochromatic X-rays with the resonance energy of P K-shell absorption edge is a useful probe to analyze the effect of direct ionization of P atoms on the formation of chromosome aberrations. In the present study, induction of chromosome aberrations was studied in cultured mammalian cells using the monochromatic X-rays with the energies of at and around the peak of of P K-shell absorption edge.

Experimental and Results

A near diploid cell line established from mouse embryos (m5S/1M) was used¹). Density-inhibited cells were irradiated with monochromatic X-rays with the energies of either below (2.145keV), above (2.157keV) or at the peak (2.151keV) of P K-shell absorption edge. The irradiated cells were dispersed by trypsin, replated and fixed after 40 hours for chromosome analysis. The results are shown in Figure 1. Dicentric yields increased with the doses in either X-rays, while the efficiency was the highest at the peak energy (2.151keV). When the dose-response curves were fitted to a linear-quadratic equation, $Y = \alpha D + \beta D^2$, the highest efficiency at the peak energy was largely due to the increase of β term as indicated in Table 1.

The predominance of β term at the absorption edge suggests that the elevated yield of chromosome aberrations at the peak energy is mainly due to the photon absorption in adjacent P atoms rather than to the contribution of dense ionization by Auger cascades. The extremely low values of α terms

commonly seen in either X-rays presently used is intriguing particularly in view of our previous finding that α term for the induction of chromosome aberrations in human lymphocytes tends to decline when the photon energy is reduced below 6.9keV²).

References

- 1) M.S. Sasaki and S. Kodama: J. Cell.Physiol., 131, 114 (1987)
- 2) M.S. Sasaki et al: Int. J. Radiat. Biol., (1989) in press

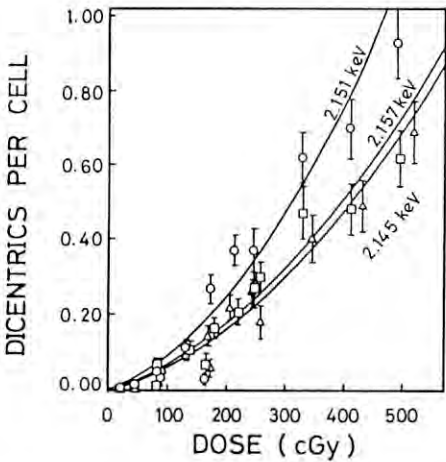


Fig. 1. Dicentric yields in m5S/1M cells irradiated with monochromatic X-rays with photon energies of 2.145keV(Δ), 2.151keV(\circ) and 2.157keV(\square).

Table 1. Coefficients for dose response relationships of dicentric yields in m5S/1M cells.

Wave length (nm)	Energy (keV)	α	β
0.5747	2.157	5.01×10^{-4}	1.94×10^{-6}
0.5763	2.151	5.75×10^{-4}	3.34×10^{-6}
0.5779	2.145	4.26×10^{-4}	1.92×10^{-6}

MOLECULAR CHANGES OF AN AMINO ACID INCLUDING SULFUR WITH IRRADIATION OF MONOCHROMATIC SOFT X-RAYS AT THE RESONANCE ABSORPTION PEAK OF SULFUR

Akinari YOKOYA, Katsumi KOBAYASHI*, Noriko USAMI and Shozo ISHIZAKA

Institute of Biological Sciences, University of Tsukuba, Tsukuba 305,

*Photon Factory, National Laboratory for High Energy Physics, Tsukuba 305, Japan

Introduction

In our previous studies, it was clearly shown that cell lethality ^{1),2)} and induction of genetic changes ²⁾ of monochromatic soft X-rays increased at the energy of resonance absorption of phosphorus. It was supposed that these biological enhancements might be due to radiation damages of macromolecules specifically produced by the inner shell excitation. Knowledge of molecular changes initiated with the inner shell excitation, however, are very scarce except in case of simple gas molecules. In order to get an evidence for molecular changes specific to inner shell excitation on biological molecules, we chose a sulfur containing amino acid, cystathionine, as a model of biological macromolecules, and surveyed molecular changes of the molecule irradiated with monochromatic soft X-rays around K-shell resonance absorption of sulfur.

Materials and Methods

Cystathionine consists of two amino acids (alanine and aminobutyric acid) linked by a sulfur atom (shown in Fig.1). Cleavage of S-C or C-C bond would produce various kind of amino acid. Therefore we could determine the location of cleavage sites by analyzing produced amino acid using high performance liquid chromatography (HPLC) as a usual technique for amino acid analysis. Each peak on the chromatogram is identified with its retention time and quantified with area of the peak. Monochromatic soft X-ray (2472 eV), which corresponds to the resonance absorption peak of sulfur in cystathionine, was chosen for irradiation. Energy of below the peak

(2466 eV), was chosen as a control experiment, which can not be absorbed by the K-shell electron of sulfur. Cystathionine was irradiated in a vacuum chamber with the monochromatic soft X-rays which were obtained with InSb double crystal monochromator at BL-11B.

Results and Discussions

Peak areas (relative yield) per unit exposure of 4 products out of 20 observed are shown at both energies in Table 1. All of them increased with the exposure (incident flux). Aminobutyric acid, which could be produced by the cleavage at the bond A in Fig.1, showed larger peak area at the resonance absorption energy of the sulfur than at the lower energy. On the other hand, glycine, which could be produced by the cleavage at the bond B, did not show any difference in their peak areas between the two energies. Furthermore two unidentified products, peak 1 and peak 2, were observed only at the resonance absorption energy. These results clearly indicate that the K-shell absorption of the sulfur changes fragmentation pattern of irradiated cystathionine. Enhanced yield of aminobutyric acid at the resonance absorption energy suggests that inner shell excitation efficiently leads to the rupture of the bond including the excited atom.

References

- 1) H. Maezawa et al., (1986) Photon Factory Activity Report, **4**, 235.
- 2) K. Kobayashi et al., (1987) Proceedings of the 8th International Congress of Radiation Research, 89.

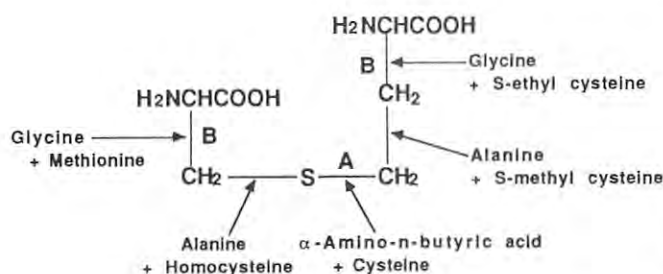


Fig.1. Molecular formula of cystathionine. Arrows show the relation between cleavage site and possible resulting products.

Table 1. Relative peak areas per unit exposure of 4 products from cystathionine irradiated with monochromatic soft X-rays around K-shell resonance absorption peak of sulfur.

Products	w/ S-abs.	w/o S-abs.	Ratio
glycine	1.10	1.10	1.00
aminobutyric acid	14.61	5.93	2.46
peak 1	1.28	not observed	—
peak 2	0.60	not observed	—

INACTIVATION ACTION SPECTRA OF *BACILLUS SUBTILIS* SPORES WITH MONOCHROMATIC SOFT X RAYS (1-6A)Nobuo MUNAKATA¹⁾, Kotaro HIEDA²⁾, Hiroshi MAEZAWA³⁾ and Katsumi KOBAYASHI⁴⁾

1) Radiobiology Division, National Cancer Center Research Institute, Tokyo 104

2) Department of Physics, Rikkyo University, Tokyo 171

3) Department of Radiation Oncology, Tokai University, Isehara 259-11

4) Photon Factory, National Laboratory for High Energy Physics, Tsukuba 305

Introduction

Synchrotron radiation is an ideal source to study biological effects of monochromatic radiations. Our goal is to obtain action spectra for inactivation and mutagenesis of *B. subtilis* spores in the entire range of X rays and vacuum UV radiations available from synchrotron radiation^{1,2,3)}. In the current project, detailed inactivation action spectra in a 1-6A wavelength range for five types of the spores are obtained and analysed. The results demonstrate the importance of K-shell electron absorption of critical target atoms in the spore in shaping the action spectra.

Experimental

Five strains of *B. subtilis* were used; UVR(uvr⁺), UVS(uvrA10 ssp-1), UVP(uvrA10 ssp-1 polA 151), RCE(recE4) and RCF(recF7). Purified 5x10⁶ spores in water were spotted on membrane filter in a circle of about 2mm-diameter₂ for irradiation. A piece of thin flake (about 13mm₂, 0.11mg/mm₂) made of spore powder was used for determination of transmittance. Two types of monochromators covered the wavelength range in question; 111-channel cut Si crystal monochromator (1-3A) and InSb crystal monochromator (4-6A). Samples were exposed in irradiation chambers in vacuo.

Results and Discussion

Survival curves were obtained for five types of the spores at ten wavelengths (1.0, 1.6, 3.0, 3.067, 3.074, 4.0, 5.747, 5.763, 5.779 and 6.0A). Each semilogarithmic curve was fitted to a straight line by linear regression analysis. Since in most cases, the y-intercept of the line is close

to 1.0, we assume a simple exponential decline of survival against exposure and, thence, the sensitivity is represented by the inactivation rate constant. Exposure determined by an ionization chamber and expressed as R is converted to photon fluence (photon/m²) so that the sporocidal effectiveness is exhibited by the inactivation rate constant per unit fluence. Results are shown in Fig. Overall patterns of the spectra are similar in all cases with abrupt changes of the sensitivity at around 3.067A and 5.763A corresponding to the peak resonance absorption by K-shell electrons of Ca and P, respectively. The sensitivities are about 3 and 2 times higher for RCE and RCF, respectively, than the other three types of the spores. This indicates the involvement of DNA-repair capacity dependent on recombination. At each K-edge, the sensitivity is highest at the wavelength corresponding to the peak of resonance absorption. Though Ca atoms are not in DNA, the event subsequent to the absorption to K-shell electrons of Ca seems to cause damage to DNA molecule in the vicinity. When the sensitivity is expressed as the inactivation rate constant per unit absorbed dose (Gy), the pattern becomes relatively flat except the changes at the K-edges of Ca and P. These results show that the pattern of action spectra is mainly determined by the K-shell absorption of Ca and P. It is intriguing that the sensitization is attained by cellular components possibly incorporated in or surrounding DNA.

References

- 1) N. Munakata et al. Photochem. Photobiol. **44**, 385.
- 2) N. Munakata et al. J. Rad. Res. **29**, 44.
- 3) N. Munakata et al. Photon Fact. Act. Rep. **1988**, 114.

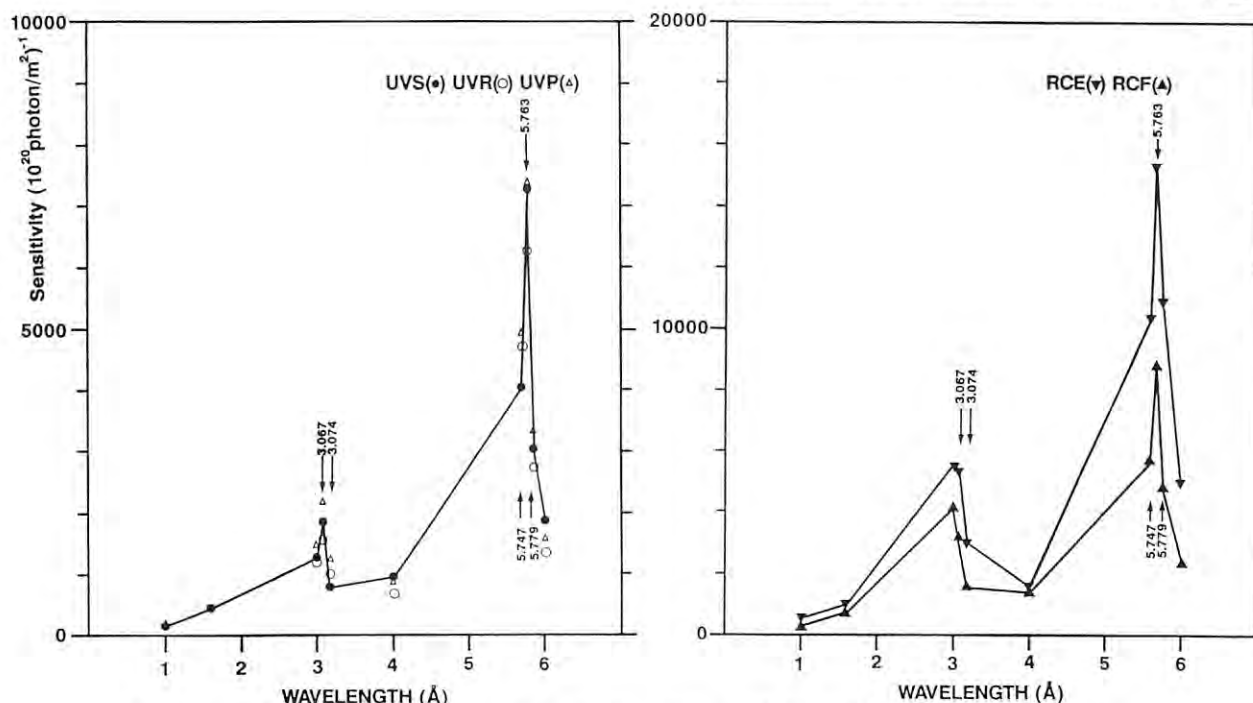


Fig. Inactivation action spectra of five types of *B. subtilis* spores.

REPAIR SUSCEPTIBILITY OF DNA LESIONS PRODUCED BY K-SHELL RESONANCE ABSORPTION OF PHOSPHORUS IN WILD TYPE AND *rad54* MUTANT OF YEAST

Noriko USAMI, Katsumi KOBAYASHI*, Akinari YOKOYA and Shozo ISHIZAKA

Institute of Biological Sciences, University of Tsukuba, Tsukuba 305,

**Photon Factory, National Laboratory for High Energy Physics, Tsukuba 305, Japan*

Introduction

Monochromatic soft X-rays at K-shell resonance absorption of phosphorus show higher lethality to various type of cells than below the absorption edge of phosphorus¹⁾⁻³⁾. In this study, we tried to characterize the nature of the lesions produced by the resonance absorption of phosphorus on the basis of susceptibility to repair of the yeast cells. Yeast cells are known to have various repair activities for DNA lesions. Since each of the activities is exclusively active to certain type of DNA lesion, type of the lesions can be identified with the effectiveness of the pathways to raise the surviving fraction of irradiated cells. Repair pathway including *rad54* gene is reported to be able to repair DNA double strand break type damage⁴⁾, which is considered one possible consequence of the resonance absorption of phosphorus in DNA. Survival curves under various conditions of repair were compared as a measure of repair susceptibilities of the damage.

Materials and Methods

A wild type (RAD) and a DNA repair deficient mutant (*rad54-3*) of diploid yeast, *Saccharomyces cerevisiae* were used. The latter shows temperature-sensitive phenotype and can repair DNA double strand breaks at 23°C while not at 36°C⁴⁾. The procedures of sample preparation and irradiation are almost same with the previous report³⁾. Both strains were irradiated with monochromatic soft X-rays at the resonance absorption peak (2153 eV) of phosphorus or below the absorption edge (2147 eV) at BL-11B or 1B. After irradiation, cells were treated with the following procedures. For the wild strain, part of irradiated cells were immediately plated on nutrient agar medium (immediate plating, IP; no time for repair), another part were kept at 30°C for 48 hrs in 67 mM phosphate buffer before plating (delayed plating, DP; sufficient time for repair). For *rad54* strain, irradiated cells were kept at 23°C (permissive for repair by *rad54* pathway) or 36°C (restrictive for repair) in 67 mM phosphate buffer for 48 hrs, then plated and incubated at 36°C. After these treatments, formed colonies were counted and obtained surviving fractions were plotted against exposure dose (incident photon flux).

Results and Discussions

In the case of wild strain (Fig.1), the surviving fractions increased with post irradiation incubation at both energies of X-rays. Repair susceptibilities defined as $D_{10}(DP)/D_{10}(IP)$ were 1.79 at 2153 eV and 2.27 at 2147 eV. In the *rad54-3* strain (Fig.2), repair susceptibilities ($D_{10}(23^{\circ}C)/D_{10}(36^{\circ}C)$) were 1.81 at 2153 eV and 1.83 at 2147 eV. The lesions

produced by resonance absorption of phosphorus might be less susceptible to the repair activities of wild type than the lesions produced by non-resonance absorption. But responsible repair pathway does not seem to be the pathway including *rad54* gene. These results indicate that the lesions induced by the resonance absorption of phosphorus include, at least in part, some specific type of lesions which are less repairable than the other.

References

- 1) Maezawa, H. *et al.*, 1987, *Proceedings of the 8th International Congress of Radiation Research*, 89.
- 2) Kobayashi, K. *et al.*, 1987, *ibid*, 89.
- 3) Kobayashi, K. *et al.*, 1987, *Photon Factory Activity Report*, #5, 287.
- 4) Budd, M. and Mortimer, R.K., 1982, *Mutation Research*, 103, 19-24.

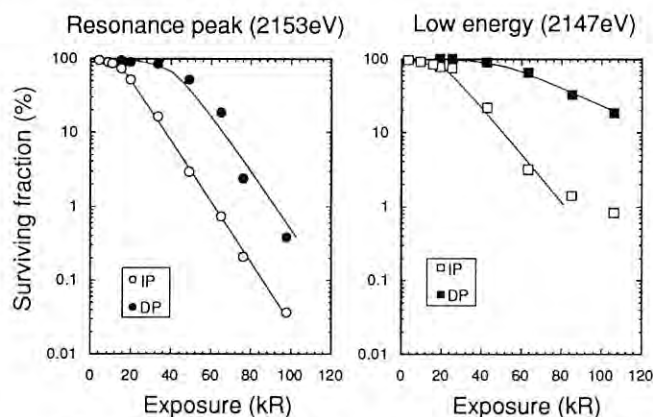


Fig.1 Survival curves of wild type yeast after immediate and delayed plating irradiated with monochromatic soft X-rays at resonance absorption of phosphorus and below the absorption edge.

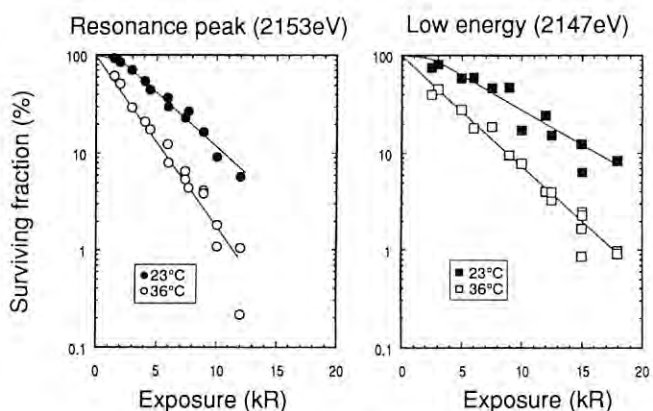


Fig.2 Survival curves of *rad54* strain after holding at 23°C and 36°C irradiated with monochromatic soft X-rays at resonance absorption of phosphorus and below the absorption edge.

IRRADIATION EFFECT ON DEOXYURIDINE-MONOPHOSPHATE INDUCED BY SOFT-X-RAYS WITH RESONANCE ENERGY OF PHOSPHORUS K-ABSORPTION EDGE

Kaoru TAKAKURA, Mitsuo ISHIKAWA, Ritsuko WATANABE, Kotaro HIEDA⁺, Hiroshi MAEZAWA⁺⁺ and Katsumi KOBAYASHI⁺⁺⁺

Department of Physics, College of Liberal Arts, International Christian University, Tokyo 181,

⁺Department of Physics, Faculty of Science, Rikkyo (St.Paul's) University, Tokyo 171,

⁺⁺Department of Radiation Oncology, School of Medicine, Tokai University, Kanagawa 259-11,

⁺⁺⁺Photon Factory, National Laboratory for High Energy Physics, Ibaraki 305.

Introduction

Phosphorus is important atom which forms a main chain in Nucleic Acids. In this study mononucleotide, deoxyuridine monophosphate (dUMP), in aqueous solution was irradiated with monochromatic soft-X-rays around resonance energy of phosphorus K-absorption edge. Radiolytic products were analysed using High Performance Liquid Chromatography (HPLC) and Nuclear Magnetic Resonance (NMR) method.

Materials and Methods

Deoxyuridine-5'-Monophosphate(dUMP) purchased from Sigma Co.Ltd. was dissolved in triply distilled water at concentration of 200 mg/cm³. A hundred μ l of solution was irradiated in a specially designed cell stirring with glass coated iron rod. Monochromatic soft-X-rays from SR at Photon Factory was used as a radiation source. Two wavelengths 5.763 Å (2.152 keV) at the resonance absorption peak of phosphorus and 5.779 Å (2.146 keV) below the K-absorption edge of phosphorus, were selected for irradiation.

The chromatogram was measured using Waters Model ALC/GPC 609G. A reverse-phase column 10mm in diameter by 100 mm in length (Waters μ bondapak C₁₈) was employed. Elution was by means of a 0.007 M K₂HPO₄ solution (pH 7.8) and the flow rate was 1 cm³/min. The spectra were monitored by optical detection at 260 nm. The chromatograph was operated at a temperature of 21 \pm 1°C. Samples of dUMP, uracil and deoxyuridine purchased from Sigma Co. Ltd. were used for reference samples. dUMP in aqueous solution was freeze-dried after irradiation and redissolved in D₂O for measurement of NMR. Spectra of FT-proton NMR were recorded at 21°C on a Varian XL-300 spectrometer.

Results

HPLC elution profiles of dUMP at 2.151 keV were shown at various exposure (Fig.1). Similar profiles were observed at 2.146 keV irradiation. (Figures were not shown) Among several signals for radiolytic products seen in the profile, a signal indicated by no.1 was identified as uracil, judging from retention times with reference sample. A signal indicated by no.2 corresponds to parent dUMP. In Fig.2, the release of uracil from irradiated dUMP per unit volume of irradiated solution of 1 cm³ was shown as the number of uracil as a function of exposure. The efficiency at 2.152 keV was 2.7 times higher than that at 2.146 keV at the exposure of 200 kR.

Proton NMR spectra of dUMP irradiated in aqueous solution with monochromatic X-rays of 2.146, 2.152 and 2.185 keV at exposure of 500 kR were shown in Fig.3. Two new signals which might corresponds to radiolytic products were observed in these spectra

as indicated by a and b. It was confirmed that these signals were neither for uracil nor deoxyuridine. The experiment to identify these signals should be examined.

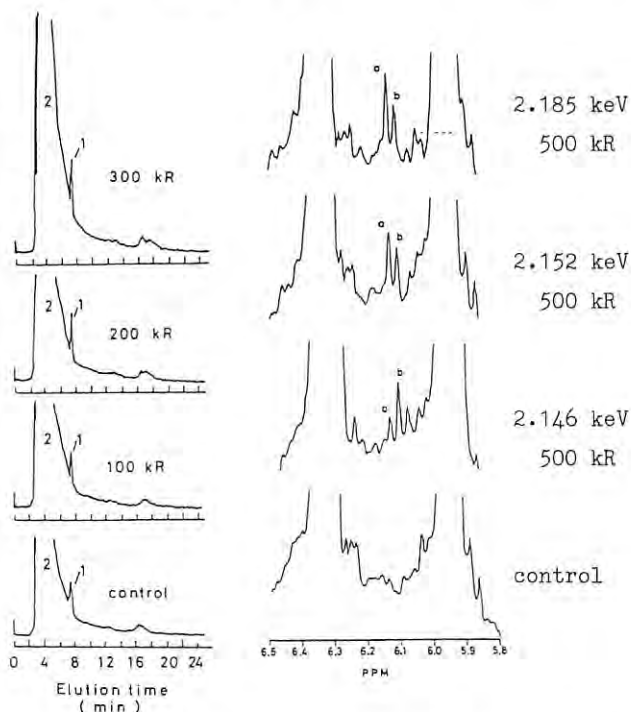


Fig.1 HPLC elution profiles of dUMP irradiated with 2.151 keV X-ray in aqueous solution. 1; uracil, 2; dUMP.

Fig.3 Proton NMR spectra of dUMP irradiated in aqueous solution with X-rays of 2.146, 1.152 and 2.185 keV at 500 kR exposure.

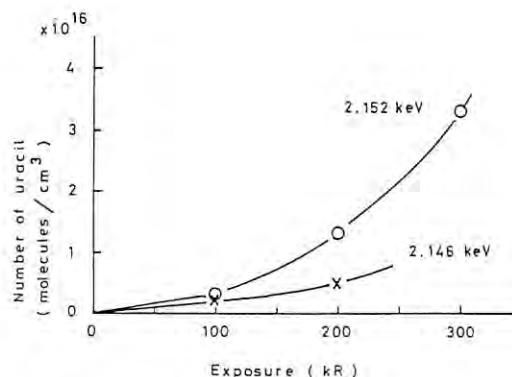


Fig.2 The number of the release of uracil from irradiated dUMP per unit volume of irradiated solution of 1 cm³ as a function of exposure with 2.152 keV (o-o) and 2.146 keV (-x-) X-rays.

FURTHER ANALYSIS OF THE SOFT X-RAY MICROIMAGES OF UNSTAINED HUMAN CHROMOSOME FIBERS DRIED WITH NO FIXATIVE

Kunio SHINOHARA, Hisako NAKANO, Atushi ITO, Yasuhito KINJO*,
Makoto WATANABE*, Sachiko KIKUCHI**, Katsumi KOBAYASHI***,
and Hideki MAEZAWA***

Tokyo Metropolitan Institute of Medical Science, Bunkyo-ku, Tokyo 113

*Tokyo Metropolitan Isotope Research Institute, Setagaya-ku, Tokyo 158

**Toshiba VLSI Research Center, Saiwai-ku, Kawasaki-shi, Kanagawa 210

***Photon Factory, National Laboratory for High Energy Physics, Ibaraki 305

Introduction

It is very important in determining real structure of cellular components to observe biological specimens at high resolution without any artifacts which may be produced by the process of fixation and staining. In the previous report, we have succeeded in observing the structure of unstained human chromosomes dried without any fixative by the use of X-ray contact microscopy (1). Here, we further analyzed the fine structure of chromosome fibers in these images.

Materials and Methods

The analyzed pictures were collected from the images obtained by the method demonstrated in the previous report (1). Briefly, chromosomes from human lymphocytes (RPMI 1788) were spread on a surface of distilled water and were whole-mounted directly on a resist, PMMA (polymethylmethacrylate), supported by a silicon base. They were then dried immediately without any fixation process. The PMMA with the transferred chromosomes was exposed to 2.98 nm monochromatic undulator radiation in a vacuum. The chromosomes were removed from the PMMA which was then developed with a mixture of methylisobutylketone and isopropanol. The developed images were observed under a transmission electron microscope by means of the replica method with a plasma polymerization film made of naphthalene produced in a glow discharge apparatus.

Results

Figure 1 shows an example of the images. Figure 1a shows an X-ray image of a stretched portion of a human chromosome. The enlarged picture of the area pointed by an arrow is shown in Figure 1b. "Beads on a string" structure was observed in Figure 1b. The size measurements were performed for the diameters of these filaments and particles of 50 sites in a couple of enlarged pictures including Figure 1b. The results were divided into two groups, namely 7-15 nm (12.2 ± 2.1 nm) filaments and 16-69 nm (31.4 ± 13.2 nm) particles.

Discussion

In stretched portions of the unstained single human chromosome fiber, we could see the "beads on a string" structure which has been observed in fixed chromosome fibers stained with uranyl acetate and examined by transmission electron microscopy (2). The average diameters of thin filaments (12.2 ± 2.1 nm) and particles (31.4 ± 13.2 nm) suggest that the thin filaments are composed of nucleosomes packed tightly side by side and that the particles correspond to superbeads (unit structure composed of a multiple association of nucleosomes) since the sizes of nucleosomes and superbeads have been reported as 10-15 nm and 15-50 nm, respectively.

The good agreement of the sizes of observed filaments and particles with those of corresponding structures reported by conventional transmission electron microscopy indicates the usefulness of X-ray microscopy for the observation of chromosome structures.

References

- 1) K.Shinohara et al., In "X-ray Microscopy II"(eds. D.Sayer et al.), Springer Series in Optical Sciences 56, Springer-Verlag, Berlin, pp.429-432 (1988).
- 2) M.Watanabe et al., In "X-ray Microscopy in Biology and Medicine" (eds. K.Shinohara et al.), Japan Scientific Societies Press, Tokyo/ Springer-Verlag, Berlin, (in press).

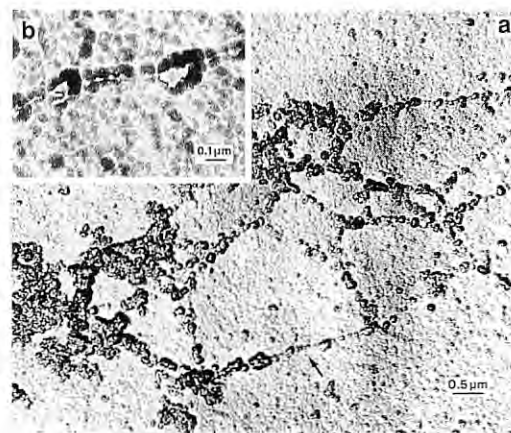


Figure 1

NONDESTRUCTIVE X-RAY FLUORESCENCE SPECTROSCOPIC IMAGING OF TRACE ELEMENTS IN ANIMAL TISSUES (II)

Izumi NAKAI, Nobuhiro SHIMOJOU*, Shino HONMA*, Takuji KAWASHIMA, and Atsuo IIDA**

Department of Chemistry, The University of Tsukuba, Ibaraki 305

*Institute of Community Medicine, The University of Tsukuba, Ibaraki 305

**Photon Factory, National Laboratory for High Energy Physics, Tsukuba, Ibaraki 305

Introduction

In our previous paper, we reported the results of two-dimensional analysis of brains of rats and guinea pigs, which were dosed with Hg and Se, to study mercury intoxication.¹⁾ Through these study we have demonstrated that SR-XRF imaging is particularly useful in the analysis of biological tissue because this technique enables us to carry out multielemental analysis of ppm levels without destroying the form of tissues.

In this study, we have extended the samples to kidney and liver of mouse and several human tissues.

Experimental

Measurements were made at BL-4A, PF utilizing energy dispersive SR-XRF system with monochromatic X-ray obtained by Si(111) double crystal monochromator. Energies of X-ray used were either 14 or 16 KeV. Two dimensional analysis was carried out by placing a slice of sample on a newly designed γ XZ stage, which allows us to measure 50x100mm² area.

Samples used are kidney and liver of mouse dosed with mercury. We have also measured human tissues including kidney, medulla oblongata of human baby and testes of adult man, etc. Photographs of the samples are shown in Figs. 1, (a) to (d).

Results and Discussion

The results of chemical imaging of the samples in Figs. 1 (a) to (d) are given in Figs. 2(a) to (d), respectively. The imaging was made for Hg, Zn, Cu and Se. The data are

represented by 16 densities of black and white image corresponding to the intensity of fluorescence X-ray of each element. As can be seen from Fig. 2a, metal concentration is high at the cortex (rim) in the mouse kidney. One of the important functions of kidney is to filter waste materials in venous blood and glomerulus in the cortex has a role of it. On the other hand, localization of the elements is not found in the liver(Fig. 2b). The liver also has a function of detoxication but whole liver cells have charge of it. In this way, good correlation was observed between elemental distribution and biological functions.

Qualitative analysis of the kidney of human baby disclosed presence of Fe, Cu, Ca, Zn, Se, Cl in the sample. It is thought that Fe came from blood remained in the tissue. The amount of Hg in the sample was negligible, but Hg was measured for future comparison with adult samples. The concentration of metals was high at the cortex of kidney similar to that of mouse. Qualitative analysis of medulla oblongata indicated the presence of Fe, Cu, and Zn, but their concentrations were lower than kidney. It seems that further discussion about relationship between elemental distribution and biological function is difficult because of the lack of literature data. Therefore, we are going to start an extensive study of biological samples to obtain background data of elemental distributions in biological tissues

References 1) I. Nakai, N. Shimojo, S. Honma, T. Kawashima, and A. Iida, PF Activity Report, #694, 141(1988).

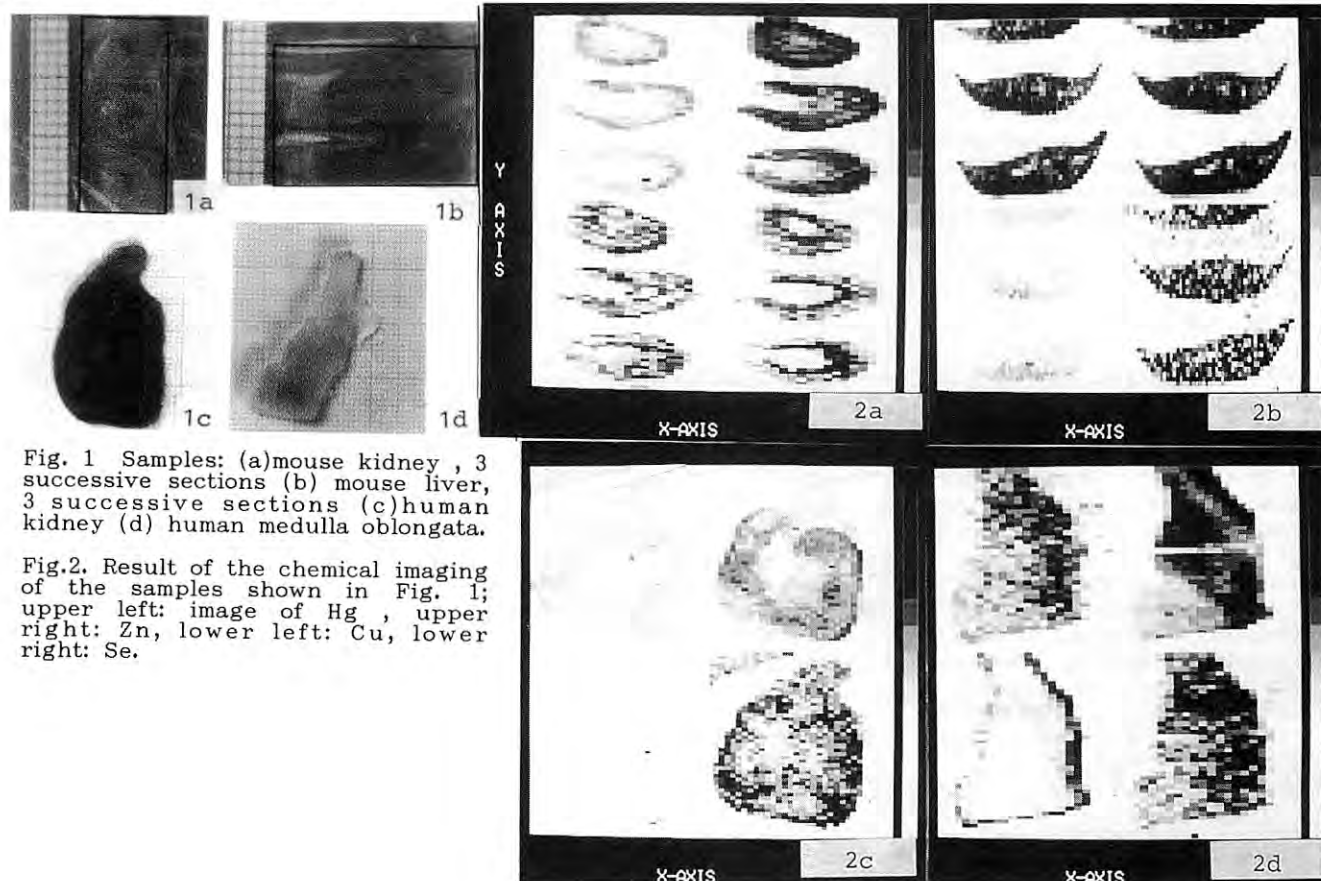


Fig. 1 Samples: (a) mouse kidney, 3 successive sections (b) mouse liver, 3 successive sections (c) human kidney (d) human medulla oblongata.

Fig. 2. Result of the chemical imaging of the samples shown in Fig. 1; upper left: image of Hg, upper right: Zn, lower left: Cu, lower right: Se.

**DETECTION OF DAMAGED DNA IRRADIATED WITH MONO-X-RAY IN THE PRESENCE OF BrdU;
PART II: EFFECT OF HEMATOPORPHYRIN OLIGOMER**

Norio MIYOSHI¹⁾, Kazumori ISHIGURO²⁾, Masaya ISHIHARA³⁾, Katsumi KOBAYASHI⁴⁾,
Takashi ITO⁵⁾, Kazuo NAKANISHI¹⁾, Masaru FUKUDA¹⁾

- 1) Department of Pathology, Fukui Medical School, Matsuoka, Yoshida-gun, Fukui 910-11.
- 2) Department of Dermatology, Fukui Medical School, Matsuoka, Yoshida-gun, Fukui 910-11.
- 3) Department of Development, Hamari Chemical Co., Kunijima, Higashiyodogawa-ku, Osaka 533.
- 4) Photon Factory, National Laboratory of High Energy Physics, Oho, Tsukuba 305.
- 5) Department of Development, Nikon Co., Nishiohi, Shinagawa, Tokyo 140.

INTRODUCTION

Recently, we have studied the detection of instability of nuclear DNA at acid hydrolysis by fluorescent staining with acridine orange (AO)^{1,2)}. Then, we examined quantitative detection in nuclear DNA damaged by mono-X-ray irradiation in the presence of bromodeoxyuridine (BrdU) and/or hematoporphyrin oligomer (HpO) using an acid hydrolysis and AO fluorescence staining method.

EXPERIMENTS

Healthy human lymphocytes (LYM), chronic myelocytic leukemia (CML) and human melanoma flow (HMF) cells were treated with 100 µg/ml BrdU for 6 hr and/or 50 µg/ml HpO for 0.5 hr before harvesting. The cells were irradiated 0.5, 1.0, 3.0, 5.0, 10 and 20 krad by mono-X-ray at 0.80, 0.918, 0.922 and 2.0 Å, respectively.

Almost immediately after the irradiation, these cells were smeared on non-fluorescent glass slide and were fixed with 70 % EtOH aqueous solution for 16 hr at 4 °C. The fixed cells were treated by an acid hydrolysis and AO fluorescence staining method mentioned in our previous reports^{2,3)}.

Fluorescence intensities of AO green and red fluorescence were measured by fluorescence cytophotometry (model QH-2, Olympus). The hydrolysis curves obtained by the photometry were fitted to the Bateman function: $y(t) = y_0 k_1 / (k_2 - k_1) \times [\exp(-k_1 t) - \exp(-k_2 t)]$ to determine the kinetic parameters; y_0 , the initial yield of apurinic acid or single-stranded DNA; k_2 , the rate constant of depolymerization, namely, the degree of DNA denaturation.

RESULTS AND DISCUSSION

The values of y_0 and k_2 were plotted against X-ray doses in the presence of BrdU and/or HpO as shown in Figs. 1 and 2. These values of y_0 and k_2 increased linearly with increase of X-ray doses. The slope of the dose response curves of CML cells was larger than that of the LYM cells (Fig. 1). Furthermore, the slope in the presence of BrdU and/or HpO was bigger than that in the absence of HpO and/or BrdU (Fig. 2). Accordingly, BrdU and HpO molecules enhanced the nuclear DNA damage for the mono-X-ray irradiation at 0.919 or 0.918 Å. The action spectrum of the DNA damage in the presence of BrdU and HpO was shown in Fig. 3. The peak of the spectrum was appeared at 0.918 Å which corresponded to the energy level of the K-shell electron of Br-atomic nuclei. In conclusion, BrdU and HpO molecules sensitized the DNA damage by mono-X-ray radiation.

REFERENCES

- 1) M. Fukuda, N. Miyoshi, et al., *Histochem.*, 84, 556-560 (1986).
- 2) N. Miyoshi, M. Fukuda, *Histochem.*, 84, 561-565 (1986).
- 3) N. Miyoshi, et al., *Photon Factory Activity Report*, 88, 96-97 (1988).

(Fig. 1)

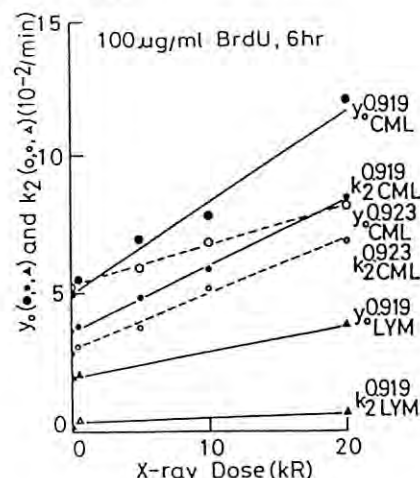


(Fig. 2)

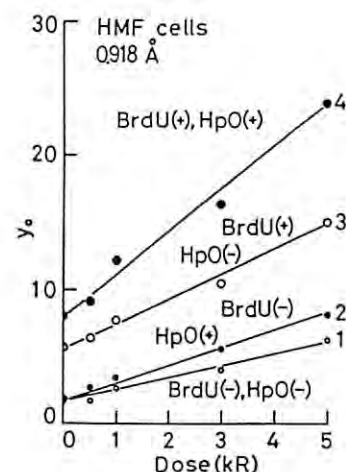
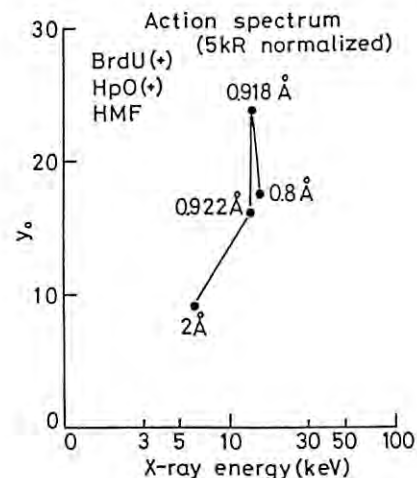


(Fig. 3)



MUTAGENIC AND TRANSFORMING EFFECTS OF SOFT-X-RAYS WITH RESONANCE ENERGY OF PHOSPHORUS K-ABSORPTION EDGE

Masami Watanabe(1), Masao Suzuki(1), Kimiko Watanabe(1), Keiji Suzuki(1),
Noriko Usami(2), Akinari Yokoya(2), and Katsumi Kobayashi(3)

(1) Division of Radiation Biology, School of Medicine, Yokohama City
University, 3-9 Fukuura, Kanazawa-ku, Yokohama 236, Japan,

(2) Institute of Biological Sciences, Tsukuba University
and

(3) Photon Factory, NLHEP, Tsukuba

INTRODUCTION

The monochromatic soft X-rays provide a useful tool for probing the mechanisms of radiation action because of their well defined initial energies and ranges. Radiation-induced mutation and morphological transformation has been supposed to be closely related to chromosome aberrations (1-3). In the present study, induction of mutation, morphological transformation and chromosome aberrations by soft x-rays in golden hamster embryo (GHE) cells were determined.

MATERIALS AND METHODS

The primary GHE cells obtained from 13-14-days embryos were used (1). The exponentially growing cells were cultured in 35mm plastic dish and were irradiated with monochromatic X-rays ranging 5.747Å - 5.779Å. After irradiation, a part of cells were inoculated into 90-mm plastic dish at cloning density (100-3,000 viable cells) to determine both frequency of morphological transformation and lethal effects. Transformation assay used in this experiment was reported previously (1,4). The frequency of transformants were expressed as the ratio of the number of morphologically transformed colonies (Type B)(1) to the total number of colonies counted. The other cells were cultured for mutation expression. When cells had divided three times, they were replated with selective medium containing 40 mM of 6-thioguanine and cultured for further 20 days to determine mutation frequency (5). Small aliquot were fixed 4 hours after irradiation and G-banding for the analysis of chromosome aberrations.

RESULTS AND DISCUSSION

The dose-response curves for survival of GHE cells irradiated with soft X-rays (5.747 Å, 5.763 Å and 5.779 Å) are shown in Figure 1. 5.763 Å X-rays, which is the resonance absorption peak of phosphorus, is more effective than the other wave lengths of X-rays for cell killing. The RBE relative to 60Co r-rays at the D₀ value is about 1.8 for 5.763 Å X-ray, 1.0 for 5.753 and 5.779 Å X-rays.

On the basis of exposure dose (R), the frequencies of mutants and chromo-

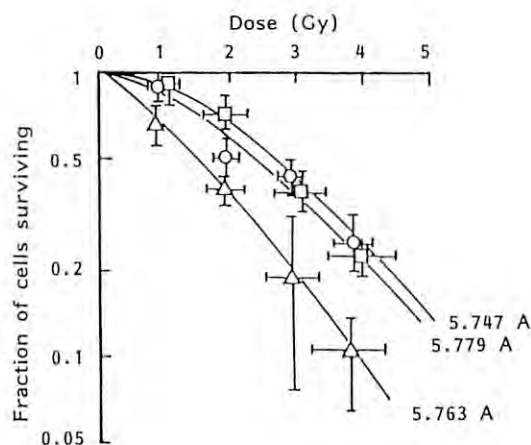


Figure 1 Survival curves of GHE cells irradiated with monochromatic synchrotron radiation.

some aberrations in cells irradiated with 5.763 Å X-rays were about 1.6 times higher than those with 5.747 and 5.779 Å X-rays. At equal survival levels, however, there were no difference in the frequencies of mutants and chromosome aberrations in cells irradiated with soft X-rays.

We also examined the relationship between frequency of transformants and the lethal effect of irradiation with soft X-rays. At equal survival levels (37 % survival), the transformation frequency in cells irradiated with 5.779 Å X-rays was 2.8 times higher than those of cells irradiated with 5.747 and 5.763 Å X-rays. These results suggest that transforming lesion is different from lethal and mutagenic lesions.

REFERENCES

- 1) M.Watanabe, M.Horikawa and O.Nikaido, *Radiat. Res.*, **98**, 274-283 (1984).
- 2) K.Suzuki, F.Suzuki, M.Watanabe and O. Nikaido, *Cancer Res.*, **49**, 2134-2140 (1989).
- 3) M.Watanabe, K. Suzuki and S. Kodama, *Cancer Res.*, **50**, in press (1990).
- 4) M.Watanabe, N.Suzuki, S.Sawada and O. Nikaido, *Carcinogenesis*, **5**, 1293-1299 (1984).
- 5) M. Watanabe and M.Horikawa, *Mutat. Res.*, **71**, 219-231 (1980).

RADIOSENSITIZATION OF 5-IODODEOXYURIDINE IN THE SOFT X-RAY REGION

Kunio SHINOHARA*, Atsushi ITO* and Katsumi KOBAYASHI**

*Dept. Radiat. Res., Tokyo Metropolitan Inst. Med. Sci., Tokyo 113;
**Photon Factory, Nat'l. Lab. High Energy Phys., Ibaraki 305.

Introduction

The sensitizing effects of halogenated pyrimidines such as 5-iododeoxyuridine (IUdR) and 5-bromodeoxyuridine (BUdR) have been well recognized in the relatively high energy region conventionally obtained by 250kVp x-ray source or ⁶⁰Co gamma-ray source. In the present study, we extended the sensitizing effect of IUdR to low energy region (12.4 keV) where photoelectric effect occurs dominantly, and compared with that in high energy region (around 1 MeV) where Compton effect is a major process.

Materials and Methods

HeLa cells were allowed to attach themselves to the surface of the plastic culture flask (Costar, #3393), and grown in Eagle's minimum essential medium supplemented with 10% fetal bovine serum in the presence of IUdR (10⁻⁵ M) and deoxycytidine (10⁻⁵ M) for 18 hr (corresponding to one generation time) at 37 °C under 5% CO₂ and 100% humidity (2.4x10⁹/cell of thymines were replaced by 5-iodouracil). The irradiation was performed on the sample scanning stage installed at the BL-4A. 12.4 keV monoenergetic radiation was obtained with a double crystal Si monochromator from synchrotron radiation. The photon energy was chosen to be unrelated to the energy absorption edge. Intensity of monoenergetic radiation was monitored by a free-air chamber. The irradiation procedure was followed as described previously (1). The surviving fraction was determined from the colony forming ability after the incubation for 10-12 days.

Results and Discussion

Figure 1 shows the survival curve of HeLa cells irradiated with monoenergetic synchrotron radiation at the photon energy of 12.4 keV in the presence or absence of IUdR. Sensitizing effect of IUdR was observed in this low energy region as was the case for high energy photons. Sensitization enhancement ratio [SER=D₁₀(-IUdR)/D₁₀(+IUdR)] defined from the ratio of D₁₀ (the dose required to show 10% survival) was 2.69. In Table 1, SER was summarized for various radiations. SER was found to increase with decreasing photon energy.

The marked wavelength dependence of IUdR radiosensitization shown here should be caused by the difference in the mode of physical interaction between atoms and photons; Compton effect is a major process in the region of ⁶⁰Co gamma-rays, Compton effect and photoelectric effect are comparable in the region of 48 keV photon energy, and photoelectric effect is dominant in the region of 12.4 keV photon energy. The higher sensitizing effect of IUdR in the region of photoelectric interaction may be attributable to Auger effect following to the photoelectric

effect. The Auger electrons and polycation produced by Auger effect are more toxic to cells and may be more reactive to iodines. The nature of iodine sensitization is now being studied with the use of radical scavengers.

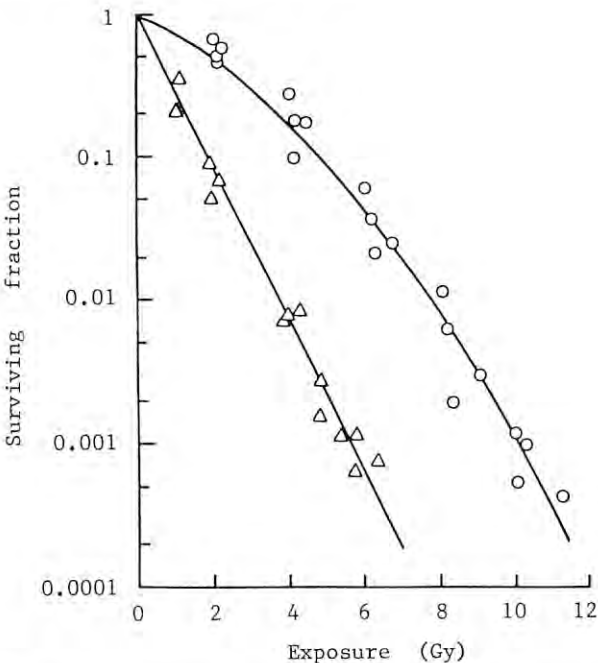


Figure 1. Survival curve of HeLa cells irradiated with 12.4 keV monoenergetic synchrotron radiation in the absence (circle) or presence (triangle) of IUdR.

Table 1. Radiosensitization of iododeoxyuridine

radiation source	SER*
⁶⁰ Co- γ (1.17, 1.33 MeV)	1.82
150kVp-X (E _{eff} =48 keV)	2.11
synchrotron radiation (12.4 keV)	2.69

*) SER is defined as D₁₀(-IUdR)/D₁₀(+IUdR).

References

1) K. Shinohara et al., Photon Factory Activity Report 1988, National Laboratory for High Energy Physics, p.99 (1989).

X-RAY CRYSTAL STRUCTURAL ANALYSIS OF TOBACCO NECROSIS VIRUS

Tomitake TSUKIHARA, Yukio YOKOTA*, Toshio ABE, Keiichi FUKUYAMA*, Hiroshi MATSUBARA* and Atsushi NAKAGAWA**

Faculty of Engineering, Tottori University, Tottori 680, *Faculty of Science, Osaka University, Toyonaka 560, and **KEK, National Laboratory for High Energy Physics, Oho-machi, Tsukuba, Ibaraki 305

Introduction

Tobacco necrosis virus is a small spherical virus about 28nm in diameter. TNV consisting of 180 copies of coat protein and a single-stranded RNA(1) was isolated with its satellite virus, satellite tobacco necrosis virus. STNV is a smaller spherical virus about 20nm in diameter consisting of 60 copies of coat protein and a single-stranded RNA(2). Tobacco leaves are infected with TNV. Although STNV can propagate only in the presence of a helper virus TNV(3). The relationships between TNV and STNV are important from virology. Crystal structure of STNV have been known at 2.5 Å resolution(4). The present study is carried out in order to elucidate three dimensional structure of TNV at a resolution as high as the case of STNV.

One hundred-eighty copies of coat protein of TNV are arranged in a T=3 icosahedral symmetry(6). The different molecular weights ranging from 22,600 to 33,300 are reported for the different strains of TNV(5,6). That of the present study exhibits a single band at 30,000 in SDS/poly acrylamide electrophoresis.

When the virus solution was dialyzed against 0.4 M-sodium phosphate buffer with the pH adjusted to 6.0, the TNV crystals grew in the form of dodecahedron, to a maximum of 1 mm in diameter, in a few weeks. The crystal belongs to a cubic space group of $P4_232$ with cell dimensions 338Å. Assuming that two particle are present in the unit cell, the V_m value(7) is 2.9Å³/dalton. Location and orientation of the virus particle in the unit cell were determined previously(7). Arrangement of coat proteins on the virus surface is described in the present paper.

Experimental

All the X-ray experiments were carried out at the BL6A2 by using Weissenberg camera with a radius of 430mm. X-ray was monochromatized to 1.488Å corresponding to the absorption edge of Ni. Diffraction intensities recorded on a imaging plate of 40x20cm² (Fuji Film Co. Ltd.) were digitized by BA100 (Fuji Film Co. Ltd.).

A crystal was mounted in a capillary to rotate about [111] axis and total of 31.62 oscillation range was covered by 21 serial Weissenberg photographs with an oscillation range of 1.62. Individual plate was overlapped by 0.12. Exposure period was 65 sec. for each shot and the crystal was translated after every seven shots to avoid deterioration of diffraction pattern. Intensities were processed by a program of Higashi(8). Total of 5,695 independent reflections, 85% of the data in the range of 8Å resolution, were obtained at the accepting criteria, $F^2 > 3\sigma(F^2)$ and whole reflection.

Results and Discussions

Fast rotation function at 10Å resolution confirmed the icosahedral symmetry and the orientation of the virus. Assuming that the coat protein is a sphere of 45Å in diameter, R-factor, $R = \sum |F_o - F_c| / \sum F_c$, was calculated at 30 Å resolution for each position on the virus surface. Unique location of coat protein was obtained from the R-factor search as shown in Fig.1. Coat protein arrangement on the virus surface are illustrated in Fig.2 by stereoscopic drawings.

References

- (1) R.E.F. Matthews (1979). Intervirology, **12**, 252
- (2) M.E. Reichmann (1964). Proc. Natl. Acad. Sci. USA, **52**, 1009-1017
- (3) B. Kassanis and H.L. Nixon (1961). J. Gen. Microbiol., **25**, 469-471
- (4) T.A. Jones and L. Liljas (1984). J. Mol. Biol., **177**, 735-767
- (5) J.K. Uyemoto and R.G. Grogan (1969). Virology, **39**, 79-89
- (6) J.A. Lesnaw and M.E. Reichman (1969). Virology, **39**, 729-737
- (7) K. Fukuyama, S. Hirota and T. Tsukihara (1987). J. Mol. Biol., **196**, 961-962
- (8) T. Higashi (1986). J. Crystallogr. Soc. Japan (in Japanese), **28**, 356-363

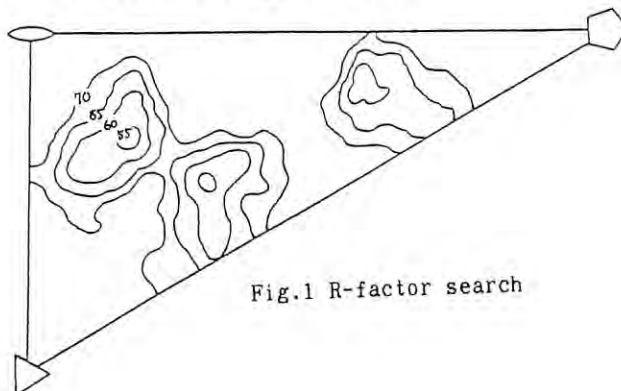


Fig.1 R-factor search

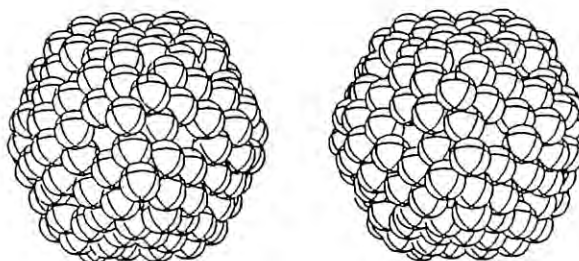


Fig.2 Arrangement of coat proteins

CRYSTAL STRUCTURE OF MYOGLOBIN RECONSTITUTED WITH SYNTHESIZED HEMES

AKIO TAKENAKA, TAKAO SATO, NOBUO TANAKA, SABURO NEYA*, NORIAKI FUNASAKI*, TADASHI HATA#, YASUYUKI KITAGAWA\$, AND YUKITERU KATSUBES\$ Department of Life Science, Tokyo Institute of Technology, Nagatsuta, Midori-ku, Yokohama 227, *Department of Physical Chemistry, Kyoto Pharmaceutical University, Yamashina-ku, Kyoto 607, #The Analytical and Metabolic Research Laboratories, Sankyo Co. Ltd., Hiromachi, Shinagawa-ku, Tokyo 140, \$Institute for Protein Research, Osaka University, Suita, Osaka 565

There are many published studies on the structure of myoglobin. Miki and Kasai (J. Cryst. Soc. Jpn. 27, 2-11, 1985) reported the crystal structures of myoglobins reconstituted with different heme modified at the β positions of pyrrole rings. In order to investigate the mobility of heme in the heme-pocket and its effect on the structure and function, we have employed several synthesized hemes with high symmetry and with no side chain at pyrrole, and have started their structural studies.

The three kinds of meso-tetra-alkyl porphines with methyl, ethyl, and n-propyl groups were synthesized and incorporated into the apoprotein. They were crystallized by the hanging-drop vapor diffusion and the microcell dialysis methods. The protein solutions with 0.1M Tris-HCl buffer (pH 7.0) were included 32-43 % saturated $(\text{NH}_4)_2\text{SO}_4$ and 10mM KCN, and the reservoir solution contained 75% saturated $(\text{NH}_4)_2\text{SO}_4$. Crystals were grown within 2 weeks at 5°C upto about 1 mm in length. Their precession photographs indicated that all the crystals were isomorphous with the space group of $\text{P}2_12_12_1$, which were different from the native one. Crystal data were summarized in Table 1.

Fresh crystals with dimensions of about $0.2 \times 0.05 \times 0.1$ mm were chosen for data collection. Diffractions of SR ($\lambda = 1.04, 1.488$, and 1.743\AA) were recorded on imaging plates packed in the Sakabe's screen-less Weissenberg camera at BL-6A of the Photon Factory. Each Weissenberg pattern was digitallized by BA-100 reader and processed by the computer program "WEIS" to assign the reflection indices and to integrate the intensities within a certain range around the Bragg peaks. The intensity data thus obtained were then combined into the same file and put on a common scale by the program "COMBINE" and "SCALE". The maximum resolution of the data were 2\AA in which 60% of the possible reflections were obtained. The number of observed reflections and their qualities are listed in Table 2.

Table 1. Crystal Data

Myoglobin	Space Group	a	b	c	β
Methyl	$\text{P}2_12_12_1$	58.85	76.58	34.05	—
Ethyl	$\text{P}2_12_12_1$	58.07	76.69	33.48	—
n-Propyl	$\text{P}2_12_12_1$	58.39	76.15	33.86	—
Native	$\text{P}2_1$	64.56	30.97	34.86	105.9

Table 2. Data Collection

Myoglobin	R _{merg} (%)	Total refl.	Unique refl.	λ (\AA)	Rotation axis
Methyl	3.66	18727	7701	1.04	c
Ethyl	4.83	19808	7390	1.04	b
n-Propyl	5.06	25636	6939	1.488	b & c
"	4.88	14757	4121	1.743	b

The crystal structure of n-propyl substituted myoglobin was solved by the molecular replacement method. The native structure without heme group was modified to be a poly-alanine for the reference molecule. Using the computer graphics, the side chains were fitted to the electron density map calculated with MR phases. The atomic parameters thus obtained were refined with the program "PROLSQ" using the $5\text{-}2\text{\AA}$ resolution data, at first, only for the apoprotein, and later the heme group found on a difference map was included. The atomic position of Fe was confirmed on the Harker section of an anomalous Patterson map using the data taken with $\lambda = 1.743\text{\AA}$. After 5 cycles of the refinement, the conventional R factor was converged to 23.9%. By the similar way, the crystal structures of the remaining methyl and ethyl substituted myoglobins were also determined. The current R factors are 25% and 27%, respectively.

The whole molecular structures of the modified myoglobins are essentially the same as that of the native protein, the root mean square deviation being 0.7\AA for overall structure. It is found that the Arg45 side chain is largely deviated to swing out of the molecule. This difference may be due to lacking of hydrogen bonds with water molecules which are hydrogen-bonded to the propionic group in the native crystal. The heme mean planes are tilted by $8\text{-}10^\circ$ from the native plane.

Difference maps omitting the hemes indicate that the meso-tetra-alkyl-porphines have a fixed orientation in the heme pocket. The electron densities, however, are remarkably low, and broaden according to the bulkyness of the substituted alkyl groups, suggesting the small mobility of modified heme in the pocket. NMR spectra of the non-substituted porphine and the methyl-porphine derivatives show a single resonance peak for eight pyrrole hydrogen atoms. The ethyl and n-propyl derivatives also show a similar spectra at 35°C and 55°C , respectively. This feature suggests a free rotation of the heme around its normal, Fe-N(His93) bond. Simple force-field calculations were performed with the program "MM2" to estimate the energy change with rotation around the Fe-N bond. Evidently, the n-propyl derivative with large bulky groups has a large barrier for such a free rotation, but there are no significant change in the non-substituted porphine derivative. We are analysing the structures at different temperatures.

We are indebted to Prof. N. Sakabe, Dr. K. Sakabe, Dr. A. Nakagawa, and Dr. N. Watanabe of the Photon Factory for their technical advice and use of the Sakabe's camera and computer programs. We also thank Dr. K. Namba of ERATO for use of a Fuji Film BA-100 system.

POLYMORPHISM OF RIBONUCLEASE RH CRYSTALS WHICH IS ENHANCED
THROUGH EXPOSURE TO SYNCHROTRON BEAM AND ITS REMEDY

Hiroyuki KURIHARA, Yukio MITSUI* and Kazuo T. NAKAMURA

Faculty of Pharmaceutical Sciences, University of Tokyo, Hongo, Tokyo 113

*Faculty of Engineering, Nagaoka University of Technology, Nagaoka, Niigata 940-21

Introduction

Ribonuclease Rh (RNase Rh) was isolated from *Rhizopus niveus* by Tomoyeda *et al*¹⁾ and purified by Komiyama and Irie²⁾. We obtained the two types of crystals of RNase Rh³⁾, Type I and Type II, which appeared even in the same droplet and they could not be morphologically distinguished from each other. Table 1 shows the crystal data for both types. Type I crystal gives sharper Bragg reflections than Type II crystal, half-widths in omega scan mode being about 0.2° and 0.4°, respectively. Moreover Type II crystal suffers serious radiation damage. Therefore, we started the structural studies on Type I crystals. Later, however, we found that a large number of crystals showed both types of diffraction patterns and it was very difficult to obtain pure Type I crystals constantly. Thus fundamental improvements in the crystallization conditions were needed.

Experimental and Results

We changed pH, temperature, protein concentration and the kinds of precipitant and buffer, using several different lots of the protein samples. Also we added the inhibitor molecules such as 2'-AMP or several ions at several concentrations. Almost all of these attempts were of no effect. However, on adding the divalent cations such as Mg²⁺, Ca²⁺ and Ba²⁺ at a concentration of 10mM, crystals with distinct morphology appeared. These crystals showed the same diffraction pattern as Type II crystal but the Bragg reflections were much sharper (Type II' crystal). Rather surprisingly, the diffraction patterns arising from the use of the three different kinds of divalent cation as mentioned above were indistinguishable from each other when comparing the precession photographs.

Data collections for Type II and Type II' crystals were carried out by using the Sakabe's Weissenberg camera at BL-6A2 using the wavelength of 1.04Å. Table 2 shows the experimental conditions for the data collections. The diffraction image was recorded on Imaging Plates and processed as usual using the computer program "WEIS".

In the case of the old Type II crystal, diffraction spots were broad at the outset and each spot split into two pieces during a few minutes of exposure to the synchrotron beam. The two pieces of spots corresponded to the diffraction patterns of Type I and Type II crystals.

In the case of the new Type II' crystal, however, high resolution data up to 1.8Å was easily collected. The diffraction spots were much sharper than those of Type II crystal and there was little sign of radiation damage. The merging R factor between the two data sets (different rotation axis) was 8.08% for 13587

independent reflections. With the help of the absorption correction referring to the corresponding diffractometer data, further improvement in the quality of the data is expected.

We do not know the mechanism of the stabilization due to the presence of the divalent cations. Considering that back-soaking the divalent-cation-containing crystals in the divalent-cation-free buffer for two to ten days makes no change to the diffraction patterns, the binding sites of these divalent cations are mostly likely non-specific. Although these divalent cations have never been described as important to stability or function of RNase Rh, they did have dramatic effect in improving the quality of the crystals. Thus, adding certain divalent cations to the crystallization media may well be one of the general recipe worth trying for improving the crystal quality.

References

- 1) M. Tomoyeda, Y. Eto and T. Yoshino, Arch. Biochem. Biophys., **131**, 191 (1969)
- 2) T. Komiyama and M. Irie, J. Biochem., **70**, 765 (1971)
- 3) H. Kurihara, Y. Mitsui and K. T. Nakamura, J. Mol. Biol., **206**, 791 (1989)

Table 1. Crystal data of RNase Rh

Type	Type I	Type II
Crystal system	orthorhombic	
Lattice constants	a=68.3 Å	a=67.7 Å
	b=73.0 Å	b=72.5 Å
	c=50.0 Å	c=44.3 Å
Space group	P2 ₁ 2 ₁ 2 ₁	

Table 2. Experimental conditions of data collection

Crystal type	Type II	Type II'	
Crystal	1	1	2
Temperature	20°C		
Crystal size (mm)	0.8×0.4	0.6×0.3	0.5×0.25
	×0.2	×0.2	×0.2
Rotation axis	a	a	b
Beam current (mA)	228-215	239-235	231-227
Wavelength (Å)	1.04	1.04	1.04
Crystal-to-film distance (mm)	430	430	430
Oscillation angle ω (deg)	12.0	12.0	12.0
Number of oscillations	5	3	3
Ratio of ω and film (deg/mm)	2.0	2.0	2.0
ω -scan speed (deg/sec)	2.0	2.0	2.0
Number of films	10	9	9
Total exposure time (sec)	684	340	340

ON THE LOCAL HETEROGENEITY IN A CRYSTAL OF HYDROGENASE

Yoshiki Higuchi, Takuya Okamoto, Yukio Morimoto, and Noritake Yasuoka

Basic Research Laboratory, Himeji Institute of Technology, 2167 Shosha Himeji Hyogo 671-22

INTRODUCTION

Protein crystals are now generally prepared in order to be determined the three-dimensional structures of themselves. The quality of the crystals, that is, the heterogeneity or mosaicity of them, have not been examined well. Recently we found that the hydrogenase crystals prepared from sulfate-reducing bacterium show the heterogeneity along the direction of the crystal growth which is parallel to *c*-axis. Here we show the experimental evidence of the local heterogeneity of the hydrogenase crystal and discuss the relationship between the heterogeneity and crystal growth.

EXPERIMENTAL AND RESULTS

Hydrogenase is an enzyme which catalyzes reversible dehydrogenation of molecular hydrogen. The hydrogenase from *Desulfovibrio vulgaris* Miyazaki F (DvMF) solubilized by trypsin digestion¹ has molecular weight of 89000, and is reported to have two or three [4Fe-4S] type clusters as unique cofactors. Single crystals ($P2_12_12_1$ $a=99.5$, $b=126.8$ $c=66.9\text{\AA}$) of freshly prepared hydrogenase were obtained by sitting-drop vapor diffusion method from 20% (w/w) polyethylene glycol 1000 buffer solution (25mM Tris-HCl, pH=7.5)². To introduce micro crystals by micro-seeding technique is essential for preparing the large size of crystals suitable for x-ray crystallography. X-ray intensity data were collected at 10°C using a Weissenberg camera designed for macromolecular crystallography by Sakabe et al³ ($r=430.5\text{mm}$) installed in BL-6A2. The wavelength of x-ray used was 1.04\AA from synchrotron radiation (SR) of National Laboratory for High Energy Physics. The diffraction patterns were recorded on Fuji Film 'Imaging Plate', and read out by a Fuji Film BA-100. The hydrogenase crystal of $0.5\times 0.5\times 3.5\text{mm}$ was mounted on goniometer head, crystal *c*-axis being parallel to the spindle ω -axis of the camera. Five screenless Weissenberg diffraction patterns in the same oscillation range ($\Delta\omega=9.6^\circ$) were obtained at the different position of the same crystal by shifting the crystal along the spindle axis. Since x-ray beam from SR progress with small divergency and the collimator used was 0.1mm in diameter, the diffraction patterns in the small local area of the crystal could be measured. The experimental conditions are shown in Figure 1. The diffraction patterns recorded on Imaging Plate are shown in Figure 2(a)-(e). They were processed by program WEIS developed by Higashi et al.⁴ to obtain indexed intensity data. The quality of a crystal may be evaluated by the number of reflections with significant intensities. The number of indexed data larger than $4\sigma(I)$ at P1, P2, P3, P4 and P5 positions are 7468, 7276, 7249, 5172 and 3834, respectively. The shapes of the diffraction spots (Fig.2) tend to be more anisotropic from the one end (left end in Fig.1)

to the other end (right in Fig.1). In the similar manner, the number of integrated intensity data which are four times larger than standard deviations decrease from P1 to P5. This observation clearly shows that there is the heterogeneity in the degree of the crystallinity along the *c*-axis. In the crystallization droplet, the P5 side of the crystal in Fig.1 was in contact with the depression glass wall on which protein droplet was set up. On the other hand, P1 side, natural end of the crystal growth, was surrounded by protein solution. These findings suggest that the crystal growth of the hydrogenase is suppressed when the heterogeneity of the crystal is reduced.

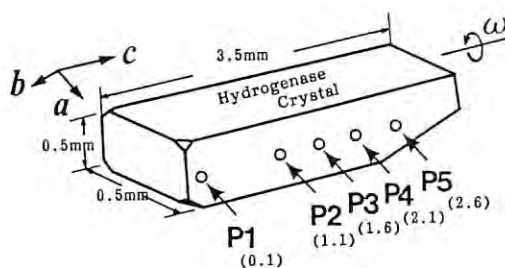


Figure 1

Schematic diagram of the setting condition for diffraction experiment. Arrows show the exposed area of the crystal by x-ray. P1-P5 are the exposed position name and the numerals in the parentheses show the absolute positions(mm) from the left edge of the crystal in this figure.

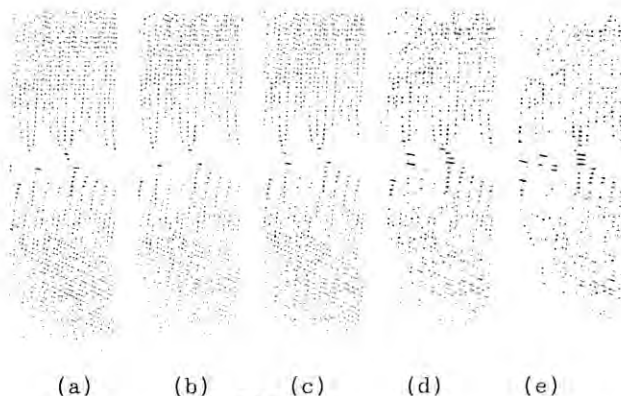


Figure 2

Diffraction patterns of hydrogenase crystal at five different positions in the same crystal.

We are indebted to Prof. Noriyoshi Sakabe, Mr. Atsushi Nakagawa for their technical advice.

References

- 1) T. Yagi et al. *J. Biochem.*, **79**, 661 (1976)
- 2) Y. Higuchi et al. *J. Biol. Chem.* **262** 2823 (1987)
- 3) N. Sakabe, *J. Appl. Cryst.*, **16**, 542 (1983)
- 4) T. Higashi *J. Appl. Cryst.*, in press.

CRYSTAL STRUCTURE DETERMINATION OF CYTOCHROME c₅₅₃ BY THE MULTI-WAVELENGTH ANOMALOUS DISPERSION METHOD

Atsushi NAKAGAWA¹⁾, Yoshiki HIGUCHI²⁾, Noritake YASUOKA²⁾,
Yukiteru KATSUBE³⁾, Tatsuhiko YAGI⁴⁾

- ¹⁾Photon Factory, National Laboratory for High Energy Physics, Oho, Tsukuba, Ibaraki 305
²⁾Basic Research Laboratory, Himeji Institute of Technology, Shosha, Himeji, Hyogo 671-22
³⁾Institute for Protein Research, Osaka University, Yamada-oka, Suita, Osaka 565
⁴⁾School of Education, Shizuoka University, Ohya, Shizuoka, Shizuoka 422

Abstracts

Multi-wavelength anomalous dispersion (MAD) phasing technique has been applied to the determination of three-dimensional structure of an electron transfer protein cytochrome c₅₅₃¹⁾ isolated from sulfate-reducing bacterium, *Desulfovibrio vulgaris* Miyazaki F²⁾. This result has proved successful through the use of synchrotron radiation at Photon Factory with accurate and high-speed data collection from the combination of the Weissenberg camera for macromolecular crystallography³⁾ and the imaging plate⁴⁾. The structure has been refined by Hendrickson-Konnert's restrained parameter least-squares refinement program⁵⁾.

Experiment

The procedure of data collection and phase determination has been reported⁶⁾.

The program FRODO⁷⁾ was used for model building procedure. The model has been refined to an *R* value of 0.226 at 6.0-1.6Å resolution including 63 water molecules.

Results and Discussions

Figure 1 shows an example of the electron density map calculated by the MAD method. This electron density map has good quality to make an atomic model.

Figure 2 shows the wire-model of the refined structure except for water molecules.

The relative locations of two helices at both N-terminal and C-terminal and style of bonding and coordination to the heme group is similar to those of other cytochromes *c*, but other parts of the structure are quite different. In this sense, the folding pattern of cytochrome c₅₅₃ shows "cytochrome *c* folding" like other cytochromes *c* superfamily but cytochrome c₅₅₃ is not classified into the same class of the other small type cytochromes *c*, for example cytochrome c₅₅₁ from *Pseudomonas aeruginosa* and so on. Its three-dimensional structure provides a novel insight into the physical and chemical properties and evolution of cytochromes *c* superfamily.

The refinement of the structure is now in progress.

Acknowledgment

The authors thank to Prof. N.Sakabe in Photon Factory for his helpful suggestion and also thank to Dr. K.Namba in ERATO for using the imaging plate reading system, BA-100.

References

- 1) Yagi, T. (1979)
Biochim. Biophys. Acta, 548, 96
- 2) Nakagawa, A. (1989)
Crystal Structure analysis of Cytochrome c₅₅₃ from Desulfovibrio vulgaris Miyazaki F
Doctoral Thesis, Osaka University, Osaka
- 3) Sakabe, N. (1983)
J. Appl. Crystallogr., 16, 542
- 4) Miyahara, J., Takahashi, K., Amemiya, Y., Kamiya, N. and Satow, Y. (1986)
Nucl. Instrum. Methods, A246, 572-578
- 5) Hendrickson, W.A. and Konnert, J.H. (1980)
In Biomolecular Structure, Function, Conformation and Evolution
(Srinivasan, R., eds.), vol.1, pp.43-57, Pergamon Press, Oxford
- 6) Nakagawa, A., Higuchi, Y., Yasuoka, N., Katsube, Y. and Yagi, T. (1988)
Photon Factory Activity Report, 6, 106
- 7) Jones, T.A. (1978)
J. Appl. Crystallogr., 11, 268-272

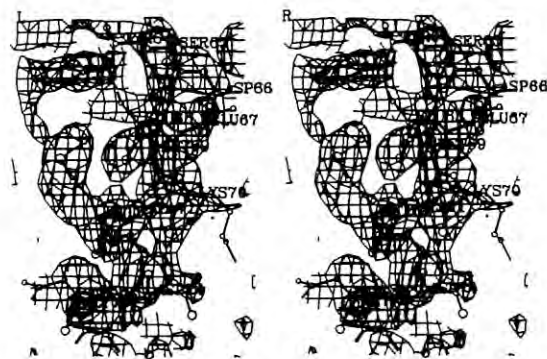


Figure 1
The MAD map showing C-terminal helix
The refined model is superimposed

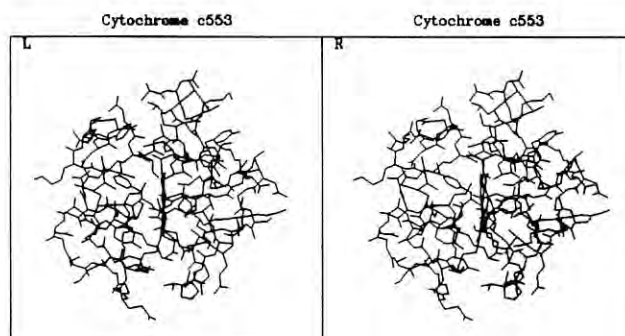


Figure 2
Wire-model of the refined structure

HIGH RESOLUTION DATA COLLECTION OF GAPDH AND IT'S DERIVATIVES WITH WEISSENBERG CAMERA SYSTEM

ZHANG Faming LIN Zhengjiong TSOU Chentlu
Institute of Biophysics, Academia Sinica, Beijing 100080, China

Introduction

As an important enzyme in both glycolysis and glyconeogenesis, D-Glyceraldehyde-3-phosphate dehydrogenase has been shown to be an allosteric enzyme. The yeast enzyme binds NAD^+ with positive cooperativity, whereas the muscle enzyme binds NAD^+ with negative cooperativity. Furthermore, the reaction between the SH group of the active site cys-149 residue of the tetrameric enzyme and certain acylating reagents shows the so-called "half-of-the-sites" reactivity typically for allosteric enzymes (1). It has been found that when the active site Cys-149 carboxymethylated derivative of GAPDH (CM-GAPDH) is irradiated with ultraviolet light in the presence of NAD^+ , a new fluorescent NAD^+ derivative (IRR-GAPDH) is formed (2). In order to deeply study the allosteric properties and the mechanism of the photochemical reaction, it is necessary to analyse the three-dimensional structures of the enzyme and its derivatives.

Experimental

Holo-GAPDH was purified from the tail muscle of *P. versicolor* lobster. The carboxymethylation and ultraviolet irradiation for producing CM-GAPDH and IRR-GAPDH were essentially the same as described for the rabbit muscle (3). Using $(\text{NH}_4)_2\text{SO}_4$ as precipitating agent, the three forms of the enzyme were crystallized by vapour diffusion method. The preliminary crystallographic studies showed that the crystals of the three forms of the enzyme are isomorphous, belong to C2 space group with unit cell dimensions $a=128.44\text{\AA}$, $b=100.10\text{\AA}$, $c=80.97\text{\AA}$, $\beta=114.44^\circ$.

All data sets were collected at BL-6A2 of Photon Factory with synchrotron radiation X-ray source-Fuji imaging plate-Sakabe's Weissenberg camera system (5). The wave length of X-ray was 1.04\AA , radius of camera 430mm, IP size $400\times 200\text{mm}^2$, scanning speed $2^\circ/\text{sec}$, the overlapping between the successive ranges 0.5° , rotation axis a+b or a-b, experimental temperature 7° . The other conditions are given in Table 1.

Table 1. Conditions of data collection

Enzyme	ΔW °	rotation range	C °/min	No. of crystals used	Exposure time	No. of IP
Holo-GAPDH	13.5	0-180°	2.5	1	13'3"	15
CM-GAPDH	13.5	0-360°	2.5	1	21'3"	24
IRR-GAPDH	10.8	0-360°	2.0	1	25'13"	28

Results and Discussions

The intensities were processed by WEIS program (6). The statistical results of the data sets are listed in

Table 2.

Table 2. Statistical results of the reflection data of the three forms of GAPDH

Enzyme	Overall Rmerge	Ntotal	Nindep.	$N(I \geq 3\sigma(I))/N_t$	
				$\infty-1.8\text{\AA}$	$2\text{\AA}-1.8\text{\AA}$
Holo-GAPDH	4.93	91438	49999	93.8%	81.4%
CM-GAPDH	6.22	132424	53524	91.8%	76.9%
IRR-GAPDH	5.77	172806	55850	92.9%	78.6%

It has been reported that the photochemical reaction leading to the formation of the new fluorophore is highly specific, and this fluorophore is a covalent adduct of the nicotinamide moiety of NAD with the enzyme protein at its active site. So there should be some conformational difference between the enzyme and its derivatives. Table 3 gives some comparison results among the three data sets.

Table 3. Merging results of diffraction data between HOLO-GAPDH, CM-GAPDH AND IRR-GAPDH

Rmerge	Holo-GAPDH	CM-GAPDH	IRR-GAPDH
Holo-GAPD	4.93	17.31	13.65
CM-GAPDH	17.31	6.22	14.79
IRR-GAPDH	13.65	14.79	5.77

From table 3, it seems that the structure difference between HOLO-GAPDH and CM-GAPDH is greater than that between HOLO-GAPDH and IRR-GAPDH. Similar results (7) have been found from the $(hk0)$ diffraction pattern comparison of procession photographs of the enzyme. The scale of intensity difference of these three forms of enzyme implies the conformational changes during modification and photochemical reaction are rather subtle. The high resolution structure analysis of the three forms of GAPDH are in progress.

Acknowledgment

We are particularly indebted to Professor N. Sakabe for generously giving us an opportunity to work at BL-6A station and cooperating in data collection. Also very grateful to Dr. A. Nakagawa for his large assistance in data processing and to Dr. K. Sakabe and Mr. N. Watanabe for their various help.

References

- (1) Ho, Y. S. et al., *Biochim. Biophys. Acta*, **613**, 250 (1980).
- (2) Ho, Y. S. & Tsou, C. L., *Nature*, **277**, 254 (1979).
- (3) Ho, Y. S. et al., *Sci. Sin.*, **22**, 207 (1979).
- (4) Gao, Y. G. et al., *Acta Biophysica Sinica*, **3**, 243 (1986).
- (5) N. Sakabe, *J. Appl. Cryst.*, **16**, 542 (1983).
- (6) T. Higashi, *J. Appl. Cryst.*, **22**, 9 (1989).
- (7) Song, S. Y., et al., *J. Mol. Biol.*, **171**, 225 (1983).

DIFFRACTION STUDIES OF THE HEAT-LABILE ENTEROTOXIN B SUBUNIT PRODUCED BY ENTEROTOXIGENIC *ESCHERICHIA COLI*

Keiichi FUKUYAMA, Takao TSUJI,[†] Yukio YOKOTA, Naoki KUNISHIMA and Atsushi NAKAGAWA^{††}

Department of Biology, Faculty of Science, Osaka University, Toyonaka, Osaka 560

[†]Research Institute for Microbial Diseases, Osaka University, Suita, Osaka 565

^{††}Photon Factory, National Laboratory for High Energy Physics, Oho, Ibaraki 305

Introduction

Heat-labile enterotoxin produced by enterotoxigenic *Escherichia coli* is structurally, functionally and immunologically similar to cholera toxin. These toxins are proteins of Mr 84,000 composed of an A subunit (Mr 28,000) and a B subunit oligomer (Mr 56,000). The A subunit consists of A₁ and A₂ fragments. The A₁ fragment increases cyclic AMP in target cells by catalyzing NAD-dependent ADP ribosylation of the regulatory GTP-binding protein of adenylate cyclase. The A₂ fragment may be bound to the B subunit oligomer. The B subunit oligomer has a function to attach the toxin to target cells and facilitates internalization of the A₁ fragment in the cell membrane (1). The relations between the functions and structures of these toxins have been studied by chemical analyses (2) and by mutagenesis of the gene of enterotoxin B subunit (3). Although detailed structures of these toxins are requisite for understanding the structure-function relationship, they are examined only by electron microscopy (4).

The oligomer of heat-labile enterotoxin B subunits has been crystallized by vapor diffusion with polyethylene glycol in the presence of the non-ionic detergent β -octylglucoside (5). The crystal is orthorhombic, space group P2₁2₁2₁, with unit cell dimensions of $a=222.7$ Å, $b=65.7$ Å, $c=119.2$ Å. Assuming that three oligomers are present in an asymmetric unit, V_m value is 2.58 Å³/dalton. The crystal diffracts X-rays to at least 2.5 Å resolution. Here we describe intensity measurement of this crystal.

Experimental and Results

All the X-ray experiments were done at the BL6A₂ using Weissenberg camera for macromolecular crystals (6). SR-ray was focused by cylindrical-bended asymmetric cut Si(111) monochrometer. The wavelength of X-ray used was 1.488 Å. The diffraction intensities were recorded on the imaging plates (40x20 cm), and read out by a Fuji film BA-100.

A crystal sealed in a glass capillary was mounted on the camera with b-axis of the crystal being parallel to the spindle axis of the camera. The oscillation range for each shot was 9° with exposure time being 68 sec. The scan speed was 2°/sec and rotation/film movement was 1°/mm. Individual plates were overlapped by 0.5°. After six exposures the crystal was translated to avoid deterioration of diffraction pattern. The intensities in the oscillation range of 94° were recorded on eleven plates.

The diffraction patterns on the imaging plates were processed by the program WEIS (7). Out of 62,466 intensities collected, 55,012 reflections whose intensities were greater than $1\sigma_I$ were accepted. The scale factor, in the form of $K \exp \{a^*(\sin\theta/\lambda)^2\}$, for each set of intensities on the plate was determined using the reflections whose intensities were greater than $5\sigma_I$. The equivalent intensities were averaged to yield 21,636 independent intensities. The R-factor for reflections with $I>\sigma_I$ was 8.05%. (R=6.36% for reflections with $I>5\sigma_I$). The result of data reduction is given in Table 1.

Table 1. Number of unique observations and percentage of possible total

Resolution range	Number of observ.		Percentage	
	$I>\sigma_I$	$I>3\sigma_I$	$I>\sigma_I$	$I>3\sigma_I$
15-7.5	2,008	1,980	93.9	92.7
7.5-5.0	4,804	4,678	86.2	84.0
5.0-3.8	5,913	5,708	59.7	57.6
3.8-3.0	6,063	5,315	33.8	29.6
Total (15-3.0)	18,788	17,681	52.8	49.7

Preparation of the heavy-atom derivatives is now in progress.

We thank Prof. Noriyoshi Sakabe for cooperating in the experiment using the Weissenberg camera and Dr. Tsuneyuki Higashi for use of computer programs.

References

- 1) J. Holmgren (1981). *Nature*, 292, 413-417.
- 2) L. K. Duffy & C. Y. Lai (1979). *Biochem. Biophys. Res. Commun.* 91, 1005-1010.
- 3) T. Tsuji, T. Honda, T. Miwatani, S. Wakabayashi & H. Matsubara (1985). *J. Biol. Chem.* 260, 8552-8558.
- 4) H. O. Ribi, D. S. Ludwig, K. L. Mercer, G. K. Schoolnik & R. D. Kornberg (1988). *Science*, 239, 1272-1276.
- 5) T. Tsuji, K. Fukuyama, H. Matsubara, T. Honda & T. Miwatani (1989). *J. Mol. Biol.* 208, 207-208.
- 6) N. Sakabe (1983). *J. Appl. Cryst.* 16, 542-547.
- 7) T. Higashi (1989). *J. Appl. Cryst.* 22, 9-18.

HIGH RESOLUTION STRUCTURE ANALYSIS OF TAKA AMYLASE A AT 1.8 Å

Masami KUSUNOKI, Hideo AGO, Yasuyuki Kitagawa, Yoshiki MATSUURA and Yukiteru KATSUBE

Institute for Protein Research, Osaka University, Suita, Osaka 565

Introduction

Taka-amylase A (TAA) is an α -amylase secreted extracellularly by *Aspergillus oryzae*. α -Amylases catalyze the hydrolysis of α -1,4-glucosidic linkage randomly along polysaccharide chains of starch, glycogen and their degradation products. The crystal structure of native TAA was already determined at 3.0 Å resolution by the methods of multiple-isomorphous replacement and molecular replacement¹⁾. We have undertaken high resolution crystal structure analysis of TAA to understand its enzyme mechanism based on the refined structure. The X-ray diffraction data to 1.8 Å for native TAA and three inhibitor complexes with TAA have been collected and processed using a macromolecular Weissenberg camera²⁾ with Fuji Imaging Plates. Refinement of atomic parameters of native TAA is under way with the current R factor of 22 % at 1.8 Å resolution.

Experimental

Diffraction data to 1.8 Å for native TAA, glucose (competitive inhibitor) TAA complex, methyl α -glucoside (non-competitive inhibitor) TAA complex, and Glu-Xyl-Xyl-Glu TAA complex were collected on a Sakabe's Weissenberg camera (BL-6A₂) with a radius of 430 mm using synchrotron radiation with a wavelength of 1.04 Å. Two or three crystals were used for the data collection of native TAA or TAA-inhibitor complex. The diffraction patterns on Imaging Plates were digitized on a Fuji-Film BA100 scanner with a raster step of 100 μ m. The diffraction images were processed to reflection data with programs WEIS and SCALE³⁾.

Results and Discussion

The merging R factor of intensity data for native TAA was 6.44 % for independent 94,090 reflections to 1.8 Å resolution. The refinement of structure of native TAA is now under way using a Hendrickson-Konnert restrained least-squares program of the fast Fourier transform version⁴⁾. The asymmetric unit of the P2₁ crystals contains three copies of TAA molecules related by a non-crystallographic 3-fold screw

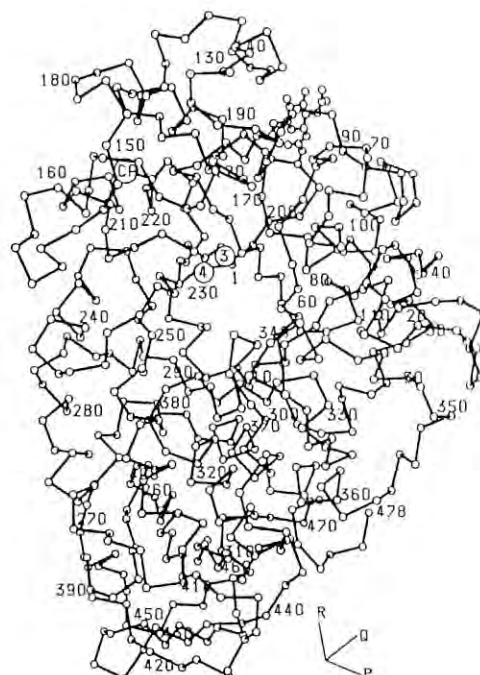
operation. The present R factor of the structure with 11,148 protein atoms and 303 water molecules is 0.224 for 91634 reflections with $F > 3\sigma(F)$. Fig. 1 shows the overall structure of the TAA molecule.

Acknowledgement

We are so much thankful to Prof. N. Sakabe, Dr. A. Nakagawa and Dr. T. Higashi for their assistance in the data collection and processing. We are also grateful to Dr. K. Namba in Houtani Project, ERATO, for the use of a BA100 film scanner.

References

- 1) Y. Matsuura, M. Kusunoki, W. Harada, M. Kakudo, J. Biochem. (Tokyo) 95, 697 (1984)
- 2) N. Sakabe, J. Appl. Cryst., 16, 542 (1983)
- 3) T. Higashi, J. Appl. Cryst., 22, 9 (1989)
- 4) B. C. Finzel, J. Appl. Cryst., 20, 53 (1987)

Fig. 1. α -Carbon atoms of Taka-amylase A

HIGH RESOLUTION DATA COLLECTION OF GLUTATHIONE SYNTHETASE FROM *ESCHERICHIA COLI* B

Hiroshi YAMAGUCHI, ^{*}Hiroaki KATO, Yasuo HATA, ^{*}Takaaki NISHIOKA, ^{*}Jun'ichi ODA,
Yukiteru KATSUBE and ^{**}Akira KIMURA

Institute for Protein Research, Osaka University, 3-2 Yamadaoka, Suita, Osaka 565 ;

^{*}Institute for Chemical Research and ^{**}Research Institute for Food Science, Kyoto University,
Uji, Kyoto 611, Japan

INTRODUCTION

Glutathione synthetase catalyzes the synthesis of glutathione from γ -L-glutamyl-L-cysteine and glycine in the presence of ATP. The amino acid sequence of glutathione synthetase of *Escherichia coli* B was deduced from DNA sequence analysis of the gsh II gene. The enzyme is a tetramer of four identical subunits composed of 316 amino acid residues. To elucidate the structure-function relationship of the glutathione synthetase, the crystal structure of the enzyme has been analyzed by X-ray diffraction method.

The crystals were obtained by microdialysis method, using ammonium sulfate as a precipitant¹⁾. They belong to a space group of $P6_322$ with cell dimensions of $a=88.0$, $c=164.2$ Å. There is one subunit per asymmetric unit. The crystal structure was determined at 2.7 Å resolution using a four-circle diffractometer set on a conventional X-ray generator. A multiple isomorphous replacement method using EMTS, $K_2Pt(CN)_4$ and $K_2Pt(NO_2)_4$ derivatives was applied to the phase calculation. In this study, about 15-20 crystals were needed for data collection of each data set, because native and derivative crystals were very sensitive to X-ray irradiation. In order to analyze the catalytic mechanism of the enzyme in detail, it is essential to determine the structures of the native enzyme and its complex with substrate, product, substrate-analogue or co-factor, at higher resolution. However, it is difficult to collect data above 2.7 Å resolution on the conventional machine because of the large cell dimensions and the X-ray sensitivity of the crystals. Thus, we tried to collect higher resolution data of these crystals by using the synchrotron radiation facilities of Photon Factory, Tsukuba, Japan.

EXPERIMENTAL AND RESULTS

Complex crystals of glutathione synthetase with ATP, GSH, or both ATP and γ -Glu-Abu (a substrate) were prepared by soaking method using 50mM potassium phosphate buffer (pH6.0) containing 40% saturated ammonium sulfate, 5mM magnesium chloride and the corresponding reagent. With the enzyme-ATP complex, a crystal was soaked in the buffer containing 10mM ATP. In the cases of GSH and ATP+ γ -Glu-Abu, crystals were soaked in a 10mM GSH solution and a mixture of 5mM ATP and 5mM γ -Glu-Abu,

respectively. Diffraction data of the native and the complexes were collected using a large Weissenberg camera with a camera-film distance of 430mm located on BL-6A₂²⁾. The temperature was controlled at 10°C during the data collections. The wavelength of 1.04 Å was used to decrease the X-ray damage. The crystals sealed in glass capillaries were mounted with the a- or c-axis parallel to the spindle axis of the Weissenberg camera. For the c-axis setting, the oscillation angle of 3.0(deg.) were selected, and for a-axis setting, the oscillation angle of 4.7(deg.) was used. Diffraction patterns were recorded on Fuji Film Imaging-plates (20 x 40 cm), and digitized on a Fuji Film BA100. This system allowed us to collect the whole data sets of each crystal using only one crystal. Data collection was summarized in table-1 and table-2. No diffraction change of the crystal was detected even after the measurement. This system is very useful for data collection of a crystal which has large cell constants and is sensitive to X-ray irradiation. The data are now under evaluation.

Table-1 Preparation of complex crystals and rotation axes

crystal	soaking condition	rotation axis
Native I	-----	a
Native II	-----	c
ATP	10mM, 4days	a
ATP& γ -Glu-Abu	5mM, 5mM, 3days	a
GSH	5mM, 5days	a

Table-2 Experimental conditions of data collection

Rotation axis	a	c
Oscillation angle (deg.)	4.7	3.0
Film moving (mm)	4.7	2.0
Coupling const. (deg./min)	1.0	1.5
Rotation speed (deg/sec)	2.0	2.0
Number of oscillation	5	5
Exposure time (sec.)	23.5	15.0
Number of films	22~24	12

REFERENCES

- ¹⁾ H.Kato, et al., J.Mol.Biol., 209, (1989).503
- ²⁾ N.Sakabe, J.Appl.Cryst., 16, (1983).542

CRYSTAL STRUCTURE ANALYSIS OF L-LACTATE DEHYDROGENASE FROM *BIFIDOBACTERIUM LONGUM*So IWATA^{1,2}, Takashi MINOWA², Takahisa OHTA², Noriyoshi SAKABE¹,

1. National Lab. for High Energy Physics, Ibaraki 305,

2. Department of Agricultural Chemistry, The University of Tokyo,
Tokyo 113.

INTRODUCTION

L-Lactate dehydrogenases (LDHs; EC 1.1.1.27) from some bacteria are allosteric enzymes activated by fructose 1,6-bisphosphate (FBP), but the enzymes from vertebrates have no dependence on the effector. To elucidate the activation mechanism of LDH, we newly purified an LDH from *Bifidobacterium longum*. *Bifidobacterium* is mesophilic and anaerobic, forms the predominant flora in human intestines, and is classified as an actinomycetes. We have already characterized the enzyme, and have cloned, sequenced, and expressed its gene^{1,2}. Recently we successfully crystallized the enzyme from a polyethylene glycol 6000 (PEG 6000) solution³. The crystals were grown in the presence of NADH (type II), both NADH and oxamate (type III), and NADH, oxamate, and FBP (type IV). All three crystal forms belong to the orthorhombic system, space group *P* 2₁2₁2. The cell dimensions of the type III crystals were *a* = 106.4 Å, *b* = 131.4 Å, *c* = 63.8 Å. Here, we report on preliminary structure study of the type III crystals of the enzyme.

EXPERIMENTAL

Crystallization was achieved by vapor diffusion using hanging drop technique. Enzyme solution contained 8.2 mg/ml protein, 5 mM Tris-HCl buffer (pH 7), and 150 mM NaCl. The reservoir solution contained 10 % (v/v) polyethylene glycol 6000, 50 mM 2-(N-morpholino)ethanesulfonic acid (MES)-NaOH buffer (pH 6.5), 2.5 mM NADH and 2.5 mM sodium oxamate (analogue of pyruvate). Drops were made from 8 µl enzyme solution and 8 µl reservoir solution. Crystals grew to about 1.0 mm in maximum length in drops within a week. Two heavy atom derivatives have been prepared by soaking crystals in each solution containing p-chloromercuribenzenesulfonate (PCMBs), and PtCl₄²⁻, respectively. All diffraction data were collected using a Weissenberg camera (BL6A2) with Imaging Plates and BA100 scanner system (Fuji Film Co.). We could collect all independent data for one axis mounting using only one crystal within 30 min exposure. The intensity data of native and derivative crystals were collected with the rotation of the crystal along *a* and *c* axes. The evaluation of the intensity data is summarized in Table I.

Table I. Evaluation of Intensity Data

	Resolution (Å)	wave length (Å)	No. of independent data	No. of anomalous data	R _{merge} (%)
Native	1.8	1.04	64,557	-	5.45
PCMBs	1.8	1.00	56,972	14,682	7.01
PtCl ₄ ²⁻	1.8	1.00	58,261	12,280	5.66

RESULTS AND DISCUSSION

The heavy atom positions were determined from difference Patterson map and cross Fourier's technique. Heavy atom parameters were refined with centric reflections. Phases for protein structure factors were calculated up to 2.5 Å resolution by the multiple isomorphous replacement method, utilizing anomalous difference data, and the over all figure-of-merit was 0.57 with 29,381 independent reflections.

Figure 1 shows two sets of composite electron density map. Tetrameric structure of the enzyme related by non-crystallographic dihedral axis are easily recognized. The dimensions of one subunit are about 40 Å × 40 Å × 45 Å. This agrees with structure of other LDHs⁴. There is a large cavity in the center of the tetramer. A Part of this cavity (probably near the contact region of dimers in the figure) is the anion binding site in the vertebrate enzyme structure and the site is thought to be an activator binding site of bacterial enzyme⁵. The tracing of the polypeptide chain is in progress.

We are greatly indebted to Dr. K. Sakabe, Dr. A. Nakagawa, and Dr. N. Watanabe for their kind help and suggestion in the data collection and processing.

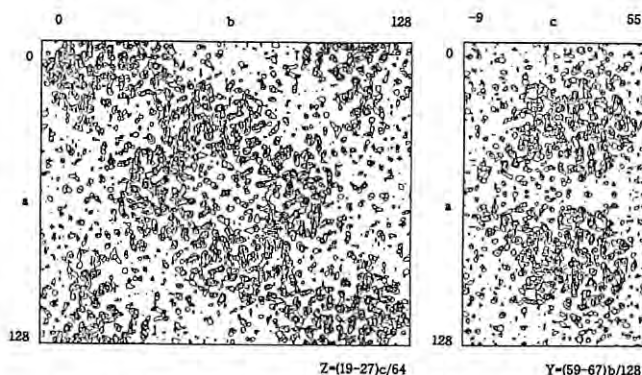


Fig. 1 Composite Fourier Map of 2.5 Å resolution

REFERENCES

1. S. Iwata, T. Minowa, H. Sakai and T. Ohta, (1989) *Agri. Biochem. Chem.* **53**, in Printing
2. T. Minowa, S. Iwata, H. Sakai, H. Masaki and T. Ohta, (1989) *Gene* **85**, 161-168
3. S. Iwata, T. Minowa, B. Mikami, Y. Morita and T. Ohta, (1989) *J. Biochem.* **106**, 558-559
4. J. J. Hollbrook, A. Liljas, S. J. Steindel and M. G. Rossmann (1975) in *The Enzymes* (Boyer, P. D., ed.) Vol.11, pp.191-292, Academic Press, New York
5. M. Matsuzawa, M. Machida, K. kunai, Y. Ito and T. Ohta (1988) *FEBS Lett.* **233**, 375-378

STRUCTURE OF A MULTIENTZYME COMPLEX FROM SPINACH CHLOROPLASTS

J.K. Sainis*, M.V. Hosur and K.K. Kannan

*Molecular Biology and Agriculture Division,
Neutron Physics Division, BARC, Bombay-400 085, INDIA.

The reported concentration of proteins in the Cytoplasm and organelles of the cell are very close to that in protein crystals. This suggests that proteins in the cell are present as multi-protein complexes. If consecutive enzymes in a metabolic pathway were to be organized as a complex, it could result in channeling of substrates to the active sites of respective enzymes, thereby avoiding the unwanted diffusion of metabolites. Indeed some such multi-enzyme complexes have been discovered experimentally (1,2). The structure of such multienzyme complexes are of utmost importance to understand the phenomenon of substrate channeling. We have observed that RuBP Carboxylase (RuBISCO), a key enzyme in photosynthetic carbon reduction cycle-copurifies with two other enzymes Viz. Phosphoribulokinase and phosphoriboisomerase of the same metabolic cycle. We have partly characterized, by biochemical methods, this multienzyme complex isolated from spinach leaves. We have grown single crystals of this complex suitable for x-ray diffraction study.

EXPERIMENTAL

Crystals of the multienzyme complex were characterized using the synchrotron X-radiation (1.04 Å wavelength) in the Photon Factory, KEK, with Sakabe's Weissenberg camera (430 mm radius). A series of image plates were collected for the c-axis mounting with an oscillation range of 7.6 deg, and for the a-axis mounting with an oscillation range of 3.45 deg and 4.6 deg. The image plates were digitized on a Fiji BA100 microdensitometer and processed further with the WEIS program package on the FACOM 360 computer. From the patterns of optical density printed by the computer it was easy to determine the unit cell dimensions which are: $a = 173$, $b = 134$, $c = 112$ Å, $\alpha = \beta = \gamma = 90^\circ$, and space group as $P2_12_12_1$. The crystal diffract to about 2.5 Å resolution and the R merge for the two data sets is 9.3%. Further work with the analysis of this data is in progress.

ACKNOWLEDGMENT

We thank Prof. N. Sakabe of the PF for the use of the Weissenberg camera and also for many useful discussions. We also thank Dr. K. Sakabe, Mr. S. Iwata and Dr. N. Watanabe for help in digitizing the image plates on BA100. Mr. A. Nakagawa's help with the WEIS program package is gratefully acknowledged. We are also thankful to Japan Society for Promotion of Science (JSPS) for the award of a short term fellowship to one of us (KKK) which made this project possible.

REFERENCES

1. B. Gontero, M.L. Cardenas & J. Ricard, Eur. J. Biochem. (1988) 173 437-443.
2. J.B. Robinson & P.A. Srere (1985) J. Biochem. 260, 10800-10805.

Structure Function-drug interaction of Carbonic Anhydrase
 High Resolution Data collection of Human Carbonic Anhydrase I and
 inhibitor Complexes and buffalo Carbonic Anhydrase II
 K.K. Kannan, Vinay Kumar, S Chakravarthy, and Padma
 Satyamurthi

Neutron Physics Division, Bhabha Atomic Research Centre, Bombay,
 400085, India.

Introduction

The Carbonic anhydrases are enzymes which catalyze the fast interconversion of CO_2 to bicarbonate and proton, with turn over rates reaching 10^6 molecules of CO_2 per enzyme molecule per sec (1).

There has been a lot of interest in the mechanism of this enzyme and especially the fast proton transfer rates achieved during catalysis. Carbonic anhydrases are inhibited by monovalent anions and also by unsubstituted aromatic and heterocyclic sulfonamides which are preventently used as drugs for treatment of glaucoma and gastric ulcers. The structure of Human Carbonic anhydrases I (HCAI) (2), HCAII (3), Buffalo carbonic anhydrase II (4), and Bovine carbonic anhydrase III (5) are known to better than 2.7 Å resolution. The present project was undertaken to collect X-ray diffraction data to higher resolution than reported, in order to elucidate the exact nature of the solvent interactions with the protein as well as to get improved atomic structure of the enzymes. Here we report the data collection on HCAI Native and complexes of HCAI-acetazol-

amide, HCAI-methazolamide, HCAI- HCO_3^- , HCAI-imidazole, HCAI at pH 6.0 and buffalo carbonic anhydrase to better than 2 Å resolution. HCAI belongs to the orthorhombic, space group $P2_12_12_1$ with cell dimensions $a=81.8\text{Å}$, $b=75.2\text{Å}$, $c=37.4\text{Å}$ $\alpha=\beta=\gamma=90^\circ$ and buffalo carbonic anhydrase belong to the space group $P2_12_12_1$ with cell dimensions $a=46.2$, $b=103.0$, $c=60.1\text{Å}$, $\alpha=\beta=\gamma=90^\circ$.

Experimental

Crystals of HCAI were soaked in the respective inhibitors or at pH 6.0 in 2.5M ammonium sulfate solution containing 0.4% protein. The crystals were mounted in Lindemann glass capillaries and sealed with mother liquor in the usual way. Crystals HCAI grow naturally along the a axis along which these crystal were mounted first and data collected for a axis rotation. Crystals were also mounted along the b axis as it was not possible to mount along the shortest c axis and data were collected for the b axis rotation. The crystals had dimensions of 0.4x0.4x0.6mm

No.	Name of crystal	Resolution of data collection (Å)	R merge (%)	Remarks
1	Human carbonic anhydrase I (HCAI) Native enzyme	1.5	7.27	a & b axes data
2.	HCAI- HCO_3^- Complex by soaking	1.7	8.13	a & b axes data
3.	HCAI-Imidazole complex by soaking	1.7	7.95	a & b axes data
4.	HCAI-pH6 crystals by soaking	1.7	7.99	a & b axes data
5.	HCAI- acetazolamide complex by soaking	1.4	5.82	a axis data only
6.	HCAI-acetazolamide complex, 2nd set of crystals prepared by direct crystallization	1.5	7.26	a & b axes data
7.	HCAI-methazolamide complex by soaking	1.6	5.55	a & b axes data
8.	Buffalo carbonic anhydrase II	2.0	6.57	a axis only

and generally diffracted to better than 1.7 Å resolution. The intensity data were collected on Sakabe's Weissenberg camera (6) with the 287mm cassette and 200x400mm Fuji imaging plate. The data were digitized on the Fuji BA100 digitizer and processed on a FACOM M360 Computer using the programs PATTERN, CONVMT, WEIS, COMBINE and SCALE (7) and electron density maps were calculated with the Munich Protein Package and viewed on a PS300 Evans and Sutherland graphics System with the FRODO program.

Results

The table below gives the result of the data collection and reduction for the different Carbonic Anhydrase crystals. The R (merge) value calculated with the SCALE program are in the range of 5.5% to 8.1% for the different crystals. The R (merge) was calculated on the basis of all the data collected to 1.3 Å resolution, as the SCALE program does not have a resolution cut off criterion. The R(merge) is very high for the large number of reflections at very high resolution resulting in a higher value of the reported R(merge) values. These are however of the order of 4-6% for the data below 2.5 Å resolution. Many of the crystals diffract to at least 1.7 Å resolution with the observed values of Intensity being more than 2 sigma level. The native HCAI, HCAI-Acetazolamide complex and HCAI methazolamide complex diffracts to better than 1.5 Å resolution as was evident from a comparison of the intensity data with calculated sigma values.

An electron density map calculated with 2020 protein atoms of HCAI and the Fobs of HCAI acetazolamide complex, clearly showed electron density of the acetazolamide molecule in the active site of the enzyme with very well resolved electron densities assignable to different atoms of the inhibitor molecule. Further work with the refinement and analysis of the structure is in progress.

Acknowledgment

We Thank Prof. N. Sakabe of the PF for the use of the Weissenberg camera and also for many useful discussions. We also thank Dr. K. Sakabe, Mr. S. Iwata and Dr. N. Watanabe for help in digitizing the Image Plates on BA100. Mr. A. Nakagawa's help with the WEIS program package is gratefully acknowledged. We are also thankful to Japan Society for Promotion of Science (JSPS) for the award of a short term fellowship to one of us (KKK) which made this project possible.

References

- 1) Papers in "Biology and Chemistry of the Carbonic Anhydrases" (ed. R. E. Tashian and D. Hewett-Emmett) Annals of the New York Academy of Sciences (1987) vol 29
- 2) Kannan, K.K., Notstrand, B., Fridborg, K., Ohlsson, A., & Petef, M. (1975). Proc. Natl. Acad. Sci. U.S.A., 72 51.
- 3) Liljas, A., Kannan, K.K., Bergsten, P.-C., Waara, I., Fridborg, K., Strandberg, B., Carlsson, U., Jarup, L., Lovgren, S. & Petef, M., (1972), Nature New Biol. 235, 131
- 4) Vinay Kumar, Kannan, K.K., and Chidambaram, R. (198) Current Science 58, 344
- 5) Eriksson, A.E., and Liljas, A (1988), in the PhD thesis, uppsala University of Eriksson, A.E.
- 6) Sakabe, N. (1983) J. Appl. Cryst. 16 542
- 7) Higashi, T. (1989) J. Appl. Cryst. 22, 9.

X-RAY ANALYSIS OF RECOMBINANT HUMAN RENIN

Howard M. EINSPAHR, Barry C. FINZEL, Keith D. WATENPAUGH,
Akihito SHODA* and Kazuo MURAKAMI*

The Upjohn Company, Kalamazoo, MI 49001 USA and

(*) Institute of Applied Biochemistry, University of Tsukuba, Ibaraki 305

Introduction

Renin is the aspartyl proteinase that specifically cleaves the decapeptide angiotensin I from the N-terminus of the protein angiotensinogen. Angiotensin I is further cleaved by another enzyme to yield angiotensin II, the octapeptide hormone that acts to increase blood pressure. Because of its critical role in the pathway to angiotensin II, renin is the target of drug design efforts that aim to produce an inhibitor of use in control of hypertension. The work we describe here is part of our effort to assist this drug design endeavor by application of crystallographic methods of structure determination. A significant advance in knowledge of the active-site region was achieved when the structure of the native renin enzyme was reported recently¹⁾. In order to apply structural knowledge in the design of renin inhibitors, however, the structure of the native enzyme is insufficient, and it is necessary to determine the structures of one or more complexes of renin with substrate analogs or candidate inhibitors.

Human renin is a protein of about 40 kD. Because it is produced in extremely small amounts in human tissue, it has been impossible to isolate in quantity. Accordingly, it has been expressed by recombinant means in a variety of cells in order to provide amounts of the protein sufficient for biochemical and biological studies. Native renin is glycosylated by post-translational modifications that attach carbohydrate chains to two asparagine sidechains. The protein we use was produced by heterologous expression of the gene²⁾ in Chinese hamster ovary (CHO) cells and was purified by published procedures³⁾. We use the protein in two different forms: a glycosylated form in which attachment of carbohydrate is under the control of the CHO cell, and a deglycosylated form in which the attached carbohydrate has been removed enzymatically.

Over the past two years, we have worked to prepare crystals of renin useful for structure determination. We have succeeded in producing large (0.7-1.0 mm) crystals of the glycosylated form of renin and have collected several data sets on these crystals in our laboratory on a Siemens area-detector diffractometer with CuK α X-rays provided by a fine-focus (0.5 mm) sealed tube operated at 1.6 KW. In no case, however, have we succeeded in collecting data at room temperature that extended beyond 4 Å resolution. These crystals are tetragonal, space group I4₁, with $a = b = 160$ Å, $c = 80$ Å. Assuming two molecules per asymmetric unit, the Matthews⁴⁾ volume (V_M) is greater than 3 Å³/dalton, suggesting a higher than average ratio of solvent to protein in these crystals. The primary goal of our experiments at the Photon Factory was to extend our data from these crystals to beyond 3 Å resolution by taking advantage of the increased X-ray beam brilliance provided by this facility over that available from conventional sources, that is, to compensate for poor scattering with a brighter beam.

We have also succeeded in producing crystals of enzymatically deglycosylated renin. While we have obtained a variety of seemingly different crystal forms from our samples of this protein, in no case have we been able to grow crystals of sufficient size to characterize by diffraction experiments in our laboratory. A secondary goal of our Photon Factory experiments was to take advantage of the increased X-ray beam brilliance provided by this facility to determine if any of these deglycosylated renin crystals could provide suitable data, that is, to compensate for small size with a brighter beam.

Preliminary Results

During the 48 hours of beamtime scheduled for our use, we examined 16 crystals and collected six data sets. All data were collected on the Weissenberg protein data collection system⁵⁾ with the help of Dr. N. Sakabe and staff.

We examined five crystals of glycosylated renin and collected full data sets on two of them. One of these data sets proved to be by far the better, and we will concentrate our further work on it. While data reduction has not been completed as yet, it is clear that the resolution of this data set will be at least 3.0 Å. Lattice constants for this data set are $a = b = 159$, $c = 80$ Å.

We also collected three data sets on small deglycosylated renin crystals. Data processing remains incomplete at this writing, but a resolution of at least 2.5 Å is observed for each of the three. Lattice constants and diffraction patterns suggest that all three data sets were produced by a single crystal form with a tetragonal, I-centered cell, and lattice constants of $a = b = 133$, $c = 42$ Å. Although conclusive proof is not presently available, we suggest that this may be the same as the crystal form of the previously reported structure determination¹⁾.

Finally, we collected a partial data set (about 75% of the data to 2.5 Å resolution) on a crystal of deglycosylated renin that had been grown in the presence of micromolar concentrations of an Upjohn renin inhibitor, U79465e (Fig. 1). The IC_{50} for U79465e is in the nanomolar range and it is highly likely that, in this crystal, the majority of renin molecules are complexed by the inhibitor. Lattice constants are $a = b = 129$, $c = 41$ Å. After we returned to our laboratory, we collected area-detector data by rotation perpendicular to the unique axis and thereby sampled the region missed at the Photon Factory, albeit at a much reduced resolution.

From these data, the space group is determined as I4. We suggest this crystal form may also be isomorphous to that used for the recent structure determination¹⁾, but with one important difference: this is likely the crystal of an enzyme-inhibitor complex.

Efforts to prepare heavy-atom derivatives are underway, as are renewed efforts to apply molecular-replacement techniques. It is likely that when crystals of heavy-atom derivatives or other renin-inhibitor complexes have been prepared, we will return to the Photon Factory for further data collection efforts.

References

- (1) A. R. Sielecki et al., *Science*, **243**, 1346 (1989).
- (2) T. Imai et al., *Proc. Natl. Acad. Sci. USA*, **80**, 7405(1983).
- (3) R. A. Poorman et al., *Proteins: Structure, Function and Genetics*, **1**, 139(1986).
- (4) B. W. Matthews, *J. Mol. Biol.*, **33**, 491(1968).
- (5) N. Sakabe, *J. Appl. Cryst.*, **16**, 542(1983).

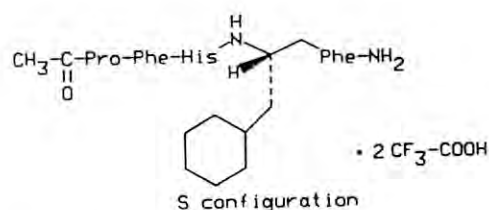


Fig.1. Chemical formula of renin inhibitor U79465e

Structural Characteristics of Cation κ -Carrageenate in Sol and Gel States as Observed by Small-Angle X-ray Scattering

K. Kajiwara¹⁾, H. Urakawa¹⁾, M. Tokita²⁾, R. Niki³⁾, Y. Hiragi⁴⁾

¹⁾ Faculty of Engineering & Design, Kyoto Institute of Technology, Kyoto, 606 Japan

²⁾ Faculty of Science, Hokkaido University, Sapporo, 060 Japan

³⁾ Faculty of Agriculture, Hokkaido University, Sapporo, 060 Japan

⁴⁾ Institute for Chemical Research, Kyoto University, Uji, Kyoto-fu, 611 Japan

INTRODUCTION

κ -carrageenan, a sulfated galactan extracted from red seaweeds, is composed of a disaccharide repeat unit of alternating 1,3-linked β -D-galactopyranose and 1,4-linked α -D-galactopyranose, where most of the former residues are sulfated on the position 4. Carrageenans form thermoreversible gels by lowering temperature, increasing solute concentration and/or adding salt, and are widely applied in the food industry. Two types of gel are available for κ -carrageenan as conventionally termed as the "strong gel" (monovalent cation induced) and the "weak gel" (bivalent cation induced) from its appearance, and various models are proposed for the gelation mechanism. The present study aims the structural characterization of κ -carrageenan chains in the sol and gel states by means of small-angle X-ray scattering (SAXS).

RESULTS and DISCUSSION

Figure 1 displays the results of small-angle X-ray scattering (SAXS) from κ -carrageenan aqueous solutions. SAXS measurements were performed from these solutions at 5°C (in the gel state) and 60°C (in the sol state) with a SAXES focusing optics installed at the BL10C of the Photon Factory, Tsukuba, Japan. No salt was added in those solutions, which were neutralized with KOH and Ca(OH)₂, respectively, yielding the strong (monovalent cation κ -carrageenate) and weak (bivalent cation κ -carrageenate) gels from the appearance. The marked difference will be noticed immediately in respective scattering envelopes for the sol and gel states of each solution with a pronounced correlation maximum around $q = 0.05 \text{ \AA}^{-1}$ in the strong gel. When salt is added to those solutions and/or the solute concentration is increased, the apparent maximum observed in the scattering envelop of the strong gel becomes less pronounced, suggesting the observed correlation maximum is caused by the electrostatic interaction which is screened by increasing the ionic strength. No such an interaction seems present in the aqueous solutions of bivalent cation κ -carrageenates. A pronounced maximum/minimum characterizes the distance distribution function of monovalent cation κ -carrageenate aqueous solutions obtained by the Fourier-transformation of scattering intensities, whereas the distance distribution function of bivalent cation κ -carrageenates exhibits a single broad maximum at ca. 130 \AA with a long tail typical of a chain molecule. The former distance distribution function may be composed of (i) a sharp distribution function with a maximum at around 20 \AA and the subsequent correlation hole characteristic of strong repulsive interactions, and (ii) a broad

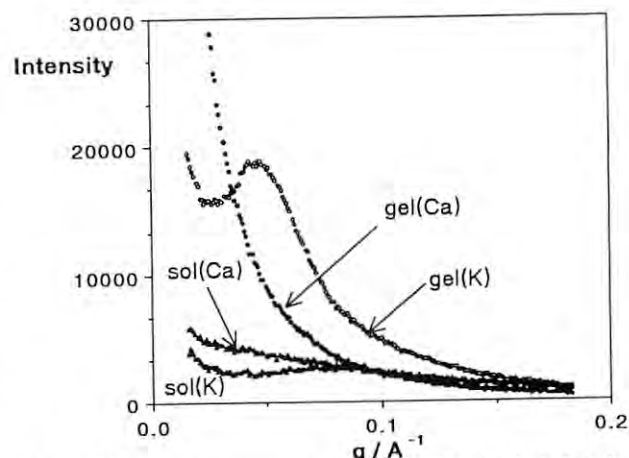


Fig.1 SAXS from κ -carrageenan aqueous solution in sol and gel.

distribution function with a single peak observed for bivalent cation κ -carrageenates. The largest dimension of the interaction unit (i.e., the crosslinking domain) is evaluated from the position of the correlation hole observed for monovalent cation κ -carrageenates as approximately $75 - 80 \text{ \AA}$ in the gel state and $30 - 50 \text{ \AA}$ in the sol state. The Guinier-plot for cross-section yielded the cross-sectional radii of gyration for monovalent and bivalent cation κ -carrageenates as 6.8 \AA and 7.2 \AA , respectively, in sol, and as 8.9 \AA and 8.8 \AA , respectively, in gel. The estimated values in the sol state of potassium or calcium κ -carrageenates are close to the expected value for κ -carrageenan double-helix. The cross-sectional radius of gyration increases to approximately 9 \AA in the gel state, which accounts for the cross-section of a triangular array of double-helices. κ -carrageenan double-helical conformation is composed of three disaccharide residues per turn with a repeating distance of 24.6 \AA and a diameter of 13 \AA (which is equivalent to 5.3 \AA in terms of the cross-sectional radius of gyration). Thus, potassium κ -carrageenates are partly double-helixed in one or two turns in the sol state to compose stiff dimerized chains, and the double-helix region grows to approximately three turns to aggregate 3-4 regions together with the sol-to-gel transition. The double-helix domain is approximated by a cylinder of $30 - 50 \text{ \AA}$ in length and 13 \AA in diameter in the sol state, and by that of $75 - 80 \text{ \AA}$ in length and 25 \AA in diameter in the gel state. The domain structure is probably same for monovalent and bivalent cation κ -carrageenates. The electrostatic interaction between double-helix domains produces the strong gel in appearance, probably due to the elastic repulsion between crosslinks.

COMPLEXATION OF LOW MOLECULAR WEIGHT AMYLOSE WITH IODINE

Mitsuhiro HIRAI*, Toshihiro HIRAI**, Sadao HAYASHI** and Tatsuo UEKI***

* Department of Liberal Art, Kanagawa Institute of Technology, Atsugi 243-02

** Faculty of Textile Science and Technology, Shinshu University, Ueda 386

***Department of Biophysical Engineering, Osaka University, Osaka 560

INTRODUCTION

In our previous report, structure change of amylose was found to be induced by complexation with iodine.¹ Further investigation on the amylose of low molecular weight revealed that the structure change was concluded to be caused by association of the amylose which is induced by the complexation. The structure of the complex was expected to be somehow a similar one which is known in the case of the crystal of iodine complex of cyclodextrin.^{2,3}

EXPERIMENTAL

Amylose whose molecular weight is 2900 was guaranteed grade, and was purchased from Nakarai Chemicals Ltd. Other reagents were guaranteed grade purchased from Wako Chemical Industries Ltd.

Small-angle X-ray scattering experiments were carried out with small-angle scattering equipment SAXES installed at BL10C line in the Photon Factory of KEK. The wavelength used was 1.49 Å, and the sample-detector distance was 65 cm. Sample solutions were put into sample cells of 1 mm path-length. The time of exposure of samples to the X-ray beam was 900 sec.

RESULTS AND DISCUSSION

In Figure 1 are shown the $\log(I_{\text{nt}})$ vs. $\log Q$ plots of the particles of the amylose or its iodine complexes. From the comparison of the scattering curves, the shape of the particle was found to change from spherical to cylindrical form with the increase of iodine concentration, and moreover, further increase of iodine lead the shape to spherical form again.

From Guinier plots, the Guinier radius was estimated, and was found to change from 23.9 Å to the maximum value of 58.9 Å, and then decreased to 24.8 Å with further addition of iodine. (Table 1)

These result shows that the amylose was induced to form an associated cylindrical structure, and further addition of iodine caused the structure break down into a short spherical structure.

As is known, cyclodextrin-iodine complexes can form crystals in which the cyclodextrins are stacked uni-

dimensionally.^{2,3} The associated long cylindrical structure which we showed in this report can also be expected to be a similar one to that of cyclodextrin-iodine complex. In the case of amylose complex, however, the complex cannot hold its cylindrically associated form under the presence of excess iodine, and changes into a small spheric, probably a monomeric, structure again with further addition of iodine.

REFERENCES

- 1) T. Hirai, M. Hirai, S. Hayashi, and T. Ueki, Photon Factory Activity Report, **5**, 136(1988).
- 2) M. Noltemeyer and W. Saenger, J. Am. Chem. Soc., **102**, (8), 2710-2722(1980).
- 3) M. Noltemeyer and W. Saenger, Nature, **259**, 629-632 (1976).

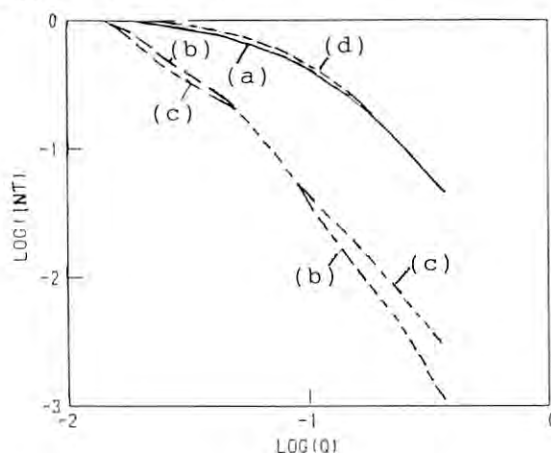


Fig.1 $\log(I_{\text{nt}})$ versus $\log Q$ plots of amylose (—) and amylose-iodine-iodide complex (---). Molecular weight of amylose was 2900. $[amylose]=0.2$ unit-mol/l, $[I_2]=(a)0$, (b)0.02, (c)0.06, and (d)0.10 mol/l, $[I_2]/[KI]=1/10$, measured at 15°C.

Table 1 Effect of Iodine Concentration on Guinier Radius (R_g)

	$[I_2](\text{mol/l}) \times 10^3$			
	0.00	2.00	6.00	10.0
$R_g(\text{Å})$	23.9	57.2	58.9	24.8

$[amylose]=0.2$ unit-mol/l, at 15°C.
 $[I_2]/[KI]=1/10$

CONFORMATIONAL CHANGE OF POLY-N⁵-(2-HYDROXYETHYL)-
L-GLUTAMINE IN SOLUTION WITH SOLVENT AND TEMPERATURE
STUDIED BY SMALL ANGLE X-RAY SCATTERING

Yoshio MUROGA¹, Hiroyuki TAGAWA², Yoshiyuki KONDO³, Tadao HAYAKAWA³

- 1) Faculty of Engineering, Nagoya University, Chikusa-ku, Nagoya, Aichi 464
- 2) Faculty of Science and Technology, Nihon University, Chiyoda-ku, Tokyo 101
- 3) Faculty of Textile Science and Technology, Sh^hshu University, Ueda, 386

Introduction

It is well known that poly-N⁵-(2-hydroxyethyl)L-glutamine, PHEG, in solution changes its conformation with temperature and/or with the composition of two solvents.¹ This conformational change is unique in that its Zimm-Bragg parameter is significantly large compared with other polymers. The purpose of the present investigation is to clarify the detail in the conformational change by studying the scattering function obtained by small angle X-ray scattering, SAXS.²

Experimental

PHEG was dissolved in water and a mixture of water and isopropanol (40 wt% isopropanol). The measurements of SAXS were carried out at various temperatures ranging from 25 to 50 °C, where the polymer chain may take different conformations.

The SAXS was carried out using a synchrotron radiation as an X-ray source, set up in the Photon Factory of the National Lab. for High Energy Phys. at Tsukuba.

Results and Discussion

The observed scattering behaviors of PHEG are the one as seen in ordinary nonionic polymers: a maximum of the scattering curves (I v.s. h) in a low angle region was not observed under all present experimental conditions. Therefore, the conformational analyses can be applied to the scattering curves over a wide scattering vector range above ca. 0.02 \AA^{-1} in h .

For PHEG in water, the radius of gyration of a cross-section of a polymer chain, R_c , was almost kept constant, when the temperature was changed, whereas, for PHEG in a mixture of water and isopropanol, R_c increased with the helical content of the polymer chain.

After the observed scattering intensities were corrected for R_c , they were represented in the form of the Kratky plot, $I \cdot h^2$ v.s. h , as shown in Fig.1. It is observed that the scattering curves are remarkably affected by the solvent and/or the temperature, reflecting the change of the conformation. The detailed conformational analyses are under progress.

References

- 1) M.Miyake, *et.al.*, Biopolymers, **13**, 1173 (1974).
- 2) Y.Muroga, *et.al.*, Macromolecules, **21**, 2751, 2756 (1988).

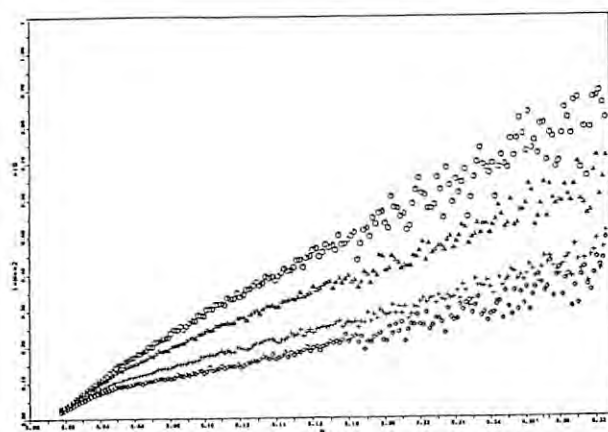


Fig.1
The dependence of the Kratky plot of PHEG in solution upon the solvent and the temperature: square, water at ambient temperature; circle, triangle and cross, a mixture of water and isopropanol at increased temperatures.

STRUCTURE OF THERMALLY DENATURED RIBONUCLEASE A BY MEANS OF SMALL-ANGLE X-RAY SCATTERING

Yuzuru,HIRAGI¹,Euiho KIM¹, Kanji Kajiwara²,Yoh SANO³,
Katsumi KOBAYASHI⁴ and Hiroshi NAKATANIS⁵

- 1)Institute for Chemical Research, Kyoto University, Uji, Kyoto 611
- 2)Faculty of Engineering and Design, Kyoyo Institute of Technology, Kyoto 606
- 3)National Institute of Agrobiological Resources, Tsukuba, Ibaraki 305
- 4)Photon Factory, National Laboratory for High Energy Physics, Tsukuba, Ibaraki 305
- 5)Faculty of Agriculture, Kyoto University, Kyoto 606

Introduction

Bovine pancreatic ribonuclease A(RNase A) is one of the important proteins for studies of reversible folding-unfolding processes. However, the shape or global structure at the denatured state is still not clear. Therefore, we examined structural differences of RNase A between native and denatured states by small-angle X-ray scattering method.

Results and Discussion

Sample solutions of 0.85% ~ 4.9% RNase A were prepared using 0.01 M HCl and 0.1 M KCl buffer(pH 2.10). Small-angle X-ray scattering measurements were carried out from 10 °C to 50 °C at BL-10C. The scattering curve from oxidized RNase A

showed drastic conformational change and somewhat aggregation even at low temperature, but the scattering curves from intact RNase A did not change from 10 °C to 50 °C as shown in Fig.1 (a) and (b). Radius of gyration(R_g) of intact RNase A from Guinier plot was almost constant (Fig.2(a)). The corresponding UV and CD spectral changes in the same buffer from 10 °C to 60 °C are shown in Fig.2(b). The apparent transition temperature is about 35 °C. Results of Fig.1 and 2 suggest that RNase A with intact S-S bridges is rather compact, not expanded nor swollen at the thermally denatured state. Informations from small-angle X-ray scattering are mainly from protein body itself without hydration sphere, because the scattering data reflect the difference of electron densities between solute and solvent. Comparing present study with previous results, a compact denatured structure with increased hydration sphere is deduced as a model of thermally denatured intact RNase A.

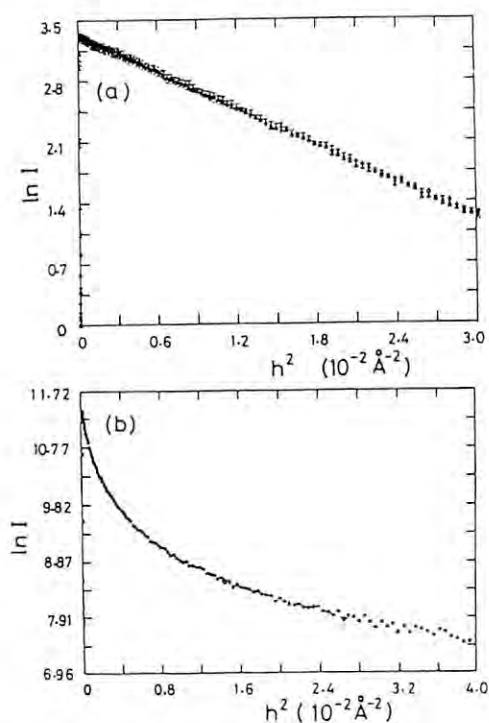


Fig.1. Guinier plot from scattering curves of intact RNase A(a) at 10 °C, 30 °C and 50 °C, and oxidized RNase A(b) at 10 °C.

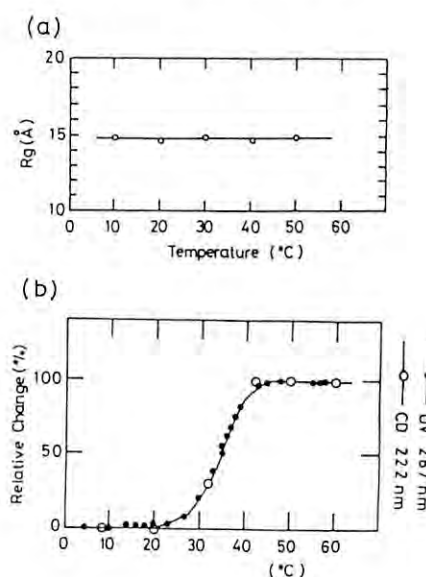


Fig.2. Temperature dependence of R_g and relative change of UV and CD spectra.

STRUCTURAL ANALYSIS OF OLIGOMERIC PROTEIN IN SOLUTION

Shinji NITANI, Tatzuo UEKI, Yoji INOKO and Katsumi KOBAYASHI*

Faculty of Engineering Science, Osaka University, Toyonaka, Osaka 560

* Photon Factory, National Laboratory for High Energy Physics, Tsukuba, Ibaraki 305

INTRODUCTION

Small-angle X-ray scattering is a technique for studying structural features of a particles in solution. In higher scattering angles, the scattering intensities are much weaker, by more than two orders, as compared with those in small-angles. In these regions (moderate-angle), however, some biological molecules with quaternary structure provide characteristic scattering profile, that has been proved to be related to the arrangement of subunits in the particle (1).

This report describes a simple analysis of the moderate-angle scattering profiles from Hb as an example of oligomeric protein, and from Mb as subunit respectively.

THEORETICAL BACKGROUND

The electron density $\rho(\vec{r})$ of a particle can be written as

$$\rho(\vec{r}) = \rho_s(\vec{r}) * \sum_i \delta(\vec{r} - \vec{r}_i)$$

where * denotes convolution operation, $\rho_s(\vec{r})$ is electron density of a subunit and \vec{r}_i the position of the i-th subunit.

The scattering intensity from the particle is

$$I(S) = \{f_s(S)\}^2 \sum_{i,j} \sin(2\pi S|\vec{r}_i - \vec{r}_j|) / (2\pi S|\vec{r}_i - \vec{r}_j|)$$

This expression is valid when subunits are taken as spherically symmetric. The first term in $I(S)$ is the form factor of subunit and the second the interference function which is related to arrangement of subunits in particle. By some way, if we could extract the values of $|\vec{r}_i - \vec{r}_j|$, we may be able to reconstruct the arrangement of subunits in particle (2).

EXPERIMENTS AND RESULTS

The X-ray scattering profiles from human Hb, and from sperm whale Mb were measured by the SAXES on BL-10C. The contrast variation experiments were carried out to separate the total scattering profile into components, "form" $I_f(S)$ and "internal" $I_s(S)$.

The scattering profiles from Hb and Mb with several sucrose concentrations are shown in Fig.1 and separated profiles $I_f(S)$ and $I_s(S)$ in Fig.2.

The outer peaks at $S \approx 0.08$ and 0.10 of scattering profile from Hb are derived from its "internal" structure, while the inner peaks are concerned with "form" term.

REFERENCES

- 1) T.Ueki et al. (1986) J.Biochem., 99,1127.
- 2) T.Ueki et al. (1988) Photon Factory activity Report, 8,112

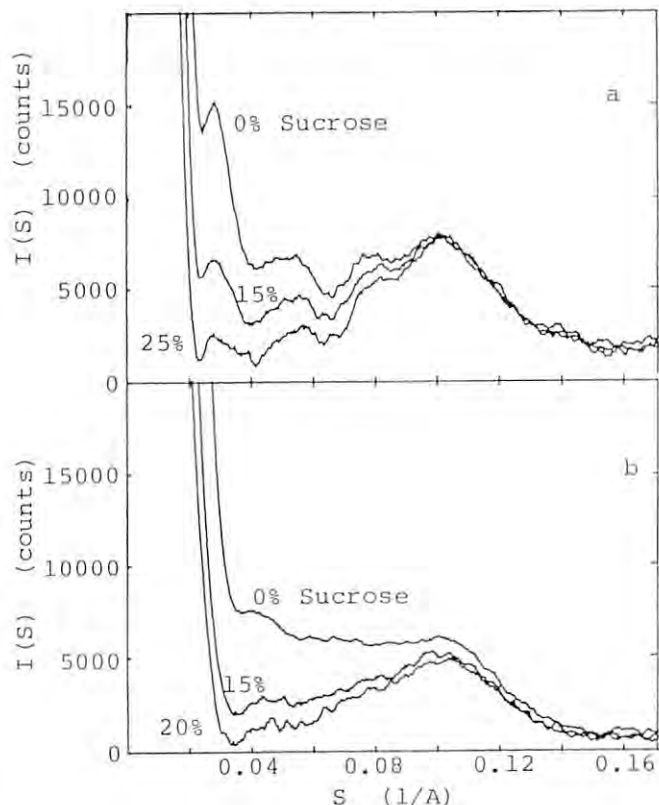


Fig.1 X-ray scattering profiles a: from Hb and b: from Mb with sucrose.

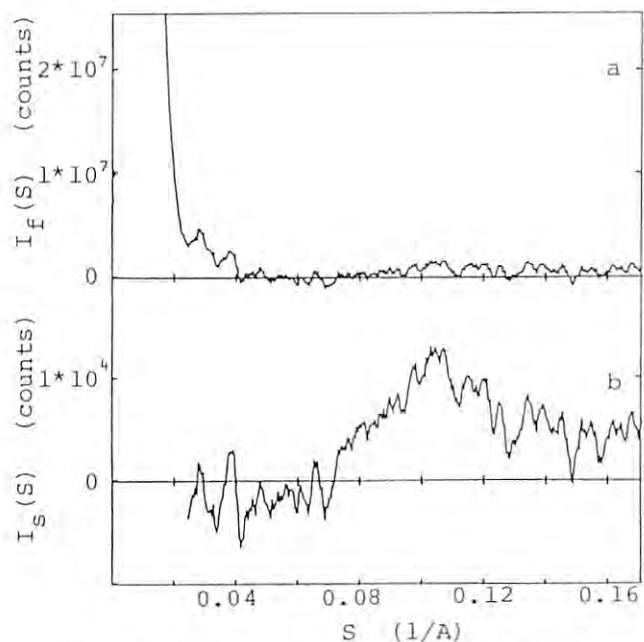


Fig.2 Components separated from profiles from Hb, a: "form" $I_f(S)$ and b: "internal" $I_s(S)$.

SMALL-ANGLE X-RAY SCATTERING STUDIES OF ISOLATED LINKER AND CORE HISTONES

Yoji INOKO, Toshio GATTO, Tatzuo UEKI and Katsumi KOBAYASHI*

Department of Biophysical Engineering, Faculty of Engineering Science, Osaka University, Toyonaka, Osaka 560

*Photon Factory, National Laboratory for High Energy Physics, Tsukuba, Ibaraki 305

Introduction

Histone H1, which plays a crucial role in chromatin condensation, is known as a very lysine-rich protein among the basic proteins found in most eukaryote chromatin. The sequence studies of H1 have shown that in free solution the molecule has three domains: an unstructured N-terminal domain (~ 40 residues, calf thymus¹⁾), a folded central domain (~ 80 residues) and a long unstructured C-terminal domain (~ 95 residues). We have performed a SAXS study on structure of histone H1 (linker histone) in solution. This report describes the X-ray scattering patterns from H1 solutions at various ionic strengths.

Experimental

Histone H1 was prepared from rat thymus nuclei according to the method of Oliver et al.²⁾ Protein was dissolved in 1 mM Tris-HCl, pH 7.5, with 0-400 mM NaCl (or MgCl_2). The SAXS experiments for solutions of H1 were carried out on a double-focusing X-ray camera for solution³⁾ installed at BL-10C, using 1.48 Å wavelength. A typical exposure time was 1800 sec at ring current of 280-160 mA and sample-to-detector distance was 75 and 200 cm.

Results and Discussion

Figure 1 shows the curves of scattered intensities, $I(S)$, in a plot of $\ln I(S)$ vs. S^2 , from H1 solutions (5.6 mg/ml) at different concentrations of NaCl. The salt concentration dependence of the scattering curve was observed. As the NaCl concentration increases up to 100 mM, the scattered intensity $I(S)$ is lowered uniformly for all scattering angle observed experimentally ($0.2 \times 10^{-2} \text{ Å}^{-1} < S < 6 \times 10^{-2} \text{ Å}^{-1}$). Above 100 mM NaCl, however, the change in $I(S)$ is reversed and at 400 mM NaCl the intensity is raised over the level of $I(S)$ at 0 mM NaCl with the exception of a slight recovery of $I(S)$ in the small angle region. In the case of MgCl_2 , the behavior of the scattering curve as a function of salt concentration is similar to that in the case of NaCl.

In all curves of Fig.1, the $I(S)$ increases steeply as S approaches zero. The tangents to the curves of the most inner parts give more than 70 Å as an apparent radius of gyration, R_g , and the zero-angle intensities, $I(0)$, obtained by their extrapolations show molecular weights corresponding to about 4 H1 molecules, indicating the occurrence of molecular aggregates in the solutions used here. The ratio of R_g to $I(0)$ for each curve differs largely from that of globular particle. On the other hand, in the higher angle region the scattering curve exhibits

a long tailing and does not drop readily to zero up to the observable upper limit ($S = 6 \times 10^{-2} \text{ Å}^{-1}$). These features of the curves observed in both small and higher angle regions suggest that aggregates of H1 and/or H1 molecule itself have elongated forms in solution.

References

- 1) P. G. Hartman, G. E. Chapman, T. Moss and E. M. Bradbury, *Eur. J. Biochem.*, **77**, 45(1977).
- 2) D. Oliver, K. R. Sommer, S. Panyim, S. Spiker and R. Chalkley, *Biochem. J.*, **129**, 349(1972).
- 3) T. Ueki, Y. Hiragi, M. Kataoka, Y. Inoko, Y. Amemiya, Y. Izumi, H. Tagawa and Y. Muroga, *Biophys. Chem.*, **23**, 115(1985).

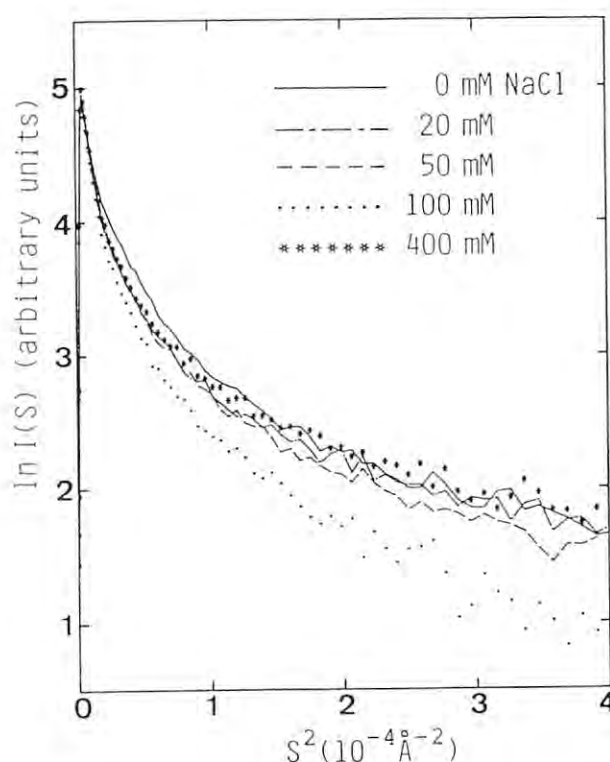


Fig.1. Logarithmic plots of scattered intensity $I(S)$ against S^2 , where $S = 2\sin\theta/\lambda$, for the solutions of H1 at various concentrations of NaCl. $I(S)$ was normalized with respect to the exposure time and the intensity of the primary beam. The sample-to-detector distance was 75 cm.

X-RAY DIFFRACTION STUDY ON THE STRUCTURE OF M-INTERMEDIATE IN THE PHOTOREACTION CYCLE OF BACTERIORHODOPSIN

Masayoshi NAKASAKO, Fumio TOKUNAGA, Mikio KATAOKA and Yoshiyuki AMEMIYA*

Department of Physics, Faculty of Science, Tohoku University, Sendai, Miyagi 980

*Photon Factory, National Laboratory for High Energy Physics, Tsukuba, Ibaraki 305.

INTRODUCTION

Bacteriorhodopsin (bR) is the sole membrane protein in the purple membrane (PM) of *H. halobium* and functions as a light-driven proton pump. The M-intermediate in the photoreaction cycle is considered to be the most important for the function. To elucidate the structural change in the intermediate with X-ray diffraction technique, the lifetime of the intermediate should be prolonged. As previously reported, we have already found the condition for the prolongation at room temperature without destruction of two-dimensional crystal structure of PM^{1,2}). The condition was further improved and we could record the diffraction profile from M-intermediate with better S/N ratio and analyze the structural change in M-intermediate.

EXPERIMENTAL

PM was isolated from R1M1 strain of *H. halobium*. PM solution was dialyzed against Arg-HCl (ca. 10mM) solution (pH 10) and dried on the sheet of mylar. After the treatment, M-intermediate can be completely accumulated under the irradiation of intense yellow light.

X-ray diffraction experiment was performed with MUSCLE diffractometer at BL-15A. The X-ray wavelength, the camera length and the receiving slit width in front of the PSPC were 1.5 Å, 647 mm and 4mm, respectively. Sample was exposed to X-ray for 300 sec. The diffraction profiles from *trans* state and M-intermediate were recorded with each other. Samples were irradiated with intense yellow light (> 530 nm) for the formation of M-intermediate and purple (410 nm) light for the *trans* state.

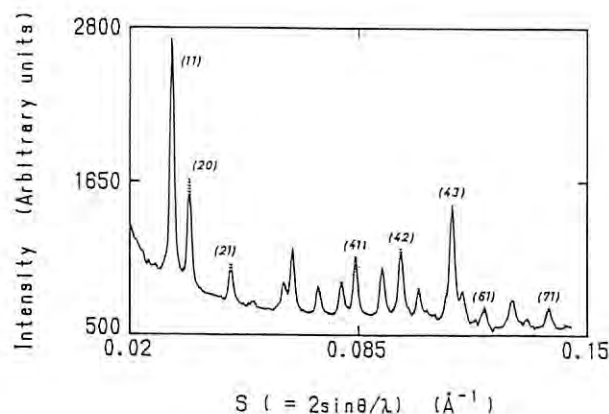


Fig. 1 X-ray diffraction profiles from PM in *trans* state (solid line) and M-intermediate (dotted line).

RESULTS

The X-ray diffraction profiles from the *trans* state and the M-intermediate are shown in Fig. 1. Small but significant differences can be seen between the profiles. The lattice constants of PM in *trans* state and M-intermediate were found to be 62.7 Å and 62.8 Å, respectively. This change in lattice constant indicated that the chromophore-chromophore interaction between adjacent trimer was weakened in the M-intermediate. The integrated intensities for each Bragg reflections were obtained through several corrections and calculation. According to the results of the electron diffraction experiment³), the structure factors were obtained from the intensity. The difference electron density map [m-*trans*] were calculated with these structure factors and phases³) (Fig. 2). We found small but significant structural change in two helices; B and G. The helix G contains some amino acid residues having significant contribution for proton-pumping⁴). These changes indicated that the helices B and G tilted to the inside of the trimer during the formation of M-intermediate.

Furthermore, the time-resolved measurement was performed during the conversion of M-intermediate to *trans* state. There was no disorder during the conversion.

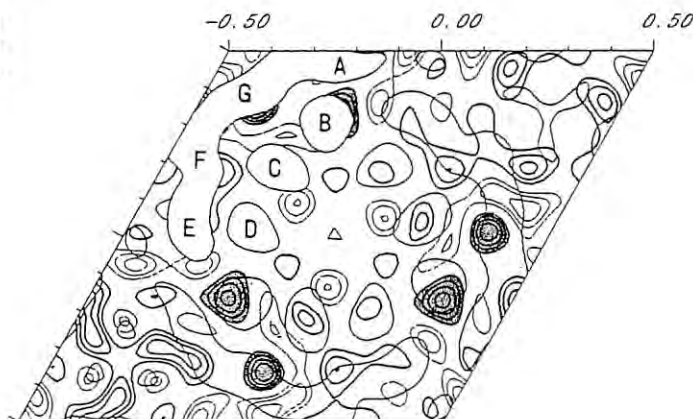


Fig. 2 Difference electron density map. The region where the electron densities increase in M-intermediate is designated with thick line.

REFERENCES

- 1) Nakasako et al., FEBS Lett.
- 2) Tokunaga et al., PF Activity Report #6.
- 3) Henderson and Gleaser, Ultramicroscopy
- 4) Mogi et al., ProNAS

Measurement of the Intensity of the First Actin Layer-line during Contraction of Frog Skeletal Muscle

N.Yagi, K.Horiuti*, S.Takemori*, M.Watanabe*,
Y.Umazume*, I.Matsubara & Y.Amemiya†

Department of Pharmacology, Tohoku University School of Medicine, Sendai, Japan.

*Department of Physiology, The Jikei University School of Medicine, Minato-ku, Tokyo, Japan.

†Photon Factory, National Laboratory for High Energy Physics, Tsukuba, Japan.

INTRODUCTION

It is known that the intensities of most of the actin layer-lines down to the axial spacing of 2.0 nm increase during contraction of frog skeletal muscle (Amemiya et al., 1987). However, the intensity of the first actin layer-line at the axial spacing of 36.0 nm, which arises from the double helix of the thin filament, has not been measured. This layer-line is overlapped by the first myosin layer-line at the axial spacing of 43.0 nm and therefore its intensity can not be measured directly. In this study, we measured the intensity profile of the first myosin layer-line to separated the contribution from the first actin layer-line to it.

EXPERIMENTAL

Sartorius muscles from Japanese frogs (*Rana nigromacrata*) were used. They were electrically stimulated at 6 °C. Experiments were done at the station BL15A of Photon Factory, Tsukuba, using the X-ray camera and the detector described in Amemiya et al. (1983). Diffraction patterns were recorded on Fuji imaging plates and scanned as described in Amemiya et al. (1987). The specimen-to-plate distance of 230 cm was used to obtain the maximal resolution. The data were analyzed on the ACOS-2020 computer and the image analysis system (RSIPS-DT) at Tohoku University Computer Center.

RESULTS

(i) Inner region (0.026-0.076 nm⁻¹)

The spacing of the first myosin layer-line in a resting muscle was 43.0 nm, which is as expected for the first myosin layer-line. The axial cross-section of the layer-line showed a Gaussian-like intensity distribution. When fitted by two Gaussian functions centered at 43.0 nm and 36.0 nm, contribution from the latter function was very small (about 2%). When the muscle contracts, the first myosin layer-line decreased in intensity to about 30% of that in the resting state. Its cross section had a asymmetrical profile with a longer tail in the higher angle side.

The center of gravity of this profile was found to be 40.1 nm. When fitted by the two Gaussian functions, contribution from that centered at 43.0 nm was 70%, while that at 36.0 nm was 30%. When the intensity of each component was compared, that of the 43.0-nm layer-line was 30% of the resting value, while that of the 36.0-nm layer-line was about 5 times as large as in the resting state.

(2) Outer region (0.082-0.142 nm⁻¹)

The cross-sectional profile of the first myosin layer-line has a broader profile in the outer part than in the inner part due to the disorientation of the filaments in the specimen. When the profile in the resting state was fitted by the two Gaussians functions centered at 36.0 nm and 43.0 nm, 33 % of the intensity was due to that at 36.0 nm. During contraction, the contribution ratio was not significantly changed and hence the peak position moved only slightly. Both the intensities of the 36.0- and 43.0-nm layer-lines decreased during contraction.

DISCUSSION

The very clear contrast between the behaviour of the inner and the outer regions of the first myosin layer-line is interpreted as due to different behaviour in the intensity of the first actin layer-line. The structural change in the thin filament due to the Ca-regulation decreases the intensity of this layer-line at around 0.10 nm⁻¹ (Yagi & Matsubara, 1989). This decrease is large enough to mask the intensity increase caused by binding of myosin heads to the thin filament. In the inner region, the structural change in the thin filament does not affect the intensity so that the intensity increase due to binding of myosin heads dominates the intensity change of the first actin layer-line.

REFERENCES

- Amemiya, Y., K.Wakabayashi, T.Hamanaka, T.Wakabayashi, T.Matsushita & H.Hashizume (1983) *Nucl. Inst. Meth.* **208** 471-477
- Amemiya, Y., K.Wakabayashi, H.Tanaka, Y.Ueno and J.Miyahara (1987) *Science* **237** 164-168
- Yagi, N. and I.Matsubara (1989) *J. Mol. Biol.* **208** 359-363.

Effects of BDM (2,3-butanedione-2-monoxime) on the Axial X-ray Diffraction Pattern from Frog Skeletal Muscle during Contraction

N.Yagi, K.Horiuti*, S.Takemori*,M.Watanabe*,
Y.Umazume*, I.Matsubara & Y.Amemiya†

Department of Pharmacology, Tohoku University School of Medicine, Sendai, Japan.
*Department of Physiology, The Jikei University School of Medicine, Minato-ku, Tokyo, Japan.
†Photon Factory, National Laboratory for High Energy Physics, Tsukuba, Japan.

INTRODUCTION

BDM (2,3-butanedione-2-monoxime) suppresses contraction of skeletal muscle by inhibiting the actin-myosin ATPase reaction (Horiuti et al., 1988; Higuchi & Takemori, 1989). The previous study on the equatorial reflections (Takemori et al., 1989) suggested that BDM may inhibit tension generation of myosin heads bound to actin. In the present study, this point was further studied by investigating the intensity changes of the myosin and actin layer-lines during contraction in the presence of BDM.

EXPERIMENTAL

Sartorius muscles of Japanese frogs (*Rana nigromacrata*) were used as specimens. They were tetanically stimulated at 6 °C either in the presence or absence of 3mM BDM. In the presence of 3mM BDM, the muscles developed tension about 40% of that in the absence of BDM. Experiments were done at the beam line 15A of Photon Factory using the X-ray camera and the detector described in Amemiya et al. (1983) and the axial diffraction patterns were recorded on Fuji imaging-plates. They were read by the scanner described in Amemiya et al. (1987). The data were analyzed on the ACOS-2020 computer and the image analysis system (RSIPS-DT) at Tohoku University Computer Center.

RESULTS

The intensities of myosin and actin layer-lines during contraction was measured in the resting and contracting states in the presence or absence (control) of 3mM BDM. The intensities during contraction divided by that in a resting state are :

	Control	3mM BDM
Myosin 1st layer-line	0.29	0.38
Myosin 2nd meridional	0.15	0.31
Myosin 3rd meridional	1.27	0.91
Actin 5.9-nm layer-line	1.21	1.05
Actin 5.1-nm layer-line	1.78	1.36

DISCUSSION

As has been known (Amemiya et al., 1987), the myosin layer-lines decrease in intensity while the actin layer-lines increases in intensity during contraction. The effects of BDM on the intensity changes of the myosin layer-lines are small considering the fact that the tension is less than half of that in normal contraction. This indicates that there are some myosin heads which are not forming the helix around the thick filament, but not contributing the tension production, either. On the other hand, the effects of BDM on the actin layer-lines are roughly proportional to those on the tension development. These results suggest that, even if there are myosin heads which are bound to actin but not producing tension, they are not contributing to the intensities of the actin layer-lines. Probably their attachment to actin is different from that during normal contraction.

REFERENCES

Amemiya,Y., K.Wakabayashi, T.Hamanaka, T.Wakabayashi, T.Matsushita & H.Hashizume (1983) *Nucl. Inst. Meth.* **208** 471-477
Amemiya,Y., K.Wakabayashi, H.Tanaka, Y.Ueno and J.Miyahara (1987) *Science* **237** 164-168
Higuchi,H. and S.Takemori (1989) *J. Biochem.* **105** 638-643
Horiuti,K., H.Higuchi, Y.Umazume, M.Konishi, O.Okazaki and S.Kurihara (1988) *J. Muscle Res. Cell Motility* **9** 156-164
Takemori,S., M.Watanabe, N.Yagi, K.Horiuti, Y.Umazume, I.Matsubara and Y.Amemiya (1989) *Photon Factory Activity Report* **6** 123

FOLDING MECHANISM OF BACTERIORHODOPSIN PEPTIDE CHAIN BY X-RAY DIFFRACTION

Fumio TOKUNAGA, Masayoshi NAKASAKO, Mikio KATAOKA and Yoshiyuki AMAMIYA*

Department of Physics, Faculty of Science, Tohoku University, Sendai, Miyagi 980

*Photon Factory, National Laboratory for High Energy Physics, Oho-machi, Ibaraki 305

INTRODUCTION

Bacteriorhodopsin (bR) of Halobacteria is one of membrane proteins and acts as a light-driven proton pump. BR forms trimer and the trimer arranged in a two-dimensional hexagonal lattice forming purple membrane (PM). BR contains seven trans-membraneous α -helix. Mitaku et al. proposed the hypothesis that structure of the membrane proteins is maintained by hydrogen bonds¹⁾. In order to elucidate this hypothesis, we performed X-ray diffraction experiments of purple membrane in alcohol-water solution with various concentrations.

EXPERIMENTAL

Purple membrane was isolated from *Halobacterium halobium*. PM was suspended in methanol or ethanol-water solution with various concentration.

X-ray diffraction experiment was performed with MUSCLE diffractometer at BL-15A.

RESULTS AND DISCUSSION

Figure 1 shows the x-ray diffraction patterns from the PM in ethanol-water solution.

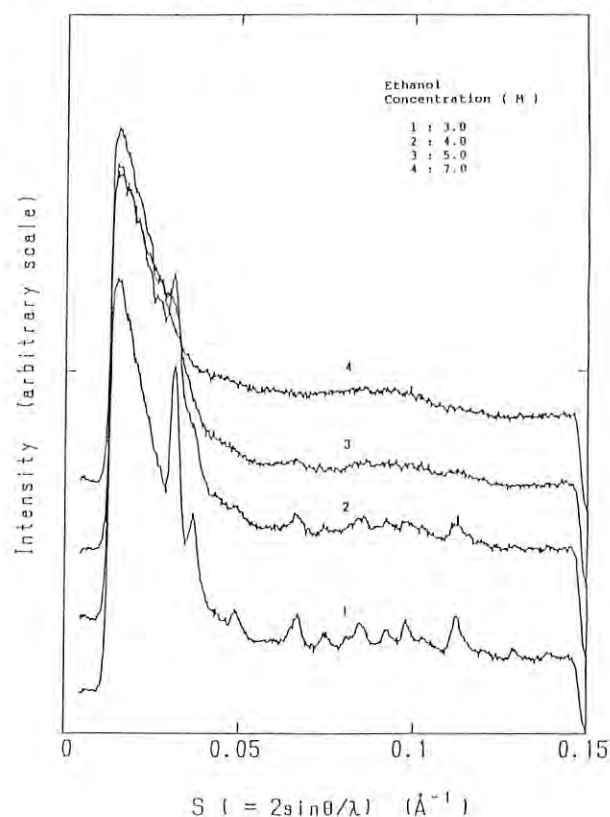


Fig. 1. X-ray diffraction pattern of the PM in ethanol-water solution.

Radial autocorrelation functions were calculated from the patterns and analyzed. With increase of the concentration of methanol or ethanol, three steps of changes were observed: In the region of low concentration of alcohol, maximum absorbance decreases and disorder is induced in the two-dimensional lattice. In the region of middle concentration, Bragg reflections disappeared, that is two dimensional crystal structure is destroyed but trimer structure is still maintained. In the region of higher concentration trimer disappeared but the correlation between helices still maintained.

Alcohol enters into the membrane and destroys stepwise the PM structure, but not intra-helical hydrogen bonds.

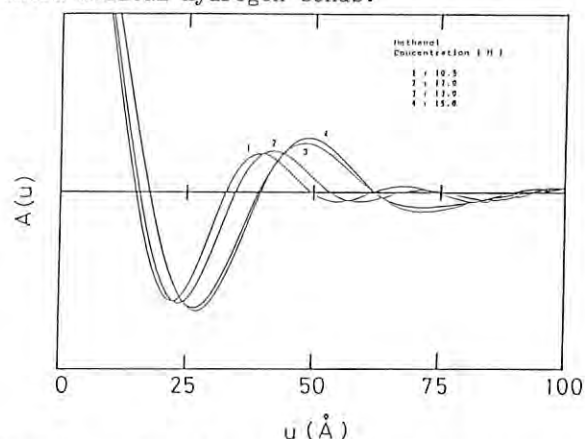


Fig. 2. Radial autocorrelation function with 20 Å resolution calculated from X-ray diffraction pattern from PM in ethanol-water solution.

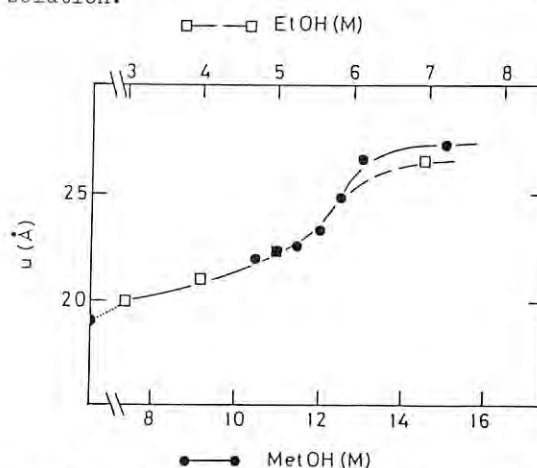


Fig. 3. Concentration dependence of first peak of radial autocorrelation function.

REFERENCE

1. S. Mitaku et al., Biophys. Chem., 30, 69-79 (1988)

Stable Lamellar Phase of 1,2-O-di-tetradecyl-3-O- β -D-glucopyranosyl-sn-glycerol

Morio AKIYAMA, Hirokuni YAMADA and Yoshiyuki AMEMIYA*

Department of Physics, Sapporo Medical College, Sapporo Hokkaido 060

*Photon Factory, National Laboratory for High Energy Physics, Tsukuba, Ibaragi 305

Introduction

The phase behaviour of lipids depends on the sort of head group. Aqueous dispersion of glycolipids form the inverted hexagonal (H_{II}) phase at high temperature¹⁾, while phosphatidylcholine does not form the H_{II} phase. The formation of the H_{II} phase in glycolipid is due to the highly developed hydrogen bond network.

The head group interaction may have also influence on the lamellar structure at low temperature. One of glycolipids, 1,2-O-di-tetradecyl-3-O- β -D-glucopyranosyl-sn-glycerol (abbreviate as 14-Glc) forms the stable lamellar (L_c) phase when 14-Glc in the metastable (L_{β}) phase (the L_{β} phase is formed as 14-Glc cooled from the lipid crystalline (L_{α}) phase) is annealed at room temperature.²⁾

We studied the transition process from the L_c phase to the L_{α} phase by using a synchrotron radiation.

Experimental

The aqueous dispersion, 66 weight % water, was sealed in a glass capillary of 1 mm diameter. X-ray diffraction study was carried out at BL-15 A station.

Results and Discussion

Figure 1 shows the x-ray diffraction patterns of 14-Glc at various temperature in the cooling process from the L_{α} phase to the L_{β} phase. The cooling rate was 0.2K/min.

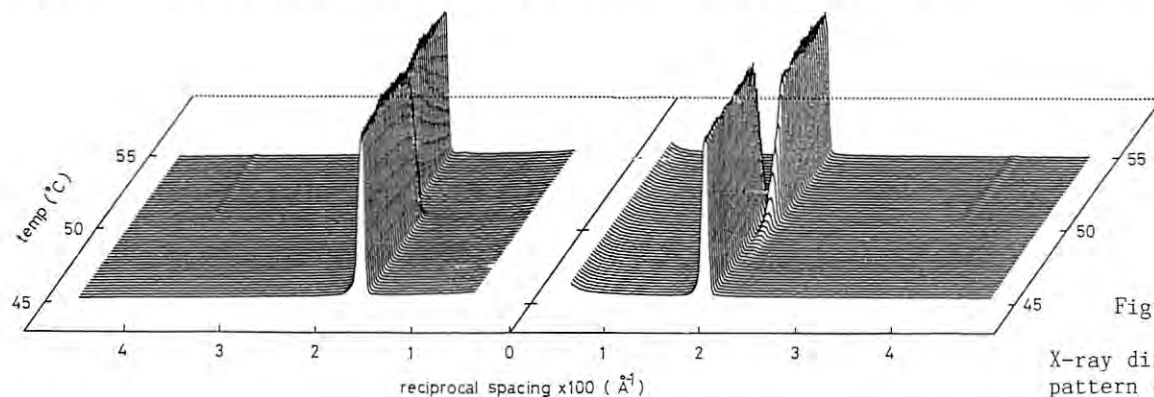


Fig.1

X-ray diffraction pattern of 14-Glc. Cooling 0.2K/min.

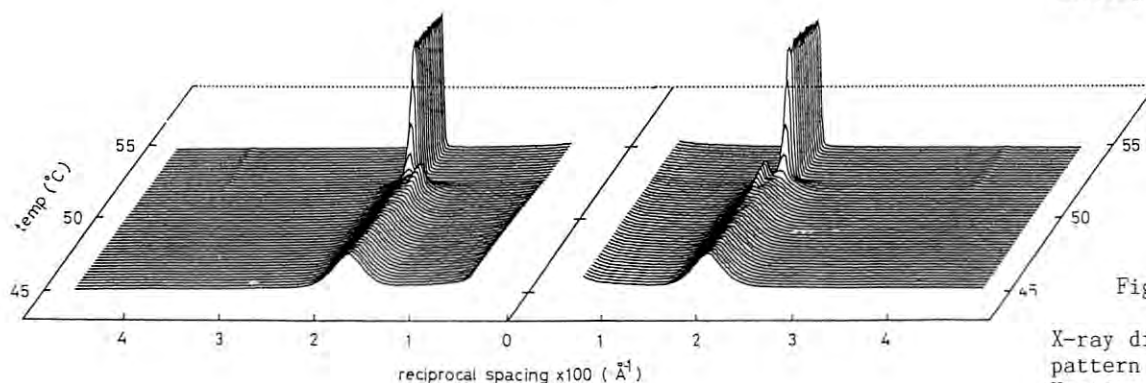


Fig.2

X-ray diffraction pattern of 14-Glc. Heating 0.2K/min.

We have already observed by using a diffractometer in our laboratory that the L_{β} phase converts to the L_c phase. It takes about 35 hours to complete the conversion at 20.5°C. The conversion is two phase conversion; on the way of the conversion, the x-ray diffraction pattern have the L_{β} phase component and the L_c phase component. This behaviour is quite different from the formation of the L_c phase in DPPC³⁾.

Figure 2 shows the x-ray diffraction patterns of 14-Glc in the heating process from the L_c phase to the L_{α} phase. In the narrow temperature region (50-52°C), the L_{β} phase appeared co-existing with the L_c phase. This behaviour also differs from that of DPPC.

The line width of the L_c phase is very much wide compared with that of the L_{β} phase, while the line width of the L_c phase in DPPC is comparable to that of the L_{β} phase.

These results suggest that the L_c phase of 14-Glc exists as the microcrystalline-like domains and that the L_c phase domain is formed by a interlamellar interaction resulting from the hydrogen bonds between head groups.

References

- 1) D. A. Mannock et al., *Biochemistry*, 27, 6852 (1988)
- 2) D. A. Mannock, *Parsonal communication*
- 3) M. Akiyama et al., *Jpn. J. Appl. Phys.*, 26, 1587 (1987)

STOPPED-FLOW X-RAY SCATTERING STUDY ON ALLOSTERIC TRANSITION OF ASPARTATE TRANSCARBAMYLASE AT SUBZERO TEMPERATURE

Hirotsugu Tsuruta¹, Takayuki Sano¹, Patrice Vachette², Patrick Tauc³,
Michael F. Moody⁴, Katsuzo Wakabayashi⁵, Yoshiyuki Amemiya⁶, Kazumoto Kimura⁷
and Hiroshi Kihara⁸

¹ Department of Materials Science, Faculty of Science, Hiroshima University

² LURE, Batiment 209d, Universite Paris-sud

³ Institut d'Enzymologie, CNRS

⁴ School of Pharmacy, University of London

⁵ Department of Biophysical Engineering, Faculty of Engineering Science
Osaka University

⁶ Photon Factory, National Laboratory for High Energy Physics

⁷ Division of Medical Electronics, Dokkyo University, School of Medicine

⁸ Jichi Medical School, School of Nursing

Structural change associated with the allosteric transition of *E.coli* aspartate transcarbamylase (ATCase) has been monitored by solution X-ray scattering. Kinetics of the structural change was monitored by stopped-flow X-ray scattering method, using acetyl phosphate, which is a substrate analogue of slow reaction rate¹⁾. Our new stopped-flow device operative at subzero temperature²⁾ has now enabled us to monitor the structural kinetics of ATCase during the physiological enzyme reaction with the native substrates, L-aspartate and carbamyl phosphate at -5 °C in the presence of 30% ethylene glycol. Stopped-flow X-ray scattering experiment was carried out at the BL-15A of the Photon Factory with a position sensitive proportional counter. All the scattering data were normalized for incident beam intensity and counting time.

Scattering patterns of the enzyme at various times after mixing are shown in Figure 1. The subsidiary maxima, whose position and intensity are specifically sensitive to quaternary structural changes, first show an increase in intensity before reaching a plateau. When the substrates have been exhausted, the maxima return to the initial level. Scattering pattern of the enzyme in the steady-state phase was thus obtained for the first time. In Figure 2 is shown a time course of the whole reaction. Both the structural change induced by the substrates binding and the reverse structural change due to the substrate consumption are seen. The higher the aspartate concentration, the longer the plateau becomes. Studies with allosteric effectors are now in progress.

1) H. Kihara, E. Takahashi-Ushijima, Y. Amemiya, Y. Honda, P. Vachette, P. Tauc, T. E. Barman, P. T. Jones, and M. F. Moody, *J. Mol. Biol.* **198**, 745 (1987)

2) H. Tsuruta, T. Nagamura, Z.-X. Wang, K. Kimura, Y. Igarashi, A. Kajita, Y. Amemiya, K. Wakabayashi, and H. Kihara, *Rev. Sci. Instrum.* **60**, 2356 (1989)

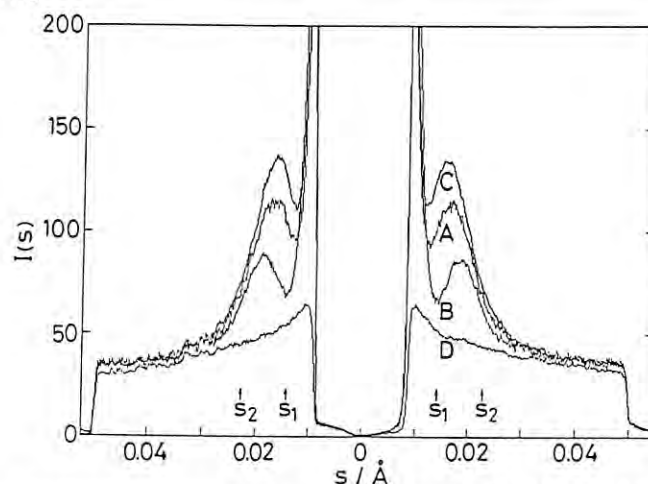


Figure 1. Time-resolved X-ray scattering patterns of ATCase during the physiological reaction. ATCase containing carbamyl phosphate was mixed with aspartate and carbamyl phosphate. Final concentration: ATCase, 60mg/ml; carbamyl phosphate, 44mM; aspartate, 89mM. 13 runs were repeated. $s = (2/\lambda)\sin\theta$, and 2θ is the scattering angle. Curve A, recorded at 16.5 s after mixing in a steady state; curve B, 78.0 s after mixing in a final equilibrium; curve C, scattering pattern of the enzyme ligated with a bisubstrate analogue PALA; curve D, background scattering.

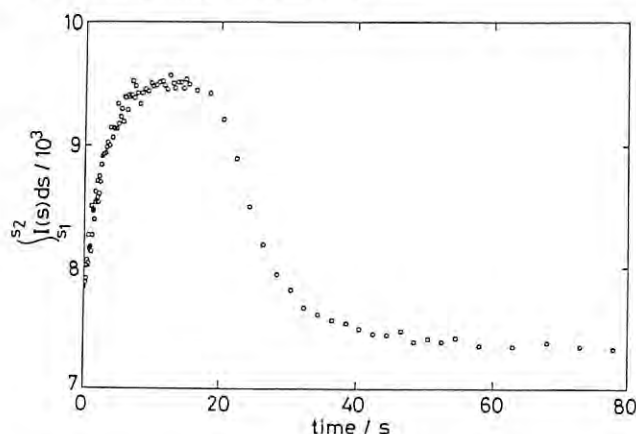


Figure 2. Reaction time course expressed as the integrated intensity over the angular range s_1 - s_2 shown in Figure 1.

OLIGOMERIZATION OF ACTIN MONOMER AT THE EARLY STAGE OF ACTIN POLYMERIZATION MEASURED BY STOPPED-FLOW X-RAY SMALL ANGLE SCATTERING

Masaaki Kuroda¹, Hirotugu Tsuruta², Yoshiyaki Amemiya³, and Hiroshi, Kihara⁴

- 1) Faculty of Science, Shimane University, Matsue 690, Japan
- 2) Faculty of Science, Hiroshima University, Hiroshima 730, Japan
- 3) Photon Factory, National Laboratory for High Energy Physics, Tsukuba 305, Japan
- 4) Jichi Medical School, School of Nursing, Tochigi 329-04, Japan

Actin, a major protein of most eukaryotic cells exists as a monomer under low salt-conditions. The monomeric actin (G-actin) assembles into helical filaments (F-actin) by the addition of neutral salts. Pioneering work done by Oosawa and colleagues (1) treated the process as a kind of a nucleation-condensation phenomenon. The nucleation-condensation mechanism contains a lag in the polymerization process. In most kinetical analysis, the lag is interpreted as a nucleation step of the polymerization. On the other hand, it is now recognized that a conformational change of actin monomer induced by the added salts precedes the nucleation step. As a consequence, the interpretation of the lag phase has become more complicated than ever. Moreover, in some reports, the entity of nuclei was doubted (for review, refer 2). In order to know the nature of oligomers formed at very early stage of actin polymerization, we measured the stopped flow X-ray scattering of actin polymerized with KCl/ MgCl₂ and found that dimerization of G-actin took place without detectable lag-phase in the kinetics.

Actin was extracted from an acetone dried powder of chicken breast muscle and purified to monomer by Sephadex G-200 column chromatography. G-actin preparation either with bound Mg or Ca in 0.1 mM ATP and 5 mM Tris-HCl of pH 7.5 were used for the experiment. For kinetic study, Ca-G-actin was polymerized with 50 mM KCl and 2 mM MgCl₂ in a stopped flow mixing chamber regulated at 25.0 C.

Static X-ray scattering measurements for monomer solution --- Guinier plots of the scattering patterns gave radius of gyration at 27.1 Å and 26.2 Å for Ca-bound G-actin at a protein concentration of 0.91 mg/ml and 2.41 mg/ml respectively. These values showed good agreement with the previously

reported estimation done by Matsudaira et al.(3) with synchrotron X-ray diffraction studies. G-actin with bound Mg also showed similar results, suggesting that species of bound metal did not affect gross conformation of G-actin.

Stopped flow X-ray scattering measurements during polymerization --- G-actin at final concentrations of 0.71 mg/ml and 1.87 mg/ml were mixed with Mg/K-polymerizing reagents in a stopped-flow mixing chamber and injected into the X-ray cell within 10 ms after the mixing. Time-resolved scattering patterns were recorded at 300ms- or 3s-intervals. Plots of the scattering intensity and the radius of gyration obtained by extrapolating observed values to zero degree versus time (frame number up to 95 frames) followed exponential curves and did not show lag period. The calculated radius of gyration of actin molecules increased from 26 Å to 30-40 Å within 300ms after the initiation of polymerization. From these data, we concluded that dimerization of actin monomers occurred at very early stage of the polymerization. The results we had obtained so far agreed well those of Matudaira et al. (3). However, a variety of methods employed for the measurements on polymerization kinetics of actin showed lag phase. The discrepancy should be elucidated by further experiments.

References

- (1) F. Oosawa and S. Asakura, *Thermodynamics of the Polymerization of Proteins* (Academic Press, New York, 1975)
- (2) T.D. Pollard, and J.A. Cooper, *Ann Rev. Biochem.*, **55**, 987 (1986)
- (3) P. Matsudaira, J. Bordas and M.H.J. Koch, *Proc. Natl. Acad. Sci. USA*, **84**, 3151 (1987)

A DYNAMIC X-RAY DIFFRACTION STUDY ON SLOW SKELETAL MUSCLE OF THE CHICK AT THE BEGINNING OF CONTRACTION

I. MATSUBARA, N. YAGI, Y. SAEKI*, N. SUDA[†] & S. KURIHARA[†]

Department of Pharmacology, University of Tohoku School of Medicine, Sendai.

*Department of Physiology, Tsurumi University School of Dental Medicine, Yokohama.

[†]Department of Physiology, Jikei-kai Medical School, Minato-ku, Tokyo.

INTRODUCTION

Two types of binding seem to occur between myosin and actin during muscle contraction (1). One is a weak binding which produces no tension and in rapid equilibrium with the dissociated state (2). The other is a strong binding which produces the contractile tension. The weak binding shifts to the strong binding, releasing an inorganic phosphate (1). This shift is considered to limit the rate of tension production in cardiac muscle (3,4). To examine whether the same shift limits the rate of tension rise in skeletal muscle, we have studied by an X-ray diffraction method the behaviour of the cross-bridges in a slow muscle, anterior latissimus dorsi (ALD), of the chick. This muscle is a wing muscle and consists almost solely of slow fibres which can maintain a tension for more than ten minutes with a very little energy expenditure. We have compared the cross-bridge behaviour in the slow muscle with that in a fast muscle, posterior latissimus dorsi (PLD). This muscle is also a wing muscle and consists almost entirely of fast fibres.

METHODS

The anterior and posterior latissimus dorsi were dissected from 4-week-old chicks. ALD was isolated with part of the wing bone, humerus, and the spinal vertebrae to which it was attached. PLD was isolated also with the spinal vertebrae, but the distal end was cut in the middle of the tendon which connected the muscle to the humerus. The muscles were held isometrically in a specimen chamber which was perfused continuously with an oxygenated Ringer solution at 32 °C. ALD was stimulated for 2 sec with a train of electrical pulses (50 Hz) given through a pair of parallel electrodes. The muscle length was adjusted to produce the maximum isometric force. PLD was stimulated for 0.5 sec also at the optimal length.

The low-angle diffraction camera (5) combined with the beam line 15A was used at a wavelength of 0.15 nm and with a specimen-to-detector distance of 2 m. A linear position sensitive counter was used to record the equatorial diffraction patterns. The time resolution was 25 ms for ALD and 20 ms for PLD. The diffraction data were accumulated over 50 contractions. From the accumulated data the integrated intensities the two main equatorial

reflections, I_{10} and I_{11} , were obtained every 25 ms (ALD) or 20 ms (PLD).

RESULTS

The basic features of the equatorial patterns from ALD and PLD were the same as those described previously (6). The 1,0 lattice spacing at the optimal muscle length was 31 nm in ALD and 30 nm in PLD.

On activation of muscle the intensity ratio I_{10}/I_{11} decreased, indicating the binding of myosin heads with actin. About 80 % of myosin heads were bound at the maximum tension in ALD and 70 % in PLD. The half maximum of the binding was obtained 40 ms after the onset of stimuli in ALD and 20 ms in PLD.

The tension started to rise simultaneously with the binding, but proceeded considerably slower than the binding in both muscles. The half maximal tension of ALD was reached 160 ms after the onset of stimuli. This was 50 ms in PLD.

DISCUSSION

The binding detected by X-ray diffraction represents both weak and strong bindings. On the other hand, the tension represents only the strong binding (4). The delay between the mid-points of binding and tension was 120 ms in ALD and 30 ms in PLD. The delay probably represents the time required for the weak binding to shift to the strong binding. Therefore our results indicate that the shift takes longer in slow muscle than in fast muscle.

REFERENCES

- (1) Eisenberg, E. & Hill, T.L. (1985). *Science* 227, 999-1006.
- (2) Brenner, B., Schoenberg, M., Chalovich, J. M., Greene, L.E. & Eisenberg, E. (1982). *Proc. Nat. Acad. Sci. USA* 79, 7288-7291.
- (3) Matsubara, I., Yagi, N., Maughan, D.W., Saeiki, Y. & Amemiya, Y. (1989). In *Muscle Energetics* (Ed. Paul, R.J.) pp. 481-486.
- (4) Matsubara, I., Maughan, D.W., Saeiki, Y. & Yagi, N. (1989). *J. Physiol.* 417, 555-565.
- (5) Amemiya, Y., Wakabayashi, K., Hamanaka, T., Wakabayashi, T., Matsushita, T. & Hashizume, H. (1983). *Nucl. Instr. Meth.* 208, 471-477.
- (6) Matsubara, I. (1974). *J. Physiol.* 238, 473-486.

STUDIES OF PHASE TRANSITION IN PHOSPHATIDYLCHOLINE-WATER SYSTEMS BY TIME-RESOLVED X-RAY DIFFRACTION AT LOW TEMPERATURE SCAN RATES.

Sinzi MATUOKA, Boris G. TENCHOV[#], Haruhiko YAO, Satoru KATO, Yoshiyuki AMEMIYA^{\$}, Ichiro HATTADepartment of Applied Physics, School of Engineering, Nagoya University
Furo-cho, Chikusa-ku, Nagoya 464-01[#]Central Laboratory of Biophysics, Bulgarian Academy of Sciences, 1113 Sofia, Bulgaria.^{\$}Photon Factory, National Laboratory for High Energy Physics Oho 1-1, Tsukuba, Ibaraki 305

Introduction

In hydrated phosphatidylcholine (PC) multilayer systems, well defined thermal phase transitions has been observed. From low temperature L_{β} phase (gel phase) P_{β} phase (ripple phase) L_{α} phase (liquid crystalline phase) appear. We have pointed out that the time-resolved low-angle X-ray diffraction at low temperature scan rates is one of the powerful methods to characterize these phase transitions. This method provides a successive X-ray diffraction profiles during phase transition and make it possible to study the temperature dependence in detail.

In this report we focus our attention on the main transition from P_{β} to L_{α} phase in the system of fully hydrated dipalmitoylphosphatidylcholine (DPPC), fully hydrated dimyristoylphosphatidylcholine (DMPC) and concentrated DMPC in which water content is about 25 wt%.

Experimental

Hydrated multilayers of PCs were prepared by the conventional method. Temperatures of the samples were controlled by the circulating water supplied from a computer controlled water bath. The temperature scan rate was 0.1°C/min and its monitoring by a chromel-alumel thermocouple showed perfectly linear temperature scans.

Small angle X-ray diffraction measurements have been performed at BL-15A station. The temperature resolution of each diffraction frame in which the exposure time was 30 s is 0.050°C at the scan rate of 0.1°C/min.

Results and Discussion

X-ray diffraction patterns of fully hydrated DPPC (water content : 75 wt%) in the heating scans at 0.1°C/min are shown in Fig. 1. The observed peak denotes the lamellar spacing. The spacing of P_{β} phase shifts to that of L_{α} phase during heating through the main transition. However its conversion shows the complicated feature as follows. In a narrow range of 0.1°C at the transition midpoint (41.25°C) a broad diffraction profile was observed. This behavior reflects to the drop of the peak intensity in the range of 41.2 - 41.3°C. In these temperatures the spacing shifts continuously from that of P_{β} phase to that of L_{α} phase. These data indicate that there is no coexistence of P_{β} phase and L_{α} phase in fully hydrated DPPC.

In fully hydrated DMPC with the water content of 55 wt %. The coexistence of P_{β} phase and L_{α} phase did not observed at the scan rate of 0.1°C/min as well.

In contrast, concentrated DMPC multilayer system with the water content of 25 wt% exhibits the two-phase coexistence at main transition temperature. Fig. 2 shows the diffraction profiles during heating scans at 0.1°C/min. Around 25.7°C two peaks originating from the coexistence of P_{β} phase and L_{α} phase appear. Such a state was stable at least 50 min. This fact indicates the stable two phase coexistence.

These differences in the behavior of phase transition caused by water contents suggest that water molecules play an important role in the nature of phase transition.

References

- (1) B.G.Tenchov, H.Yao and I.Hatta Biophys.J. (1989) 56 757-768.

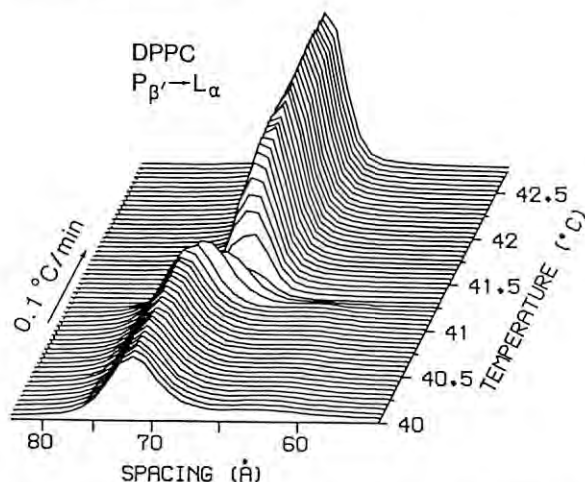


Fig. 1 : The main transition in fully hydrated DPPC multilayers recorded by low-angle X-ray diffraction at heating rate of 0.1°C/min.

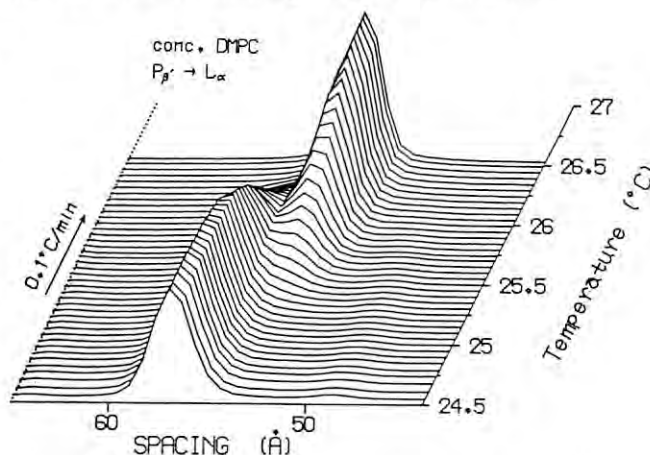


Fig. 2 : The main transition in concentrated DMPC multilayers recorded by low-angle X-ray diffraction at heating rate of 0.1 °C/min.

X-RAY DIFFRACTION OF THE LIVE SQUID RETINA IN THE DARK AND LIGHT

Toshiaki HAMANAKA*, Yuji KITO**, Masatsugu SEIDOU**, Katsuzo WAKABAYASHI*
and Yoshiyuki AMEMIYA***

- * Department of Biophysical Engineering, Faculty of Engineering Science, Osaka University, Toyonaka, Osaka 560
 ** Department of Biology, Faculty of Science, Osaka University, Toyonaka, Osaka 560
 *** National Laboratory for High Energy Physics, Tsukuba, Ibaraki 305

Introduction

The initial step of the visual process is the absorption of light by the visual pigment. The squid visual pigment is located in microvilli which are cylindrical extensions of the cell membrane, arranged hexagonally within the rhabdomes. Until now, only a few papers have been published on the structural study of invertebrate rhabdomes by x-ray diffraction. In those, however, the retina fixed by glutaraldehyde was used, because this tissue disintegrated within 1 hour of dissection. In the previous report¹⁾, it was described that we could succeed in recording the x-ray diffraction pattern from unfixed retina by the use of the synchrotron radiation and a storage phosphor screen, the imaging plate. In the present study, we have investigated the structural response of photoreceptors to the light stimulation.

Experimental

Living, active specimens of the squid, *Watasenia scintillans* were captured at Toyama Bay of the Japan Sea and brought to Tsukuba within several hours. The squids were decapitated and their retinas dissected in dim red light. For the x-ray experiment, a 1-mm thick slice of retina was kept in an artificial seawater chamber with Mylar windows at 4°C. Schematic diagram of a slice of squid retina was shown in the previous report¹⁾. The artificial seawater containing D-glucose was oxygenated and gently circulated through the sample chamber during the experiment. A 100-W halogen lamp in conjunction with an interference filter and a heat filter, was used for light stimulation (about 500 nm in wavelength).

X-ray experiments have been performed with a mirror-monochromator optics (the Muscle Diffractometer) at BL-15A1²⁾. The wavelength of the radiation was 0.150 nm. The sample-to-detector distance was 2276 mm. X-ray diffraction intensity was recorded on the imaging plate and stored on magnetic tape after converting to the digital signals with the image reader and the image processor³⁾. The exposure time was 4 minutes and each recording finished within 40 minutes after the decapitation.

Results

Figure 1 shows the x-ray diffraction patterns from outer segments of a live squid retina in the dark (*left*) and light (*right*), which were reproduced and photographed from the stored images with the image writer. The low angle x-ray diffraction spots are due to the oblique lattice of microvilli. Upon light

illumination, the prominent changes have been observed in the lattice constants and the x-ray intensity distribution. The analysis of these data by model calculations suggests that the diameters of microvilli increase as well as the spacings among microvilli in response to the light stimulation.

References

- 1) T. Hamanaka et al., PF Activity Report, No.6, 124 (1988)
- 2) Y. Amemiya et al., Nucl. Instrum. Methods, 208, 471 (1983)
- 3) Y. Amemiya et al., Nucl. Instrum. Methods, A266, 645 (1988)

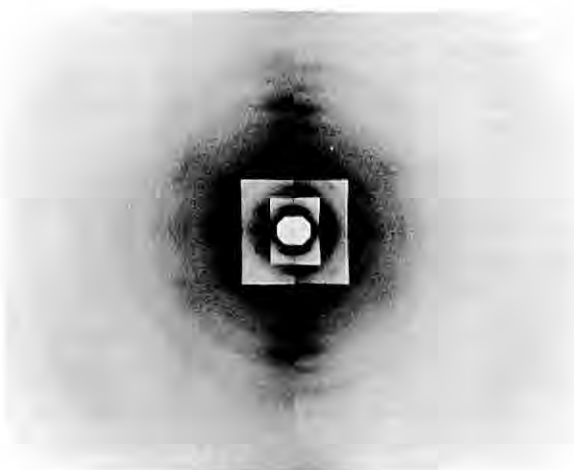


Figure 1. The x-ray diffraction patterns from a live squid retina in the dark (*left*) and light (*right*). The x-ray diffraction spots are due to the oblique lattice of microvilli. The lattice constants are $a=60.0$ nm, $b=59.0$ nm and $\gamma=118^\circ$ in the dark, and $a=65.5$ nm, $b=64.0$ nm and $\gamma=118^\circ$ in light, respectively. The storage ring was operated at 2.5 GeV with a beam current of 300 mA. The exposure time was 4 minutes for each pattern. The recording of both patterns has finished within 40 minutes after the decapitation.

X-RAY DIFFRACTION FROM INSECT FLIGHT MUSCLE IN A PARTIALLY RELAXED CONDITION

Richard T. TREGGAR, Katsuzo WAKABAYASHI*, Hidehiro TANAKA**, Hiroyuki IWAMOTO**, Mary C. REEDY***
Michael K. REEDY***, Yoshiyuki AMEMIYA**** and Haruo SUGI**

AFRC Institute of Animal Physiology and Genetics Research, Babraham, Cambridge CB2 4AT, U.K.

* Department of Biophysical Engineering, Faculty of Engineering Science, Osaka University, Toyonaka, Osaka 560

** Department of Physiology, School of Medicine, Teikyo University, Itabashi-ku, Tokyo 173

*** Department of Cell Biology, Duke University Medical School, Durham, NC 27710, U.S.A.

**** Photon Factory, National Laboratory for High Energy Physics, Tsukuba, Ibaraki 305

Introduction

Our interest is in the movement of the muscle crossbridges, the heads of the myosin molecules that cause contraction in a muscle. These can be particularly well seen in insect flight muscle. In order to simulate the positions taken up transiently by the crossbridges in active contraction for long enough to be able to see them by X-ray diffraction we have recorded the low-angle X-ray diffraction pattern from *Lethocerus* flight muscle fibres in rigor or under two conditions that modify crossbridge structure and behaviour, aqueous AMPPNP and AMPPNP + calcium in an ethylene glycol-water mixture.

Experimental

For this purpose we used the Photon Factory low-angle diffraction line 15A, and observed the diffraction pattern either on a linear position-sensitive counter or on a Fuji imaging plate; use of film produced unacceptable deterioration in the specimen before the data could be collected. Restriction of exposure to that needed to observe the inner layer lines of the pattern allowed comparative observation of different stages of relaxation in a single specimen.

Results and Discussion

The effects of relaxation on the 38.7 nm layer-line peaks (hk.6) of the diffraction patterns were studied in detail. In aqueous AMPPNP at room temperature, a condition in which rigor tension drops to half without loss of stiffness, the peaks remained nearly as intense as in rigor except for the 10.6, which dropped to half. In 20% ethylene glycol-AMPPNP + 100 μ M Ca^{2+} at 23°C, a condition which removed muscle tension but left stiffness close to the rigor value, the 10.6 and 11.6 peaks greatly decreased but the 31.6 remained relatively high. The 14.5 nm meridional peak (00.16) became stronger on addition of AMPPNP and again on adding glycol + calcium. Considered in terms of diffraction amplitude, these results show a progressive increase in thick-filament based order with relaxation (squares, Fig. 1) and a progressive decrease of the thin-filament based order (closed circles, Fig. 1). The exchange of diffracting mass between the two ordering filaments appears to be quite precise, as if each part of the crossbridge took up one or the other order but did not become disordered; note that the sum of the squares and filled circles remains approximately constant in Fig. 1B.

We compared the X-ray diffraction patterns and crossbridge structure seen in the electron microscope under the same chemical conditions. The electron micrographic model of redistribution of mass within attached crossbridges as re-

laxation approaches was confirmed by the X-ray diffraction results. However, in near-relaxed conditions the X-ray diffraction showed that more crossbridge mass was attached in an orderly manner to the actin than could be seen in the electron micrographs.

Our data indicate that the position of the myosin crossbridge is strongly constrained by its relationship to both thick and thin filaments, even when a muscle is partially relaxed. It follows that contraction may well be a highly-ordered process within the head of the myosin molecule, consisting of several stages of internal motion.

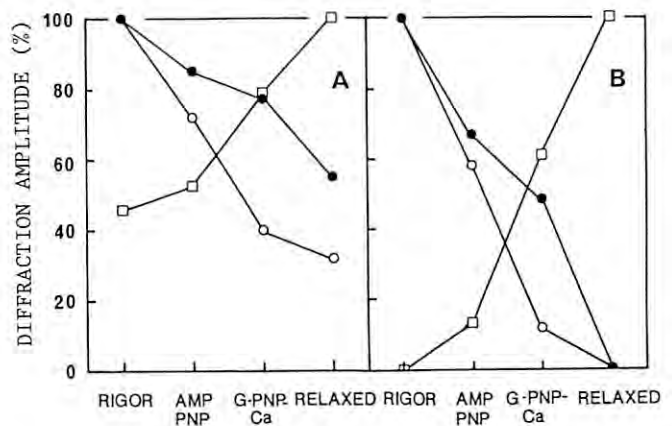


Fig. 1. Amplitudes of electron density components derived from the changes in X-ray diffraction. Average actin marking derived from the 31.6 reflection (closed circles), 38.7 nm-periodic marking derived from the 10.6 reflection (open circles) and 14.5 nm-periodic marking derived from the 00.16 reflection (squares). A, total amplitude expressed as a fraction of the maximum seen; B, the variable component re-normalised.

FREQUENCY AND TEMPERATURE DEPENDENCE OF THE INTENSITY CHANGES IN THE 14.3 NM MERIDIONAL AND THE EQUATORIAL 1,0 AND 1,1 REFLECTIONS FROM A TETANIZED FROG MUSCLE DURING SINUSOIDAL LENGTH CHANGES

Katsuzo WAKABAYASHI, En-Zhong WANG, Hidehiro TANAKA*, Hiroyuki IWAMOTO*, Takakazu KOBAYASHI*, Toshiaki HAMANAKA, Yoshiyuki AMEMIYA**, Haruo SUGI* and Toshio MITSUI

Department of Biophysical Engineering, Faculty of Engineering Science, Osaka University, Toyonaka, Osaka 560

* Department of Physiology, School of Medicine, Teikyo University, Itabashi-ku, Tokyo 173

** Photon Factory, National Laboratory for High Energy Physics, Tsukuba, Ibaraki 305

Introduction

In order to clarify the molecular motion of the myosin heads during muscle contraction, we have investigated the effect of sinusoidal length changes on a contracting frog skeletal muscle by time-resolved X-ray diffraction method. As reported previously [1], distinct periodic intensity changes were observed in the 14.3 nm myosin meridional and the equatorial 1,0 and 1,1 reflections. In the present study we have found that the change of the 14.3 nm reflection at ca. 1% length amplitude contains less harmonics than in the case of larger amplitude [1,2], and that intensity changes in these three reflections from tetanized frog muscles depend significantly upon frequency and temperature.

Experimental

Time-resolved X-ray diffraction studies were done using the small-angle diffractometer at the beam line 15A1. Diffraction patterns were recorded on a 1D-PSD. The sartorius muscle of the bullfrog was used and isometrically stimulated with 3 ms current pulses at 30Hz at the full overlap length. When the steady tetanic tension was reached, sinusoidal length changes of frequencies of 2, 5 and 10Hz at ca. 1% amplitude were applied to a contracting muscle at 4°C and 17°C. Intensity and tension data were measured with 10 ms (for 5 and 10Hz) and 20 ms (for 2Hz) time resolutions.

Results and Discussion

As the frequency of the sinusoidal length change increases, the amplitude of the 14.3nm change became larger (Fig. 1) and the level around which its oscillatory change takes place became lower than the tetanus level of the intensity (Fig. 2) and the phase shift of the intensity change became markedly larger at 17°C (Fig. 3). The I(1,0) change was nearly in phase with the tension change, whereas the I(1,1) change was almost in antiphase with it [1]. The I(1,0) change was smaller than the I(1,1) change. The amplitude of I(1,1) became larger with increase in frequency (Fig. 1). The oscillation levels of I(1,0) and I(1,1) were very close to their tetanus levels at the three frequencies (Fig. 2). No distinct phase shift was observed in both reflections as the frequency increases. Decrease of I_{14.3nm} in stretch phase became remarkably larger by about 40% at 4°C than 17°C (Fig. 1). The level of the intensity oscillation was markedly lowered below the tetanus level at 4°C (Fig. 2). At 4°C the intensity peak during length oscillation tended to become doublet and its tendency was more distinct in the higher frequency, showing increase of the second harmonic in I_{14.3nm} [1,2]. The amplitude of I(1,0) and I(1,1) changes became slightly larger at 4°C than 17°C (Fig. 1). No distinct phase shift of both reflections was observed by changing the temperature.

The obtained results were explained on the assumption that weakly bound myosin heads move in quite a different manner from strongly bound

myosin heads.

References

- 1] K. Wakabayashi et al., *Biophys. J.*, **49**, 581 (1986).
- 2] T. Mitsui et al., *Photon Factory Act. Rep.*, **3**, 177 (1984/85).

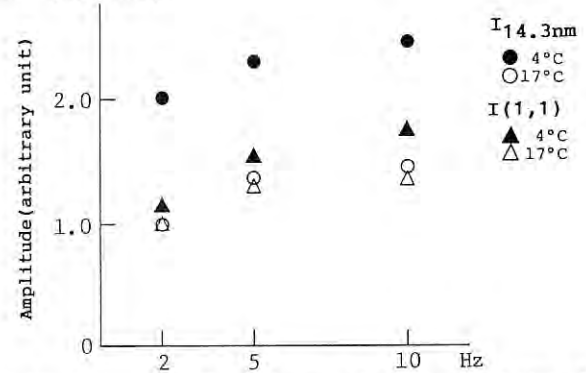


Fig. 1. Frequency dependence of the amplitude of the I_{14.3nm} and I(1,1) changes during sinusoidal length changes at 17°C and 4°C.

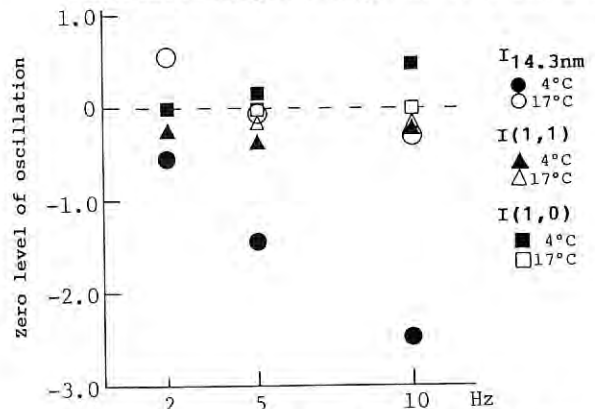


Fig. 2. Frequency dependence of the oscillation levels of I_{14.3nm}, I(1,0) and I(1,1) during sinusoidal length changes. Dashed line, the tetanus level of intensity.

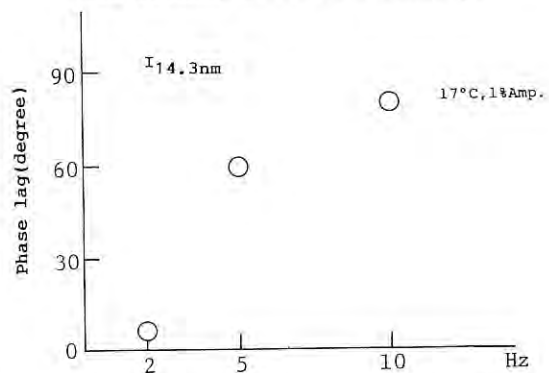


Fig. 3. Frequency dependence of the phase lag of the I_{14.3nm} change relative to the tension change during sinusoidal length change.

X-RAY DIFFRACTION STUDIES OF THE MODIFIED PURPLE MEMBRANE DURING ITS PHOTOCYCLE

Tomoya URUGA, Toshiaki HAMANAKA, Katsuzo WAKABAYASHI,
Yoshiyuki AMEMIYA* and Toshio MITSUI

Department of Biophysical Engineering, Faculty of Engineering
Science, Osaka University, Toyonaka, Osaka 560, Japan

* Photon Factory, National Laboratory for High Energy Physics,
Oho, Tsukuba, Ibaraki 305, Japan

Introduction

Bacteriorhodopsin (bR) is a sole protein existed in the purple membrane (PM) of *Halobacterium halobium*. In the PM, bR molecules aggregate to trimers and form a two-dimensional crystalline array, P3, together with lipids. bR functions as a light-driven proton pump during its photocycle consisted of several photo-intermediates (K, L, M, O etc.).

We have examined the structure of M intermediate by X-ray diffraction study. The treatments of PM with cross-linking agent and/or detergents caused the elongation of the lifetime of M. Also, using intense X-ray generated from synchrotron radiation, the concentration of sample suspension used in the X-ray experiment could be lowered. These made possible that the large population of bR existed as M state in the X-ray sample under continuous intense light irradiation.

We previously reported on the diffraction changes of several modified PM due to irradiation (1,2). In this report, we present the results on the other modified PM and compare them with previous data.

Materials and Methods

The native and/or cross-linked PM by glutaraldehyde were treated with deoxycholate (DOC) and/or Triton X-100 as described (3,4). Part of Triton-treated cross-linked PM was further treated with Bio-Beads SM-2 to adsorb Triton (5). The modified PM suspensions were concentrated to 9-13mg bR/ml. X-ray diffraction experiments were performed at BL15A. Experimental procedures were the same described in previous report (1).

Results

The detergent treatment of PM caused a shrinkage of the unit cell of membrane crystalline array by extracting boundary layer lipids. Triton-treated cross-linked PM dispersed without Triton had a similar unit cell dimension, 58.1Å of lattice constant, to that of Triton-treated PM or DOC-treated PM. However, when it was dispersed in 0.25% Triton-containing solution, the lattice constant increased by 0.5-0.7Å. The treatment of this sample with Bio-Beads caused further reduction of the unit cell to 56.7Å of lattice constant. The populations of M state in the X-ray samples under irradiation were estimated by measuring the visible absorption change. About 40-80% of bR were photoconverted to M state.

Figure 1 shows diffraction patterns from Triton-treated cross-linked PM dispersed in 0.25%

Triton before irradiation, under irradiation and during 5-10min after terminating irradiation. These are almost the same as previously reported (2). Due to light, the larger changes in diffraction patterns were observed, which involve the enlargement of lattice constant by about 1Å and the worse of crystalline order. However, such diffraction changes were not observed in the cross-linked PM, DOC-treated PM, Triton-treated PM and Triton-treated cross-linked PM dispersed without Triton. In Triton-treated cross-linked PM dispersed in 0.25% Triton, the light-induced structural changes might be caused as the followings. The slightly larger unit cell of this sample in comparison with the other modified PM may cause the enhancement of the movability of bR. Alternatively, bR in photoconverted state may further interact with Triton in solution to enlarge the unit cell together with crystalline disorder.

References

- 1) Uruga et al., PF Activity Report#5, 326 (1987)
- 2) Uruga et al., PF Activity Report#6, 129 (1988)
- 3) Lam et al., Archives of Biochem. Biophys. **221**, 557 (1983)
- 4) Hwang et al., J. Membr. Biol. **53**, 325 (1977)
- 5) Holloway, Anal. Biochem. **53**, 304 (1973)

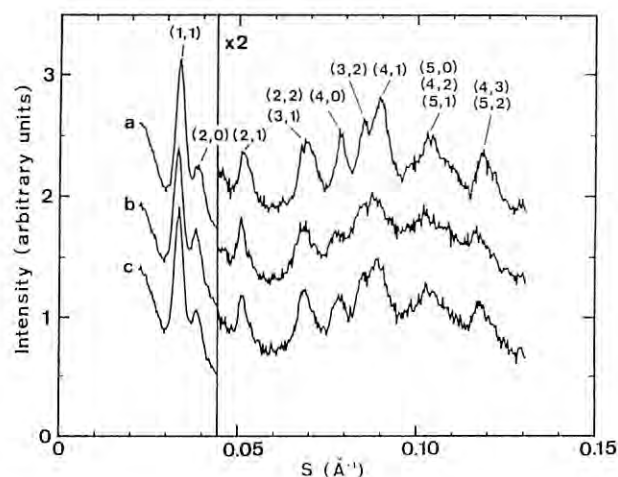


Fig. 1 X-ray diffraction patterns from Triton-treated cross-linked PM in 0.25% Triton. Curves: (a) before irradiation; (b) under irradiation; (c) during 5-10min after terminating irradiation. Total counting time was 40min for each curve. Concentration of sample, 11mg bR/ml; Temperature, 5 C; PH, 7.0.

X-RAY SMALL ANGLE SCATTERING OF ALPHA-2-MACROGLOBULIN AFTER TREATMENT WITH 2,4-DINITROPHENYL THIOCYANATE

Atsushi IKAI¹, Hideo ARAKAWA¹, Hiroyuki KYUSHIKI, Hiroshi KIHARA², Hirotsugu TSURUTA³, Katsuzo WAKABAYASHI⁴ and Yoshiyuki AMEMIYA⁵

- 1) Laboratory of Biodynamics, Tokyo Institute of Technology
Nagatsuta, Midoriku, Yokohama
- 2) Jichi Medical College, Tochigi-ken
- 3) Hiroshima University, Hiroshima
- 4) Osaka University, Toyonaka, Osaka
- 5) Laboratory for High Energy Physics, Tsukuba, Japan

INTRODUCTION

Alpha-2-macroglobulin has internal thiolester bond which becomes exposed and hydrolyzed spontaneously when the bait region is attacked by proteinases. The proteinases that split the peptide bonds in the bait region sequence become trapped by alpha-2-macroglobulin when the latter undergoes a major structural change subsequent to the bait region hydrolysis. Similar structural change can be induced by artificially breaking the thiolester bond with externally added methylamine but the structurally altered alpha-2-macroglobulin no longer has the capacity to entrap proteinases. If 2,4-dinitrophenyl thiocyanate coexists with methylamine and the thiolester is made cyanylated, the capacity of alpha-2-macroglobulin to entrap proteinases is reduced to half of the normal level.

In this experiment, the x-ray scattering curves of alpha-2-macroglobulin in four different states, namely, 1) native, 2) cyanylated (CN-alpha-2-macroglobulin), 3) methyl amine treated (MA-alpha-2-macroglobulin), 4) chymotrypsin treated (CHY-alpha-2-macroglobulin) were taken and structural differences between them were compared.

similar scattering pattern to MA-alpha-2-macroglobulin except in the very inner part of the scattering curve. When CN-alpha-2-macroglobulin was reacted with chymotrypsin the scattering curve showed a time dependent change with a half-life of about 0.3-0.4 sec and the final state was similar to alpha-2-macroglobulin directly reacted with chymotrypsin.

Scattering curve of fatty acid synthetase was also taken in the absence and presence of substrate, malonyl CoA. Little difference was observed between the two state in terms of x-ray scattering but when the enzyme was specifically cross linked at two active sites, there was a change indicating that the enzyme became more compact after cross-linking.

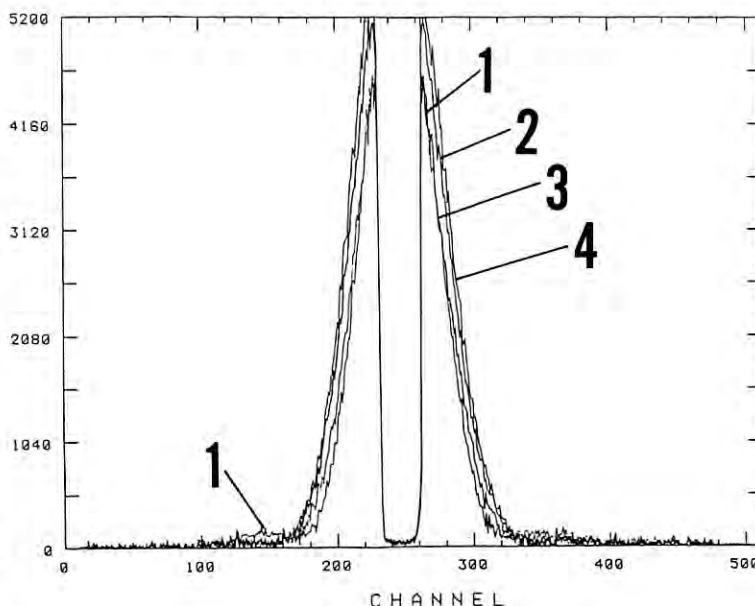
Figure 1. X-ray Small Angle Scattering Curves of Four Different States of Alpha-2-Macroglobulin. 1) Native, 2) MA-, 3) CN-, and 4) CHY-alpha-2-macroglobulin.

METHODS

A stopped flow cell built by Kihara et al. for the time resolved x-ray small angle scattering experiment was used and the scattering curves were recorded with intervals of 100 ms or 200ms. Scattering curves were taken at protein concentration of 10mg/ml, 7.7mg/ml, 5mg/ml, 2.5mg/ml, and 1.2mg/ml for each sample.

RESULTS

The scattering curve of alpha-2-macroglobulin has a characteristic side peak which is partially lost in MA-alpha-2-macroglobulin. The result was slightly different from the published data of Osterberg and his coworkers who has reported that the side peak is completely lost in MA-alpha-2-macroglobulin. CN-alpha-2-macroglobulin has a



STUDIES OF THE MEDIUM ANGLE X-RAY PATTERN FROM A TONICALLY CONTRACTING MOLLUSCAN SMOOTH MUSCLE

Yoshiko TAJIMA and Yoshiyuki AMEMIYA*

Department of Physics, Tokyo Metropolitan University, Setagaya-ku, Tokyo 158

* Photon Factory, National Laboratory of High Energy Physics, Oho, Tsukuba-shi, Ibaraki 305

The X-ray pattern from the anterior byssus retractor muscle of *Mytilus edulis* (ABRM) shows layer lines from the thin filaments at small and medium angles up to 0.145 \AA^{-1} . By small angle X-ray studies of the tonically contracting ABRM¹⁾, structure change of actin has been suggested to occur as in the contracting striated muscle of bullfrog²⁾. By medium angle studies structure change of actin may be examined more precisely at a scale of interpeptide-chain distance.

Tonic contraction was produced by stimulation with acetylcholine. X-ray patterns were recorded in a 60 s exposure on Fuji imaging plates by using the point focusing camera at BL15A-1. The X-ray wave length was 1.504 \AA .

Change of the medium angle pattern by tonic contraction depends on tension level. Figure 1 shows a medium angle pattern from a muscle generating tonic tension of 7.3 Kg/cm^2 . At this tension the thin filaments are changed in structure almost uniformly¹⁾. The strong 9.3 \AA layer line characterizes the medium angle pattern. In the tonically contracting state, the 9.5 \AA layer line appears under the 9.3 \AA layer line. A weak layer line at a period of 11.5 \AA also appears under the 11.3 \AA layer line. These layer lines increase in intensity with increase in tonic tension. The 6.9 \AA layer line conversely decreases in intensity with increase in tonic tension.

In Fig. 2 the intensities of the four layer lines with the 0th Bessel order, the layer line corresponding to the axial period of actin, 27 \AA , and the higher order reflections, are compared with the intensities in the resting state. The intensities are integrated within the cross sections perpendicular to the layer lines, and shown on scales on which the intensity peaks of the small angle 59 \AA layer line in the resting and tonically contracting states coincide in the height. While the 1st, 2nd and 4th layer lines are flattened at the meridian, the 3rd layer line shows a peak which rises at the meridian. The scattering amplitudes from the inner and outer domains of actin are probably in phase on the third layer line, and out of phase on the other layer lines at the meridian due to axial shift of the two domains. The very narrow peaks at the meridian on the 1st and 2nd layer lines indicate the presence of a small mass on the outer shoulder of the outer domain. The small mass and the main part of the outer domain are staggered axi-

ally by about $1/2$ of the axial period of actin so as to correct the phase difference at the meridian between the scattering amplitudes from the two parts due to difference in the dimension.

The maps in Fig. 3 show the cylindrically averaged difference autocorrelation functions for the cylindrically averaged density distributions of the thin filaments. The maps were obtained by inverse transform of the intensities shown in Fig. 2. The solid lines are positive contours, and the broken lines are 0 and negative contours. In both maps disk-like peaks are oriented horizontally about the longitudinal z-axis along the filament axis, suggesting horizontal orientation of peptide chains. Because the positive areas which are distant from the z-axis is a little expanded along the z-axis in the tonically contracting state as compared with the resting state, the peptide chain direction is probably tilted against the filament axis in the outer domain as a result of structure change by tonic contraction.

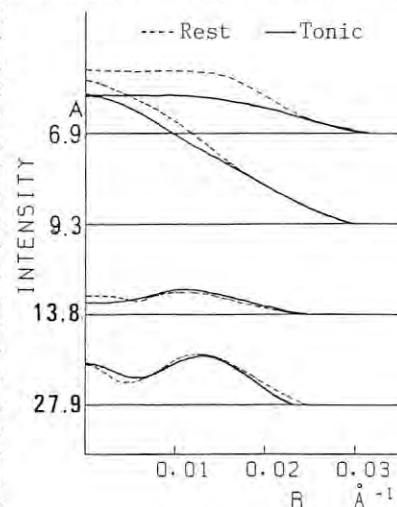


Fig. 2

The reflections from the paramyosin cores of the thick filaments are also changed in intensity. For example, the two reflections indicated by the arrows have been reversed in the order of intensity with increase in tonic tension.

- 1) Y. Tajima et al., *J. Appl. Cryst.* **22**, 72(1989).
- 2) K. Wakabayashi et al., (1989), In *Molecular Mechanism of Muscle Contractions*, ed. H. Sugi & H. Pollack, p. 353, New York: Plenum Press.



Fig. 1

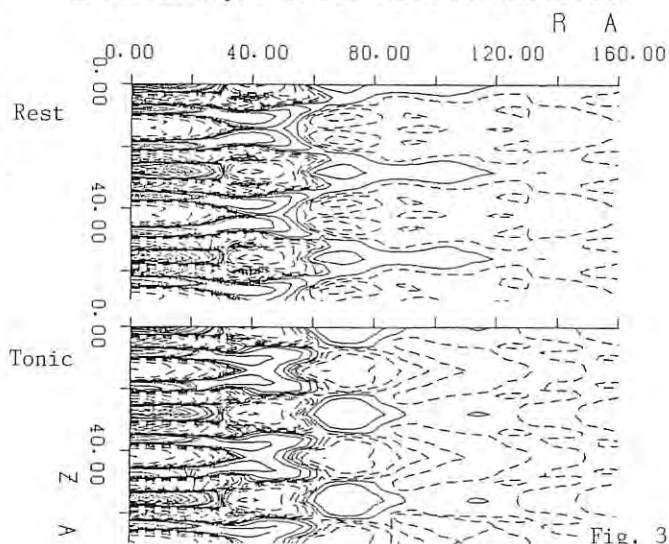


Fig. 3

Solution X-ray Scattering Study on Dissociation of *Eisenia foetida* (earthworm) Hemoglobin at Acidic and Alkaline pH

Yoshihiko Igarashi¹⁾, Kazumoto Kimura²⁾, Kaoru Ichimura¹⁾, Akihiko Kajita¹⁾, Hirotsugu Tsuruta³⁾, Katsuzo Wakabayashi⁴⁾, Yoshiyuki Amemiya⁵⁾ and Hiroshi Kihara⁶⁾

1) Department of Biochemistry, and 2) Division of Medical Electronics, Dokkyo University School of Medicine, Mibu, Tochigi 321-02, Japan

3) Faculty of Science, Hiroshima University, Hiroshima 730, Japan

4) Faculty of Engineering Science, Osaka University, Toyonaka, Osaka 560, Japan

5) Photon Factory, National Laboratory for High Energy Physics, Tsukuba 305, Japan

6) Jichi Medical School, School of Nursing, Tochigi 329-04, Japan

X-ray scattering study on the dissociation of *Eisenia foetida* (earthworm) hemoglobin has been proceeded [1]. In the static study, Rg value of the native CO hemoglobin was estimated to be 109.7 ± 0.46 Å. The protein dissociates into smaller units below pH 3.3 (25°C) and above pH 11.2 (10°C). Typical scattering patterns at acidic, neutral and alkaline pH are shown in Fig. 1. Subpeaks observed at neutral pH diminished at both extreme pH, suggesting remarkable changes in their conformations.

Acidic dissociation of the hemoglobin was monitored kinetically at 25°C by pH-jump method with the stopped-flow X-ray scattering apparatus [2]. Partially integrated amplitude of the dissociation process was monitored and plotted in Fig. 2. The decay process was multiphasic, of which half decay time was 35 s.

In contrast, the alkaline dissociation was too fast to be monitored at room temperature [1]. The dissociation rate, then, was slowed down by reducing the temperature to -10°C in the presence of antifreezer (30% ethylene glycol). Thus, the dissociation process could be observed with a half decay time of 42 s, as shown in Fig. 2.

We also carried out scattering experiments in the oxy, CO and deoxy forms at neutral pH. Rg values are estimated as 109.6 Å, 109.7 Å, and 109.9 Å, respectively, indicating no significant differences between their conformations. Further analyses are now in progress.

REFERENCES

1. Y. Igarashi et al. (1989) PF Activity Report **6** 134.
2. H. Tsuruta et al. (1989) Rev. Sci. Instrum., **60** 2356-2358.

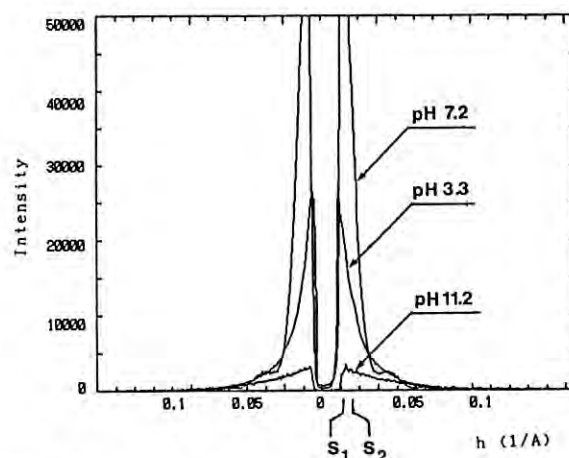


Fig. 1. Normalized scattering patterns of *E. foetida* hemoglobin at pH 3.3 (25°C), 7.2 (25°C) and 11.2 (10°C). Exposed 100 s, 5 min after the mixing. *E. foetida* hemoglobin 4×10^{-2} g/ml.

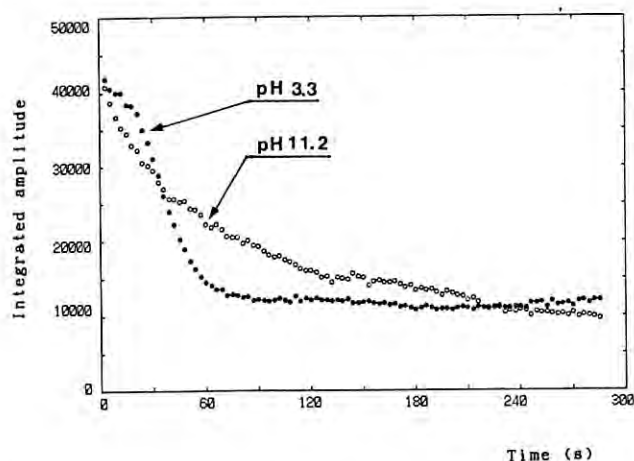


Fig. 2. Time course of the partially integrated amplitude (between s_1 and s_2 in Fig. 1). At pH 3.3; 25°C. At pH 11.2; -10°C in the presence of 30% ethylene glycol.

X-RAY DIFFRACTION STUDIES ON THE CHEMICALLY-MODIFIED GLYCERINATED FIBERS OF RABBIT SKELETAL MUSCLE

Hidehiro TANAKA, Takakazu KOBAYASHI, Shigeru CHAEN, Kazuhiro OOIWA,
Katzuzo WAKARAYASHI*, Yoshiyuki AMEMIYA** and Haruo SUGI

Department of Physiology, School of Medicine, Teikyo University Itabashi Tokyo 173

* Dept. Biophys. Engi., Faculty of Engineering Science, Osaka Univ. Toyonaka, Osaka 560

** Photon Factory, National Laboratory for High Energy Physics, Tsukuba, Ibaraki 305

Introduction

Within a muscle fiber the two globular heads of a myosin molecule extend radially from the rod part of the thick filament to form "crossbridge" between the thick and thin filaments. Considerable effort have been made to see a possibility of cooperative interaction between the two heads. However, the role of the double headed structure of the myosin molecule in muscle contraction is still not clear.

A bifunctional thiol reagent, p-PDM(p-phenylenedimaleimide), was known to react with reactive sulphhydryls on the myosin head, and to result in the loss of its ability to bind to F-actin and to hydrolyse ATP [1-3]. Recently it was suggested that the isometric force in Ca-activated fibers may be generated only by the myosin molecule with two native heads, while there may be no cooperative interaction between the two heads in catalyzing ATP hydrolysis [4]. In this study an X-ray technique was applied to solve this problem using p-PDM treated glycerinated muscle fibers.

Materials and methods

The glycerinated rabbit psoas muscle fibers dissected into small bundle of about 0.5 mm (diameter) were mounted horizontally between a force transducer and a glass shaft attached to an X-ray cell. The sarcomere length of the fiber bundle was adjusted to 2.4 μ m using a laser light diffraction technique. Relaxing solution contained 125 mM KCl, 20 mM PIPES (pH 7.0), 4 mM ATP, 4 mM MgCl and 4 mM EGTA and contracting solution was prepared by adding 4 mM CaCl.

At first, the fiber bundle mounted on the X-ray cell was washed with the relaxing solution to take the relaxed (control) equatorial pattern. Then it was treated with various concentrations of p-PDM for 10 min. After washing out free p-PDM with the relaxing solution, the equatorial pattern was again taken from the p-PDM treated fiber, and finally the contracting pattern was

taken from the fiber when the Ca-activated tension reached a plateau level which was determined by the extent of modification.

Results and discussion

Full modification of myosin heads caused decreases in both I(1,0) and I(1,1), resulting in the decrease in the intensity ratio, I(1,0)/I(1,1) (from \circ to \bullet in Fig.1). The Ca-activated tension of the fully modified fiber fell to nearly zero, and the equatorial pattern from the fiber was similar to that from the relaxed one (Fig.1).

Fig.2 shows a relation between the individual intensities and the isometric force level which is controlled by the amount of modification. The individual intensities were normalized relative to the intensity of each reflection in the relaxed (unmodified) state. These normalized intensities were found to vary in a reciprocal way on activation: I(1,0) decreased while I(1,1) increased throughout the range of force level studied. These gradual changes in I(1,0) and in I(1,1) with force level were very similar to those obtained by Yu et al [5], in which force levels were controlled by caffeine according to the rapid cooling method.

References

- 1) M. Burke, E. Reisler and W.F. Harrington Biochemistry **15**, 1923 (1976).
- 2) R. Lamed, A. Oplatka and E. Reisler Biochim. Biophys. Acta, **427**, 688 (1976).
- 3) E. Reisler, M. Burke, S. Himmelharf and W.F. Harrington Biochemistry **13**, 3837 (1974).
- 4) S. Chaen, M. Shimada and H. Sugi J.Biol.Chem. **261**, 13632 (1986).
- 5) L.C.Yu, J.E.Hartt and R.J.Podolsky **132**, 53 (1979).

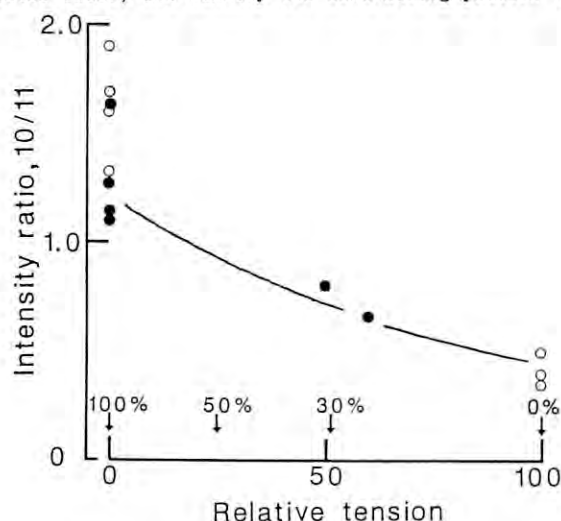


Fig.1 Relation between the intensity ratio and the relative force. Numerals with the arrows mean the amount of modification. \circ , unmodified; \bullet modified.

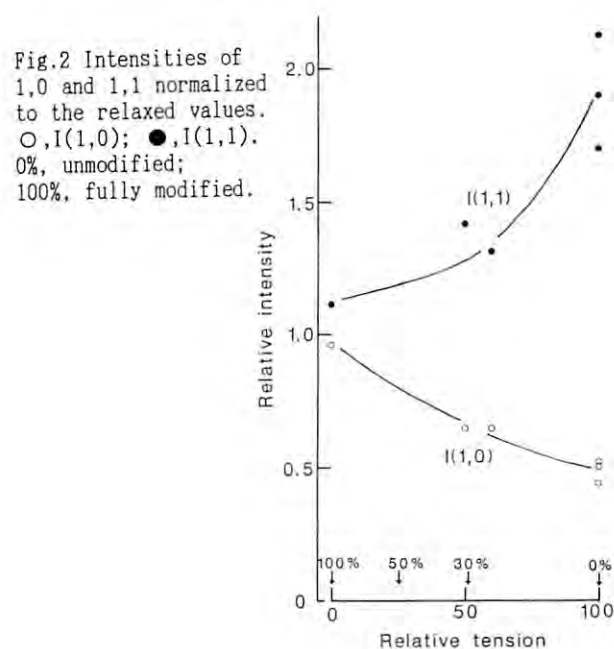


Fig.2 Intensities of 1,0 and 1,1 normalized to the relaxed values. \circ , I(1,0); \bullet , I(1,1). 0%, unmodified; 100%, fully modified.

Real Time K-edge Subtraction X-ray Imaging - Animal Experiment

Hiroshi FUKAGAWA, Toshinori KOZAI, Yoichi SUZUKI, Shin HASEGAWA,
Kazuyuki HYODO*, Masami ANDO*, Yasuro SUGISHITA**,
Masaaki KAKIHANA**, Sadanori OHTUKA**, Toru TAKEDA**, Masayoshi AKISADA**,
Katuyuki NISHIMURA***, Fukae TOYOFUKU**** and Eiichi TAKENAKA*****

The University of Electro-Communications, Chofu, Tokyo 182
*National Laboratory for High Energy Physics, Tukuba, Ibaraki 305
**The University of Tukuba, Tukuba, Ibaraki 305
***Saitama Medical School, Moroyama, Saitama 350-04
****Kyushu University, Fukuoka, Fukuoka 812
*****National Self Defence Medical College, Tokorozawa, Saitama 356

In our previous paper on K-edge subtraction television system, some results of the phantom experiments were reported.¹⁾ The system has been improved to show the clear image of animal vessels.

K-edge subtraction imaging

After injection of contrast material (iodine), the subject is irradiated by monochromatized dual energy X-ray flux closely bracket the K-edge of iodine, alternately. The subtraction images derived from each pair of the X-ray images visualize contrast material only.

Experimental results

In the animal experiment, two images are acquired with 2ms exposure of X-ray flux with the same interval time as shown in Fig.1, and each image is memorized as digital data (256x240,8bits). A series of 32 pairs of image data is memorized at the rate of 30 pairs per second, displaying rough subtraction images in real time.

Stored data are processed to show the improved subtraction images after data acquisition. This system was used in an anesthetized dog (14.5kg), and the obtained images are shown in Fig.2 and Fig.3. During the experiment, the SOR system was running at 5.8GeV electron energy and 25mA current.

Reference

- 1) H.Fukagawa, et al, Rev. Sci. Instrum., 60, 2268 (1989).

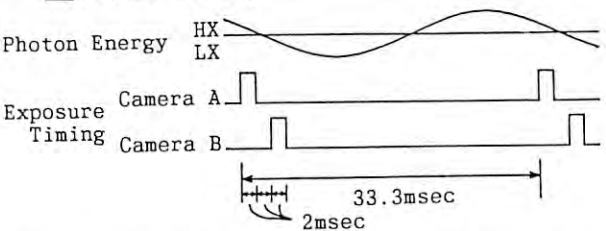


Fig.1 Timing of energy change and exposure.

Table 1 Experimental conditions.

SOR energy and current	5.8GeV 25mA
Size of irradiated area	64mm x 55mm
Weight of dog	14.5kg
Injected contrast material	Urografin 76% 10ml (at rate of 10ml/s)

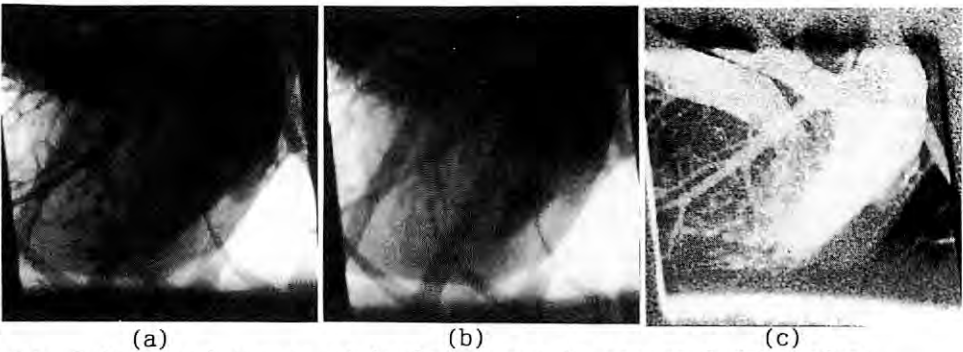


Fig.2 Acquired images at higher x-ray in camera A (a) and at lower X-ray in camera B (b), and the subtraction image (c).

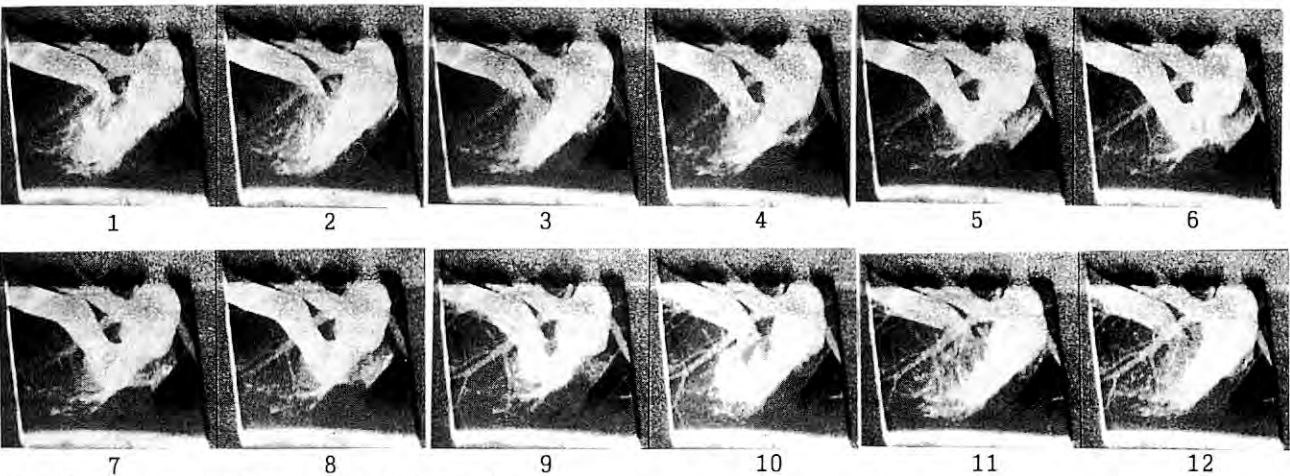


Fig.3 A series of 12 subtraction images.

OPTIMUM ENERGY SEPARATION IN K-EDGE ENERGY SUBTRACTION ANGIOGRAPHY

Katsuyuki NISHIMURA, *Kazuyuki HYODO, *Hideaki SHIWAKU, **Shin HASEGAWA, *Masami ANDO
Saitama Medical School, Moroyama, Iruma, Saitama 350-04

* Photon Factory, National Laboratory for High Energy Physics (KEK), Tsukuba, Ibaraki 305
** University of Electro-Communication, Chofu, Tokyo 182

Introduction

Several methods to perform K-edge subtraction angiography using synchrotron radiation have been reported¹⁻⁶⁾. In K-edge energy subtraction, monochromatic X-ray energy is switched between energies above and below the K-edge of iodine. It should be noted that the energy separation affects on the quality of a subtracted image.

In this paper the optimum energy separation is discussed in relation to various factors such as stereo effect, contrast difference of bone image, reflection-angle spread at crystal, energy distribution in a x-ray image field and a source spot size. For simplicity, the effect of the number of photons is excluded in this discussion. The enough number of photons are assumed to be available.

From the Bragg condition the small amount of change in the incident beam angle corresponds to the change of reflected energy as,

$$\Delta E = \alpha \cdot \Delta \theta \quad [1]$$

where $\alpha = \cot \theta / E$. $\theta = 0.114$ rad for the energy of 33.16 keV and for reflecting plane of Si (311), so that $\alpha = 2.90 \times 10^{-5}$ (eV/rad).

The Factors Limiting Lower Bounds of EnergySeparation(1) Energy distribution in the X-Ray Field

Main factor to determine the lower bounds of energy is the energy distribution in the field. This distribution arises when the fan beam is incident onto a crystal with parallel reflection lattice.

When a source spot size is negligibly small, a vertical half width of incident beam angle is expressed as,

$$\Delta \theta_v = y/R, \quad [2]$$

where R is a distance between the source and the crystal and y is a vertical field size.

Typically $R = 1500$ cm and $y = 1.0$ cm in AR ring at KEK. This corresponds to 193 eV in energy.

(2) Angle Spread in Reflected Beam in the Crystal

The angle spread $\Delta \theta_o$ is dependent on the roughness of crystal surface and the degree of crystal imperfection. ΔE_o corresponding to $\Delta \theta_o$ ranges from 30 eV to 100 eV which depends on various degree of surface preparation.

(3) Source Spot Size

As the source size depending on electron beam size is finite, the penumbra forms within the angle like

$$\Delta \theta_s = s/R, \quad [3]$$

where the source spot size is denoted by s and the length between the source and the object by R.

As these above three factors are additive and independent, the energy separation have to satisfy the relation as,

$$\Delta E \geq \alpha \sqrt{(\Delta \theta_v)^2 + (\Delta \theta_o)^2 + (\Delta \theta_s)^2} \quad [4]$$

The Factors Limiting Upper Bounds of EnergySeparation(1) Stereo Effect

We assume the expected spatial resolution in the vertical direction is less than the pixel size

L/N, where L denotes the x-ray field size, N the number of pixels along the vertical line. Stereo effects arises when a reflection crystal is rotated in order to change monochromatic x-ray energy. Let the path length in a human body be X_b (cm). Maximum misregistration amounts to $2 \cdot X_b \Delta \theta_r$, where $\Delta \theta_r$ is a rotation angle. As the misregistration must be less than L/N, the relation

$$\Delta \theta_r \leq L/(2 \cdot N \cdot X_b) \quad [5]$$

is required to be satisfied.

(2) Contrast in Subtracted Image of Bone

We assume that the overall signal to noise ratio is expected less than R (e.g. $R=10^{-3}$). Bone signal will be suppressed to a factor of $\exp(-\Delta \mu_B X_B)$ by subtraction. As the attenuation coefficient of bone is continuous around the K-edge of iodine, for the small amount of change in x-ray energy

$$\Delta \mu_B = (\delta \mu_B / \delta E) \Delta E. \quad [6]$$

Subtracted signal G in the presence of bone is expressed as

$$G = G_B \cdot \exp(-(\delta \mu_B / \delta E) \Delta E \cdot X_B) \\ = G_B \cdot (1 - (\delta \mu_B / \delta E) \Delta E \cdot X_B), \quad [7]$$

where G_B is a subtracted signal without bone layer. Contrast between the images for above and below the K-edge in the presence of bone layer should be less than the expected value R like

$$\Delta E \leq R / |(\delta \mu_B / \delta E) X_B|. \quad [8]$$

Discussion

Unless the parameters for imaging would be carefully chosen, there would be a possibility that lower bounds exceed upper one.

Dominant factors are the distribution of energy and the angle spread at the reflection crystal. The lower limit is made smaller by using a bent crystal to decrease $\Delta \theta_v$ or by using a mirror-polished surface to decrease $\Delta \theta_o$.

From the point of view of upper limit, the smaller the energy separation is, the better the results on image qualities are. If the lower bounds exceed upper one, then the degree of cancellation of bone and soft tissue or the degree of misregistration will depend on $\Delta \theta_v$ or $\Delta \theta_o$.

References

- 1) Rubenstein, E. et al, 1981, SPIE 314, 42.
- 2) Nishimura, K., 1985, Medical & Biological Engineering & Computing (Proc. XIV Int. Conf on Med. Bio. Engineering and VII Int. Conf. Med. Phys.), 23 Suppl., 1521.
- 3) Hyodo, K. et al, 1985, Medical & Biological Engineering & Computing (Proc. XIV Int. Conf on Med. Bio. Engineering and VII Int. Conf. Med. Phys.), 23 Suppl., 1523.
- 4) Akisada, M. et al, 1986, Nucl. Instrum. Methods Phys. Research, A246, 713.
- 5) Suwa, A. et al, 1988, Japanese Journal of Applied Physics, 27, 1989.
- 6) Nishimura, K. et al, 1989, Rev. Sci. Instrum., 60, 2260.

SOFT X-RAY STANDING WAVE MEASUREMENTS OF CLEAN AND OXYGEN
ADSORBED GaAs(111) SURFACES

Koichi IZUMI, Seishi KIKUTA, Masaharu OSHIMA ,
Tomoaki KAWAMURA*, Yasuko YAMADA-MARUO*, and Satoshi MAEYAMA*

Department of Applied Physics, Faculty of Engineering,
University of Tokyo, Hongo, Bunkyo-ku, Tokyo 113

* NTT Applied Electronics Laboratories, Midori-cho,
Musasino-shi, Tokyo 180

Introduction

Soft X-ray standing wave method is useful especially for the not so perfect crystal because the angular width of the Bragg diffraction is large compared with that for the usual X-ray energy. Moreover the sensitivity of the surface atoms is very high, depending on the large cross section¹⁾. In this study we demonstrated this method for the clean and oxygen adsorbed GaAs(111) surfaces.

Experimental

We used the surface combined characterizing system at BL1A. The diffraction was detected by photomultiplier set at 45° from the incident X-ray. Bragg angle was fixed at 67.5° . The Auger electrons of Ga, As, and O were analyzed by semi-spherical electron energy analyzer set at 21° from the incident direction. The sample cleaning was carried out by Ar^+ bombardment in the UHV chamber. After that we can observed the 1×1 pattern by LEED and cannot detected the any Auger signals except for Ga and As. Oxygen was adsorbed by DC discharge in the O_2 gas

of 0.6 Torr for 5 minutes.

Results

The diffraction curve from the GaAs(111) was measured by scanning the incident photon energy (Fig. 1). The full width at half maximum was about 4eV. Next we measured the Ga LMM (1067eV) and As LMM (1225eV) Auger electrons from the clean surface as a function of the incident X-ray energy shown in Figs. 2 and 3. The slight difference between two figures can be seen. Fig. 4 shows the profile of O KLL (510eV) Auger electron signal as a function of the incident photon energy from the oxygen coated surface. This curve is similar to that of Ga. However the more studies are needed in order to obtained the conclusions about the position of oxygen atoms on the surface.

Reference

- 1) T. Ohta, H. Sekiyama, Y. Kitajima, H. Kuroda, T. Takahashi, and S. Kikuta, Jpn. J. Appl. Phys., **24** L475 (1985).

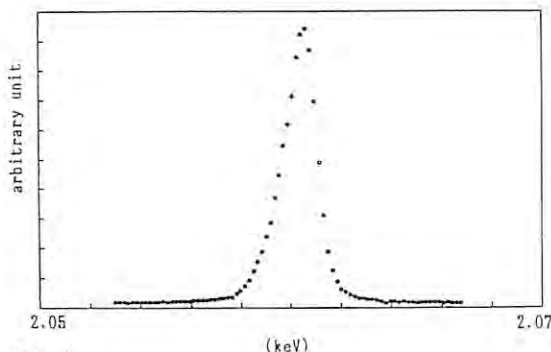


Fig. 1

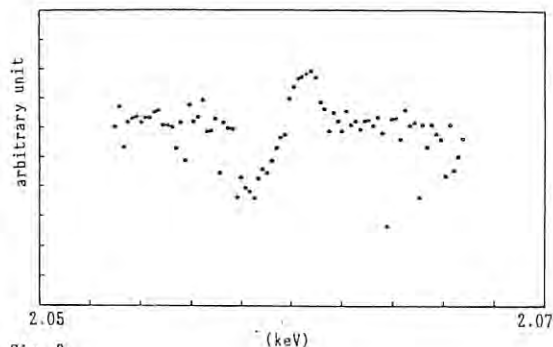


Fig. 3

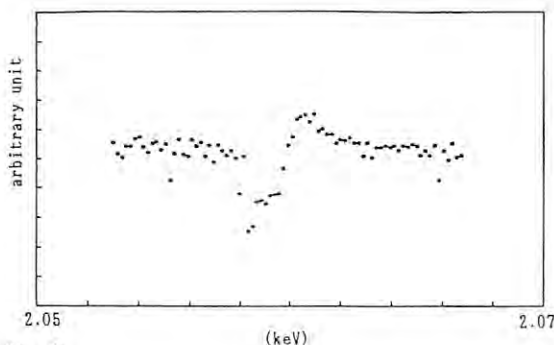


Fig. 2

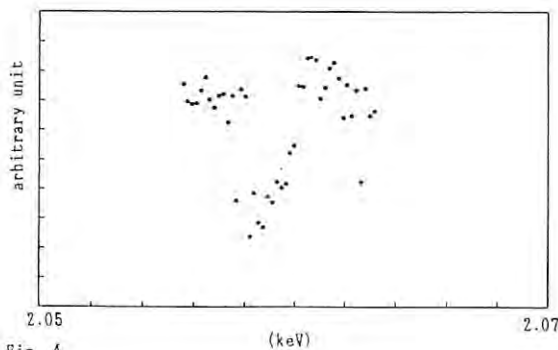


Fig. 4

SOFT X-RAY STANDING WAVE MEASUREMENTS OF $\text{NiSi}_x/\text{Si}(111)$
AT THE BRAGG ANGLE OF $\pi/2$

Koichi IZUMI, Seichi KIKUTA, Masaharu OSHIMA ,
Tomoaki KAWAMURA*, Yasuko YAMADA-MARUO*, and Fumihiko MAEDA*

Department of Applied Physics, Faculty of Engineering,
University of Tokyo, Hongo, Bunkyo-ku, Tokyo 113

* NTT Applied Electronics Laboratories, Midori-ku,
Musashino-shi, Tokyo 180

Introduction

The angular width of the diffraction for the Bragg angle of $\pi/2$ is very large. Especially in the case of soft X-ray that becomes about few degree. On the contrary the width in the energy scale is very narrow¹⁾. For this reason the $\pi/2$ Bragg angle diffraction can be used for the characterization of the not so perfect crystal combined with X-ray standing wave method. For example, the structural analysis of large misfit interfaces can be studied. In this work we demonstrated this method to Ni-Si system on the Si(111) crystal.

Experimental

The experiments were carried out by using the surface combined characterizing system at BL1A. The intensity of the incident X-ray was monitored by the current from the gold coated tungsten mesh in the path. The energy of the X-ray was calibrated by the fluorescent X-ray from Ni and Si. Bragg angle was fixed at 90° . InSb(111) double crystal were used as a monochromator. This monochromator was set at the optimum position where the mesh current was maximum. Auger electron was analyzed by semi-spherical electron energy analyzer. Si(111) wafers were prepared by Siraki method in the air. The sample

was bombarded by Ar^+ ions and heated in the UHV till the 7×7 pattern was observed and no Auger signals except Si were detected. Ni was deposited on this sample by the simple source. After that only Ni Auger signal was detected. This sample was annealed at about 500°C for few minutes, and we can observed the 1×1 pattern by LEED and detected Ni and Si Auger signals. The interface was observed by TEM after these studies and it was very smooth.

Results

Figs. 1 and 2 are the Si KLL (1617eV) and Ni LVV (852eV) Auger yields as a function of the incident photon energy, respectively. Two curves are very similar. Although we cannot detected the Bragg diffraction in the condition of the large Bragg angle, we can obtained 90° of the Bragg angle and observed the dynamical effects from the figures. This method is understood to be useful for the characterization of interfaces.

Reference

- 1) K. Kohra and T. Matsushita, Z. Naturf., **27a**, 484 (1972).

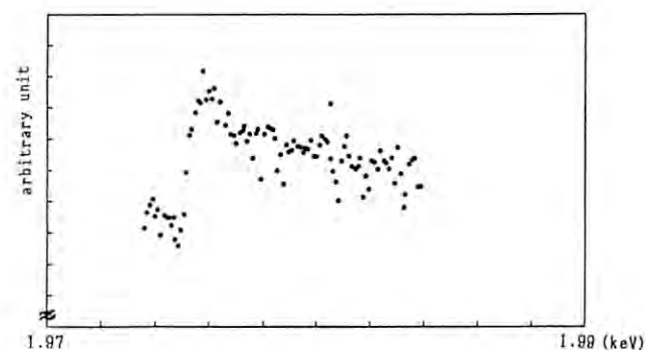


Fig. 1

Si KLL Auger yield as a function of the incident X-ray energy.

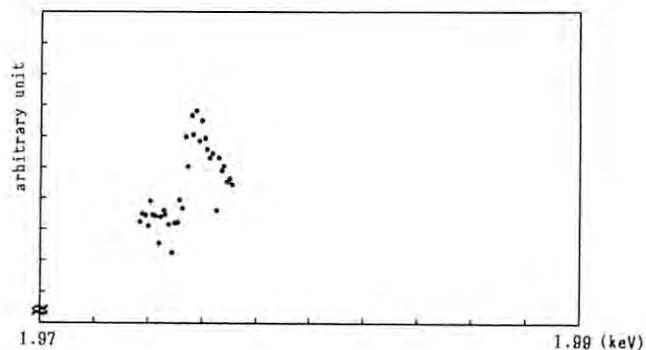


Fig. 2

Ni LVV Auger yield as a function of the incident X-ray energy.

STRUCTURE-REFINEMENT OF ORTHORHOMBIC SUPERSTRUCTURE OF TRIDYMITE: AN APPLICATION OF THE POWDER DIFFRACTION METHOD

Tsuyoshi Motoyama, Kuniaki Kihara, Hiroki Okudera, Hirokazu Nakae,
Masayuki Okuno, Takeo Matsumoto, Takamitsu Yamanaka* and Toshibumi Ashida*
Department of Earth Sciences, Faculty of Science, Kanazawa University,
Kanazawa 920

* College of General Education, Osaka University, Toyonaka, Osaka 560

Introduction

Monoclinic tridymite, a silica polymorph, shows successive structure-transitions as temperature changes. The O-II form appear in the temperature range from about 100 to 160°C, and has superstructure cells three times larger than that of the hexagonal prototype structure. In this research project, we aim at establishing the method of structural study of superstructures by the analysis of powder-diffraction profiles taken with SR. We have chosen O-II as the target of the present study, because its superstructure cell-size is moderate, but not too much complicated, and its structure at 428K has been already studied by a single-crystal diffraction technique¹. The detailed information about the sample used, the method of preparation and the measuring conditions of the diffraction profiles have been

given already², except temperature. The sample was heated through the whole measurement, between 413 and 420 K, on a stage with an electric resistance heater.

Refinement

The space group of O-II is $P2_12_12_1$ and the superstructure cell contains 24 formula of SiO_2 , which are grouped into 6 symmetrically independent formula. Since all atoms occupy general positions, we have 54 positional parameters, and 18 or 108 temperature factors if isotropic or anisotropic thermal vibrations are assumed respectively. Structure refinement was carried out by a computer program PFLS-M kindly supplied by Dr. H. Toraya of Nagoya Institute of Technology. This program enable us to vary all the structural parameters including cell constants, and also some profile parameters. Atomic scattering factors were

those for spherical neutral atoms³. In short, we have repeated so many different schemes of least-squares calculations to obtain good fits, and the calculations are still going on. So far we have succeeded to refine the cell constants, but not succeeded yet to fit the atomic parameters. Hence in this report, the powder diffraction profile, calculated from the atomic positions and equivalent isotropic thermal parameters¹, is compared to the observed one.

Results and discussion

The cell constants were fitted as $a = 26.212(2)$, $b = 4.9901(4)$ and $c = 8.2055(8)\text{\AA}$. The calculated and observed diffraction profiles from $2\theta = 18$ to 60° are shown in Fig. 1, where crosses and lines indicate observed and calculated profiles, respectively. The R-values are 0.29 for profile intensity. The atoms in this structure should undergo highly anisotropic thermal vibrations or be disordered so as to result in anisotropic thermal parameters¹. The R-value obtained here is not a calamity, because we have not invoked yet anisotropic thermal parameters. Our problem should be on the fitting procedure itself. The profile data should be extended to much higher angles for the least-squares method to work properly.

Reference

- 1) K. Kihara (1977), *Zeit. Krist.* 146, 185-203.
- 2) K. Kihara, H. Okudera, H. Nakae, T. Motoyama, H. Sugaya, M. Okuno, T. Matsumoto, M. Masanori, T. Yamanaka and T. Ashida, Photon Factory Activity Report, No.6 (1988).
- 3) J. Ibers and W. Hamilton (1974), *International Tables for X-ray Crystallography*, Vol. IV. Kynoch Press, Birmingham.

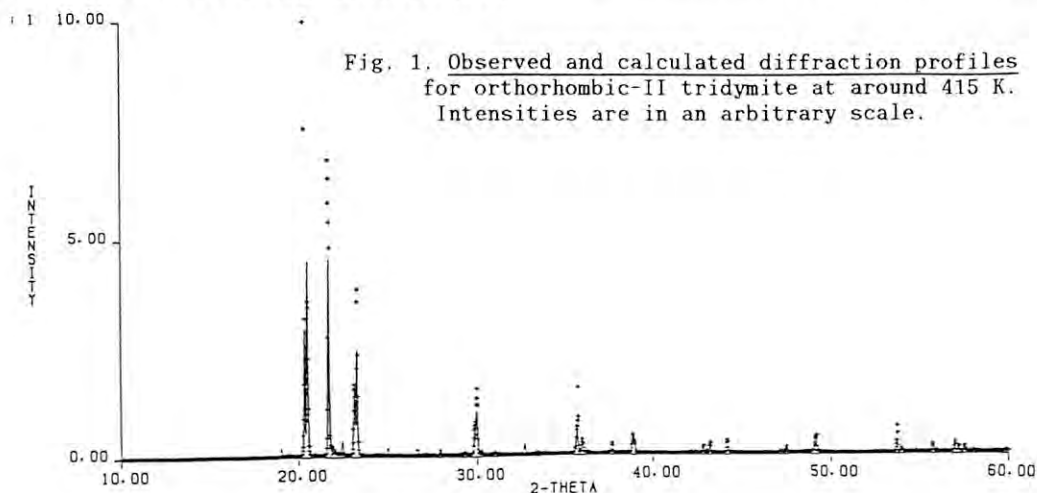


Fig. 1. Observed and calculated diffraction profiles for orthorhombic-II tridymite at around 415 K. Intensities are in an arbitrary scale.

X-Ray Fluorescence Analysis using a Crystal Spectrometer with a Position Sensitive Proportional Counter

Atsuo IIDA, Syunji KISHIMOTO, Kazutaka OHASHI*, Mamoru TAKAHASHI*, and Yohichi GOHSHI*

Photon Factory, National Laboratory for High Energy Physics, O-ho, Tsukubashi, Ibaraki

* Department of Industrial Chemistry, University of Tokyo, Bunkyo, Tokyo

Introduction

Most of the X-ray fluorescence (XRF) analysis using synchrotron radiation (SR) have adopted an energy dispersive type detection where the Si(Li) detector is almost exclusively used. But the Si(Li) detector measurement is inefficient for those samples in which the line interference occurs and the major fluorescence line is dominant. A crystal spectrometer with a position sensitive detector is promising for practical applications because of its high energy resolution, multielemental nature, high efficiency and matching with high brilliance SR source. In this report, analytical aspects of the crystal spectrometer with the position sensitive proportional counter (PSPC) is described.

Experimental

The experiment was done at the beam line 4A. The experimental arrangement is schematically shown in Fig.1. The sample is mounted on the xyz stage for the alignment and the positioning. A flat single crystal (Ge(111)) and a linear PSPC (50 mm effective length, 0.2 mm spatial resolution) were mounted on the 0-20 goniometer. Pulse height analysis was made using the signal from an anode wire. The effects of the spectrum of the excitation X-rays, X-ray beam dimensions, polarization of the incident beam, and geometrical arrangement were studied.

Results and Discussion

The energy resolution of a present crystal spectrometer is determined by the dimension of the irradiation area (X-ray source size for the spectrometer), the distance between the sample and the detector, and the spatial resolution of the detector. For the typical experimental arrangement (0.2 mm horizontal excitation beam

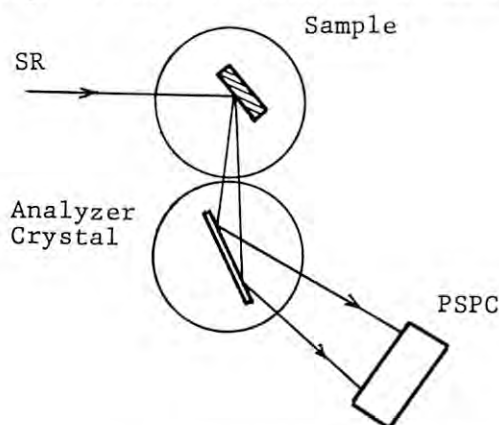


Fig.1. Experimental arrangement.

size, 40 cm sample to detector distance), the energy resolution of 30 eV was obtained at 8 keV. The spectra in Fig.2 shows the comparison of the energy resolution between the Si(Li) detector and the crystal spectrometer. Mn Kb (6.49 keV) and Fe Ka (6.40 keV) lines are clearly separated with the crystal spectrometer, while those are hard to be separated with the Si(Li) detector.

The origin of the background was systematically studied. For the white excitation, scattered radiation from the sample and around the sample was so high, careful shielding was needed to reduce the background. When the reflecting mirror is used before the sample, the high signal to background ratio as well as the radiation damage reduction was achieved. The minimum detection limit is 0.3 A for the thin film sample and the minimum detection limit in the absolute amount is improved by a factor of a few hundreds compared to the conventional crystal spectrometer with X-ray tube.

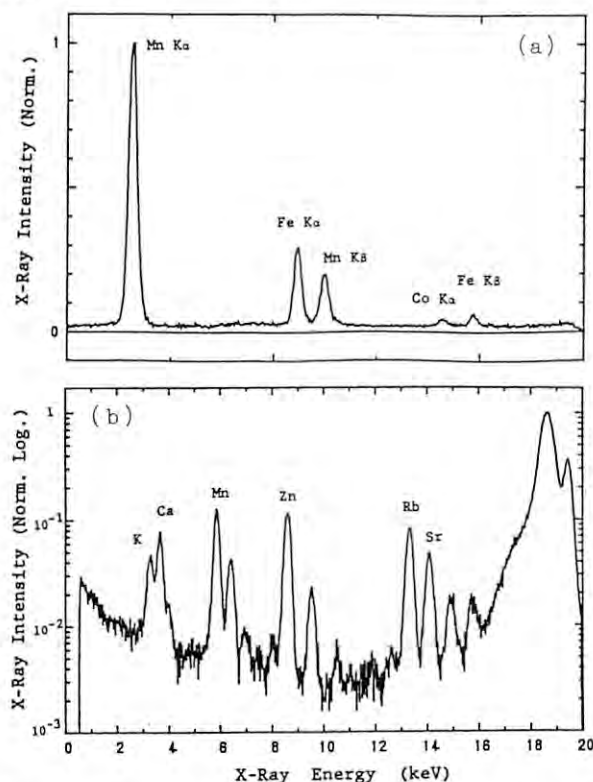


Fig.2. X-ray fluorescence spectra from Pepperbush (National Institute for Environmental Studies, Certified Reference Materials, NO.1). (a) A crystal spectrometer with white excitation and (b) Si(Li) detector with monochromatic excitation.

X-RAY FLUORESCENCE IMAGING BY IMAGE RECONSTRUCTION TECHNIQUE

Mamoru Takahashi, Atsuo Iida* and Yohichi Gohshi

Department of Industrial Chemistry, Faculty of Engineering, University of Tokyo, Hongo, Tokyo 113

*Photon Factory, National Laboratory for High Energy Physics, Oho, Tsukuba-shi, Ibaraki 305

INTRODUCTION

X-ray fluorescence (XRF) imaging is made by the image reconstruction technique using a line-shaped incident X-ray beam, in which the elemental distributions are obtained from the XRF data measured with the rotational and translational scanning of the sample^{1,2,3}). The advantage of this technique is an increased signal intensity compared with the technique using a point-shaped beam.

We developed a high spatial resolution XRF imaging with monochromated x-ray excitation by this image reconstruction technique. To achieve this end, we used an asymmetric reflection in combination with a sagittal focusing monochromator as a beam demagnifier.

In this report, the spatial resolution and the incident photon flux are optimized for practical applications.

EXPERIMENTAL

The experiment was carried out on the beam-line 4A. A schematic arrangement is shown in Fig.1.

To achieve the high resolution XRF imaging, it is necessary to obtain narrow line-shaped X-ray beams with the sufficient photon flux. We used a sagittal focusing double crystal monochromator and an asymmetric Si crystal (C2) for the horizontal and vertical beam demagnifier respectively.

An asymmetric factor (b) of the asymmetric crystal is given by $b = \sin(\theta - a) / \sin(\theta + a)$, where θ is the Bragg angle and a is the angle between the crystal surface and the reflecting plane. By using the asymmetric reflection as shown in Fig.1, the beam height is reduced by a factor of b while the intensity loss is only a factor of \sqrt{b} .

We used the asymmetric crystal of an asymmetric factor of 1/50 at 8.83 keV ($a = 12.45^\circ$). The distance between the asymmetric crystal and the sample was 30 mm. The height of the slit before the crystal was 500 μm .

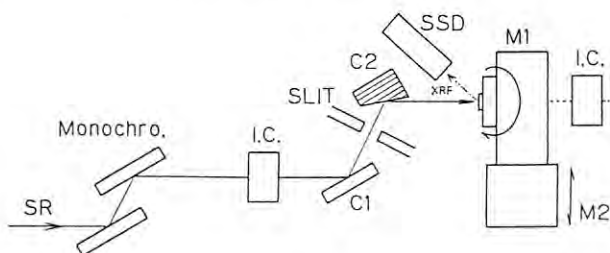


Fig.1 Experimental arrangement for the high spatial resolution XRF image reconstruction.

A sample was mounted on the x-y translational stage for the positioning, and the sample stage itself was mounted on the rotational (M1) and z- translational stage (M2) for scanning. The XRF signal from the sample was detected by a Si(Li) detector under the atmospheric condition.

RESULTS AND DISCUSSION

The beam height was estimated at about 10 μm , which agrees well with the designed one considering the broadening due to the angular divergence of reflected X-rays.

The high resolution XRF imaging by the image reconstruction technique was made. Fig.2 shows the reconstructed Ni XRF and transmission X-ray image of the Ni grid (1000 mesh, 25 μm period). Measurement conditions were as follows; beam size 10 μm x 160 μm , 90 rotational steps ($2^\circ/\text{step}$), 80 translational steps (2 $\mu\text{m}/\text{step}$), and 1 sec measurement time at a step. The highest counts of Ni Ka intensity was more than 6×10^3 cps. Fig. 2 shows that the spatial resolution of about 10 μm was actually achieved. The contrast of transmission image was degraded for thin or dilute sample and cannot be obtained for thick samples. The Fe XRF image of the sintered iron ore was also obtained. The application to the chemical state imaging with the high spatial resolution is now underway.

The authors thank Mr. M. Sato for preparing an asymmetric crystal.

REFERENCES

- 1) N. Cruker, X-Ray Spectrom. 8, 149 (1979)
- 2) M. Takahashi et al, Activ. Rep. No.6, 145 (1988)
- 3) A. Iida et al, Rev.Sci.Instrum. 60,2458 (1989)

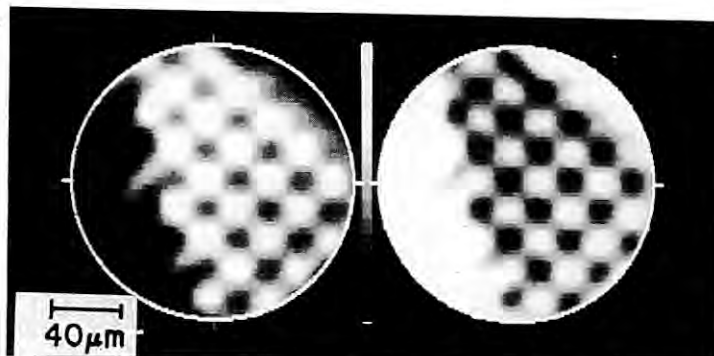


Fig.2 Ni Ka Fluorescence reconstructed image (left) and transmission image (right) of a Ni 1000 mesh per inch grid.

DETERMINATION OF TRACE RUTHENIUM
IN METEORITIC MINERALS BY MICROBEAM X-RAY FLUORESCENCE SPECTROMETER

Jun SAITO, Osamu HIDAKA, Hiroshi TAKEDA, Tomoki NAKAMURA, Akira YAMAGUCHI, Haruhiko SATO, Atsuo IIDA*
Mineralogical Inst., Faculty of Science, Univ. of Tokyo, Hongo, Tokyo 113

*Photon Factory, National Lab. for High Energy Phys., Oho-machi, Tsukuba City, Ibaraki 305

Introduction

Our reconnaissance work to determine trace elements with a microbeam X-ray fluorescent (XRF) analysis by SOR developed by Iida¹⁾ revealed that a few ppm order of Ru within a 0.5 X 0.5 mm region can be determined by this equipment²⁾. Only bulk amounts of Ru in a few meteorites were measured³⁾. Geochemical behavior of Ru has not been too well known partly because of this analytical difficulty. Because Ru is expected to have a behavior similar to but different from Ir as a siderophile element, we can obtain more insight into the differentiation processes of meteorites. In addition, we can determine Ru in coexisting mineral grains. We report a determination of Ru in iron meteorites and nickel-iron metal grains in chondrites and achondrites. We also located a Ru-bearing fremdling in the CAI in Allende without destruction and coating.

Samples and Analytical Techniques.

The microbeam XRF unit on BL-4A was used for the XRF intensity measurements the same as those described in the previous report^{1,2)}. Sliced chips of meteorites were fixed with Wevo plastic to a silicon wafer and the surface was polished. The samples were irradiated by X-ray of excitation energy fixed at 22.5 KeV, counting times ranging from 900 to 1000 sec., and the beam diameters range from 0.25 X 0.25 mm to 0.40 to 0.40 mm squares. Standard samples of Ni-Fe alloy (Fe 90: Ni 10 wt. %) doped with Ru (1, 0.1, 0.01 wt. % Ru) have been prepared by the courtesy of Tanaka Precious Metal Co. in Tokyo.

Iron meteorites we measured in this experiments are IAB type, including Zogora (New Morocco), Bocaiuva, Toluca, Yamato 791694, ALH77283. Metal grains in Saint Severin (LL6) chondrite were also measured to test the small size of the beam. A white inclusion (CAI) 4 X 5 mm in size in a chip of Allende carbonaceous chondrite has been used to locate Ru-bearing fremdling.

Results

Standard Ni-Fe alloys have been measured to obtain a calibration curve for Ru. The measured X-ray counts for 1 wt. % Ru was not on a line for 0.1 and 0.01 %. The concentrations of Ru in unknown iron meteorites were calculated by a ratio method by employing the counts of 0.01 % Ru, which is the closest to the Ru concentrations of unknown samples.

Bocaiuva contains approximately 10 ppm Ru. ALH77283 and Toluca contain 2 to 5 ppm Ru, but Y791694 and Zogora IAB irons do not reveal detectable peaks of Ru. A metal grain in Saint Severin chondrite contains about 2.5 ppm Ru.

A search for Ru-bearing fremdlings (refractory metal) in CAI in Allende was performed by moving the stage until we observe detectable counts of Ru. One metal-looking area shows

the highest peak of Ru among observed meteorite specimens (Fig. 1). In comparison with the Ru in the Ni-Fe alloy standard, the X-ray counts of this fremdling amounts to about 150 ppm Ru.

Discussion

With 22.5 keV X-ray, it was possible to determine Ru down to 2 ppm in iron meteorites using the $K\alpha$ line. The advantage of micro-XRF is that we can excite particular $K\alpha$ lines of Pt-group elements within a small area. Since we could irradiate selected region with large kamacite within the etched specimen, the Ru content of ALH77283 may represent almost entirely of that of kamacite. The data of Zogora may show bulk Ru contents of the mixed phases of kamacite and thin taenite lamellae.

The bulk Ru contents of IAB irons reported previously range from 5 to 10 ppm³⁾. Because the modal abundance of taenite in the IAB irons is low, the Ru contents of kamacite may be the same order of amounts as those of the bulk analysis of the IAB irons. Our measured values are slightly smaller than those of the bulk analysis.

The low Ru content of Y791694 may suggest that the higher the Ni contents of the IAB irons, the low the Ru contents. Ru in the metal grain in the Saint Severin chondrite may be the first value ever reported. Further studies will be required to compare the Ru contents of metals between irons and chondrites, but it is no doubt that the micro-analysis will be useful to unravel the problem of such meteorites.

References

- 1) Iida A. et al., Nucl. Instrum. and Methods 228, 556 (1985).
- 2) Hidaka O. et al., PF Activity Report No.6, 146 (1988).
- 3) Scott E. R. D., Geochim. Cosmochim. Acta 36 1205-1236 (1972).

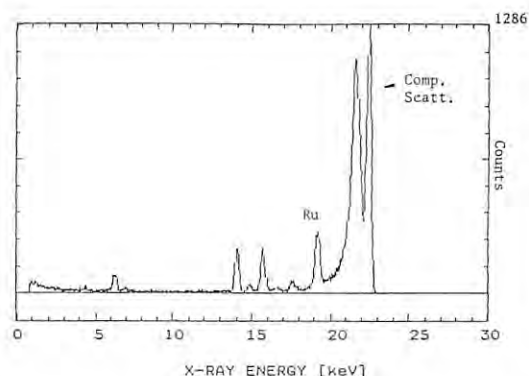


Fig. 1 XRF spectrum of a Ru-bearing fremdling in a CAI of Allende. Total count 66164.

X-Ray Microbeam by Multilayer Zone Plate

Kazuya SAITOH, Koji Oishi, Atsuo IIDA*

Institute for Super Materials, ULVAC JAPAN Ltd., Tsukuba 300-26

*Photon Factory, National Laboratory for High Energy Physics, Tsukuba 305

Introduction

Multilayer zone plate which was fabricated using sputtering and slicing techniques, could focus hard X-ray of Å order wave length¹⁾. Theoretically an X-ray spot size focused by a zone plate is determined by the outermost zone width of about 2000 Å^2). But an X-ray spot size actually measured with a multilayer zone plate in the previous report³⁾ was $3 \mu\text{m}$. It is considered that the spot size was determined by SR source size. In this report, we realize $1 \mu\text{m}$ spot size of focused X-ray using an aperture in the beam line.

Experimental

Experiments were performed on BL-4A. The schematic view of the experimental configuration is shown in Fig.1. 8 keV SR with a double crystal monochromator was used for the experiment. X-rays transmitted through a $10 \mu\text{m}$ diameter pinhole were impinged on a multilayer zone plate and focused to a spot. The pinhole was located 3 meters in front of the zone plate, 10 m from the SR source. For the zone plate, the SR source size virtually becomes small.

To estimate the focused X-ray spot size, transmitted X-rays were counted with a scintillation counter while a $2.5 \mu\text{m}$ diameter tungsten wire was scanned across the X-ray spot on focal plane and then a calculated result was fitted to a measured X-ray intensity profile. Another pinhole was set behind the zone plate to select a region around the spot and to suppress scattered X-rays and zero-th order diffraction.

It is assumed in the calculation that the intensity distribution of the focused X-ray spot is one dimensional gaussian and that the tungsten wire cross section is a circle. Values used for

the calculation is as follows ; tungsten density : 19.3 g/cm^3 , tungsten attenuation coefficient : $172 \text{ cm}^2/\text{g}$.

Result and Discussion

A series of measurements was done by changing the distance between the zone plate and the wire to find a focal point. A typical measured X-ray intensity profile, which had minimum FWHM of absorbing peak, is shown in fig.2 as a solid line.

A calculated result (a convolution profile) is also shown as dashed line in fig.2. A FWHM of X-ray spot size was about $1 \mu\text{m}$ according to the profile fitting.

It became clear by this experiment that a focused X-ray spot size strongly depends on the X-ray source size. This was also confirmed by observations of spot images with and without the pinhole.

In this experiment, the distance between the pinhole and the zone plate was 3 m. If the pinhole can be set closer to the SR source, a focused spot size will become smaller than $1 \mu\text{m}$. To achieve both higher incident photon flux and micron spot size, higher brightness SR source is preferable.

The authors are grateful to Mr. S. Hayakawa for providing us with the computer programs for the experiment.

References

- 1) K.Saitoh, K.Inagawa, K.Kohra, C.Hayashi, A.Iida, and N.Kato, Jpn.J.Appl.Phys. **27**, L2131 (1988).
- 2) A.G.Michette, Optical Systems for Soft X-rays (Plenum, New York, 1986), p.186.
- 3) K.Saitoh, K.Inagawa, K.Kohra, C.Hayashi, A.Iida, and N.Kato, Rev.Sci.Instrum. **60**, 1519 (1988).

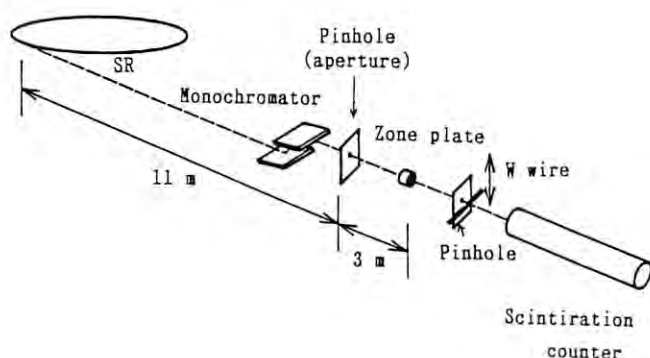


Fig.1 Schematic view of the experimental configuration.

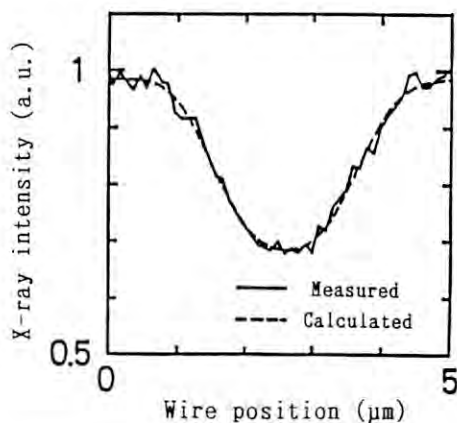


Fig.2 Intensity profile of transmitted X-rays.

ANALYSIS OF ULTRA TRACE ELEMENTS IN MARINE ECOLOGICAL SAMPLES BY SR
MONOCHROMATIZED X-RAYMasafumi ISHIKAWA^{*1}, Atsuo IIDA^{*2}, Kenji OHKOSHI^{*3} and Gunzo IZAWA^{*4}

- *1 National Institute of Radiological Sciences, Division of Marine Radioecology, Isozaki 3609, Nakaminato, Ibaraki-ken, 311-12, Japan
 *2 KEK, Photon factory, National Laboratory for High Energy Physics, Oho-machi, Ibaraki-ken, 305, Japan
 *3 Ishinomaki Sensyu University, Faculty of Science and Technology, Shinmito 1, Minamisakai, Ishinomaki-shi, Miyagi-ken, 986, Japan
 *4 Utsunomiya Bunsei Junior Collage, Kamitomatsuri 4-8-15, Utsunomiya-shi, Tochigi-ken, 320, Japan

INTRODUCTION

A recently facilitated SR monochromatized X-ray beam of sub-millimeter dimensions with a bi-dimensional scanner is effective when examining trace characterization, especially for biological samples such as marine fish.

Detailed information of elemental locality in tissue may suggest migration, transportation and history of elements and may introduce the solution of physico-chemical behavior of elements in the environment.

In this study, to supply necessary data for radioecological evaluation on the elemental uptake by organisms, trace characterization was implemented for major and critical elements.

EXPERIMENTAL

- 1). Target sample: Detailed procedures for the sample target preparation can be referred to our previous report.(1) A 500 μ m thick cross section cut out from the 11th vertebra of a flat fish, *Paralichthys olivaceus*, was mounted on a 2 μ m Makrofol film, then coated with carbon.
 2). Scanning: 17 keV SR monochromatized X-ray was focussed into a beam of 200x200 μ m² by a Si(111) double crystal monochromator installed on the BL-4A.(2) An area of 10000x10000 μ m² was covered by this analysis with a 200 μ m step. At each step, signal accumulation was made for 3 seconds.

RESULTS AND DISCUSSION

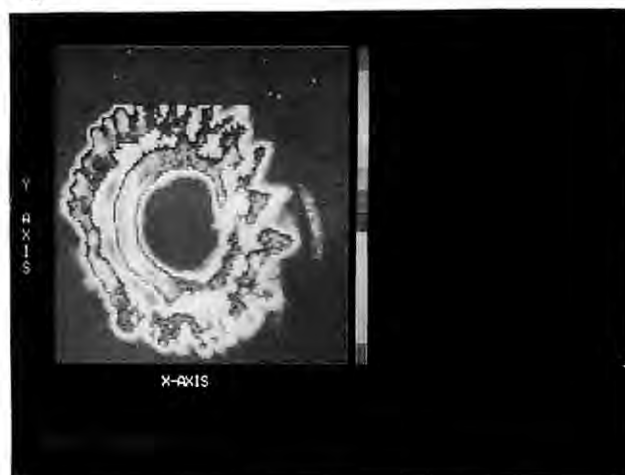
The 17 keV monochromatized X-ray beam sufficiently submitted characteristic X-ray signals due to the elements K, Ca, etc. until the energy of 14 keV emitted from Sr. The essential elements P, Ca, Mn, Fe, Zn and Sr were therefore scanned for determining their locality.

Fig. 1 shows the distribution pattern of Ca on the cross section target. During the scanning, the ring current decreased about 12 % from the initial strength. The difference does not affect the graphical representation, because the color reflects the elemental concentration when double X-ray signals are counted between positions.

The two dimensional Ca distribution pattern clearly indicates that even elements considered the main physiological component have locality characteristics, although our previous paper stated, (1) using PIXE scanning analysis towards one direction, that the element Ca presents a uniformly concentrated level in the vertebra.

This pattern indicates that the specific deposit of Ca observed at the edge and around the intervertebrale foramen starts to form along with the certain regularity, i.e. Ca deposits are high

Fig. 1



like spines radiated from the center of the vertebra to its surface, and the deposit around the intervertebrale foramen is independent of the former accumulation.

The tendency was identical when the element was Mn, Fe and Sr, while Zn was independent of this category. The concentration level of the element was low, but it developed homogeneously over the scanned surface. The details are described in a separate paper.(3)

The distributional results suggest, from the observation of Ca and Sr, that for the infant fish, alkali-earth metals are particularly necessary. Since they are classified as the essential elements, the requirement can also be high during the growth, but the observed pattern negates the estimation. The active accumulation again occurs a few years after the period.

With superficial observation it is possible to point out that the high deposit of the elemental bands are formed by a concentric circle with a few years interval. The solid geometry suggests that, elements Ca consequently forms multi-cylindrical hard layers like annuluses of trees and fish scales. This estimation can clearly be supported with sufficient data by a high spacial resolution SR beam.

REFERENCES

- 1) M. Ishikawa, T. Ishii, S. Uchida and K. Kitao, Biol. Trace Elem. Res., 3, 43(1987)
 2) Y. Goshi et al., Adv. in X-ray Anal. 3, 495(1988)
 3) M. Ishikawa, A. Iida, K. Ohkoshi and G. Izawa, in press

X-RAY ABSORPTION NEAR EDGE STRUCTURE (XANES) OF CuInSe_2 BY PHOTOACOUSTIC METHOD

Taro TOYODA¹, Tsutomu MASUJIMA², Hideaki SHIWAKU³, Atsuo IIDA³, Hiroshi KAWATA³,
Masami ANDO³, Hisayuki NAKANISHI⁴, Saburo ENDO⁵, and Taizo IRIE⁵

1. Department of Applied Physics and Chemistry, The University of Electro-Communications, Chofu, Tokyo 182
2. Institute of Pharmaceutical Science, Hiroshima University, School of Medicine, Hiroshima 734
3. Photon Factory, National Laboratory for High Energy Physics, Tsukuba, Ibaraki 305
4. Department of Electrical Engineering, Faculty of Science and Technology, Science University of Tokyo, Noda, Chiba 278
5. Department of Electrical Engineering, Faculty of Engineering, Science University of Tokyo, Shinjuku-ku, Tokyo 162

Introduction

Recently, the heat generation by X-ray absorption has been detected by a photoacoustic method using synchrotron radiation with pure Cu metal in the K-edge region. It was found that the spectra of the heat production included fine structure in the region, i.e. EXAFS. This report presents detailed studies of X-ray absorption spectra with a photoacoustic detector in the region near the K-edge of Cu in CuInSe_2 , compared with that of pure Cu metal as a reference. The ternary semiconducting compound CuInSe_2 has a chalcopyrite structure, and the excellent reliability and high power-conversion efficiency of polycrystalline thin film CuInSe_2 solar cells have stimulated research on fundamental properties of this material.

Experimental and Results

Single crystals of CuInSe_2 were prepared by melting the elements in an evacuated quartz ampoule followed by directional freezing. The cylindrical photoacoustic cell has a sample chamber at the center with volume of 0.16cm^3 and two Be windows together with an electret type microphone. The experiments were carried on at the Beam Line 4A. In order to measure the absorption spectra simultaneously, the ion chambers were set at both sides of the photoacoustic cell. The photoacoustic signal intensity was always divided by the first ion chamber current for normalization against photon flux. The X-ray beam intensity was modulated by a rotating Pb plate chopper at a frequency of 9 Hz.

Fig.1 shows the X-ray photoacoustic spectrum of CuInSe_2 powder together with that of Cu metal near K-edge region. Fig.2 shows the absorption spectrum in the same energy region. Fig.2 shows the fine structure in both cases which corresponds to XANES. It shows that the information in XANES is also included in the X-ray photoacoustic spectrum, so that the heat production process is also reflected in XANES. We cannot observe small structure at the shoulder part of the spectrum in CuInSe_2 , which is considered to be the $1s \rightarrow 3d-4s$ band transition. The first energy peak value of CuInSe_2 is smaller than that of pure Cu metal, indicating a chemical shift.

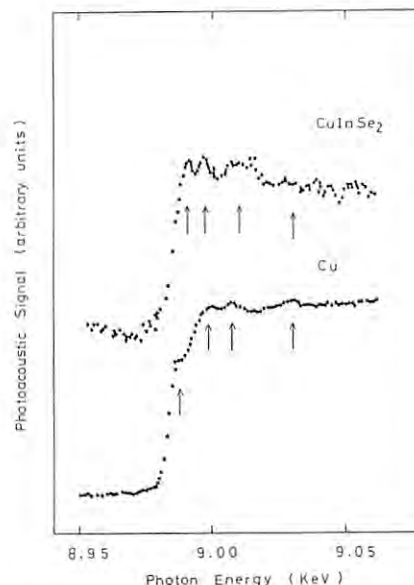


Fig.1 X-ray photoacoustic absorption spectra for CuInSe_2 (powder) and Cu(10 μm foil).

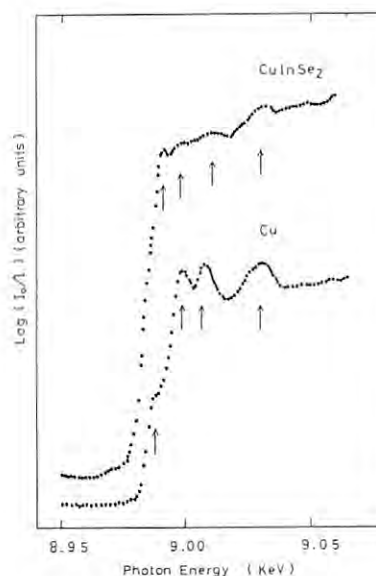


Fig.2 X-ray absorption spectra for CuInSe_2 (powder) and Cu(10 μm foil).

X-RAY PHOTOACOUSTIC ABSORPTION SPECTRA OF BRASS AND PHOSPHOR BRONZE

Taro TOYODA¹, Tsutomu MASUJIMA², Hideaki SHIWAKU³, Atsuo IIDA³, Hirohi KAWATA³,
and Masami ANDO³

1. Department of Applied Physics and Chemistry, The University of Electro-Communications, Chofu, Tokyo 182
2. Institute of Pharmaceutical Science, Hiroshima University, School of Medicine, Hiroshima 182
3. Photon Factory, National Laboratory for High Energy Physics, Tsukuba, Ibaraki 305

Introduction

Due to the availability of a tunable source of X-rays in the form of synchrotron radiation, X-ray spectroscopy has been thriving in the last decade. All the techniques measure a signal which is linked to the excitation probability of a core electron. Since the absorption of X-rays in a sample results in the generation of heat, photo-thermal spectroscopy should provide another method of studying X-ray absorption. Recently, microphones have been utilized to obtain the X-ray absorption spectra with acoustic detection. This report presents detailed studies of X-ray absorption spectra with a photoacoustic detector in the region near the K-edge of Cu in brass (Cu: 65wt.%; Zn: 35wt.%) and phosphor bronze (Cu: 94wt.%; Sn: 6wt.%), compared with that of Cu metal as a reference.

Experimental and Results

Brass, phosphor bronze and Cu foils of 10 μm were used as samples. The cylindrical photoacoustic cell has a sample chamber at the center with volume of 0.16 cm^3 and two Be windows together with an electret type microphone. The experiments were carried out at the Beam Line 4A. In order to measure the absorption spectra simultaneously, the ion chambers were set at both sides of the photoacoustic cell. The photoacoustic signal intensity was always divided by the

first ion chamber current for normalization against photon flux. The X-ray beam intensity was modulated by a rotating lead plate chopper at a frequency of 9Hz.

Fig.1 shows the X-ray photoacoustic absorption spectra of brass and phosphor bronze together with that of Cu metal near K-edge region. Fig.2 shows the absorption spectra of them in the same energy region. Fig.2 shows the fine structure which corresponds to XANES. It shows that the information in XANES is also included in the X-ray photoacoustic spectra, so that the heat production process is also reflected in XANES. Energy peak values of brass and phosphor bronze show the same values of Cu metal, indicating that there are no chemical shifts in such Cu alloys. The results suggest that the crystal structure difference between brass and Cu metal is not reflected in XANES. There are small structures at the shoulder part of brass, phosphor bronze and Cu metal, indicating the transition of $1s \rightarrow 3d-4s$ band which is characteristic in pure Cu metal. Fig.3 shows the phase changes in brass, phosphor bronze and Cu metal near the K-edge region. The phase spectra show sudden changes at the K-edge. It shows that the phase change of phosphor bronze is twice as those of Cu metal and brass. It suggests that the delay time of phosphor bronze is twice as those of Cu metal and brass.

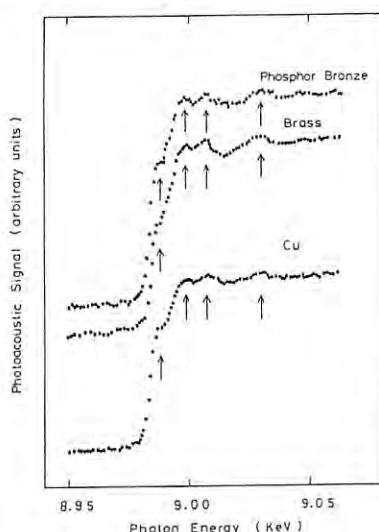


Fig.1: X-ray photoacoustic spectra for brass, phosphor bronze and Cu foils (10 μm each).

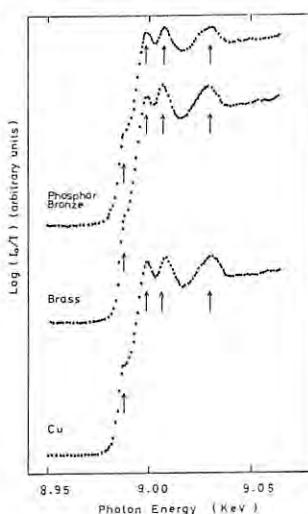


Fig.2: X-ray absorption spectra for brass, phosphor bronze and Cu foils (10 μm each).

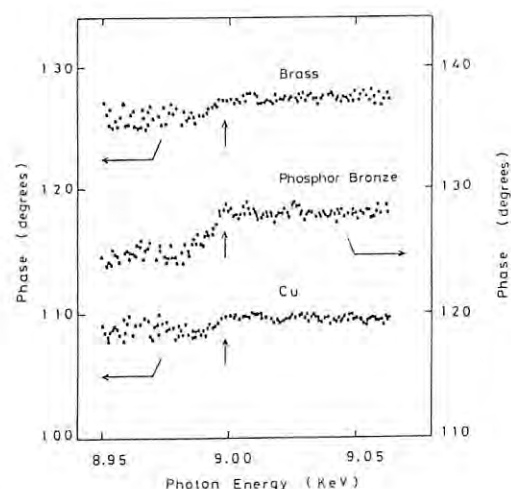


Fig.3: X-ray photoacoustic phase spectra for brass, phosphor bronze and Cu foils (10 μm each).

PHOTOACOUSTIC EXAFS OF BRASS (Cu-Zn ALLOY)

Taro TOYODA¹, Tsutomu MASUJIMA², Hideaki SHIWAKU³, Atsuo IIDA³, Hiroshi KAWATA³,
and Masami ANDO³

1. Department of Applied Physics and Chemistry, The University of Electro-Communications, Chofu, Tokyo 182
2. Institute of Pharmaceutical Science, Hiroshima University, School of Medicine, Minami-ku, Hiroshima 734
3. Photon Factory, National Laboratory for High Energy Physics, Ibaraki 305

Introduction

In X-ray absorption spectroscopy, the extended X-ray absorption fine structure (EXAFS) method is now widely employed as a powerful tool for structure analysis. As a further effect of X-ray absorption, heat generation should be considered. Recently, the heat generation by X-ray irradiation was detected by means of a microphone photoacoustic method (PAS), and further spectroscopic study showed a fine structure in its primitive spectrum. In these circumstances, further study using Cu alloys, brass, was performed in order to check the generality of this phenomenon and to study common futures.

Experimental and Results

Brass foil of 10 μm was used as a sample (Cu 64.7wt.%, Zn 35.3wt.%). The experiment was carried on at the Beam Line 4A. In order to measure the normal absorption spectra simultaneously, the ionization chambers were set at both sides of the photoacoustic cell.

The photoacoustic signal intensity was always divided by the first ionization chamber current for normalization against photon flux. The X-ray beam intensity was modulated by a rotating lead plate chopper at a frequency of 9Hz.

Figs. 1 and 2 show the X-ray photoacoustic and normal absorption spectrum of brass, respectively. Both of them show fine structures over the K-edge of Cu and Zn which correspond to EXAFS. It shows that the information in EXAFS is also included in the X-ray photoacoustic spectrum in alloy system like brass (Cu-Zn alloy) so that the heat production process is also reflected in EXAFS even in Cu alloy. Figs. 3 and 4 show the X-ray photoacoustic and absorption spectrum near Zn K-edge region. Both of them show fine structures which correspond to XANES. It shows that the information in XANES is also included in the X-ray photoacoustic spectrum not only at Cu K-edge region but at Zn K-edge region in Alloy system.

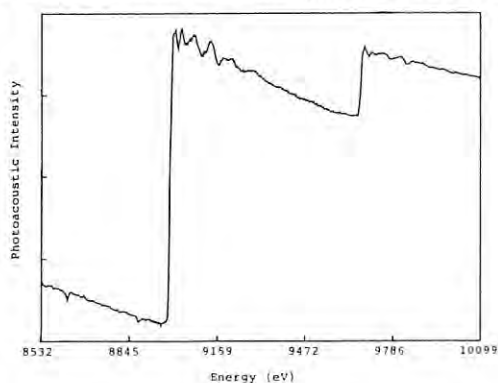


Fig.1: X-ray photoacoustic spectrum for brass.

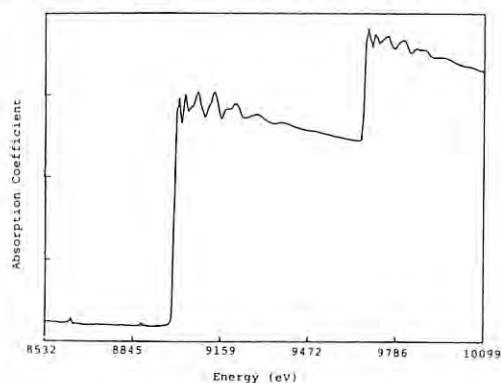


Fig.2: X-ray absorption spectrum for brass.

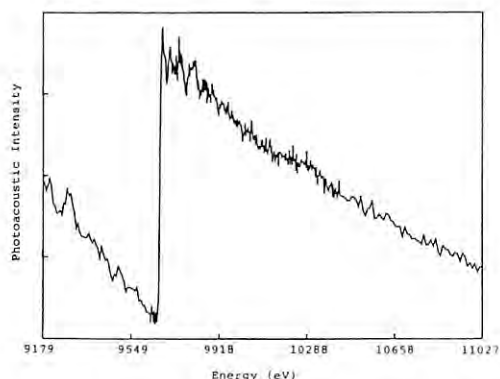


Fig.3: X-ray photoacoustic spectrum for brass near Zn K-edge region.

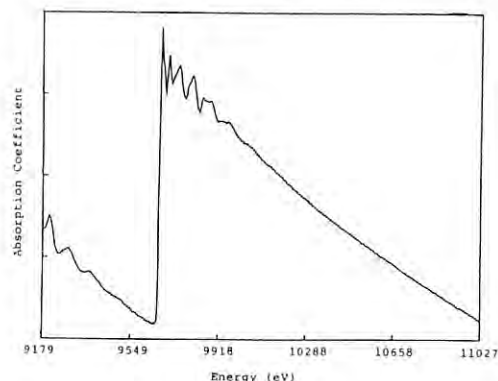


Fig.4: X-ray absorption spectrum for brass near Zn K-edge region.

EXAFS IN PHOTOACOUSTIC PHASE SPECTRUM

Tsutomu MASUJIMA¹, Hideaki SHIWAKU², Masami ANDO², Taro TOYODA³, Hideo IMAI⁴,
Gen TAMAI⁴, Shin'ichi KAWANO¹, and Atsuo IIDA²

1. Institute of Pharmaceutical Science, Hiroshima University, School of Medicine, Minami-ku, Hiroshima 734
2. Photon Factory, National Laboratory for High Energy Physics, Tsukuba, Ibaraki 305
3. Department of Applied Physics and Chemistry, The University of Electro-Communications, Chofu, Tokyo 182
4. Faculty of Pharmaceutical Science, Fukuyama University, Higashimura-cho, Fukuyama 729-09

Introduction

It was found that X-ray photoacoustic spectrum of Cu foil shows fine structure similar to EXAFS, and Fourier analysis of the spectrum reveals the identical radial dispersion to that of conventional absorption spectrum¹⁾. This method has unique potential to be applied to depth profiling. Another potential source of information in the photoacoustic signal is the phase angle of the signal with respect to the modulation phase of the incident light beam. By measuring the phase angle of the photoacoustic signal, it is possible to calculate the quantitative absorption spectrum if in addition only the sample thermal diffusivity is known. This report presents detailed studies of X-ray photoacoustic phase spectrum for thick Cu foil (100 μm).

Experimental and Results

The cylindrical photoacoustic cell has a sample chamber at the center with volume of 0.16 cm^3 and two Be windows together with an electret type microphone. The experiments were carried out at the Beam Line 4A. In order to measure the absorption spectrum simultaneously, the ionized chambers were set at both sides of the photoacoustic cell. The photoacoustic signal intensity was always divided by the first ionized chamber current for normalization against photon flux. The photon flux was of the order of 10^9 - 10^{10} cps at 9 keV.

The X-ray beam intensity was modulated by a rotating lead plate chopper at a frequency of 9 Hz. The driving of the monochromator and data handling of the photoacoustic signal, and of ionization chamber currents were controlled and processed by a microcomputer using the interfacing electronic instrument. The wave form of the photoacoustic signal was also monitored by a storage oscilloscope.

Fig.1 shows the X-ray photoacoustic phase spectrum. Fig.2 shows the X-ray photoacoustic spectrum which indicates EXAFS. EXAFS like fine structure is shown in phase spectrum. The arrows indicate the maximum peak of the fine structure. The peak values in X-ray photoacoustic phase spectrum in Fig.1 corresponds to those of X-ray photoacoustic spectrum in Fig.2. Also, the phase spectrum shows sudden change at the K-edge of Cu just like photoacoustic intensity change. The heat which is needed for propagation to the surface can be detected as the phase-lag. The phase signal is related to the delay time of the response to the incident signal. Experimental result suggests that the delay time of the response has a information on EXAFS which corresponds to local atomic arrangement. EXAFS information is included not only in photoacoustic intensity but also in phase.

- 1) T. Masujima et al., Rev. Sci. Instrum. **60**, 2522 (1989).

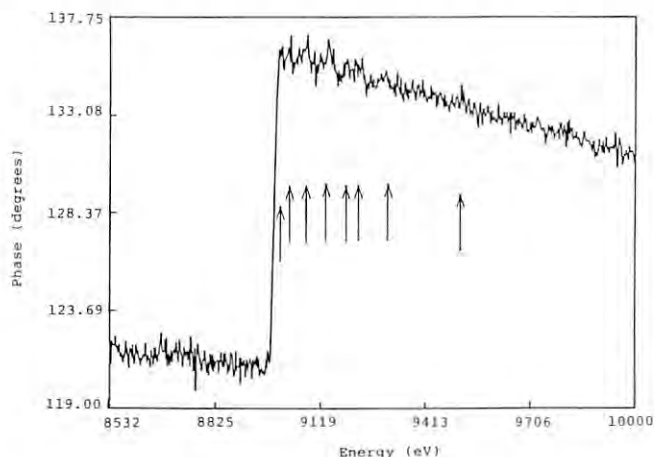


Fig.1: X-ray photoacoustic phase spectrum for Cu foil (100 μm) at frequency of 9 Hz.

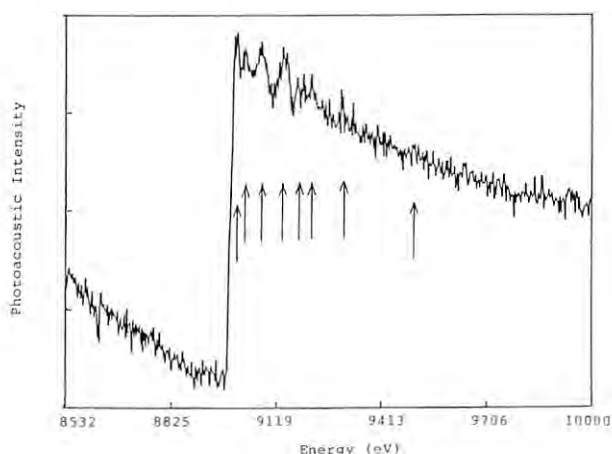


Fig.2: X-ray photoacoustic spectrum for Cu foil (100 μm) at frequency of 9 Hz.

CHEMICAL STATE IMAGING AND TRACE ELEMENT ANALYSIS OF METEORITES BY X-RAY FLUORESCENCE SPECTROSCOPY

Izumi NAKAI, Akira TSUCHIYAMA* and Ritsuro MIYAWAKI**

Department of Chemistry, University of Tsukuba, Ibaraki, 305

*Department of Geology and Mineralogy, Kyoto University, Kyoto 606

**Ceramic Technology Department, Government Industrial Research Institute, Nagoya Kita, Nagoya 462

Introduction

An XRF (X-ray fluorescence analysis) technique based on the selective excitation of specific chemical species by tunable synchrotron radiation was recently developed by Sakurai et al.¹⁾ and named as SIXES (selectively induced X-ray emission spectroscopy). This technique was successfully applied to a geological problem in our previous study²⁾.

Knowledge of chemical states of elements and distribution of trace elements in a mineral is useful to estimate origin of the mineral and its formation condition. The present paper reports a further application of this technique to geological problems including meteorites. High sensitivity of SR-XRF technique is also utilized in trace element analysis of the meteorites.

Experimental

XRF measurement was carried out at BL-4A at PF utilizing the energy dispersive XRF system with Si(Li) detector. Monochromatic X-ray with desired energy and beam size was obtained with Si(111) double crystal monochromator and a set of vertical and horizontal slit. Two dimensional analysis was carried out by placing a sample on a computer controlled XZ stage normal to the orbital plane of SR.

Sample used are pseudomorph of goethite after pyrite (Fig. 1a) and two chondrites: Allende (Fig. 2a) and Murchison meteorites. Reference samples as standards for iron in various oxidation states include Fe metal, FeS₂, Fe₃O₄, FeOOH, Fe₂SiO₄, olivine and YFeO₃.

XANES spectra of the reference samples were measured by X-ray fluorescence detection. Excitation energies were determined to be 7112.3eV for selective excitation of metal, 7117.0eV for that of metal and Fe²⁺, and 7598.9eV for total iron. The pyrite/goethite sample was excited at the latter two energies and the meteorite samples were at the three energies. Two dimensional Fe image at each energy was measured: beam size ca. 0.2x0.2mm², 47x59 points, 0.2mm step, and 2s/point for pyrite/goethite; 0.13x0.13 mm², 0.1mm step, 2s/point and 57x40 points for Allende and 39x50 for Murchison).

Results and Discussion

A selected image of each oxidation state of iron is obtained by a simple mathematical treatment of the above data¹⁾. The results are shown in Fig. 1 b-c and Fig. 2 b-f, where Fe concentration was scaled with 8 densities of black and white image. Fig. 1b indicates distribution of divalent Fe, which corresponds well with pyrite, FeS₂, while Fig. 1c indicates trivalent iron corresponding to goethite, FeOOH. This result is consistent with assumed formation process that the goethite formed under oxidizing conditions as a weathering product of pyrite.

Distributions of metallic, divalent and trivalent iron in Allende meteorite are shown in Figs. 2b, c, d, respectively. Figs. 2e and f show distribution of trace elements, Cu and Zn (beam size 0.2x0.2mm², 27x21 points, 5s/point, 0.2mm step). Allende meteorite is composed of chondrules, inclusion and matrix minerals. A separate SEM-EDX analysis using the same sample showed that the chondrule is rich in Mg, Si, the inclusion is fine grained CAI (Ca, Al rich inclusion) and matrix is rich in Fe and Si. The present analysis indicates that Cu and Cr concentrated at the region rich in metallic Fe, but not vice versa. Zinc is concentrated in the fine grained CAI.

The authors thank Dr. A. Iida and Mr. S. Hayakawa for their kind help in the measurements.

References

- 1) K. Sakurai, A. Iida, M. Takahashi and Y. Gohshi, Jap. J. Appl. Phys., 27, L1768(1988).
- 2) I. Nakai, Y. Suzuki, and A. Iida, Photon Factory Activity Report #6, 141 (1988).

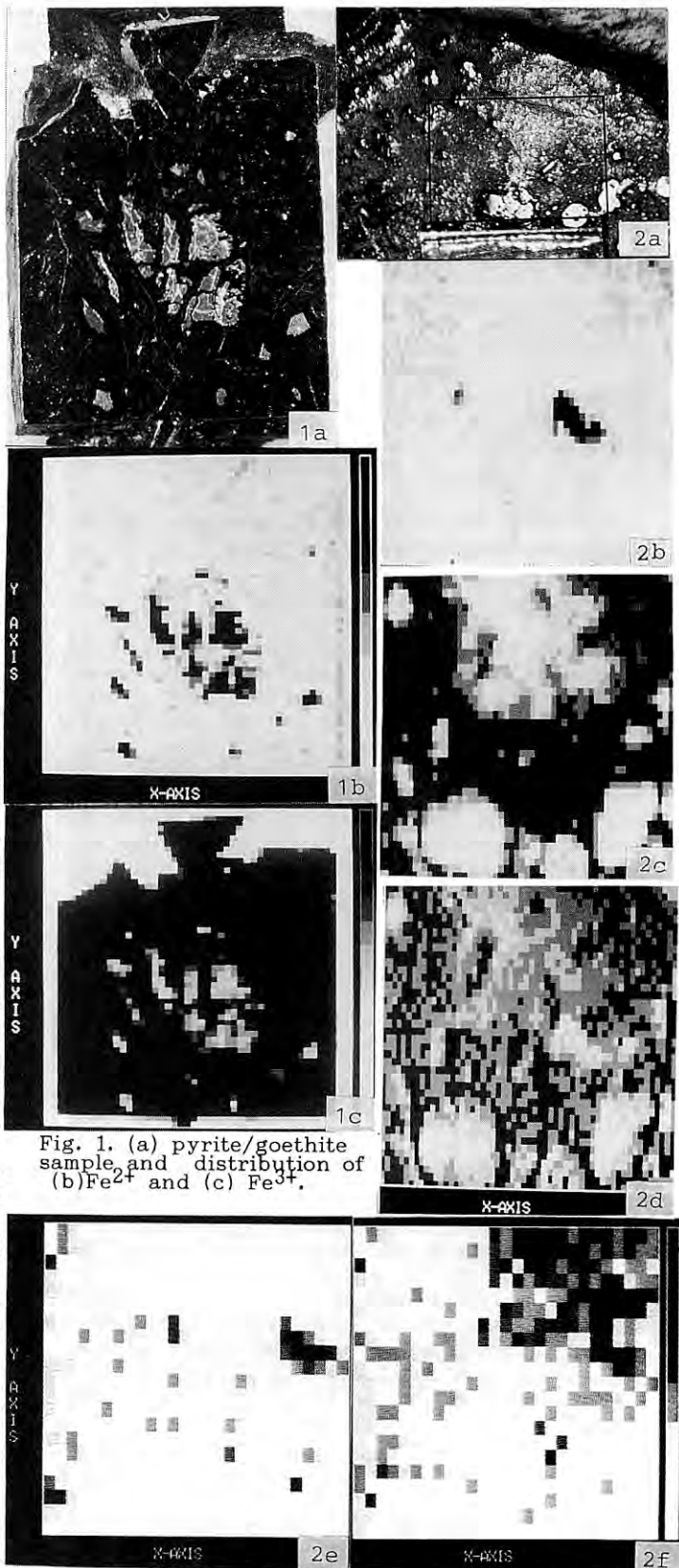


Fig. 1. (a) pyrite/goethite sample and distribution of (b)Fe²⁺ and (c) Fe³⁺.

Fig. 2. (a)Allende meteorite and distribution of (b)Fe⁰, (c)Fe²⁺, (d)Fe³⁺, (e)Cu and (f) Zn.

MICRO FLUORESCENCE EXAFS/XANES FROM ROCK SAMPLE

S. HAYAKAWA, Y. GOHSHI, A. IIDA*, S. AOKI** and K. SATO***

Department of Industrial Chemistry, Faculty of Engineering, University of Tokyo, Tokyo

*Photon Factory, National Laboratory for High Energy Physics, Tsukuba, Ibaraki 305.

**Institute of Applied Physics, University of Tsukuba, Tsukuba, Ibaraki

***Geological Survey of Japan, Tsukuba, Ibaraki

Introduction

An intense monochromatic microbeam can realize various kinds of X-ray spectroscopies, and micro-EXAFS is one of the most promising methods for the characterization of a heterogeneous sample. The combination of a mirror and a double crystal monochromator realizes a monochromatic micro beam with a fixed beam position when the energy of the incident beam is continuously scanned.

Though we have realized a micro X-ray beam using Wolter mirror system¹⁾, the maximized photon flux in the 10 μm beam spot was obtained using a single ellipsoidal mirror and a pinhole at the expense of spatial resolution. Monochromatic micro beam has been applied to micro-XANES and micro-EXAFS measurement using the fluorescence detection method.

Experimental

Experiments were carried out on the BL-4A. A single ellipsoidal mirror ($M=1/9.5$) was installed in the beamline and a pinhole of 10 μm in diameter was placed in the experimental hutch. A Si(111) double crystal monochromator was used and the energy of the incident beam could be selected in the region up to the cut-off energy of the mirror (about 10 keV). The photon flux through the 10 μm pinhole was more than 100 times intense than that with unfocused condition for 8 keV X-rays.

We have used a single Si(Li) detector to collect the fluorescence signals under atmospheric condition as in the micro X-ray fluorescence (Micro-XRF) analysis. Detection geometry and data acquisition time for the micro-XANES and micro-EXAFS were evaluated by comparing the data of Cu thin films between with the fluorescence method and with the transmission method.

Results and Discussion

A rock sample (peridotite) was analyzed with 10 keV monochromatic X-rays. Fig. 1 shows XRF images of Cr, Fe, Ni and Zn in a region of 900 μm * 900 μm . It was easily understood that there were three minerals in this region, and micro-XRF and micro-XANES spectra were measured at each position of interest on XRF images by using the xy scanning system. Micro-XANES spectra of Fe were collected at the three spots marked on the photograph in Fig. 2. In the region c, Fe is not the main component and the counting rate was 1/10 of that in region a. However, a XANES spectrum of high SB ratio was obtained by using the fluorescence method. From the XRF and XANES spectra, these minerals could be easily assigned to chromite, olivine and diopside

respectively.

The local structural analysis with micro-EXAFS is now in progress, and elemental, chemical and structural information can be obtained simultaneously with trace element sensitivity.

Reference

- 1) S. Hayakawa et al., Rev. of Sci. Instrum. 60, 2452(1989).

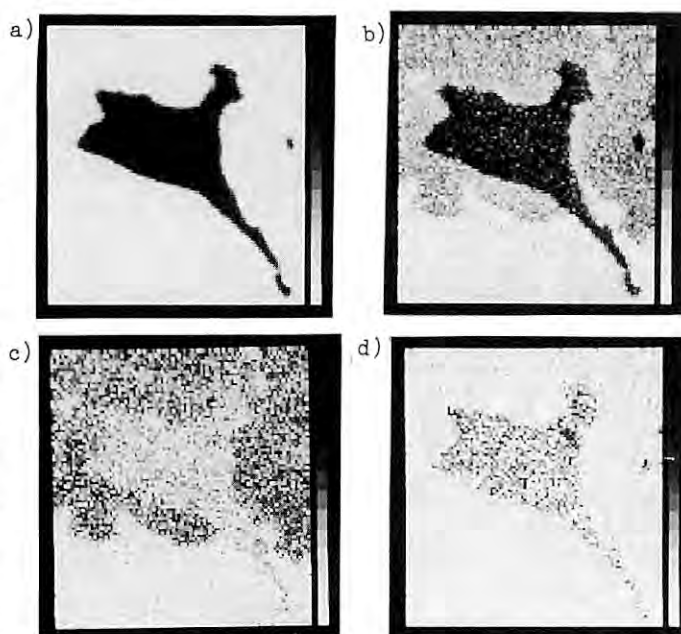


Fig. 1 XRF images of a peridotite. a) Cr K α , b) Fe K α , c) Ni K α and d) Zn K α signals were collected for 1 sec/pixel using 10 keV monochromatic X-ray beam. The analyzed area was 900 μm * 900 μm .

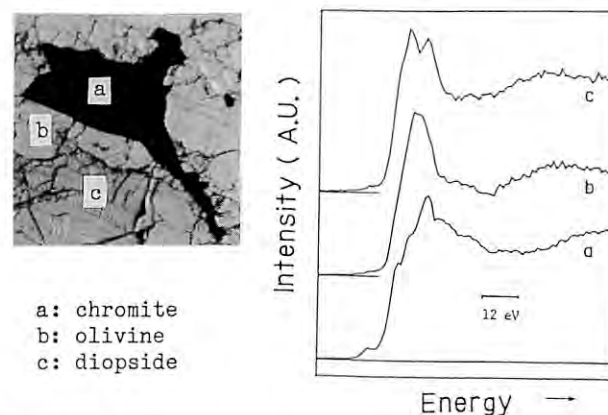


Fig. 2 Optical micrograph and micro fluorescence XANES spectra of Fe taken in the spots marked on the photograph of the rock sample.

NEAR-SURFACE CHEMICAL CHARACTERIZATION USING GRAZING INCIDENCE X-RAY FLUORESCENCE

Kenji SAKURAI and Atsuo IIDA*

*National Research Institute for Metals, Sengen, Tsukuba, Ibaraki 305

Photon Factory, National Laboratory for High Energy Physics, Oho, Tsukuba, Ibaraki 305

Introduction

The Grazing Incidence X-ray Fluorescence technique (GIF) are suitable for the analysis of the thin films and near surface of the materials because of the shallow penetration of X-rays (10-1000 Å) around the critical angle.¹⁾ However, conventional fluorescent experiments do not give any information on chemical state of the elements. This report shows the results of near surface chemical characterization by the GIF technique used in conjunction with the selectively induced X-ray emission spectroscopy (SIXES)^{2,3)}, which employs absorption edge shifts for chemical state analysis.

Experimental and Results

The experiment was carried out on the beam line 4A. A Si(111) double crystal sagittal focusing monochromator was used. The apparatus for GIF was described in detail elsewhere.¹⁾ In this experiment, the X-ray absorption spectrum was measured in terms of fluorescent intensity as a function of the incident energy scanned around the absorption edge. The sample used was Cr[200Å]/Cr₂O₃[2000Å] thin film evaporated on a flat, smooth synthetic quartz plate.

Angular dependence of the reflectivity is shown in Fig.1. Below the absorption edge, high reflectivity was obtained due to little absorption in the film. The curve shows interference oscillations mainly due to the reflection at the Cr₂O₃/SiO₂ interface. Good agreement was obtained with the calculation based on the Fresnel's theory. In contrast, above the absorption edge, strong absorption smears the angular dependence of the reflectivity.

Cr K α fluorescent intensity was measured at various glancing angles by scanning incident X-ray energy through the absorption edge. Figure 2 shows the near edge absorption spectrum measured at an extremely low angle of less than 4 mrad. and the one obtained at 45 deg. incidence angle (B). The standard spectra of Cr metal and Cr₂O₃ thin films are also shown. The Cr₂O₃ absorption curve locates higher energy side of the Cr curve, since the position of the absorption edge shifts to a higher energy as the oxidation number increases.

The curves A and B are clearly different, though the sample is the same. For the 45 deg. incidence angle, the penetration depth is in the order of μm above the absorption edge. Therefore B corresponds to information for the whole film, i.e., Cr metal 200 Å layer plus Cr₂O₃ 2000 Å layer. On the other hand, in the grazing incidence condition, the penetration depth become extremely shallow and is estimated to be about 100 Å for A. That is, curve A indicates the chemical state of the near-surface layer of the sample. Actually, it is close to

the spectrum of Cr metal. The difference between A and the Cr metal spectrum might be explained by considering the formation of the surface Cr₂O₃ layer by natural oxidation. Assuming that curve A consists of two components of Cr and Cr₂O₃ spectra, thickness of the surface Cr₂O₃ layer can be calculated and was estimated to be about 40 Å. From these results, it is concluded that we can analyze the chemical nature of near-surface layer separated from the bulk material information using the grazing incidence condition. The authors would like to thank Prof. Gohshi of the Univ. of Tokyo for his valuable discussion.

References

- 1) A. Iida et al.: Nucl. Instr. and Methods **A246**(1986)736.
- 2) K. Sakurai et al.: Anal. Sci. **4**(1988)37.
- 3) K. Sakurai et al.: Adv. in X-Ray Anal. **32**(1989)167.

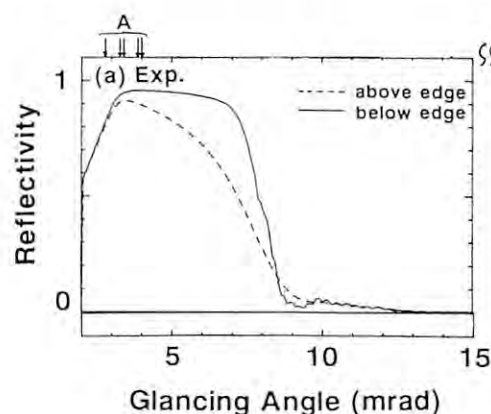


Fig.1 Angular dependence of the reflectivity at lower (solid line) and higher (dashed line) energy side of the absorption edge.

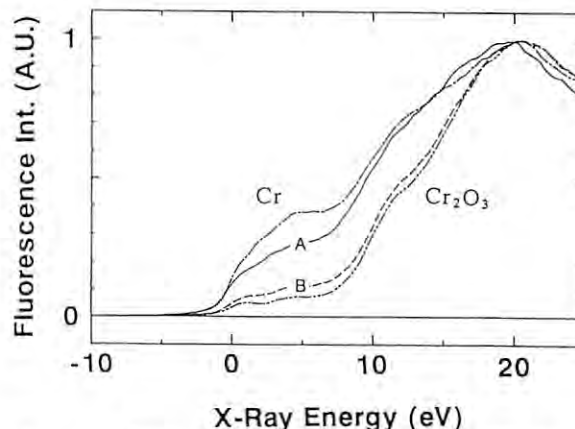


Fig.2 Near edge absorption spectra of Cr[200Å]/Cr₂O₃ [2000Å] thin film using the GIF setup. A: extremely small glancing angle less than 4 mrad. (See Fig.1), B: 45 deg. incidence.

X-RAY DIFFRACTION ANALYSIS ON LOCAL STRUCTURE CHANGES OF AMORPHOUS ALLOY

Toshio NASU, Kunio NAGAOKA, Toshiharu FUKUNAGA*, Masaki SAKURAI**, Fumitake ITOH**, Kenji SUZUKI** and Kazumasa OHSUMI***

Faculty of Education, Yamagata University, 1-4-12 Kojirakawa, Yamagata 990 Japan

*Faculty of Engineering, Nagoya University, Furoh-cho, Chikusa-ku, Nagoya 464 Japan

**Institute for Materials Research, Tohoku University, 2-1-1 Katahira, Sendai 980 Japan

***Photon Factory, National Laboratory for High Energy Physics, Oho-machi, Tsukuba 305 Japan

Introduction

The deformation behaviours of amorphous alloy are completely different from those of crystalline in both the elastic and plastic regions. The previous EXAFS measurement confirmed that the anelasticity can occur on the atomic scale by the irreversible rearrangement of atoms⁽¹⁾. The results of positron annihilation measurement suggest that the free volume in amorphous alloy increase by plastic deformation⁽²⁾. "Work softening" of amorphous alloy seems to be based on this increase of the free volume by plastic deformation.

The purpose of this report is to investigate the structural changes with plastic deformation by means of X-ray diffraction.

Experimental

$\text{Pd}_{83}\text{Si}_{17}$ amorphous ribbon (2.7 mm wide and 0.03 mm thick) was prepared by splat quenching from the molten state using a single-roll technique. X-ray structure factors $S(Q)$ of $\text{Pd}_{83}\text{Si}_{17}$ amorphous alloy in the various states of plastic deformation were measured by using synchrotron radiation at the beam line 4B of Photon Factory of KEK. The amorphous ribbon was reduced in thickness by cold rolling along the direction of the long ribbon. The degree of plastic deformation was defined as the relative increase of length. The degree of deformation were 0 (as prepared), 5.0 and 10.0 %. The direction of Q vector of X-ray coincide with the direction of rolling.

Results and Discussion

Figure 1 shows the total structure factors of as prepared and cold-rolled $\text{Pd}_{83}\text{Si}_{17}$ amorphous alloy. Figure 2 shows the differences of total

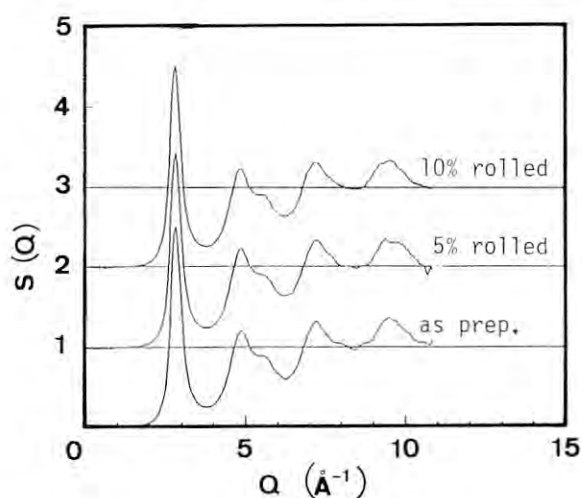


Fig.1 Total structure factors $S(Q)$ of cold rolled $\text{Pd}_{83}\text{Si}_{17}$ amorphous alloy.

structure factors, $\Delta S(Q)$

where $\Delta S(Q) = S(Q)_n - S(Q)_0$, where $S(Q)_0$ denotes the structure factor for as prepared specimen, and $S(Q)_n$ denotes that for the cold rolled specimen with the deformation degree of n %. The behaviour of $\Delta S(Q)$ indicates that the height of the first peak in $S(Q)$ decreases by cold rolling of 5 %. Increasing the degree of plastic deformation more than 5 %, the height of the first peak in $S(Q)$ returns back closer to the original value of as prepared alloy. These results suggest that a much more disordered atomic structure is produced by the deformation of 5 % than that is produced by the deformation of 10 %.

References

- (1) T. Nasu et al., Materials Science and Engineering, **98**, 553(1988).
- (2) T. Nasu et al., J. Phys. Soc. Jpn., **58**, 894(1989).

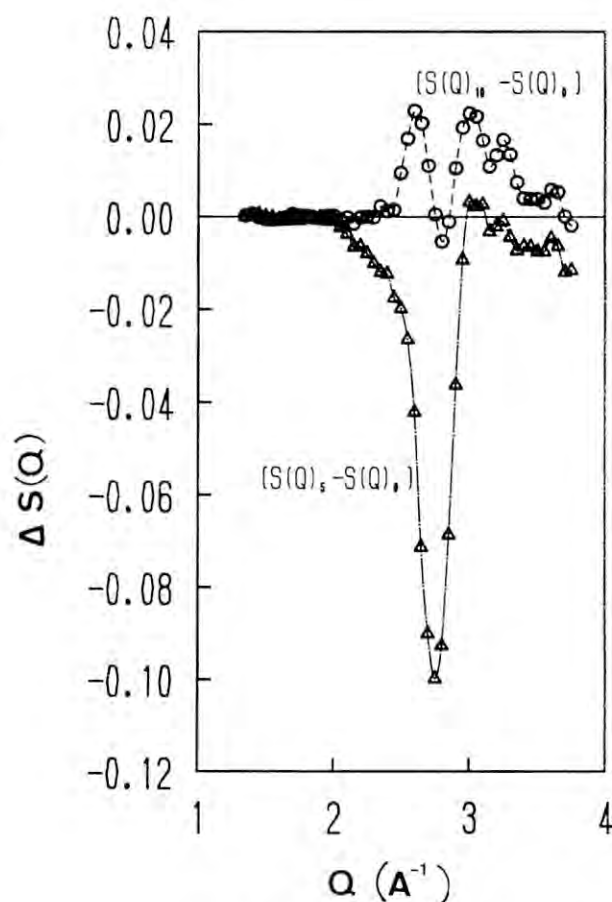


Fig.2 Differences in the total structure factors $\Delta S(Q)$ (=rolled alloy - as prepared alloy).

PRESSURE INDUCED AMORPHIZATION OF $\text{Ca}(\text{OH})_2$

Takamitsu YAMANAKA, Osamu OHTAKA, Shinji KAWASAKI and Toshifumi ASHIDA*

College of General Education, Osaka UNIV. Toyonaka 560

*Faculty of Engineering, Tokushima Univ. Tokushima 770

INTRODUCTION

Since an amorphization of H_2O ice I was discovered under pressure, many interests about the process have been attracted for the premonitory phenomenon of the structure transformation.

Recently pressure-induced amorphizations of SiO_2 , SnCl_4 and LiKS04 have been also reported by diffraction studies under high pressure. However, the amorphization mechanism has not been clarified with respect to thermodynamical and mechanistic aspects.

Many of the above mentioned structures consist of array of molecules of AX_4 . The decomposition to micro-domains under high pressure may induce the amorphization.

We have observed the crystalline-to-amorphous transition of $\text{Ca}(\text{OH})_2$ (Fig. 1), which is an isostructure to CdI_2 . This structure is not composed of any molecular structures therein.

The present experiment aimed to disclose the process of the crystalline-to-amorphous phase transition.

EXPERIMENT

Energy dispersive (ED) diffraction studies of the pressure-induced amorphization of $\text{Ca}(\text{OH})_2$ has been undertaken using the diamond anvil pressure cell which set on the powder diffractometer PFPD at BL-4B. The diamond anvil was installed on the sample spinner with 1/20 rpm, which is prepared for the randomization of the preferred orientation of sample and reduction of the effect of the grain growth under high pressure. Gasket of udmitt-700 and pressure transmission medium of mixture of methanol and ethanol were used. Pressure was measured by the ruby fluorescence method.

In situ observation of the ED spectra up to 16 GPa was carried out by intrinsic Ge SSD in the energy range 10keV-40keV. Energy resolution and counting efficiency were tested in advance by radio active isotope.

Diffraction profile of the ED spectrum after the subtraction of the background was expressed by the pseudo-Voigt function.

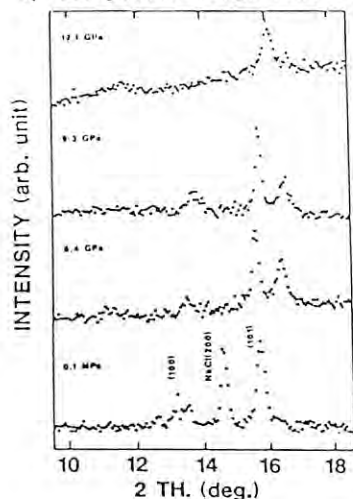


Fig. 1

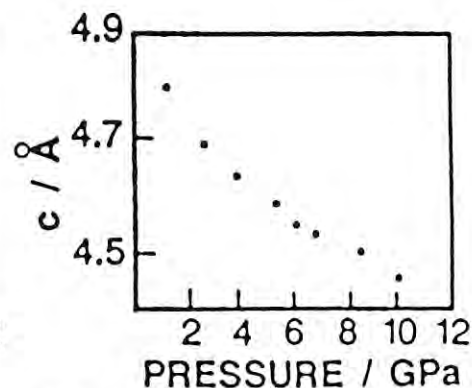
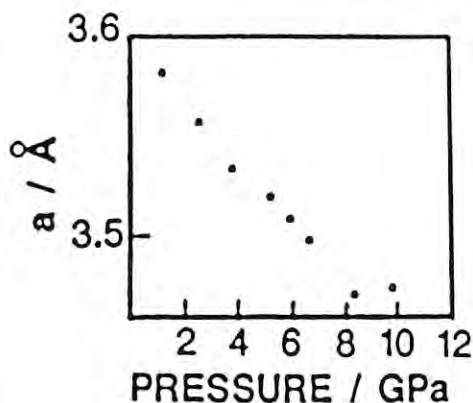


Fig. 2

The relation between energy and inter-spatial distance was calibration with the X-ray fluorescence of several metal elements. The lattice constant of $\text{Ca}(\text{OH})_2$ under pressure was calculated by six diffraction peaks of 001, 100, 101, 102, 110 and 111.

The diffractometer and ED measuring system were previously detailed in PF Act. Rep. #5 143 (Yamanaka, et al.) and 144 (Uno, et al.) and #4 147 (Yamanaka, et al.)

RESULT

(1) The diffraction peaks were observed up to 10 GPa but could not be detected at above 12 GPa. This indicates that the critical pressure of the crystalline-to-amorphous transition is placed between 10 GPa and 12 GPa at room temperature.

(2) The lattice constants of $a(\text{\AA})$ and $c(\text{\AA})$ of $\text{Ca}(\text{OH})_2$ almost linearly decreased with pressure (Fig. 2). The ratio of c/a as a function of pressure decreased with pressure, which implies that the sample was more easily compressed along the direction of the c axis than the a axis, and that the deformation from the hexagonal closest packing of oxygen atoms becomes more extreme.

(3) A bulk modulus of $\text{Ca}(\text{OH})_2$ was calculated to be $K_0 = 39.2 \text{ GPa}$ from the volume compressibility.

(4) Full width half maximums (FWHM) of the diffraction peak profiles became linearly broadened and the integrated diffraction intensities were decreased with pressure.

(5) The amorphous phase stayed in all through the experimental range up to 16 GPa at room temperature. It is an interesting problem to determine whether the phase is thermodynamically stable at high pressure. The phase was confirmed to be metastable under the thermally activated condition and we found a new phase at 10 GPa and 450 K. Probably the amorphous phase is in the premonitory state of the transformation to the high pressure phase. The structure of the new phase has not been determined yet.

THE STRUCTURE STUDY OF GeO₂-P₂O₅ GLASSES WITH THE ANOMALOUS X-RAY SCATTERING(II)

Yutaka SHIMIZUGAWA, Hideki MORIKAWA, Fumiyuki MARUMO, Akihiko NUKUI* and Kazumasa OHSUMI**

Research Laboratory of Engineering Materials, Tokyo Institute of Technology, Yokohama 227

*National Institute for Research in Inorganic Materials, Tsukuba, Ibaraki 305

**Photon Factory, National Laboratory for High Energy Physics, Tsukuba, Ibaraki 305

INTRODUCTION

As to the GeO₂-P₂O₅ glass system, it was reported that a part of Ge atoms change their coordination numbers from 4 to 6 on introduction of the P₂O₅ component in the glasses. We have estimated the fraction of six-coordinated Ge atoms from the Ge-O distances obtained by Ge K EXAFS analysis.¹⁾ In this article, we report the Ge-O distances estimated by the radial distribution function (RDF), which were obtained making use of the anomalous scattering of Ge atoms.

EXPERIMENTAL

The chemical composition of three kinds of GeO₂-P₂O₅ glasses examined are given in Table 1. The intensity measurements were performed on the powder diffractometer installed on BL-4B. The details of the experiment were described in our previous report.²⁾ The energy employed in this study were 11.091KeV ($f'_{Ge}=-7.395$) and 10.240KeV ($f'_{Ge}=-2.265$).

RESULTS

The experimental data were put on a common scale by dividing measured values with monitor intensities, corrected for the absorption and Compton scattering, and then normalized in an electron unit. Analytic approximations were used for atomic scattering and Compton scattering factors. The low r contribution to the RDF was corrected analytically. In the conventional RDF, there was no obvious difference in the first peak distance among the three kinds of samples, the peak being contribution of P-O and Ge-O pairs.

Fig.1 shows $I_{coh}-f^2$ of the GEP3 sample. The difference depending on X-ray energy shows the effect of the anomalous scattering of Ge atoms. The differential reduced intensities $S\Delta i(S)$ was derived from these curves, by taking the difference(Fig.2). $S\Delta i(S)$ is defined as follows,

$$S\Delta i(S)=\Delta(I_{coh}-f^2)/2C_{Ge}\Delta f'_{Ge}f,$$

where C_{Ge} is the atomic ratio of Ge and $\Delta f'_{Ge}$ is the difference between f' factors of Ge at two energies.

With Fourier transformation of $S\Delta i(S)$, the differential distribution function(DDF) has been obtained(Fig.3). The Ge-O distances estimated on Fig.3 are also given in Table 1. The values show the same tendency as those obtained with EXAFS.

In conclusion, the change of coordination number has been confirmed by the two different methods. A detailed discussion will be made elsewhere.

REFERENCES

1) Y.Shimizugawa, C.D.Ying, M.Okuno, H.Morikawa, F.Marumo, Y.Udagawa, N.Mochida, T.Sekiya, Yogyo-Kyokai-Shi, 95, 418(1987)
2) Y.Shimizugawa, K.Itoh, S.Yamazaki, H.Morikawa, F.Marumo, A.Nukui, H.Ozawa, R.Uno and K.Ohsumi, P.F. Activity Report, 6, 158(1988)

Table 1. Chemical composition and Ge-O distances

Sample	Chemical Composition(mol%)		Ge-O distance(A)	
	GeO ₂	P ₂ O ₅	EXAFS	DDF
GeO ₂ (Glass)	100	—	1.73	1.74
GEP1	79.6	20.4	1.74	1.73
GEP2	66.0	34.0	1.76	1.76
GEP3	60.8	39.2	1.77	1.78
GeO ₂ (Trigonal)	100	—	(1.74)	
GeO ₂ (Tetragonal)	100	—	(1.89)	

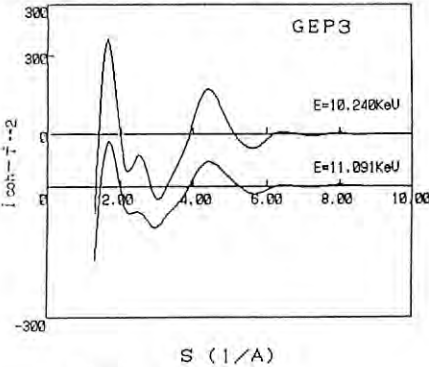


Fig 1. $I_{coh}-f^2$ curve of GEP3 sample

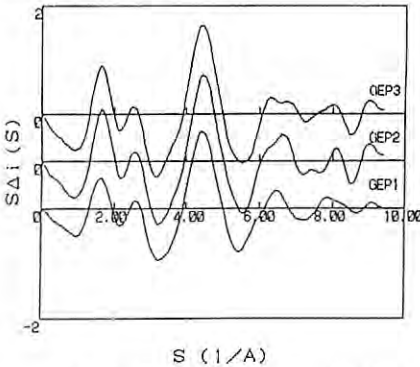


Fig 2. $S\Delta i(s)$ curve obtained from $I_{coh}-f^2$ curve

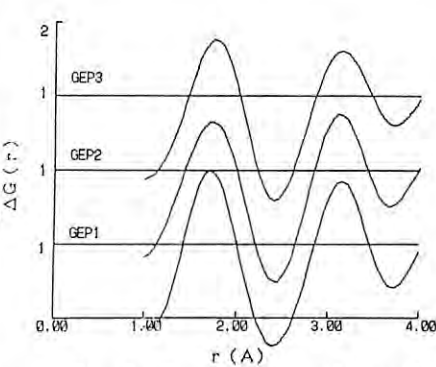


Fig 3. Fourier transform of $S\Delta i(s)$

A Synchrotron Radiation Beam Following System of the X-ray Powder Diffractometer for the Photon Factory.

Haruo Ozawa, Ryosei Uno and Kazumasa Ohsumi*

College of Humanities and Sciences, Nihon Univ. Sakurajosui, Setagaya, Tokyo 156.

*Photon Factory, National Laboratory for High Energy Physics, Tsukuba, Ibaragi 305.

Introduction

One of the advantages of the synchrotron radiation(SR) beam as an X-ray source of the powder diffractometry is that a diffraction measurement at an arbitrary wavelength can be carried out.

In the case of our diffractometer, the wavelength of the incident X-rays can be set within the error of 0.0001 \AA and can be measured within 0.00002 \AA . However, if the beam moves 1 mm vertically, an angle of incidence to the monochromator varies by about 0.003 deg at the BL-4B hutch and the wavelength of the exit beam from the monochromator changes by about 0.0003 \AA . To make the accuracy of the real part of the anomalous dispersion correction more than two digits just near the absorption edge, for example 0.001 \AA shorter than the K absorption edge of Ga atom, the accuracy of the wavelength more than 0.0001 \AA is required. Therefore the diffractometer should follow the SR beam when the beam moves more than 0.3 mm . To achieve this requirement a new system was developed.

Design of the SR beam following system

The detector of a position of the beam is an X-ray TV camera. To reduce the intensity of the SR beam, a small piece of a copper plate was set as a scatterer in the plane of incidence on a side of an incident slit of the monochromator at 45 deg to the SR beam, as shown in Fig. 1. The X-rays from the scatterer was detected by the camera through a horizontal slit of 0.5 mm width put near the middle point between the scatterer and the camera. The camera was fixed to the

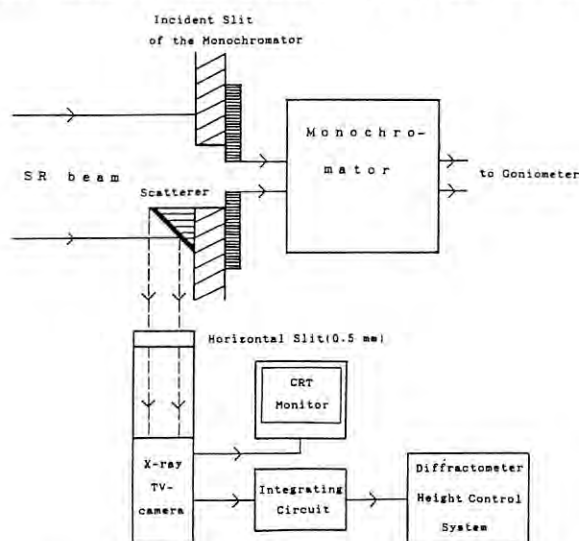


Fig. 1. A block diagram of the SR beam following system.

diffractometer in order to detect the relative shift of the SR beam to it. The output of the camera was monitored by the CRT and the vertical position of the SR beam was stored in memories of 640 channels. The data in a single scanning line can be added up to 256 times to get the time-integrated intensity. The position of the center of the beam was estimated from a middle point of FWHM of the beam pattern. The sensitivity of the beam shift was about 0.03 mm , which was enough to control the shift of the beam within 0.3 mm .

Results and Discussion

An example of the shifts of the SR beam and the results of the beam following operation on 7th July 1989 is shown in Fig. 2. The diffractometer displaced upwards at about 8:20 am. Three downwards displacements were performed from 2:20 pm to 4:15 pm.

These results show that our SR beam following system works satisfactorily and also the system is necessary for the measurements at the neighbourhood of the absorption edge.

Acknowledgement

This work was supported by the Grant-in-Aid for General Scientific Research. The authors are grateful to members of the Hitachi Denshi, Ltd and Rigaku, Ltd for the cooperation in the process of designing the system.

Reference

- 1) H. Ozawa et al: Rev. Scie. Instr. 60(1989) 2382.

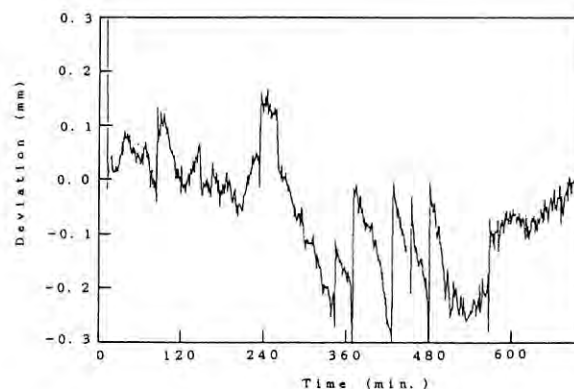


Fig. 2. An example of shifts of the beam and displacements of the diffractometer.

Evaluation of Dimensional and Orientational Distribution of Crystallites in Powder Specimen

Haruo OZAWA, Ryosei UNO and Ken YUKINO*

Department of Physics, College of Humanities & Sciences, Nihon University, Tokyo 156

*National Institute for Research in Inorganic Materials, Ibaraki 305

Introduction

The preferred orientation and the size effect of the crystallites in the powder sample are ones of the important problems in the X-ray powder diffractometry. A method of evaluating them, called " ϵ -scan" method, is proposed by K. Yukino et al.¹⁾ and successfully applied to the focussing geometry of the diffractometer.

In the ϵ -scan method, a thick tabular powder specimen is rocked about the θ axis of a diffractometer while the detector is fixed at a Bragg peak position $2\theta_B$. When the powder specimen is homogeneous and infinite in thickness, the total intensity of a Bragg reflection, $I(\epsilon)$, is given by

$$I(\epsilon) = I(0) \cdot A(\epsilon),$$

$$A(\epsilon) = 1 - \cot \theta_B \cdot \tan \epsilon,$$

$$-\theta_B \leq \epsilon \leq \theta_B,$$

where $I(0)$ is the total intensity in the case of symmetry reflection, $A(\epsilon)$ the absorption factor at a angle ϵ . Only a part of the total intensity can be actually measured because of a finite area of the receiving slit of the detector. Figure 1 shows the absorption factor at some Bragg angles, calculated under the conditions shown in the figure, in the kinematical theory. The angular dependence of the orientational distribution $r(\epsilon)$ is given by

$$r(\epsilon) = I_{\text{ex}}(\epsilon) / I_{\text{c}}(\epsilon)$$

where I_{ex} is the experimental intensity, I_{c} the calculated one. $r(\epsilon)$ reflects actually the inhomogeneities of the powder specimen as grain size, orientation and packing density.

Experimental

Intensity measurement was performed at BL-4B station by using the high-resolution powder diffractometer (PFPD) with the parallel geometry.²⁾ The conditions of the experiment were as follows: IS=0.2mm, RS=10mm, $\lambda=1.5409$ Å.

The sample spinner was very useful to average the effects of the orientation and the packing density. In the case of the NBS standard Si powder 640B, the fluctuation of the reflection intensity was less than 4% using the spinner while it was about 30% without the spinner. Therefore all intensity measurements were performed using the spinner. The species measured

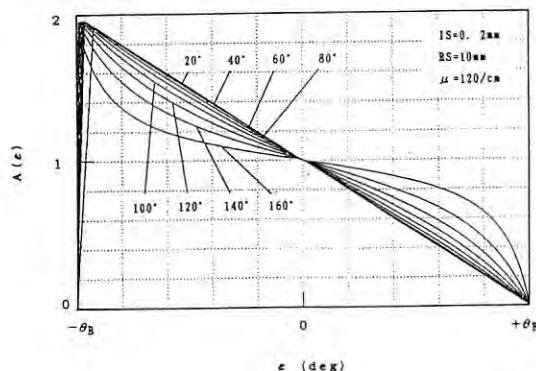


Fig.1. Absorption factors calculated at some Bragg angles $2\theta_B$ in the ϵ -scan method.

were LiF, Si and hot pressed BN.

Results and Discussion

LiF was expected to be homogeneous because it was cubic in the form and less than $5\mu\text{m}$ in the grain size by the observation of the SEM. The result on LiF (111) plane is shown in Fig. 2. The same result was obtained for all the other planes. Thus, the homogeneity was confirmed for LiF. In order to find the size effect, the Si powders of the various grain size ($2\sim 3\mu\text{m}$, $\sim 5\mu\text{m}$, $\sim 10\mu\text{m}$, $\sim 20\mu\text{m}$) were measured. The fluctuation of the intensity for the powder of the grain size more than $\sim 10\mu\text{m}$ was estimated to be more than 30% even if the sample spinner was used. It was possible to correct the preferred orientation for the powder of the grain size of $\sim 5\mu\text{m}$. The preferred orientation for that of less than $3\mu\text{m}$ could be neglected. The angular dependency of the orientational distribution was found for the hot pressed BN, as shown in Fig. 3. Gaussian may be the good fitting curve for it.

References

- 1) K. Yukino and R. Uno, Jpn. J. Appl. Phys., **25**, 661(1986)
- 2) R. Uno et al., Aust. J. Phys. **41**, 133(1988)
H. Ozawa et al., Rev. Sci. Instrum. **60**, 2382(1989)

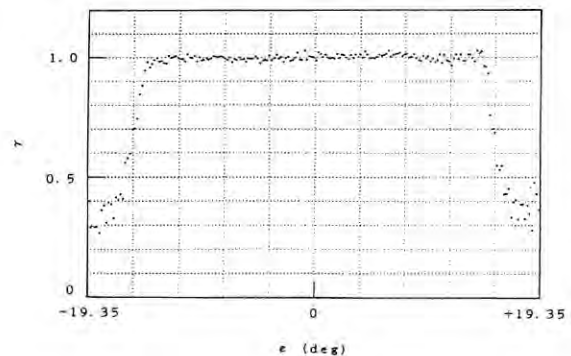


Fig.2. Homogeneity of LiF(111)

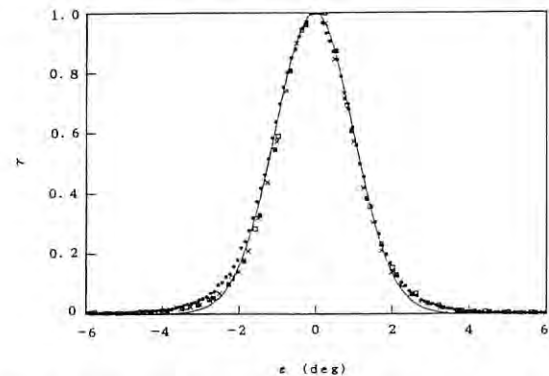


Fig.3. Angular dependency of orientational distribution of (001) plane of hot pressed BN. (● — 002, × — 004, ■ — 006, □ — 008). The solid line expresses the fitted Gaussian.

TEXTURE ANALYSIS OF SILVER HALIDE PHOTOGRAPHIC GRAIN

Toshihiko YAGI, Takamitsu YAMANAKA*, Osamu OHTAKA*, Toshifumi ASHIDA**
and Kazumasa OHSUMI***

Development Center KONICA Co. Tokyo Hino 191

* College of General Education, Osaka Univ. Toyonaka 560

** Faculty of Engineering, Tokushima Univ. Tokushima 770

*** Photon Factory, National Laboratory for High Energy Physics Tsukuba 305

INTRODUCTION

AgBr_{1-x}I_x powder, photo-sensitive materials has been investigated for collar film substance. The crystallite size, texture and AgI concentration give large effects to the image quality and photo-sensitivity. The procedure of the sample preparation also gives a significant effect. Assembly of the submicron grains having several different compositions is designed to form a zonal structure of a few micron in diameter. The composition of the substance is finely controlled. It has been known that AgBr (B1 type structure) has a wide solid solution range with AgI (wurtzite type structure). The procedure of the sample preparation condition

Analysis of the crystallite size, strain in the crystal lattice and chemical composition can be made by the precise profile analysis and measurement of the lattice constant. Anomalous dispersion study can also confirm a texture of the zonal structure. An integrated diffraction intensity makes a quantitative analysis of the thickness of the layer.

EXPERIMENT

A powder diffractometer PFPD designed for the high angular resolution diffraction study with in $\pm 0.0005^\circ$ (PF Act. Rep. #5, 144) was used for the profile analysis. A monolithic Si (111) monochromator with fixed exit beam position supplies an extremely precise wave length of the incident X-ray source (less than 10-5Å) with 1.54330Å, which is similar to the characteristic X-ray of CuK α . We selected the wavelength for the comparison with the diffraction study using the conventional X-ray source in laboratory. An evacuation of all optical path including the sample chamber reduces a background noise. Sample spinner with 3 rpm was employed for the randomization of sample orientation. Step counting technique of $0.01^\circ / 5\text{sec}$ was applied.

Profile analysis employed a pseudo-Voigt distribution function, which was previously found to be the most optimum profile function.

Well characterized AgBr_{1-x}I_x samples with different grain size consisted of the submicron crystallite were prepared the double-jet method. Observation by scanning electron microscope revealed that all samples were of homogeneous grain size and that several different crystal forms, octahedron, hexahedron, didodecahedron and spherical, were crystallized by the sample preparation.

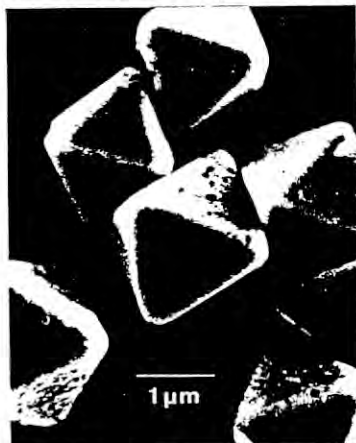
RESULT

- (1) With respect to AgBr samples, end specimen of the solid solution, having diameters from $0.8\mu\text{m}$ to $2.0\mu\text{m}$ determined by SEM, profile analyses of the line broadening caused by the crystallite-size effect reveals that FWHM of the Lorentzian part of the peaks 111, 311, 331, 440, 531, 620 of each sample increased with diameter.
- (2) A pure AgBr showed much longer tail of peak profile than the sample containing AgI molecule. This is probably because the lattice distortion of the former sample is exceedingly large. This is coincident with the noticeable diffuse streak of the Bragg reflections of the single crystal. (Noticed that AgBr crystal is a well known ion conductor.)
- (3) A lattice constant of the solid solution is very sensitive for the concentration of AgI molecule because of the large difference of halogen ionic radii. A linear relation between the lattice constant and the concentration is presented by

$$a(\text{\AA}) = 5.7748 + 0.00368X \quad (X:\text{mole}\%)$$

- (4) AgBr_{1-x}I_x grain of $2\mu\text{m}$ in diameter was grown, having seven-layered zonal structure with an octahedral form (Fig.1). Each layer has a different composition between $x=0.03$ and 20.0 , as shown in Fig.2. A high angular resolution with PFPD disposed the separated peaks of 420 reflection from the individual layered compound (Fig.3). Integrated intensity of each peak indicate the mass ratio related to the thickness of the layer of the zonal structure.

These analyses could not be performed by the conventional X-ray source.



AgX grains

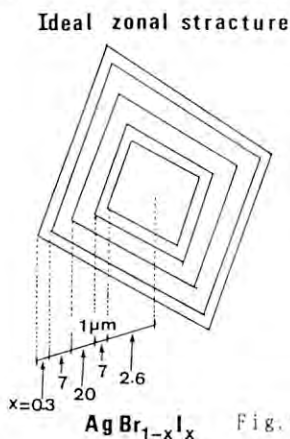


Fig. 1

AgBr_{1-x}I_x Fig. 2

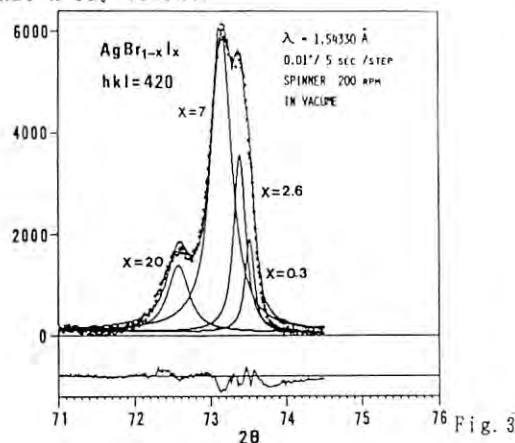


Fig. 3

Local structure and valence states of Tl-Ba-Ca-Cu-O superconductors

Hirotaaka Yamaguchi, Hiroyuki Oyanagi, Hideo Ihara, Ryoji Sugise* and Takehiko Shimomura**

Electrotechnical Laboratory, Umezono, Tsukuba, Ibaraki 305

**Ube Industries Ltd., Ube, Yamaguchi 755*

***Unitika R&D Center, Uji, Kyoto 611*

INTRODUCTION

Tl-Ba-Ca-Cu-O superconductors, $\text{Tl}_m\text{Ba}_2\text{Ca}_{n-1}\text{Cu}_n\text{O}_{m+2n+2}$ consist of stacking Cu-O layers between which Ca layers are sandwiched, and they form perovskite-like layered units. The units are separated by Tl-O monolayers and bilayers in $m=1$ and $m=2$ systems, respectively. The superconducting transition temperature T_c depends on the number of Cu-O layers in the perovskite-like unit and the highest T_c occurs at 122 K in $\text{TlBa}_2\text{Ca}_3\text{Cu}_4\text{O}_{11}$ (1234). We have measured the Cu K-edge absorption fine structure to study the valence state of Cu ions and local structure around them. We have also measured the Tl L_3 -near-edge structures to discuss the origin of hole carriers.

EXPERIMENTAL

The samples were prepared by mixing powders of Tl_2O_3 , BaO, CaO and CuO. Well mixed powders were cold pressed into pellets and sintered at 890 °C in an oxygen atmosphere for 30-50 minutes.¹ X-ray absorption measurements were performed at the BL-4C beam line. Both Cu K- and Tl L_3 -edge spectra were measured with powdered samples by transmission mode at 300 K and 30 K. The measurements of the temperature variance of Cu K-EXAFS of 1234 were also carried out between these temperatures.

RESULTS AND DISCUSSION

The near-edge spectrum of $\text{Tl}_2\text{Ba}_2\text{Ca}_2\text{Cu}_3\text{O}_{10}$ (2223) is shown with those of La_2CuO_4 , $\text{Ba}_2\text{YCu}_3\text{O}_{6.96}$ and Nd_2CuO_4 in Fig. 1. La_2CuO_4 and Nd_2CuO_4 are typical compounds composed of Cu-O octahedra and planes, respectively while $\text{Ba}_2\text{YCu}_3\text{O}_{6.96}$ is of both of Cu-O pyramids and planes. The near-edge structure of the 2223 is found to be very similar to that of $\text{Ba}_2\text{YCu}_3\text{O}_{6.96}$, which reflects the similar average coordination environment of the Cu ions comprising the layers and pyramids. The absorption edge of the 2223 is 0.47 eV higher in energy than that of La_2CuO_4 . The Cu valence is estimated at 2.2 by using the value of average edge shift of 2.47 eV/valence.² The edge positions of the $m=1$ -system lay slightly higher in energy than those of the $m=2$ -system. On the other hand, the systematic variations of the near-edge structure with n were not found. The Tl L_3 -near edge spectrum of 2212 has both features of Tl^{+1} and Tl^{+3} and the edge position, which is defined by a midpoint of absorption, lies between those for Tl^{+1} and Tl^{+3} in energy. This suggests the occurrence of Tl^{+1} and agrees with the results of the photoelectron spectroscopy.³

In the Fourier transform of the Cu EXAFS, the most dominant peak indicates the contribution of

the nearest planer-coordinated oxygen ions while the peak corresponding to the apical oxygens of CuO_5 pyramid is hardly found. This is because the apical oxygens are fewer in number and located further than those in plane. We performed the Fourier filtering of the contribution of the first-nearest oxygen in $k^3\chi(k)$ between 1.0 and 2.3 Å, and fitted it using single-shell model. No anomaly in the temperature dependence of the Debye-Waller factor σ of the 1234 was found between 30 K and 300 K and it was fitted to the Einstein model with the Einstein temperature $\Theta_E=577$ K.

1. R. Sugise, M. Hirabayashi, N. Terada, M. Jo, T. Shimomura and H. Ihara: Jap. J. Appl. Phys **27**, L1709 (1988).
2. H. Oyanagi, Y. Nishihara, K. Murata, H. Yamaguchi, H. Unoki, H. Ihara, T. Matsushita, M. Tokumoto and Y. Kimura: J. Phys. Soc. Jpn **58**, 3324 (1989).
3. T. Suzuki, M. Nagoshi, Y. Fukuda, Y. Syono, M. Kikuchi, N. Kobayashi and M. Tachiki: Phys. Rev. B **40**, 5184 (1989).

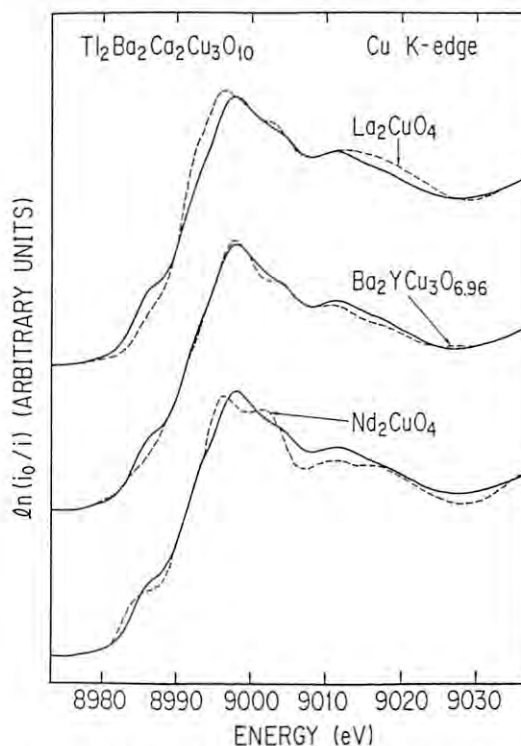


Fig. 1 The Cu K-XANES spectrum of $\text{Tl}_2\text{Ba}_2\text{Ca}_2\text{Cu}_3\text{O}_{10}$ compared with those of La_2CuO_4 , $\text{Ba}_2\text{YCu}_3\text{O}_{6.96}$ and Nd_2CuO_4 (dashed lines).

Ge/Si Monolayer Superlattices on Si(100) Studied by Surface-Sensitive EXAFS

Hiroyuki OYANAGI, Tsunenori SAKAMOTO, Kunihiro SAKAMOTO,
Hirotaka YAMAGUCHI and Takafumi YAO

Electrotechnical Laboratory, Umezono, Tsukuba, Ibaraki 305, Japan

INTRODUCTION

Ge/Si strained-layer superlattices exhibit unique optical properties. In particular, the origin of the lowest electroreflectance transition at 0.80 eV observed for $\text{Ge}_4\text{Si}_4(100)$ superlattice¹⁾ has attracted much attention. However, whether this strong transition originates from the indirect $\Gamma_V\text{-}\Delta_C$ excitation or the folded-in direct transition is not established yet. To further characterize the electron states of the Ge/Si superlattices dominated by strained Ge layer, we have studied the local structure around Ge atoms in $\text{Ge}_n/\text{Si}(100)$ superlattices ($n < 8$) using surface-sensitive XAFS.

EXPERIMENTAL

Ge_n/Si monolayer superlattices were prepared on a well-oriented p-type Si(100) (4 ohm-cm) surface in an UHV MBE growth chamber with a base pressure of 1.3×10^{-7} Pa. A single-domain Si(100) 2×1 structure was obtained by annealing at 1000°C for 20 min. Two-dimensional growth of Ge and Si layers were performed with an electron gun and a PBN Knudsen cell, monitoring the oscillation of RHEED specular beam intensity. Surface-sensitive XAFS experiments utilized a fluorescence-detection technique and a total reflection geometry. As a fluorescence detector, a Si(Li) solid state detector (SSD) was used to filter out the scattered photons and diffractions.

RESULTS AND DISCUSSION

In Fig. 1, the Ge K EXAFS oscillations of Ge_n/Si superlattices are plotted as a function of photoelectron wavenumber k for (a) $n=2$, (b) $n=4$ and (c) $n=8$. The EXAFS profile indicates that the Ge-Ge bond increases with n since the backscattering amplitude of Si peaks at low k and falls off sharply with the increase of k , while that of Ge has a maximum at $k=6.7\text{\AA}^{-1}$ and extends to $k > 15\text{\AA}^{-1}$. The ideal Si/Ge ratio is 0.5 ($n=2$), 0.33 ($n=4$) and 0.14 ($n=8$) without a chemical disorder along the [100] direction. The EXAFS profile for $n=2$ indicates,

however, that the Ge-Si bonds still dominate for $n=2$ as in case of $n=1$ ²⁾. These results indicate the presence of substitutional disorder along the [100] direction due to interdiffusion. Second, the Fourier transform analysis of EXAFS data show that the Ge-Ge bondlength decreases as the Ge layers are strained, in agreement with the elastic energy minimization. This rules out a possible superlattice structure proposed by Wong et al.³⁾ in which the Ge-Ge bondlength of bulk Ge is conserved. In summary, The present results demonstrate that the chemical disorder exists along the perpendicular direction which relaxes the k -conservation rules along the [100] direction enhancing Γ -X mixing.

1) T.P.Pearsall, J.Beck, L.C.Feldman, J.M.Bonar and J.P.Mannaerts; Phys.Rev.Lett.58(1987)729.

2) H.Oyanagi, T.Sakamoto, K.Sakamoto, T.Matsushita, T.Yao and T.Ishiguro; J.Phys.Soc.Jpn. 57(1988)2086.

3) K.B.Wong, M.Jaros, I.Morrison and J.P.Hagon; Phys.Rev.Lett.60(1988)2221.

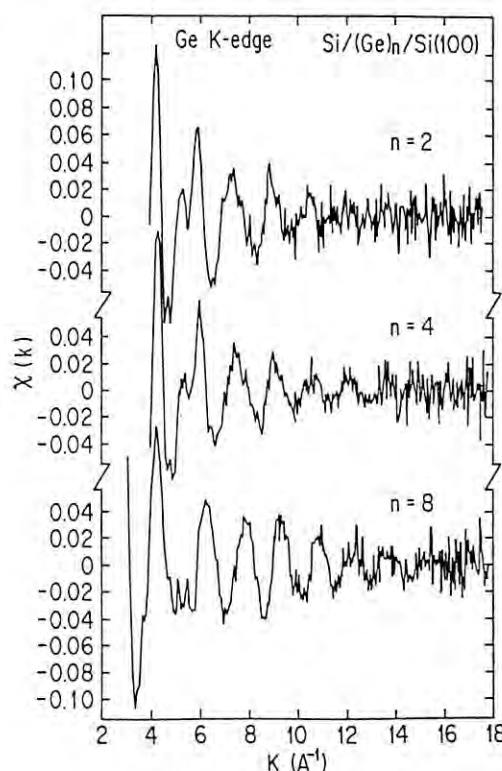


Fig. 1 Ge K-EXAFS oscillations of Ge_n/Si monolayer superlattices for (a) $n=2$, (b) $n=4$ and (c) $n=8$.

SINGLE-CRYSTAL DIFFRACTOMETRY WITH POLYCRYSTALLINE SAMPLES

A. W. Stevenson, S. W. Wilkins, J. Harada*, M. Sakata* and K. Ohshima**

CSIRO, Division of Materials Science and Technology, Locked Bag 33, Clayton, Victoria, 3168, Australia

* Department of Applied Physics, Nagoya University, Chikusa-ku, Nagoya 464-01, Japan

** Institute of Applied Physics, University of Tsukuba, Sakura, Ibaraki 305, Japan

The current experiments were based on the application of triple-crystal geometry to cases of polycrystalline or powder samples. Using triple-crystal diffraction data from powder samples it is hoped that one can study the diffraction process in individual crystallites. In this way information on particle size and characteristics, and strain can be obtained. Another aim of such studies is to be able to investigate the nature of extinction in powders.

The application of triple-crystal diffractometry and topography to polycrystalline materials, and in particular ceramics and metals is very promising. Such studies may be able to shed light (non-destructively) on the processes of crack nucleation and propagation, and fatigue

The experiments were carried out on BL-4C. The wavelength selected was 1.4 Å. A quartz powder sample (crystallite size $< 140 \mu\text{m}$) was studied initially. The 100 and 101 reflections were selected. A Si 111 analyzer crystal was used. ω scans revealed many peaks, associated with individual crystallites. Fig. 1 shows the 2 dimensional intensity distribution for 101 quartz reflection. The various crystallites are clearly visible along the ω -direction. The values of 2θ for the crystallites show very little variation, consistent with little or no strain (lattice-parameter variation).

In an attempt to induce strain in the quartz powder, we heated the sample to 20, 50, 120, and 160°C. The changes to the peak positions (2θ) were very consistent between the three crystallites examined. These changes were quite significant with 2θ decreasing by 0.006° (20–50°C), 0.008° (50–120°C), and 0.008° (120–160°C). These changes can be shown to be in reasonable accord with the expected thermal expansion behaviour of quartz.

The next sample to be examined was a Lucalox ceramic sample (Al_2O_3) which contained a (macro-) crack directed along its length. The particle size was typically around 30 to 40 μm . A wedge was positioned so that it could be driven into

the crack with a micrometer, thereby increasing the stress field at the crack tip and forcing the crack to propagate. The sample was mounted on the diffractometer so that the X-ray beam was incident on the sample just ahead of the crack tip. We located six crystallites which we "kept track of" as the wedge was driven into the crack. These particles were clearly resolved in the diffractometer angles $\omega, 2\theta, \chi$. Fig. 2 is a schematic diagram of the experimental configuration. The aim of this experiment was to use the diffraction properties of the individual particles in the ceramic to monitor strain and deformation behaviour as the crack propagated.

Fig. 3 shows the two-dimensional intensity distributions for one of the six crystallites as the wedge is driven into the crack. The contours represent intensity levels which are 90, 80, 70, 60, 50, 40, 30, 20, 10, 5, 2 and 1% of the maximum count. The positions of the peaks in ω are, to some extent, arbitrary since adjusting the micrometer may cause some change in ω for the entire sample. The most significant changes in 2θ occurred for the crystallite displayed in Fig. 3, which also exhibits the largest changes in morphology. Another crystallite is seen to be diffracting in step 3 and to a greater extent in step 4. It is very tempting to suggest that this crystallite has actually split into two smaller crystallites (the main peak intensity does indeed decrease significantly from step 3 to step 4). It is not, however, possible to prove this conclusively.

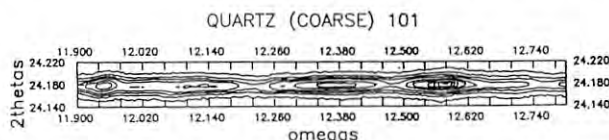


Fig. 1 2D intensity distribution for the 101 quartz reflection.

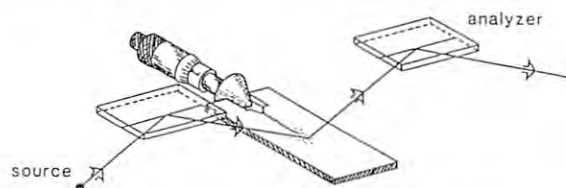


Fig. 2 Schematic diagram of the experimental configuration.

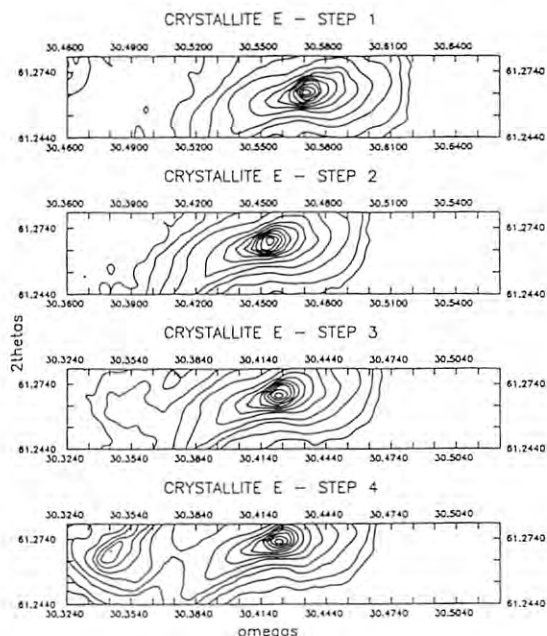


Fig. 3 003 intensity distribution for a crystallite of the Lucalox sample as the wedge is driven into the crack.

X-Ray Diffraction from GaAs/AlAs/GaAs Grown on GaAs(001) by MBE

Yasuharu KASHIHARA, Kenjiro IKEDA and Jimpei HARADA

Department of Applied Physics, Nagoya University, Chikusa-ku, Nagoya 464.

Introduction

The lattice spacing of the sandwiched AlAs layers between the GaAs layers in $(\text{GaAs})_m(\text{AlAs})_n$ superlattice layers grown on GaAs(001) substrates is elongated along the epitaxial-growth direction due to a Poisson expansion¹⁻³⁾. It is also interesting to investigate whether a similar lattice expansion exists or not in a single bunch of AlAs layers sandwiched between two GaAs layers.

Experimental

The sample investigated was a GaAs/AlAs/GaAs multilayer structure grown on a GaAs(001) substrate by MBE. The nominal numbers of molecular layers of the GaAs and AlAs layers were 1240 and 125, respectively. The thickness of the cap layers of GaAs was equal to that of basal epitaxial layers of GaAs.

In the X-ray diffraction measurements, a synchrotron radiation source was employed at beamline 4-C in which a vertical-type Huber four-circle diffractometer was installed. The wavelength of radiation selected was 1.542 Å. The scattering intensities from the sample were measured by the θ - 2θ scanning mode with step sizes of 0.001° (θ).

Results

The diffraction patterns obtained from the scan along the $\langle 001 \rangle$ direction through the 002 Bragg point of GaAs(001) are shown by the dotted line in Fig.1. The sharp peak denoted by 002 represents the Bragg reflection from the GaAs(001) substrates. The axis of abscissa represents the scattering vector normalized by the lattice spacing between successive cation layers of the substrate of GaAs ($a_1=2.827\text{Å}$). The three broad peaks in which a small oscillatory structure is seen represent the scattering profile from the GaAs/AlAs/GaAs

epitaxial layers.

In the framework of the kinematical theory of the diffraction, the scattered intensity from such a one-dimensional array of the multilayer lattice is given by

$$FF^* = |F_1|^2 + |F_2|^2 + |F_3|^2 + (F_1^*F_2 + F_1F_2^*) + (F_2^*F_3 + F_2F_3^*) + (F_3^*F_1 + F_3F_1^*), \quad (1)$$

where F_1 , F_2 and F_3 represent the scattering amplitude from the cap layers of the GaAs, from the AlAs layers and from the GaAs layers including the GaAs substrate, respectively. The numerical calculation was made on the basis of eq. (1). The result is shown by the solid line in Fig.1 in which the lattice spacings between successive cation layers of the GaAs and AlAs regions are assumed to be $a_1=2.827\text{Å}$ and $a_2=2.835\text{Å}$, respectively. They are cited from the values obtained from the analysis of the $(\text{GaAs})_{28}(\text{AlAs})_{24}$ superstructure lattice¹⁾. We can see that not only the position of the broad peaks but also the period of a small oscillatory structure observed are well reproduced by the calculation performed on the basis of eq. (1). From these facts we see that the number of molecular layers of the cap layers of GaAs and of those of the AlAs layers are in agreement with the nominal numbers of 1240 and of 125, respectively. In the calculation, the lattice spacing between the successive cation layers in the AlAs layers is used to be $a_2=2.835\text{Å}$. This is the lattice spacing which is expected from the simple Poisson expansion of AlAs spacing so as to compensate the lattice mismatch between GaAs and AlAs perpendicular to the growth direction.

In general the ratio of the structure factor of AlAs to that of GaAs is $|f_{\text{AlAs}}| : |f_{\text{GaAs}}| \approx 10:1$ in the vicinity of the 002 Bragg point of the GaAs. Thus, the main terms which contribute to the scattered intensity of eq. (1) are $|F_2|^2$, $(F_1^*F_2 + F_1F_2^*)$ and $(F_2^*F_3 + F_2F_3^*)$. The broad peaks in Fig.1 come from $|F_2|^2$ representing a well known Laue function of the AlAs layers. The small oscillatory structure in Fig.1 comes from $(F_1^*F_2 + F_1F_2^*)$ representing the interference effect between the cap layers of the GaAs and the AlAs layers.

We thank Prof. H. Terauchi of Kwansei-Gakuin University for providing us with a very high-quality sample.

References

- 1) Y. Kashihara, T. Kase and J. Harada: Jpn. J. Appl. Phys. **25** (1986) 1834.
- 2) Y. Kashihara and J. Harada: Jpn. J. Appl. Phys. **27** (1988) 522.
- 3) A. Segmüller, P. Krishna and L. Esaki: J. Appl. Cryst. **10** (1977) 1.

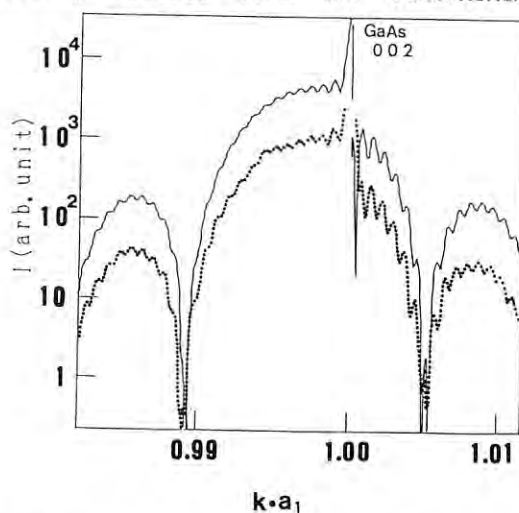


Fig. 1. Observed (dotted line) and calculated intensity (solid line) vs the scattering vector along 001 in the vicinity of the 002 GaAs reflection. The scattering vector is normalized by the lattice spacing between successive cation layers in GaAs, a_1 .

DIFFRACTION PATTERNS OF THIRD-ORDER FIBONACCI SERIES

H. TERAUCHI, K. KAMIGAKI, T. OKUTANI, Y. NISHIHATA,* H. KASATANI and H. KASANO**
 Department of Physics, Kwansei-Gakuin University, Nishinomiya 662

Introduction

From a physical point of view, the one-dimensional quasiperiodic lattice is interesting since it is, in some sense, the projection of a quasicrystal onto a line. We discussed the diffraction patterns of the one-dimensional second-order Fibonacci series grown by a technique of the molecular beam epitaxy (MBE).¹⁾ Many satellite peaks have a self-similar feature associated with the golden mean τ (a diagonal value of a regular pentagon). Here we report the diffraction patterns of the one-dimensional third-order Fibonacci series, i.e.

$$S_1 = A, S_2 = C, S_3 = CBA, S_4 = CBACBC, \dots, \\ S_n = 2S_{n-1} - S_{n-3} + S_{n-2} \quad (1)$$

in which the secular equation of the transformation matrix is given by

$$x^3 - 2x^2 - x + 1 = 0 \quad (2)$$

with the solutions $-\alpha/\beta$, $1/\alpha$ and β (α and β are diagonal values of a regular heptagon). Note that $1/\alpha + 1/\beta = 1$. The equation (2) corresponds to the equation that gives τ , $x^2 - x - 1 = 0$, in the second-order Fibonacci series.

Experimental

The third-order Fibonacci lattices were grown by MBE on the (001) GaAs substrate following the sequence given in eq. (1). The thickness of alternating layers d_A , d_B and d_C are $5a_0/2$ (AlAs), $9a_0/2$ (Al_{0.5}Ga_{0.5}As), $11a_0/2$ (GaAs), respectively, where a_0 is the average lattice constant. The thickness ratio is almost $1 : \alpha : \beta$. The ratio of numbers of A, B and C included in the lattice is also $1 : \alpha : \beta$. The average quasiperiodicity is then defined as $d_0 = (5/2 + 9\alpha/2 + 11\beta/2)a_0 = 22.97a_0$.

The preliminary measurement of the x-ray diffraction pattern of the present lattice was made by a conventional double axis x-ray diffractometer with Cu-K α radiation. The observed diffraction pattern around the fundamental (004) reflection is shown in the inset of Fig. 1. The high resolution measurement was carried out by using synchrotron radiation (SR) available at PF. Radiation ($\lambda = 1.54$ Å) was monochromatized by a pair of Si(111) and focused by a sagittal focusing mechanism (beam line 4C). Figure 1 shows the diffraction pattern scanned from $2\theta = 66.50^\circ$ to 68.70° .

Results and Discussion

The several satellite peaks observed by a conventional method are assigned by $q_0/\alpha^m\beta^n$, ($n=0,1$, $m=-1,0,1,2$), $q_0 = \alpha\beta(2\pi/d_0)$, as shown in the inset of Fig. 1. By using SR, we found many satellite peaks in the small region

of 2θ as shown in Fig. 1. These satellite peaks are also assigned by $q_0/\alpha^m\beta^n$ ($n=-3,\dots,1$, $m=2,\dots,8$), implying that there is a self-similarity in the third-order Fibonacci lattice.

In the Fibonacci lattices there are no long range period, but strong correlations extending up to a long distance give the sharp diffraction patterns.²⁾ The patterns show the self-similarity and are assigned by the projection onto a line.

The authors wish to express their thanks to staffs of the MBE group of Kwansei-Gakuin University and the crystal physics group of PF for their fruitful discussion.

* Department of Physics, Okayama University

** Department of Physics, Yamaguchi University

1) H. Terauchi, Y. Noda, K. Kamigaki, S. Matsunaka, M. Nakayama, H. Kato, N. Sano and Y. Yamada: J. Phys. Soc. Jpn. **57** 2416-2424 (1988).

2) H. Terauchi: Solid State Phys. **24** 467-481 (1989), in Japanese.

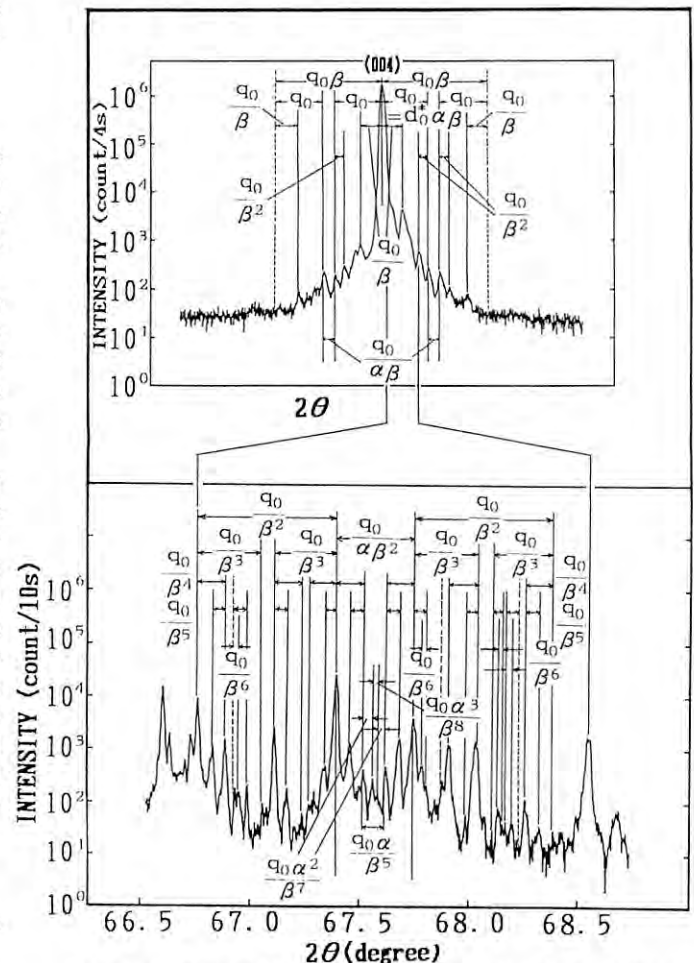


Fig. 1. Diffraction pattern of the third-order Fibonacci lattice. An inset shows the pattern at low resolution.

STUDY ON THE PRECURSIVE PHENOMENA OF PHASE TRANSITION FROM LAYERED COMPOUNDS

Ken-ichi OHSHIMA, Yoshihiro KUROIWA, Kenji KOGA and Hiroshi MAETA*

Institute of Applied Physics, University of Tsukuba, Tsukuba 305

* Department of Physics, Japan Atomic Energy Research Institute, Tokai, Ibaraki 319-11

Introduction

The layered disulfides of Ti and Ta transition metals are intercalated with various ions and molecules between the sulfur layers which are normally separated through the Van der Waals interaction. These intercalation compounds are of interest because of their quasi two-dimensional properties and because of their application as electrodes in cells. In the present study, we report the result of X-ray measurements on the in-plane and intra-plane correlations from stage-2 Ag_xTiS_2 single crystal.

Experimental

The Ag_xTiS_2 single crystal was prepared electrochemically by immersing TiS_2 single crystal in a 0.1 mole AgNO_3 solution with Ag metal as the anode. Mosaic spread of it parallel to the c axis was less than one degree. The composition of the specimen used was determined through an analysis of the 00L Bragg intensities by a least-squares fitting procedure and given as $x=0.15$.

Data collection of diffuse scattering was performed on a Huber 5020.4 four-circle diffractometer with HOPG crystal analyser installed at BL-4C. A new versatile cryostat was mounted on a centering device on a Huber Eulerian cradle with off set χ circle.

Results

Rodlike diffuse scattering parallel to c^* at $1/3 \ 1/3 \ 0$, $2/3 \ 2/3 \ 0$ and their equivalent positions was observed on the diffraction pattern at room temperature. It reveals the two-dimensional feature of intercalated Ag atoms in the compound. These diffuse intensity distributions parallel to the c^* direction centered on $5/3 \ 2/3 \ 0$ were measured from 350 to 90 K.

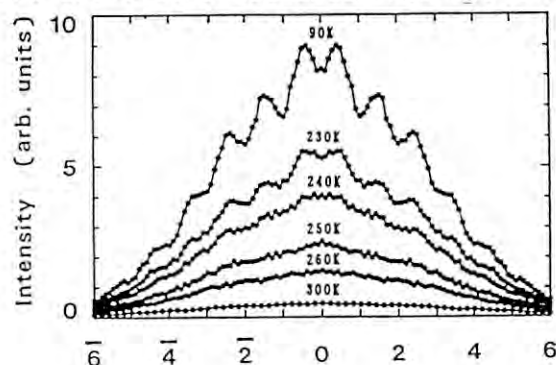


Fig.1

Fig.1 shows a typical result of diffuse rod at six different temperatures, where the range of the scan was from $l=-6$ to 6. It is clearly seen that intensity modulation on the diffuse rod appears slightly at 250 K, enhances with decreasing temperature and does not develop at 180 K furthermore. It means an enhancement of three-dimensional nature below 250 K.

In Fig.2 intensity distributions in $(hk0)$ plane of reciprocal space are shown in arbitrary units at 350, 300, 280 and 250 K. As seen from a series of intensity maps diffuse maximum at $1/3 \ 1/3 \ 0$ reciprocal point is increasing with decreasing temperature. By performing the Fourier inversion of intensity, two-dimensional order parameters were determined. Based on these parameters, local arrangements of Ag atoms in the compound are discussed.

Reference

- 1) Y. Kuroiwa, K. Ohshima and H. Maeta, J. Appl. Cryst. (1990) in printing.

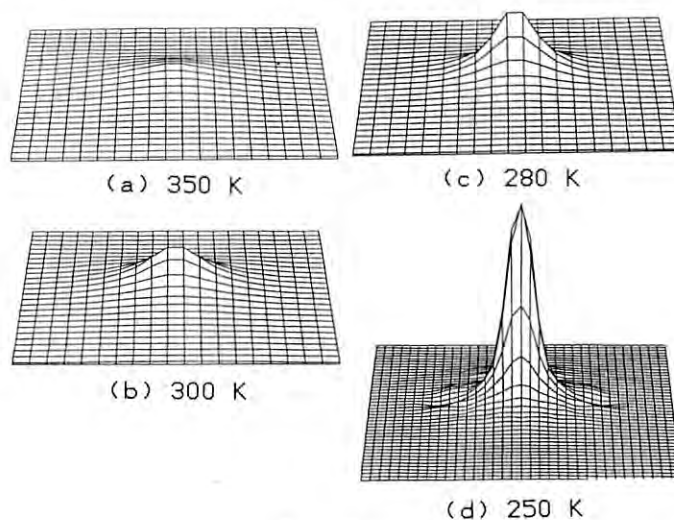


Fig.2

Fig.1. A typical result of diffuse rods at six different temperatures.

Fig.2. Intensity distributions in $(hk0)$ plane in arbitrary units at 350, 300, 280 and 250 K.

Determination of the low temperature phase diagram of the Fe-Ni alloy system

Shinya HASHIMOTO, Hiroaki MORITA, Yasuo FUJINAGA, Kumi MOTAI,
Hiroyasu FUJIMORI and A. Chamberod*

Institute for Materials Research, Tohoku Univ., Sendai 980

*Department de Recherche Fondamentale, Section de Physique du Solide

Centre d'Etudes Nucleaires de Grenoble, F-38041 Grenoble Cedex, France

Introduction

The phase diagram below 800 K is not well understood because of the slow atomic diffusion in the alloy. To overcome this problem, Morita, et al. tried to get the equilibrium state enhancing the diffusion by the electron-irradiation technique¹⁾. They prepared foil samples with different compositions of 10 to 60 at%Ni which were electron-irradiated at temperatures between 470 and 770 K. They measured the magnetic properties and determined the phase boundaries as drawn with solid lines in Fig. 1. We performed X-ray diffraction experiments on the same samples to identify each phase. Since Fe and Ni have almost the same atomic scattering factors, it is hard to detect the superlattice reflection intensities if the conventional X-ray generator is used. We employed synchrotron radiation as a tunable high-intensity source to take advantage of the anomalous scattering effect.

Experimental

Samples were the same ones that Morita, et al. used for the magnetic property measurements.¹⁾

For X-ray measurements, we used the multipurpose four-circle diffractometer at BL-4C²⁾ in an X-ray optical geometry of Fig. 2. The wavelength of radiation was adjusted to $\lambda = 1.7444$ Å after calibrating the absorption edge of Fe (1.7435 Å). The diffraction pattern on the plane (in reciprocal space) nearly normal to the sample surface was surveyed by the imaging plate (IP) in an oscillation method ($\Delta\omega = \pm 5^\circ$ and exposure time=20 min.). This IP method was very powerful for the electron-irradiated thin foil samples with enhanced grain growth and strongly preferred orientation in polycrystalline structure.

Results and Discussion

We examined the samples marked with circles in Fig. 1. The full circles indicate the samples

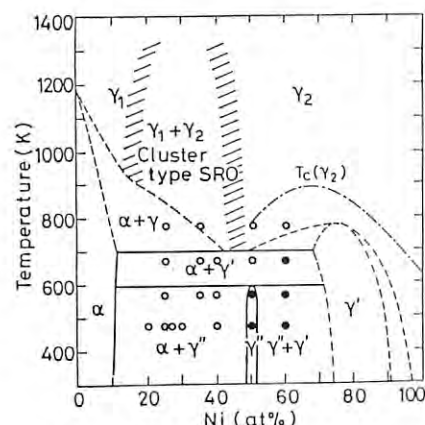


Fig. 1. Solid lines were determined by Morita, et al.¹⁾. Circles indicate the compositions and electron irradiation temperature of the samples.

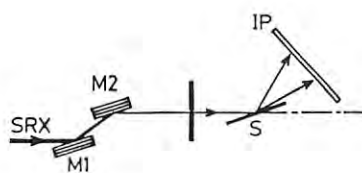


Fig. 2. X-ray optical geometry.
IP: imaging plate,
M1, M2: monochromators,
S: sample.

which showed diffuse scattering maxima at the superlattice reflection positions of the f.c.c. based alloy. Fig. 3 is a typical IP pattern, which was given from the Fe-50at.%Ni alloy irradiated at 570 K. The diffuse maximum indicated by an arrow is thought to be the 100 superlattice reflection of the γ'' phase (L1₀ type). The broadening of the maximum might be due to an intermediate state of ordering into a single ordered domain. The average diameter of the ordered domains was estimated to be 200 Å from the line profile measured by the θ -2 θ scan method. We also observed such intensity maxima for Fe-50at.%Ni (470 K) and Fe-60at.%Ni (470, 570 and 670 K). Other samples marked by the open circles in Fig. 1 did not show any diffuse maxima, indicating the absence of detectable ordered arrangements. Particularly, the disappearance of the 100 superlattice reflection at 670 K for the Fe-50at.%Ni alloy indicates that the γ'' phase never exists above 670 K. On the other hand, the Fe-60at.%Ni alloy exhibited a diffuse maximum at 670 K which is thought to be the superlattice reflection for the γ' phase (L1₂ type). Thus, the present results strongly support the diagram predicted by the magnetic measurements¹⁾.

We were not successful, for the present, in finding 1) a trace of reflection of the α phase for the samples with more than 30 at%Ni and 2) any superlattice reflection for the γ'' phase in the range from 25 to 40 at%Ni including the stoichiometric Fe₃Ni concentration. We are planning more detailed examination for the Fe-Ni low temperature phase diagram as the next step.

References

- 1) H. Morita, A. Chamberod and H. Fujimori, to be published in Proceedings of TMS-AIME (1989).
- 2) H. Iwasaki, et al., Rev. Sci. Instrum., 60 (1989), 2406.

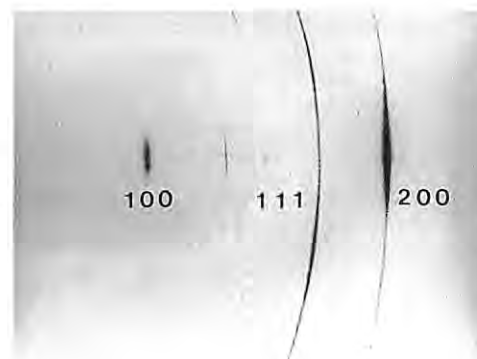


Fig. 3. Imaging plate pattern for the Fe-50at.%Ni electron-irradiated at 670 K. The 100 diffuse maximum is characteristic.

APPEARANCE OF SUPERSTRUCTURE IN FERROELECTRICS AT LOW TEMPERATURE BELOW THE INCOMMENSURATE-COMMENSURATE TRANSITION

Hiroyuki MASHIYAMA, Mamoru SAKAMOTO, Hazime NAKAMURA, Hironobu KASANO,
Takanao ASAHIM*, Katsuhiko HASEBE* and Shunji KISHIMOTO**

Department of Physics, Faculty of Science, Yamaguchi University, Yamaguchi 753

* Department of Physics, Faculty of Liberal Arts, Yamaguchi University, Yamaguchi 753

**Photon Factory, National Laboratory for High Energy Physics, Tsukuba 305

Introduction

Thiourea is a well-known ferroelectrics that performs an incommensurate-commensurate phase transition at $T_C=169\text{K}$.¹⁾ In the incommensurate phase the dielectric constant has a sharp peak where the modulation locks-in the commensurate phase with $1/8c^*$. However the temperature range of this eightfold phase is very narrow without applied electric field.²⁾ On the other hand, a peculiar dielectric anomaly at $T_X=161\text{K}$ in the ferroelectric phase has been interested recently. In the temperature range between T_C and T_X , the diffuse scattering has been observed by using a usual two circle diffractometer with a tube X-ray source.^{2,3)}

In order to clarify the modulated structure in the incommensurate phase and the diffuse scattering, we performed a high resolution X-ray scattering experiment by the use of synchrotron radiation.

Experimental

A platelet specimen with size of $3\times 3\times 1.2\text{mm}^3$ perpendicular to the polar b axis was cut from a single crystal grown from an ethanol solution by slow evaporation and mounted in a cryostat cooled by a cryogenics (APC DE202), which was attached on a four circle diffractometer (Huber 5020.4) at the station of BL-4C.⁴⁾ The X-ray wavelength was adjusted as 0.9997\AA for a parallel beam.

The satellite reflections were measured by a c^* -scan with $\phi=\text{constant}$ to avoid the excess tilt of the cryostat. The diffuse scattering around $(0\ 2\ 0)$ main reflection was investigated by ω -scan (effectively c^* -scan). Here reflections and the reciprocal space are represented by references to the unit cell of the ferroelectric phase ($\text{Pb}2_1\text{m}$).

Results and Discussion

Figure 1 shows a scattering distribution along the c^* -direction in the modulated phase at 178K . Satellite reflections are characterized by the commensurate wavenumber of $1/8$. All order of satellites were recognized at first time. The HWHM of the satellite reflection is the same as that of main ones.

Below the lock-in temperature $T_C=169\text{K}$, satellite reflections disappear. Instead, the diffuse scattering appear around main reflections as shown in Fig.2. The width of the diffuse scattering becomes narrower with further decreasing temperature. If the temperature is increased from 100K , then the width remains constant. And above T_C , the excess diffuse scattering disappears.

The observed diffuse scattering is considered to be caused by the random distribution of the discommensurations in the ferroelectric phase. Therefore, the experimental result of this work supports the idea that the dielectric anomaly at $T_X=169\text{K}$ is caused by the pinning or depinning of the remaining discommensurations in the ferroelectric phase.³⁾ However, more detailed and highly resolved observation of the diffuse scattering is required to discuss quantitatively.

We thank Prof. H Terauchi, Dr. S. Hashimoto and Dr. K. Ohshima for their advice and help to operate the instruments.

REFERENCES

- 1) F. Denoyer and R. Currat, in *Incommensurate Phases in Dielectrics*, edited by R. Blinc & A. P. Levanyuk (North-Holland, Amsterdam, 1986), Vol.2, Ch.14, pp.129, and references therein.
- 2) H. Mashiya, S. Jida and S. Tanisaki, *Ferroelectrics*, (1989) in press.
- 3) H. Mashiya, M. Sakamoto and S. Jida, *Ferroelectrics*, (1990) in press.
- 4) H. Iwasaki, S. Sasaki, S. Kishimoto, J. Harada, M. Sakata, Y. Fujii, N. Hamaya, S. Hashimoto, and K. Ohshima and H. Oyanagi, *Rev. Sci. Instrum.* **60** (1989) 2406.

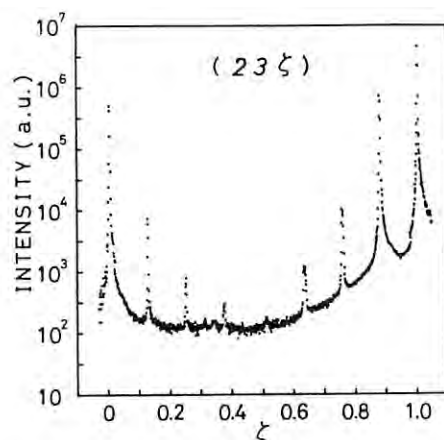


Fig.1 Intensity profiles between $(2\ 3\ 0)$ and $(2\ 3\ 1)$ main reflections from thiourea at 178K .

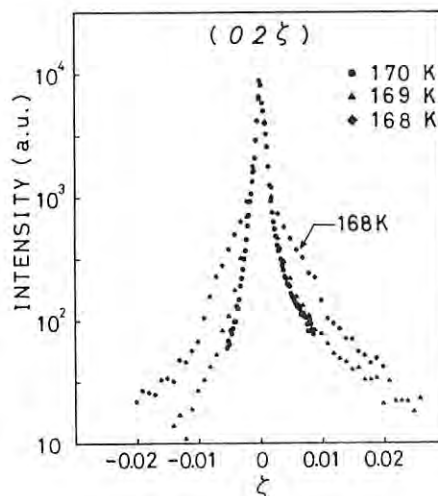


Fig.2 Scattering distributions scanned along the c^* direction around $(0\ 2\ 0)$ from thiourea.

AB INITIO STRUCTURE ANALYSIS OF 5-AMINOVALERIC ACID BY X-RAY POWDER DIFFRACTION

Masayasu KURAHASHI, Kazumasa HONDA, Midori GOTO

Analytical Chemistry and Standard Division, National Chemical Laboratory for Industry,
Higashi 1-1, Tsukuba, Ibaraki 305Introduction

Up to now only a few structures have been solved ab initio from powder diffraction data. We attempt to determine the crystal structure of 5-aminovaleric acid(5-AVA) by using monochromated synchrotron radiation and a large radius Weissenberg camera. The crystal structure of this compound has remained unsolved owing to difficulty of growing its single crystals.

Experimental

The X-ray powder diffraction experiment was performed at the Photon Factory BL-6A2. Powder sample was sealed in a 0.5-mm ϕ glass capillary and mounted on a Sakabe's Weissenberg camera with a Fuji Imaging Plate (IP; 40.96 x 20.48 cm) in its cylindrical film cassette of 28.65-cm radius. X-ray beam with a wavelength of 1.0418(4) Å was used. The diffraction recorded on the IP after 6 minutes exposure was digitized at every 100x100- μ m pixel by using a Fuji BA-100SF IP reader. Intensities involved in the same 2θ value were accumulated and averaged along with correction for the Lorentz and polarization. Thus I vs 2θ data were obtained for 2° to 65° in every 0.01° step.

Structure Determination

Crystal system and lattice constants were preliminarily determined from low angle peaks. Index assignments were then extended to higher angles, and the space group was assumed for Pnam or Pna 2_1 by the extinction of ($h=0, k+l=2n$) and ($k=0, h=2n$). 55 integrated peak intensities with unambiguous indexing were obtained. The Patterson map revealed that intramolecular C-C chain locates parallel to the a-b plane. Position of the chain on the plane was next determined by the trial and error method. Five carbon and one nitrogen atoms were located after the successive Fourier synthesis. At this stage, the original diffraction pattern was compared with a simulation pattern based on the $|F_c|$ values, and 21 reflections which were consistent with the calculation were added to the Fo data set. Remaining oxygen atoms were located by further Fourier synthesis. The structural parameters were finally refined by a Rietveld analysis. The program used was RIETAN, which was modified for the present study. The peak profile was assumed to be a single Gaussian function. No correction was performed for the preferred orientation.

Results and Discussion

A model assumed for space group Pna 2_1 yielded better fit than that for Pnam. Final cell parameters obtained were $a=17.358(7)$, $b=4.523(2)$ and $c=7.447(3)$ Å, $U=584.7(4)$ Å³, $D_c=1.33$ g cm⁻³ for $Z=4$ (C₅H₁₁NO₂, MW=117.15), and $R_p=0.079$ and $R_f=0.028$. The result of the Rietveld

refinement is shown in Fig. 1. The crystal structure is illustrated in Fig. 2. The molecule approximately possesses a mirror symmetry perpendicular to the c-axis, but two oxygen atoms apart from the mirror do not locate at the position of the symmetry to each other. Short intermolecular N...O contacts of 2.77(7), 2.86(6), and 2.89(6) Å were observed.

In conclusion, no K α doublet, single-Gaussian peak profile, and no preferred orientation lead to rapid and stable convergence in the Rietveld refinement. These excellent performance will allow further application to studying the crystal structure of more complex and larger organic compounds, such as higher alcohols, lipids, polypeptides, etc.

The authors thank Prof. N. Sakabe and Drs. A. Nakagawa and N. Watanabe of the Photon Factory for their kind help and suggestions in data collection with the camera.

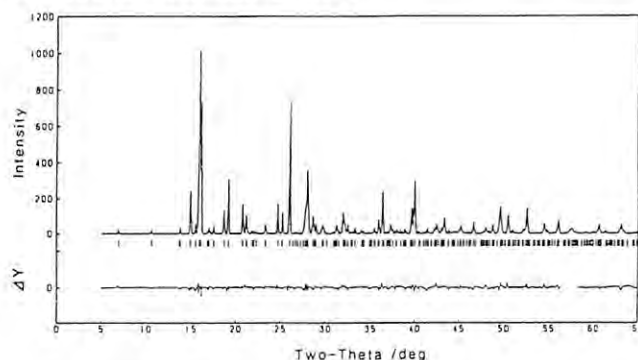


Fig. 1. Observed (points; background-subtracted), calculated (bold) and difference profiles for 5-AVA. Unit weight was employed in the refinement. Range of $56.3^\circ < 2\theta \leq 58.3^\circ$ was excluded from the calculation because of the blind region of the camera.

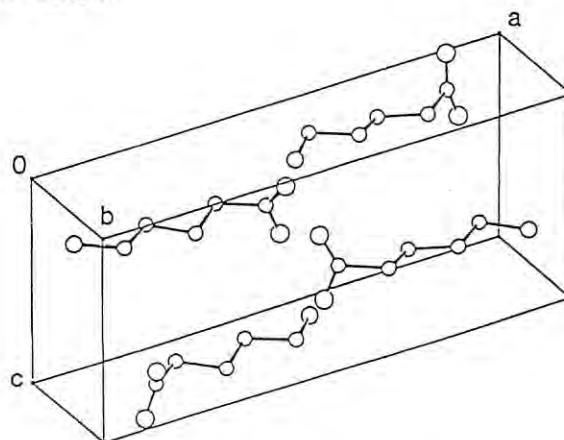


Fig. 2. Perspective view for the crystal structure of 5-AVA.

NEW TECHNIQUE FOR THE OBSERVATION OF X-RAY CTR SCATTERING USING IMAGING PLATE DETECTOR

Jimpei Harada, Takayoshi Shimura, Yasuharu Kashiwara,
Masaki Takata, Makoto Sakata and Nobuo Kashiwagura

Department of Applied Physics, Nagoya University
Chikusa-ku, Nagoya, 464-01, Japan

In the X-ray scattering from a flat surface of a crystal, rod shaped scattering emanating from each Bragg point in a direction normal to the crystal surface is observed. This scattering has been understood as the diffraction effect due to the abrupt truncation of the charge density at the crystal surface and is referred to as the crystal truncation rod (CTR) scattering^{1,2)}. In general the intensity of CTR scattering is strong if the crystal surface is flat and smooth. It depends very much on the surface condition so that the investigation of this scattering provides diverse information about the lattice modulation at a crystal surface, such as the surface morphology and surface lattice relaxation of an atomic scale. But the intensity of the CTR scattering is generally very weak comparing with the Bragg reflection. Thus, the observation is laborious, taking unexpectedly much beam time.

We examined whether the CTR scattering from several crystal surface can be easily observed or not by using Imaging Plate (IP) detector since IP is known to be effective also for the observation of very weak X-ray scattering, having high-quantum efficiency, unlimited count-rate capacity, high spatial resolution, a wide dynamical range ($1 \sim 10^5$) and high sensitivity (approximately 30 times that of normal photographic X-ray film) if it is in conjunction with synchrotron radiation X-ray source.

We tested three samples of Si single crystal of which surface are formed in different way. Two of them are the natural (111) facet faces of the seed cone which is formed during the crystal growth process by using the CZ method. One of them is the (111) facet face of the crystal grown by a magnetic-field-applied CZ method and the other one is that by a usual CZ method. We will refer to as MCZ facet plane and CZ facet plane, hereafter another sample is the (111) Si wafer of which surface has been treated mechano-chemically according to the ordinary wafer making process. This sample is used as a reference since the surface of such a sample has been characterized already by ordinary diffraction method.

In the observation we employed the Weissenberg Camera for Macromolecular Crystallography (Sakabe's X-ray Camera) installed to the BL-6-A2 at PF, and the IP were developed by BA-100 (Fuji Photo Film Co.). Oscillation photographs were taken around the 111 Bragg point with the oscillation angle $\Delta\omega = \pm 10$ degree around the axis perpendicular to the [111] axis and with the incident beam monochromated to be 1.02 Å.

In Fig.1 three oscillation photographs are shown: a) taken from the (111) natural facet face of the MCZ single crystal, (b) taken from that of the usual CZ single crystal and c) taken from a mechano-chemically (MC) polished (111) surface of a silicon wafer just for reference. Since the MC

polished surface of the silicon wafer had been characterized by the measurement of the CTR scattering, this sample could be used for reference. In the photographs the 111 Bragg points are represented by the index. The intensity contours represented is in logarithmic scale. Elliptical shape contours seen around the Bragg point are the well known thermal diffuse scattering (the X-ray phonon scattering from low energy acoustic branches) and the rod shaped scattering emanating from the Bragg point along both the [111] and the $[\bar{1}\bar{1}\bar{1}]$ directions is the CTR scattering which is especially remarkable in a) and c). If we compare three of them, we notice that the CTR scattering is extending to almost the same region in the reciprocal space in a) and c) while it is not in b). According to Kashiwagura et al.³⁾ and Harada⁴⁾ this fact suggests that the surface of the natural facet face seen on the seed cone of the MCZ crystal has the same degree of flatness as that of the MC polished (111) surface, whereas a similar natural facet face on the seed cone of the CZ crystal is rather poor in the flatness on an atomic scale.

References

- 1) J. Harada, N. Kashiwagura, M. Sakata and H. Miyatake: J. Appl. Phys. 62 (1987) 4159
- 2) I. K. Robinson: Phys. Rev. B33 (1986) 3830
- 3) N. Kashiwagura, Y. Kashiwara, M. Sakata, J. Harada, S. W. Willkins and A. W. Stevenson: Jpn. J. Appl. Phys. 26 (1987) L2026
- 4) J. Harada and N. Kashiwagura: J. de Physique to be published



a) taken from the (111) natural facet face of the MCZ single crystal



b) taken from the (111) natural facet face of the usual CZ single crystal



c) taken from a mechano-chemically (MC) polished (111) surface

Fig.1 three oscillation photographs

STRUCTURAL INSTABILITY OF PbSe/SnSe SUPERLATTICES UNDER PRESSURE

Yasuo OHISHI¹⁾*, Noriko SHINGAKI¹⁾, Yasuhiko FUJII²⁾, Zenji HIRO¹³⁾,
Noriaki NAKAYAMA³⁾, Yoshichika BANDO³⁾, and Teruya SHINJO³⁾

1) Fac. Eng. Sci., Osaka Univ., Toyonaka, Osaka 560

2) Inst. Mater. Sci., Univ. Tsukuba, Tsukuba, Ibaraki 305

3) Inst. Chem. Res., Kyoto Univ., Uji, Kyoto 611

Introduction

Synchrotron x-ray diffraction experiments have revealed successive phase transitions in epitaxially-grown PbSe/SnSe superlattices. A bulk of PbSe and SnSe compounds has the cubic B1(NaCl)- and the orthorhombic B16(GeS)-type structures stable at atmospheric pressure, respectively. The B16 lattice is realized as a denser structure by doubling the B1 lattice along the $\langle 100 \rangle$ axis¹⁾. In fact, PbSe undergoes the B1-to-B16 phase transition at 4.3 GPa while SnSe has the B16 structure at lowest up to 34 GPa²⁾. At atmospheric pressure the [PbSe/SnSe] superlattices have four kinds of structures as [B1/B1], [B1/B16], [B16(distorted)/B16] and [B16/B16] depending upon the ratio of the layer thickness. The cubic (100) plane is known to be the stacking-layer in the present case. The purpose of the present study is to investigate the effect of hydrostatic pressure applied to the negatively-pressured SnSe layer as well as the conversely positively-pressured PbSe one in the PbSe/SnSe superlattices.

Experimentals

A specimen film 300 $\mu\text{m}\phi$ was mounted in a high pressure chamber of a diamond anvil cell(DAC) specially-developed for layered-materials³⁾. X-ray diffraction experiments were performed on the Beam Line 6B. The incident beam was monochromatized($\lambda = 1.089 \text{ \AA}$) and focused by a sagittally-focussing Si(111) double-crystal monochromator. Diffraction patterns were measured by a scintillation counter with the $\theta - 2\theta$ scanning mode along the layer-stacking direction at room temperature.

Results

Figure 1 shows the linear compression of [PbSe(40A)/SnSe(40A)]₂₅ (B1/B16 type structure in its as-grown state). One can see a discontinuity at pressure 4.3 GPa, which results from the B1-to-B16 structural transition of PbSe layer. Figure 1(b) shows the result for [PbSe(36A)/SnSe(12A)]₁₉ which has the B1/B1 type structure in its as-grown state. One can see two discontinuities in its compression, which indicate the B1-to-B16 structural transition successively taking place in SnSe and PbSe layers upon compression. Similar measurements were also carried out for several other superlattices with different layer-thickness.

Figure 2 summarizes the observed B1-to-B16 transition pressure(P_c) as a function of the number of the (100) planes deposited in the PbSe layer(n). The dashed line at 5.2 GPa is the transition pressure observed in the present vacuum-deposited PbSe film(1000A in thickness). It is different from the previous data of the bulk(4.5 GPa)³⁾. One can see

the systematic variation of P_c as a function of n , but no systematic behavior is seen between P_c and m .

In the present work, we have observed that the negatively-pressured SnSe layer is forced to take the B1 structure while the conversely positively-pressured PbSe one transforms to the B16 structure at pressures lower than its bulk value. We are now under way to evaluate the interatomic forces acting at the interface between the PbSe and SnSe layers based on these systematic variation of the transition pressures.

References

Present address : *Sumitomo Chem. Co., Ltd., Tsukuba Res. Lab., Tsukuba, Ibaraki, 300-32.

1) Fujii, Y. et al.: Solid State Commun. Appl. **49**, 135(1984)

2) Chattopadhyay, T. et al.: Revue Phys. Appl. **19**, 807(1984)

3) Fujii, Y. et al.: J. Phys. Soc. Jpn. **55**, 251(1986)

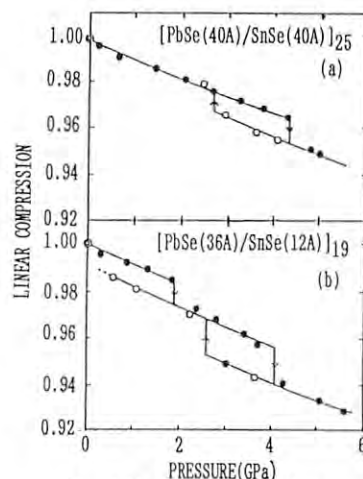


Fig. 1 Linear compression Δ/Δ_0 observed on (a) [PbSe(40A)/SnSe(40A)]₂₅ and (b) [PbSe(36A)/SnSe(12A)]₁₉.

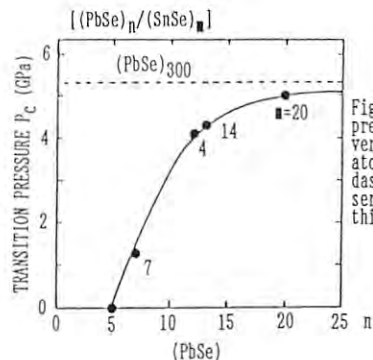


Fig. 2 The B1-B16 transition pressure(P_c) of the PbSe layer versus the number of its (100) atomic planes deposited. The dashed line at 5.2 GPa is P_c observed on the PbSe film (1000A in thickness).

DETERMINATION OF THE ENVIRONMENTAL STRUCTURE AROUND A SPECIFIC ATOM
IN DISORDERED MATERIALS BY THE ANOMALOUS X-RAY SCATTERING

Yoshio WASEDA, Eiichiro MATSUBARA, Kazumasa SUGIYAMA and Shin-ichi TAKEDA*

Research Institute of Mineral Dressing & Metallurgy (SENKEN), Tohoku University, Sendai 980, JAPAN.
* Department of General Education, Kyushuu University, Fukuoka 810, Japan.

Amorphous Al-based ternary alloys are usually known to be very brittle and their tensile strength is as low as about 50 to 150 MPa. However, Inoue et al.¹⁾ recently found that a new amorphous Al-Y-Ni alloy shows extremely high strength and good ductility. The specific strength defined as a ratio of the fracture strength to its density is as high as 38, which is much higher than that for conventional duralumin and alloy steels. Thus, the structural information on this new amorphous alloy is strongly desired to reveal the origin of the particular properties at a microscopic level.

The anomalous X-ray scattering (AXS) technique at the Y K-absorption edge was applied to a structural study of new amorphous $\text{Al}_{87}\text{Y}_8\text{Ni}_5$ which shows the highest fracture strength in Al-Y-Ni system. The scattering intensities measured at 17.0126 and 16.7380 keV below the Y K-edge in the ternary $\text{Al}_{87}\text{Y}_8\text{Ni}_5$ alloy are shown in Fig. 1. The fundamental features of both profiles represent a typical non-crystalline structure. A distinct feature observed in these profiles is a pronounced prepeak at $Q=13 \text{ nm}^{-1}$ which is indicated by an arrow in Fig. 1. The presence of a prepeak has been qualitatively interpreted as one of the compound-forming behaviors. The differential intensity profile at the Y K-edge is shown in the top of Fig. 1. The prepeak is still observed in the differential profile, which implies the presence of certain local ordering structure formed by Y and Al atoms.

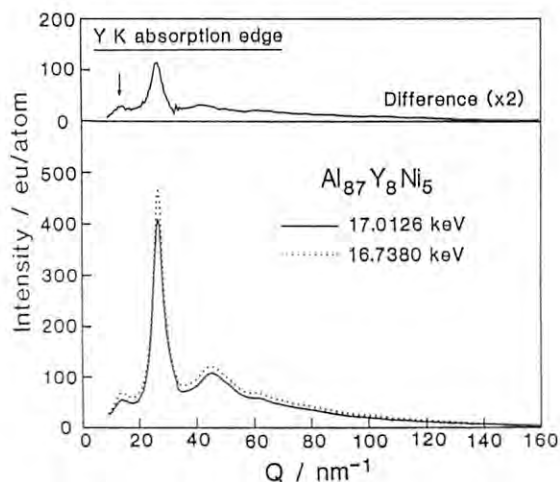


Fig. 1 Differential intensity profile of amorphous $\text{Al}_{87}\text{Y}_8\text{Ni}_5$ alloy

In order to obtain insight into the structural features of this ternary alloy, the environmental RDF around Y as well as the ordinary RDF were estimated and given in Fig. 2. The nearest neighbor distances of pairs calculated from the metallic bonding distances of Al, Y and Ni are indicated in Fig. 2. For comparison, the ordinary RDF for a binary amorphous $\text{Al}_{90}\text{Y}_{10}$ alloy²⁾ is also drawn in a dotted curve. It is found that the first peak of the ternary alloy extends to lower r than that of the binary alloy. By comparing the peak positions calculated from the atomic sizes, this tail at the lower- r side corresponds to Ni-Ni and Ni-Al pairs which are not included in the binary Al-Y alloy, because the environmental RDF around Y only contains three partial RDFs of Y-Ni, Y-Al and Y-Y. This is clearly seen in the profiles of the first peaks of the RDFs in Fig. 2, since the atomic positions of pairs unrelated with Y disappear in the environmental RDF around Y.

These experimental results suggest that there is a certain local ordering structure which differs from the one given by the random mixing of the constituents in these Al-based amorphous alloys.

- 1) A. Inoue, K. Ohtera, A. P. Tsai and T. Masumoto, Japanese J. App. Phys. **27**, L479 (1988).
- 2) E. Matsubara, Y. Waseda, A. Inoue, H. Ohtera and T. Masumoto, Z. Naturforsch. **44a**, 814 (1989).

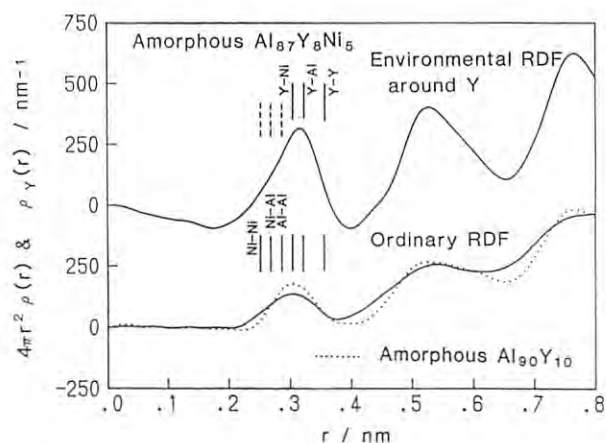


Fig. 2 Environmental radial distribution function (RDF) around Y (top) and ordinary RDF (bottom) of amorphous $\text{Al}_{87}\text{Y}_8\text{Ni}_5$ alloy.

PRESSURE-INDUCED MOLECULAR DISSOCIATION IN IODINE AT LOW TEMPERATURES

H. Fujihisa¹⁾, Y. Fujii^{1,6)}, K. Hase^{1,7)}, Y. Ohishi^{1,8)}, N. Hamaya^{1,6)}, K. Tsuji²⁾
K. Takemura³⁾, O. Shimomura³⁾, H. Takahashi⁴⁾ and T. Nakajima⁵⁾

- 1) Faculty of Engineering Science, Osaka Univ., Toyonaka, Osaka 560
- 2) Department of Physics, Keio Univ., Yokohama, Kanagawa 223
- 3) National Institute for Research in Inorganic Materials, Tsukuba, Ibaraki 305
- 4) ISSP, Univ. Tokyo, Roppongi, Minato-ku, Tokyo 106
- 5) Photon Factory, KEK, Tsukuba, Ibaraki 305
- 6) Institute of Materials Science, Univ. Tsukuba, Tsukuba, Ibaraki 305
- 7) Murata Mfg. Co., Ltd., Nagaokakyo, Kyoto 617
- 8) Sumitomo Chem. Co., Ltd., Tsukuba Res. Lab., Tsukuba, Ibaraki 305

INTRODUCTION

Solid iodine undergoes the diatomic-to-monatomic phase transition, called molecular dissociation, at 21 GPa and room temperature. Recently, Pasternak et al. carried out Mössbauer experiments of iodine at high pressures and low temperatures¹⁾. They have claimed that at 4 K the molecular phase still persists at pressures up to 30 GPa, although some arguments have arisen^{2,3)}. In order to settle such arguments, we have carried out x-ray diffraction experiments for exploring the phase boundary at low temperatures.

EXPERIMENTAL

Iodine and NaCl (pressure standard) powder were mounted together in a DAC (150 μm ϕ gasket hole) driven by He gas⁴⁾. Temperature was measured by a thermocouple directly attached to the DAC. The energy dispersive x-ray diffraction experiment with SSD was made by the use of white radiation from a bending-magnet (BL-6C₁). The incident beams were collimated 70 μm ϕ .

RESULTS AND DISCUSSION

The patterns on the right hand side of Fig. 1 (scattering angle $2\theta=15.0^\circ$) were measured at $T=298\text{K}$ as a reference, where the transition is well known to take place at about 21 GPa. The pressure was reliably determined by the NaCl 200 reflection. Upon compression several new peaks (marked with arrow) start emerging at $P_S=21\text{GPa}$ and the transition is completed at $P_f=25.4\text{GPa}$. Left four patterns were measured at $T=33\sim 46\text{K}$ and they change quite similarly to those at $T=298\text{K}$. This fact offers the direct evidence that also at low temperatures the molecular dissociation takes place.

All data at several temperatures on compression are plotted in the P-T diagram as shown in Fig. 2. The open and closed squares represent the molecular and monatomic phases, respectively. Two solid lines represent P_S and P_f . The extrapolation of thus determined phase boundary to the lower temperatures implies that the monatomic phase must be realized at $P=30\text{GPa}$ and $T=4\text{K}$ (asterisk in Fig. 2), where Pasternak et al. have claimed the persistence of the molecular phase.

REFERENCES

- 1) M. Pasternak et al.: Phys. Rev. Lett. **58**, 575 (1987).
- 2) M. Pasternak et al.: Phys. Rev. Lett. **59**, 945 (1987).
- 3) K. Takemura et al.: Phys. Rev. Lett. **59**, 944 (1987).
- 4) K. Tsuji: Solid State Physics under Pressure, ed. by S. Minomura (KTK Sci. Pub., 1985) P. 375.

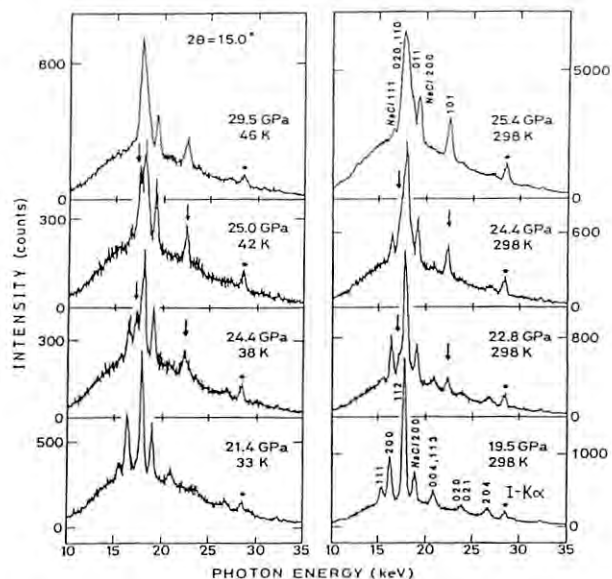


Figure 1 Pressure dependence of diffraction patterns of iodine and NaCl observed at room temperatures and low temperatures. Diffraction indices assigned to the bottom and top figures are based on the orthorhombic molecular (D_{2h}^{18} -Cmca) and the monatomic (D_{2h}^{25} -Immm) phases, respectively.

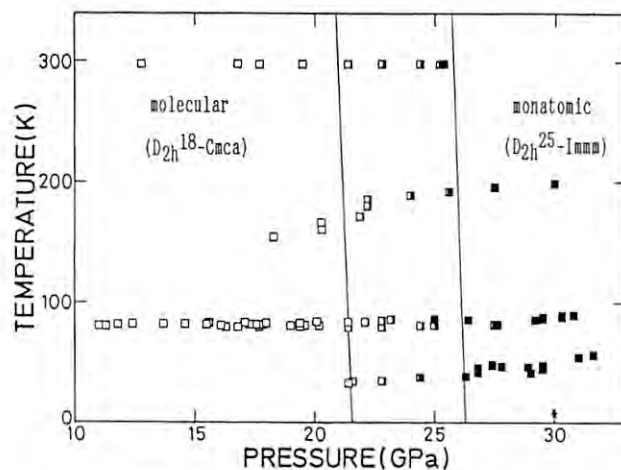


Figure 2 P-T phase diagram of iodine. The asterisk shows the location where the Mössbauer experiment was reported to be made.

Alternate Abstraction of Rotatory Polarized SR X-Rays with Different Helicity and Its Utilization

Tetsuo NAKAJIMA, Masami YOSHIKAWA* and Tomoe FUKAMACHI*

Photon Factory, National Laboratory of High Energy Physics, 1-1 Oho, Tsukuba-shi, 305 JAPAN

*Saitama Institute of Technology, 1690 Fusaiji, Okabe-machi, Oosato-gun, Saitama-ken, 369-02 JAPAN

One of the characteristics in born SR X-rays is a well-defined continuous polarization from right- to left-circular polarization through linear polarization in the plane of the electron orbital in the storage ring. As one of the utilizations of the circularly polarized X-rays, Cooper group¹⁾ had tried to measure the magnetic Compton scattering (MCS) in iron. We undertook to construct SR X-ray optics system to abstract the right-circularly polarized X-rays (RCPX) and left-ones (LCPX) alternatively, to attempt an expansion of the applied polarized X-ray physics. The schematic diagram of main parts of the optics is shown in Fig. 1. The first thing (A) in Fig. 1 divide the white X-rays into the two circularly polarized parts with inverse helicity, in electron orbital plane symmetry. The lowest limits of the wave length were regulated by the several effective thicknesses of beam catchers made of tantalum. Behind the beam catcher both beams are cut by chopper with the definite periodic interval. Two silicon single crystals with 111 plane in the second part (B) monochromatize both beams, which are controlled to be focussed at the same position of the specimen, shown in the third thing (C) arranged to be used for MCS. The geometrical relation in the optics system shown in Fig. 2 is described as follows:

Using the scattering angle θ_s adjusted based on wave length wanted to be and tilt angle ϕ and

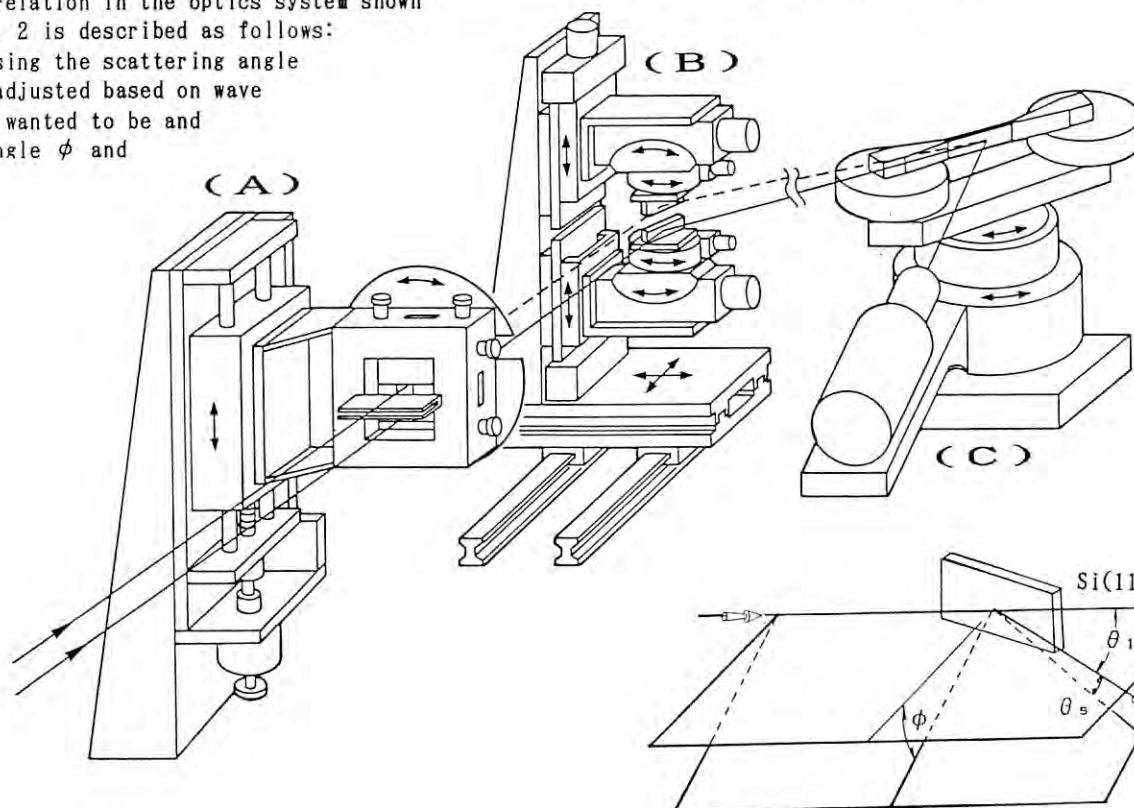


Fig. 1. Schematic arrangements of optical elements to abstract rotatory polarized SR X-rays.

θ_s at θ_{111} rotation around the incident beam, we could get the relation

$$\sin(\theta_s/2) = \sin 2\theta_{111} \sin(\phi/2).$$

From the Bragg relation $\tau_{111} = 2k \sin \theta_{111}$, we obtain the following relation between ϕ and θ_s

$$\phi = [k/\tau_{111} \{1 - (2k/\tau_{111})^2\}^{1/2}] \theta_s.$$

By the translations and the rotations (shown by arrows) of monochrometers driven by a personal computer within the reasonable small θ_{111} , both RCPX and LCPX were abstracted and focussed continuously on the constant position in a space occupied by a specimen.

The third thing (C) is a small special type of electromagnet installed on a ω - 2θ goniometer. This arrangement is used for MCS measurement to determine the degree of the polarization of rotatory polarized X-rays by use of RCPX and LCPX. The further detailed description including the test study will be presented elsewhere.

1) For example, R. S. Holt et al., Nucl. Instrum. & Methods A243 (1986) 608-610

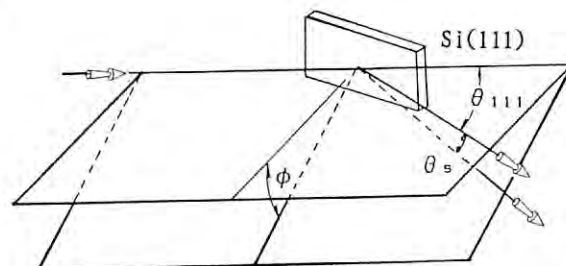


Fig. 2. monochromatising and focussing by the plane 111 of silicon single crystals.

LOW-TEMPERATURE AND HIGH-PRESSURE X-RAY STUDY ON THE PRESSURE-INDUCED PHASE TRANSITION OF AMORPHOUS SEMICONDUCTORS

Motoharu IMAI, Takeshi MITAMURA, Kenichi YAOITA and Kazuhiko TSUJI

Department of Physics, Faculty of Science and Technology,
Keio University, Hiyoshi, Kohoku-ku, Yokohama 223

Introduction

Amorphous silicon and germanium prepared by vacuum evaporation (a-Si and a-Ge) are known to show a pressure-induced semiconductor-to-metal transition at 10 GPa and 6 GPa, respectively.^{1,2} At these pressures, peaks of white-tin structure appear in amorphous pattern. The high-pressure phase of a-Si below 15 GPa returns to the amorphous state on releasing the pressure. In this sense, the transition of a-Si is reversible. For amorphous silicon made by glow-discharge decomposition (a-Si:H), the transition is also reversible.³ On the other hand, the transition of a-Ge is irreversible; the high-pressure phase transforms to a BC-8 structure when pressure is released.^{2,4}

To understand the mechanism of these phase transitions, it is important to investigate the temperature and the concentration dependence of transition behavior of amorphous silicon-germanium alloys.

In this work, we measured x-ray diffraction for amorphous silicon-germanium alloys prepared by glow-discharge decomposition ($a\text{-Si}_x\text{Ge}_{1-x}$, $x=0.9, 0.6$) and for sputtered a-Ge at room temperature and at 77 K at various pressures up to 18 GPa.

Experimental

Powder samples, pressure marker (NaCl) and pressure transmitting medium (4:1 methanol-ethanol mixture) were compressed in a diamond-anvil cell. This cell was driven by He gas to allow the continuous pressure control at low temperatures.^{5,6}

Results and discussion

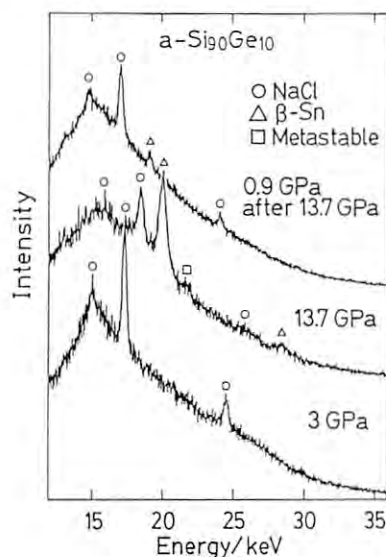


Fig.1

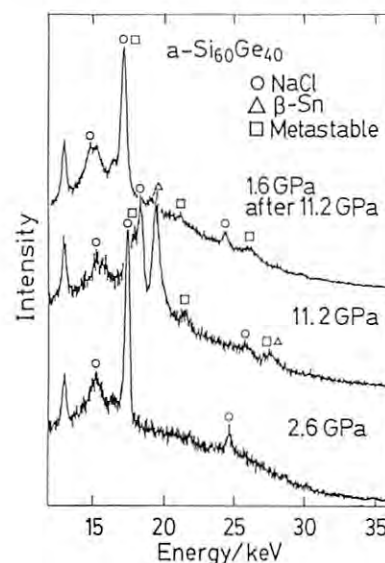


Fig.2

In a-Ge at room temperature, peaks of high pressure phase (white-tin structure) appear at 7.6 GPa with increasing pressure. On depressurizing from 9 GPa to 1.8 GPa, the white-tin structure transforms to a metastable ST-12 structure. At 77 K, a-Ge transforms to the white-tin structure at 11.6 GPa, and this phase still remains even when the pressure is reduced to 8 GPa. Figures 1 and 2 show pressure dependences of x-ray diffraction patterns at room temperature of $a\text{-Si}_{0.9}\text{Ge}_{0.1}$ and $a\text{-Si}_{0.6}\text{Ge}_{0.4}$, respectively. For $a\text{-Si}_{0.9}\text{Ge}_{0.1}$, the phase transition is reversible: it transforms to the high-pressure phase at 13.3 GPa and returns to amorphous state on releasing pressure. For $a\text{-Si}_{0.6}\text{Ge}_{0.4}$, however, the phase transition is irreversible: the ST-12 structure appears at 8.2 GPa and the white-tin structure at 9.7 GPa with increasing pressure. With decreasing pressure, the peaks of the white-tin structure become weak and those of the ST-12 structure grow.

References

- 1) K. Tamura, J. Fukushima, H. Endo, S. Minomura, O. Shimomura and K. Asaumi, *J. Phys. Soc. Jpn.*, **36**, 558 (1974)
- 2) O. Shimomura, S. Minomura, N. Sakai, K. Asaumi, K. Tamura, J. Fukushima and H. Endo, *Philos. Mag.*, **29**, 547 (1974)
- 3) K. Tsuji, M. Imai, O. Endo and K. Yaoita, *P.F. Activity Report 1987*, 163 (1987)
- 4) S. Minomura, *J. de Physique*, **42**, C4-181 (1981)
- 5) N. Sakai, T. Kajiwara, K. Tsuji and S. Minomura, *Rev. Sci. Instrum.*, **53**, 499 (1982)
- 6) K. Tsuji, *Solid State Physics under Pressure*, ed. S. Minomura (KTK, Tokyo, 1985) p.375

Research Study of Cooling down to mK Region by He-3 Dilution Refrigerator
Used for SR X-ray Diffraction Experiments

Tetsuo NAKAJIMA, Haruhiko SUZUKI* and Kitomi TSUTSUMI**

Photon Factory, National Laboratory for High Energy Physics, Tsukuba, 305 JAPAN

*Department of Physics, Faculty of Science, Tohoku University, Sendai, 980 JAPAN

**Department of Physics, Faculty of Science, Kanazawa University, Kanazawa, 920 JAPAN

As was briefly reported in Photon Factory Activity Report 1988 #6, He-3 dilution refrigerator (He-3DR) model NS200 purchased from Oxford Inc. has been continuously arranged to use X-ray diffraction, since the virgin test was performed in the last summer. Some of our initial purposes of the very low temperature X-ray diffraction experiments is to get better understanding of the physical picture of solid helium single crystal as is called quantum solids, structural transformation related with the nuclear spin ordering, precursor phenomena in the nuclear spin ordering in praseodymium etc.

As is well-known thermodynamically, the entropy of the concerned system tends to zero, as the temperature tends to zero. Hence, the specific heats and thermal conductivity tend to zero unlimitedly, too. From these, it means that the cooling power and its velocity of He-3 DR become smaller, because of the entropy reduction of the coolant, including the extra effect of the Kapitza resistance. Moreover, we have nothing to insulate the inflow of the heat. Ultra low temperature measurement is ceaselessly challenge to the techniques to control finely temperature stability.

In July of 1989, we tried to observe the heat-

ing effects on a test specimen, for example, NaCl as a standard material of the lattice spacings measured by the energy dispersive X-ray diffraction. Fig. 1 shows the behaviour of heating up at the mixing chamber, which is thermal engine in He-3 DR to produce the base temperature, measured by uncalibrated carbon resistor thermometer. The ordinate represents decrease of resistance in the carbon resistor by rising temperature and the abscissa flying hours of the X-ray irradiation. The starting temperatures in the curve (a) and (b) are about 14.6 and 50 mK, respectively. Every interval from point to point is plotted by 10 seconds.

The former temperature in this run is the base temperature, which is not reproducible because of circumstances effect of mechanical vibration and eddy current Joule heat by electromagnetic waves in the shield room position. The shield room for X-rays made of 6 mm thick pure iron plates is not effective for protection of electromagnetic waves.

To make a gentle change of temperatures, thick aluminum absorbers to 6 mm thick were used. And taking the topographs of $\text{Cs}_2\text{NaHoCl}_6$ (elpasolite) was tried by polaroid films for about 60 seconds exposure. In this run, we could not find an optimum condition on thickness of absorber and length of the exposure time.

The lower topographs in Fig. 2 were taken at 14.6 mK and about 4.2 K under the same condition of Fig. 1 (exposure time: 10 sec.). It is considered that $\text{Cs}_2\text{NaHoCl}_6$ has structural transformation at 150 mK. Its evidence may be confirmed from these photographs. Detailed report will be presented elsewhere.

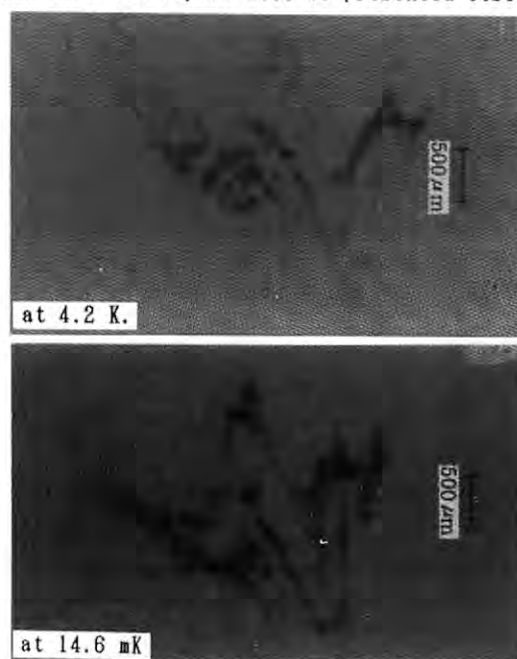
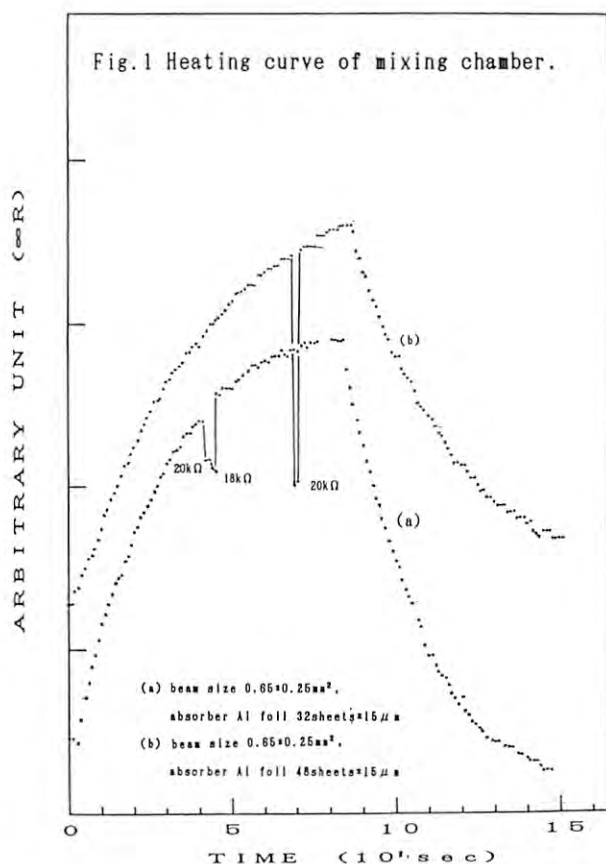


Fig.2 Topographs of elpasolite

KINETICS OF PHASE TRANSITION IN GRAPHITE INTERCALATION COMPOUNDS
-- FIRST ORDER TRANSITION IN A ONE-DIMENSIONAL SYSTEM --

N.Metoki, H.Suematsu, Y.Murakami, Y.Ohishi*, Y.Fujii*, and T.Matsushita**

Dept. of Physics, University of Tokyo, Hongo, Bunkyo, Tokyo 113,
*Faculty of Engin. Science, Osaka University, Toyonaka, Osaka 560,
**Photon Factory, KEK, Tsukuba, Ibaraki 305.

INTRODUCTION

Graphite intercalation compounds(GIC) exhibit various kinds of phase transitions, that is, staging, in-plane melting and stacking transitions. The stacking ordering is regarded as a one-dimensional(1D) system along the c-axis.

In this work we have studied the first-order stacking order-order transition in stage 1 Rb-GIC. The compound has the four-layer-stacking phase($\alpha\beta\gamma\delta$) at a low temperature(T) and the two-layer-stacking phase($\alpha\beta$) at a high T. These two structures correspond to the 1D ferromagnetic(AAAA..) to antiferromagnetic(ABAB..) states when $\alpha\beta$ and $\gamma\delta$ layers are denoted by A and B; B is shifted to A in the transition, and vice versa. The present work is the first investigation of the kinetics in the 1D first-order transition.

EXPERIMENTS

The stacking transition can be controlled by sample T and the vapor pressure of Rb(P)¹. In the present measurements the time(t) dependence of structures were observed by changing P across the critical pressure P_c from the $\alpha\beta\gamma\delta$ - to $\alpha\beta$ -side, and vice versa. X-ray diffraction measurements were carried out at BL7C with using a vertical two-axis goniometer and a two-T furnace. Monochromatic X-rays were used($\lambda = 0.8216\text{\AA}$). The stacking structures $\alpha\beta\gamma\delta$ and $\alpha\beta$ were observed by c*-scans at (103) and (104), respectively: these reflections were used to get a higher resolution, instead of (101) and (100) in the previous measurements. The acquisition time was reduced to 60 sec per scan by improving the gear system of the goniometer($\sim 5^\circ/\text{sec}$).

RESULTS AND DISCUSSIONS

Fig.1 shows the t-dependence of the (101) diffraction spectrum obtained for the transition from $\alpha\beta\gamma\delta$ to $\alpha\beta$ phase and $\Delta P = -1.6\text{ Pa}$. The (104) peak intensity of $\alpha\beta$ phase grows with time while the (103) peak of $\alpha\beta\gamma\delta$ decreases. The (104) reflection is characteristic of the Bragg peak even at the beginning stage of the transition, indicating that nuclei of $\alpha\beta$ phase are stabilized to have a enough large grain size in the matrix of the metastable $\alpha\beta\gamma\delta$ phase.

The t-dependence of the integrated intensity $I(t)$ of $\alpha\beta$ phase can be scaled for various ΔP by a unified function when t is normalized by $\tau = t/t_{1/2}$, where $t_{1/2}$ is the time that $I(t)$ grows to a half the intensity at the completion of the transition. The observed scaling function is in agreement with the result of Avrami's theory for the 1D system.² Furthermore, the structure factor $S(q)$ can be scaled by a unified function very close to the squared Lorentzian, which is in agreement with the theoretical prediction.³ These observations are the first evidence of the scaling for nucleation

growth(NG) in the 1D non-conserved order-parameter system.

Fig.2 shows the t-dependence of nuclear size R of the growing phase which was determined from the linewidth corrected by experimental resolution. R shows the logarithmic t-dependence from a critical size ($\sim 60\text{ \AA}$) to a final size ($\sim 300\text{ \AA}$). This observed dependence of R is inconsistent with the Avrami's assumption of a constant growing rate of nuclear size, the physically reasonable assumption and also the basis of the recent microscopic theories. So the observed logarithmic t-dependence is quite unique.

The authors greatly thank A.Koyama and M.Nomura for their technical advices. The work was partially supported by the Grant-in-Aid of the Ministry of Education.

References

- 1) N.Metoki and H.Suematsu, Phys.Rev.B38, 5310 (1988).
- 2) M.Avrami, J.Chem.Phys. 7,1103(1939). *ibid*, 9,177(1941).
- J.D.Axe and Y.Yamada, Phys.Rev. B34, 1599 (1986).

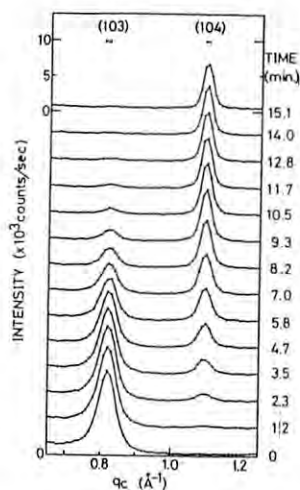


Fig 1

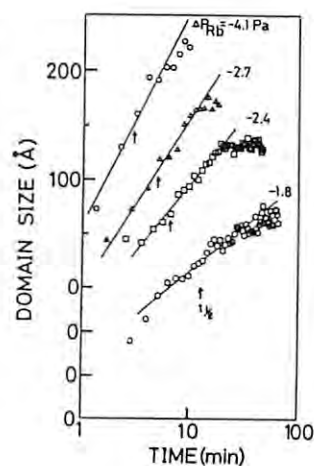


Fig 2

A CINE K-EDGE SUBTRACTION CORONARY ANGIOGRAPHY IN THE RABBIT EXPERIMENT

Tohoru TAKEDA, Masayoshi AKISADA, Teiichi NAKAJIMA, Izumi ANNO,
*Ken UEDA, *Keiji UMETANI

Institute of Clinical Medicine, University of Tsukuba, Tsukuba-shi, Ibaraki-ken, 305 Japan

*Central Research Laboratory, Hitachi Ltd. Kokubunji, Tokyo, 185 Japan

Introduction

The iodine K-edge energy subtraction angiographic system with synchrotron radiation, is now being constructed [1-4]. The coronary artery will be demonstrated clearly and safely with intravenous injection of contrast material. By using a cine K-edge subtraction angiographic system, a preliminary experiment was done in 1988 [4-6]. In this paper, our results of rabbits' experiments will be described.

Method and materials

The cine K-edge subtraction angiographic system was constructed at beam line of 8C of Photon Factory in Tsukuba, consisted of movable silicon (111) monocrystal, image intensifier (II)-TV and digital memory system. X-ray TV images were digitized into 256 x 256 pixel matrix with an 8 bit depth by using an 8 bit AD converter. Image processing and control of the system were performed by the computer (HD-68000 as a micro-processor unit).

The energy of the beams was adjusted in 250 eV above and below the iodine K-edge by rotation of the silicon monochromator crystal. Asymmetric reflection at silicon planes expanded the beam size 25 times, produced 50 x 60 mm monochromatic X-ray beam. Photon energy between above and below iodine K-edge was changed within 16.7 msec. During this experiment, the electron storage ring was operated at 2.5 GeV with an electron current of approximately 200 mA.

The rabbits were anesthetized with phenobarbital, and 5F catheter (0.8 mm in diameter) was inserted into the inferior vena cava via the right femoral vein. The aortogram was also done. 1.5 ml/kg of contrast material (Conraxin H 80%) was injected by the injector at the rate of 0.75 ml/sec. Examination was carried out in an anterior, a left and right anterior oblique projection.

Results

The clear K-edge subtracted images of coronary artery are obtained in the rabbits' studies. The right coronary artery, left main trunk and left circumferential artery ($\Phi 0.4$ mm) can be revealed. Fig.1 showed the image of left circumferential artery. The coronary artery overlapping in the ventricular chamber, can not be seen. The aortogram demonstrates the right coronary artery, the left anterior descending coronary artery and circumferential artery (Fig.2). At the end diastolic and the end systolic phase, images are sharp, but blur is seen at other cardiac phase owing to the cardiac wall motion.

Reference

- 1) Rubenstein E, Hughes EB, Campbell LE, et al: Synchrotron radiation and its application to digital subtraction angiography. SPIE 314: 42, 1981
- 2) Akisada M, Ando M, Hyodo K, et al: An attempt at coronary angiography with a large size monochromatic SR beam. Nuclear Instruments and Methods in Physics Research A246: 713-718, 1986
- 3) Thompson AC, Rubenstein E, Zeman HD, et al: Coronary angiography using synchrotron radiation. Rev. Sci. Instrum. 60, 1674-1679, 1989
- 4) Ueda K, Umetani K, Takeda T, et al: A cine K-edge subtraction angiographic system for animal studies. Rev. Sci. Instrum. 60: 2272-2275, 1989
- 5) Takeda T, Akisada M, Anno I, et al: High speed iodine K-edge subtraction angiography; A preliminary experiment with rats. Medical Imaging Technology 6: 400-406, 1988
- 6) Takeda T, Akisada M, Anno I, et al: High speed iodine K-edge subtraction angiography in the animal experiment. Photon Factory Activity Report 6: 169, 1988



Fig. 1. K-edge subtraction image



Fig. 2. Aortogram

△ RCA
□ LAD
○ LCx

OBSERVATION OF FIBERS IN LONG FIBER REINFORCED METAL MATRIX COMPOSITES
BY X-RAY COMPUTED TOMOGRAPHY USING SYNCHROTRON RADIATIONC. Masuda* , Y.Tanaka*, K.Usami**, T.Hirano**,Y.Imai***,I.Shiota****,
E.Furubayashi* and H.Iwasaki***** Materials Characterization Division,National Research Institute for
Metals,Tokyo.** Materials Characterization Research Center, Hitachi Research Laboratory,
Hitachi Ltd.,Hitachi.

*** Physical Properties Division,National Research Institute for Metals,Tokyo.

**** Photon Factory ,National Laboratory for High Energy Physics, Tsukuba.

Introduction

In order to make clear the fracture process of long fiber reinforced metal matrix composites, X-ray CT images for same composites were obtained in two energy range.

Experiment

Boron(B)(carbon core filament) and silicon carbide(SiC)(carbon filament) fibers reinforced aluminum or titanium matrix composites were fabricated by hot press and cut into the specimens in which those sizes were calculated on the base of the coefficient of X-ray absorption for metallic elements of composites and boron or silicon carbide fibers. The Si(400) channel cut type monochromator was used in the energy range from 20 to 29 Kev. The specimen set up on the holder was rotated at the range of angle from 0 to 180 degrees by 1 degree step and the transmitted X-ray was detected by X-ray sensing pick up tube and cross sectional image was re-constructed by back projection method.

Result and discussion

For B/6N01, SiC/Al and SiC/6061(Al-0.5Si-0.5Mg) aluminum matrix composites boron and silicon carbide fiber were clearly found at the energy level of 20 Kev as shown in Fig.1(a), (b) and (c), while for SiC/Ti-6Al-4V titanium matrix composite silicon carbide

fiber was also observed at the energy level of 29 Kev as shown in Fig.1(d). In Fig.1(a) dark areas are the boron fibers(90 micron meter in diameter) and white area is the aluminum alloy matrix, while in Fig.1(b),(c) and (d) dark areas are the carbon core filament in the silicon carbide fiber and white areas around carbon filaments are the silicon carbides fiber(140 micron meter in diameter). Slightly dark area in comparison to silicon carbide fibers are aluminum or aluminum alloy matrix. On the other hand, in Fig.1(d) the most dark areas were carbon filament, the most white areas were titanium alloy matrix and others were the silicon carbide fibers. These contrast were followed by the coefficient of X-Ray absorption for the element of each materials.

3-dimensional image used 5 cross sectional images were constructed by image processor as shown in Fig.2 for B/6N01 composite. Six boron fibers deviate from the specimen axis. It is suggested that 3-dimensional images could be point out the fracture parts of the fiber or debonded parts at the fiber/matrix interface. We tried to observe the fracture process of fiber in metal matrix composites and in future we will try to observe the particles containing metal matrix composites and in-situ observation of fiber containing composites will be tried.

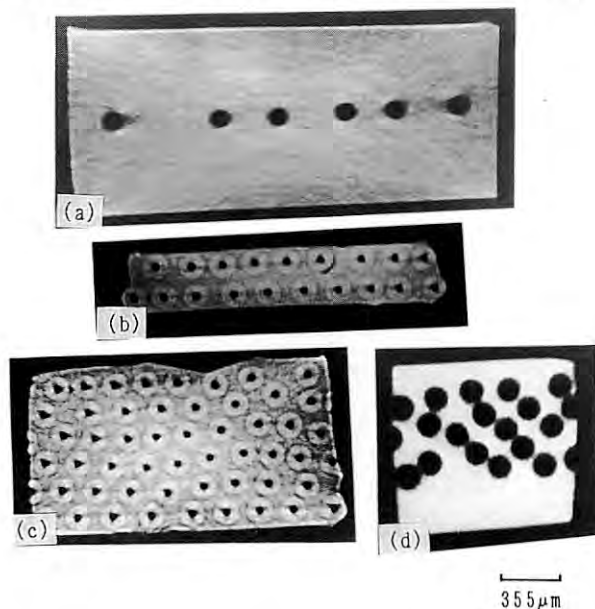


Fig.1 Monochromatic X-ray CT images of (a)B/6N01, (b)SiC/Al, (c)SiC/6061 and (d)SiC/Ti-6Al-4V.

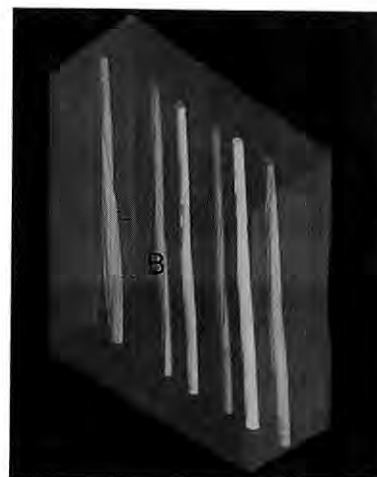


Fig.2 3-dimensional image constructed from 5 monochromatic X-ray CT images for B/6N01 aluminum composite.

OBSERVATION OF METEORITES BY MONOCHROMATIC X-RAY CT BASED ON SYNCHROTRON RADIATION

Minoru Funaki¹, Tatsumi Hirano², Takeshi Nagata¹, Isamu Taguchi³,
Hiroki Hamada⁴, Katsuhisa Usami⁵ and Kazunobu Hayakawa⁵

- 1: National Institute of Polar Research
- 2: Hitachi Research Laboratory, Hitachi, Ltd.
- 3: National Museum of Japanese History
- 4: Analysis Research Laboratory, Nippon Steel Corporation
- 5: Hokkaido University

Introduction

Three-dimensional CT images with a high resolution of 10 μ m using monochromatic X-ray based on synchrotron radiation (SR-CT) are very useful for understanding of internal structures of materials. Allende carbonaceous chondrite is one of the primitive chondrite which includes volatile matters, chondrules, metallic and iron-sulfide grains, silicate aggregates and many kinds of silicate fragments. The configuration of these materials may indicate history of the parent body of the Allende in the early solar system. We elucidated internal structure and configuration of materials in the Allende using the three-dimensional SR-CT images and elemental image obtained by computer-aided microanalyzer (CMA). The slice thickness of SR-CT was 37 μ m and the slice plains were spaced at 110 μ m intervals. After observation by SR-CT, 7th slice plain was cut and polished for CMA analysis.

Experimental results

Three dimensional SR-CT image indicated that the Allende includes nearly spherical chondrules (typical diameter of 0.1-0.5mm and largest one of about 2mm in diameter). This meteorite is very dense, and has no cracks without open spaces of more than 10 μ m in size. The mineral compositions are estimated from the X-ray attenuation coefficient of individual elements. The largest chondrule is surrounded by two kinds of iron sulfide, and a part of them extends into the matrix field. It may suggest the metamorphism of the Allende in the parent body. The most heavy element, probably metallic FeNi grains, is observed in its sample. Two humps are observed on the surface of the largest chondrule (Fig.1). Probably they are formed due to collision among chondrules in space. Well crystallized barred

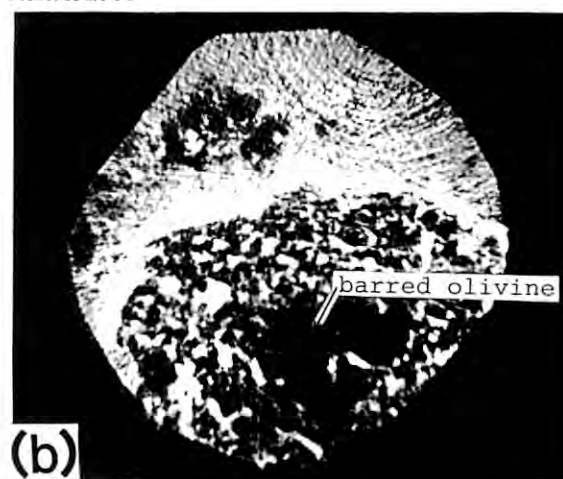
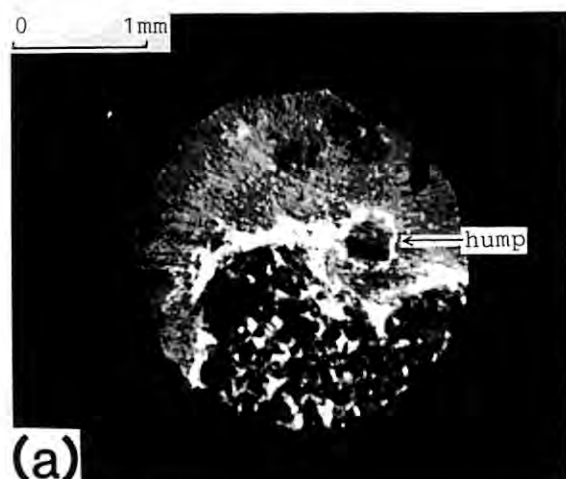
minerals (probably olivine) are observed in the center of the largest chondrule. Almost all small chondrules consist of only light element (silicate). Matrix seems to consist of relative heavy elements compared with silicate in chondrules.

Chemical compositions of Fe, Ni, Mg, S and Si were measured by CMA. From the configurations in the elemental, individual minerals could be identified. Iron sulfide limb of troilite and pentlandite are recognized around the largest chondrule, which consists of fine grained metallic FeNi, olivine, troilite and pentlandite. The small chondrules consist mainly of Si and Mg. Si and Fe are uniformly distributed in the matrix. These observation results seem to be good agreement with those of the SR-CT image.

Conclusions

1. Three dimensional observation by monochromatic X-ray CT based on synchrotron radiation is available for identification of precise internal structure of the stony meteorites.
2. Mineral compositions estimated by SR-CT give good agreement with the results by CMA analyses.
3. Complicate internal texture of the Allende Carbonaceous chondrite elucidates some history in the early solar system; weak metamorphism of the parent body and collision among chondrules.

Fig. 1 SR-CT images of the 7th and 17th slice planes for Allende carbonaceous chondrite. Bright localized features are regions of high attenuating elements. (a): 7th plane showing a hump on the chondrule, (b): 17th plane showing barred olivine in the center of the chondrule.



Three-Dimensional Monochromatic X-ray CT Based on Synchrotron Radiation

Tatsumi Hirano, Minoru Funaki†, Isamu Taguchi††, Katsuhisa Usami and Kazunobu Hayakawa†††

Hitachi Research Laboratory, Hitachi, Ltd., Hitachi-shi, Ibaraki 319-12

†National Institute of Polar Research, Itabashi-ku, Tokyo 173

††National Museum of Japanese History, Sakura, Chiba 285

†††Catalysis Research Center, Hokkaido University, Kita-ku, Sapporo 060

Introduction

X-ray computed tomography (CT) is a nondestructive method to observe internal structures of objects. We have also developed a high resolution, tunably monochromatic X-ray CT based on synchrotron radiation (SR-CT) and obtained CT images of several industrial materials with the resolution of 10 μm .¹⁾ Further, in order to examine the spatial fine structures of objects, the SR-CT should be able to measure CT images at many slice planes with a single scan of the object. A one-time scan offers advantages such as reduction of radiation damage to objects and shorter measuring time. This report describes the development of the three-dimensional SR-CT measurement system and its application to observation of spatial structures in Allende meteorite.

Experimental and Results

Fig. 1 shows a schematic diagram of the SR-CT for measuring the three-dimensional CT image. It was installed on the beam line 8C₂ in the KEK Photon Factory. SR was monochromatized through a Si(400) channel cut monochromator and applied to a specimen. The two-dimensional projection image, corresponding to an intensity distribution of the X-rays transmitted through the specimen, was detected by an X-ray sensing pickup tube (HS501X, Hitachi Denshi Ltd.), which is a two-dimensional X-ray detector. The output signal from the pickup tube through the camera controller was stored in a 2-Mbyte frame memory. The projection image in the frame memory consisted of 1024 x 960 elements.

A large number of two-dimensional

projection images irradiated at different angles produces a three-dimensional CT image of a specimen. CT images are fundamentally reconstructed from every scanning line. However, an enormous amount of memory capacity and calculation time are necessary. We improved the measurement software system, which condenses the two-dimensional projection image of 960 scanning lines to a maximum of 40 slice planes by accumulating several scanning lines. Slice position, slice width and slice interval between the slice planes can be arbitrarily selected in the condensation work. Then the projection image, consisting of selected slice planes, is stored in the memory region of the image processing computer. By rotating the specimen, 180 projections, at 1 degree intervals, are measured by rotating it.

As an application of the three-dimensional SR-CT system to materials, spatial fine structures of Allende meteorite were observed. Fig. 2 displays three CT images of the Allende meteorite at the sixth to eighth slice planes from among twenty slice planes measured. The spatial structures and configurations of substances such as metallic minerals, matrix and chondrules in the Allende meteorite could be observed.²⁾

References

- 1) T. Hirano and K. Usami: Jpn. J. Appl. Phys., 28 (1989) 263.
- 2) T. Hirano et al.: submitted to Fourteen Symposium on Antarctic Meteorites

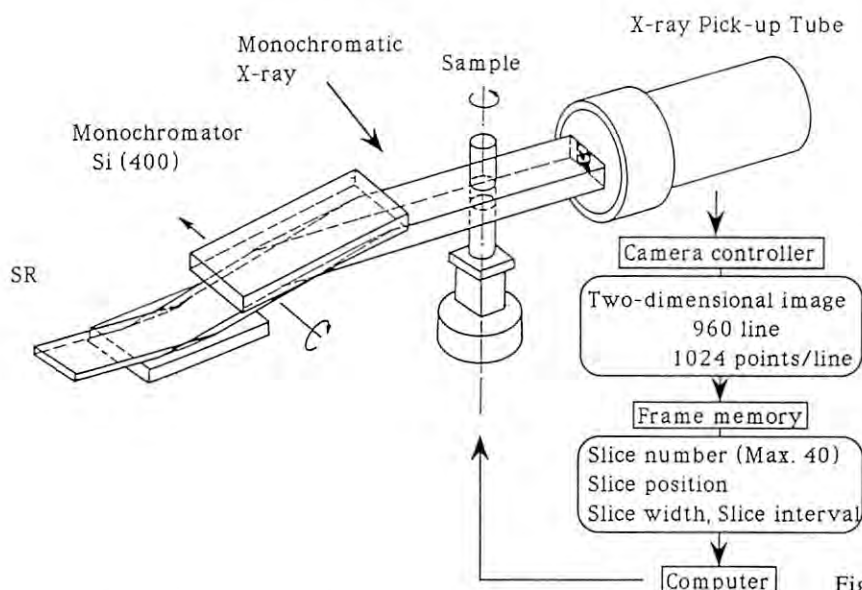


Fig.1 Schematic diagram of SR-CT system for measuring three-dimensional CT images.

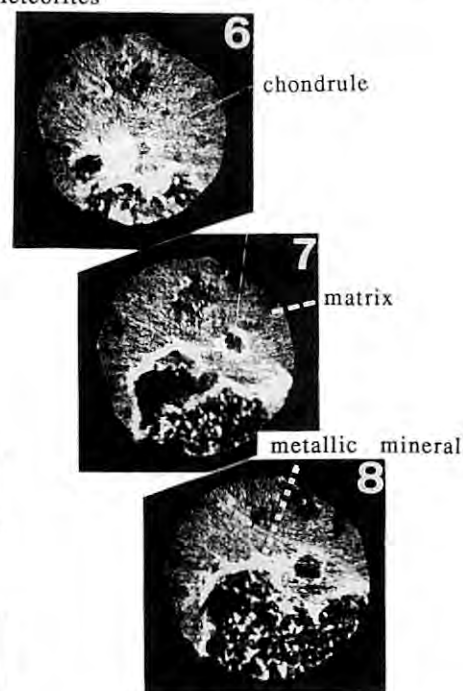


Fig.2 Consecutive CT images of Allende meteorite measured at 30 keV with slice thickness of 30 μm and slice plane interval of 110 μm .

X-Ray Microprobe with a pair of Elliptical Mirrors

Yoshio Suzuki, Fumihiko Uchida[†] and Yasuharu Hirai

Advanced Research Laboratory, Hitachi Ltd., Kokubunji, Tokyo 185

[†]Central Research Laboratory, Hitachi Ltd., Kokubunji, Tokyo 185Introduction

X-ray microprobes should be a basic tool in various X-ray analysis fields. Fresnel zone plates, multilayer reflectors or grazing-incidence mirrors are used to focus the X-ray beam. Among them, the grazing-incidence total-reflection mirror system has several advantages. A broad wavelength band can be accepted with high reflectivity, and the optical element can be used at a fixed focal length that is independent of the X-ray wavelength.

This report describes grazing incidence optics for an X-ray microprobe. The mirror system produces a demagnified image of the X-ray source.

Optical System

In 1948, Kirkpatrick and Baez¹⁾ devised a simple optical system for high-resolution X-ray microscopy. Their scheme used two crossed spherical (or cylindrical) mirrors. The K-B system can remove most of the astigmatism from the grazing incidence optics with concave mirrors. The principal limitation to the spatial resolution is spherical aberration.

The most effective and simplest way to eliminate spherical aberration is use of aspheric (in this case, elliptical) mirrors. As shown in Fig.1, an output beam from focal point F_1 is focused on another focal point F_2 by an elliptical mirror, and demagnification can be approximately defined as a/b . When a mirror with an elliptical cylinder shape is used, the point source is focused on a line image. As shown in Fig.2, with a pair of elliptical mirrors in the K-B configuration, a point image can be generated from a point source. Although coma aberration and field obliquity are still strong, they are not relevant in microprobe usage.

Numerically-controlled fly-cutting technique was used to fabricate the elliptical mirrors. Details of the flycutting machine have been described elsewhere.^{2,3)}

Focusing Properties Test

Focusing properties for the elliptical K-B mirror system were tested at BL-8C. Synchrotron radiation passing through a Si(111) symmetric double-crystal monochromator is focused by the mirror system. Profiles of the focused beam are

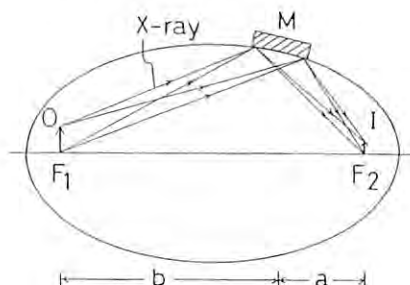


Fig.1. Focusing by an elliptical mirror.

measured by a knife-edge scan through a focused beam. A steel knife is set on a two-axis stepping-motor-driven translating stage. Transmitted X-rays are detected by a scintillation counter. The knife-edge profile is differentiated to give a line-spread function of the optical system. As shown in Fig.3, the measured FWHM is $5.5\mu\text{m}$ horizontally and $4.2\mu\text{m}$ vertically at a wavelength of 2.0\AA .

References

- 1) P. Kirkpatrick and V. Baez: J. Opt. Soc. Am. **38** (1948) 766.
- 2) S. Moriyama, E. Seya and F. Uchida: Opt. Eng. **27** (1988) 1008.
- 3) F. Uchida, S. Moriyama and E. Seya: Seimitu-Kougakukai-Shi **55** (1989) 179 [in Japanese].

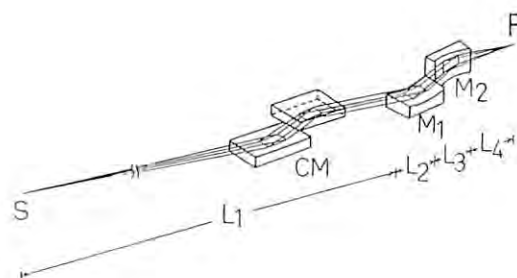


Fig.2. Schematic diagram of optical system. X-ray source S, crystal monochromator CM, elliptical mirrors M_1 and M_2 . Distance between the source point and front end of the mirror, L_1 , is 27970 mm. Mirror lengths, L_2 and L_3 , are 30 mm. Distance between rear end of the mirror and focal point, L_4 , is 15mm.

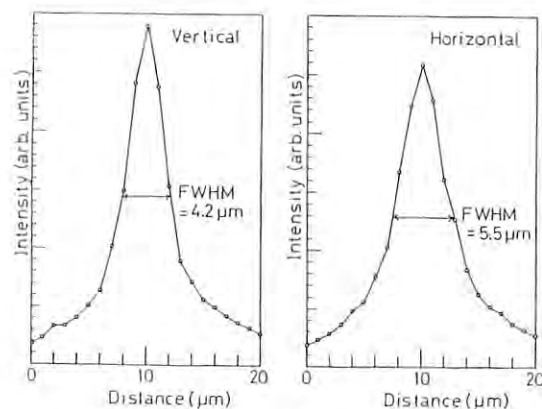


Fig.3. Beam profiles obtained from knife-edge scanning.

STRUCTURAL STUDY ON SiO₂/Si INTERFACE

Ichiro HIROSAWA, Koichi AKIMOTO, Jun'ichiro MIZUKI, Toru TATSUMI* and Junji MATSUI**
Fundamental Research Laboratories, NEC Corporation, Miyukigaoka, Tsukuba, Ibaraki

* Microelectronics Research Laboratories, NEC Corporation, Miyazaki, Miyamae-ku, Kawasaki

** Research and Development Group, NEC Corporation, Miyukigaoka, Tsukuba, Ibaraki

Silicon is a dominant material in electronic devices for the high quality of its oxide. To control the electronic character, the atomic structure at the SiO₂/Si interface must be cleared. We introduced a grazing incidence X-ray diffraction (GID) method to study SiO₂/Si interface.

Two types of samples were prepared. One had a 50Å thick SiO₂ layer which was deposited by a molecular beam deposition (MBD) method. The other was a thermally oxidized Si(100), whose SiO₂ thickness was 50Å.

GID experiments were performed at BL-9C. The monochromatized X-rays (1.5Å) reflected from Si(111) were used. The incident beams, with a horizontal divergence of about 1 mrad and a vertical divergence of about 0.04 mrad, was monitored with an ion chamber. The beams impinged a sample surface with a glancing angle of 0.23°. Scattered beams from the samples were collected by a scintillation counter through 3 mrad Soller slits.

Some fractional-order reflections, which indicate existence of 2x1 interface superstructures, were observed in the MBD sample as shown in Fig.1. On the other hand, there was neither fractional-order reflection nor diffraction peak indicating the existence of crystalline SiO₂ in thermally oxidized sample.

In this report, we refer to the (011) and (011) indices as (-1 0) and (0 1), respectively. Structure factors were obtained from the integrated intensities through correction procedures. Figure 2 is a map of the observed structure factors of the SiO₂/Si(100)-2x1 sample. The radius of each solid circle is proportional to the magnitude of observed structure factor, and stars indicate fundamental reciprocal lattice points. At the points of open circles, no clear diffraction peak was observed.

To explain observed data, several models were considered. In our discussion, an R factor was defined as in the following formula to judge the agreement of the model with the observed data;

$$R = (\sum |F_{obs}| - |F_{cal}|) / (\sum |F_{obs}|)$$

We first considered the crystalline SiO₂ models. Recently, the observation of cristobalite-like and tridymite-like crystalline phases at the SiO₂/Si(100) interface were reported^{1,2}. But neither of them could not explain our observed data.

Among other several models, the following three models were selected. Atomic arrangements of these three models are shown in Fig.3a, 3b and 3c.

Model 1 is a dimer model like a clean surface. Through the fitting procedure to decrease R factor, the arrangements that gave an R factor of 15% were obtained. The difference between calculated and observed structure factors is rather large at (-2 ± 1/2) reciprocal lattice points.

Model 2 employs the bonding sequence of atoms in the [011] direction proposed by Ohdomari et al³, in a 2x1 unit cell (the atomic sequence of Si-O-Si-Si-O-Si). Two additive oxygen atoms and one additive silicon atom are taken into account

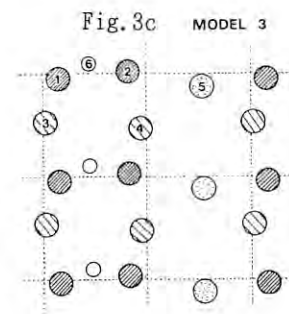
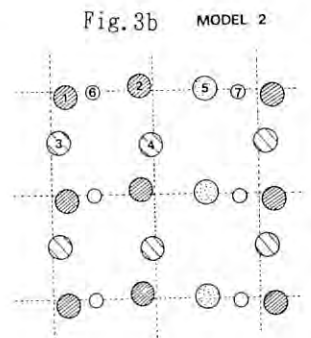
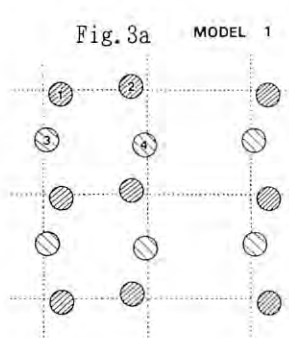
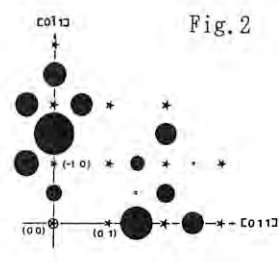
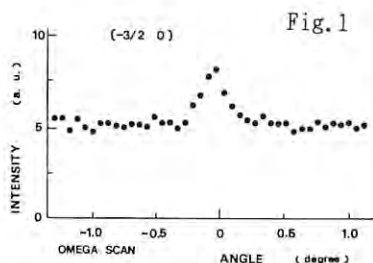
in the unit cell. This model resulted in the optimum atomic arrangements with a 14% R factor.

Model 3 is modified from the model 2. It contains only one additive oxygen atom and one additive silicon atom in a 2x1 unit cell. The optimum arrangements give an R factor of 9%. Although model 3 gives the smallest R factor, the other two models cannot be denied completely, because each observed structure factor contained about 15% ambiguity as its statistical error.

Further experiments, such as the measurements of the crystal truncation rods for determination of the depth profile, are required in order to clarify the detailed atomic arrangements at the interface.

Reference

- 1) A. Ourmazd et al., Phys. Rev. Lett. 59, 213, (1987).
- 2) P. H. Fuoss et al., Phys. Rev. Lett. 60, 600, (1988).
- 3) I. Ohdomari et al., J. Appl. Phys. 62, 3751, (1987).



● top layer Si
○ 2nd layer Si
● deposited Si
○ deposited O

ANALYSIS OF DIFFUSE X-RAY SCATTERING FROM THE OMEGA PHASE IN TITANIUM ALLOYS

Masahiko MORINAGA¹, Naohisa TAKESUE¹, Masato KATO¹, Natsuo YUKAWA¹,
Ken-ichi OHSHIMA², Jimpei HARADA³, Satoshi SASAKI⁴ and Shuji HANADA⁵

- 1) Toyohashi University of Technology, Toyohashi, Aichi 440, Japan
- 2) Institute of Applied Physics, University of Tsukuba, Tsukuba, Ibaraki 305, Japan
- 3) Department of Applied Physics, Nagoya University, Chikusa, Nagoya 464, Japan
- 4) Photon Factory, National Laboratory for High Energy Physics, Oho, Tsukuba, Ibaraki 305, Japan
- 5) Institute for Materials Research, Tohoku University, Sendai 980, Japan

Introduction

The omega phase appears metastably in certain b.c.c. alloys (e.g. Ti and Zr alloys) upon quenching from high temperatures. Some criteria for the occurrence of the omega phase have been discussed by electron theory¹⁾.

It is known that there are co-operative displacements of atoms along $\langle 111 \rangle$ directions in this phase. However, as yet detailed structural model has not been found. In the present study, diffuse intensities have been measured with single crystals of Ti-15mass% Mo and Ti-24mass% V alloys quenched from 1273 K. Attention has been directed towards the computer simulation on the local atomic displacements relevant to the omega phase.

Experimental

The diffuse intensities were obtained in a volume in reciprocal space in absolute units with monochromatic radiation (wavelength = 1.2Å). The measurements were performed at the beam line 10A. A total number of measured points was about 13,000 for each alloy. Further details on the measurements will be seen in our paper²⁾.

The observed intensities were analyzed by a least square method. Several parameters to represent local structures were determined quantitatively.

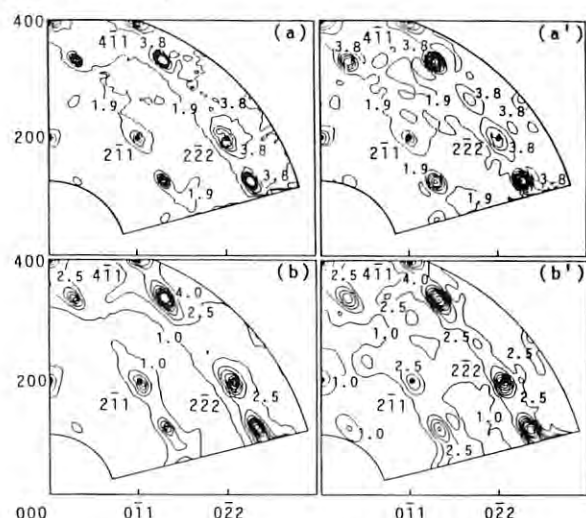


Fig.1 Contour maps of the diffuse X-ray intensity distribution on (011) b.c.c. reciprocal lattice plane; (a) observed, (a') analyzed intensity for Ti-15mass% Mo alloy, and (b) observed, (b') analyzed intensity for Ti-24mass% V alloy. The labels of the curve indicate the intensities in electron units per atom / f_{av}^2 (f_{av} : the average atomic scattering factor).

Results

Fig.1 (a-b') are the contour maps of diffuse intensities on the (011) reciprocal plane; (a), (a') and (b), (b') show the observed and analyzed intensities for Ti-15mass% Mo and Ti-24mass% V alloys, respectively. The diffuse scattering peaks appeared near $2/3$, $2/3$, $2/3$ type positions. There is good agreement between (a) and (a'), and also between (b) and (b').

For either Ti-Mo or Ti-V alloy, short-range order intensity was very small. For Ti-Mo alloy it was estimated to be less than 5% of total intensities. A large portion of the observed intensities was attributable to the thermal diffuse scattering and Huang scattering. This result is consistent with the observation of large temperature parameters ($1.6-1.9 \text{ Å}^2$) of these alloys.

Fig.2 shows one example of the displacement parameters determined in the present study. There is strong resemblance between Ti-Mo and Ti-V.

Based on these parameters, structural simulations are carried out using a new computer program with the simplex method. As this is a completely new way for treating atomic displacements, the validity and usefulness of the simulation is now investigated extensively.

References

- 1) M. Morinaga, H. Ezaki, M. Kato, N. Yukawa and H. Adachi, Trans. JIM (Suppl.) 29, 237 (1988).
- 2) K. Ohshima, J. Harada, M. Morinaga, P. Georgopoulos and J. B. Cohen, J. Appl. Cryst., 19, 188 (1986).

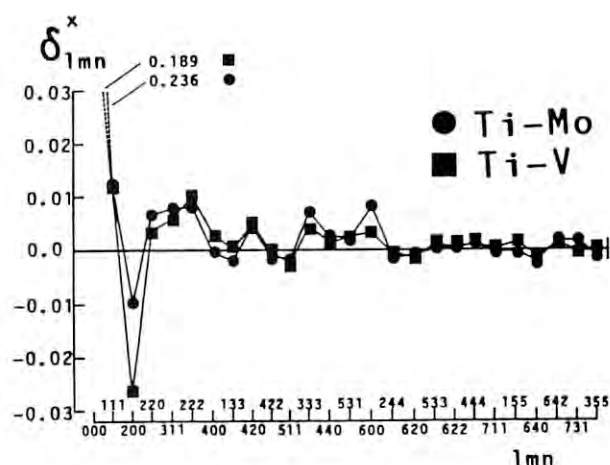


Fig.2 Change of displacement parameter, $\delta_{l mn}^x$, with interatomic vector, $l mn$.

OBSERVATION OF CRITICAL SCATTERING FROM NaNO_3 SINGLE CRYSTAL UNDER HIGH PRESSURE ON SYNCHROTRON RADIATION SOURCE

A. OKAZAKI, H. IWASAKI*, S. HASHIMOTO AND S. SASAKI*

Institute for Materials Research, Tohoku University, Sendai 980

* Photon Factory, National Laboratory for High Energy Physics, Tsukuba 305

NaNO_3 is known to undergo structural phase transition at 548 K in which ordering and disordering in the orientation of the NO_3 radicals are involved. The transition is of a second order and structural fluctuation which is observed as an X-ray critical scattering occurs at temperatures just above the transition temperature T_c ⁽¹⁾. Octopole-octopole interaction between the radicals is responsible for the transition and a decrease in the inter-radical distance with the application of pressure is expected to give an influence on the transition. We made an investigation on how the pressure effect appears through the measurement of the intensity of reflection which is sensitive to the orientational order of the radicals using single crystals on synchrotron radiation source. The measurement was extended to detect the critical scattering under high pressure.

Figure 1 shows a cross section of the high-temperature diamond-anvil cell used for the measurement. The sample crystal 0.1 mm in size is immersed in fluid paraffin and squeezed in between a pair of the diamonds. In order to prevent a release in pressure on heating the cell, the tightening screws are made of Invar metal having small thermal expansivity. The cell was mounted on the ϕ -table of the four-circle diffractometer at BL-10A and monochromatized beam 0.09 nm in wavelength and 0.3 mm in cross sectional diameter was incident to the sample.

The reflection chosen was $11\bar{3}$ and the temperature dependence of its integrated intensity was measured at a pressure of 1 GPa along with the intensity of $02\bar{2}$ reflection which was insensitive to the orientational order and used as a standard reflection. The results show that the degree of the orientational order decreases with increasing temperature and finally goes to zero at a temperature of 610 K, higher by 62 deg than T_c at atmospheric pressure. What is notable is the manner of the decrease and the order begins to fall appreciably when temperature approaches more closely to T_c . In other words, the application of pressure makes the nature of the transition in NaNO_3 closer to that characteristic of the first order type.

Figure 2(a) shows the result of an intensity scan at a temperature of 610.5 K across the region where the critical scattering appears. Although very weak, one can clearly see a peak of the scattering with the breadth three times narrower than that observed at atmospheric pressure. When the sample temperature was raised by 1 deg, the scattering completely disappeared, as shown in Fig. 2(b). This is in a striking contrast to what is observed at atmospheric pressure, at which the scattering exists over a temperature range of 5 deg above T_c . This also suggests the gradual change in the nature of the transition with the application of pressure.

References

- (1) H. Terauchi and Y. Yamada: J. Phys. Soc. Japan **33** (1972) 446.

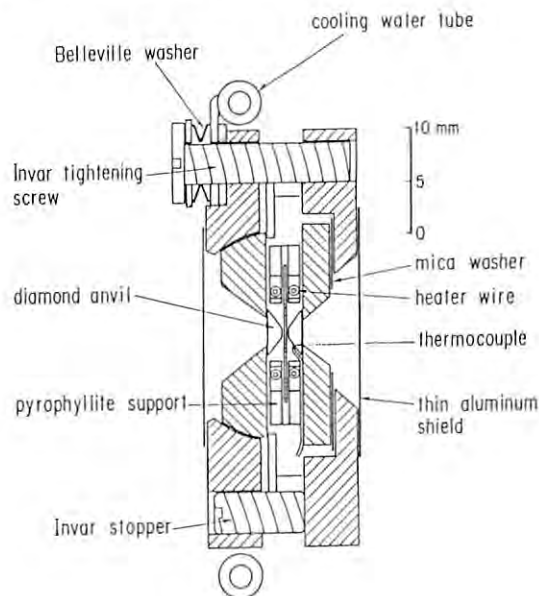


Fig. 1 High-temperature diamond-anvil cell used for the measurement of critical scattering.

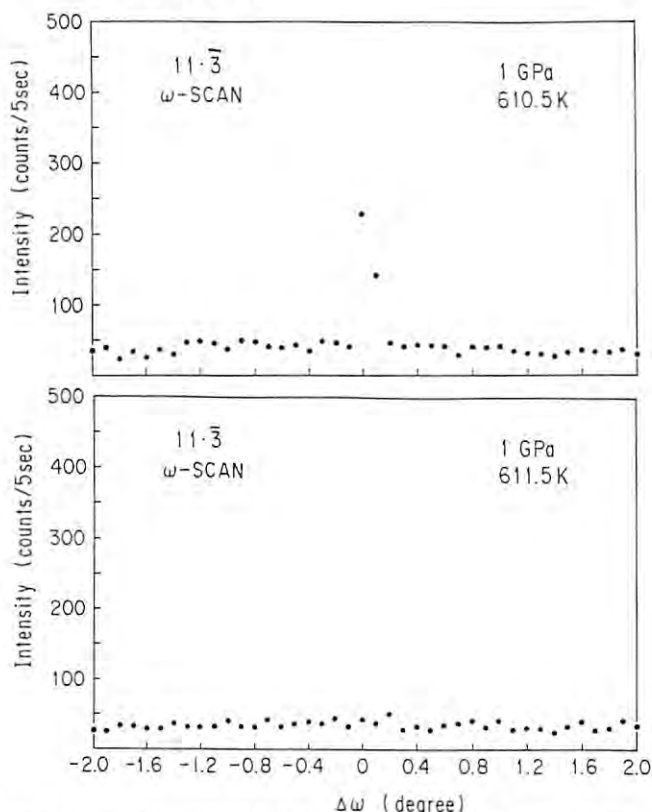


Fig. 2 (a) Intensity profile of the critical scattering from NaNO_3 at a pressure of 1 GPa and a temperature of 610.5 K. (b) Intensity profile at a pressure of 1 GPa and a temperature of 611.5 K, showing that the critical scattering disappears.

STUDIES ON THE PROCESS OF REACTION IN CRYSTALS BY SR.

--Dehydration of alpha-FeOOH.--

Masaaki.OHMASA, Kenji.HAGIYA, Sizuo.SAITO and Satoshi.SASAKI*

Institute of Materials Science, University of Tsukuba, Japan

*Photon Factory, National Laboratory for High Energy Physics, Japan

Introduction

In order to study the process of reaction in crystals, it is necessary to observe decomposition of precursor and formation of the product during the transformation. Since such change is related to the structures of the both phases, X-ray diffraction is the most powerful tool for this purpose. However, not only Bragg reflections but diffuse scattering or satellite reflections are observed occasionally in the early stage of the process and intensities of such scattering are too weak to measure though they are important to analyze the process. Therefore use of synchrotron radiation is desirable to study those problems.

There are many compounds which show topotaxy during phase transformation. Since the product of such transformation is formed in an oriented manner under influence of the structure of precursor, diffraction patterns of the product are similar to those of a single crystal and anomaly of the diffraction can be easily detected. Alpha-FeOOH is one of the compounds which shows topotaxy during the dehydration and the product indicates satellite reflections in the early stage of formation. We have consequently studied the process of dehydration in alpha-FeOOH by observation of diffracted X-ray.

Experimental

Single crystals from Colorado, U.S.A. were selected for the investigation. Since preliminary results obtained by quenching method indicates that the intensity of satellites is too weak to measure on a conventional diffractometer and that the satellites shift towards the main reflection after longer heating, the process of dehydration was observed at elevated temperature

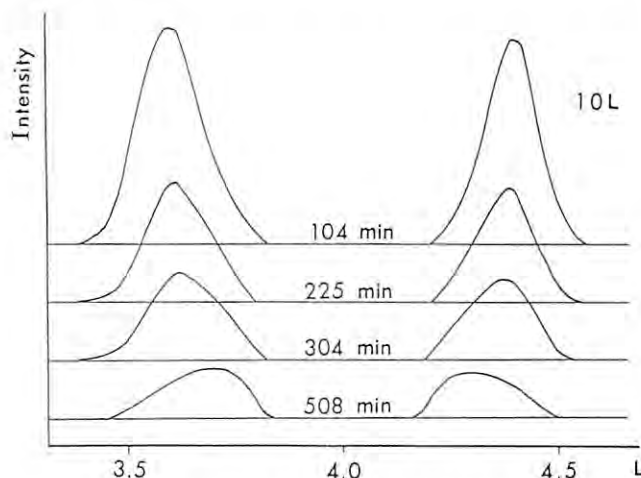


Fig.1 Profiles of satellites

by X-ray diffraction with strong SR beam of Photon Factory in KEK. The experiments have been done using the vertical four-circle diffractometer on the BL-10A. A small furnace was attached on the diffractometer to keep the specimen at a definite temperature.

Results

For Al-analogue we have found that the satellites being attributed to the periodic change of the Al-occupancy change their profile as the stage of the dehydration and that the modulation specimens were heated longer and that they overlapped to the main reflections finally. These phenomena were interpreted as a kind of a one-dimensional stacking disorder, because the structure of the product can be regarded as a layer structure (Ohmasa et al., 1988). Similar phenomena were observed for Fe-analogue in the present studies. The change of profiles of the satellites are illustrated in Fig.1 where the heating period is given in minutes. We calculated the change of the profile of the satellites with the following formula:

$$I = \sum (N - |m|) \text{tr} V F P^m \exp(-2\pi i m \gamma),$$

where N is number of fundamental layers, V a matrix of structure factors of the layers, F probabilities of existence of the layers, P sequence of the layers and tr a trace of a matrix. Fig.2 the obtained relation between period of the diffuse maxima (period of the mean modulation wave) and a probability gamma. When gamma increase, the layers with the same cation occupancy increase: that is, the layers with less occupancy are filled with cation according to the diffusion.

References

M.Ohmasa, et al., KEK Prog. Rep. 88-3, 173, 1988.

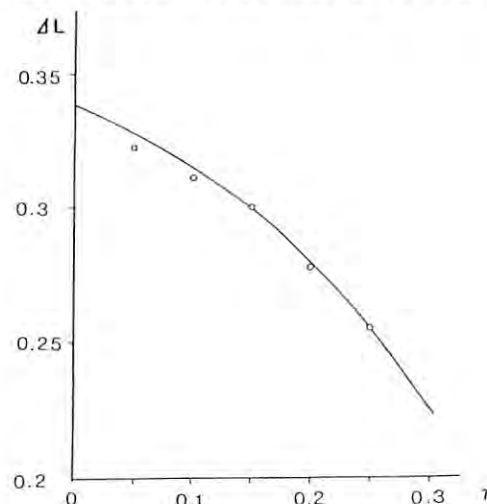


Fig.2 Relation of distance between main reflection and diffuse maximum to gamma

Cu K-EDGE ABSORPTION SPECTRA OF A NOVEL SUPERCONDUCTING OXIDE :
 $\text{Nd}_{2-x}\text{Ce}_x\text{CuO}_{4-y}$ II. REDUCED SAMPLES

Nobuhiro KOSUGI¹, Yoshinori TOKURA², Hidenori TAKAGI³ and Shinichi UCHIDA³

1.Division of Molecular Engineering, Kyoto University, Yoshida, Kyoto 606 (JAPAN)

2.Department of Physics, The University of Tokyo, Hongo, Tokyo 113 (JAPAN)

3.Engineering Research Institute, The University of Tokyo, Hongo, Tokyo 113 (JAPAN)

To induce superconductivity in $\text{Nd}_{2-x}\text{Ce}_x\text{CuO}_{4-y}$ (NCCO), electron doping by the reduction ($y \neq 0$) is necessary in addition to the Ce substitution ($x \sim 0.15$)^{1,2)}. This indicates breakdown of the rigid-band and single-band models in which both the substitution and the reduction should induce the same change in electronic (band) structure. In the present work,³⁾ we have studied how the reduction induce changes in the electronic and geometrical structures in NCCO by means of X-ray absorption spectroscopy (XANES) at the Cu K-edge.

The spectra for the reduced NCCO samples ($x=0.12, 0.15$) are not identical with those for the unreduced ones. We have tried to extract XANES spectra for reduced components. The extracted XANES spectra for the reduced components can be obtained as follows:

$$([\text{red.}] - b [\text{"unred."}]) / a \quad (a = 1 - b).$$

As shown in Fig.2.1, the extracted XANES spectra for the reduced components show a single $1s-4p\pi$ (P) and a single $1s-4p\sigma$ (Q) transitions, irrespective of the values of a . This indicates that the reduction yields monovalent species unlike the Ce substitution. Examination on various values of a has revealed that the reduced components correspond mainly to Cu_2O -like species.

In Fig.2.1 the extracted spectra are best fitted to the spectrum of pure Cu_2O . The resultant values of a are 0.07~0.08. This means that $y=0.24\sim 0.28$ (for example, $[\text{CuO}_{3.72}] = 0.92[\text{CuO}_4] + 0.04[\text{Cu}_2\text{O}]$). The value of y obtained with the XANES analysis is much larger than that obtained with the iodometric titration technique²⁾ which has revealed that the oxygen content decreases from $y=0\sim 0.01$ to $y\sim 0.04$ after the reduction when $x\sim 0.15$. Most of the oxygen deficiencies correspond to a tiny Cu_2O impurity phase (1~2%) found with powder X-ray diffraction²⁾; that is, $0.99[\text{CuO}_4] + 0.005[\text{Cu}_2\text{O}] = [\text{CuO}_{3.965}]$. This is consistent with no remarkable difference found in the lattice parameters between the samples before and after the reduction. The discordance of the values of y obtained with the XANES analysis and with the iodometric titration and powder X-ray diffraction techniques probably arises from the difference in sensitivity to impurity phases and from the experimental and analytical errors.

On the other hand, Cu 2p XPS spectra for unreduced and reduced samples ($x=0.15$) show that the satellite-to-main peak intensity ratios I_s/I_m are 0.25 and 0.21⁴⁾, respectively, indicating that monovalent species are included up to 16 % after the reduction and $y=0.56$ if they are all Cu_2O ($[\text{CuO}_{3.44}] = 0.84[\text{CuO}_4] + 0.08[\text{Cu}_2\text{O}]$). The values of y obtained with XPS are much larger than those obtained with XANES, iodometric titration and powder X-ray diffraction. This means that the monovalent

species are impurity phases such as surface contamination and grain boundary segregation since photoabsorption (transmission-mode) and photoelectron spectroscopies are bulk-sensitive and surface-sensitive, respectively, and there is extrinsic Cu^+ contamination mainly at the surface and grain boundary.

The essential effect of the reduction to induce the superconductivity in NCCO has not yet been revealed.

- 1) Y.Tokura, H.Takagi and S.Uchida, Nature 337 (1989) 345
- 2) H.Takagi, S.Uchida and Y.Tokura, Phys. Rev. Lett. 62 (1989) 1197.
- 3) N.Kosugi, Y.Tokura, H.Takagi and S.Uchida, Phys.Rev.B 41 (1990) in press
- 4) A.Fujimori et al., unpublished

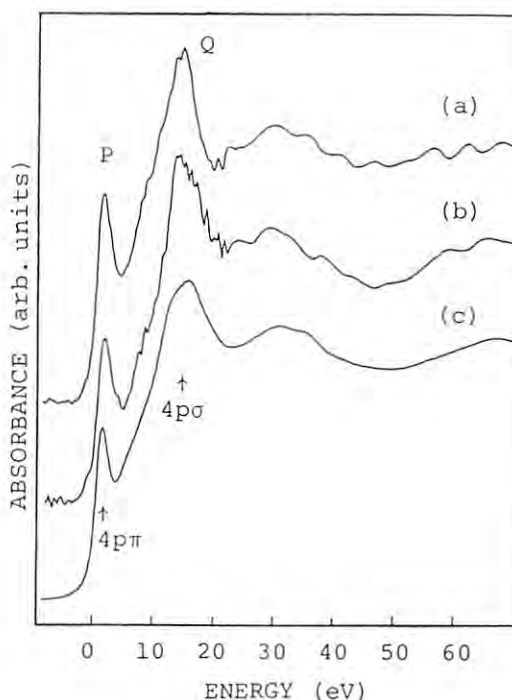


Fig.2.1. Extracted XANES spectra for impurities introduced with the reduction from the spectra of the unreduced $\text{Nd}_{2-x}\text{Ce}_x\text{CuO}_4$ and reduced $\text{Nd}_{2-x}\text{Ce}_x\text{CuO}_{4-y}$ ($y \neq 0$):
 $([\text{red.}] - b [\text{"unred."}]) / a \quad (a = 1 - b).$
 (a) $x=0.12$, $a=0.08$, (b) $x=0.15$, $a=0.07$, (c) Cu_2O .

TERTIARY STRUCTURE OF CALMODULIN FRAGMENTS IN SOLUTION

Yoshinobu Izumi, Masayoshi WAKITA, Hidenori YOSHINO*, and Norio MATSUSHIMA**,

Department of Polymer Science, Faculty of Science, Hokkaido University, Sapporo 060.

* Department of Chemistry, Sapporo Medical College, Sapporo 060.

** Department of Physics, School of Allied Health Professions, Sapporo Medical College, Sapporo 060.

Introduction

The solution X-ray scattering (SOXS) has been applied to study the conformation of calmodulin (CaM) in solution¹⁻⁴. This technique has brought a remarkable refinement in the quality of data compared with the results in conventional laboratories. The purpose of this paper is to present a further verification of previous results throughout the SOXS study of the sizes and shapes of fragments and the complex formed by the interaction of each fragment and mastoparan.

Experimental

The tryptic fragments F12 and F34 of calmodulin were prepared according to the method previously reported⁵. The SOXS profiles were recorded with synchrotron radiation from a storage ring at the Photon Factory of the National Laboratory for High Energy Physics, Tsukuba. The scattering profiles for fragments F12 and F34 and the complexes were calculated on the basis of the crystal coordinates. The calculations were carried out with a computer program which uses Debye's formula for models composed of spherical subunits⁶. Each spherical subunit is substituted by a circle of 3.7Å radius, which approximately represents the volume occupied by one residue of polyalanine.

Results and Discussion

Fig. 1 shows the moderate-angle X-ray scattering (MAXS) profiles for fragment F34 of CaM. Upon binding mastoparan, the MAXS profile of Ca^{2+} -saturated F34 differs remarkably from those of Ca^{2+} -free and/or Ca^{2+} -saturated F34 without mastoparan: a prominent decrease of a minimum near $s=0.045$, was observed, where s is the inverse Bragg spacing. Ca^{2+} -saturated F12 with mastoparan showed almost the same behavior as that of F34 with mastoparan.

Fig. 2 shows the theoretical SOXS profiles for fragment F34 in the presence of Ca^{2+} and in the presence of both Ca^{2+} and mastoparan. The theoretical scattering profiles calculated for F34 with or without mastoparan are very similar to the corresponding MAXS profiles shown in Fig. 1. That is, the theoretical profiles for F34 without mastoparan show a minimum, a maximum, and another minimum at $s=0.05$, 0.06 , 0.08 , respectively. Upon binding mastoparan, theoretical profile also shows a prominent minimum near $s=0.045\text{\AA}^{-1}$. Ca^{2+} -saturated F12 with mastoparan showed almost the same theoretical behavior as that of F34 with mastoparan.

Comparing with the model calculation by Persetich-

ini and Kretsinger suggests⁷ that mastoparan in α -helical state is located to interact with hydrophobic patch in each fragment as in their model but the center-to-center distance between mastoparan and each fragment is shorter by several angstrom than that in their model and that mastoparan in α -helical state binds to both domains of intact calmodulin with a large bend of the long central helix connecting the domains.

References

- 1) Y. Izumi et al, Rept. Prog. Polym. Phys. Jpn. 31, 571 (1988).
- 2) Y. Izumi et al, Housha-Kou 2, 23 (1989).
- 3) N. Matsushima et al, J. Biochem. (Tokyo) 105, 883 (1989).
- 4) H. Yoshino et al, J. Biol. Chem. 264 (1989) in press.
- 5) O. Minowa & K. Yagi, J. Biochem. (Tokyo) 96, 1175 (1984).
- 6) P. Debye, Ann. Physik 46, 809 (1915).
- 7) A. Persechini & R. H. Kretsinger, J. Cardiovasc. Pharmacol. 12, (Suppl. 5) S1-S12.

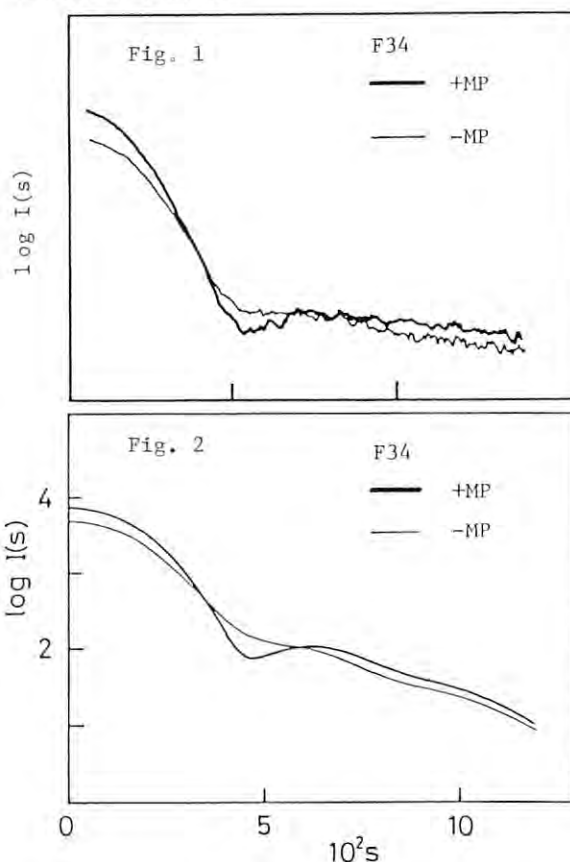


Fig. 1. The SOXS profiles of the fragment F34 in the presence and absence of mastoparan.

Fig. 2. The calculated profiles for the fragment F34 in the presence and absence of mastoparan.

X-RAY PHOTOACOUSTIC SPECTROSCOPY FOR DETERMINATION OF IRON IN POWDERED SAMPLES

Kenji KATO* and Yoshinori SUGITANI**

* National Chemical Laboratory for Industry, Tsukuba, Ibaraki 305

** Department of Materials Science, Kanagawa University, Tsuchiya, Kanagawa 259-12

Introduction

In the X-ray region elemental analysis can be conducted using the characteristic absorption of atoms. Measurements based on X-ray absorption are suitable for the determination of heavy elements in light matrices. One of the problems in photoacoustic measurement for powdered sample is that the effect of scattering of exciting beam is severe for fine particles. However, this is not serious in X-ray region, because refractive index of materials for X-ray is almost 1 so that the scattering at the sample surface will scarcely occur. Moreover, the intensity of photoacoustic signal depends on the thermal diffusion length, μ , which can be varied by changing the chopping frequency. Therefore, the frequency response of the photoacoustic signal involves information concerning the diameter of powder particles and the distribution of elements in powder particle.¹

Experimental

The photoacoustic measurements were conducted at beam lines BL-10C (1.7-1.8Å) and BL-15A (1.504Å). The powdered sample was packed in a concavity (18mm in diameter and 0.5mm in depth) of the sample holder and covered with polymer adhesive tape. The photoacoustic signal was detected by a condenser microphone. Active alumina powder containing iron was used as sample. Elemental composition of the sample was checked by spectrophotometric method and thermogravimetric analysis.

Results and Discussion

The photoacoustic signal intensity for the sample without iron was large at a low chopping frequency, and showed a tendency to decrease at a high chopping frequency. The signal intensity for the sample without iron was subtracted from the raw signal intensities as the background. Figure 1 shows the signal intensities plotted as

a function of the iron content. Plots for high chopping frequencies show good linearity and low background. This suggests that measurements at a high chopping frequency is preferable to quantitative analysis.

Figure 2 shows the change in the signal intensity versus the chopping frequency, f . The signal intensity decreased as f^{-1} for samples with iron added. On the other hand, the signal intensity decreased as $f^{-3/2}$ for samples without iron. According to the RG theory², the photoacoustic signal intensity varies as f^{-1} on the condition that $\mu > 1/\beta$ (thermally thin case) and as $f^{-3/2}$ on the condition that $\mu < 1/\beta$ (thermally thick case), where β is optical absorbance of the sample. Thus, the aluminum hydroxide gel powder without iron was thermally thick, while the samples with iron added were thermally thin. These facts suggest that iron was concentrated at the surfaces of particles or in small particles.

X-ray photoacoustic spectra is also obtained. This is an approaches to eliminate the background contribution. Figure 3 shows the X-ray photoacoustic spectra for the active alumina powder with iron added. The absorption edge can be designated with the magnitude, R_j and the wavelength λ_j of the jump. Experimental value of λ_j fitted to that for Fe $K\alpha$. But, the experimental value of R_j was larger than the calculated value using mass absorption coefficients which do not take into account the effect of EXAFS. This disagreement is considered to be due to the presence of fine structure (EXAFS) and the concentrated iron at the surface of the particles or in the small particles.

References

- 1) K. Kato and Y. Sugitani, Anal. Sci., in press (1989).
- 2) A. Rosencwaig and A. Gersho, J. Appl. Phys., 47, 64 (1976).

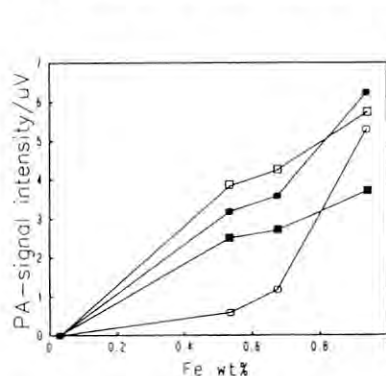


Fig.1. Corrected photoacoustic intensities versus the iron contents for various chopping frequencies. ○:10Hz, ●:20Hz, □:40Hz, ■:80Hz.

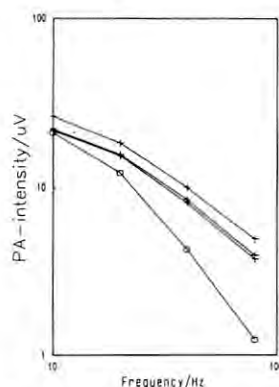


Fig.2. Photoacoustic intensities versus the chopping frequencies for the samples with(+) and without(O) iron addition.

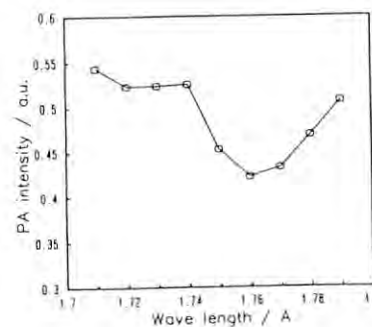


Fig.3. X-ray photoacoustic spectra of active alumina with iron added (Fe 1.72wt %) near the absorption edge of Fe $K\alpha$.

COMPOSITION FLUCTUATION WITH SMALL WAVE LENGTH IN EARLY
STAGE SPINODAL DECOMPOSITION OF POLYSTYRENE/POLY(2-CHLOROSTYRENE) BLEND SYSTEMS

Masato Takahashi^{*1}, Mamoru Okada^{*2}, Shuichi Nojima^{*3}, Takuhei Nose^{*2} and Tamaichi Ashida^{*3}

^{*1} Department of Industrial Chemistry, Tokyo Metropolitan University, Setagaya-ku, Tokyo 158

^{*2} Department of Polymer Chemistry, Tokyo Institute of Technology, Meguro-ku, Tokyo 152

^{*3} Department of Applied Chemistry, Nagoya University, Chikusa-ku, Nagoya 464

Introduction

A huge number of experimental investigations on kinetics of phase separation have been made by using light scattering technique. Investigation of shorter wave length behavior is needed to clarify the early stage of spinodal decomposition, i.e. effect of thermal noise, relation between the maximum wave number k_m and the critical wave number k_c , etc. In the present study, we measured the time evolution of the small angle X-ray scattering in the phase separation process of polystyrene(PS)/poly(2-chlorostyrene)(P2-ClS) blends to investigate the composition fluctuation with small wave length in the early stage of spinodal decomposition.

Experimental

PS was the product of Pressure Chemical Co. with the weight average molecular weight $M_w = 5.00 \times 10^4$ and molecular weight distribution $M_w/M_n < 1.06$. P2-ClS was prepared by radical polymerization using AIBN as an initiator and was fractionated. Its M_w and M_w/M_n were determined by GPC using PS as the standard to be 9.9×10^4 and 1.1, respectively. The measured compositions of blends were 41 and 50 wt%PS. Temperature jump was made by transferring the sample to the heating block controlled at a temperature within the two phase region. The scattered intensity was detected by PSPC with the sensor length of about 20cm. The distance from samples to the detector was 200cm. The temperature of samples was controlled within $\pm 0.1^\circ\text{C}$.

Fig.1 shows the scattered intensity $I(k,t)$ from 50 wt%PS sample at the wave number $k = 1.27 \times 10^{-3}$, 1.65×10^{-3} and $2.03 \times 10^{-3} \text{ \AA}^{-1}$ as a function of time t after the temperature was jumped to $T = 152.3^\circ\text{C}$. The scattered intensity $I(k,t)$ increased initially (early stage), and then decreased (intermediate stage). The time period in which $I(k,t)$ increased depends on the wave length and is longer at the small wave numbers. The temperature dependence of the length of this period is opposite in the two composition, namely, this time period became longer with decreasing the quench depth for 41wt%PS, while it became longer with increasing the quench depth for 50wt%PS.

In early stage of spinodal decomposition, the composition fluctuation of phase separation is expected to obey the linearized diffusion equation, so-called the Cahn-Hilliard-Cook's (CHC) theory¹⁾. The CHC theory predicts the following equation

$$I(k,t) = (I(k,t) - I(k, \infty)) \exp(2R(k)t) + I(k, \infty) \quad (1)$$

for the time development of $I(k,t)$, where $I(k,0)$ and $I(k, \infty)$ are the scattered intensity at $t = 0$ and $t = \infty$, respectively. Fig.2 shows the rate constant $R(k)$ obtained from the non-linear least squares fitting to eq.(1) as a function of k . The deviation from the linearity predicted by the CHC theory may be responsible for the contribution of the non-linear term neglected in CHC theory. This term may give non-negligible contribution in high wave number region because of the wave number dependence of the time period of the early stage.

Results and Discussion

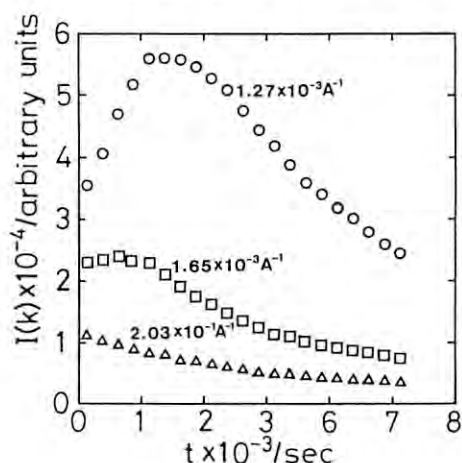


Fig.1

References

- 1) H. E. Cook, Acta Metall., 18, 297 (1970).

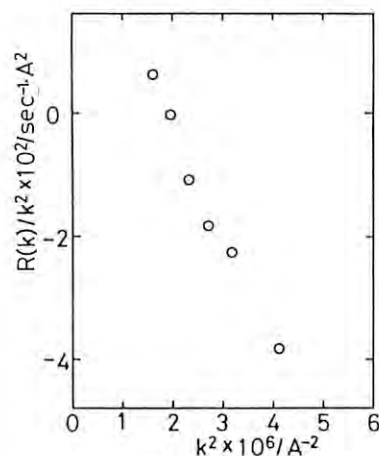


Fig.2

Imaging by Semi-pulse X-ray Photoacoustic Method

Tsutomu MASUJIMA¹, Taro TOYODA², Hideaki SHIWAKU³,
 Masami ANDO³, Katsumi KOBAYASHI³, Yoshiyuki AMEMIYA³,
 Tadashi HIRAGA¹, Norihisa ISHIBASHI¹, Shin-ichi KAWANO¹

- 1.Inst. Pharmaceutical Sci., Hiroshima Univ. School of Med.,
Kasumi, Hiroshima 734 JAPAN
- 2.Dept. Applied Phys. Chem., Univ. Electro-Communications,
Chofugaoka, Chofu 182 JAPAN
- 3.Photon Factory, National Laboratory for High Energy Physics,
Oho, Tsukuba 305 JAPAN

INTRODUCTION

Pulse method, which analyzes the transient response of photoacoustic signal on a pulse-wise X-ray irradiation on to samples, is shown to be useful for depth-profiling¹⁾.

The synchrotron radiation X-ray was chopped pulse-wise by a rotating blade at audio frequencies. Thus we called this method as "Semi-pulse method".

This semi-pulse method was adopted for imaging by stepwise scanning of the focused X-ray beam on the sample, at the Beam Line 15 A and 10 C.

EXPERIMENTAL

The experimental set up was the same as that of imaging method²⁾. An circle blade which has two slits ($12^\circ \times 2/360^\circ$) along its periphery was rotated at 9 Hz. The response signal at each point (every each 0.5 mm step) on the way of scanning was averaged by a digital storage oscilloscope.

RESULTS and DISCUSSION

Figure 1 shows the scheme of a model Ni sample half of which is covered with 50 μm thick poly-ethylene terephthalates (PET) film. X-ray was scanned from Ni side to PET covered side. The series of primitive photoacoustic signals are shown in Fig.1(a). In contrast to the sharp rising followed by exponential rise-down in the Ni region which is typical for monolayered region, small and convex signals were observed in PET region. In this PET coated region, the amplitude of rising signal was decreased whose contribution is from surface PET and subsurface Ni.

Primary (surface) component of these signals was extracted as shown in Fig.1(b), according to the signal shapes at separate experiments using Ni and PET only. These signal shapes in Fig.1(b) were subtracted from the primitive signal shapes (in Fig.1(a)) and the difference signals are shown in Fig.1(c). Delayed rise-up of the difference signal shows that the Ni layer is locating under the PET region

at 30-70 μm thick.

This method is quite useful for non-destructive and three dimensional analysis of various layered materials. When the energy of incident X-ray is changed at K-edge region, the atomic species can be discriminated. The study of three dimensional atomic component analysis is under development by improving this method.

REFERENCES

- 1) T.Masujima, E.M.Eyring et al., Photon Factory Activity Report, 6, 195 (1988).
- 2) T.Masujima, H.Shiwaku et al., Rev.Sci. Instrum., 60, 2468 (1989).

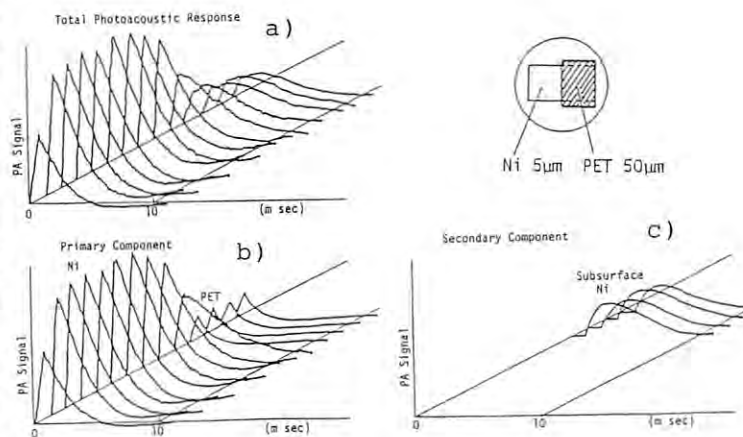


Figure 1. Semi-Pulse X-ray Photoacoustic Imaging

(a): Series of primitive photoacoustic signal responses.

(b): Primary component signals from surface layers.

(c): Subtracted secondary component which comes from subsurface layer.

SUBTRACTION IMAGING BY X-RAY PHOTOACOUSTIC METHOD

Hideaki SHIWAKU¹, Masami ANDO¹, Tsutomu MASUJIMA², Taro TOYODA³, Shin-ichi KAWANO², Kayo IKEDA², Ikue WADA², Katsumi KOBAYASHI¹, Yoshiyuki AMEMIYA¹

1. Photon Factory, National Laboratory for High Energy Physics, Oho, Tsukuba 305 JAPAN

2. Inst. Pharmaceutical Sci., Hiroshima Univ. School of Med., Kasumi, Hiroshima 734 JAPAN

3. Dept. Applied Phys. Chem., Univ. Electro-Communications, Chofugaoka, Chofu 182 JAPAN

INTRODUCTION

It was suggested that the photoacoustic imaging method with scanning the focused X-ray beam enables us to analyze the localization of various components in two-dimension¹⁾. Furthermore, three dimensional analysis with depth profiling should be possible by phase analysis of photoacoustic signals²⁾. In this paper, a subtraction image was obtained from above and below K-edge energy region's images.

EXPERIMENTAL

This study was performed at Beam Line 15A and 10C. In order to improve the resolution, the focused X-ray beam was cut down into 0.5-0.9mm ϕ by lead apertures which were set just in front of the photoacoustic cell. Monochromatic X-ray beam was used at 1.37 \AA (above Cu K-edge energy) and at 1.39 \AA (below Cu K-edge energy) at modulation frequency 9 - 49Hz. The photoacoustic cell was set on the scanning X-Z stage which was settled perpendicular to the surface of an iron-base table with vibration -insulating mounts. The photoacoustic signals were monitored by the two phase lock-in amplifier which gave amplitude images and phase images of photoacoustic signals, simultaneously.

RESULTS AND DISCUSSIONS

Figure 1 shows one of example of this study. This model sample have a copper/zinc/tin foil (phosphor bronze) at right upper quarter, a brass foil at left upper quarter and a copper foil at lower half. Above Cu K-edge energy, any region of various metal foils show higher signal intensity (as shown in figure 1(a)), however, it shows especially the highest signal intensity at copper foil region. The K-edge subtraction image shows signal intensity corresponding to copper contents at each region (as shown in figure 1(b)).

The spatial resolution ($\sim 1\text{mm}$) and the quality of imaging were still poor due to poor S/N ratio, however, these results seem to promise the potentiality of this method for three-dimensional analysis.

References

- 1) T.Masujima et al., Photon Factory Activity Report 5, 347 (1987)
- 2) T.Masujima et al., Rev. Sci. Instrum. 60(7), July 1989

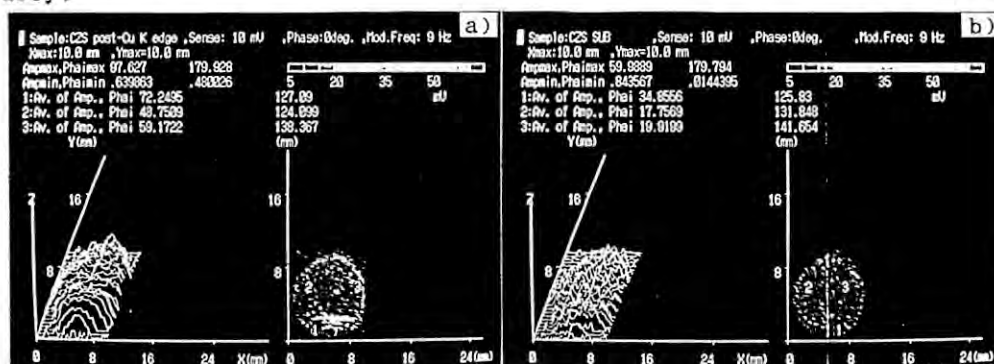


Figure 1. X-ray photoacoustic imaging of the model sample at 9Hz.
a) above Cu K-edge image, b) subtraction image.

Surface Structure Analysis of $\text{Si}(111)\sqrt{3}\times\sqrt{3}\text{-Ag}$
by Transmission X-Ray Diffraction

Toshio TAKAHASHI, Shinichiro NAKATANI, Naoko OKAMOTO,
*Tetsuya ISHIKAWA and *Seishi Kikuta

Institute for Solid State Physics, University of Tokyo,
Roppongi, Minato-ku, Tokyo 106

*Department of Applied Physics, Faculty of engineering,
University of Tokyo, Hongo, Bunkyo-ku, Tokyo 113

The structure of the $\text{Si}(111)\sqrt{3}\times\sqrt{3}\text{-Ag}$ surface is in controversy although extensive studies have been made. Hitherto, two kinds of models have been proposed, that is, a honeycomb model with two Ag atoms in the unit cell and a trimer model with three Ag atoms in the unit cell.

In a previous work¹⁾, the authors have measured the intensity changes along the integral and fractional order rods in a reflection geometry, and determined the arrangement of Ag atoms and the adsorption site with respect to the unreconstructed Si crystal: any honeycomb model with two Ag atoms in the unit cell was rejected and a modified trimer model, HCT (honeycomby chained triangle) model, was proposed although the positions of the reconstructed Si atoms were not fully analyzed. The result is shown in Fig. 1(a) and (b), where the height of the Ag layer from the unreconstructed first layer of Si is about 2.9 Å, and the parameter x/a indicating the size of a trimer is about 0.44. The R-factor was slightly better for the model (a) than for the model (b).

In this work, the diffraction spots were observed for the first time in a transmission geometry as shown in Fig. 2, and the adsorption site with respect to the unreconstructed Si atoms was

uniquely determined.

The experiments were made at BL-10C. The intensity change along the $(0\bar{1})$ rod was measured around the $1\bar{1}1$ Bragg points, as hatched in Fig. 3. The observed intensities (dots in Fig. 4) changed asymmetrically around the $1\bar{1}1$ Bragg point. The lines in Fig. 4(a) and (b) were obtained by calculations according to the models in Fig. 1(a) and (b). The results clearly reject the adsorption site in Fig. 1(b).

Recently a similar atomic arrangement of Ag atoms was obtained by E. Vlieg et al.²⁾ But a different result is obtained as for the adsorption site. The reason will be that they have observed only the fractional order spots.

References

- 1) T. Takahashi et al.: Jpn. J. Appl. Phys. 27 (1988) L753.
- 2) E. Vlieg et al.: Surf. Sci. 209 (1989) 100.

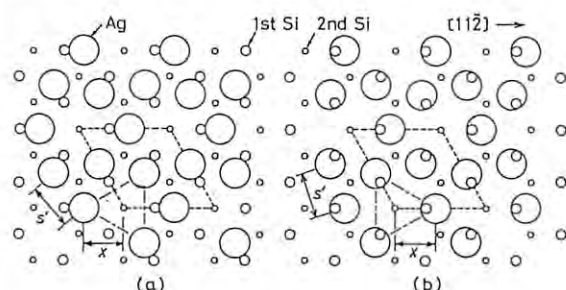


Fig. 1

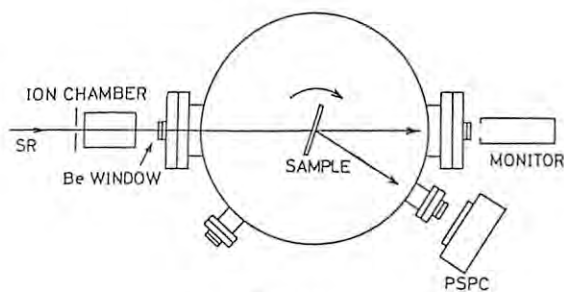


Fig. 2

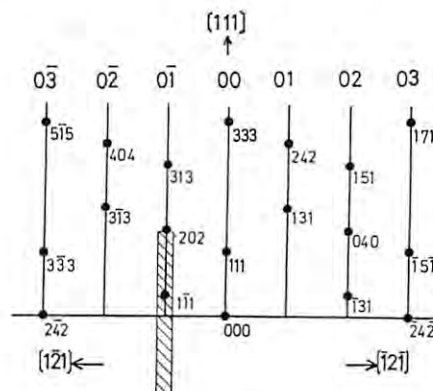


Fig. 3

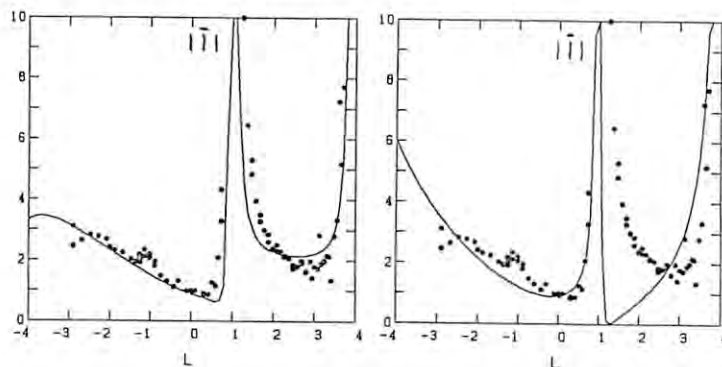


Fig. 4(a)

Fig. 4(b)

ANISOTROPIC EFFECTS IN X-RAY RAMAN SCATTERING

Yasuo UDAGAWA and Kazuyuki TOHJI

Institute for Molecular Science, Okazaki, Aichi 444

Introduction

Very recently we have reported EXAFS-like wiggles in the x-ray Raman spectra of graphite and diamond, and showed that they coincide very well with those observed in soft x-ray absorption¹⁻³; thus it was proved for the first time that x-ray Raman scattering is capable of providing the same information as absorption.

For anisotropic materials additional information can be obtained, since the momentum transfer or scattering vector plays the same role as the polarization vector in the absorption. Scattering may be superior to absorption in revealing anisotropy because of several experimental reasons.

Experimental and Results

The experimental conditions are the same as those described previously¹⁻³, except for BL16, which is a multipole wiggler line, was used as well as BL10C. Measurements at BL 16 reduced the time required to collect photons by more than an order of magnitude. The sample employed is a monochromator graphite from Union Carbide. Scattering was collected at 60° from the sample, which was mounted in such a way that the c-axis of graphite is either parallel or perpendicular to the scattering vector \vec{s} . The c-axis of graphite is perpendicular to the ring plane; in-plane transitions are forbidden for $\vec{s} // \vec{c}$, while those perpendicular to the plane are forbidden for $\vec{s} \perp \vec{c}$.

Figure 1 shows x-ray Raman spectra from graphite with the scattering vector either parallel or perpendicular to the c-axis. The two spectra show remarkable differences in edge energy as well as in extended fine structure. The edge shift of the $\vec{s} // \vec{c}$ spectrum is about 7 eV smaller than that of $\vec{s} \perp \vec{c}$. Nagasawa et al. has also reported a difference of 6 eV in his polarization study on near edge structure⁴. Hence, the transitions to the lowest states are in the ring plane, while transitions perpendicular to the ring plane start at a few eV higher in energy.

In addition, there are prominent differences in the extended fine structure. A complicated structure is observed for $\vec{s} \perp \vec{c}$ while the oscillation for $\vec{s} // \vec{c}$ is simple and has a rather short interval. An oscillation observed in the soft x-ray absorption of graphite

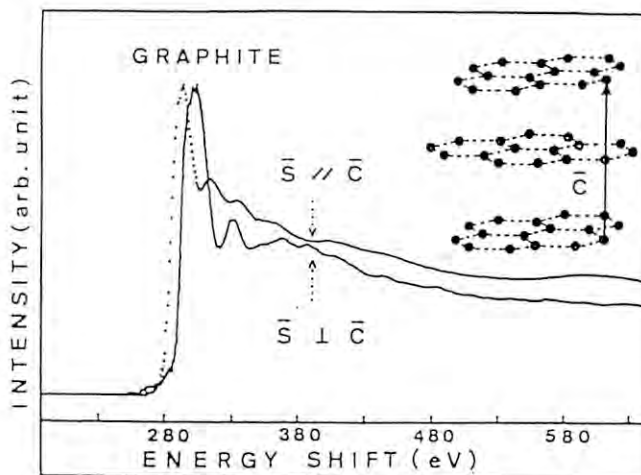


Figure 1. X-ray Raman scattering spectra of graphite with the scattering vector $\vec{s} // \vec{c}$ and $\vec{s} \perp \vec{c}$.

with polarization parallel to the c-axis has already been reported⁵, and a comparison of the two reveals without doubt that they are substantially the same. On the other hand, no polarized absorption study perpendicular to the c-axis is available.

A more detailed analysis⁶ employing standard procedures for EXAFS analysis shows that intra and inter-layer structural information can be separately obtained from the anisotropy in the fine structure reported here.

REFERENCES

1. K. Tohji and Y. Udagawa, Phys. Rev. B36, 9410 (1987).
2. K. Tohji and Y. Udagawa, Phys. Rev. B39, 7590 (1989).
3. Y. Udagawa and K. Tohji, PF Activity Report 6, 177 (1988).
4. H. Nagasawa, S. Mourikis, and W. Schule, J. Phys. Soc. Jpn. 58, 710 (1989).
5. G. Comelli, J. Stohr, W. Jark, and B. B. Pate, Phys. Rev. B37, 4383 (1988).
6. K. Tohji, Y. Udagawa, T. Matsushita, M. Nomura, and T. Ishikawa, submitted to J. Chem. Phys.

SMALL-ANGLE X-RAY SCATTERING STUDY OF RECONSTITUTION PROCESS OF TOBACCO MOSAIC VIRUS PARTICLES

Yoh SANO¹, Hideo INOUE², Yuzuru HIRAGI³, Kanji KAJIWARA⁴ and Hiroshi URAKAWA⁴

1 National Institute of Agrobiological Resources, Tsukuba City, Ibaraki 305

2 Shimadzu Corporation, Kyoto 604

3 Institute for Chemical Research, Kyoto University, Kyoto 611

4 Kyoto Institute of Technology, Kyoto 606

Introduction

Tobacco mosaic virus (TMV) is reconstituted in vitro into an infective virion from its constituents RNA and coat protein (TMVP). The reconstitution of TMV from its constituents occurs in two steps: formation of the initial complex by interaction of the 5'-end of RNA with 20S disk aggregate of TMVP and growth of the helical rod by sequential addition of TMVP. This assembly process has been mainly investigated by electron microscopy and turbidity, and the reaction is thought to complete approximately within 20-40 min under physiological conditions. TMV particles reconstituted were observed in a dried state by the former method, and the latter method gave little information about the size and shape of the particles in solution. A small-angle X-ray scattering (SAXS) method is exceedingly useful for this case. The growth of aggregates of TMVP and RNA to rodlike particle is suspended completely by lowering the solution temperature to about 5°C. We shall be able to determine an aggregation state at each reaction time, if we quench the sample at 5°C after growing the aggregate by keeping the sample at 20°C for each reaction time(min) and carry out the ordinary static SAXS experiments at 5°C.

Experimental

TMV coat protein, prepared from TMV by the usual acetic-acid method, was dialyzed against phosphate buffer (PB) whose concentration was increased stepwisely and final concentration was 100mM at pH 7.2. TMV-RNA was prepared by the extraction method with phenol. All the equipments and buffer solutions were sterilized with autoclave just prior to preparing of sample solutions. We prepared eleven samples varying incubation times at 20°C for SAXS, as shown in Fig.1. The reactions of TMVP and RNA were immediately stopped after a fixed period of incubation by dipping the samples into ice water. The mixing ratio of TMVP to RNA was 20 in 100mM PB at pH 7.2.

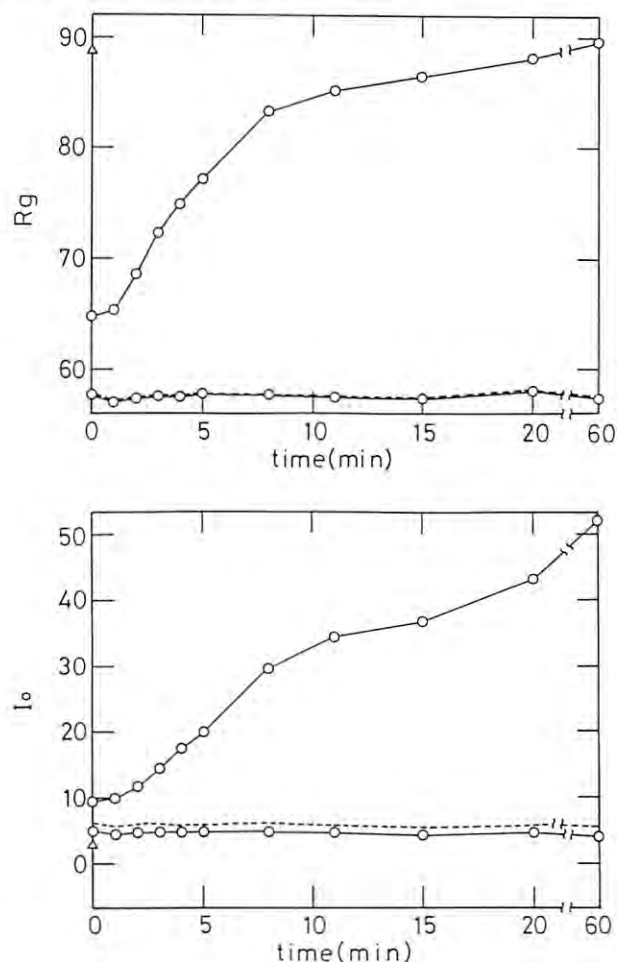
SAXS experiments were performed with the SAXS at station BL-10C at 5°C in order to stop the further growth of the aggregates. The z-average radius of gyration and intensities at zero scattering angle, I_0 , proportional to weight-average molecular weight of the aggre-

gates, were obtained from the initial slope and the intercept of the Guinier plot, respectively

Results and Discussion

The time courses of R_g and I_0 are shown in Fig.1. There is no appreciable change of R_g and I_0 in the case of TMVP only. However, the mixture of TMVP and RNA showed the gradual increase in R_g and I_0 with incubation time, whose values are much larger than those (broken line) calculated by assuming the ideal (no interaction) mixture of each component (shown with lower curves for TMV protein and triangles for RNA in Fig.1). The reaction lag is also observed at the initial reaction time.

The detailed reaction mechanism is now under analysis with the present data.



X-RAY DETECTION CHARACTERISTICS OF MICROCHANNEL PLATES IN THE ENERGY RANGE FROM 0.06 TO 0.6 KEV

Naohiro YAMAGUCHI, Teruji CHO, Mafumi HIRATA, Eiichi TAKAHASHI, Syoichi MIYOSHI,
Takashi KONDOH*, Sadao AOKI**, Hideki MAEZAWA*** and Akira YAGISHITA***

Plasma Research Center, University of Tsukuba, Tsukuba, Ibaraki 305

* Japan Atomic Energy Research Institute, Naka-machi, Naka-gun, Ibaraki 311-02

** Institute of Applied Physics, University of Tsukuba, Tsukuba, Ibaraki 305

***Photon Factory, National Laboratory for High Energy Physics, Tsukuba, Ibaraki 305

Introduction

A microchannel plate (MCP) is one of the useful detectors for x-ray measurements in fusion researches, because of its high gain, fast time response, high degree of immunity to magnetic fields as well as its compactness. MCPs have often been applied to x-ray imaging^{1, 2)} or spectroscopic measurement³⁾. Studies of x-ray detection characteristics of MCPs have been carried out in the 0.6 to 82 keV energy range⁴⁾. We extend the measurement on current response of MCPs in the 0.06 to 0.6 keV energy.

Experimental and Results

The experiment has been carried out by using synchrotron radiation in XUV and soft x-ray region which is supplied at the beamline having a 2-m grasshopper monochromator (BL-11A). In order to suppress stray and higher order radiation, four different thin filters (Cu, Ag, C and Be) have been used. The MCP to be calibrated, Hamamatsu F1943-22MX, has a tandem configuration and is coated with normal electrode materials (Fe and Cr), whose channel diameter is $15\mu\text{m}$, length to diameter ratio 40, and channel bias angle 13° . The MCPs have been operated under the condition of the unsaturated current detection mode. The gold photocathode is mounted in an NBS-type diode with a cylindrical anode. This is utilized for calibration of the incident photon flux.

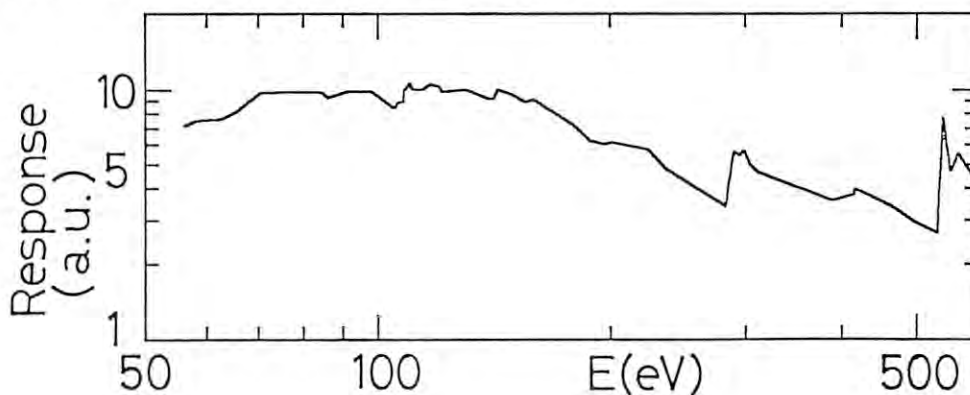
The current response of MCPs has been obtained as shown in Fig.1 for the photon energy from 60 eV to 600 eV. The data have been taken for the case of normal incidence to the MCP surface; therefore, the incident angle of photons to the channel axis is 13° (the bias angle of the MCPs). The general feature of the MCP current response curve is summarized as follows: there is a maximum around 100 eV. The response decreases with increasing the photon energy beyond 150 eV as a whole, except the

structures originated from the absorption edges of constituent elements of MCP glass material. In particular, the O K-edge structure is very clear accompanying with an EXAFS-like oscillatory structure. The penetration length of photons in this energy range is estimated to be on the order of 1000 Å for the MCP glass. Therefore, the surface composition of the MCP glass throughout a channel wall would strongly affect the MCP response. It is considered that the surface of channel wall consists of a SiO_2 layer of 100 Å thick, whose bulk side composition is lead glass⁵⁾. The measured MCP response might be explained qualitatively from the surface composition of a channel wall, that is, there are a small jump above Si L II, III -edge (100.6 eV), a clear jump near the O K-edge energy (531.7 eV) and a hump around 400 eV which is considered to correspond to the Pb N-edge (413 eV). Finally it should be mentioned about a jump near C K-edge energy because carbon is not the explicit ingredient of MCP glass. A possible origin of carbon is a rare impurity included in anode material or some contamination on the MCP channel wall. Providing that the surface of channel which is consisted of a SiO_2 layer of 100 Å thick is covered with a thin carbon layer, a 30 Å thick carbon layer can explain the jump ratio of 1.6 at the edge from the absorption characteristics below and just above C K-edge.

References

- 1) N. Yamaguchi et al., Jpn. J. Appl. Phys. **24**, 1065 (1985).
- 2) T. Kondoh et al., J. Appl. Phys. (1990) to be published.
- 3) J. L. Schwob et al., Rev. Sci. Instrum. **58**, 1601 (1987).
- 4) N. Yamaguchi et al., Rev. Sci. Instrum. **60**, 2307 (1989).
- 5) G. W. Fraser, Nucl. Instrum. Methods **195**, 523 (1982).

Fig.1
Current response
of the MCPs as a
function of the
incident photon
energy from 60 eV
to 600 eV.



THE ENERGY RESPONSE OF A SILICON SURFACE BARRIER DETECTOR (0.06-0.9 KEV)

T. Cho, N. Yamaguchi, M. Hirata, E. Takahashi, T. Kondoh, S. Miyoshi,
S. Aoki¹, H. Maezawa², and A. Yagishita²

Plasma Research Centre, University of Tsukuba, Ibaraki 305

¹Institute of Applied Physics, University of Tsukuba, Ibaraki 305

²National Laboratory for High Energy Physics, Tsukuba, Ibaraki 305

ABSTRACT

The detection efficiency of a silicon surface barrier (SSB) detector, η_{SSB} , has been investigated in the 0.056-0.900 keV energy region. The experimental data are compared with the theoretically calculated results using the SSB-detector parameters. As a whole, the data points agree well with the theoretical results except an oscillatory structure for the 0.07-0.17 keV region. In this energy region, sharp edge structures in η_{SSB} are observed near the Al L_{II} and L_{III} absorption edges as well as the Al L_I edge. In particular, XANES is observed near the Al L_I edge.

DETECTION EFFICIENCY OF THE SSB DETECTOR

The detection efficiency data of the SSB detector for a unit incident photon flux, η_{SSB} , are plotted by the dots in fig. 1. Also, the result from theoretical calculations is depicted by a dashed curve. These experimental data are obtained from the following process: The experimental results of the normalized detection currents of I_{SSB}/I_0 and I_{Au}/I_0 give the energy response of I_{SSB}/I_{Au} for the normalized incident photon flux. Here, I_{SSB} denotes the detection current of the SSB detector. The quantum efficiency of gold, $QE(E)$, is proportional to the normalized energy response of I_{Au} to the incident photon flux; therefore, the relative value of η_{SSB} is calculated from I_{SSB}/I_{Au} multiplied by $QE(E)$. (Here, in our paper, the $QE(E)$ values of gold are based on the Day et al. data from 0.05 keV to 0.9 keV; also, the $QE(E)$ data from Henke et al. are

utilized for the 0.20-0.28 keV region as well.)

The theoretical values of η_{SSB} are written as:

$$\eta_{SSB} = \exp(\mu_e \cdot \rho_e \cdot x_e) \times \exp(\mu_d \cdot \rho_d \cdot x_d) \times [1 - \exp(\mu_{dep} \cdot \rho_{dep} \cdot x_{dep})] \times E, \quad (1)$$

where μ , ρ , and x denote the mass absorption coefficients, mass densities and thicknesses of the following layers. The subscripts of e , d , and dep indicate the electrode, the dead layer, and the depletion layer, respectively.

Now, we compare the experimental results and the theoretical calculations. As a whole, the experimental data points agree well with the theoretical curve except a detailed structure near the Al absorption edges. Near the Al L_{II} (73 eV) and L_{III} (72 eV) absorption edges, a sharp edge structure of η_{SSB} is seen, and the height of the jump in η_{SSB} agrees quite well with the theoretical estimation. The next sharp jump near the Al L_I absorption edge (87 eV), however, is not expected by the calculations. Also, it is noted that this sharp edge is accompanied by an oscillatory structure (XANES).

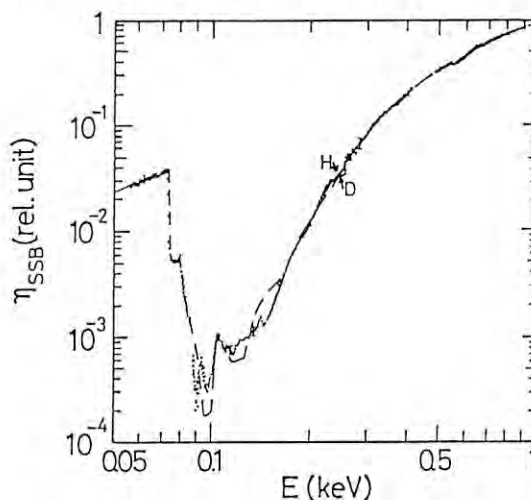


fig. 1

TIME-RESOLVED TWO-DIMENSIONAL OBSERVATION OF THE CHANGE IN X-RAY DIFFUSE SCATTERING
USING AN IMAGING PLATE ON SYNCHROTRON RADIATION SOURCE

H. IWASAKI, Y. MATSUO*, K. OHSHIMA** and S. HASHIMOTO***

Photon Factory, National Laboratory for High Energy Physics, Tsukuba 305

* Faculty of Science, Nara Women's University, Nara 630

** Institute of Applied Physics, University of Tsukuba, Tsukuba 305

*** Institute for Materials Research, Tohoku University, Sendai 980

Introduction of Imaging Plate, a highly sensitive area detector recently developed, into X-ray diffraction experiments has opened various new fields of structural study. When combined with synchrotron radiation, it has enabled us to take two-dimensional diffraction pattern within a short period of time and thus to do time-resolved measurement of structure change in materials. The measurement was hitherto concerned with Bragg reflections having relatively strong intensity. In the present study we made an attempt to observe a change in the intensity distribution of weak diffuse scattering from an alloy single crystal and succeeded in following the time evolution of whole process of phase transition.

The diffraction geometry adopted is as follows: an AgZn single crystal having the B2-type structure is mounted on the ϕ -table of the four-circle diffractometer at the BL-14A and monochromatized synchrotron radiation beam, 0.3 nm in wavelength, is incident to the crystal at such an angle that the Ewald sphere is nearly tangent to the (111) relplane. Radiation scattered from the crystal is captured by Imaging Plate, 250 mm \times 200 mm in size, placed on the 2 θ -arm set at an angle of 80 deg so that the plate is nearly parallel to the (111) relplane to be explored. The sample crystal is rotated by an angle of ± 5 deg by changing ω -angle of the diffractometer during exposure. This movement makes the Ewald sphere intersect the (111) relplane and the intensity distribution on the plane is mapped and projected onto the plate.

The diffuse scattering was so weak that it took longer than 500 sec to get its readable image. The alloy crystal was kept at a temperature of first 330 K and then 353 and 373 K using a small heater attached to the goniometer head to induce the transition from the β' phase into the ζ phase. Change in the intensity distribution on the (111) relplane was observed by making successive exposures.

Figure 1 shows the patterns selected from a series of two-dimensional patterns thus obtained. At the beginning of the transition there are only three strong Bragg reflections with diffuse streaks emanating from each of them in the pattern. There is also a weak diffuse intensity sheet of a triangular shape with the corners at the three Bragg reflection peak positions. The diffuse scattering arises from thermal vibration of atoms. As the transition proceeds, weak but relatively sharp spots appear superimposed on the diffuse intensity sheet without any modulation in the intensity distribution, as seen in the middle of the pattern. The spots grow in their intensity with many additional spots and the diffuse scattering gradually loses its intensity. The observation shows that the transition is of a nucleation and growth type and the new phase has a definite orientation relationship to the parent phase.

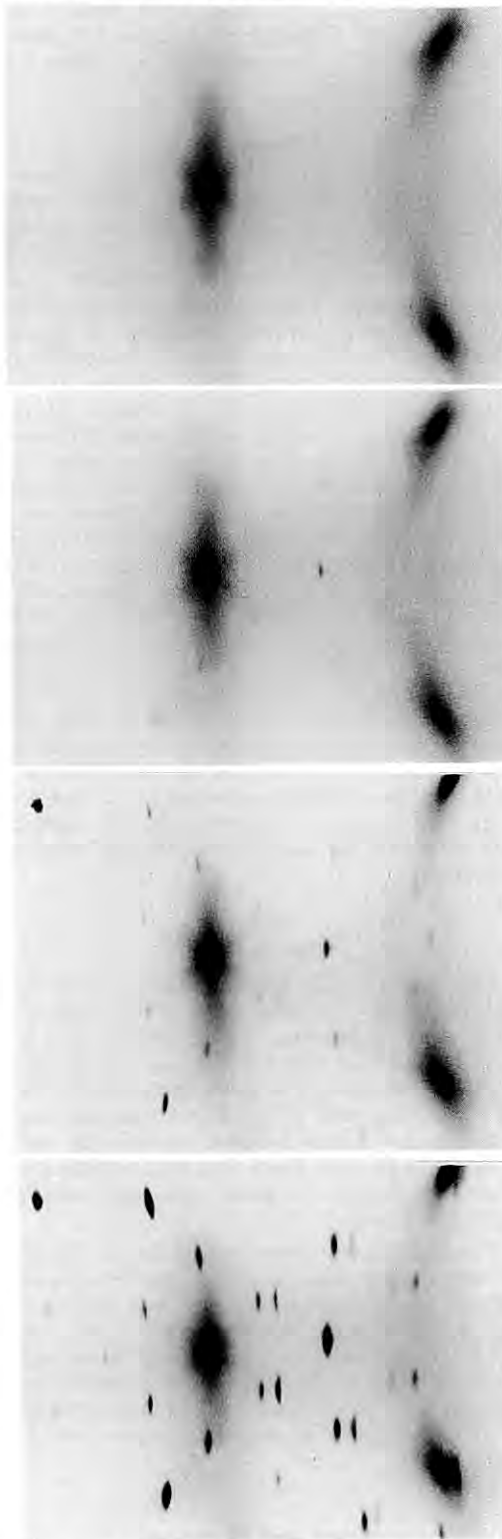


Fig. 1 A series of time-resolved two-dimensional patterns taken with Imaging Plate showing the time evolution of the scattering intensity distribution on the phase transition in AgZn.

X-RAY STANDING WAVE ANALYSIS OF GaAs/Si(111) INTERFACE

Tomoaki KAWAMURA, Masaharu OSHIMA, Yukio FUKUDA, Yoshiro OHMACHI,
Keiichi HIRANO*, Koichi IZUMI*, Tetsuya ISHIKAWA* and Seishi KIKUTA*

NTT Applied Electronics Laboratories,
Midori-cho, Musashino-shi, Tokyo 180

* Department of Applied Physics, Faculty of Engineering,
University of Tokyo, Hongo, Bunkyo-ku, Tokyo 113

Introduction

The X-ray standing wave method was known as the powerful tool for structure analysis of surface and interface^{1,2}. However, There are some limitation in interface analysis with using X-ray standing wave; (1) high quality substrate crystals are necessary, (2) small lattice mismatch is necessary between substrate and epitaxial layer, (3) interface structure is abruptly changed. In the case of GaAs and Si, (1) and (3) were usually gratified but (2) was not satisfied enough because of the different lattice constant of 4% between GaAs and Si crystals. In previous report, the interface structure of GaAs/Si(100) was investigated and Ga and As K α signals were same as Bragg reflection in the case of 50 Å thickness GaAs/Si(100) samples.³ This is due to the averaging of fluorescence signals from X-ray standing wave through epitaxial layer and no information gives about epitaxial film and interface structure. To avoid averaging fluorescence signals, ultra thin film sample should be used for X-ray standing wave. The limitation thickness was about 20 Å in Si and GaAs combination. Furthermore, it is difficult to get precise information of Ga and As position in interface because of the equivalent position of Ga and As atoms in (400) reflection. On the other hand, Ga and As fluorescence profile are supposed to be distinguishably different for GaAs film on Si(111) substrate because of different position of Ga and As about 25%. In this report, the investigation of GaAs/Si(111) interface structure by using X-ray standing wave method was described.

Experimental

The GaAs/Si(111) sample was prepared by MBE method. To clarify the initial surface structure of Si substrate, As was evaporated at first after substrate was cleaning. This surface which was known as As passivated surface, is stable though in the atmosphere⁴. The thickness of GaAs film was set to about 4 atomic layers to avoid the effect of lattice mismatch between Si and GaAs. From the TEM images, GaAs film had grown continuously from Si substrate in atomic order and interface may be abruptly changed.

The experiments were carried out at BL-14B. The optical system were almost same as previous experiments³ but all Si(111) reflection geometry was selected in this experiments. The asymmetry factor b was set at about 30 with 7.345° Bragg angle. The wavelength was set 0.800 Å to avoid the effect of the Compton and elastic scattering into Ga and As fluorescence. The Ga and As fluorescence yield was measured with rotating samples during Bragg reflection region.

Result and Discussion

Figure 1 shows the normalized fluorescence yield of Ga and As K. The intensity of Ga K α was 0.5 to As. This may be caused from the absorption coefficient of Ga and

As. Obviously, the different profile of Ga and As K α fluorescence was due to the dissimilar position of Ga and As atoms in the unit cell of zinc blend structure.

The least square analysis was performed to decide Ga and As atomic position. The parameters used in this analysis were coherent parameter, position of marked atom and background. From the least squares of Ga and As position, the displacement of Ga and As atoms to Si (111) net plane are 3.14 Å and 1.05 Å, respectively.

Figure 2 shows the interface model of GaAs/Si(111). The distance of Ga is nearly equal to lattice constant of Si(111) net plane, but the distance of As is 25% large than the Si(111) lattice distance. This may be due to the surface relaxation of silicon. Because of lattice mismatch of Si and GaAs, the distance of top Si atoms and second Si atoms are expanded and the distance of first and second Si atoms are larger than bulk Si atoms. In this case, the distance of top Si atoms and first As atoms are small than which was decided by least square.

References

1. B. W. Batterman, Phys. Rev., **133**(1964) A759.
2. K. Akimoto, T. Ishikawa, T. Takahashi, and S. Kikuta, Nucl. Inst. Meth., **A246**(1986) 755.
3. T. Kawamura, M. Oshima, Y. Ohmachi, K. Izumi, S. Kikuta, and T. Ishikawa, Photon Factory Activity Report, **6**(1988) 188.
4. R. I. G. Uhrberg, R. D. Bringans, M. A. Olmstead, and R. Z. Bachrach, Phys. Rev. B, **35**(1987) 3945.

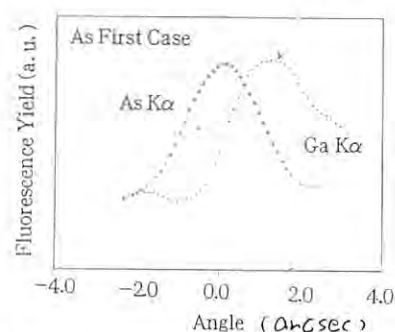


Fig.1 Normalized fluorescence yield of Ga and As K α .

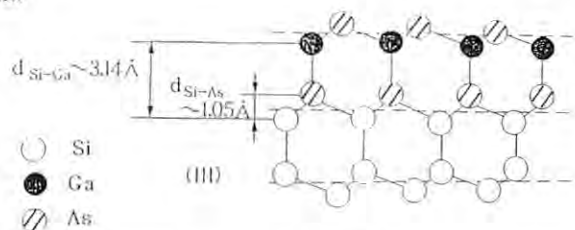


Fig.2 Structure model for the GaAs/Si(111) interface.

X-RAY REFLECTIVITY AND FLUORESCENCE YIELD FROM A PERFECT GERMANIUM CRYSTAL AT GRAZING-INCIDENCE BRAGG CONDITION

H. Hashizume, O. Sakata, H. Sakuma, I. Kawamoto and M. Sugiyama

Research Laboratory of Engineering Materials, Tokyo Institute of Technology, Yokohama 227

X-ray standing waves produced from a nearly perfect crystal at grazing-incidence Bragg conditions provide a means to accurately determine the in-plane positions of surface atoms. To investigate the feasibility of such an experiment, we have measured Ge K fluorescence yields from a bulk germanium crystal with a mechano-chemically polished (111) surface. Prior to the measurement, the surface was etched in HF solution to remove oxide layers and passivated by bromine. Bragg reflection for the (220) plane, nearly perpendicular to the surface, was excited by 17 keV photons, which had angular divergences of 5 μ rad and 70 μ rad in the $\Delta\theta$ and ϕ_0 directions, respectively. Here $\Delta\theta$ and ϕ_0 denote the deviation angle from exact Bragg incidence and the glancing angle against the crystal surface, respectively. The experimental arrangement and procedures have been detailed elsewhere [1].

Figure 1 plots observed reflectivities for the specular and diffracted beams, R_s and R_h , together with simultaneously measured fluorescence yields by rocking the sample through the Bragg position at three different values of ϕ_0 close to the off-Bragg critical angle ϕ_c , which is equal to 2.5 mrad. Solid lines show theoretical profiles calculated using the dynamical diffraction theory for a perfect crystal, where the incident-beam profile and the macroscopic curvature of the sample surface are taken into account. The observed reflectivity and fluorescence data show general behaviors predicted by the theory, but there are obvious discrepancies. In

particular, no dip exists in the Ge K α data for the lowest ϕ_0 angle examined. To examine the effect of near-surface strain, we repeated the measurements after chemically etching the sample to remove a layer of 2000 Å. However, no noticeable change occurred in the observed reflectivity profiles and the fluorescence curves. The observed specular reflectivities could be accounted for by including microscopic surface roughness in the existing dynamical theory. It seems difficult, however, to explain the discrepant fluorescence yields in terms of surface roughness.

Calculations indicate that fluorescence yields are determined by the standing-wave field intensities in a shallow penetration depth of several tens Angstroms close to the surface. Unlike in the conventional Bragg-case diffraction, we have here two separate wave fields, one with the standing-wave antinodes at the atomic planes and the other with the nodes at the atomic planes. At $\Delta\theta \simeq 0$ and $\phi_0 \lesssim \phi_c$ crystal waves have complex amplitudes because of total external reflection, which lead to a shift of the standing-wave position. It can be shown that the shifts are in the opposite directions for the two wave fields at $\Delta\theta > 0$, while at $\Delta\theta < 0$ they are in the same direction parallel to the diffracting vector. The shifts amount to 10% of the Bragg-plane spacing.

Reference

- [1] H. Hashizume and O. Sakata : Rev. Sci. Instrum. 60, 2373 (1989).

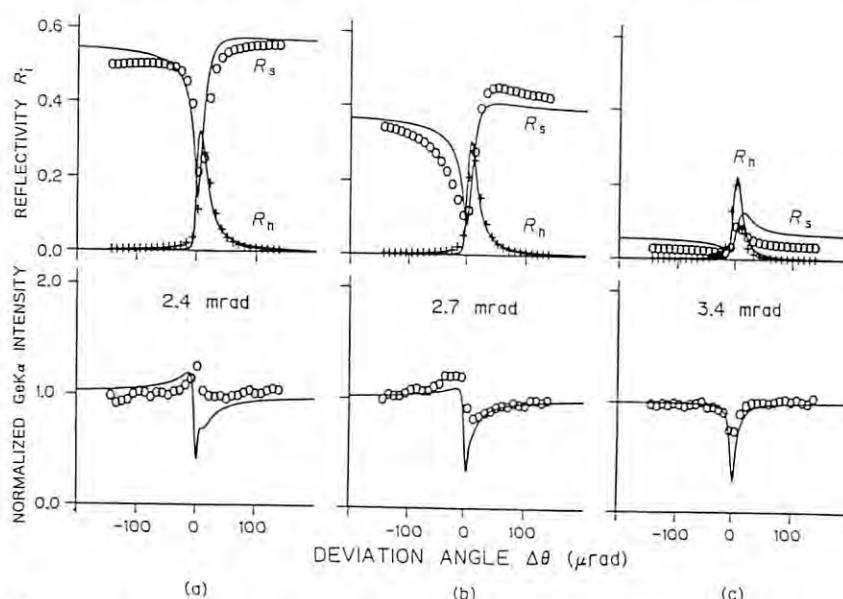


Fig. 1. Observed (open circles and plus signs) and calculated (solid line) reflectivities curves and fluorescence yields for $\phi_0 = 2.4, 2.7$ and 3.4 mrad. R_s : specular beam, R_h : diffracted beam.

STUDY OF LATTICE DISTORTION OF POROUS SILICON LAYERS BY MEANS OF X-RAY DIFFRACTOMETRY

Osamu NITTONO, Hiroshi SUGIYAMA and Tetsuya FUSHIMI
Department of Metallurgy, Tokyo Institute of Technology,
Oh-okayama, Meguro-ku, Tokyo 152

Introduction

Porous silicon layer (PSL) is known to be effectively used for the full dielectric isolation of electronic devices because of its being easily oxidized. Therefore, formation conditions and relevant physical properties of oxidized PSL have been also investigated. Previous studies showed that the crystalline quality of PSL formed on the (001) wafer of resistivity as low as $0.01\Omega\text{cm}$ was superior to that on the wafer of resistivity more than $0.1\Omega\text{cm}$. X-ray diffraction studies of PSL showed that the lattice spacing of PSL was about ten times smaller on the wafers with lower resistivities than on the wafers with higher resistivities. Recently, the authors¹⁾ have investigated crystalline property of PSL formed on (111) and (001) wafers with various resistivities more than $0.5\Omega\text{cm}$ by means of well-defined X-ray goniometry, and demonstrated that the crystalline quality of PSL formed on the (111) wafers was superior to that of the (001) wafer irrespective of wafer resistivity, and also that the crystalline quality of PSL was inferior to that of the silicon substrate but was not so heavily degraded. These results, together with the previous results, suggest that the crystalline property of PSL is related to wafer orientation and wafer resistivity. In this study, therefore, in order to confirm this more clearly, we examined the crystalline property of PSL's on (111) and (001) wafers of 0.01 to $33\Omega\text{cm}$, together with annealing effect on the crystalline property of PSL's by means of X-ray diffraction technique.

Experimental

In order to have a porosity of about 50% for each PSL, p-Si wafers of $0.01\Omega\text{cm}$ were anodized in a 25%HF with $30\text{mA}/\text{cm}^2$ and wafers of more than $0.1\Omega\text{cm}$ were anodized in a 50%HF with $100\text{mA}/\text{cm}^2$. Anodized wafers with $15\mu\text{m}$ thick PSL were studied by X-ray multiple-crystal diffractometry. Rocking curves were measured mainly with the reflection planes parallel to the wafer surfaces: 111 and 333 reflections for (111) wafers and 004 reflections for (001) wafers.

Experimental Results and Discussion

Diffraction rocking curves are found to be composed of two peaks: one at a lower angle side is for the PSL, and the other at a higher angle for Si substrate. This indicates that the PSL is a monolithic single crystal and has a slightly larger lattice spacing than the substrate, being under compressive stress. The PSL showed a comparatively narrow FWHM, indicating that the crystalline quality is not so heavily degraded. On the contrast, the change in lattice spacing of PSL's formed on wafers of more than $0.1\Omega\text{cm}$ was $\Delta d/d=10^{-3}$. From these results, we can conclude that the crystalline property of PSL is not due to preparation conditions including HF concentration and current density, but is affected by the wafer resistivity. It was also found that the PSL was easily affected by spontaneous oxidation of inner pore surfaces in PSL's formed on the wafers with various resistivities.

Figure 1(a) shows 004 rocking curves from an anodized (001) wafer of $0.01\Omega\text{cm}$. The features of rocking curves are almost the same: angular separation appears larger, but this separation corresponds to the same change in lattice spacing as that of PSL formed on the (111) wafers. PSL is found to be under compression, resulting in an elastic bending shown in the inset. Figure 1(b) reproduces rocking curves from the same wafer after annealing at 400°C for 10 min. The lattice spacing of PSL is found to be greatly affected by successive annealing in a vacuum. It has been reported that a lot of hydrogen-silicon bonds such as SiH , SiH_2 and SiH_3 are produced in PSL during anodization and the dissociation of Si-H bonds takes place at elevated temperatures higher than about 250°C . Our preliminary results concerning the size distribution of pores in PSL measured by a gas adsorption technique showed that no remarkable change in size distribution was detected before and after annealing.

Detailed studies of relations between hydrogen concentration and lattice spacing of PSL, and also of crystallographic features of lattice distortion around pores in PSL's are now in process by using SR X-ray diffraction technique.

Reference

- 1) H. Sugiyama & O. Nittono, ISIJ International, 29(1989) 223-228.

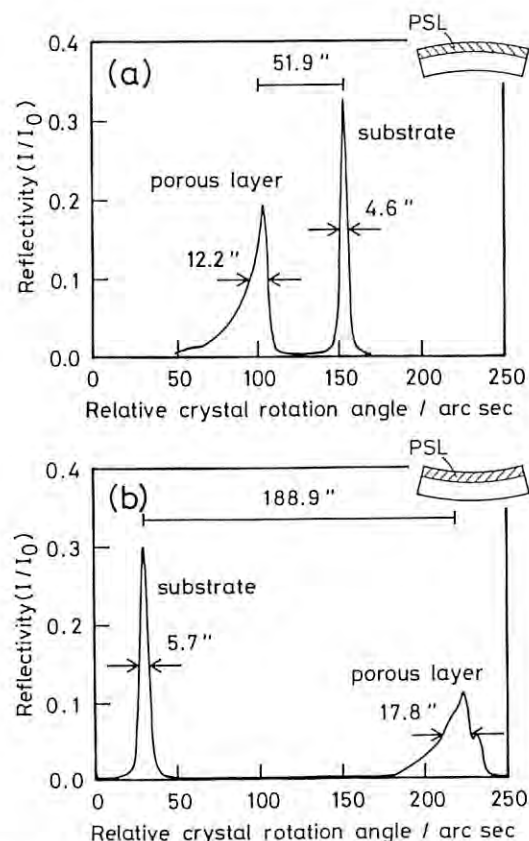


Fig. 1 Rocking curves from PSL and Si substrate.

STRUCTURE OF LIQUID SELENIUM UNDER PRESSURE

Kazuhiko TSUJI, Kenichi YAOITA, Motoharu IMAI, Osamu SHIMOMURA*,
Kozaburo TAMURA** and Hirohisa ENDO***

Department of Physics, Faculty of Science and Technology, Keio University, Yokohama 223

* National Institute for Research in Inorganic Materials, Tsukuba 305

** Faculty of Integrated Arts and Sciences, Hiroshima University, Hiroshima 730

***Department of Physics, Faculty of Science, Kyoto University, Kyoto 606

Introduction

The pressure dependence of the melting temperature of selenium shows a maximum point. This phenomenon (melting-curve maximum) is interpreted in terms of a two-species model^{1,2)} which assumes the liquid as a mixture of high- and low-pressure solid phases. The aim of this work is to measure diffraction for liquid Se under high pressure to test the propriety of this model for selenium.

At atmospheric pressure and room temperature, selenium has a crystal structure consisting of spiral chains. Each chain consists of tightly bonded two-fold Se atoms, and is bonded to adjacent chains with weak *van der Waals* force. This crystal shows a pressure-induced semiconductor-to-metal transition. Though a diffraction measurement was made for the high-pressure phase³⁾, the structure was not determined. It can be thought, however, on the analogy of tellurium that an atom in high-pressure Se is bonded to interchain neighbors as well as to the intrachain neighbors so that the coordination number is larger than that of the low-pressure phase. It is at least natural to think that a dense high-pressure phase has a larger coordination number than a sparse phase. Therefore, it is expected from the two-species model that the coordination number of liquid Se increases with raising pressure.

In previous reports, we obtained the structure factor $S(Q)$ of liquid selenium under various pressures^{4,5)}. We report here some newly investigated results derived by further data analysis.

Experimental

MAX80, a cubic-type high-pressure apparatus was used. Used light sources are a vertical wiggler on PF and a bending magnet on AR. Details of experiment and data analysis are described elsewhere⁶⁾.

Results and Discussion

Structure factor $S(Q)$ for liquid Se at various pressures have been obtained^{4,5,7,8)}. Fig. 1 shows pair distribution function $g(r)$ derived from Fourier transformation of $S(Q)$. A high first peak and a succeeding sharp dip of $g(r)$ appeared at 0 GPa became less prominent with increasing pressure. The coordination number N_1 and the position r_1 of the first neighbors obtained from Fig. 1 are plotted as Fig. 2. The increase in N_1 can be explained by the expected formation of interchain bonds. It seems unnatural that r_1 increases with pressure. However, this may be explained by an overlap of the peaks of inter- and intrachain distances: a peak position can seem to shift when another peak approaches. These results imply that liquid Se under high pressure consists of two species; i.e., the two-fold low-pressure phase and the high-pressure phase of higher coordination.

References

- 1) E. Rapoport, J. Chem. Phys., **46**, 2891 (1967).
- 2) E. Rapoport, J. Chem. Phys., **48**, 1433 (1968).
- 3) G. Parthasarathy and W. B. Holtzapfel, Phys. Rev., **B38**, 10105 (1988).
- 4) K. Tsuji, O. Shimomura, K. Tamura, N. Nakamura, T. Ishihara, H. Endo and S. Akimoto, PF Activity Rep., **3**, 114 (1985).
- 5) K. Tsuji, O. Shimomura, K. Tamura, H. Endo, M. Imai, O. Endo, S. Hosokawa, M. Inui, Y. Katayama and S. Akimoto, PF Activity Rep., **4**, 285 (1986).
- 6) K. Tsuji, K. Yaoita, M. Imai, O. Shimomura and T. Kikegawa, Rev. Sci. Instrum., **60**, 2425 (1989).
- 7) K. Tsuji, O. Shimomura, K. Tamura and H. Endo, Z. Phys. Chem. Neue Folge, **156**, 495 (1988).
- 8) K. Tsuji, J. Non-Crys. Sol., (to be published).

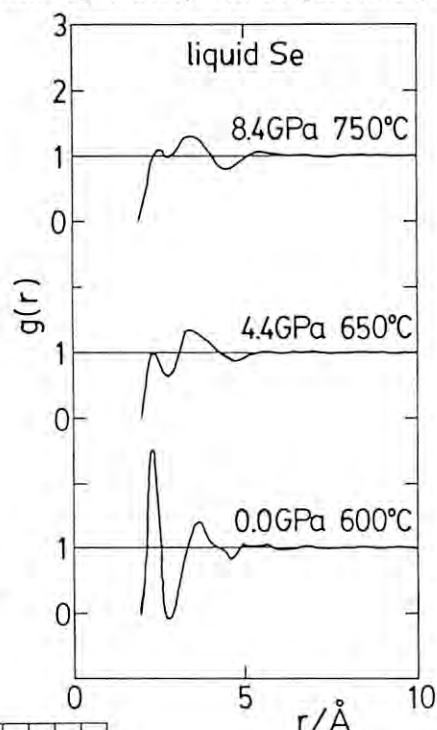


Fig. 1.

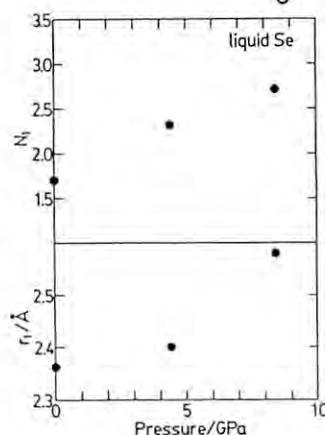


Fig. 2.

SECTION TOPOGRAPHY USING A HIGH-ORDER REFLECTION AND ITS APPLICATION

Yoshimitsu SUGITA, Satoshi IIDA, Nobuo KASAGI, Kazuhiro UEDA, Kouhei OKITSU,
Gu CHANGJIANG, and Hiroshi KAWATA*

Department of Physics, Toyama University, 3190 Gofuku, Toyama 930

*Photon Factory, National Laboratory for High Energy Physics, Tsukuba, Ibaraki 305

Introduction

We have measured the static Debye-Waller factor (SDWF) of dislocation-free silicon crystals by analyzing the Pendellosung fringes in the section topography.¹⁾²⁾ In this investigation various FZ- and CZ-silicon crystals having micro defects and growth striations were examined by the section topography with an extremely large scattering vector, such as 18 18 0 or 24 0 0, using synchrotron radiation from a vertical wiggler.

Experimental

Experiments were carried out using 0.4 Å x-ray beam monochromated with a triangle-shaped silicon bent monochromator in the asymmetric 111 reflection. Section topographs were taken in the 440 to 18 18 0 and 800 to 24 0 0 reflections and recorded on nuclear plate or imaging plate. Various silicon crystals were examined; as-grown FZ crystals having D-defects, which have been speculated to be vacancy agglomerates, and growth striations; heat treated FZ crystals with D-defects; CZ crystals containing clusters of point defects formed by rapidly quenching the ingot during crystal growth.

Results and Discussion

Figure 1 shows a series of the section topographs of the as-grown FZ-crystal having D-defects and growth striations. From the difference in the period of the Pendellosung fringes between the V-region containing D-defects and the I-region, the SDWF was determined to be 0.014 for the 14 14 0 reflection. The nature of D-defects was inferred from the model calculation of the SDWF made on the basis of two models of vacancy clusters, spherical cluster and dislocation

loop. These results were given in Fig. 2 and Table 1. As shown in Fig. 1, growth striations were observed in the I- and S-regions. These growth striations were analyzed using computer simulation technique based on the Takagi-Taupin equation and with the assumption that the growth striation is represented as sinusoidally varying function of strain. The results indicated that the growth striations could be simulated with the amplitude of strain, 8×10^{-8} , though the origin of the growth striations is uncertain. We tried the quenched CZ-crystals but satisfactory results have not yet been obtained.

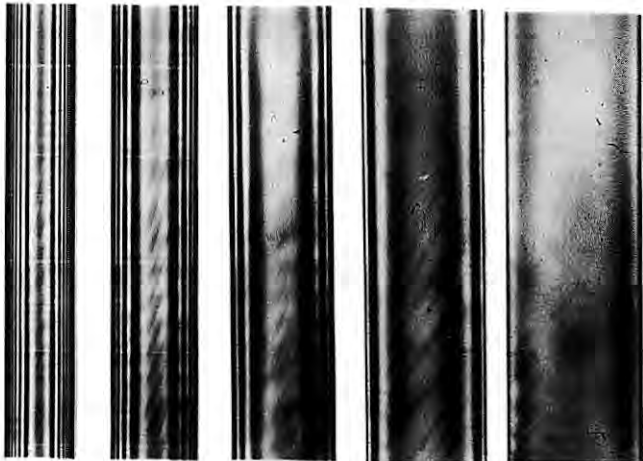
References

- 1) Y.Sugita et al.:Jpn.J.Appl.Phys.26(1987)1903.
- 2) S.Iida et al.:Jpn.J.Appl.Phys.27(1988)1081.

Table 1

Estimation of the average size of vacancy type dislocation loops from the experimental results. The average radius, R, and the concentration of vacancy necessary for the creation of the dislocation loops, C_v , are given as a function of the concentration of the dislocation loops, N.

$N(\text{cm}^{-3})$	10^{13}	10^{14}	10^{15}	10^{16}
$R(\text{\AA})$	69.5	32.3	14.9	6.8
$C_v(\text{cm}^{-3})$	8.7×10^{15}	1.9×10^{16}	4.0×10^{16}	8.4×10^{16}



880 10 10 0 12 12 0 14 14 0 16 16 0

Figure 1

A series of section topographs of an as-grown FZ-wafer.

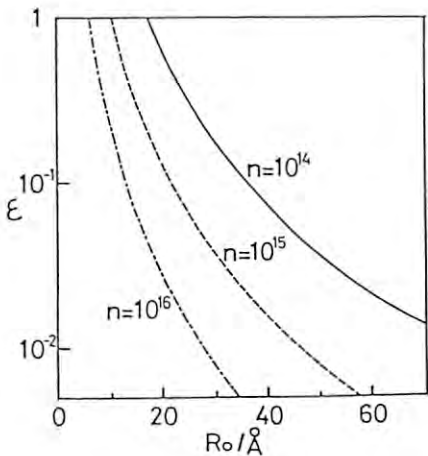


Figure 2

Estimation of the average radius of spherical vacancy clusters, R_0 ; n is the concentration of the clusters and ϵ is the mismatch parameter.

HIGH RESOLUTION PAIR DISTRIBUTION FUNCTION OF $\text{Al}_{68}\text{Mn}_{20}\text{Ru}_8\text{Si}_4$ ICOSAHDRAL PHASE

Yoshiharu SAKURAI, Yoshikazu TANAKA, Yasuhiro WATANABE, Osamu TSUDA,
Chan Wuk KIM, Hiroshi NOMATA, Susumu NANAŌ, Hiroshi KAWATA* and Masami ANDO*

* Inst. of Industrial Science, University of Tokyo, Minato, Tokyo 106, Japan
Photon Factory, National Laboratory for High Energy Physics, Tsukuba,
Ibaragi 305, Japan

1. Introduction

In order to improve the atomic structure model for an icosahedral phase, it is necessary to obtain a high resolution pair distribution function experimentally. The high resolution pair distribution function can be provided by the achievement of X-ray diffraction measurements from $q=0$ to more than 20 \AA^{-1} with appropriate angle resolution. We report here an attempt to measure an X-ray diffraction profile from $q=0$ to 40 \AA^{-1} with the resolution of 0.01 \AA^{-1} at 3 \AA^{-1} , at BL-14C.

2. Experimental

Figure 1 shows a schematic setup for the X-ray diffraction measurement. A monochromated X-ray of 43.57 keV is used for an incident X-ray beam. The horizontal slit S1 is fixed at 0.4 mm and S2, S3 is varied from 0.05 mm to 0.2 mm in such a way to keep an appropriate angle resolution. SSD1 detects the intensity of Compton scattered X-rays from the Kapton film to monitor the intensity of the incident X-ray beam. X-ray diffraction profile was measured for a powdered samples of $\text{Al}_{68}\text{Mn}_{20}\text{Ru}_8\text{Si}_4$ icosahedral phase.

3. Results

After corrections for air scattering, Compton and multiple scattering, the X-ray structure factors were obtained. The structure factor of $\text{Al}_{68}\text{Mn}_{20}\text{Ru}_8\text{Si}_4$ icosahedral alloy is shown in figure 2. The scattering peak width of (211111) and (221001) are 0.030 and 0.042 \AA^{-1} in FWHM, respectively. The pair distribution function of this alloy is shown in figure 3.

Improvement of atomic structure model for $\text{Al}_{68}\text{Mn}_{20}\text{Ru}_8\text{Si}_4$ icosahedral alloys is now in progress.

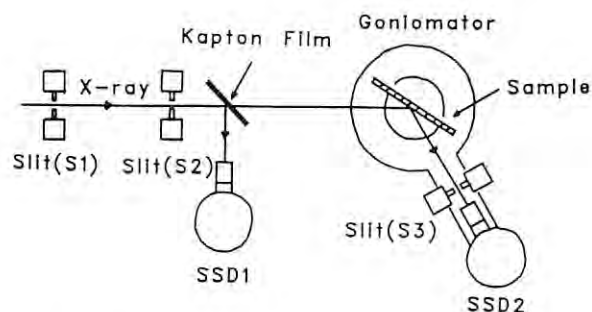


Fig. 1

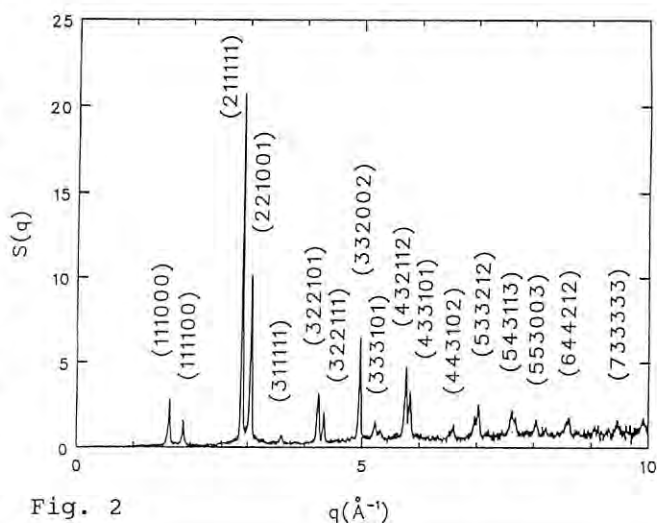


Fig. 2

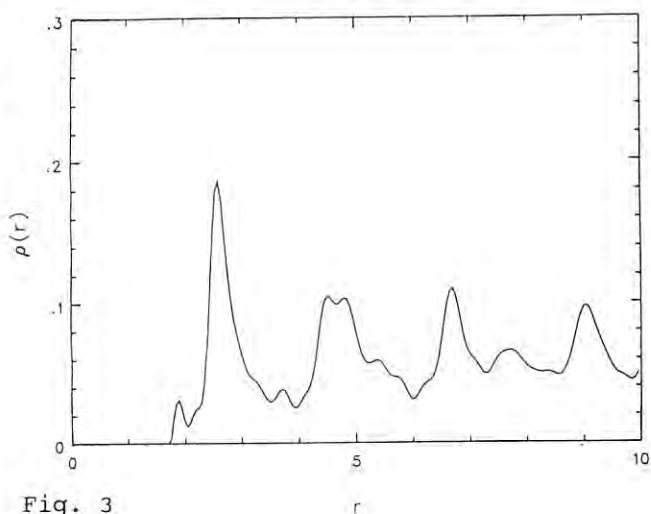


Fig. 3

DEVELOPMENT OF SYNCHROTRON RADIATION DOSIMETRY TECHNIQUES

Hiroshi NAKASHIMA¹, Shun-ichi TANAKA¹, Hideo HIRAYAMA²,
 Syuichi BAN², Nobuteru NARIYAMA³ and Michio YOSHIZAWA¹

1. Japan Atomic Energy Research Institute, Tokai, Ibaraki 319-11
2. National Laboratory for High Energy Physics, Oho, Tsukuba, Ibaraki 305
3. Ship Research Institute, Tokai, Ibaraki 319-11

The features of SR, the high brightness, the well directivity and the wide energy range up to ultraviolet, bring interesting but difficult issues in the radiation dosimetry, differing from that of conventional X rays. In the present work, fundamental researches, the development of absolute flux intensity monitor systems and dosimetry techniques for SR, were made using monoenergetic SR.

Concerning with the radiation dosimetry technique, a total absorption calorimeter was developed as an absolute flux intensity detector of SR, and a parallel-plate free-air ionization chamber which has been used as a beam monitor in SR experiments was tested. The calorimeter has the performance to measure the energy deposition up to a few microwatt by detecting the differences of the heat flow between the beam absorber and reference made of Ag. The experimental configuration using X rays from BL-14C line is shown in Fig. 1. The experiments with 20 to 50 keV SR demonstrated that the total absorbed energy of about 10 microwatt corresponding to the intensity of 1.25×10^9 photons/sec of 50 keV photons could be measured with an accuracy of a few % with the calorimeter and Fig. 2 shows the example of the calorimeter output for 50 keV photons. Furthermore, the absolute values with the ionization chamber agreed with 1 to 2 % with those of the calorimeter as tabulated in Table 1, when a correction was made for the ion-recombination using a relationship between current vs. collection field strength. The arrangement of the guards and the collecting plate is shown in Fig. 3. As the results, it was convinced that the calorimeter as a standard absolute detector and the ionization chamber as an in-situ monitor for monoenergetic SR would be used in the experiments of SR.

Next, the basic properties; energy response, linearity, and dose rate effect of $\text{Li}_2\text{B}_4\text{O}_7$ TLD with 15 micro-meter thickness, and of film-type alanin dosimeter with 120 micro-meter were examined using SR less than 50 keV for low and high dose measurements in various purposes. The linearity for the radiation dose was obtained up to 30 Gy.

Table 1

Energy (keV)	FIC	Calorimeter	
	Absolute Flux Intensity (photons/sec)	Thermal Power (μW)	
20.0	$1.14 \pm 10^*$	1.19 ± 10	38.01
30.0	1.17 ± 10	1.18 ± 10	56.81
50.0	4.40 ± 9	4.30 ± 9	34.50

* Read as 1.14×10^{10}

FIC : Free Air Ionization Chamber

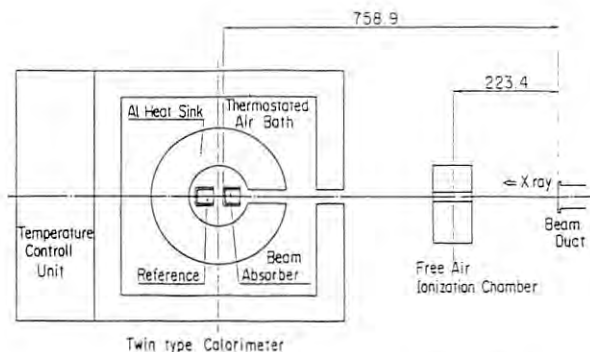


Fig. 1

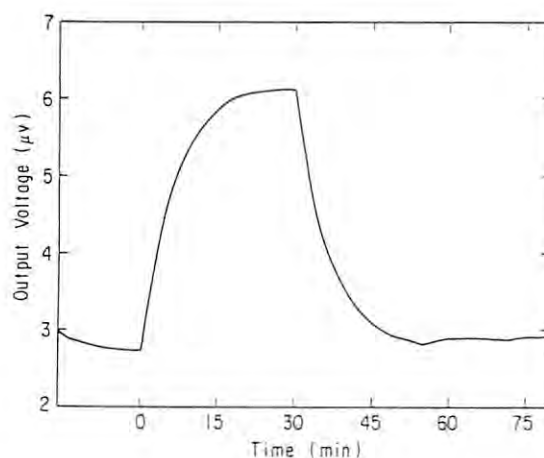


Fig. 2

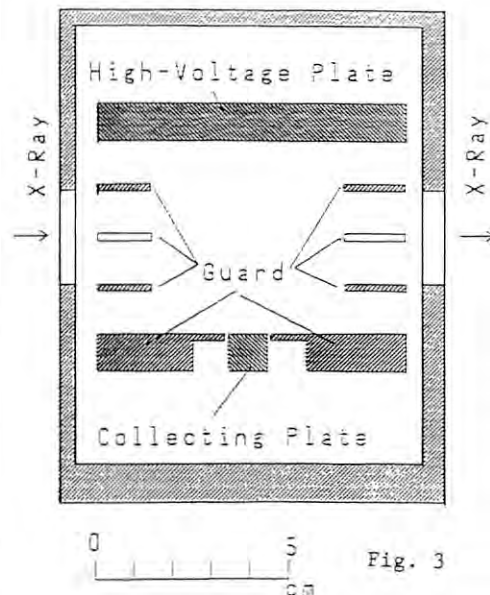


Fig. 3

TWO-STAGE TEMPER EMBRITTLEMENT OF AMORPHOUS Fe-B-Si ALLOYS AND STRUCTURAL CHANGES EXAMINED BY SR-SMALL ANGLE X-RAY SCATTERING

Tohru Yamasaki*, Yoshikiyo Ogino*,
Terukazu Honda** and Yoshiyuki Amemiya***

*Himeji Institute of Technology, 2167 Shosha Himeji 671-22, JAPAN.

**Graduate Student, Himeji Institute of Technology, Himeji, JAPAN.

***Photon Factory, National Laboratory for High Energy Physics,
1-1 Oho, Tukuba 305, JAPAN.

Introduction

Fe-based amorphous alloys are known to be severely embrittled by annealing at temperatures well below the crystallization temperature. Although many studies have been performed on this subject, the relationship between embrittlement and structural relaxation has not yet been well understood. Further, some of the previous studies examined the embrittlement only at room temperature. Since Fe-based amorphous alloys exhibit the ductile-brittle transition (1), it is desirable to examine the embrittlement on the basis of the ductile-brittle transition temperature.

The present study determined the dependence of DBTT on annealing and analyzed the structural changes induced by annealing of Fe-B-Si amorphous alloys. For detecting the structural changes, a small angle X-ray scattering method using synchrotron radiation was employed. This is a powerful means for this purpose since the structural change during annealing can be almost continuously followed.

Experimental

Fe-B-Si alloys were melted in silica tube and rapidly quenched by using a single roller type melt spinning apparatus. The amorphous specimens were isothermally annealed at temperatures between 523 K and 653 K. In order to determine DBTT, the fracture strain was measured by a simple bend test at various temperatures. The SR-SAXS experiments were performed

during heating at the rate of 0.33 K/s. The selected X-ray wavelength was $\lambda = 0.15$ nm, and each spectrum was measured with a counting time of 20 s by using a position sensitive proportional counter.

Results

As-quenched $\text{Fe}_{77}\text{B}_{13}\text{Si}_{10}$ amorphous alloy is quite ductile at 77 K. After annealing, the alloy exhibits the DBTT at temperatures above 77 K. At temperatures above DBTT, the specimen is quite ductile ($\epsilon_f = 1.0$). At temperatures below DBTT, the fracture strain significantly decreases. Also, the rising behavior of DBTT depends on the annealing temperature.

As shown in Fig.1 for the case of the $\text{Fe}_{77}\text{B}_{13}\text{Si}_{10}$ amorphous alloy, DBTT saturates to about 290 K when annealed below 623 K. On the other hand, when annealed above 633 K, DBTT rises up to about 290 K at the initial periods of annealing and then steadily rises with increasing annealing times. These results indicate that the embrittling reaction proceeds in two stages: below about 620 K, only the first-stage embrittlement occurs and at the higher temperatures the second-stage occurs following the first-stage reaction.

On the other hand, as shown in Fig.2, the SAXS intensity begins to increase from 620 K which well coincides with the starting temperature of the second-stage embrittlement. The increase of the intensity above 850 K is due to crystallization, as confirmed by the DSC measurement.

1) R.S. Williams et al.: Proc. of RQ3, Vol.1, 214(1978).

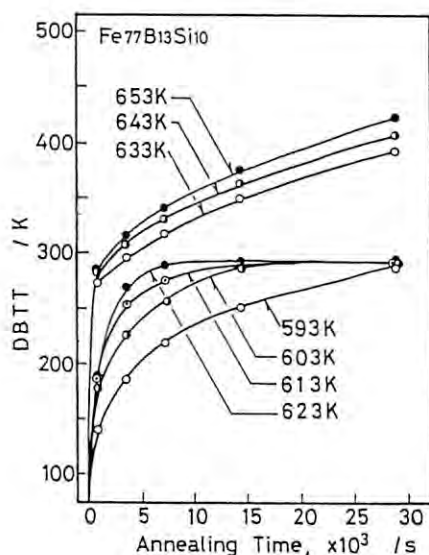


Fig.1 The change of DBTT as a function of ann. time at various ann. temp. in $\text{Fe}_{77}\text{B}_{13}\text{Si}_{10}$ alloy.

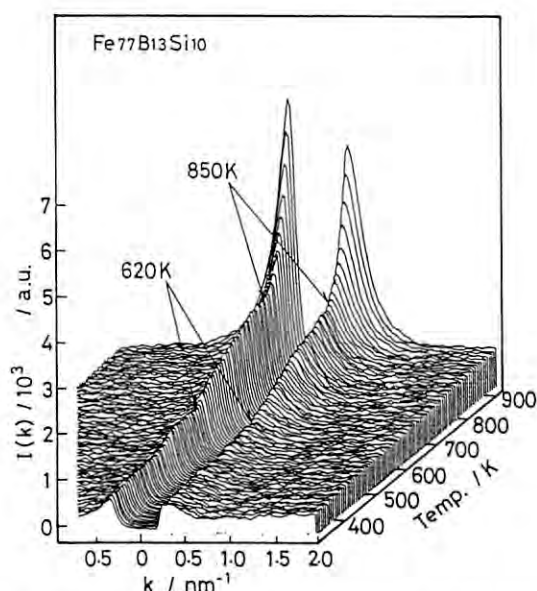


Fig.2 The change of SAXS intensity during heating.

X-RAY PHOTOACOUSTIC IMAGING OF SUBSURFACE LAYER AND CORRELATION SPECTRA

Yoshinori SUGITANI* and Kenji KATO**

* Department of Materials Science, Kanagawa University, Tsuchiya, Kanagawa 259-12

** National Chemical Laboratory for Industry, Tsukuba, Ibaraki 305

Introduction

Photoacoustic measurement is sensitive to the thermal properties of samples such as thermal conductivity and heat capacity. Using the two dimensional scanning technique, X-ray photoacoustic image of the sample was obtained, which resulted from the subsurface structure as well as from the variation in absorbance for the exciting beam. Correlation photoacoustic measurement gives impulse response characteristics of heat generated in the sample caused by X-ray absorption without any use of pulsed X-ray source^{1,2)}. The impulse response is referred to as the first kind of correlation photoacoustics³⁾, which gives more detailed information on thermal and structural properties of the sample material than the lock-in method.

Experimental

Experiments were conducted at the beam line of synchrotron radiation, BL-15A. The X-ray beam was monochromated to 1.504 Å and was narrowed with the use of a lead slit of 1mm in diameter and was chopped with a rotating sector. Photoacoustic cell was mounted on an XZ-stage, which was controlled by a desktop computer (NEC, PC9801). The photoacoustic signal was detected with a condenser microphone and preamplified. Then the signal was introduced to a lock-in amplifier (NF CIRCUIT BLOCK INC., LI575). The output signals of amplitude and phase were read on an A/D converter and stored in the memory of the computer. memory of the computer.

In the measurement of correlation spectra X-ray beam was modulated by a mechanical random chopper (containing 2 series of M-sequence, $n=31$). Chopper speed was 4RPS. The preamplified photoacoustic signal and the reference signal from the chopper were introduced into FFT analyzer (ADVANTEST, TR9403), where the cross correlation between these signals was calculated with accumulation of 1024 times.

Results and Discussion

Figure 1 shows X-ray photoacoustic images of the laminated sample of aluminum and lead foils.

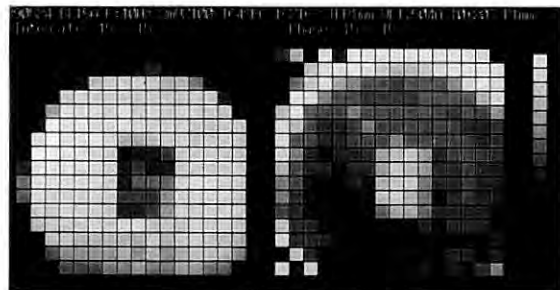


Fig.1. X-ray photoacoustic images of the laminated sample of lead and aluminum foil. A, amplitude and B, phase images.



Fig.2. X-ray photoacoustic image (amplitude image) of the flexible print circuit board.

The shape of the subsurface lead layer was clearly visualized. In the amplitude image, signal intensity was weak in the center part of the specimen where the hole of the lead foil was open. In the phase image, phase delay was small in the center of the specimen and large in the surroundings. This is considered as follows: 1) X-ray absorption occurred largely in the lead foil at deep layer in the surroundings of the specimen showing the large phase delay and X-ray absorption mainly occurred in the surface aluminum layer in the center of the specimen showing the small phase delay.

Figure 2 shows the X-ray photoacoustic image of the flexible print circuit board. The print pattern of copper strip at surface layer was visualized in the amplitude image. But, the print pattern below polymer layer was not observed in the experiment with spatial resolution of 1mm. In a photoacoustic image with 0.5mm spatial resolution, print pattern below the surface polymer layer was visualized both in amplitude and phase images.

Figure 3 shows a correlation photoacoustic spectra obtained for the laminated sample of lead and aluminum foils. The correlation spectra measured at the center of the specimen, where the hole pattern was opened, is different from that for the surroundings of the hole. This is due to change in the depth of heat generation between two position.

References

- 1) Y. Sugitani and K. Kato, Photon Factory Activity Report, p350 (1987), p181 (1988).
- 2) K. Kato and Y. Sugitani, Anal. Sci., 4, 59 (1988), in press (1989).
- 3) Y. Sugitani, A. Uejima and K. Kato: J. Photoacoust. 1, 217 (1982).

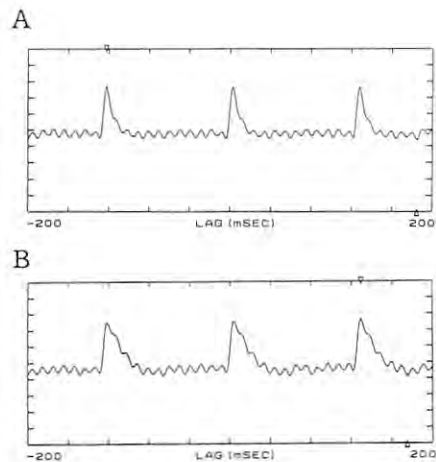


Fig.3. Impulse response of laminated sample. A, center of the specimen and B, the surroundings.

DIFFUSION OF SELF-INTERSTITIALS IN ICE UNDER HYDROSTATIC PRESSURE

Takeo HONDOH, Ryoji HOSHI, Akira GOTO and Hironobu YAMAGAMI

Department of Applied Physics, Hokkaido University, Sapporo 060

Introduction

We have developed a new method using high speed X-ray topography for determining diffusion coefficients of point defects (vacancies or self-interstitials) ^{1) 2)}. The method involves observation of dislocation climb under supersaturation (or undersaturation) of the defects, and the diffusion coefficient *D* is determined from the climb distance vs. time plot. We applied the method to ice crystal, and determined migration energy and entropy of self-interstitials successfully. The most important unknown parameter for self-interstitials in ice is an activation volume, *V_m*, involved in the migration process. For determining *V_m* by the above method, in situ X-ray topographic observations under high pressure is desirable. In the present study, the first attempt for such observations was made.

Experimental

In the present method, a specimen dimension is essentially important. A suitable thickness of the specimen is around 2 mm for ice ¹⁾, and a diameter has to be much larger than twice the thickness. Therefore, a high-pressure cell should necessarily have a large capacity in it. Figure 1 shows the cell and the pressure apparatus used in the present experiments. The cell was compressed by an oil actuator of which load capacity was 80 kN. The maximum pressure achieved in the cell was 250 MPa, which is higher than the phase transition pressure from Ih to III (210 Mpa at 251K). The pressure in the cell was calculated simply from the compression force and the cross-sectional area of the cell. Pressure melting was observed in order to confirm the pressure calculated.

The cell was cooled by blowing cold nitrogen gas evaporated from liquid nitrogen. Temperature of the sample was monitored by a thermocouple embedded in the steel sleeve, and was controlled by changing the evaporation rate of the liquid nitrogen.

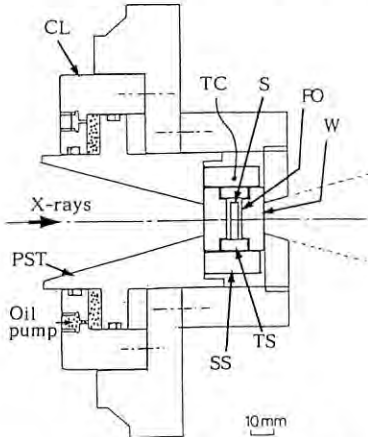


Fig.1 A high pressure apparatus for X-ray topo.
CL:cylinder,PST:piston, TC:thermocouple, S:specimen
PO:silicon oil, W:PMMA window, TS:teflon sleeve
SS:steel sleeve (pressure ring)

Results and Discussion

Sufficient supersaturation (or undersaturation) of the self-interstitials were introduced by a rapid change in temperature. Climb motion of dislocations was observed by a monitor TV and was recorded on a video tape intermittently. Figure 2 shows $\ln(L_f - L)$ vs. time plot, where *L* is the climb distance and *L_f* is the final value of *L*. The gradient of this plot is equal to $-\pi^2 D/d^2$, where *d* is the specimen thickness.

The values of *D* were determined as a function of pressure *P* as shown in Fig.3. *D* decreases as *P* increases, i.e., negative activation volume for the migration results in ice. Further analysis of the data is underway.

References

1)K.Goto et al., Jpn.J.Appl.Phys.25, 351(1986)
2)T.Hondoh et al.,Rev.Sci.Instrum.60, 2494(1989)

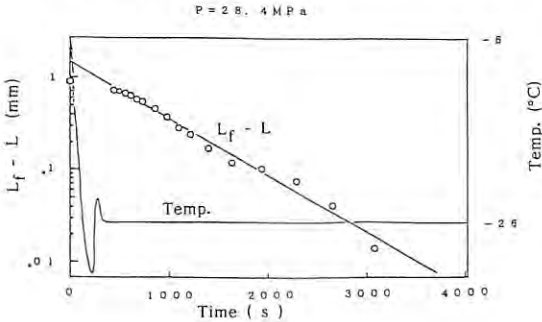


Fig.2 A climb distance vs. time plot
The sample was cooled from -6°C to -26°C, and then climb motion of a dislocation was observed. *L* is the climb distance and *L_f* the final value of *L*.

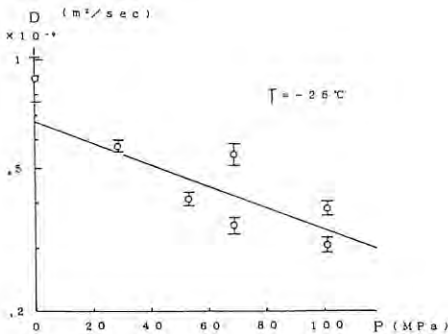


Fig.3 Diffusion coefficient *D* vs. pressure *P*
The plot indicates a negative activation volume for self-interstitial migration in ice.

DISLOCATION MOTION IN ICE UNDER STRESS

Pierre PIMIENTA, Takeo HONDOH, Akira GOTO, Ryoji HOSHI and Takayuki ONO

Department of Applied Physics, Hokkaido University, Sapporo 060

Introduction

In situ synchrotron radiation X-ray topography experiments were carried out in order to measure dislocation velocity in ice. The very high X-ray flux allows the observation of lattice defects by X-ray TV system¹⁾ and reduces the exposure time for the film method to approximately one second. The utilization of an image processor allows to increase the contrast by integrating several tens frames and to measure quite easily the displacement of the defects by comparing two images.

Experimental

A specimen chamber mounted on the goniometer is cooled by cold nitrogen gas evaporated from liquid nitrogen in a Dewar vessel. The temperature is controlled by a programmed regulation. The loading machine specially designed is schematically shown in Fig.1. The maximum load admitted by the load cell is 50N. The applied constant load and the loading period were controlled by computer.

Several artificial single crystals and bicrystals with a very low dislocation density were studied. Sample length was 30mm for all specimens but with a different section of 3x3, 6x3 or 6x6 mm². Single crystals were cut with the c-axis parallel, normal and inclined with regard to the sample axis. No dislocation movement was observed in the first two cases even at high stresses (1MPa) and high temperature (-5°C). These results are in good agreement with previous mechanical tests. Many velocity data were obtained when basal planes were subjected to shear stress (the third case).

Bicrystalline samples were also used for a study of interaction between dislocations and a grain boundary. In all the bicrystalline samples we observed a subboundary intersecting a large-angle grain boundary. We studied dynamical behaviour of the subboundaries also.

Results and discussion

Figure 2 is an example of the TV topograph which shows dislocation motion in a single crystal. This photograph was made by overlapping two TV images which were taken before and after deformation. The dislocation A moved to A' along the basal plane by the deformation while other dislocations did not move at all. A linear relationship between dislocation velocity and the applied shear stress was obtained in a stress range between 0.05 and 0.6 MPa. We have also studied the stress and temperature dependence of the subboundary migration velocity in the region indicated in Fig. 3. During migration, some rotation of the subboundary was observed. Since the subboundary intersected a large-angle grain boundary, this rotation can be explained by a dragging at the intersection. A relaxation was also observed, i.e., the subboundary rotated backward after removal of stress.

At each temperature and stress, several loadings were carried out. The calculated velocity are similar to those of Yamamoto obtained on individual dislocations in single crystals²⁾. However the linear relationship between the velocity and the applied stress was not always observed (the stress exponent at some temperature is lower than unity). This fact may be explained by the possible drag due to the grain boundary. The temperature dependence of the subboundary mobility in a bicrystal is also equivalent to that of individual dislocations in a single crystal.

References

- 1) S. Suzuki et al., Nucl. Instrum. Meth. Phys. Res., 227, 584 (1984).
- 2) Y. Yamamoto, M.S. Thesis, Hokkaido University.

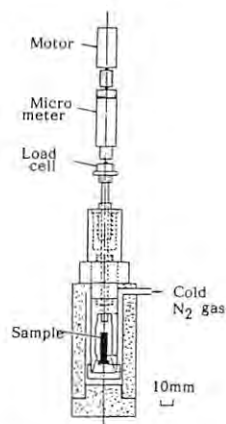


Fig.1 A deformation apparatus



Fig.2 Glide motion of a dislocation
The dislocation A moved to A' by a compression stress of 0.5 MPa for 180s.

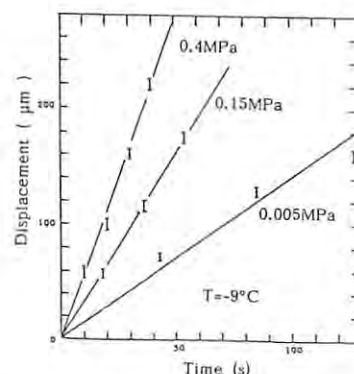


Fig.3 Subboundary migration curve

X-RAY MAGNETIC SCATTERING STUDIES ON THE $R_2Fe_{14}B$ INTERMETALLIC COMPOUNDS.

Hitoshi YAMAZAKI, Kazumichi NAMIKAWA,* Hiroshi MARUYAMA, Akihisa KOIZUMI, Manabu FUJITA, Koichi MORI,† Masami ANDO,† Hiroshi KAWATA† and Hironobu MAEDA#.

Department of Physics, Faculty of Science, Okayama University,
 # Department of Chemistry, Faculty of Science, Okayama University,
 3-1-1 Tsushima-Naka, Okayama-shi, Okayama 700.
 * Department of Physica, Tokyo Gakugei University,
 4-1-1 Nukuikita-machi, Koganei-shi, Tokyo 184.
 † Photon Factory, National Laboratory for High Energy Physics,
 1-1 Oho, Tsukuba-shi, Ibaraki 305.

INTRODUCTION

Intrinsic magnetic properties of $R_2Fe_{14}B$ compounds have been extensively studied in connection with the sintered R-Fe-B permanent magnet, which is applied to insertion device as a synchrotron radiation light source. In the series of the compound, spin reorientation transitions have been observed in the compounds with R-Nd, Ho, Er and Tm. These transitions have been ascribed to competition between crystalline electric field of the R^{3+} ions and molecular field due to exchange interaction.

Although the crystal structure of the compound has been studied by neutron diffraction, magnetic structure is not still clear because of absorption of neutron by Boron and rare earth. Recently, X-ray magnetic scattering technique is available to study magnetic structure. It is favorable to investigate spin structure with long period because of high resolution in k-space. When the incident X-ray energy is tuned through an absorption edge, a resonant enhancement of Bragg peak is observable. The polarization of spin density near Fermi level or the orbital and spin contributions in magnetic materials is studied from resonant magnetic scattering.

In the present work, we study magnetic and band structures of $R_2Fe_{14}B$ by means of X-ray magnetic scattering technique.

EXPERIMENTAL and RESULT

(1) $Nd_2Fe_{14}B$.

The single crystal of the $Nd_2Fe_{14}B$ was grown in an infrared image furnace by the floating zone melting technique. The crystal structure is tetragonal. The high-field magnetization measurements along the three principal directions have been done in the temperature range from 4.2 up to 300K. The spin reorientation and Curie temperatures are 130 and 588K, respectively. The magnetic structural transition from ferromagnetic to conical structure takes place at 130K with decreasing temperature.

(2) X-ray magnetic Bragg scattering.

The experiments have been done at R.T. and 13K by using the three-axes diffractometer installed at BL-15B. The Si(110) channel-cut monochromator was used. The energy of the incident X-ray was tuned to 10 keV ($\lambda=1.24 \text{ \AA}$). The sample was a disc of $Nd_2Fe_{14}B$ single crystal with the (001) plane, 5 mm in diameter and 1 mm in thickness. To arrange the magnetic domain, the sample was attached on a $SmCo_5$ permanent magnet. Magnetic satellite peak associated with the magnetic structural transition has been searched in the (001) plane at 13 K in comparison with the scans at R.T. Unfortunately, the satellite peak has not been observed yet.

(3) X-ray resonant magnetic scattering.

The Resonant magnetic scattering has been measured on $Nd_2Fe_{14}B$ single crystal with the (110) plane. The incident X-ray energy was scanned below and above Nd L_2 absorption edge by a step of 1 eV, and the Bragg condition was corrected every time the energy was changed. The magnetic field (2.5 kOe) was applied parallel to the easy [001] direction and perpendicular to the scattering plane. Intensity of (330) reflection was measured with alternating the direction of magnetic field. The period of the alteration was 30 - 45 sec and the repetition of the measurement was 20 times. The asymmetric ratio defined by $R_a = (I^\uparrow - I^\downarrow) / (I^\uparrow + I^\downarrow)$, where I^\uparrow and I^\downarrow is the intensity of the Bragg reflection when the spin is parallel to $k \times k'$ and antiparallel to it, reflects the difference of spin density above Fermi level. The fluorescent X-ray spectrum was simultaneously measured to compare with R_a . They are indicated in Fig.1. It gives the information about the exchange splitting of Nd 5d-band in $Nd_2Fe_{14}B$.

ACKNOWLEDGMENT

The authors are indebted to Dr. S.Hirosawa of Sumitomo special metals Co. Ltd. for supplying the single crystal of $Nd_2Fe_{14}B$.

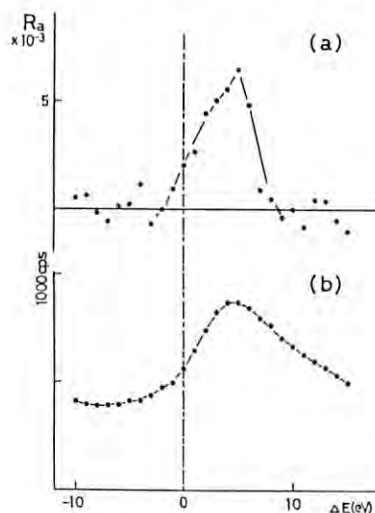


Fig.1 (a) Asymmetric ratio of (330) Bragg reflection obtained from resonant magnetic scattering. (b) Fluorescent X-ray spectrum at Nd L_2 absorption edge.

STUDY OF CRYSTAL MOIRÉ

Junichi YOSHIMURA and Tetsuya ISHIKAWA*

Institute of Inorganic Synthesis, Faculty of Engineering, Yamanashi University, Kofu, Yamanashi 400

*Department of Applied Physics, Faculty of Engineering, University of Tokyo, Hongo, Tokyo, 113

Introduction

It has recently been reported^{1,2)} that X-ray moiré fringe patterns are not exactly a projected figure thrown to the wave-traveling direction in vacuum, in contradiction to the theoretical prediction. The purposes of this study are to see whether such nonprojective moiré fringes are also observed using good-natured SR X-rays, and to elucidate the characteristics of that nonprojectiveness.

Experimental

The experiment was conducted on the beam line 15C. X-rays of wavelength 0.72 \AA were selected by the Si(111) and (220) monochromators set in a (+, -) setting, with the wavelength spread $\Delta\lambda/\lambda = 6 \times 10^{-4}$ and the angular spread $0.34''$ arc. This X-ray beam was incident on the specimen (Fig.1) aligned in the parallel setting with the downstream monochromator of Si(220). The specimen was a monolithic bicrystal of the total thickness $3350 \mu\text{m}$ and gap width $225 \mu\text{m}$. The rear component of the bicrystal was rotated unforcedly about the z axis relative to the front component due to the mass difference between the two. This deformation is the main cause for produced moiré fringes. Further, the rear component was pulled at a point on its side by the weight W , so as to be rotated about the y axis. Moiré patterns were recorded simultaneously on about ten X-ray films placed parallel each other but at different z_d (distance from the specimen). Exposure time was 25-35 sec.

Results and discussion

Figures 2(a) and (b) show moiré patterns recorded on each successive four films of two sets of topographs taken simultaneously when the pulling weight W was -0.2 and $+0.2 \text{ g}$, respectively, where the negative value refers to the operation of weight $W(-)$ (see Fig.1) and the positive value to the operation of $W(+)$. Figures 3(a) and (b) show the slope angles of moiré fringes (angle between the fringe line and the X axis) measured on these two sets of topographs.

(1) In Fig.2(a), by comparing moiré fringes in the limited field between vertical lines (Area II), we can visually recognize that the direction and position of moiré fringes are changed between the topographs. This inspection and the plots in Fig.3(a) show that the nonprojective oscillation of moiré fringes is observable, similarly to the previous studies, with SR X-rays which are linearly polarized and well collimated and monochromatized. The oscillation amplitude in this case was a few to 13 deg of arc for the fringe-direction change.

(2) It should be noted in Fig.3(a) that the oscillation amplitude is large for fringes (Nos.1-7) in the lower field in the topographs, but becomes much smaller for fringes in the upper field. This was a common tendency observed in other areas on the specimen and in other sets of topographs.

(3) In contrast to Fig.2(a), the change in the fringe direction and position in Fig.2(b) is not easily recognized by visual inspection except for No.1 fringe. In agreement with this, the amplitude of the slope-angle change in

Fig.3(b) is all less than 4° . Like this, a notable difference in the oscillation amplitude was observed between the opposite weight-loading directions.

The findings (2) and (3) give clues for the further investigation hereafter.

References

- 1) J. Yoshimura: Acta Crystallogr. **A43** (1987) C221.
- 2) J. Yoshimura: J. Phys. Soc. Jpn. **58** (1989) 1283.

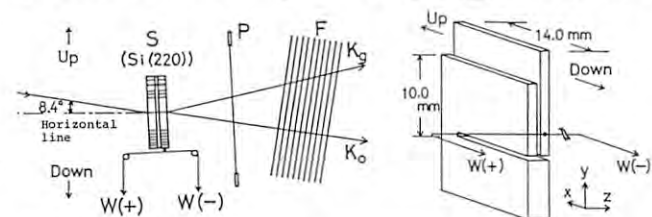


Fig.1. S: Specimen; P: Frame stretching thin Pt wires; F: X-ray films. $x//[1\bar{1}0]$, $y//[11\bar{2}]$, $z//[111]$.

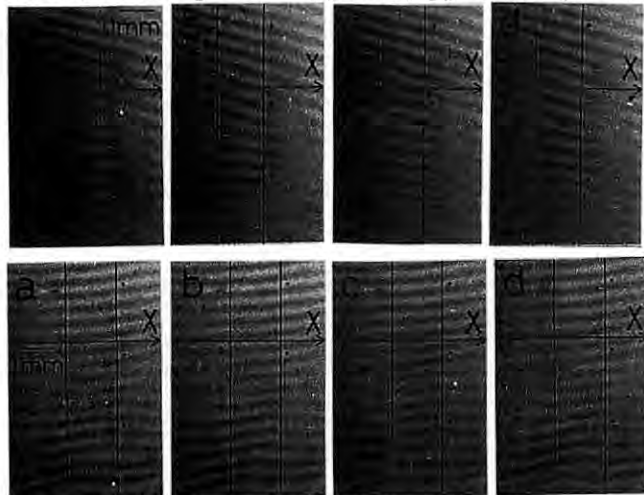


Fig.2. Upper row: (a) Exposure No.14 ($W=-0.2 \text{ g}$); Area II; $z_d = 60.5$ (a), 60.8 (b), 61.2 (c), 61.8 mm (d). Lower row: (b) Exposure No.8 ($W=+0.2 \text{ g}$); Area II; $z_d = 60.6$ (a), 60.9 (b), 61.3 (c), 61.8 mm (d). G-beam images. Moiré fringes are numbered from the bottom. Nos.5, 10, 15 fringes are marked by dot.

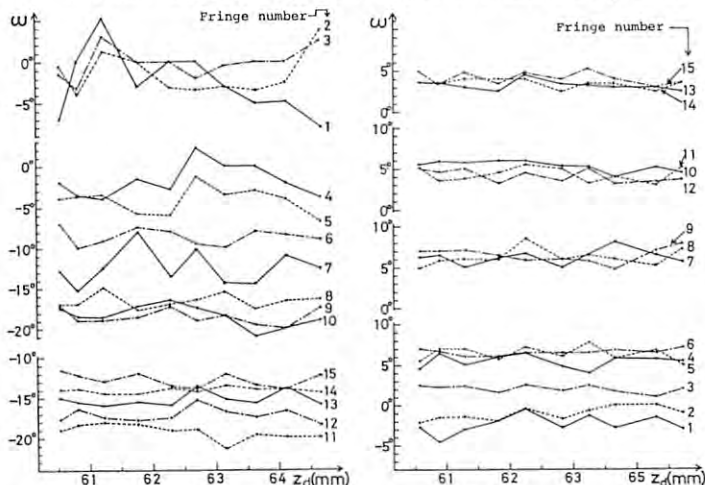


Fig.3. Slope angle ω vs. z_d . Left: (a) Exposure No.14. Right: (b) Exposure No.8. G-beam images. Area II.

LATTICE SPACING MEASUREMENT AROUND DISLOCATIONS IN UNDOPED GaAs CRYSTAL

Tomohisa KITANO*, Tetsuya ISHIKAWA** and Junji MATSUI***

Fundamental Research Laboratories*, Research & Development Group***,
 NEC Corporation, 34 Miyukigaoka, Tsukuba, 305
 **Department of Applied Physics, University of Tokyo,
 7-3-1, Hongo, Bunkyo-ku, Tokyo, 113

Introduction

Dislocations in undoped GaAs crystal form a typical cellular structure. The cell walls act as a source as well as sink for vacancies, and as a gettering center for some residual atoms. Point defects such as anti-site atoms, interstitial atoms and vacancies are also generated. At the same time, these point defects interact with the dislocations, which affects the inhomogeneity in electrical and optical properties. In this work, lattice spacing variations were measured around the dislocations in the aim of studying point defect behaviors around them.

Experimental

The experimental arrangement, schematically shown in Fig.1, was set up at beam line 15C. The 0.08nm wavelength x-rays were monochromatized by C1 crystals. Since the lattice spacings for Si (553) and GaAs (008) are very close¹⁾, the (+n, -n, n) triple crystal setting is made up between the collimator, sample and analyzer crystals. A series of topographs were taken at individual angle positions around the Bragg peak of the analyzer crystal, with respect to a fixed angle of the sample crystal. Other series of topographs were repeatedly taken in the same way, after rotating the sample crystal to the next angle position. From this experiment, the scattering vectors, which are related to the angular deviations from the Bragg angle for the sample and analyzer crystals, can be represented as "reciprocal points" in q_x - q_y reciprocal space²⁾.

Results and Discussion

Figure 2 shows a typical cellular structure observed in these topographs. The local reciprocal lattice points giving meaningful intensities for the regions A~D are necessarily deviated due to imperfection from that for an

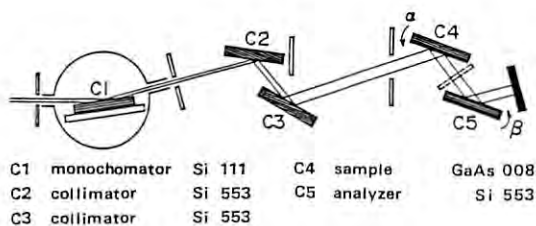


Fig.1

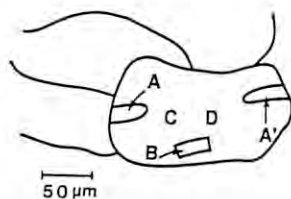


Fig.2

ideal undoped GaAs crystal. Their deviations are obtained by plotting the reciprocal points which give strong black contrast for individual regions, as shown in Fig.3. The rows of reciprocal points for individual regions lie parallel to the q_x axis. This implies that contrast observed in the regions A~D is derived from a dynamical diffraction effect. Individual row centers correspond to the reciprocal lattice points of the regions A~D. Considering position shift of the row centers of the regions A~D, two kinds of features are found. One is the position shift along the q_x axis, which represents a variation in the length of the reciprocal lattice vector due to lattice spacing variation. The other is that along q_y axis, which represents a variation in the direction of the reciprocal lattice vector due to lattice inclination variation. In the dislocation-free regions C and D, the row center positions are located near the average reciprocal lattice point. That is, the lattice spacings in these regions show the average value. In the dislocation-related regions, the lattice spacing in the region A is smaller than the average value by 3×10^{-6} , and the lattice spacing in the region B is larger than the average value by 6×10^{-6} . It is plausible that the lattice spacing contraction observed in the region A is due to vacancies, while, the lattice spacing dilatation observed in the region B is due to interstitial atoms. In addition, the vacancies in the region A is expected to be associated with the existence of dislocations because dislocation climbing motion frequently occurs near the cell walls, after forming sessile dislocations³⁾.

References

- 1) T. Ishikawa et al. Jpn. J. Appl. Phys. 24 (1985) L559.
- 2) A. Iida et al. Phys. Stat. Sol. (a) 51 (1979) 533,
- 3) H. Ono et al. Appl. Phys. Lett., 51 (1987) 801

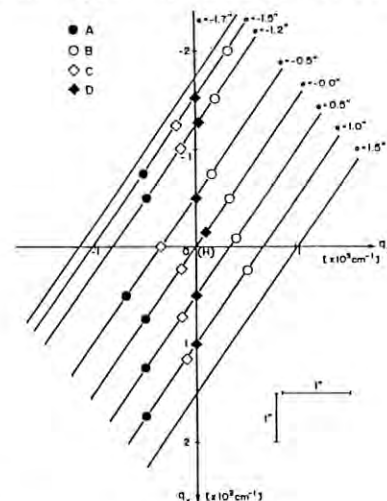


Fig.3

CONTRAST FORMATION MECHANISM AROUND THE CELL WALLS IN EQUI-LATTICE-SPACING MAPPING X-RAY TOPOGRAPHS FOR AN UNDOPED GaAs CRYSTAL

Tomohisa KITANO*, Tetsuya ISHIKAWA** and Junji MATSUI***

Fundamental Research Laboratories*, Research & Development Group***, NEC Corporation, 34 Miyukigaoka, Tsukuba, 305

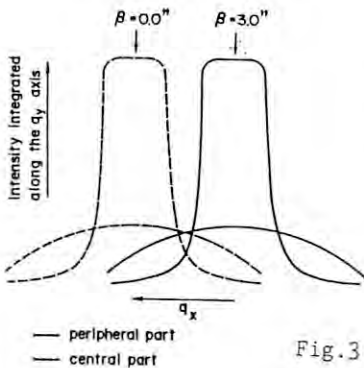
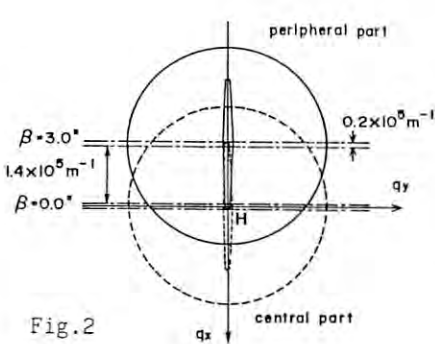
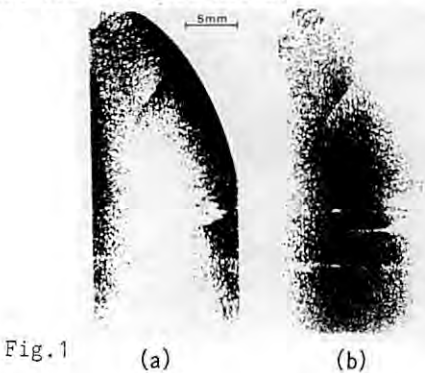
**Department of Applied Physics, University of Tokyo, 7-3-1, Hongo, Bunkyo-ku, Tokyo, 113

Introduction

We have proposed equi-lattice-spacing mapping x-ray topography (ELSMXT) to observe two-dimensional lattice spacing variations over the GaAs wafers, irrespective of lattice inclination¹⁾. The macroscopic lattice spacing variation was observed using this method. However, the contrast formation mechanism around the cell walls still remains to be unsolved. In this work, the contrast formation mechanism, which was observed microscopically at the cell interiors and the cell walls, is discussed.

Summary of ELSMXT

Fig.1(a) and (b) show two ELSMXT taken at analyzer angle positions of $\beta=3.0^\circ$ and 0.0° . Black contrast is observed at the peripheral part in Fig.1(a) and at the central part in Fig.1(b), where the diffraction condition is satisfied. From these results, we concluded that lattice spacing was longer at the peripheral part than at the central part, by $\Delta d/d=1 \times 10^{-5}$. Microscopically, the cell interiors are imaged in black contrast when the diffraction condition is satisfied (the peripheral part at $\beta=3.0^\circ$ and the central part at $\beta=0.0^\circ$). However, the cell walls are imaged in black contrast when the diffraction condition is not satisfied (the peripheral part at $\beta=0.0^\circ$ and the central part at $\beta=3.0^\circ$). Thus, contrast reversal is observed between the cell interiors and the cell walls.



Analysis

Fig.2 shows the schematic representation of extents of dynamical and kinematical diffraction profiles in reciprocal space. The dynamical diffraction, which dominates at the cell interiors where the crystal is nearly perfect, is represented as streak pattern along the q_x axis. The kinematical diffraction, which dominates on the cell walls where the crystal is heavily distorted, is represented as isotropic pattern for simplicity. The dash-dotted lines show the momentum resolution determined by the intrinsic diffraction width of the analyzer crystal. Fig.3 shows the dynamical and kinematical diffraction intensities integrated along the q_y axis in Fig.2, which vary dependent on the q_x values. When the intrinsic diffraction width of the analyzer crystal covers the centers of the integrated diffraction intensity profiles (the peripheral part at $\beta=3.0^\circ$ and the central part at $\beta=0.0^\circ$), the integrated dynamical diffraction intensities are much larger than the kinematical ones. Accordingly, black contrast at the cell interiors is a result of x-ray enhancement by the dynamical diffraction effect. At the same time, white contrast at the cell walls is only due to a minor kinematical diffraction effect. The opposite phenomenon occurs when the intrinsic diffraction width of the analyzer crystal covers the off-center portions of the integrated diffraction intensity profiles (the peripheral part at $\beta=0.0^\circ$ and the central part at $\beta=3.0^\circ$). The results described above are summarized in Table 1. In this way, contrast reversal observed between the cell interiors and the cell walls is explained by preference of two kinds of diffraction effects.

References

1) T. Ishikawa et al. J. Appl. Cryst. 20 (1987) 344.

Table 1 Contrast observed between the cell interiors and the cell walls

	peripheral part		central part	
	cell interiors	cell walls	cell interiors	cell walls
$\beta=3.0^\circ$	black (DE>KE)	white	white (DE<KE)	black
$\beta=0.0^\circ$	white (DE<KE)	black	black (DE>KE)	white

DE: Dynamical Diffraction Effect
KE: Kinematical Diffraction Effect
 β : Analyzer Angle Position

TIME-RESOLVED X-RAY DIFFRACTION FROM A GERMANIUM CRYSTAL IRRADIATED BY A VISUAL PULSED-LASER

Shigeru KOJIMA, Seiji KAWADO, Tatsuo CHIJIMATSU*, Tetsuya ISHIKAWA*,
Toshio TAKAHASHI** and Seishi KIKUTA*

Sony Corporation Research Center, Hodogaya-ku, Yokohama 240

*Department of Applied Physics, Faculty of Engineering,

The University of Tokyo, Hongo, Bunkyo-ku, Tokyo 113

**The Institute for Solid State Physics, The University of Tokyo,
Roppongi, Minato-ku, Tokyo 106

Introduction

Using the time-resolved x-ray diffraction method, we have studied the lattice deformation in semiconducting materials caused by pulsed laser irradiation.^{1,2)} This report describes the time-change behavior of rocking curves from a Ge crystal under visual pulsed-laser irradiation.

Experimental

The experimental arrangement was the same as reported previously.²⁾ The sample used was a 2 mm-thick Ge crystal with the [111] orientation which was aligned to give the symmetric 111 reflection. We irradiated the sample surface with a Q-switched Nd:YAG laser beam with a wavelength of 0.53 μm and a pulse width of about 20 ns at a 10 Hz repetition rate. The power of the laser beam 6 mm in diameter was about 15 mJ/pulse. Time-resolved rocking curves were measured using the TAC technique, and the time dependence of the diffracted x-ray intensity at a fixed angular position of the sample was examined using the MCS technique.^{1,2)}

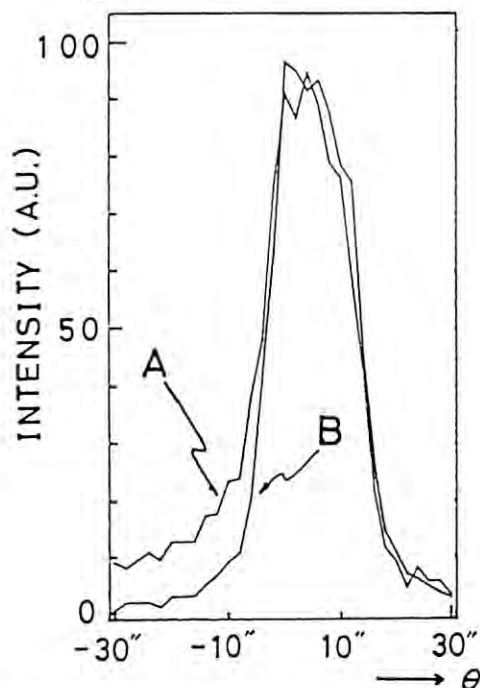


Fig.1. Time-resolved rocking curves measured by the TAC technique. A: just laser irradiation, B: 10 μs after the laser irradiation.

Results

Figure 1 shows time-resolved rocking curve profiles of the symmetric 111 reflection measured by the TAC technique with a time resolution of 50 ns. When the laser beam was irradiated onto the sample surface, the enhancement of x-ray intensity was observed at the lower angle side of the Bragg peak, but the peak shift was not observed (curve A). This intensity enhancement disappeared 10 μs after the laser irradiation (curve B). The FWHM of the measured rocking curve was about 17''. The penetration depth of x-rays was estimated to be about 2 μm for a wavelength of 1.54 \AA .

Figure 2 shows the time dependence of x-ray intensity examined by the MCS technique at a fixed angular position ($\theta = -9''$) of the sample. The time resolution was 200 ns and it took 20,000 times accumulation of a single scanning profile to obtain this MCS profile. The x-ray intensity was rapidly increased just after the laser irradiation and then gradually decreased. It took about 4 μs to relax the lattice strain due to the laser irradiation.

References

- 1) S.Kojima et al., Jpn.J.Appl.Phys., **27**, L1377 (1988).
- 2) S.Kawado et al., Rev.Sci.Instrum., **60**, 2342 (1989).

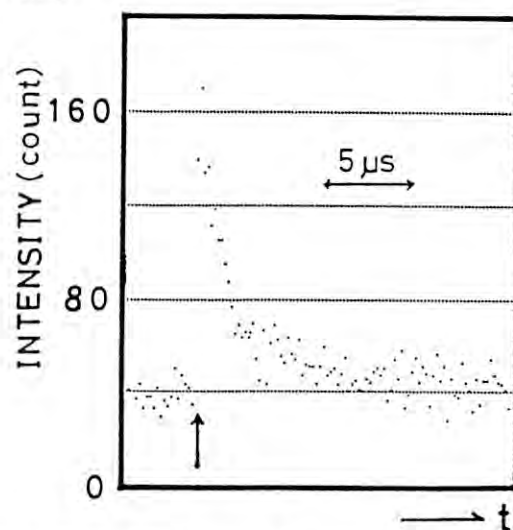


Fig.2. Time dependence of x-ray intensity examined by the fast MCS technique at an angular position $\theta = -9''$. Arrow indicates the laser irradiation time.

HIGH-RESOLUTION DIFFRACTION PROFILES OF SILICON SINGLE CRYSTALS MEASURED BY HIGHLY COLLIMATED X-RAY BEAMS

Seiji KAWADO, Shigeru KOJIMA and Tetsuya ISHIKAWA*

Sony Corporation Research Center, Hodogaya-ku, Yokohama 240
 *Department of Applied Physics, Faculty of Engineering,
 The University of Tokyo, Hongo, Bunkyo-ku, Tokyo 113

Introduction

X-ray diffraction topography using highly collimated x-ray beams provides a useful technique to observe growth striation and microdefects in as-grown FZ, CZ and MCZ silicon single crystals.^{1,2)} When a dynamical diffraction occurs in Laue geometry with a highly collimated beam, a rocking curve of a nearly perfect silicon crystal has an oscillatory profile. In this report we describe the influence of crystal defects to this high-resolution diffraction profile of silicon.

Experimental

The experimental arrangement was the same as that of ultra-plane wave x-ray diffraction topography.^{1,2)} The (+m,-n,+n) separated three-crystal monochromator gave about 40 nanoradian collimation of the incident x-ray beam ($\lambda=0.72 \text{ \AA}$). The silicon sample 300 μm thick with the [001] surface orientation was aligned to give symmetric 220 reflection in the Laue geometry for a non-dispersive parallel setting. Rocking curve measurements were carried out using the diffracted x-ray beam reduced to 0.4 mm \times 1.0 mm with a slit in front of the scintillation counter.

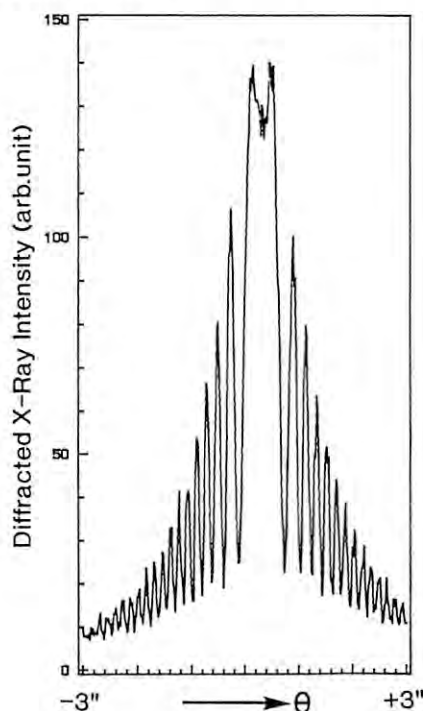


Fig.1. Rocking curve for the symmetric 220 reflection of as-grown MCZ silicon in the Laue geometry.

Results

Figure 1 shows a rocking curve of the sample prepared from a high-grade, B-doped MCZ silicon crystal with an oxygen concentration of 18×10^{17} atoms/cm³ (old ASTM). This curve gives an oscillatory profile predicted by the dynamical theory of x-rays, and it has subsidiary peaks with a half-width of about 0.1°.

High temperature annealing generates oxygen-precipitates in CZ and MCZ silicon crystals. Two examples of rocking curves obtained from heat-treated MCZ silicon are shown in Fig.2. The sample which was annealed at 1000°C for 25 h in N₂ gave a profile showing a decrease in the intensity of subsidiary peaks (Fig.2a), while the sample which was annealed at 750°C for 50 h gave a remarkably reduced oscillatory-profile (Fig.2b). Both samples contained oxygen-precipitates with a density of $10^6 \sim 10^7 / \text{cm}^3$, but they showed different profiles of rocking curves. This result indicates that the change in the high-resolution diffraction profile gives new information about crystal imperfection.

References

- 1) T. Ishikawa, Rev. Sci. Instrum., 60, 2490 (1989).
- 2) S. Kawado et al., to be published in Proc. Int. Conf. on Science and Technology of Defect Control in Semiconductors (Yokohama, 1989).

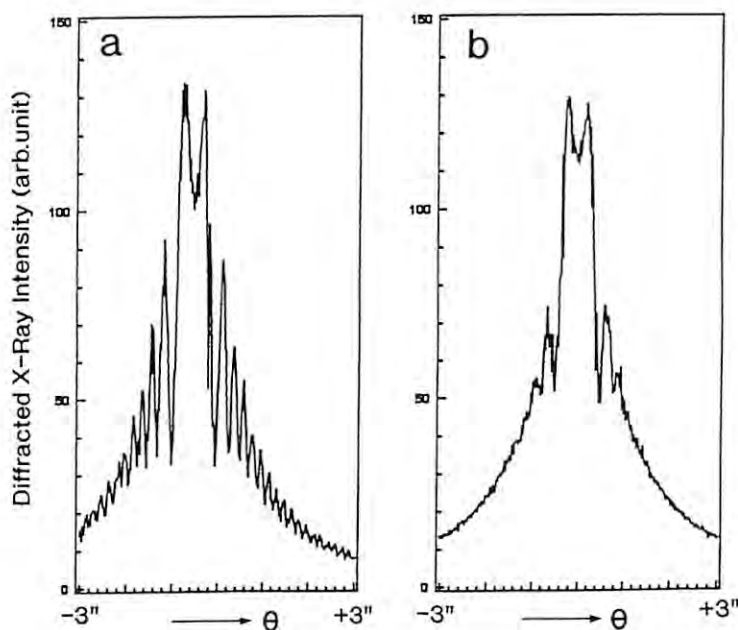


Fig.2. Rocking curves of MCZ silicon crystals annealed a) at 1000°C for 25 h and b) at 750°C for 50 h.

GRAZING INCIDENCE DIFFRACTION FROM MONOLAYERS OF ARACHIDIC ACID ON WATER SURFACES AND GLASS SUBSTRATES

T. Matsushita, A. Iida, K. Saito*, S. Kuroda*,
H. Oyanagi* and M. Sugi*

Photon Factory, National Laboratory for High Energy Physics, Oho,
Tsukuba, Ibaraki 305

*Electrotechnical Laboratory, Umezono, Tsukuba, Ibaraki 305

Langmuir-Blodgett(LB) films are built-up multilayers prepared by transferring monolayers spread on water surfaces to solid substrates. In order to understand correlation between the in-plane structure of arachidic acid monolayers on water surfaces and that of LB films(1, 3 and 13 monolayers of cadmium arachidate on glass substrates in the present case), grazing incidence diffraction(GID) experiments were performed on a bending magnet(BL-4C) and a mutipole wiggler(BL-16) beamlines. The X-ray beam was deflected downwards by a flat mirror and was incident onto the water or substrate surface with a glancing angle of 1.8 mrad. The diffracted beam was measured by a scintillation counter before which a Sollar slit(0.118°) was placed. The temperature of the trough was controlled at $20.0 \pm 0.1^\circ\text{C}$.

Figures 1 and 2 show background-subtracted diffraction curves from monolayers of arachidic acid on pure water and for 10^{-4} CdCl_2 in the subphase at various surface pressures. In the case on pure water, the peak position shifts to higher angles as the pressure is raised up to 27 mN/m and stays nearly constant above it. The lattice(d -) spacing changes from 4.31\AA (~ 0.0 mN/m) to 4.11\AA (50.0 mN/m). The pressure dependence of d -spacing is very similar to the results reported by Kjaer et al.¹⁾. The FWHM becomes wider at higher pressures suggesting formation of a deformed lattice. In the presence of Cd^{2+} ions in the subphase, the peak position was almost stationary below 30 mN/m with corresponding d -spacing of $4.11 - 4.10\text{\AA}$. At 25 to 30 mN/m, another peak appeared around $2\theta = 23.0^\circ$ corresponding to a d -spacing of 3.73\AA . It should be noted that this peak was observed in some scans, but was not in others. At 50.0 mN/m, the main peak shifts to 21.62° ($d = 3.97\text{\AA}$) and becomes sharper.

For a single monolayer of cadmium arachidate transferred onto a glass substrate at 25mN/m, we observed a diffraction peak which corresponds to a d -spacing of 4.10\AA . This value is very close to that for arachidic acid on the surface of water containing 10^{-4} M Cd^{2+} . For 3 and 13 monolayers of cadmium arachidate on glass substrates, we also observed a peak giving a d -spacing of 3.74\AA . This is close to that for the peak at 23.0° in Fig.2. The intensity ratio between these two peaks(for $d = 4.10\text{\AA}$ and

$d = 3.74\text{\AA}$) was strongly dependent on the in-plane orientation of molecular rows giving Bragg reflection. This would suggest reorientation of two dimensional crytalline powders in the process of transferring monolayers from water surface to glass substrates.²⁾

- 1) K. Kjaer, J. Als-Nielsen, C. A. Helm, P. Tippman-Krayer and H. Mohwald, J. Phys. Chem. 93(1989)3200.
- 2) M.Sugi, N. Minari, K. Ikegami, S. Kuroda, K. Saito and M. Saito, Thin Solid Films 178(1989)157.

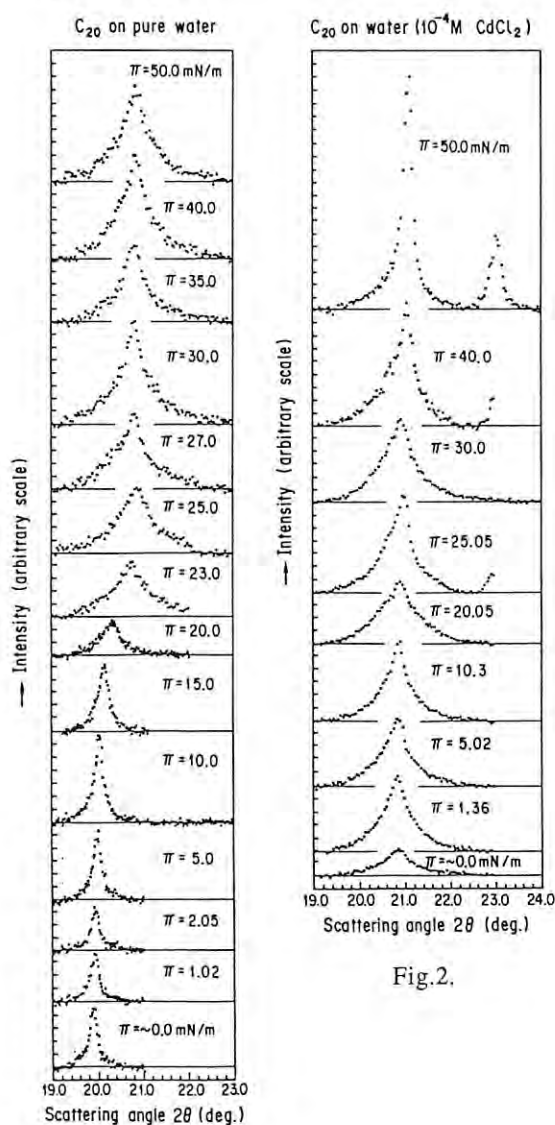


Fig.2.

Fig.1.

A NEW DRICKAMER-TYPE CELL FOR IN-SITU X RAY STUDIES AT HIGH PRESSURE AND TEMPERATURE

K. Leinenweber, W. Utsumi, T. Yagi, K. Omura,
H. Suzuki*, and T. Kikegawa**

Institute for Solid State Physics, Roppongi, Minato-ku, Tokyo 106
*Dept. of Geophysics, Faculty of Science, Tokyo University,
Hongo, Tokyo 113

**Photon Factory, National Laboratory for High Energy
Physics, Oho, Tsukuba 305, Japan

Introduction

The in-situ observation of materials at high pressure and temperature is important in the Earth sciences and high-pressure materials science. In-situ X-ray diffraction is used for pressure measurement, the observation of unquenchable phases, and the measurement of compressibility and thermal expansion. In this study, an internally heated Drickamer-type pressure cell is developed, which is designed for in-situ X-ray diffraction studies at simultaneous pressures and temperatures higher than those attainable by previous methods.

Experimental

The design of the cell is shown in the first figure. The sample (d) is compressed by applying a uniaxial load to two anvils (b), which are made of tungsten carbide or sintered diamond. The pressure medium (c) is boron epoxy resin, with an MgO or pyrophyllite sleeve around the sample. Heat is applied using resistance heaters, which are in contact with the sample. Sample temperature is measured with a Pt/Pt 13% Rh thermocouple.

The incident X-ray beam (e) enters through a hole in the outer cylinder (a). Diffracted X-rays pass through a 15 degree slit in the outer cylinder, and are collected by a solid state detector for energy dispersive analysis. X-ray measurements for the present study were made at the accumulator ring at KEK.

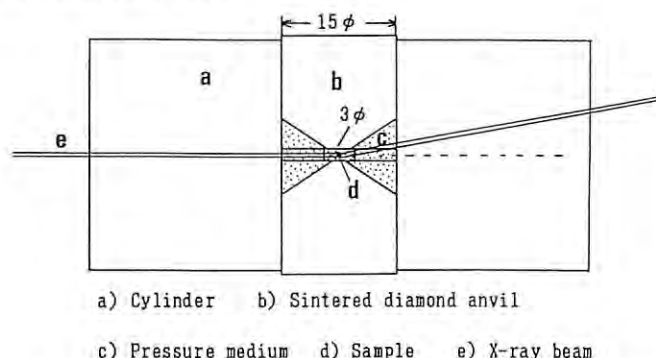
Results and Discussion

Pressure generation curves at room temperature were collected using a mixture of NaCl and Au. A typical X-ray exposure is shown in the second figure. The pressure results for sintered diamond anvils are shown in the third figure. The anvils survived to a pressure approaching 30 GPa, with no reduction in the efficiency of pressure generation. Tungsten carbide anvils, in contrast, generated up to 16 GPa.

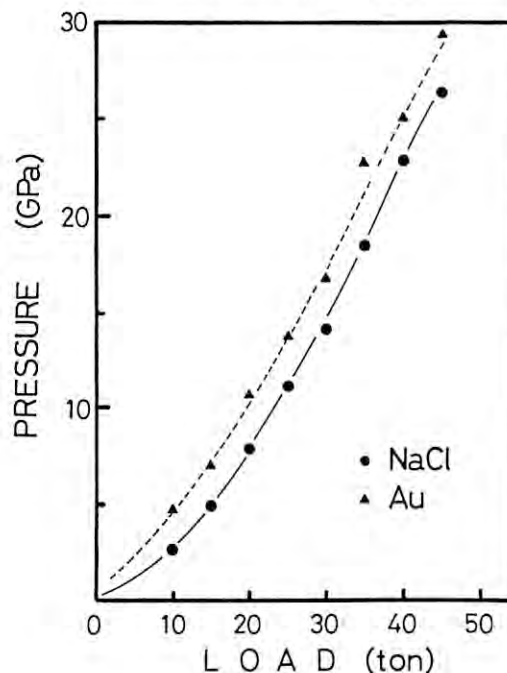
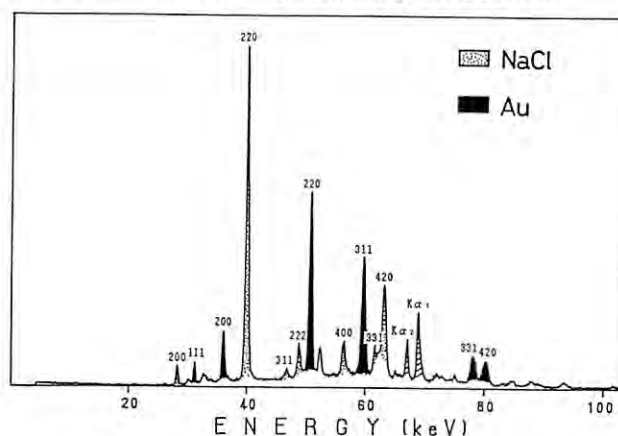
The difference in pressure values measured for gold and sodium chloride standards may result from the inhomogeneous elastic response of the mixture to high pressure or high stress. Previous calibrations at lower pressures agree more closely with the data for NaCl.

Temperature was raised to 600 degrees C at 4 GPa, and X-ray patterns were taken for a sintered disc of MgO under these conditions.

These trials show the feasibility of taking X-ray patterns at high P and T using this system. We are working on two improvements: 1. Stable alignment of the cell is needed, to minimize breakage of the anvils, and 2. The furnace has been redesigned and is now stable to temperatures above 1000 degrees C.



A131 [#131:DR1 1 DR8-7-1 PH=7.25
1989-07-03 23:21:52
P[mV]=36 T[C]=25 2THETA=10.00 t[sec]=300



ACCURATE DETERMINATION OF PHASE BOUNDARY OF RUTILE- α PbO₂ TRANSITION IN TiO₂ AT HIGH PRESSURES AND HIGH TEMPERATURES²

Masaki AKAOGI¹, Jun-ichi SUSAKI², Keiji KUSABA³, Masanori MATSUI⁴,
Takehiko YAGI², Toshiyuki ATO³, Hitoshi YUSA¹ and Takumi KIKEGAWA⁵

- 1) Department of Earth Sciences, Kanazawa University, Kanazawa 920
- 2) Institute for Solid State Physics, University of Tokyo, Tokyo 106
- 3) Institute for Materials Research, Tohoku University, Sendai 980
- 4) Kanazawa Medical University, Uchinada, Ishikawa 920-02
- 5) Photon Factory, National Laboratory for High Energy Physics, Tsukuba 305

Introduction

High pressure transitions of rutile-structured dioxide are of considerable interest to predict post-stishovite transition in the earth's interior. Rutile- α PbO₂ transition of TiO₂ is an important example of the post-rutile transition. However, this transition boundary in TiO₂ has not yet been well constrained in the previous studies. The purpose of this study is to determine accurately the equilibrium phase boundary of the TiO₂ transition by in situ x-ray diffraction experiments.

Experiments

Experiments were carried out using the cubic anvil apparatus (MAX80) at the beam line AR-A2 with 4mm truncation anvils. The sample assembly was similar to that in the previous study¹. A mixture of rutile and α PbO₂ types of TiO₂, synthesized by shock loading², was inserted in a tubular graphite furnace. Pressure was measured from a lattice parameter of NaCl which was also embedded in the furnace. Temperature was monitored by a Pt/Pt-Rh thermocouple. X-ray diffraction patterns were measured in traversing the phase boundary at pressures up to 8.5GPa and temperatures to 900 °C.

Results

Typical diffraction patterns are shown in Fig.1. When the sample was kept at 4.7GPa and 800 °C, it was observed that the transition of α PbO₂ phase to rutile phase proceeded in about 60min. The results of the present experiments are summarized in Fig.2. Open circles represent the runs in which relative amount of α PbO₂ phase increases, while closed circles show the runs of rutile phase. The phase boundary is represented as $P(\text{GPa}) = 3.5 + 0.0038T(^{\circ}\text{C})$. This boundary, which is quite different from that determined by the synthesis experiments³, can be used as new pressure calibration points at high temperatures.

References

- 1) J. Susaki et al., Geophys. Res. Lett., 12, 729 (1985).
- 2) K. Kusaba et al., Phys. Chem. Min., 15, 238 (1988).
- 3) F. Dacheille et al., Am. Min., 53, 1929 (1968).

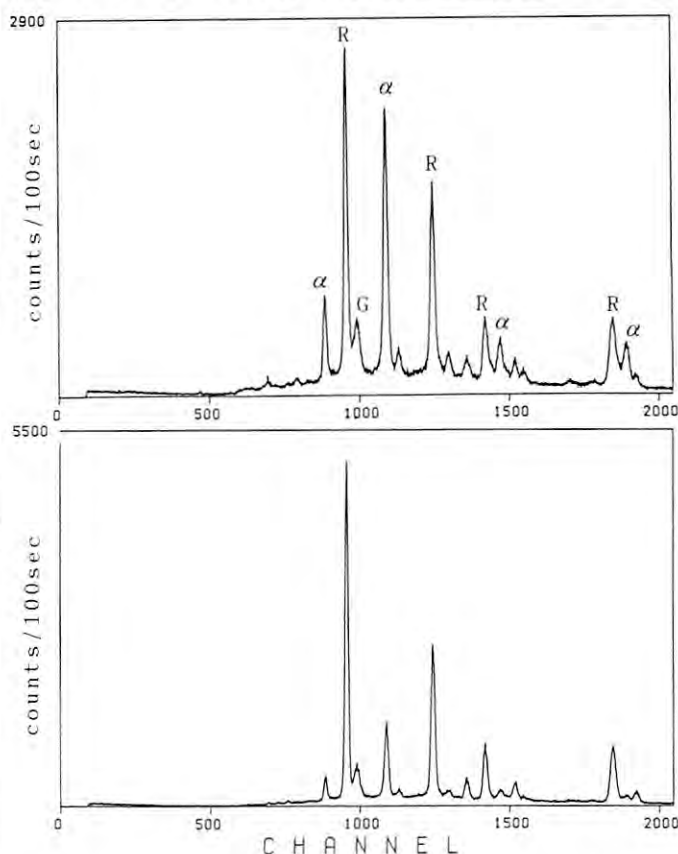


Fig.1. Diffraction patterns of the sample kept at 4.7GPa and 800 °C. Above: initial.. Below: after 55min.

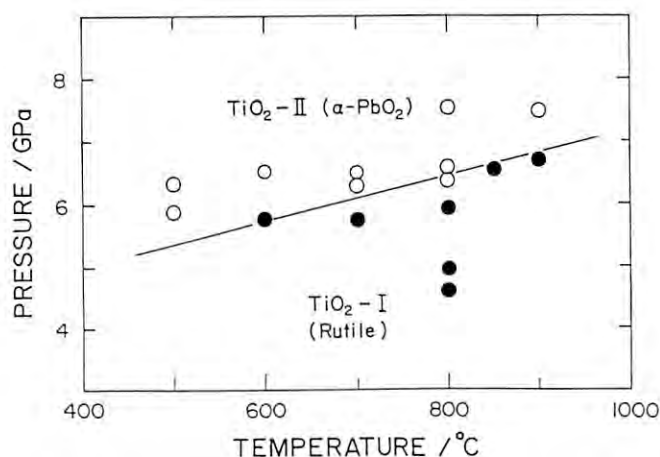


Fig.2. Phase diagram for the rutile- α PbO₂ transition in TiO₂.

INVESTIGATION OF THE PHASE TRANSFORMATIONS IN Au-Ge AND Au-Si ALLOYS BY IN-SITU HIGH-PRESSURE X-RAY DIFFRACTION

Yasuo FUJINAGA, Keiji KUSABA, Shinya HASHIMOTO, Kazuhiro UEKI, Kumi MOTAI,
Takumi KIKEGAWA*, Hiroshi IWASAKI* and Yasuhiko SYONO

Institute for Materials Research, Tohoku University, Sendai, 980

*Photon Factory, National Laboratory for High Energy Physics, Tsukuba, Ibaraki, 305

Introduction

Au-Ge and Au-Si systems are known to have eutectic phase relations in their equilibrium phase diagrams with only two terminal solid solutions of limited solubility, α , having the fcc structure and β , having the diamond structure. However, earlier investigations on the Ag-Ge system, which has also an eutectic phase relation, showed the formation of an intermediate phase by quenching after application of high pressures^{1,2)}. The result suggests that such an intermediate phase may be formed in the Ag-Ge and Au-Si systems under high pressures.

Experimental

Au-20,30%Ge and Au-20,30%Si alloys about 50 mg weight each, were prepared by melting the elements together in ceramic tubes in vacuum. The melts were followed by cooling to room temperature within a few minutes. The alloys were crashed about 0.3 mm thick, then a part of it was used as a sample for the compression. The sample was placed in a cube-shaped pressure transmitted medium of 8x8x8 mm³ in size and subjected in a cube type multi-anvils MAX80. First, room temperature compression runs were made up to the desired pressure. Next, temperature was raised stepwise at 50 K intervals and maintaining for about 10 min in each stage, while the alloy sample was subjected to the pressure. During the heating in-situ X-ray diffraction experiments were carried out.

Results and Discussion

Fig.1(a) shows an X-ray diffraction profile of Au-20%Ge alloy before high pressure annealing. Diffraction lines indexed in terms of the fcc structures are due to the α (Au) and β (Ge) phases. When the alloy sample was kept at 5.4 GPa and 473 K, a new intermediate phase appeared. After further heating at 523 K for several minutes, the multi-phase state was converted into a single phase. The diffraction lines were indexed in terms of the hcp structure as shown in Fig.1(b). When the temperature was raised at 673 K, the alloy was melted. Lattice parameters of the hcp phase were estimated to be $a=0.2864$ nm and $c=0.4686$ nm with $c/a=1.636$ at 5.4 GPa and 523 K.

When the Au-30%Si alloy was kept at 4.2 GPa and 473 K, another new intermediate phase appeared. Fig. 2 shows an X-ray diffraction profile of the new phase and α phase at 523 K. The new phase, designated X, usually coexisted with the α phase up to the melting temperature, that is, the Si content in the X phase is more than 30%Si. The structure was not identical with that of the hcp phase in the Au-Ge system. Many diffraction lines shown in Fig.2 suggests that the structure of the X phase is complex. When it was aged at ambient pressure and room

temperature, it was transformed into another metastable X' phase having a complex structure. Therefore, in the case of Au-Si system the in-situ measurement of phase transformation is important to study equilibrium phase relations under high pressures.

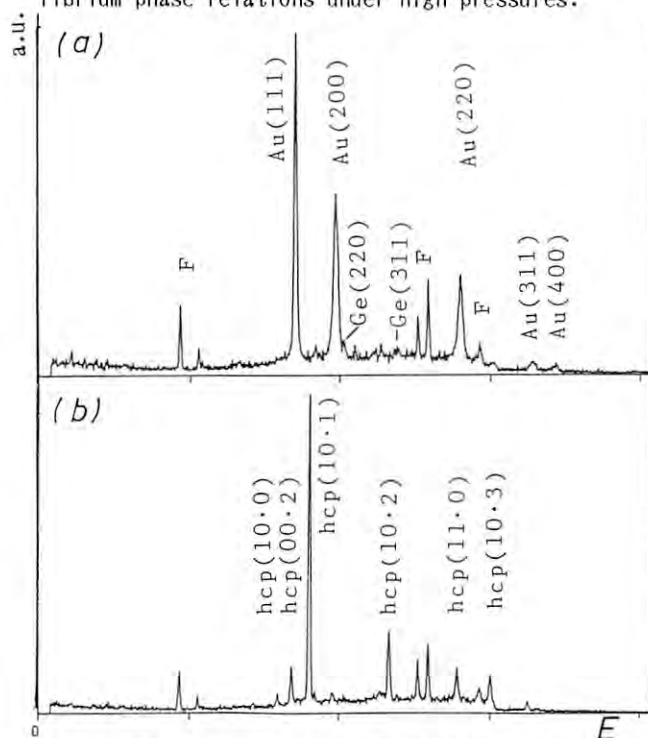


Fig.1 Diffraction profiles of the Au-20at%Ge alloy, (a) at ambient pressure and room temperature, (b) at 4.2 GPa and 473 K.

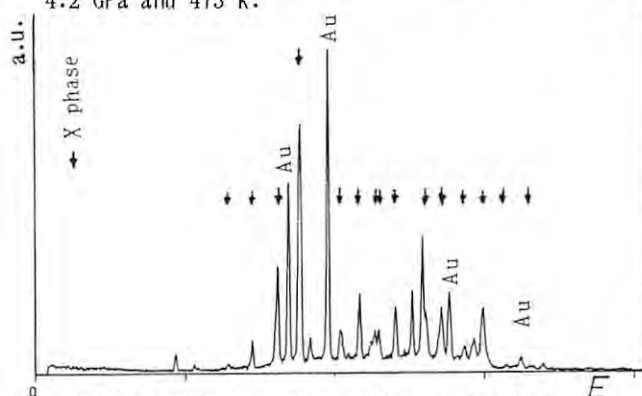


Fig.2 Diffraction profile of the Au-30at%Si alloy at 4.2 GPa and 473 K.

References

- 1) Y.Fujinaga, H.Iwasaki, K.Fukamichi and Y.Syono : Proceedings JIMIS-5, Non equilibrium Solid Phases of Metals and Alloys, Supplement to Trans. JIM, 29, 191(1988).
- 2) G.V.Chipenko and V.F.Degtyareva : Sov. Phys. Solid State, 26, 735(1984).

COMPTON-PROFILE OBSERVATION OF NEGATIVE SPIN POLARIZATION OF CONDUCTION ELECTRONS IN FERROMAGNETIC Ni METAL

Nobuhiko SAKAI, Masahisa ITO, Hiroshi KAWATA⁺, Toshiaki IWAZUMI⁺,

Nobuhiro SHIOTANI^{*}, Fumitake ITOH^{**}, Yoshiharu SAKURAI⁺⁺,

Yoshikazu TANAKA⁺⁺, Susumu NANA⁺⁺, and Masami ANDO⁺

The Institute of Phys. and Chem. Research, Wako, Saitama 351-01.

⁺ Photon Factory, KEK, Oho, Tsukuba, Ibaraki 305.

^{*} Tokyo University of Fisheries, Minato, Tokyo 108.

^{**} Institute for Materials Research, Tohoku Univ., Sendai 980.

⁺⁺ Inst. of Industrial Science, The Univ. of Tokyo, Minato, Tokyo 106.

Introduction

Hitherto, measurements of Compton profiles of magnetic electrons have been intensively made on a typical ferromagnet of iron, stimulated by interest in the spin-dependent momentum distribution of 3d, 4s, and 4p electrons¹⁻⁴. However, no magnetic-electron Compton profiles (MCP) have been made on another characteristic ferromagnet of nickel except preliminary ones⁵⁻⁷, because the small magnetization of this ferromagnet have prevented us to measure the MCP with sufficient statistical accuracy.

Recently, an elliptical multipole wiggler was installed at the 6.5-GeV storage ring (AR) of TRISTAN complex, and intense circularly polarized 60-keV x rays with a brightness of 10^{13} photons/s.mm².0.1 b.w. became available⁸. The following is our first report on experimental observation of anisotropic negative spin polarization of 4s,p conduction electrons of ferromagnetic Ni.

Experimental

Circularly polarized 60-keV x rays monochromatized by a quasi-double-bent crystal array⁹ were focused on a specimen. The specimen was a single-crystalline Ni disk 12 mm in diameter and 2 mm in thickness. The crystal axes $\langle 100 \rangle$, $\langle 110 \rangle$, and $\langle 111 \rangle$ are at an angle of about 7° above the surface of the specimen, so that the scattering vector chosen is parallel to one of these crystal axes. The energy spectra of Compton-scattered x rays were measured by a conventional solid-state detector and an amplifier with a pile-up rejector. The overall momentum resolution was 1.0 a.u.

Results and Discussion

In Fig. 1 are shown the MCPs of ferromagnetic Ni. The directional profile along the $\langle 100 \rangle$ direction shows the deepest hollow around $p_z = 0$, indicating a large amount of negative spin polarization of s,p-like conduction electrons. The solid lines in Fig. 2 are the band-theoretical profiles calculated by the full-potential linearized augmented-plane-wave (FLAPW) method¹⁰. The present agreement between the experiment and theory shows that the FLAPW method gives better spin-dependent momentum distribution than a previous theoretical calculation¹¹, which was made by using a constant potential outside of the atomic potentials together with LCAO wave functions for 3d electrons and OPW wave functions for s,p-like electrons.

References

- 1) N. Sakai and K. Ono, Phys. Rev. Letters 37, 351(1976), J. Phys. Soc. Jpn. 42, 770(1977).
- 2) N. Sakai, and H. Sekizawa, Phys. Rev. B36, 2164(1987).
- 3) M. J. Cooper, S. P. Collins, D. N. Timms, A. Brahmia, P. P. Kane, R. S. Holt, and D. Laundy, Nature 333, 151(1988).
- 4) N. Sakai, H. Kawata, T. Iwazumi, M. Ito, N. Shiotani, F. Itoh, Y. Sakurai, S. Nanao, and M. Ando (these activity reports).
- 5) D. M. Mills, Phys. Rev. B36, 6178(1987).
- 6) N. Sakai, N. Shiotani, M. Ito, O. Mao, F. Itoh, T. Sugawa, H. Sakurai, Y. Sakurai, Y. Tanaka, S. Nanao, H. Kawata, T. Iwasumi, M. Ando, S. Yamamoto, H. Kitamura, K. Hyodo, and Y. Kitazima, The second annual meeting of the Japanese Society of Synchrotron Radiation Research(Setagaya, Tokyo), April,(1989).
- 7) M. Cooper, private communication.
- 8) S. Yamamoto, H. Kawata, H. Kitamura, M. Ando, N. Sakai, N. Shiotani, Phys. Rev. Letters 62, 2672(1989).
- 9) H. Kawata, T. Miyahara, S. Yamamoto, T. Shioya, H. Kitamura, S. Sato, S. Asaoka, N. Kanaya, A. Iida, A. Mikuni, M. Sato, T. Iwazumi, Y. Kitazima, and M. Ando, Rev. Sci. Instrum. 60, 1885(1989).
- 10) Y. Kubo, private communication.
- 11) P. Rennert, G. Carl, and W. Hergert, Phys. stat. sol. (b) 120, 273 (1983).

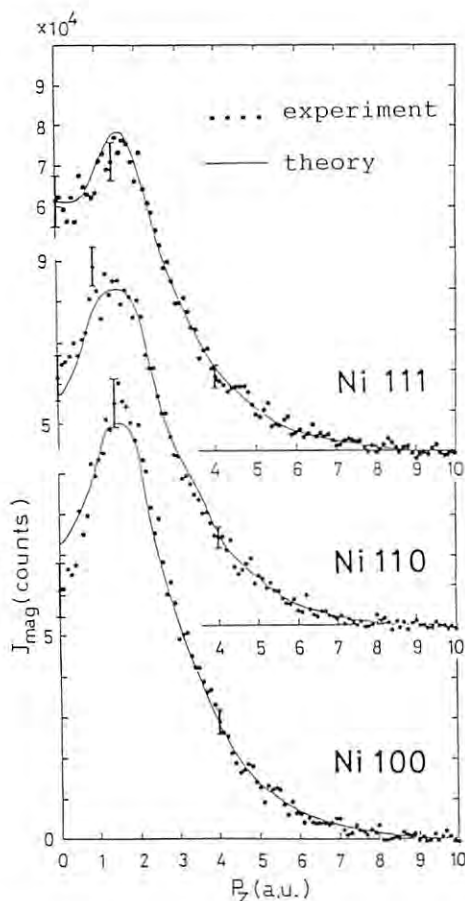


Fig. 1. Magnetic-electron Compton profiles of Ni.

IMPROVED MEASUREMENT OF MAGNETIC-ELECTRON COMPTON PROFILES OF FERROMAGNETIC Fe

Nobuhiko SAKAI, Hiroshi KAWATA⁺, Toshiaki IWAZUMI⁺, Masahisa ITO,
Nobuhiro SHIOTANI^{*}, Fumitake ITOH^{**}, Yoshiharu SAKURAI⁺⁺,
Susumu NANO⁺⁺, and Masami ANDO⁺

The Institute of Phys. and Chem. Research, Wako, Saitama 351-01.

⁺ Photon Factory, KEK, Oho, Tsukuba, Ibaraki 305.

^{*} Tokyo University of Fisheries, Minato, Tokyo 108.

^{**} Institute for Materials Research, Tohoku Univ., Sendai 980.

⁺⁺ Inst. of Industrial Science, The Univ. of Tokyo, Minato, Tokyo 106.

Introduction

Circularly polarized x rays interact with electron spins in the process of Compton scattering, and the scattering intensity becomes spin-dependent. At the same time, the energy distribution of Compton-scattered x rays reflects the momentum distribution of electrons, and yields the so-called Compton profile. Thus the Compton profile of circularly polarized x rays provides the information of magnetic-electron momentum distribution in ferromagnetic materials.

One of the difficulties in measuring a magnetic-electron Compton profile (MCP) had been a low count rate due to relatively low flux of circularly polarized photons^{1,2)}. Recently, this difficulty was largely overcome by an elliptical multipole wiggler installed at a 6.5 GeV storage ring of TRISTAN complex³⁾. A measured degree of circular polarization was 0.8 for 60-keV x rays emitted along the spiral orbital axis.

Experimental

Figure 1 shows the measured MCPs of magnetized Fe with extreme statistical accuracy. Two single crystal specimens of Fe with 3 % Si with dimensions of 9 x 20 x 0.15 mm³, and 20 x 20 x 0.2 mm³ were used. The crystal axes <100>, <110>, and <111> are in the surface of the specimen, and transmission geometry was adopted for the MCP measurement. The accumulation time was about 20 hrs. for each direction.

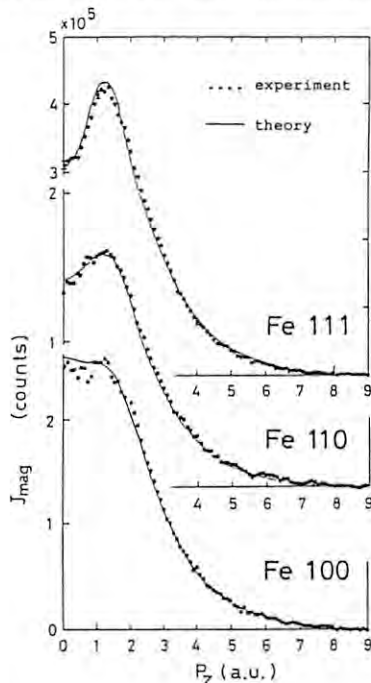


Fig. 1. Magnetic-electron Compton profiles of Fe measured by using 60-keV circularly polarized x-rays. The momentum resolution is 1.0 a.u.

Results and Discussion

The solid lines in Fig. 1 are band-theoretical profiles calculated by the full-potential-linearized augmented-plane-wave method (FLAPW)⁴⁾. An excellent agreement is obtained between the experiment and theory: It should be noted that no theoretical calculations have ever succeeded in getting correct profiles in the region $|p_z| < 2.0$ a.u., where appears the momentum distribution of the negative spin polarization of s,p-like conduction electrons. This result demonstrates that the careful band-theoretical calculation with suitable non-constant potentials in the region outside the atomic spheres can explain the momentum distribution of magnetic electrons in Fe.

The anisotropy in the magnetic-electron Compton profile between <100> and <111> direction is examined and shown in Fig. 2. Within the statistical accuracy, good agreement between the experiment and theory is found. The FLAPW calculation gives much better agreement than the previous APW calculation⁵⁾.

References

- 1) N. Sakai, and H. Sekizawa, Phys. Rev. B36, 2164(1988).
- 2) N. Sakai, N. Shiotani, M. Ito, F. Itoh, H. Kawata, Y. Amemiya, M. Ando, S. Yamamoto, and H. Kitamura, Rev. Sci. Instrum. 60, 1666(1989).
- 3) S. Yamamoto, H. Kawata, H. Kitamura, M. Ando, N. Sakai, and N. Shiotani, Phys. Rev. Letters 62, 2672(1989).
- 4) Y. Kubo, Private communication.
- 5) S. Wakoh, and Y. Kubo, J. Magn. Magn. Materials 5, 202(1977).

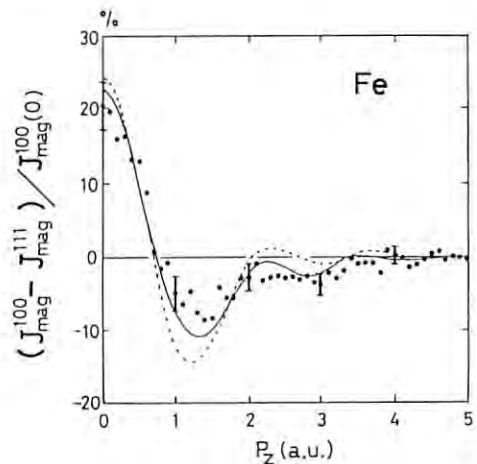


Fig. 2. Anisotropy of magnetic-electron Compton profile between Fe<100> and Fe<111> profile. The solid line shows the FLAPW anisotropy⁴⁾, and the dotted line the previous APW one⁵⁾.

HIGH RESOLUTION COMPTON SPECTROMATOR AT AR-NE1

Yoshiharu SAKURAI, Nobuhiro SHIOTANI*, Nobuhiko SAKAI**, Masahisa ITO**, Teruo URAI**, Fumitake ITOH⁺, Susumu NANA0, Toshiaki IWAZUMI⁺⁺, Hiroshi KAWATA⁺⁺ and Masami ANDO⁺⁺

Inst. of Industrial Science, University of Tokyo, Minato, Tokyo 106, Japan

* Tokyo University of Fisheries, Monato, Tokyo 108, Japan

** Inst. of Physical and Chemical Research, Wako, Saitama 351-01, Japan

+ Inst. for Materials Reserach, Tohoku University, Sendai 980, Japan

++ Photon Factory, National Laboratory for High Energy Physics, Tukuba, Ibaragi 305, Japan

Installation of a multipole wiggler¹ in the 6.5GeV AR and a quasi-double-bent monochotomator² in the NE1 beam line have enabled us to use intense linearly or elliptically polarized X-rays in the energy range from 50keV to 70keV. We reprot here a Compton spectromator designed for studies of electronic structures of metals and alloys both magnetic and non-magnetic. It has been known theoretically but not well established experimentally that a three-dimensional electron momentum distribution can be reconstructed from a group of Compton profiles which are measured along different crystalline directions. The characteristic feature of this spectromator is that we can measure four Compton profiles of different crystalline directions simultaneously. With this we can obtain twelve to sixteen profiles within a reasonable beam time.

A schematic view of the spectromator is shown in Fig.1. The system for analyzing the scattered X-rays consists of a Cauchois bent-crystal analyzer (Si 422) and an Imaging Plate or PSPC as a position sensitive detector. The scattering angle is fixed to 160 degrees. The

distance from a sample to a crystal analyzer is 500mm. The analyzer plate with 1.5mm in thickness is cut in a triangular shape so that the direction of Bragg diffracted X-rays having the Compton-peak energy (48.9keV) is normal to the surface of the analyzer plate. The plate is cylindrically bent to a radius of 2500mm. In order to improve the ratio of signal to back ground, a four-quadrant slit is placed in the path between the analyzer and the detector. The position of the slit is determined by analyzing the paths of signals from the sample to the detector through the analyzer. Figure 2 shows the results of the path analysis and the position of the slit. The slit minimamizes the amount of the X-rays which come from the analyzer without being energy-analyzed.

References

- (1) S.Yamamoto, H.Kawata, H.Kitamura, M.Ando, N.Sakai, N.Shiotani, Phys. Rev. Lett. **62**(1989)2672
- (2) H.Kawata, T.Miyahara, S.Yamamoto, T.Shioya, H.Kitamura, S.Sato, S.Asaoka, T.Iwazumi, Y.Kitazima and M.Ando, Rev. Sci, Instrum. **60**(1989)1885

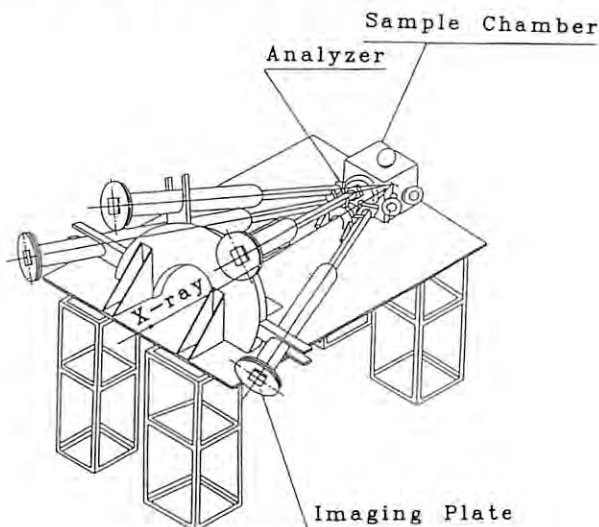


Fig. 1

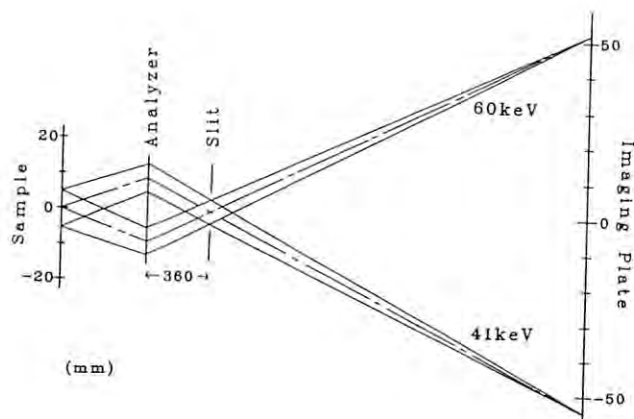


Fig. 2

STRUCTURE OF LIQUID GALLIUM UNDER PRESSURE

Kazuhiko TSUJI, Kenichi YAOITA, Motoharu IMAI, Osamu SHIMOMURA* and Hirohisa ENDO**

Department of Physics, Faculty of Science and Technology, Keio University, Yokohama 223

* National Institute for Research in Inorganic Materials, Tsukuba 305

**Department of Physics, Faculty of Science, Kyoto University, Kyoto 606

Introduction

There are three known stable phases of gallium¹⁾. The atmospheric-pressure phase, GaI has an orthorhombic structure consisting of a stacking of distorted hexagonal layers. Since the inter-layer bonds are much stouter than the intra-layer bonds, this structure can be assumed to consist of Ga_2 molecules. The phase behavior of gallium has been a subject of some confusion because of the capricious appearance of metastable phases. However, a face-centered tetragonal (fct) structure which is identical to the indium's has been proposed for a high-pressure phase (GaII or GaIII) by several investigators²⁻⁴⁾.

The melting point of GaI descends with increasing pressure. A two-species model⁵⁾ was proposed to interpret such negative slope of melting curve. According to this model, liquid consists of high- and low-pressure solid phases, gradually changing the concentration with pressure. Thus this model suggests that high-pressure solid phase can be found in liquid at pressure lower than the transition pressure. This can be tested by measuring diffraction for liquid varying pressure.

Previously we reported the structure factor $S(Q)$ of liquid gallium under various pressures⁶⁾. We report here some newly investigated results derived by further data analysis.

Experimental

The experiment was carried out using a cubic-type high-pressure apparatus MAX80, settled at AR. Details of the experiment and data analysis are described elsewhere⁷⁾.

Results and Discussion

The structure factor $S(Q)$ for liquid gallium was obtained at various pressures, which suggests that there was the high-pressure phase (fct) in liquid state at lower pressure than the transition pressure^{6,7)}. The subpeak appeared at the high- Q side of the principal peak of $S(Q)$ shifted toward the principal peak with raising pressure so that c/a ratio of the corresponding fct structure decreased toward unity, that of fcc. This is in contrast with the result for liquid bismuth⁸⁾, whose subpeak of $S(Q)$ shifted toward opposite direction.

Using Fourier transformation, pair distribution function $g(r)$ was derived from $S(Q)$ and plotted in Fig. 1. And Fig. 2 shows the first coordination number N_1 and the first coordination distance r_1 estimated from $g(r)$, versus pressure. With increasing pressure, N_1 increases and r_1 decreases. Being satisfactory for a result of compression, however, this is also in contrast with the result for liquid bismuth, whose r_1 does not change with pressure^{9,10)}.

References

- 1) A. Jayaraman, W. Klement, Jr., R. C. Newton and G. C. Kennedy, *J. Phys. Chem. Solids*, **24**, 7

- (1963).
- 2) L. F. Vereshchagin, S. S. Kabalkina and Z. V. Troitskaya, *Dokl. Akad. Nauk. SSSR*, **158**, 1061 (1964) [*Sov. Phys.-Dokl.*, **9**, 894 (1965)].
- 3) C. E. Weir, G. J. Piermarini and S. Block, *J. Chem. Phys.*, **54**, 2768 (1971).
- 4) L. Bosio, *J. Chem. Phys.*, **68**, 1221 (1978).
- 5) E. Rapoport, *J. Chem. Phys.*, **46**, 2891 (1967).
- 6) K. Tsuji, K. Yaoita, M. Imai, O. Endo, O. Shimomura and H. Endo, *PF Activity Rep.*, **6**, 205 (1988).
- 7) K. Tsuji, K. Yaoita, M. Imai, O. Shimomura and T. Kikegawa, *Rev. Sci. Instrum.*, **60**, 2425 (1989).
- 8) K. Yaoita, K. Tsuji, M. Imai, T. Kikegawa and O. Shimomura, *High-Press. Res.*, (to be published).
- 9) K. Tsuji, K. Yaoita, M. Imai, T. Mitamura, T. Kikegawa and O. Shimomura, (this volume).
- 10) K. Tsuji, *J. Non-Crys. Sol.*, (to be published).

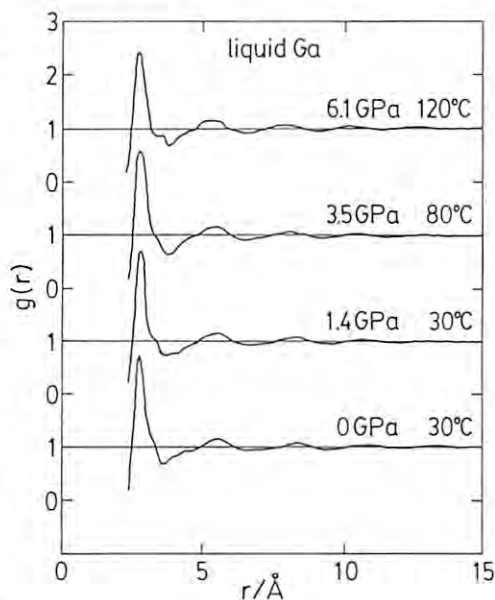


Fig. 1.

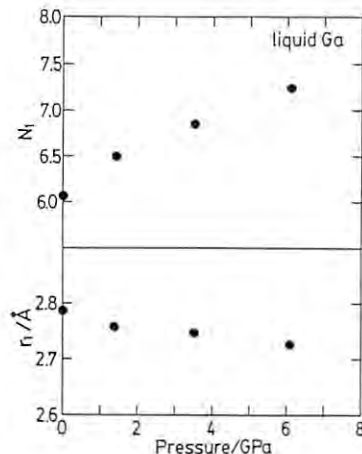


Fig. 2.

STRUCTURE OF LIQUID BISMUTH UNDER PRESSURE

Kazuhiko TSUJI, Kenichi YAOITA, Motoharu IMAI, Takeshi MITAMURA,
Takumi KIKEGAWA* and Osamu SHIMOMURA**

Department of Physics, Faculty of Science and Technology, Keio University, Yokohama 223

* Photon Factory, National Laboratory for High Energy Physics, Tsukuba 305

** National Institute for Research in Inorganic Materials, Tsukuba 305

Introduction

Bismuth tends to crystallize in structures related to simple cubic structure since the bonds between bismuth atoms are formed mainly by *p*-electrons spread along *x*-, *y*- and *z*-directions. In fact, Bi I and Bi II¹⁾ have a rhombohedral and a monoclinic structure, respectively, both of which can be regarded as distorted simple cubic structures. Under sufficiently high pressures, however, bismuth crystallizes in a bcc structure (Bi V) which is no longer simple-cubic related. Structures of intermediate-pressure phases (Bi III and Bi IV) are not known, though diffraction measurements have been done^{2, 3, 4)}, which have yielded very complicated patterns. As solid bismuth shows so many pressure-induced phase transitions, it is interesting to see the behavior of structure of liquid bismuth with varying pressure.

Melting temperature of Bi I decreases with increasing pressure. A two-species model⁵⁾ was proposed to explain such negative slope of melting curve. This model assumes liquid as a mixture of high- and low-pressure solid phases. Thus existence of high-pressure phase at pressure lower than the transition pressure of solid is predicted. The propriety of this model can be tested by measuring diffraction for liquid under high pressures. Here lies the second reason why the structure of liquid bismuth under high pressure is of interest.

Experimental

The high pressure experiment was carried out using MAX80, a cubic-type high-pressure apparatus. Details of experiment and data analysis are described elsewhere⁶⁾.

Results and Discussion

Fig. 1 shows obtained structure factor $S(Q)$ for liquid bismuth at various pressures⁷⁾. At

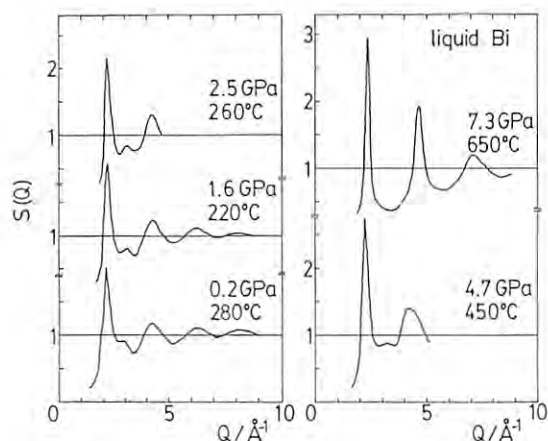


Fig. 1.

pressures below 4.7 GPa $S(Q)$ shows a subpeak at high- Q side of the principal peak. The position of the subpeak is same as that of some diffraction peaks of Bi II, Bi III or Bi IV, while there is no significant peak of Bi I on that position. This is consistent with the prediction of the two-species model.

Fig. 2 shows pair distribution function $g(r)$ below 4.7 GPa derived from Fourier transformation of $S(Q)$, and the first coordination number N_1 and the first coordination distance r_1 estimated from $g(r)$ are plotted in Fig. 3. While N_1 increases with pressure, r_1 seems almost constant. This is in contrast with the result for liquid gallium⁸⁾, whose r_1 decreases with pressure.

The $S(Q)$ at 7.3 GPa shows a pattern totally different from ones at lower pressures. It has extremely high peaks and no subpeak. It should be noticed that the peak positions of this pattern does not satisfy the pattern for bcc, which is the structure of Bi V.

References

- 1) R. M. Brugger, R. B. Bennion and T. G. Worlton, *Phys. Lett.*, **24A**, 714 (1967).
- 2) V. K. Fedotov, E. G. Ponyatovskii, V. A. Somenkov and S. Sh. Shil'shtein, *Sov. Phys. Solid State*, **20**, 628 (1978).
- 3) K. Tsuji, K. Yaoita, M. Imai, O. Endo, T. Kikegawa and O. Shimomura, *PF Activity Rep.*, **6**, 206 (1988).
- 4) K. Tsuji, *J. Non-Crys. Sol.*, (to be published).
- 5) E. Rapoport, *J. Chem. Phys.*, **46**, 2891 (1967).
- 6) K. Tsuji, K. Yaoita, M. Imai, O. Shimomura and T. Kikegawa, *Rev. Sci. Instrum.*, **60**, 2425 (1989).
- 7) K. Yaoita, K. Tsuji, M. Imai, T. Kikegawa and O. Shimomura, *High-Press. Res.*, (to be published).
- 8) K. Tsuji, K. Yaoita, M. Imai, O. Shimomura and H. Endo, (this volume).

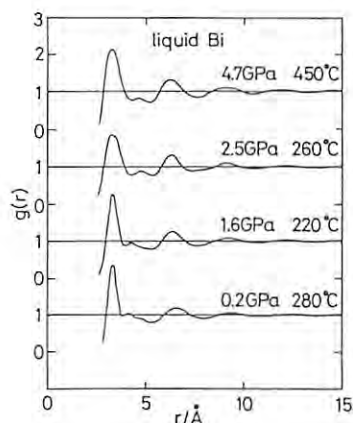


Fig. 2.

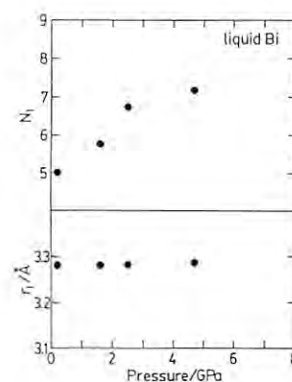


Fig. 3.

STRUCTURE OF LIQUID CESIUM UNDER PRESSURE

Kazuhiko TSUJI, Kenichi YAOITA, Motoharu IMAI, Takeshi MITAMURA,
Takumi KIKEGAWA*, Osamu SHIMOMURA** and Hirohisa ENDO***

Department of Physics, Faculty of Science and Technology, Keio University, Yokohama 223

* Photon Factory, National Laboratory for High Energy Physics, Tsukuba 305

** National Institute for Research in Inorganic Materials, Tsukuba 305

***Department of Physics, Faculty of Science, Kyoto University, Kyoto 606

Introduction

As the compressibility of cesium is very large ($V/V_0 = 0.4$ at 4.3 GPa), the electron number density n increases remarkably with compression. This increase in n changes the screening length and the Fermi level. Moreover, it causes an electronic transition from $6s$ - to $5d$ -band. These changes in the electronic structure reflect on the ion-ion pair potential $\phi(r)$, and consequently, on the atomic structure.

There are two maxima in the pressure dependence of the melting point of cesium. Melting-curve maximum has been discussed in terms of a two-species model^{1,2)}. This model assumes liquid phase as a mixture of high- and low-density phases. If the high-density phase is realized as a high-pressure solid phase, a similar structure, on a short range order basis, can appear in the liquid at pressures lower than the transition pressure of solid. Isoconcentration lines in the p - T plane were constructed for liquid cesium²⁾, which proposed a sudden change in liquid state at pressure around 3 GPa.

The aim of this work is to measure x-ray diffraction for liquid cesium under high pressure to get information about the pressure-induced structural change predicted from these two points of view, viz., from the electronic transition and from the two-species model.

Experimental

The experiment was carried out using MAX80, a cubic-type high-pressure apparatus set at a bending-magnet beam line on AR. The experiment and data analysis were done in previously described way^{3,4)}. As cesium was chemically reactive, the sample container had to be made by Teflon, and construction of the sample assembly had to be done in Silicone oil to prevent oxidation of the sample.

Results and Discussion

Obtained structure factor $S(Q)$ and pair distribution function $g(r)$ are shown in Figs. 1

and 2, respectively. The height of the first peak of $S(Q)$ increases with compression below 2.9 GPa, then decreases between 2.9 GPa and 4.3 GPa. The width of the first peak of $g(r)$ also shows a pressure dependence with an abnormality at pressure between 2.9 GPa and 4.3 GPa. This abnormality can be clearly seen in Fig. 3 which shows the first coordination number N_1 and the first coordination distance r_1 derived from Fig. 2. N_1 shows a sharp drop at pressure between 2.9 GPa and 4.3 GPa.

At 2.9 GPa, r_1 shows a value larger than expected from a continuous compression. It should be noticed that the two-species model predicts an abrupt change around this pressure²⁾. As a phase transition of solid cesium at 2.3 GPa is associated with increase in the atomic radius⁵⁾, the abnormality of r_1 can also be interpreted as a result of similar transition occurred in liquid state. If this interpretation is realistic, N_1 should increase at the transition since the transition in solid is from bcc to fcc. In fact, broadened high- r side of the first peak of $g(r)$ taken into account, N_1 shows a peak at 2.9 GPa⁶⁾.

Thus it is concluded that liquid cesium has two abrupt pressure-induced structural changes: one at about 2 GPa corresponding to the bcc-fcc transition or the abrupt concentration change of the high-pressure species, and the other at pressure between 3 GPa and 4 GPa possibly caused by the electronic transition.

References

- 1) E. Rapoport, J. Chem. Phys., **46**, 2891 (1967).
- 2) E. Rapoport, J. Chem. Phys., **48**, 1433 (1968).
- 3) K. Tsuji, K. Yaoita, M. Imai, O. Shimomura and T. Kikegawa, Rev. Sci. Instrum., **60**, 2425 (1989).
- 4) K. Tsuji, J. Non-Crys. Sol., (to be published).
- 5) H. T. Hall, L. Merrill and J. D. Barnett, Science, **146**, 1297 (1964).
- 6) K. Tsuji, K. Yaoita, M. Imai, T. Mitamura, T. Kikegawa, O. Shimomura and H. Endo, J. Non-Cryst. Sol., (to be published).

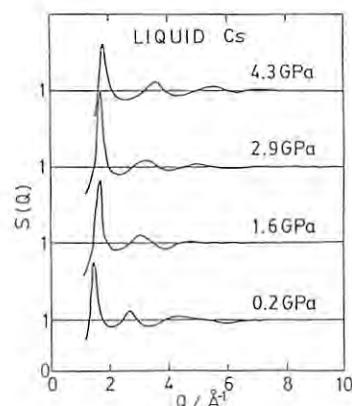


Fig. 1.

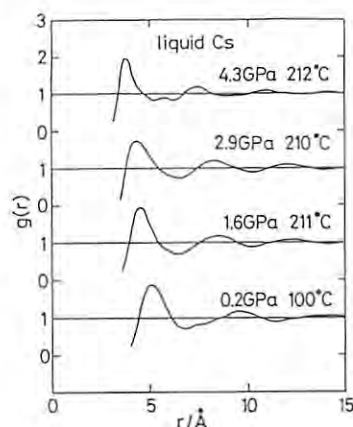


Fig. 2.

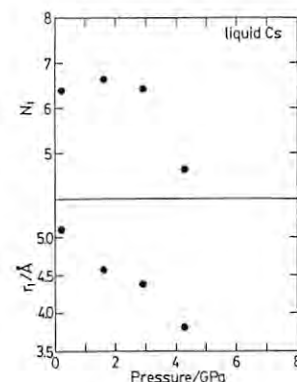


Fig. 3.

PICOSECOND SYNCHROTRON RADIATION PULSE RADIOLYSIS

Seiichi TAGAWA, Hiromi SHIBATA, Yoichi YOSHIDA*, Side YAO, Atsushi OGATA**,
Ken'ichi KANAZAWA**, Kenji ITO**, and Noriyuki KOUCHI***

Research Center for Nuclear Science and Technology, The University of Tokyo,
Tokai-mura, Ibaraki 319-11

* Nuclear Engineering Research Laboratory, The University of Tokyo,
Tokai-mura, Ibaraki 319-11

** National Laboratory for High Energy Physics, Tsukuba, Ibaraki 305

***Tokyo Institute of Technology, Meguro-ku, Tokyo 152

INTRODUCTION

When ionizing radiation interacts with matter, short-lived reactive intermediates such as electrons, ions, excited states and radicals are produced in the matter. Reactions of these intermediates are so complicated that the elucidation of detailed formation mechanisms of final radiolytic products is formidably difficult without the direct observation of reactive intermediates.

A pulse radiolysis technique, which can directly measure reactive intermediates, is very powerful method for studies on the primary processes of the radiolysis. In this method, the reactive intermediates are generated by the pulsive radiation, and their time-dependent behavior is observed and analyzed spectroscopically.

Recently picosecond phenomena in radiolysis of aqueous solutions, organic molecules and polymers using electron pulse radiolysis, and the primary processes of LET effects (excitation density effects) using ion beam pulse radiolysis have been investigated extensively. The first picosecond synchrotron radiation pulse radiolysis is starting for studies on above materials, and we intend to compare with these results and to clarify the differences of effects between excitation sources.

EXPERIMENTAL

The picosecond synchrotron radiation pulse radiolysis experiments have been started at the NE9 beam line of the Accumulation Ring of the TRISTAN accelerator. The SR pulse width (FWHM) is below 150 psec and the time separation between neighboring bunches is 1.25 usec. The X-ray pulse from the AR was introduced to a target sample through a lmm-thick Be window without a monochromator.

The UV emission from liquid or solid sample was detected by a photomultiplier (PMT) with multi-channel plates (MCP) (Hamamatsu photonics, R2809U-02), whose rise time was about 150 psec, combined with a band pass filter. The time-dependent signal from PMT was observed by an oscilloscope (Tektronix 11403 1GHz digitizing oscilloscope or 7854 oscilloscope with S-6 sampling head).

RESULTS AND DISCUSSION

Fig. 1 shows a typical time-behavior of the fluorescence from liquid n-dodecane after a SR pulse irradiation. The rise time of the fluorescence was equal to the time resolution of the detection system, and the decay was 3.6 nsec. This value was smaller than the results obtained by electron pulse radiolysis (4.3nsec).

The formation processes of excited states in n-alkanes, which are mostly the geminate ion recombination and partially direct excitation, complete within the time resolution of the detection system of our SR pulse radiolysis.

In the case of low-LET radiation, such as high energy electron beam, the ionization and excitation take place in a localized spatial region (so-called "spur"). On the other hand, the excitation energy in this experiment is from 5 to 20 keV. Therefore, as the spur may be overlapped by the comparably high LET effect, the interaction between the excited states may shorten the lifetime of the fluorescence. This speculation is agreement with the lifetime of 2.7 nsec obtained by the irradiation of high LET ion beam.

REFERENCES

- 1) A.Ogata and S.Tagawa,
Rev. Sci. Instrum., **60**, 2197 (1989).

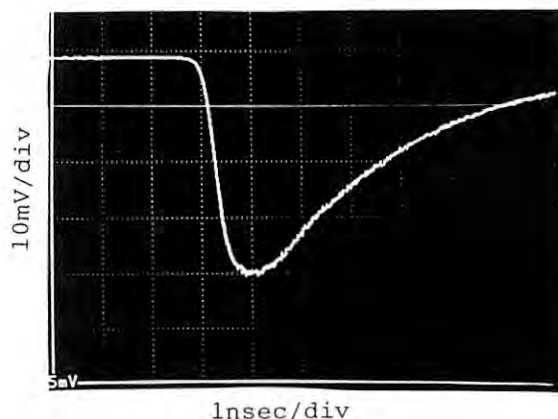


Fig.1 Typical time-behavior of the fluorescence from liquid n-dodecane after the SR pulse irradiation.

PHOTOELECTRON SPECTROSCOPY OF RbF- AND LiF-COVERED GaAs(100) SURFACES

Ruth KLAUSER*, Masakazu KUBOTA and Yoshitada MURATA
 The Institute for Solid State Physics, The University of Tokyo,
 Roppongi, Minato-ku, Tokyo 180, Japan
 Masaharu OSHIMA, Yasuko YAMADA MARUO, Tomoaki KAWAMURA and
 Tsuneaki MIYAHARA** NTT Laboratories, Musashino, Tokyo 180, Japan
 ** KEK Photon Factory, Tsukuba 305, Japan
 * present address: NTT Laboratories, Musashino, Tokyo 180, Japan

Introduction

RbF and LiF are among the alkali fluorides those with the smallest (0.2%) and the largest (28.8%) lattice mismatch to the GaAs-lattice. Lattice matching plays an important role in the discussion about epitaxial growth and the quality of the interface. We studied the interface properties of RbF/GaAs(100) and LiF/GaAs(100) against annealing temperature and deposition thickness and compared the results with our previous investigations of NaF and KF on the same surface^{1,2}.

Experimental

Photoemission experiments were performed at BL-1A of the Photon Factory. Angle-integrated spectra were taken at a photon energy of 115.4 eV. X-ray photoelectron spectra and low-energy electron diffraction (LEED) were additionally monitored. We used Ar⁺-sputtered and annealed GaAs(100) wafer surface. RbF and LiF powders were evaporated from tungsten basket.

Results and Discussion

Fig. 1 and 2 show the surface-sensitive F2p peak for the interfaces RbF/GaAs and LiF/GaAs, respectively. In the case of RbF on GaAs the F2p peak is for monolayer deposition centered at 8.7 eV binding energy (BE). At higher BE the Rb4p peak at 16.1 eV appears. Annealing the sample a second F2p peak at 2.3 eV to lower BE is observed and increases with increasing temperature. For the same sequence the Ga3d peak shows a shoulder to higher BE. This shoulder is

getting more distinct also with increasing annealing temperature. From these results and from the fact that the LEED pattern for the whole sequence is 4x1, which is the same as that for the clean surface, we conclude the formation of Ga-F bonds at the interface. Since the lattice constants of RbF and GaAs crystal are almost the same, RbF lattice can be easily commensurate with and epitaxially grown onto GaAs(100). At the interface the F atom couples with the dangling bonds of two Ga atoms and the RbF(100) surface is prepared.

In the case of LiF the F2p spectra of monolayer and multilayer (fig. 2A and C) deposition show the typical double peak structure of LiF-lattice deposition. After annealing the sample the LEED pattern changes from a very diffuse 4x1 into a sharp 2x1 pattern and again a second peak at 3.5 eV lower BE than the F2p appears. Further annealing causes a preferential desorption of fluorine whereas Li atoms remain on the surface. We assume that during the annealing process LiF partially dissociates and a reconstruction of the GaAs surface is induced³.

References

- 1) R. Klauser et al., PF Activity Report, No.6, 226(1988).
- 2) R. Klauser et al., Surf.Sci. **211/212**, 759 (1989).
- 3) R. Klauser et al., Phys.Rev.B Vol.**40**(5), 3301 (1989).

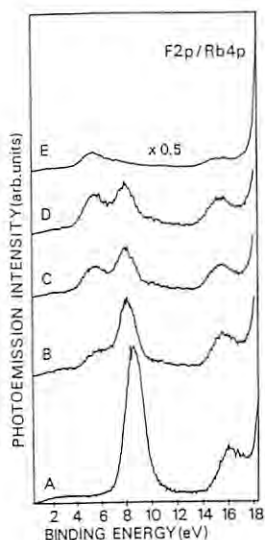


FIG. 1. Photoelectron spectra from F2p and Rb4p core levels of RbF on GaAs(100). (A) Monolayer deposition. (B)-(E) After annealing the initial monolayer deposition up to 200, 250, 300, and 350°C; a second F2p peak at lower BE appears and the intensity increases with increasing annealing temperatures. For all spectra a 4x1 LEED pattern was observed, which is the same for the clean surface.

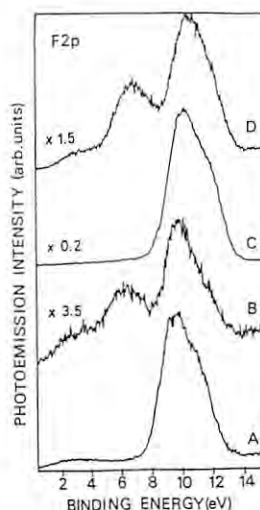


FIG. 2. Photoelectron spectra from the F2p core level of LiF on GaAs(100). (A) Monolayer deposition. (B) After annealing the initial monolayer deposition up to 400°C. (C) Multilayer deposition. (D) After annealing the initial multilayer deposition up to 400°C.

DYNAMICAL X-RAY DIFFRACTION IN BACKREFLECTION GEOMETRIES AND ITS APPLICATION TO THE REGISTRY OF OVERLAYER ATOMS

H. Hashizume, T. Nakahata, O. Sakata, H. Sakuma

M. Oshima*, T. Kawamura*, S. Maeyama*, Y. Maruo*, F. Maeda* and H. Takenaka*

Research Laboratory of Engineering Materials, Tokyo Institute of Technology, Yokohama 227

* NTT Applied Electronics Laboratories, Midori-cho, Musashino, Tokyo 186

X-ray diffraction in backreflection geometries are highly insensitive to mosaic structures in the diffracting crystal. Although discovered in early 1970s [1], this property has never been given adequate experimental confirmations nor found useful applications until recently. The lack of a bright, tunable X-ray source has prohibited careful experiments. Also, no practical means was found to detect and measure reflected X-rays at near 180° scattering angles without blocking the primary beam. These difficulties are removed on BL-1A, where a UHV compatible InSb crystal monochromator delivers high-intensity photons in the 2500-4000 eV range from a bending magnet source [2].

A simple but direct way of demonstrating the predicted high insensitivity is to observe diffraction profiles from crystals with different mosaicities [3]. Experiments were carried out on Cu(111) crystals with 1.2° and 0.4° mosaic spreads by scanning the photon energy in the vicinity of 2970 eV for fixed near-normal directions of the incident beam on the sample. A photoemissive grid allowed the incoming and backreflected X-rays to pass through and thereby be measured simultaneously. Very similar near-Gaussian profiles were observed from the two crystals at normal incidence angles. Their nearly equal widths were dominated by the photon energy resolution of BL-1A, which was found to be 2.1 eV (FWHM) at 3 keV. On the other hand, the two crystals showed distinct behaviors at off-normal angles. While profile widths, ΔE_p ,

observed from the 0.4° -mosaic crystal remained virtually unchanged when the off-normal angle was increased up to 3° , the 1.2° -mosaic crystal showed ΔE_p 's markedly dependent on off-normal angle (Fig.1). The different rates of insensitivity loss with increasing off-normal angles are in quantitative agreement with the prediction of dynamical diffraction theory [4].

The backreflection geometry has a unique advantage in the application of the X-ray standing-wave technique to surfaces other than semiconductors. The high mosaic insensitivity removes the demanding requirement of a high degree of crystalline perfection in the sample [5]. Coupled with an improved beamline energy resolution, this technique allows routine data collection from various Bragg planes for the study of atom registry at substrate-overlayer interfaces [6].

References

- [1] K. Kohra et al.: Z. Naturforsch. 27a, 484 (1972).
- [2] T. Kawamura et al.: Rev. Sci. Instrum. 60, 1928 (1989).
- [3] T. Nakahata et al.: Jpn. J. Appl. Phys. 28, L1300 (1989).
- [4] H. Hashizume et al.: Jpn. J. Appl. Phys. 27, L1568 (1988).
- [5] D.P. Woodruff et al.: Phys. Rev. Lett. 58, 1460 (1987).
- [6] P.L. Cowan et al.: Submitted to 1989 NSLS annual report.

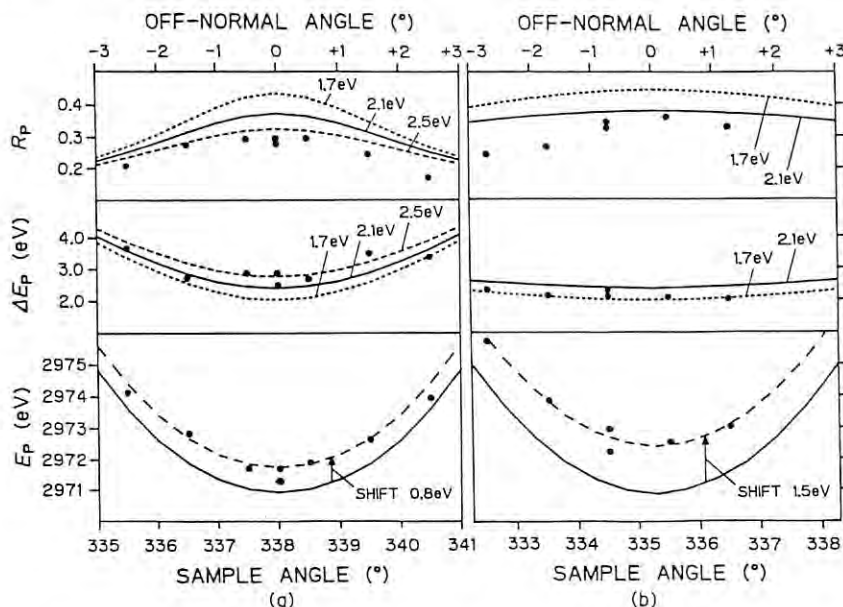


Fig.1 Peak position, E_p , peak widths (FWHM), ΔE_p and peak reflectivities, R_p of diffraction curves observed from Cu(111) crystals with mosaic spreads of 1.2° (a) and 0.4° (b) (data points), compared with calculations assuming the indicated photon energy resolutions (lines). Taken from [4].

Photoelectron Emission Study on $(\text{NH}_4)_2\text{S}_x$ -treated GaAs

Yasuo NANNICHI, Hidemi SHIGEKAWA, Haruhiro OOIGAWA, NIE Heng Yong,
Tadashi FUKASE, Yasushi KURATA, Masaharu OSHIMA*, Hirohiko SUGAHARA*,
and Tomoaki KAWAMURA*

Institute of Materials Science, University of Tsukuba, Ibaraki 305
*NTT Applied Electronics Laboratories, Musashino 180

INTRODUCTION

The surface/interface of GaAs has long been uncontrollable with the state density on the order of $10^{13}(\text{cm}^{-2})$ until we successfully reduced it down to 1×10^{11} by means of sulfur treatment¹⁾. There arises an interesting question on the bonds of surface/interface atoms, and the synchrotron radiation photoemission is the exact means to obtain the information needed.

EXPERIMENTAL

Chemically-mechanically polished surface of GaAs was etched and rinsed before dipped into the solution of $(\text{NH}_4)_2\text{S}_x$, $1 < x < 3$, at 60 C for 2 hours. The sample was kept in rough vacuum for a few tens of minutes so as not to contaminate the measuring system at BL-1A, with sublimating sulfur.

For the photon energy of 209.4 eV, photoemission spectra of Ga3d, As3d, and S2p were measured in respect to the effect of the sulfide treatment. Also measured were those of Al2p during the aluminum Schottky barrier formation.

Results and Discussions

Figure 1 shows the As3d spectra on various surfaces. On Na_2S -treated surface is seen the presence of oxygen, while the $(\text{NH}_4)_2\text{S}_x$ -treated surface is free from oxygen.

Gallium, arsenic and sulfur bonds were observed to change with heat-treatment at 360 C as shown in Fig. 2. Before heating, As-S bonds dominate over Ga-S bonds and S-S signal is also observable. But after heating the Ga-S bond becomes dominant, while As-S and

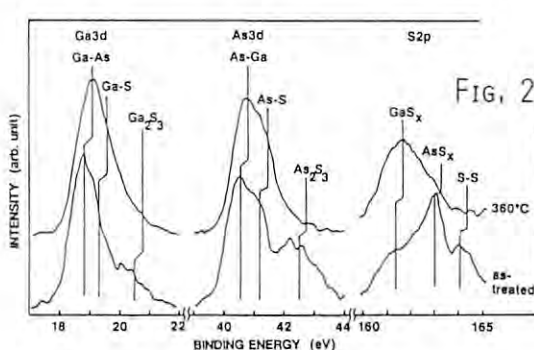
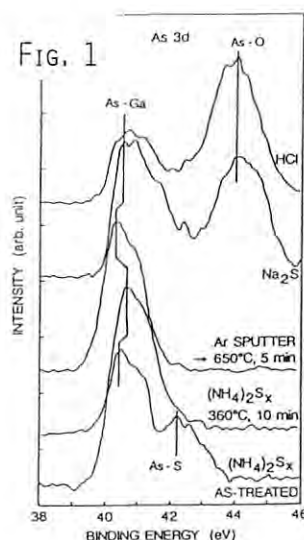
S-S bonds disappear. This is the result corresponding to the previous data²⁾ that the heat treatment brings about the surface reconstruction and that sulfur adatoms are more heat-resistant on (111)A than on (111)B plane. Switching the bonds is observed when atomic layer of aluminum is evaporated onto the $(\text{NH}_4)_2\text{S}_x$ - and heat-treated GaAs. Figure 3 shows the build-up of Al-S signal which is eventually buried with the accumulation of Al layer. This is a very important information, in that S adatoms are not easily lost on the deposition of foreign atoms to form an interface. This is in good supporting accordance with our previous observation that both in the MIS¹⁾ and MS²⁾ structures the surface trap density of GaAs at the interface is considerably reduced by the $(\text{NH}_4)_2\text{S}_x$ treatment.

We also observed the surface band bending with the deposition of sub-atomic layer of metals. However, the discussions on band bending should be done with a good reference data on the ideally cleaved surface which remains unsuccessful.

The intensive experiment with synchrotron radiation, though time-limited, supplied valuable evidences supporting the previous hypotheses⁴⁾ on the effect of sulfur treatment.

References

- 1) J. F. Fan et al., J. J. Appl. Phys., **27**, L1331 (1988)
- 2) H. Oigawa et al., *ibid.*, **28**, L340 (1989)
- 3) J. F. Fan et al., *ibid.*, **27**, L2125 (1988)
- 4) Y. Nannichi et al., *ibid.*, **27**, L2367 (1988)

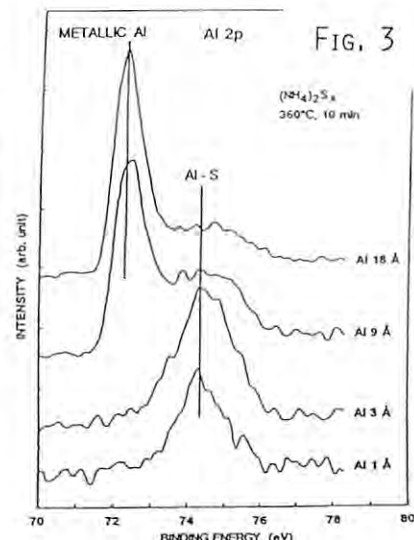


Photoelectron Spectra ($E_p = 209.4 \text{ eV}$):

Fig. 1. $(\text{NH}_4)_2\text{S}_x$ -treatment effect on As-O.

Fig. 2. Changes in the bonds by heat-treatment.

Fig. 3. Al-S bond formation on Al deposition.



PHOTOEMISSION ANALYSIS FOR $(\text{NH}_4)_2\text{S}_x$ -TREATED GaAs WITH A PHOTON ENERGY OF 80 eV

Hirohiko SUGAHARA, Masaharu OSHIMA, Haruhiro OIGAWA,* Hidemi SHIGEKAWA,* and Yasuo NANNICHI*

NTT Applied Electronics Laboratories, 3-9-11 Midori-cho, Musashino-shi, Tokyo 180

* Institute of Materials Science, University of Tsukuba, Tsukuba, Ibaraki 305

Introduction

Chemistry of $(\text{NH}_4)_2\text{S}_x$ -treated GaAs surfaces and metal/ $(\text{NH}_4)_2\text{S}_x$ -treated GaAs interfaces has been investigated with great interest, because the surface state density is dramatically reduced by the $(\text{NH}_4)_2\text{S}_x$ treatment.¹⁾ We have found that Ga-S and Al-S bonds play an important role for $(\text{NH}_4)_2\text{S}_x$ -treated n-GaAs surfaces by using synchrotron radiation with a photon energy of about 210 eV.^{2,3)} We have also analyzed the In/ $(\text{NH}_4)_2\text{S}_x$ -treated n-GaAs interfaces and $(\text{NH}_4)_2\text{S}_x$ -treated p-GaAs surfaces, adjusting the photon energy to 80 eV to minimize the escape depth of Ga3d, As3d, and In4d core electrons. In this report, the chemistry and band bending of these systems are discussed.

Experimental

All of the experiments described here were carried out at BL-1A. The photon energy was adjusted to 80 eV by using the grating/crystal monochromator.⁴⁾ Ga3d and As3d photoemission spectra for $(\text{NH}_4)_2\text{S}_x$ -treated n- and p-GaAs were measured before and after annealing at 360°C for 10 min in vacuum. In4d spectra were also measured after monolayer-order In deposition.

Results and Discussion

As3d photoemission spectra for $(\text{NH}_4)_2\text{S}_x$ -treated n-GaAs are shown in Fig. 1. The As-Ga main peak energy for as-treated n-GaAs (100) is about 0.4 eV lower than that for cleaved n-GaAs (110), indicating the upward band bending of as-treated GaAs. The band bending is relaxed by annealing in vacuum and also by monolayer-order In deposition, which corresponds to the relatively low (i.e.; metal work function-dependent) barrier height of the In/ $(\text{NH}_4)_2\text{S}_x$ -treated n-GaAs Schottky contacts.⁵⁾

Figure 2 shows As3d photoemission spectra for $(\text{NH}_4)_2\text{S}_x$ -treated p-GaAs. It is obvious that As-S bonds are broken by annealing at 360°C in vacuum, suggesting that the chemistry of the $(\text{NH}_4)_2\text{S}_x$ -treated GaAs surfaces does not depend on the carrier type except that a small amount of As-O bonds exist on p-GaAs surfaces. A peak shift of about 0.4 eV toward higher binding energy is observed after annealing, which indicates that the downward band bending is enhanced by annealing. The mechanism of this change is not clearly understood at present.

In summary, It is found that the band bending relaxation is occurred for $(\text{NH}_4)_2\text{S}_x$ -treated n-GaAs by monolayer-order In deposition and that the downward band bending is enhanced for $(\text{NH}_4)_2\text{S}_x$ -treated p-GaAs by annealing at 360°C in vacuum. The results can be explained by our previous work for n-GaAs, however further investigation is necessary for p-GaAs.

References

- 1) J. Fan *et al.*, Jpn. J. Appl. Phys. **27**(7), L1331 (1988).
- 2) H. Sugahara *et al.*, "Extended Abstracts of the 21st Conference on SSDM" (Tokyo, 1989) p.547.

- 3) Y. Nannichi *et al.*, "PF Activity Report 1989".
- 4) T. Kawamura *et al.*, Rev. Sci. Instrum. **60**(7), 1928 (1988).
- 5) H. Oigawa *et al.* (unpublished).

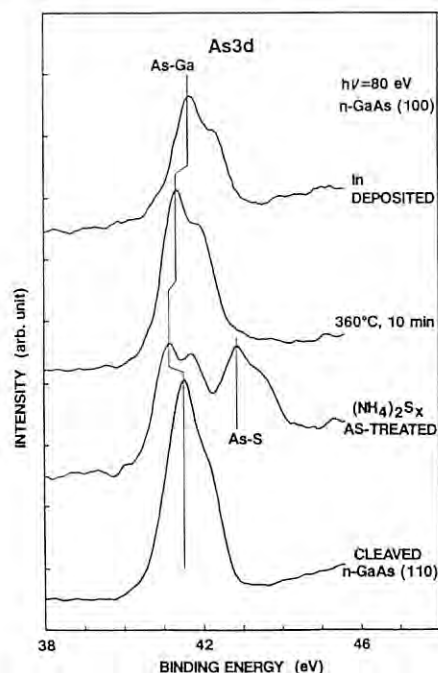


Fig. 1. As3d photoemission spectra for $(\text{NH}_4)_2\text{S}_x$ -treated n-GaAs.

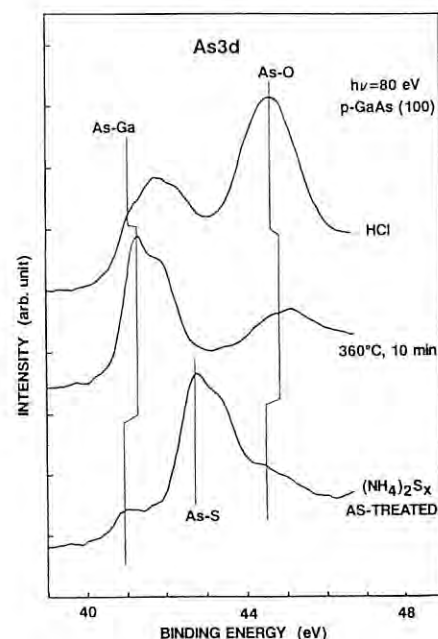


Fig. 2. As3d photoemission spectra for $(\text{NH}_4)_2\text{S}_x$ -treated p-GaAs.

INITIAL STAGE OF Au SCHOTTKY BARRIER FORMATION ON $(\text{NH}_4)_2\text{S}_x$ -TREATED n-GaAs

Hirohiko SUGAHARA, Masaharu OSHIMA, Haruhiro OIGAWA,* Hidemi SHIGEKAWA,* and Yasuo NANNICHI*

NTT Applied Electronics Laboratories, 3-9-11 Midori-cho, Musashino-shi, Tokyo 180

* Institute of Materials Science, University of Tsukuba, Tsukuba, Ibaraki 305

Introduction

Shottky barrier heights of metal/ $(\text{NH}_4)_2\text{S}_x$ -treated GaAs diodes are reported to be dependent on the metal work function.¹⁾ We found that $(\text{NH}_4)_2\text{S}_x$ -treated GaAs surfaces are terminated by Ga-S bonds after annealing at 360°C in vacuum and that Al-S bonds are formed at Al/ $(\text{NH}_4)_2\text{S}_x$ -treated GaAs interfaces.^{2),3)} In this report, the initial stage of Au Schottky barrier formation on $(\text{NH}_4)_2\text{S}_x$ -treated GaAs is discussed comparing with the Al/ $(\text{NH}_4)_2\text{S}_x$ -treated GaAs system.

Experimental

Photoemission spectra of Ga3d, As3d, S2p, and Au4f for the Au/ $(\text{NH}_4)_2\text{S}_x$ -treated n-GaAs system were measured before and after monolayer-order Au deposition at BL-1A. Photon energy was adjusted to about 210 eV to obtain surface sensitive information for S2p core electrons. MgK α characteristic x-ray was also used to confirm the SR photoemission spectra.

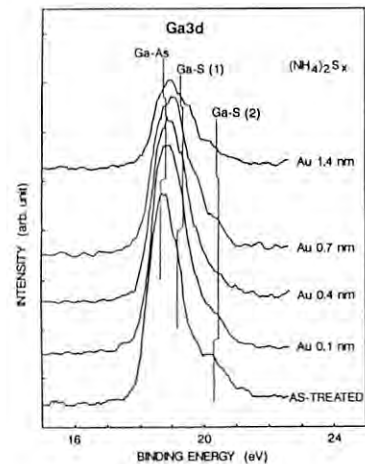
Results and Discussion

Ga3d, As3d, and S2p photoemission spectra are shown in Fig. 1(a)-(c). It is obvious that a Ga-S shoulder peak in Ga3d and an elemental As peak in As3d increase as Au thickness increases, and that As-S peaks in As3d and S2p are still remained even after Au deposition. This indicates that the interfacial chemistry for the Au/ $(\text{NH}_4)_2\text{S}_x$ -treated n-GaAs system is different from that for the Al/ $(\text{NH}_4)_2\text{S}_x$ -treated n-GaAs system in which the peak intensities of elemental As and As-S are relatively small.^{2),3)} The observed Au4f peak shift of about 0.4 eV suggests that AuGa alloy is formed at the Au/GaAs interfaces. Ga3d and As3d peak shifts of at most 0.2 eV toward higher binding energy for the Au/GaAs system is smaller than that for the Al/GaAs system.^{2),3)} This indicates that the band bending relaxation is relatively small for Au, which corresponds to the barrier height of this system determined by I-V and C-V characteristics of Schottky diodes.¹⁾

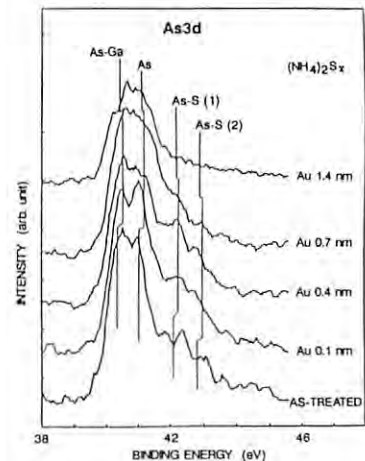
In summary, it is found that AuGa alloy is formed at the interface of Au/ $(\text{NH}_4)_2\text{S}_x$ -treated n-GaAs and that a relatively large amount of elemental As atoms, Ga-S and As-S bonds are remained at this system. The electrical characteristics of Au/ $(\text{NH}_4)_2\text{S}_x$ -treated n-GaAs are thought to be closely related to these bonding states of the interfacial Ga and As atoms.

References

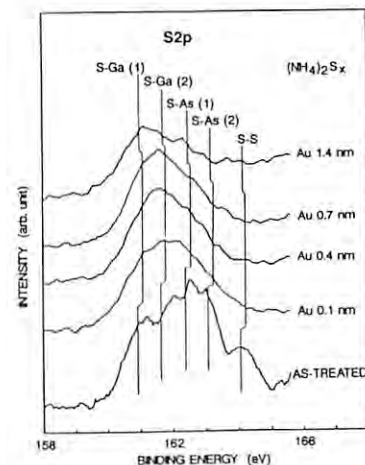
- 1) H. Oigawa *et al.*, "Extended Abstracts of the 20th Conference on Solid State Devices and Materials" (Tokyo, 1988) p.263.
- 2) H. Sugahara *et al.*, "Extended Abstracts of the 21st Conference on Solid State Devices and Materials" (Tokyo, 1989) p.547.
- 3) Y. Nannichi *et al.*, "PF Activity Report 1989".



(a) Ga3d



(b) As3d



(c) S2p

Fig. 1. Photoemission spectra of (a) Ga3d, (b) As3d, and (c) S2p for Au/ $(\text{NH}_4)_2\text{S}_x$ -treated n-GaAs.

Synchrotron Radiation Photoelectron Spectroscopy of $\text{Nd}_{1.80}\text{Ce}_{0.20}\text{CuO}_{4-y}$ Single Crystals

Fumihiko MAEDA, Masaharu OSHIMA, Yoshikazu HIDAKA* and Akihiko YAMAJI*

NTT Applied Electronics Laboratories, Midoricho, Musashino, Tokyo, 180

*NTT Opto-Electronics Laboratories, 162 Tokai, Ibaraki, 319-11

Introduction

The results of many experiments suggest that CuO_2 -planes play a key role in high- T_c superconductivity of Cu oxides. The carriers in these materials are holes. However, in a recently discovered superconductor¹⁾, $\text{Nd}_{2-x}\text{Ce}_x\text{CuO}_{4-y}$, the carriers are electrons. Differences are expected in the electronic structure of the valence band, especially the structure near the Fermi level. We report results of measurements on $\text{Nd}_{1.80}\text{Ce}_{0.20}\text{CuO}_{4-y}$ (NCCO) single crystals for the first time by photoelectron spectroscopy using synchrotron radiation and conventional X-ray sources to clarify the valence band structure.

Experimental

Photoelectron measurements were carried out at BL-1A of the Photon Factory. Total energy resolution was 0.2eV-0.4eV depending on the photon energy of the synchrotron radiation, 40eV-100eV.

The samples were $\text{Nd}_{1.80}\text{Ce}_{0.20}\text{CuO}_{4-y}$ single crystals²⁾, which showed metallic conductivity, but were not superconducting. The clean surface was obtained by heating for 10 minutes at 350°C in ultra-high vacuum. Photoelectron measurements were made after confirming a 1×1 LEED pattern.

Results and Discussion

Figure 1 shows photoelectron spectra of NCCO using synchrotron radiation with photon energy in the range 42-100eV and using $\text{MgK}\alpha$ X-ray. In order to compare these spectra intensities, the spectra taken with 42-100eV photon energy are normalized with photo-current measured by an Au mesh. Binding energy (BE) of the XPS spectrum is determined by aligning the XPS $\text{Nd}5p$ peak position with the corresponding peak for synchrotron radiation.

The peak marked TBS at 13.6eV of BE is enhanced at a photon energy of 76eV because of the resonance photoemission due to $\text{Cu}3p$ - $3d$ excitation. This is the valence band satellite due to the two-hole bound state of Cu 3d, which is also observed in hole-doped superconductors³⁾. The valence band located from 0eV to 10eV of BE has three structures, A, B and C. The valence band is expected to consist of $\text{O}2p$, $\text{Cu}3d$, $\text{Ce}4f$ and $\text{Nd}4f$. $\text{Ce}4f$ is unlikely to be observed since the quantity of $\text{Ce}4f$ is very small. Structure C can be assigned as $\text{O}2p$, because the photoionization cross section of $\text{O}2p$ drastically decrease in the energy range from 42eV to 100eV, while the cross sections of $\text{Cu}3d$ and $\text{Nd}4f$ remain almost unchanged. Since the photoionization cross section of $\text{Cu}3d$ is three times larger than that of $\text{Nd}4f$ in the photon energy of 1253.6eV, structure A is assigned as $\text{Cu}3d$. Therefore B is assigned as $\text{Nd}4f$. The peak positions of $\text{Cu}3d$, $\text{O}2p$ and TBS show no big differences from hole-doped type high- T_c cuprates.

Spectra with photon energy around 76eV are more surface sensitive than XPS spectra because the mean free path of the photoelectron is minimum. In these spectra, a peak maximum exists at structure B, that is $\text{Nd}4f$. Thus it is concluded that the topmost layer of the clean surface is an Nd-O layer.

The photoelectron spectra around the Fermi level in the photon energies of 42eV, 76eV and 100eV are shown in Fig.2. We can recognize very low densities of states (DOS) near the Fermi level and the Fermi edge is not observed. These results

indicate that the cross section of DOS near Fermi level is very low in this photon energy range, and that the Nd-O layer is not metallic. Furthermore, the intra-atomic Coulomb interaction between $\text{Cu}3d$ electrons, U_{dd} , is determined to be 7.2eV, which is a little larger than that for hole-doped type superconductor.

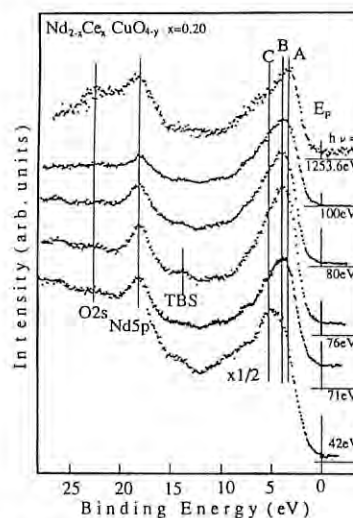


Fig.1 Photoelectron spectra of $\text{Nd}_{1.80}\text{Ce}_{0.20}\text{CuO}_{4-y}$ with $\text{MgK}\alpha$ and synchrotron radiation photon energy from 42 to 100eV.

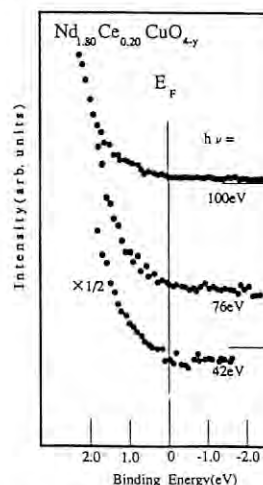


Fig.2 Photoelectron spectra of $\text{Nd}_{1.80}\text{Ce}_{0.20}\text{CuO}_{4-y}$ near Fermi level measured at photon energy of 42, 76 and 100eV.

References

- 1) Y. Tokura, H. Takagi and S. Uchida, Nature 337 345-347 (1989)
- 2) Y. Hidaka and M. Suzuki, Nature 338, 635-637 (1989)
- 3) F. Maeda, T. Kawamura, M. Oshima, Y. Hidaka and A. Yamaji, J. J. A. P. 28, L361-L363, (1989)

INITIAL OXIDATION OF METAL/Si(100) SURFACES BY ULTRA CLEAN OXYGEN GAS

Masaharu OSHIMA, Hirohiko SUGAHARA, Naoki KAWAMURA*, Norikuni YABUMOTO* and Kazushige MINEGISHI*

NTT Applied Electronics Laboratories, Musashino-shi, Tokyo 180

*NTT LSI Laboratories, Atsugi-shi, Kanagawa 243-10

INTRODUCTION

We found there is a possibility that n-Si(100) surfaces contaminated with Fe and other metals during Ar sputtering process are more easily oxidized and show more remarkable dependency on oxygen grade than less contaminated surfaces[1]. In this study, metal overlayers were formed on the n-Si(100), and initial oxidation features by ultra clean oxygen gas in comparison with normal grade gas were studied with photoemission spectroscopy.

EXPERIMENTAL

Experiments were performed at BL-1A of the Photon Factory. Photoemission spectra of Si2p and In4d core levels and valence band were taken with photon energy of 127.6 eV.

Samples chemically treated were annealed with electron bombardment from the rear side. 2x1 LEED patterns were obtained on the annealed surfaces. Then, Ag and In were deposited on the clean surfaces.

An ultra clean oxygen was supplied with a gas purifying system consisting of a double pipe system and a molecular sieve[1].

RESULTS AND DISCUSSION

Various surfaces were exposed to 10^5 L of ultra clean oxygen gas. Si2p photoemission spectra taken with the photon energy of 127.6 eV are shown in Fig. 1. The thickness of deposited Ag layer is estimated to be 6 Å. In comparison with each other, it can be said that n^+ -Si wafer ($5 \times 10^{13} \text{ cm}^{-3}$) is easier to be oxidized, and that Ag overlayer plays a role of enhancing surface oxidation, while In overlayer has no effect of oxidation catalyst. It should be noted that the oxide on the Ag/Si surface consists of more highly oxidized states such as Si^{4+} , while the oxide on the n^+ -Si surface is composed of rather intermediate oxidized state. Actually, according to peak deconvolution[2] by a computer, Si^{4+} ratio for the Ag/Si case is 24%, while that for the n^+ -Si case is 11%.

On the contrary, In-covered Si(100) surface shows almost no effect of oxidation enhancement. Judging

from the results of In4d core level spectra, the metallic In was immediately oxidized by 10^3 L oxygen exposure, while the Si substrate was only slightly oxidized. Thus, In overlayer has no oxidation enhancement effect.

The enhancement effect by Ag overlayer is thought to be attributed to breaking of Si SP^3 hybrid bonds and formation of Ag-Si bonds which may be easier to be oxidized. Figure 2 shows Si2p spectra from the oxidized Ag/Si surfaces. These spectra were normalized with SR ring current. When Ag overlayer was deposited on the clean Si surface, Si2p showed peak shift towards lower binding energy, and this shift gradually increased up to 0.3 eV as the Ag amount increased. There are two possibilities to explain the peak shift as follows; (1) chemical shift of Si because of Ag-Si bond formation, and (2) upward band bending by the Ag/Si Schottky barrier formation. It is difficult to determine which is favorable at the present stage.

In the course of oxidation, Si2p peak position moves towards higher binding energy. This is probably due to band bending towards more flat band condition. A similar tendency in the oxidation feature was observed by J.J.Yeh et al[3].

In the initial oxidation of Ag/Si(100), a clear difference between ultra clean oxygen and normal grade oxygen was observed, as shown in Fig. 3, although the difference is not so remarkable as the Ar-sputtered Si surface. Therefore, it may be said that metal-disrupted surface shows more remarkable dependency on moisture in oxygen.

In conclusion, Ag-deposited Si(100) surfaces are found to be more easily oxidized and show clearer dependency on oxygen grade than the clean Si surface.

REFERENCES

- [1] N.Kawamura et al. PF Activity Report 1989.
- [2] F.J.Himpsel et al. Phys. Rev. B 38,6084(1988).
- [3] J.J.Yeh et al. J.V.S.T. A4,1479(1986).

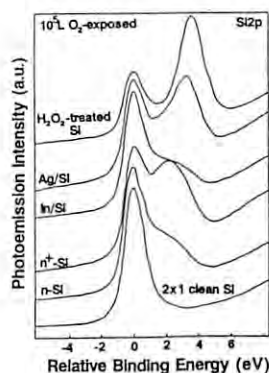


Figure 1 Si2p spectra from various surfaces exposed to ultra clean oxygen of 10^5 L.

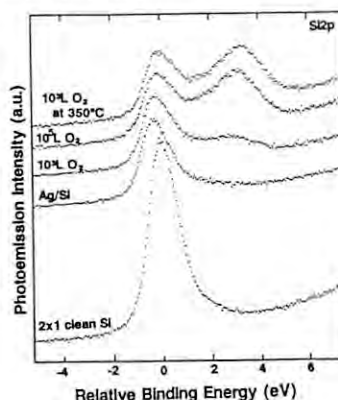


Figure 2 Si2p spectra from clean and Ag-deposited Si surfaces exposed to ultra clean oxygen.

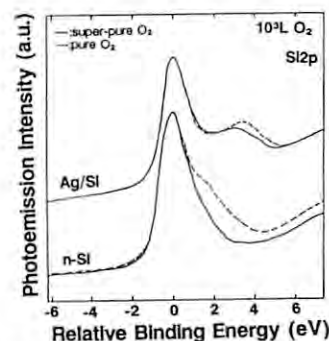


Figure 3 The difference of Si2p spectra between ultra clean oxygen and normal grade oxygen on Ar-sputtered clean Si and Ag/Si.

SYNCHROTRON RADIATION PHOTOIONIZATION OF SPUTTERED NEUTRALS

Masaharu OSHIMA, Satoshi MAEYAMA, Tomoaki KAWAMURA, and Tetsuya MARUO,
NTT Applied Electronics Laboratories, Musashino-shi, Tokyo 180

Introduction

Various attempts have been made at enhancing the ionization probability to improve an analysis sensitivity and accuracy in SIMS analysis by post-ionizing the sputtered neutrals.

In this study, we successfully used synchrotron radiation to investigate the possibility of the photoionization of sputtered neutrals for the first time.¹⁾ The results are compared with the calculated values.

Experimental

Experiments were performed at BL-1A of the Photon Factory. The beamline consists of the first paraboloidal mirror, the monochromator, the second paraboloidal mirror and an exit slit. In this experiment, a 600-g/mm grating was used.

A synchrotron radiation photoionization chamber containing an ion gun, a SR inlet port with a large bellows nipple, a highly sensitive mass spectrometer, an SR photocurrent monitor and a manipulator was made to detect photoionized ions. The samples used were Al, Si, GaAs, Al₂O₃, Pb, and Au. The zeroth-order synchrotron radiation beam at the photoionization chamber was focused at the sample. The beam size was about 8 mm x 2 mm.

Theoretical considerations

A schematic diagram of the synchrotron radiation photoionization process is shown in Fig. 1. Ion intensity I_{ion} is expressed by $I_{ion} = \alpha * (\eta * N^0 v + \tau * \int_{10}^{1000} c * q(E) * \sigma(E) dE * N^0 v)$. Here, α is a detection efficiency of the mass spectrometer. η is a secondary ionization yield. N^0 is the density and v is the velocity of sputtered atoms in space. τ is the duration in which sputtered neutrals pass through the 2-mm-wide SR beam flux. σ is the photoionization cross section (cm²). The photon density $c * q$ can be calculated by $\int_{10}^{1000} c * q(E) dE = \int_{10}^{1000} f(E) * R(E) dE / (0.8 \times 0.2)$ (ph/cm²/s). $f(E) = 2 \pi \sigma_y * \sigma_x * \text{Brilliance} * \alpha_s * \alpha_v$. $R(E)$ is the total reflectivity of the beamline. The total photon flux was calculated to be 1.84×10^{19} photons/sec by integrating these curves from 10 eV to 1000 eV.

Next, we calculated photoionization cross sections, based on the reported data.²⁾ Then, $\int_{10}^{1000} c * q(E) * \sigma(E) dE$ was calculated to be $1.8 \times 10^{-2} \text{ sec}^{-1}$ for Si and $1.5 \times 10^{-1} \text{ sec}^{-1}$ for Au. α was experimentally determined to be 1.4×10^{-4} for the Au sample. Based on

these values, the number of detected ions of photoionized sputtered neutrals were estimated to be $I(\text{Si}) = 6.6 \text{ cps}$ and $I(\text{Au}) = 1.1 \times 10^3 \text{ cps}$.

Results and discussion

First, an Al sample was Ar-sputtered with the SR beam, and no detectable difference between with and without SR was observed.

Then, a Au sample was used. Figure 2 shows ¹⁹⁷Au⁺ mass spectra measured with and without SR beam irradiation 5 mm above the sample surface. For 2-keV Ar ion energy, a signal about 4 times larger than the secondary ion peak was observed.

Figure 3 shows the ¹⁹⁷Au⁺ mass signal intensity from a Au sample as a function of photon flux. The Ar ion energy was 1 keV. When the entrance slit was completely closed, almost no ¹⁹⁷Au⁺ signal was detected. However, the signal drastically increased by opening the slit. The measured ¹⁹⁷Au⁺ intensity is about an order of magnitude smaller than the calculated ¹⁹⁷Au⁺ intensity of $1.1 \times 10^3 \text{ cps}$. However, the degradation of reflectivities of mirrors should be taken into account. The measured photocurrent of about 3 μA comes to about an order of magnitude smaller photon flux than the calculated value of $1.84 \times 10^{15} \text{ ph/s}$. Therefore, these phenomena can be explained by SR photoionization. These SR photoionization processes were also observed for the Pb sample.

When the sample was irradiated by the SR beam, the SR photoionized ion intensity decreased drastically. This phenomenon is attributed probably to the neutralization process of ions by photoelectrons from the sample surface.

In conclusion, the SR photoionization effect of sputtered neutrals was observed for the first time, and photoionized ion intensities were compared with calculated values. This technique will be applicable to understanding the features of sputtered neutrals and precise in-depth profiling.

References

- 1) M. Oshima et al. to be published in J.V.S.T. 1990.
- 2) J. J. Yeh and I. Lindau, Atomic Data and Nuclear Data Tables, 32 (1985)7.

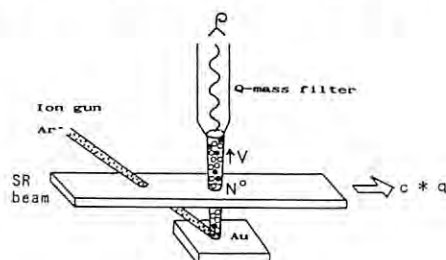


Fig.1 Schematic diagram for the SR photoionization process of sputtered neutrals.

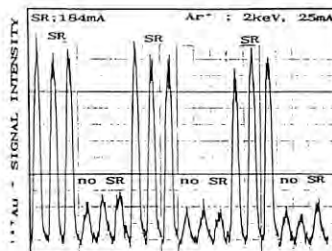


Fig.2 ¹⁹⁷Au⁺ mass spectra measured with and without SR beam. Ar ion energy was 2keV.

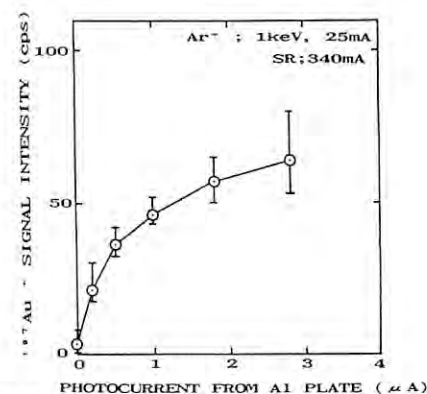


Fig.3 ¹⁹⁷Au⁺ mass signal intensity as a function of photon flux.

INITIAL OXIDATION OF Si(100) SURFACES BY ULTRA-CLEAN OXYGEN

Naoki KAWAMURA, Norikuni YABUMOTO, Kazushige MINEGISHI

Masaharu OSHIMA*, Hirohiko SUGAHARA*

NTT LSI Laboratories, Atsugi-shi, Kanagawa 243-01

*NTT Applied Electronics Laboratories, Musashino-shi, Tokyo 180

INTRODUCTION

Many studies have been carried out to elucidate the initial oxidation processes of Si(100) surfaces. However, initially oxidized states caused by the same amount of oxygen exposure are extremely varied. One of the reasons for these scattered results is considered to be the grade of gas. Ohmi et al.[1] reported that the barrier height of thermal oxide films grown by ultra-clean oxygen is higher than that of films grown by normal-grade oxygen.

In this paper, we investigate the relationship between the Si2p photoemission spectra and oxygen gas grade with surface sensitive photoemission spectroscopy using synchrotron radiation.

EXPERIMENTAL

The experiments were carried out at BL-1A of the Photon Factory. Photoemission spectra were taken with a photon energy of 127.6 eV to obtain surface-sensitive information.

The samples were cut from n-type Si(100) wafers. After $\text{H}_2\text{SO}_4 + \text{H}_2\text{O}_2$ cleaning, they were dipped in 5% HF for 2 min and in H_2O_2 for 5 min. These HF and H_2O_2 treatments were repeated twice. Then, the samples were dried in air after rinsing in deionized water.

Ar ion sputtering and annealing were repeated until 2x1 LEED patterns were observed on the sample surfaces. At this time, almost no Si2p sub-oxide peaks were observed in the photoemission spectra.

The moisture concentration of the oxygen was especially notable in the experiments: ultra-clean oxygen contains less than 20 ppb moisture, while normal-grade oxygen contains 72 ppm moisture. To obtain ultra-clean oxygen, the gas supply system shown in Fig.1 was prepared. The point to note about this system was that fresh oxygen, purified by a 13X molecular sieve, flowed at variable leak valve continuously. The moisture concentration was monitored by a dew-point meter.

The samples were exposed to the ultra-clean oxygen and the normal-grade oxygen at various substrate temperatures between room temperature and 650 °C.

RESULTS AND DISCUSSION

The Si2p photoemission spectra on Si(100) surfaces exposed to ultra-clean oxygen and normal-grade oxygen for 10^5L at room temperature are shown in Fig.2. We performed peak deconvolution of these spectra using a computer. A clear difference between the two oxidation cases is observed for the Si2p chemically-shifted peaks. The normal grade oxygen-exposed Si surface shows a higher Si^{3+} ($\Delta E = 2.5\text{ eV}$) peak than the Si^{2+} ($\Delta E = 1.8\text{ eV}$) peak. By contrast, the ultra-clean oxygen-exposed surface exhibits a smaller Si^{3+} peak than the Si^{2+} peak and a negligibly small Si^{4+} (SiO_2 state) peak, indicating that moisture content in the oxygen might play an important role to make the higher oxidized state. This relationship is also observed, when 10^3L oxygen is exposed at room temperature and the substrate temperature is elevated. Thus, the difference due to the oxygen gas grade is found to mainly appear in the uptake of Si^{3+} and Si^{4+} . This relationship is almost identical to the relationship between wet-oxidation and dry-oxidation.

Figure 3 shows the Si2p photoemission spectra of Si(100) surfaces exposed to normal-grade oxygen at different temperatures. The metallic Si2p peaks are shifted 0.2 eV towards higher binding energy with oxidation, while that in the case of ultra-clean oxygen remains unshifted. This means that the Si surface oxidized with moist oxygen is bent 0.2 eV towards a flat band condition.

In the case of n-type Si(100) surface cleaned without Ar ion sputtering, no dependence of oxidation rate on the grade of oxygen gas was observed, while the identical band bending with oxidation occurred. Therefore, the above mentioned differences due to the grade of gas might be due to such metal contaminants as Fe, Cr and Ni derived from Ar sputtering which were detected by SIMS and Total reflection X-Ray Fluorescence (TXRF). Further study is needed to investigate these phenomena in detail.

REFERENCES

- [1] T. Ohmi et al, Extended Abstracts 173rd Electrochem. Soc. 387(1988)
- [2] F.J. Himpsel et al, Phys. Rev. B 38, 6084(1988)

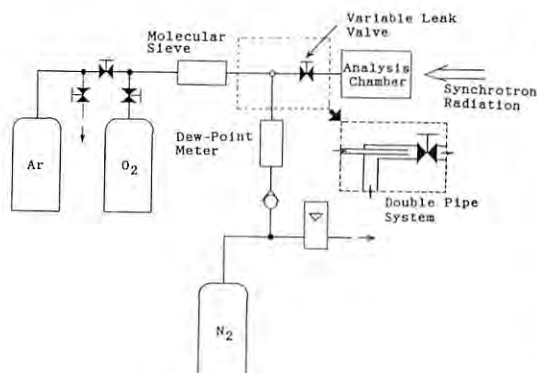


Figure 1 Diagram of the ultra-clean oxygen gas supply system.

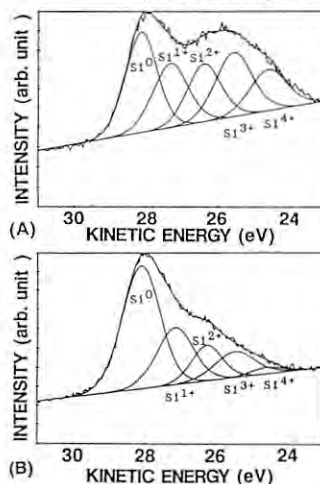


Figure 2 Photoemission spectra of Si2p from (A) 10^5L ultra-clean oxygen, (B) 10^5L normal-grade oxygen exposed n-type Si(100) substrate surface.

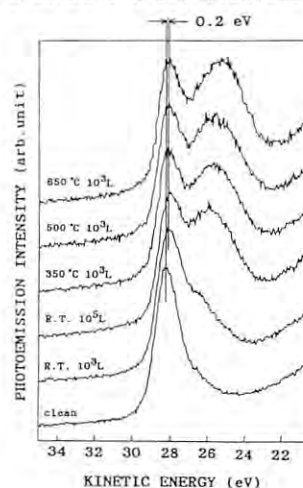


Figure 3 Photoemission spectra of Si2p from normal-grade oxygen exposed at various substrate temperatures.

ANGLE SCANNING X-RAY STANDING WAVE ANALYSIS IN HIGH VACUUM

Tomoaki KAWAMURA, Satoshi MAEYAMA and Masaharu OSHIMA

NTT Applied Electronics Laboratories, Midori-cho, Musashino, Tokyo 180

Introduction

The X-ray standing wave method was known as powerful tools for analysis surface and interface structure[1,2]. There are some rigorous limitations in X-ray standing wave method; (1) highly perfect substrate crystals are necessary, (2) abruptly interfaces should be changed. The perfections of substrate crystals are more important for X-ray standing wave method in hard X-ray region because of the small value of natural width of rocking curve. To avoid these restriction, X-ray standing wave method applied to samples in soft X-ray region [3]. In this region, the natural width of rocking curve is about hundred arcsec and the effect of defects which enlarge the natural width of rocking curve are ignored. To measure the X-ray standing wave signals in soft X-ray region, the incident X-ray energy was usually changed instead of changing incident angles because of convenience. However energy scanning X-ray standing wave method has some problems; (1) the refinement of incident X-ray beam properties should be necessary, (2) the overhead of changing incident X-ray energy is not negligible. To solve these problems, the angle scanning X-ray standing wave method was desirable. However, there were many difficulties to perform angle scanning X-ray standing wave method because of the lack of high accuracy rotation mechanisms in vacuum. To realize angle scanning X-ray standing wave method, we developed direct rotating goniometer with X and Y stage and 2 swivel stage. In this report, the performance of goniometer and preliminary result of angle scanning X-ray standing wave method was described.

Experimental

The angle scanning X-ray standing wave instrument was designed both X-ray standing wave and EXAFS. The wide area Si(Li) solid state detector was set for monitoring fluorescence yield due to X-ray standing wave and EXAFS. The rotation movement was introduced directly into vacuum through differential feedthrough shown in Figure 1. The differential feedthrough was pumped by ion pump to avoid excess vibration. The present pressure is about 10^{-8} Torr and the pressured was only restricted by the outgas of solid state detector. The accuracy of rotation was 0.72 arcsec in main rotation axis and the accuracy is sufficient for angle scanning X-ray standing wave.

GaAs (001) samples was set on the goniometer and (111) reflection was used for X-ray standing wave method. The incident X-ray wave length was set at 5.76 \AA (θ_B is about 62.3°). In this arrangement, the angle of surface were 7.6° and 63.0° . The fluorescence yield was measured in both cases.

Results and Discussion

Figure 2 shows the As L fluorescence yield corresponding to angles. Obviously, specular fluorescence yield profile corresponding to X-ray standing wave was observed. The peak to peak angles of profile was about 85 arcsec and this value was same in order as the calculated natural width of rocking curve of GaAs (111) reflection.

The possibility of angle scanning X-ray standing wave in high vacuum was confirmed with using the direct rotating mechanism in high vacuum. This method may be easily applied to angle scanning X-ray standing wave even in UHV environment with using UHV compatible fluorescence detector.

References

1. P. L. Cowan, J. A. Golovchenko, and M. F. Robbins, Phys. Rev. Lett., **44**(1980) 1680.
2. K. Akimoto, T. Ishikawa, T. Takahashi, and S. Kikuta, Nucl. Inst. Meth., **A246**(1986) 755.
3. T. Ohta, Y. Kitajima, H. Kuroda, T. Takahashi, and S. Kikuta, Nucl. Inst. Meth., **A246**(1986) 760.

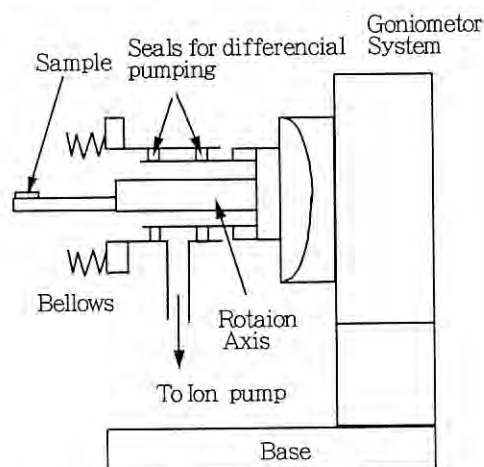


Fig. 1 Schematic diagram of the direct rotating mechanism in high vacuum.

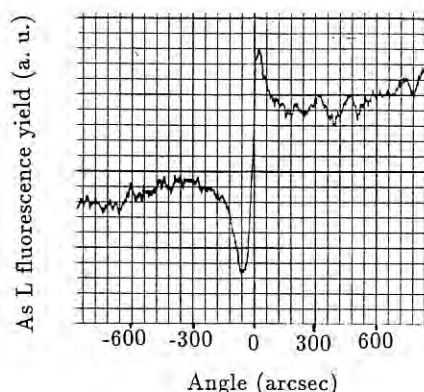


Fig. 2 Fluorescence yield of As L corresponding to X-ray standing wave in GaAs crystals.

PHOTOIONIZATION CROSS SECTIONS OF XENON IN THE L EDGE REGION

Tetsuo KOIZUMI, Tatsuji HAYAISHI*, Takashi MATSUO#, Kunihiro SHIMA+,
Hiroyuki TAWARA**, Tadao TONUMA## and Akira YAGISHITA++

Department of Physics, Faculty of Science, Rikkyo University, Toshima-ku, Tokyo 171

*Institute of Applied Physics, University of Tsukuba, Tsukuba-shi, Ibaraki 305

#Medical Research Institute, Tokyo Medical and Dental University, Bunkyo-ku, Tokyo 113

+Institute of Applied Physics and Tandem Accelerator Center, University of Tsukuba, Tsukuba-shi, Ibaraki 305

**National Institute of Fusion Science, Chikusa-ku, Nagoya 464-01

##Institute of Physical and Chemical Research, Wako-shi, Saitama 351-01

++Photon Factory, National Laboratory for High Energy Physics, Tsukuba-shi, Ibaraki 305

Inner-shell photoionization processes of atom have been extensively studied theoretically as well as experimentally for some time. It is well known that a model calculation assuming independent inner-shell electrons yields the ionization cross section having a photon energy dependence of E^{-n} . Such model calculations show reasonable agreement with most experimental results.

In our previous work, we reported the charge state distributions of xenon ions created by multiple photoionization in the L-shell ionization region¹⁾. During the study, we had noticed that the photon energy dependence of the measured total photoion yield deviates from a simple power law. In the present experiment, total photoionization cross sections of xenon have been measured in the L-shell ionization region, covering the photon energy from 4.6 to 6.1 keV with the step width of wavelength scans of about 0.0025 Å.

Details of the present experimental set-up have been already described¹⁾. Undulator radiations emitted from the 2.5 GeV electron ring at the Photon Factory in the National Laboratory for High Energy Physics were monochromatized by an InSb(111) double crystal monochromator and crossed a beam of xenon atoms introduced into the ionization region through a nozzle. The resulting photoions were extracted from the ionization region by an electric field and detected by a micro-channel plate after passing through a drift space.

Figure 1 shows total photoionization cross sections for xenon obtained in this work. As the present cross sections correspond to the photoabsorption cross sections, the absolute values of the present cross sections were obtained by normalizing them to the absorption cross sections of Wuilleumier²⁾ at the photon energies of 4.65 and 6.10 keV. The previous result of McCrary et al.³⁾ and Wuilleumier, and theoretical curve of Scofield⁴⁾ are also shown in Fig.1 for comparison.

In the present data are clearly seen sharp peaks at the L_3 and L_2 edges, which had not been observed in previous experi-

mental and theoretical work. It can be suggested that these peaks are due to the photoexcitation of 2p electrons to the unfilled higher levels. This conclusion shows agreement with the analysis of Breining et al.⁵⁾. Their model calculation reveals that the 2p-nd ($n=5, 6$, and 7) excitations are important process at the Xe L_3 and L_2 absorption edges. Furthermore, a structure above the L_3 edge which suggests deviations from the power law-like energy dependence predicted by an independent electron model can be seen in the present data. This structure might be due to simultaneous two electron excitation. Full detailed discussion of these results is given in our recent publication.⁶⁾

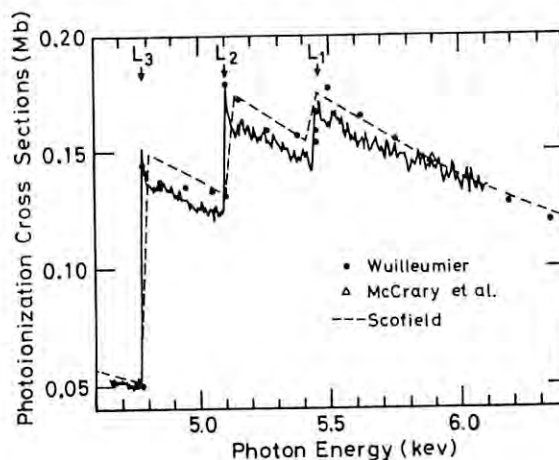


Fig. 1

References

- 1) T. Tonuma, A. Yagishita, H. Shibata, T. Koizumi, T. Matsuo, K. Shima, T. Mukoyama and H. Tawara: J. Phys. B20, L31(1987).
- 2) F. Willeumier: Phys. Rev. A6, 2067(1972).
- 3) J. H. McCrary, L. D. Looney, C. P. Constanten, and H. F. Atwater: Phys. Rev. A2, 2489(1970).
- 4) J. H. Scofield: Lawrence Livermore Radiation Laboratory Report No. UCRL-51326 (1973).
- 5) M. Breining, M. H. Chen, G. E. Ice, F. Parente, and B. Crasemann: Phys. Rev. A22, 520(1980).
- 6) T. Koizumi, T. Hayaishi, T. Matsuo, K. Shima, H. Tawara, T. Tonuma and A. Yagishita: J. Phys. Soc. Jpn. 58, 13(1989).

MULTIPLE-PHOTOIONIZATION OF NEON IN THE K-EDGE REGION

Tetsuo KOIZUMI, Tatsuji HAYAISHI*, Yukikazu ITIKAWA+, Yoh ITOH#, Takashi MATSUO\$, Tetsuo NAGATA**, Yusuke TAKIZAWA, Akira YAGISHITA++, and Masuhiro YOSHINO##

Department of Physics, Faculty of Science, Rikkyo University, Nishi-Ikebukuro, Toshima-ku, Tokyo 171.

*Institute of Applied Physics, University of Tsukuba, Tsukuba-shi, Ibaraki 305.

+Institute of Space and Astronautical Science, Sagami-hara-shi, Kanagawa 229.

#Faculty of Science, Josai University, Keyakidai, Sakado-shi, Saitama 350-02.

\$Medical Research Institute, Tokyo Medical and Dental University, Yushima, Bunkyo-ku, Tokyo 113.

**Department of Science and Technology, Meisei University, Hino-shi, Tokyo 191.

++Photon Factory, National Laboratory for High Energy Physics, Oho, Tsukuba-shi, Ibaraki 305.

##Faculty of General Education, Shibaura Institute of Technology, Ohmiya-shi, Saitama 330.

In the course of experimental study for multiple photoionization of atoms, we present here the result for neon atom in the K-shell ionization region.

The details of experimental apparatus and procedure have been described previously¹⁾. Undulator radiation, emitted from the 2.5 GeV electron ring at the Photon Factory, was monochromatized by an InSb(111) double crystal monochromator and crossed a beam of neon atoms which were introduced into the ionization region through a nozzle. The resultant photoions were mass-analyzed by a time-of-flight spectrometer. The relative intensities for the different charge state of the ion were measured as a function of photon energy in the region around 1s ionization threshold.

Figure 1.(a) and (b) shows the ion yield spectra obtained in this experiment. The ion yield curve for Ne⁺ shows prominent peaks corresponding to the excitation of 1s electrons to bound np(n=3,4,5) states. At the resonance energy, the single charged ions are produced by resonance Auger process. For Ne²⁺, the resonance peaks could not be distinguished clearly with the resolution of present experiment. The doubly charged ions, however, can be observed at the resonance energy. These doubly charged ions are produced by two step Auger decays from the 1s-np excited states. Above 1s ionization threshold, main product is doubly charged ion produced by normal Auger decay process from 1s hole state.

The formation of triply charged ions is very interesting. The yield of Ne³⁺ seems to increase stepwisely above lowest 1s-np resonance energy. This means that the Auger shake-off process from the 1s hole state is main process for Ne³⁺ formation in this energy region. Above the photoelectron shake-off (1s_{nl}⁻¹) threshold (about 910 eV), the triply charged ion yield increases to about twice the value in the region just above the 1s ionization threshold.

Detailed analysis of the results is still in progress.

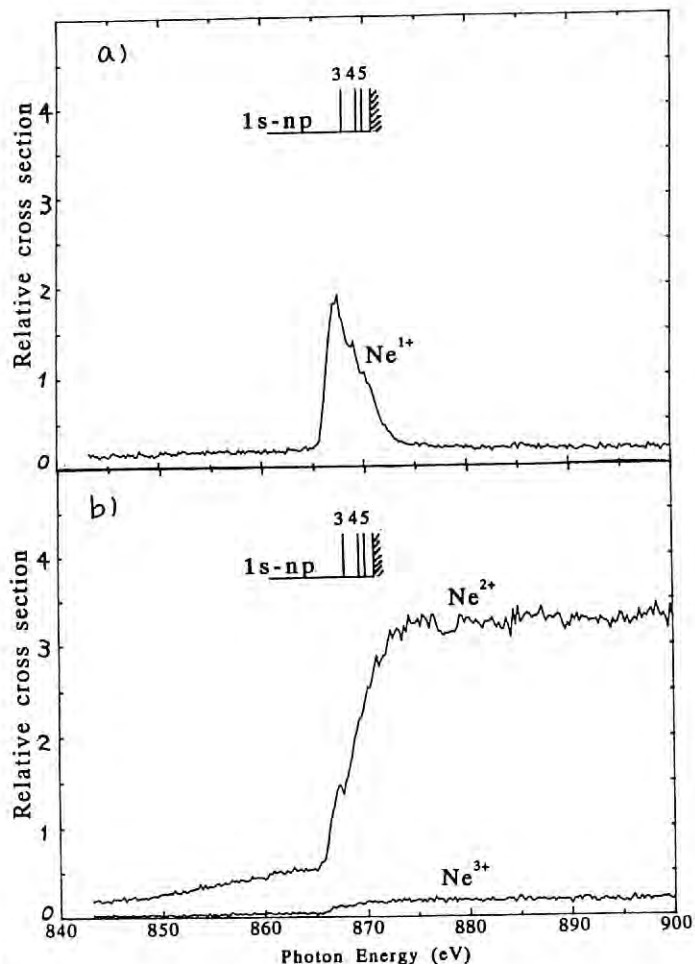


Fig. 1. The relative photoion yield curves of Ne in the K-edge region: a) Ne⁺, b) Ne²⁺ and Ne³⁺.

Reference

- 1) Y. Sato et al. J. Phys. B **18**, 225 (1985)

MEASUREMENT OF THE MASS OF THE ELECTRON NEUTRINO USING ELECTRON CAPTURE IN ^{163}Ho

Shinjiro YASUMI^{a,g}, Hideki MAEZAWA^a, Shunji KISHIMOTO^a, Manabu FUJIOKA^b, Koichiro SERA^b, Takeshi OMORI^b, Kunihiro SHIMA^c, Takeshi MUKOYAMA^d, Yosuke INAGAKI^e, and Gunzo IZAWA^f

^aNational Laboratory for High Energy Physics, KEK, Ibaraki 305; ^bTohoku University, Sendai 980; ^cUniversity of Tsukuba, Ibaraki 305; ^dKyoto University, Kyoto 611; ^eTsukuba Institute of Science and Technology, Tsuchiura 300; ^fUtsunomiya Bunsei Junior College, Utsunomiya 320; ^gTeikyo University, Tokyo 192-03.

Introduction

The mass of the electron neutrino ($m_{\nu e}$) has been recently investigated using electron capturing isotopes including ^{163}Ho and ^{198}Pt .^{1,2,3)} Our method^{4,5)} to determine the electron neutrino mass is based on the $m_{\nu e}$ -dependence of decay rates of the transition $^{163}\text{Ho} \rightarrow ^{163}\text{Dy}$. When we reconstruct an M X-ray spectrum from ^{163}Ho per atom per second using two spectra S_{M1} and S_{M2} , the M X-ray spectra of dysprosium when there is one vacancy in the M1 and M2 subshell, the coefficients of S_{M1} and S_{M2} correspond to λ_{M1} and λ_{M2} respectively, which are the partial M1-capture and M2-capture decay constants. Using λ_{M1} , λ_{M2} and λ_t (total decay constant) which was measured separately with isotope-dilution mass spectrometry,^{6,7)} as three constraints, the $m_{\nu e}$, the Q-value, and the nuclear matrix element for the decay of ^{163}Ho can be simultaneously solved from three equations of the electron capture rate.

The present experiments are aiming at an experimental determination of the S_{M1} and S_{M2} spectra of Dy. These two spectra can be reduced from fluorescence M X-ray spectra of dysprosium, $S_{E\alpha}$ ($\alpha = a, b$), using the "Photon Subtraction Method" as described in page VI-1 of PF Activity Report (1983/84).

Experiments

Undulator radiations from BL-2A line were monochromated by a double reflection crystal monochromator made of InSb and directed onto a Dy target. The incident photon beams were counted with a photon counter which consists of a xenon proportional counter and a Be-absorber array. M X-rays emitted by dysprosium excited with the incident photon beams, were measured with the same Si(Li) detector as that which was used for measuring a photon spectrum from a ^{163}Ho source.²⁾

Results and Discussions

We accumulated S_{Ea} , S_{Eb} and S_{Ec} spectra having an enough statistics for a thin Dy target (10 $\mu\text{g}/\text{cm}^2$ thick) deposited on a mylar. As an example of these spectra, a S_{Eb} spectrum is shown in Fig. 1, where an elastic part was already subtracted using the response function of the Si(Li) detector.⁸⁾ We also succeeded in estimating the number of very intense incident photons (1 keV \sim 2.5 keV) using the combination of the photon counter above-mentioned and a slit system.

Our method of determining the mass of the electron neutrino using electron capture in ^{163}Ho is based on the assumption that two spectra S_{M1} and S_{M2} are the same for the following two cases; electron capture in ^{163}Ho and photoionization of Dy. In order to check the validity of this assumption, the energy of

the 5p - 3s line⁵⁾ was measured for both cases as shown in Fig. 2.⁵⁾ The energy difference between two cases was found to be less than a few eV, indicating an evidence on the validity of the method for measuring the $m_{\nu e}$. An analysis for the other data taken during the present experiments is now going on.

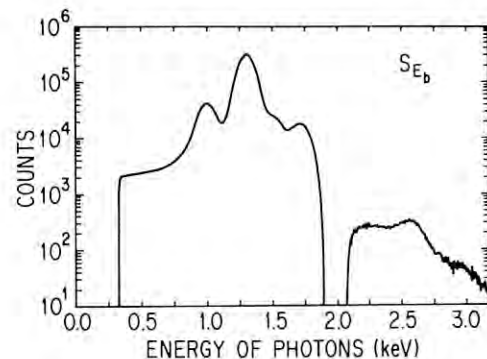


Fig. 1 S_{Eb} spectrum. Some peaks seen in the right are caused by piling up.

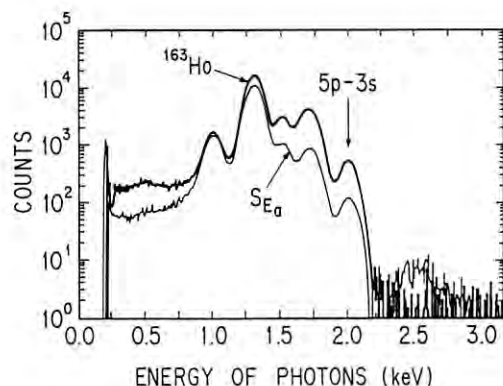


Fig. 2 The 5p-3s line in a ^{163}Ho and S_{Ea} spectra.

References

- 1) Particle Data Group, Phys. Lett. 204B (1988)
- 2) S. Yasumi et al., Phys. Lett. 181B, 169 (1986)
- 3) B. Jonson et al., Nucl. Phys. A396, 4790 (1983)
- 4) S. Yasumi et al., Proc. Neutrino '84, Nordkirchen near Dordmund, June 1984, p. 202.
- 5) S. Yasumi et al., Proc. Int. Europhys. Conf. on High Energy Physics, Madrid, Spain, 6-13 September 1989, to be published in Nuclear Physics B.
- 6) P.A. Baisden et al., Phys. Rev. C28, 337 (1983)
- 7) O. Kawakami et al., Phys. Rev. C38, 1857 (1988)
- 8) Y. Inagaki, K. Shima and H. Maezawa, Nucl. Instr. and Meth. B27, 353 (1987)

TWO-DIMENSIONAL PATTERN DEMAGNIFICATION BY ASYMMETRIC BRAGG REFLECTION

Mitsuaki MORIGAMI, Mitsuaki HARADA, Shun-ichi KOBAYASHI, Shuji FUJIWARA,
Shingo TERAOKA, Masayoshi OGURA, Osamu KITAMURA, Kazuhiro KANEDA,
Takashi GOTO, Ryu SHIMIZU, Shigeo SUZUKI, Hideki MAEAWA* and Masami ANDO*

Tsukuba Research Center, Sanyo Electric, Co.Ltd.

Koyadai, Tsukuba-shi, Ibaraki 305

*Photon Factory, National Laboratory for High Energy Physics
Oho, Tsukuba-shi, Ibaraki 305

Introduction

For X-rays in the energy region of a few keV, there is no material which acts as a refractive lens. Therefore one-to-one proximity printing technique has been studied in X-ray lithography.

There are many problems to be solved in making X-ray masks for production of ULSI. These will be minimized if pattern demagnification by the optical system can be made possible.

We have tried to reduce the size of the image by using the asymmetric Bragg reflection of the crystal¹, and reported only one dimensional pattern demagnification by using this method before^{2,3}. In this report we show the optical system for two dimensional pattern demagnification and some experimental results.

Experimental

Fig.1 shows the optical system for two dimensional pattern reduction used in our experiment.

This method needs highly parallel, bright and monochromatic X-rays. We used X-rays from the undulator (BL-2A). X-rays emitted from the undulator was monochromatized by a double crystal monochromator. A mask was set in the incident beam. The width of the X-ray beam which passed through the mask was reduced in horizontal direction by the first Si mirror and in vertical direction by the second Si mirror. The second reduction mirror and the second crystal of the monochromator were set in the (+,+) arrangement to restrict the range of wavelength and the beam divergence. The distance from the mask to resist film along the path of the X-ray beam was about 15mm.

We have chosen wavelength $\lambda=3.5\text{\AA}$, the offset angle $\alpha=22^\circ$ and 111 reflection ($\theta=34^\circ$). Then the reduction ratio n is 0.25.

A mask pattern used is a set of line and space whose width are $10\mu\text{m}$, $5\mu\text{m}$, $3\mu\text{m}$ and $2\mu\text{m}$ parallel to vertical and horizontal directions (Fig.2). The absorber was Au of $1.2\mu\text{m}$ thick supported on SiN membrane and the expected contrast was about 45 for $\lambda=3.5\text{\AA}$.

Resist films which we used in this experiment were positive type EBR-9 (TORAY). The thickness of the resist film was $2,600\text{\AA}$.

Results and Discussion

A replicated image is shown in Fig.3. Exposure dose described by a ring current in milliamps multiplied by exposure time in hours was about $250\text{mA}\cdot\text{h}$. A pattern size was reduced to 1/4 of the original size in two directions. Line and space pattern whose width are $10\mu\text{m}$ (at the mask pattern) were resolved, but whose width are $3\mu\text{m}$ and $2\mu\text{m}$ weren't resolved. Horizontal line and

space pattern whose width are $5\mu\text{m}$ were resolved, but vertical pattern weren't resolved. Resolution is different between vertical and horizontal direction. A cause of this phenomenon is diffraction of X-ray. The distance from the first (horizontal) reduction mirror to resist is longer than the distance from the second (vertical) reduction mirror to resist. Another cause is the beam divergence. The monochromator restrict only the range of vertical beam divergence. It is necessary to use the two sets of monochromators, one in horizontal direction and the other in vertical, and to make the distance from mask to resist shorter.

Reference

- ¹S.Suzuki et al. PF Activity Report #5,312(1987)
- ²S.Suzuki et al. PF Activity Report #6,267(1988)
- ³J.Nishino et al. Rev.Sci.Instrum.60(7), July 1989

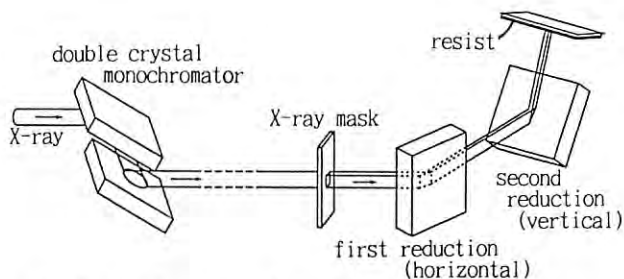


Fig.1 Optical system for two dimensional pattern demagnification by a pair of Si crystals.

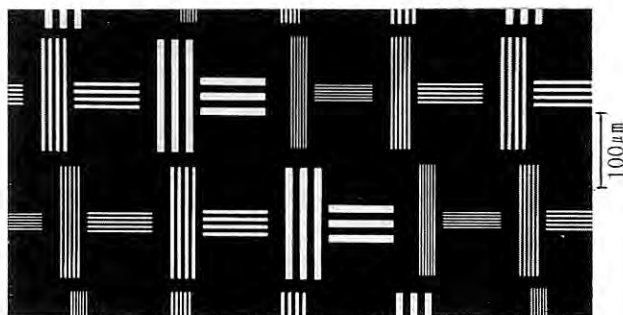


Fig.2 A mask pattern.

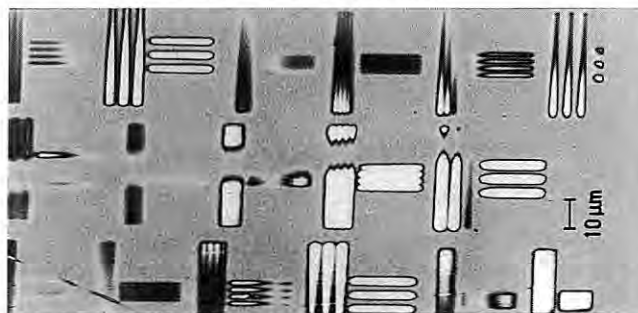


Fig.3 A replicated image.

P.A SCATTERING OF SOFT X-RAY BY SOLIDS OF LIGHT ELEMENT

Atsushi TANOKURA, Tadasu SUZUKI, Yasuo IGUCHI*, Kazumichi NAMIKAWA**
Koichi MORI*** and Hideki MAEZAWA***

Department of Physics, Sophia University, Kioi-cho, Chiyoda-ku, Tokyo 102

*Department of Systems Engineering, Toa University, Ichinomiyagakuencho,
Shimonoseki-shi, Yamaguchi 751

**Department of Physics, Tokyo Gakugei University, Nukuikita-machi, Koganei-shi, Tokyo 184

***Photon Factory, National Laboratory for High Energy Physics, Oho-machi, Tsukuba-gun, Ibaraki-ken 305

Introduction

The theory^{1), 2)} of inelastic scattering of soft X-ray suggests that it is possible to detect the effect of p.A term. Fig.1 shows the predicted results of the theory. The cross section of scattering by p.A term increases characteristically as the energies of incident X-rays become lower, while in the same region that by the A^2 term decreases. Thus measurements of the cross section of the p.A term are required to know the characteristic features of the X-ray scattering in the soft X-ray region; this could lead to the direct measurement of the life time of the inner shell hole²⁾.

Experimental result

In a recent experiment, we analysed scattering intensity of a polycrystalline beryllium for soft X-rays with wave-length between 350nm and 750nm by filter method. The energy of incident soft-Xray was 407 eV(30.5 Å). The scattering angle was 90 degrees. The result, contrary to the theoretical prediction, shows that the scattering intensity is flat for the radiation with the wave-lengths in the above mentioned region. We consider the effect of stray light from the monochromator. Fig.2 is the experimental arrangement for estimating stray light. The M-valve has a quartz window, so when the M-valve is closed, soft X-rays cannot pass through this valve, while light does. Table 1 shows the result of this experiment. The contribution of the stray light is of the order of 1/100 of the incident beam. The experimental result agrees with the calculated value of absorption of soft X-rays and light at glancing angles of 20° or 60°, but we cannot explain the data obtained at the symmetrical position of 45°. Integrated intensity of scattering from 300 nm to 800 nm by experiment is about 10^{-2} smaller than that of incident soft X-ray, and the signal by p.A term is much smaller, so we will re-examine the spectra in this energy region.

θ_s	I/I ₀ closed	I/I ₀ open	exp.	cal.
60	0.008	0.025	1	1
45	0.042	0.046	?	1.65
20	0.006	0.071	3.95	3.82

Table 1 Estimation of stray light. θ_s is glancing angle.

Discussion

Recently Marchetti and Franck³⁾ observed the spectrum of inelastically scattered X-rays by copper K-shell electrons. The incident beam of 70 KeV X-rays was used from wiggler radiation of CHESS. The spectrum of scattered X-rays observed by them in coincidence with K-shell is reported to be due to the A^2 term and to accelerated secondary electron emission. They concluded that the p.A term is not observable for copper, which has a large value of the ion charge Z. Due to the recent progress of the experimental instruments, it has become possible to use windowless SSD as a detector; this helps to perform experiments in the energy range given by Fig.1 to detect the scattering by p.A term. Probably, SSD will work well in the energy range larger than 300 eV. Incident energy of 1.1 KeV meets the condition for p.A term required theoretically. Fig.3 shows theoretical spectrum of inelastic scattering that is corrected by SSD sensitivity (solid line). As shown here, if we observe the tail in the lower energy side of the spectrum due to the A^2 term, it agrees with the theoretical prediction²⁾. If successful, our investigation gives for the 1st time the spectra of the p.A term in this region of the infrared divergence.

References

- 1) Y.Ohmura and T.Suzuki:
J.Phys.Soc.Japan **53**(1984)2807
- 2) Y.Ohmura and T.Suzuki:J.Phys.Soc.Japan **55**(1986)699
- 3) V.Marchetti and C.Franck:Phys.Rev.A **39**(1989)647

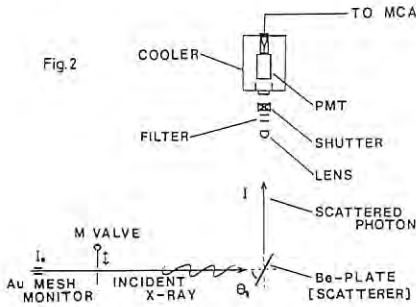
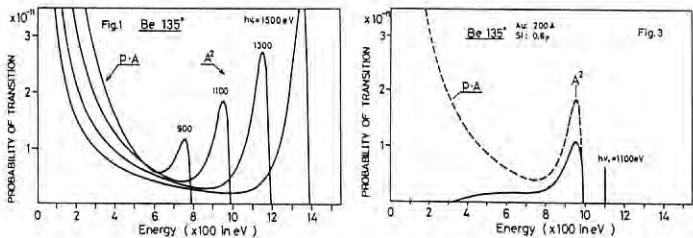


IMAGE FORMATION IN A ZONE PLATE MICROSCOPE USING UNDULATOR RADIATION

Yasushi Kagoshima, Sadao Aoki, Masami Kakuchi*, Hideki Maezawa**, and Masami Ando**

Institute of Applied Physics, University of Tsukuba, Tsukuba, Ibaraki 305

*NTT LSI Laboratories, Atsugi, Kanagawa, 243-01

**Photon Factory, National Laboratory for High Energy Physics, Tsukuba, Ibaraki 305

INTRODUCTION

A soft x-ray microscope using zone plates (ZP's) as imaging devices is in operation at the undulator beamline, BL-2B¹⁾. The undulator radiation (UR) consists of successive harmonics with a narrow band. A ZP produces not only the primary order diffraction but also positive and negative higher order ones. Therefore, the resultant images observed in an image plane are very confusing. This report briefly describes image formation by the ZP in the case of a one-dimensional transmission grating (TG) illuminated by UR and the experimental result. The detailed description will be published²⁾.

EXPERIMENTAL

The m -th order focal length of a ZP is given by $f_m = f_1/m$, where f_1 is the primary focal length. f_1 is given by $f_1 = r_1^2/\lambda$, where r_1 is the radius of the innermost zone and λ the wavelength of incidence. Since the wavelength of the n -th harmonic of UR is λ_1/n , where λ_1 is that of the first harmonic, the m -th order focal length of ZP for the n -th harmonic can be written as $f_{mn} = nf_1/m$. Fig.1 shows the optical path when a one-dimensional TG is illuminated by UR. The n -th harmonic proceeds in parallel to an optical axis at a distance of R . The ray firstly deflected by TG toward P_{1n} is deflected by ZP toward the secondary source point, namely, maximum of a Fraunhofer pattern S_{1mn} . It finally arrives at Q_{1mn} in the image plane. If λ_1 is much smaller than the groove spacing d , x_{1n} can be given by $x_{1n} = \lambda_1 a / nd$. D_{1m} is given by $D_{1m} = 1/\lambda_n f_{mn} / d = 1/r_1^2 / md$. Since it passes through two points P_{1n} and S_{1mn} , the coordinates of Q_{1mn} (X_{1m} , Y_{1m}) have the following relation.

$$X_{1m} = -\frac{\lambda}{m} \frac{r_1^2}{d} \frac{a}{b} \left(\frac{Y_{1m}}{R} + \frac{1}{2} \left(\frac{b}{a} - 1 \right) \right)^2 + \frac{1}{4} \frac{\lambda}{m} \frac{r_1^2}{d} \frac{a}{b} \left(1 + \frac{b}{a} \right)^2 \quad (1)$$

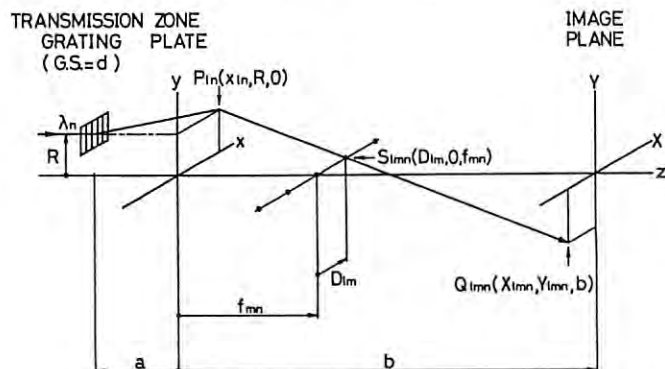


Fig.1 Ray tracing for the determination of the positions of the diffraction spots.

This equation means that every ray appears on various parabolic curves determined by the orders l, m and n .

The experiment was performed in order to confirm the above analysis. λ_1 was fixed at 2.66 nm. Main parameters of a ZP are as follows; r_1 is 5.0 μm and the number of zones is 100. Therefore, its diameter is 100 μm and f_{+1} is 9.40 mm. The primary magnification M_{+1} ($=b/a$) was 195. The outer area of a large ZP was used as TG. The groove spacing d of this area was 0.72 μm in average. A 20 μm diameter pinhole was used as an off-axis diaphragm. Fig.2(a) shows the arrangement of diffraction spots in the image plane when the pinhole was set 30 μm from the optical axis. Fig.2(b) shows the result calculated by eq.1 to explain the arrangement in Fig.3(a). l, m and n are the diffraction order of TG, that of ZP and harmonic order of UR, respectively. Dotted lines represent several parabolic curves determined by eq.1. The primary magnified image of TG can be observed in the lower side. Because of the weak continuous spectrum of UR, the spots are not completely separated. This picture clearly shows that the experimental result agrees well with calculation.

REFERENCES

- 1) Y. Kagoshima et al., Rev. Sci. Instrum. **60** (1989) 2448.
- 2) Y. Kagoshima et al., to be published in JJAP. **29** No. 1 (1990)

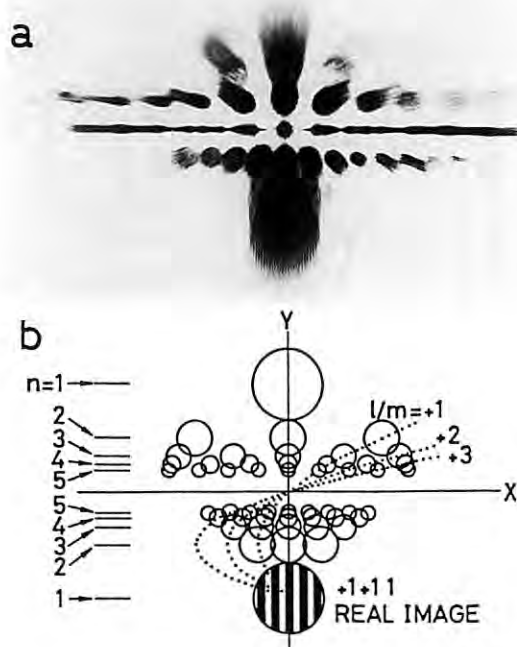


Fig.2 Arrangement of diffraction spots
(a) experimental result (b) predicted by eq.1

DETERMINATION OF CO ORIENTATION ON A Ni(7 9 11) STEPPED SURFACE BY NEXAFS

Yuji OKAWA, Hidetoshi NAMBA and Haruo KURODA

Department of Chemistry and Research Center for Spectrochemistry, Faculty of Science, the University of Tokyo, Hongo, Bunkyo-ku, Tokyo 113

Introduction

Steps and kinks on a vicinal surface can be a model of active sites of catalysis. Near Edge and Surface Extended X-ray Absorption Fine Structure (NEXAFS and SEXAFS) combined with vibrational spectroscopy by HREELS can be powerful techniques to determine a local structure of molecules adsorbed at those sites. So, we applied an apparatus of HREELS with an angle resolved electron spectrometer to measurements of NEXAFS and SEXAFS.

We report preliminary results of determination of CO orientation adsorbed on a Ni(7 9 11) vicinal surface by means of polarization dependence of NEXAFS.

Experimental

The measurement was performed at the soft X-ray beam line BL-7A¹⁾. NEXAFS spectra were recorded in the Auger detection mode.

The samples were prepared from a single crystal nickel rod. Samples were cleaned by repeated cycles of Ar ion-bombardment and annealing. CO was admitted on a sample cooled by liquid nitrogen.

In the present experiments, LEED patterns of a sample surface with no carbon and oxygen showed a twice of step periodicity of an ideal Ni(7 9 11) surface. This surface rearrangement may be due to hydrogen adsorption²⁾. CO was adsorbed on this reconstructed surface. LEED patterns was not changed by CO adsorption.

Results and Discussion

It has been suggested that CO adsorbs at a step site of Ni(7 9 11) stepped surface³⁾ at about 0.3L of CO, and at a terrace site above 3L. Fig.1 shows oxygen K-edge NEXAFS of 3L CO dosed on the reconstructed surface. The position of π^* resonance peak, σ^* resonance peak and absorption edge are deconvoluted as shown by the dotted lines. Each peak is resolved at 537.4, 557 and 541eV respectively. Fig.2 shows the polarization dependence of the intensity of π^* resonance peak divided by the edge jump. The data points of the present spectra are statistically disperse. This is due to weak signal intensity because of angle resolved measurements. However we suggest by the polarization dependence of NEXAFS and HREELS (not mentioned in this report) that CO molecules are perpendicularly adsorbed on bridge sites and/or on-top sites on the terrace plane. At 0.3L, the spectra are noticeably different from that of 3L CO, although the data points are much disperse. The polarization dependence is also different. We think a new adsorbed state of CO is detected. We tentatively assign that the polarization dependence of this π^* resonance peak intensity is due to tilted CO molecules adsorbed at a step site as suggested by Erley. The tilt angle of CO obtained from the polarization dependence is about 20° relative to the terrace normal. Improvement of statistical errors by modifying the detection system is planned in the near future.

References

- 1)H.Namba et al., Rev.Sci.Instrum.,60,1909(1989)
- 2)H.Namba et al., to be published
- 3)W.Erley et al., Surf. Sci., 83, 585(1979)

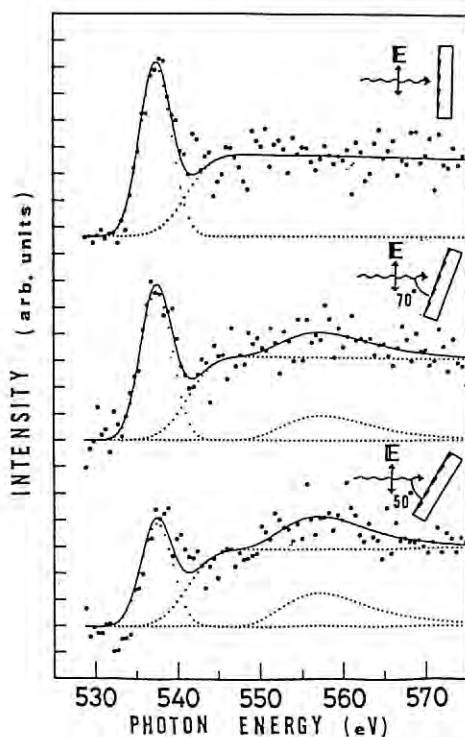


Fig.1. Oxygen K-edge NEXAFS of 3L CO dosed on a Ni(7 9 11)

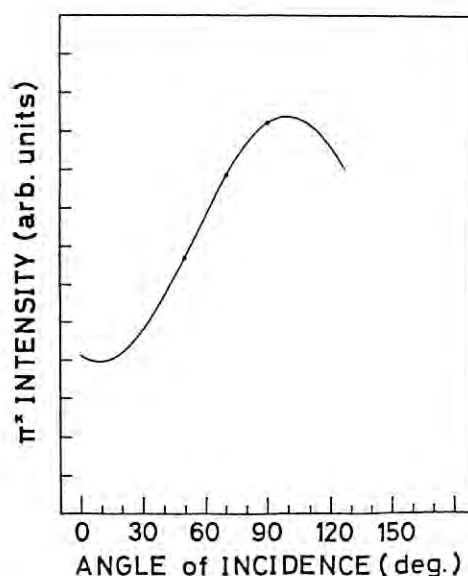


Fig.2. Polarization dependence of π^* resonance peak intensity

TWO ELECTRON EXCITATION PROCESS OF H^+ DESORPTION FROM H_2O ADSORBED ON $Ge(100)$

Hidetoshi NAMBA and Haruo KURODA

Research Centre for Spectrochemistry and Department of Chemistry,
The University of Tokyo, Bunkyo-ku, Tokyo 113

Introduction

More than ten experimental results of H^+ desorption from OH adsorbed on surfaces excited by photons and electrons in the valence region have been reported. However the excitation process leading to H^+ desorption is still ambiguous. One reason of this is due to overlap of a few possible optical transition because the excitation energy of the energy levels of adsorbate and of substrate is in a similar energy range. We chose two examples H_2O adsorbed on $Si(100)$ ¹⁾ and on $Ge(100)$ in order to resolve each process. Si has no sharp absorption edge near 25 eV, but Ge has 3d absorption edge near 30 eV. We report a part of photon stimulated desorption (PSD) of H^+ from H_2O adsorbed on $Ge(100)$.

Experimental and Results

The present experiment has been performed at BL-7B in Photon Factory.²⁾ Desorbed H^+ were detected by a quadrupole mass analyser. The present PSD was measured on the $(2 \times 1)-H_2O$ dissociatively adsorbed sample at the saturation coverage.

Fig.1 shows the H^+ yield as a function of photon energy above 20 eV. Two large peaks are found. Each threshold energy is determined at 31 (Peak A) and 23 eV (Peak B), respectively. Three small peaks (indicated by arrows in the figure) on Peak A are reproducibly resolved. The total electron yield spectrum (TEY) measured on the same sample is shown in Fig.1. Similar shape of two large peaks (Peak C and D) and three peaks on the high energy Peak C with those shown in Fig.1 is found. A remarkable difference is the energy shift of the high energy peaks Peak A to Peak C. The energy shift is 0.7 to 0.8 eV. No clear shift is resolved for the low energy ones Peak B to Peak D.

Discussion

The high energy peak Peak C measured on the $(2 \times 1)-OH$ covered surface corresponds to the TEY peak measured on the clean $Ge(111)$ surface, except for the surface sensitive peak.³⁾ Three peaks have also been detected on the peak. It has been interpreted that the peaks have been caused by transition of 3d electrons to the empty conduction bands of Ge. The small peaks have been agreed with the maxima of the density of states of the empty bands of Ge. So Peak C is caused by the excitation of 3d electrons to the empty conduction band of Ge substrate. The energy shift of Peak A

to Peak C is in good agreement of the band gap energy of Ge. We interpret that the energy shift is due to the simultaneous excitation of 3d electrons to the empty conduction band and the interband transition from near the Fermi level to the empty band. So the optical transition making H^+ desorption is the two electron excitation of from a Ge 3d electron to the empty conduction band and the interband transition.

Peak B is also due to desorption from HO-Ge species. The origin of Peak B is not so clear from an experimental point of view. From the viewpoint of the energy conservation, a transition of O 2s level to the vacuum level is not realistic, a transition to the empty conduction band may be opened. However, in this case, we are not sure whether the final state of the transition is dissociative and repulsive to desorb H^+ , or not. In the desorption of H_2O in a gas and a condensed phase, H^+ desorption in this energy range is considered by predissociation of H_2O after two electron excitation.⁴⁾ We assign that Peak B is due to two electron excitation of Ge-OH chemisorption bond.

References

- 1) H. Namba et al., Photon Factory Activity Report 6, 229 (1988).
- 2) H. Namba et al., Rev. Sci. Instrum. 60, 1917 (1989).
- 3) D.E. Eastman et al., Phys. Rev. Lett. 33, 1601 (1974).
- 4) J.O. Noell et al., Surface Sci. 157, 119 (1985).

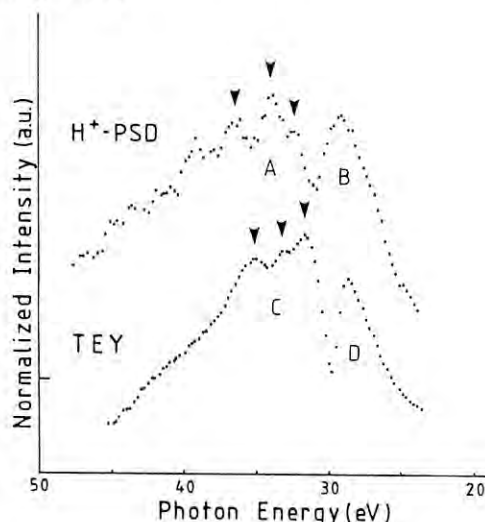


Fig.1 Comparison of H^+ desorption with total electron yield measured on $H_2O/Ge(100)$.

HIGHER-HARMONICS SUPPRESSION SYSTEM FOR SOFT X-RAYS

Izumi WAKI, Yasuharu HIRAI and Atsushi MOMOSE
Advanced Research Laboratory, Hitachi, Ltd., Kokubunji, Tokyo 185

Introduction

Higher-order photons, contained in the soft x-ray beam from grazing-incidence monochromators, degrade the quality of data in experiments using SR. Spectroscopy using undulators suffer from higher harmonics as well, as they generate intense harmonics themselves. In order to enable precise spectroscopy even in the presence of such harmonics, we have developed a higher-harmonic suppressor for soft x-rays.

Design

To suppress higher harmonics, we have employed grazing-incidence mirrors, which filter out higher harmonics with photon energy above the cut-off of total reflection. Figure 1 shows a schematic diagram of the higher-harmonics suppressor. The ambient pressure is below 10⁻⁷ Pa. The cross section of the incident beam is 30 mm horizontally and 3 mm vertically.

Higher harmonics are suppressed through two reflections by a pair of identical mirrors. The exit beam is parallel to and 8 mm lower than the incident beam. Eight sets of double mirrors are mounted on an octagonal prism. Its rotation selects one of the double mirrors to be in the beam path. The 8 sets, each with different coatings and incidence angles, cover the energy range of 80-1600 eV.

In order to suppress higher harmonics efficiently, we have selected reflecting materials and incidence angles so that the absorption edges of mirror-coating elements are located just above the critical energies of total reflection. Table 1 shows the parameters for the eight sets of double mirrors. The reflecting materials are deposited on the optical-flat substrates made of synthetic fused silica. Each mirror set is designed to transmit more than 50% of the fundamental photons and less than 3% of the second harmonics (calculated values are after Henke¹⁾ et al.). The higher-harmonics suppressor is installed at the soft x-ray branch line BL-8A.

Performance

We measured the transmission efficiencies of the double-mirrors. The measured transmission efficiencies of the double-mirrors coated with C, Ni, Al, Si, and Pt satisfied the design values. On the other hand, BN, TiN, and MgF₂ mirrors had transmission lower by factors of 2-10 than expected, owing to ambiguities of the optical constants and to imperfections of the deposited films.

Next, we examined the effect of the suppressor upon measurement of reflectivity of a MgF₂ mirror using a reflectometer²⁾. Figure 2 shows the reflectance spectra of a plane mirror coated with MgF₂ at 2° grazing-incidence angle. The reflectivity measured without the higher-harmonics suppressor is reduced between 330 and 700 eV. This is due to the second-harmonics with energy higher than 660 eV, where the reflectivity suddenly decreases due to the total reflection and the F K-shell absorption edge at 686 eV. The results measured with the higher-harmonics suppressor show that the reduction of the reflectivity disappears. Thus, the harmonics suppressor reduces the effects of higher harmonics in measuring reflectivities.

References

1)B.L.Henke et al., AIP Proc. 75, 340 (1981).
2)Y.Hirai et al., Rev.Sci.Instrum. 60, 221(1989)

Table 1. Parameters for the double mirrors

Harmonics suppression energy (eV)	Reflection material	Grazing incidence angle(deg.)	Absorption edge(eV) [element]
80- 150	BN	7.5	188[B]
130- 250	C	4.5	284[C]
210- 340	TiN	4.0	399[N]
			455[Ti]
310- 540	MgF ₂	3.0	686[F]
400- 690	Ni ²	3.0	855[Ni]
600-1100	Al	1.5	1560[Al]
900-1600	Si	1.0	1839[Si]
None	Pt	1.0	

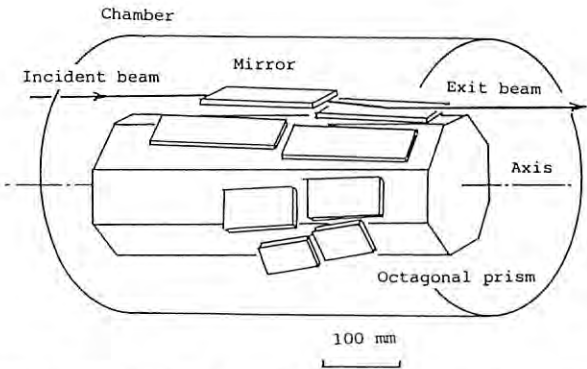


Fig.1 Schematic diagram of the higher-harmonic suppressor with 8 sets of double mirrors.

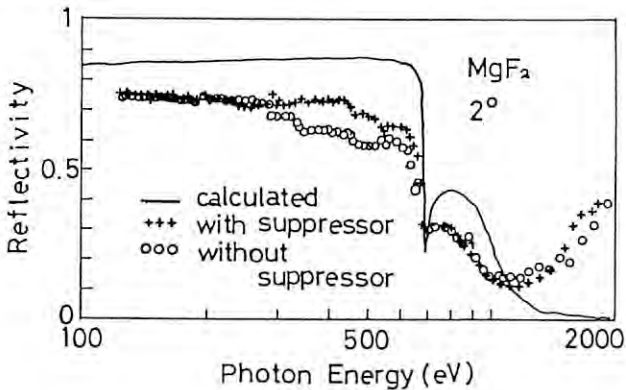


Fig.2 Reflectivities of a MgF₂ mirror at a grazing-incidence angle of 2 degrees.

EVALUATION OF THICKNESS AND ITS UNIFORMITY IN LANGMUIR-BLODGETT (LB) FILMS USING SOFT X-RAY REFLECTION

Atsushi MOMOSE, Yasuharu HIRAI, Izumi WAKI, Shuji IMAZEKI and Yasushi TOMIOKA
Advanced Research Laboratory, Hitachi Ltd., Kokubunji, Tokyo, 185Introduction

Soft X-ray reflectivities of LB films were measured using SR. Thickness and its uniformity in LB films were determined by analyzing oscillatory profiles of reflectivity vs. wavelength or grazing incidence angle, which is due to an interference of two waves reflected at the film surface and at the film-substrate interface. Thickness and its uniformity are basic parameters to characterize LB films, and the obtained results provided suggestions about the mechanism of film deposition.

Three types of LB film fabrication have been considered: the "Y-type" is defined as a floating monolayer is transferred to a substrate at both down-strokes and up-strokes in dipping cycles, and the "X(Z)-type" as the monolayer is transferred at only up(down)-strokes. In some conditions, Y-type deposition changes and approaches an X-type one gradually and spontaneously during the process, but X-ray diffraction analyses revealed the same bilayered structure of the deposited film¹⁾ as pure Y-type films.

Experiments and Results

At BL-8A, reflectivities of LB films were measured using a reflectometer for soft X-rays²⁾. Cadmium arachidate $[(CH_3(CH_2)_{18}COO)_2Cd]$ LB films were prepared on optically flat borosilicate glass substrates. Millipore filtered water added $4 \times 10^{-4} M$ $CdCl_2$ and $5 \times 10^{-5} M$ $KHCO_3$ was used as a subphase at 19 to 20°C (pH 6.5). The surface pressure of a floating monolayer was kept constant at 15 dyn/cm, and dipping speed of substrates was 0.6 to 0.7 mm/min.

Figure 1 shows the measured reflectivity (•) and its fitting curve (—) of a film which was nominally deposited as 39 monolayers (that is, the substrate was passed through the floating monolayer 39 times). Although the deposition of the film was Y-type at the beginning of fabrication, a gradual transition to an X-type appeared after the 10th stroke, which was monitored by the area decrease of the floating monolayer (see Figure 2). At first, the fitting calculation included parameters for reflectivity loss due to roughness of the film surface and the nonmonochromatic

component contained in the incident beam. However, the fitting was not successful by assuming that the thickness, or the number of layers, was uniform. Therefore, the measured reflectivity was fitted by also taking account of thickness distribution weight as a parameter. The obtained film thickness distributions as a percentage of the film surface are shown in Figure 3. Furthermore, the obtained average thickness corresponded not to the number of strokes but to the area decrease of the floating monolayer.

Discussions

To explain the transition from Y-type to X-type deposition, a molecular overturning model³⁾, a hole creation model⁴⁾ and a molecular peeling model⁵⁾ have been proposed. Experimental verification has not been successful enough to determine model validity. Our experiment shows that the film consisted of areas where the thickness varied, and that all molecules which disappeared from the air-water interface were deposited to the substrate. The molecular overturning model seems the most satisfactory one to the authors to explain these experimental results^{6),7)}.

References

- 1) C. Holley and S. Bernstein, *Phys. Rev.*, **52** 525 (1937)
- 2) Y. Hirai, I. Waki, A. Momose and K. Hayakawa, *Rev. Sci. Instrum.*, **60** 2219 (1989)
- 3) E. P. Honig, *J. Colloid Interface Sci.*, **43** 66 (1973)
- 4) H. Hasmonay, M. Vincent and M. Dupeyrat, *Thin Solid Films*, **68** 21 (1980)
- 5) J. B. Peng, J. B. Ketterson and P. Dutta, *Langmuir*, **4** 1198 (1988)
- 6) A. Momose, Y. Hirai, I. Waki, K. Hayakawa, S. Imazeki, Y. Tomioka and M. Naito, *Thin Solid Films*, (to be published)
- 7) J. B. Peng: Recently, he insists that it is possible to explain the experimental data within his model.(private communication)

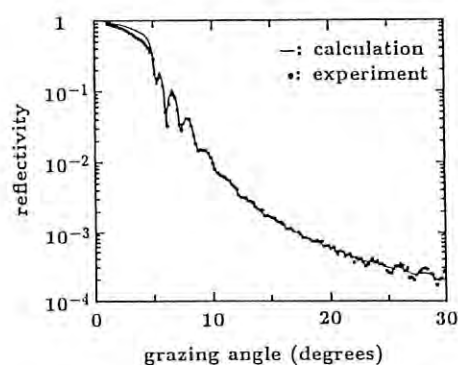


Fig.1 Measured reflectivity and its calculated fitting curve for 10nm soft X-rays.

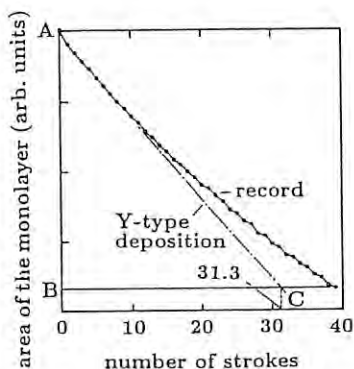


Fig.2 Film area decrease during fabrication process.
o → •: up-stroke.

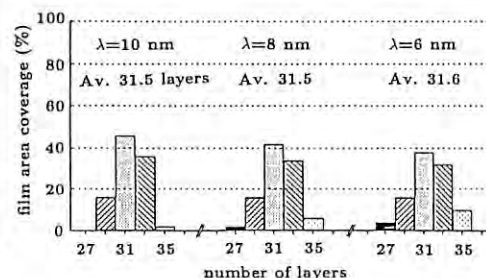


Fig.3 Obtained thickness distribution using 10nm, 8nm and 6nm soft X-rays. The average number of layers is the number of strokes minus 7.5.

SOFT X-RAY ANALYSIS SYSTEM: PERFORMANCE TEST OF A REFLECTOMETER

Yasuharu HIRAI, Izumi WAKI, Atsushi MOMOSE and Fumihiko UCHIDA^{*}
 Advanced Research Laboratory, Hitachi, Ltd., Kokubunji, Tokyo 185
^{*}Central Research Laboratory, Hitachi, Ltd., Kokubunji, Tokyo 185

Introduction

Soft x-rays are useful probes to evaluate optical elements and characterize materials and surfaces. Therefore, we have developed a soft x-ray analysis system equipped with a reflectometer and detectors for absorption-induced emissions. In the following, we describe the design and the results of performance tests for the reflectometer through measurements of reflectivities and scattering distributions of Cu plane mirrors prepared by a diamond-turning machine.

Experimental

A soft x-ray analysis system consists of three chambers: analysis, evaporation, and sample introduction. Figure 1 shows a schematic diagram of the analysis chamber equipped with the reflectometer. Pressure is 10^{-10} Pa. A sample and a detector rotate with an angular accuracy of 0.01° and resolution of 0.001° .

The reflectometer is installed at the soft x-ray branch line BL-8A. We measured angle-resolved scattering and reflectivities of diamond-cut plane copper (OFHC) mirrors. They

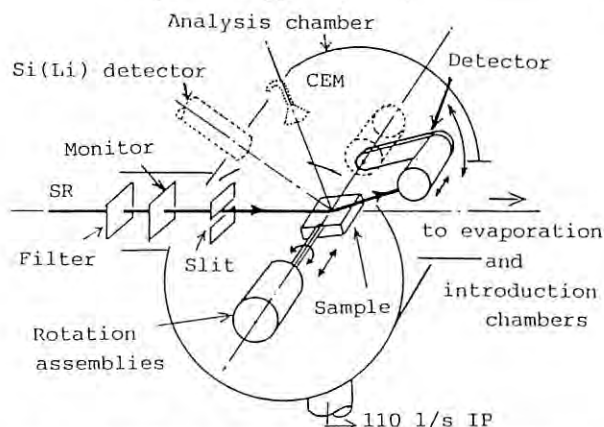


Fig.1 Schematic diagram of the reflectometer. Si(Li) detector and CEM are not used here.

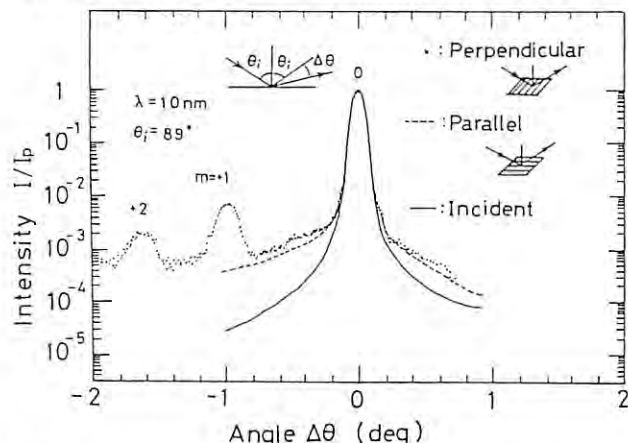


Fig.2 Angle-resolved scattering of diamond-cut copper mirrors. Cutting marks are oriented either perpendicular or parallel to the plane of incidence. In the perpendicular case, diffraction peaks appear (order number m).

were fabricated with a fly-cutting machine¹⁾ without additional polishing or coating. S-polarized beam was used for all the measurements.

Results and Discussion

Figure 2 shows the results of angle resolved scattering measurements with an angle step of 0.01° , an incidence angle of 89° , and an wavelength of 10 nm. All the curves are normalized to their peak intensities. The origin of the angle is set at each specular peak. Cutting marks are oriented parallel and perpendicular to the plane of incidence. Diffraction peaks appear for the perpendicular case because of cutting marks, the period length of which is estimated to be $22.33 \mu\text{m}$. This value agrees with the tool-feed rate.

Figures 3(a) and 3(b) show the energy spectra of reflectivities of these mirrors. Solid curves are calculated using the optical constants of Henke et al.²⁾. The large discrepancy between the observed and calculated results in Fig.3(b) is due to diffraction. With selection of a cutting direction parallel to the plane of incidence, diamond-cut mirrors can be utilized in soft x-ray grazing-incidence optics systems.

References

- 1) S. Moriyama et al., SPIE Proc. 830, 98 (1987).
- 2) B. L. Henke et al., AIP Proc. 75, 340 (1981).

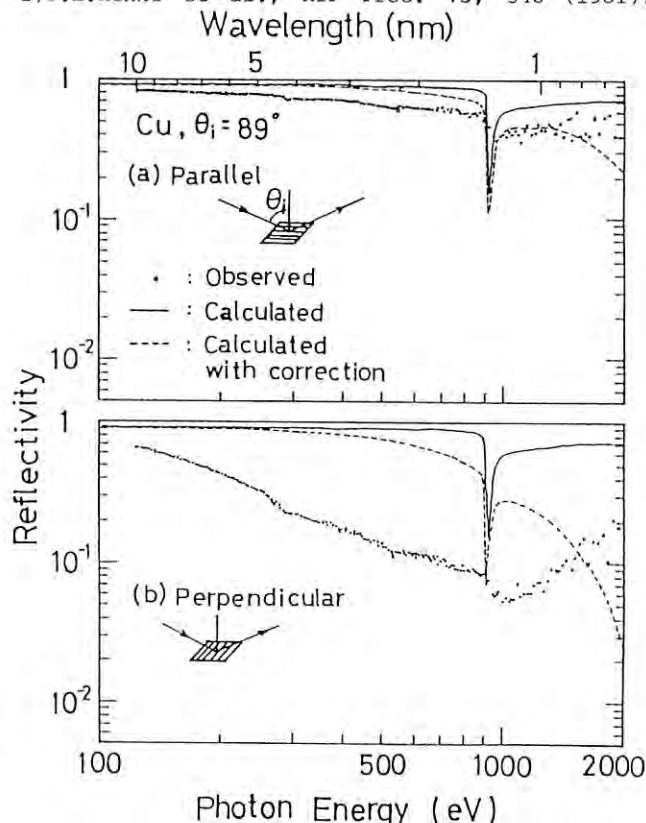


Fig.3 Reflectivities of diamond-cut copper mirrors for (a) parallel and (b) perpendicular cases. Broken curves are calculations corrected with the effect of surface roughness.

Investigations of Si Oxidation Process by XPS and XANES Using Synchrotron Radiation

Hideo SEKIYAMA, Masatoshi NAKAZAWA and Susumu KAWASE*

Central Research Laboratory, Hitachi Ltd., Kokubunji, Tokyo 185

*Present address : Hitachi Research Institute, Chiyoda-ku, Tokyo 101

Introduction

There has been considerable interest in the mechanism of Si surface oxidation from fundamental and applied points of view. In the present study, XPS and surface-sensitive XANES spectroscopy have been used for probing the local electronic structures in the initial stages of Si oxidation.

Experimental

Measurements of XPS and XANES spectra were carried out at the soft X-ray beamline(BL-8A), where a grazing-incidence monochromator¹⁾ equipped with a varied-space plane grating is used. XANES spectra were measured with the Auger-electron-yield method²⁾, which provides high surface sensitivity. Clean Si(100) and Si(111) surfaces were obtained by several cycles of Ar ion sputtering and annealing at $\sim 1000^\circ\text{C}$. The oxidation of Si surfaces was carried out at various temperatures between room temperature and 700°C .

Results and Discussion

Figure 1 shows Si 2p XPS spectra ($h\nu=130\text{eV}$) for Si(100) and Si(111) surfaces exposed to oxygen at room temperature. In this case, the escape depth of the photoelectron (kinetic energy : $E_{\text{kin}}=25\text{eV}$) for the Si 2p level is about 0.6 nm. The peaks of intermediary oxidation states (Si^{1+} , Si^{2+} , Si^{3+}) for the Si(111) surface have greater intensity ratios than those for the Si(100) surface. This indicates that, at room temperature, the oxidation of clean Si(111) surfaces proceeds much faster than that of the clean Si(100) surface because of the difference between surface structures of Si(100) and Si(111)³⁾.

Figure 2 shows oxygen K-XANES spectra for progressive oxidation process of Si(100) and Si(111) surfaces. Oxygen K-XANES spectra for molecular oxygen⁴⁾ and thermally grown silicon dioxide($\sim 200\text{nm}$ thick on a Si surface) are also shown in Fig.2. Oxygen K-XANES spectra for Si surfaces are more similar to the XANES spectrum for SiO_2 than that for molecular oxygen. This indicates that oxygen is atomically adsorbed onto the Si surfaces, and that oxygen-silicon bonds are formed by the oxygen exposure at room temperature. The intensity of band B attributed to the continuum shape resonance increases with increasing oxygen exposure. The change in the intensity of band B suggests that an effective potential barrier⁵⁾ is formed because of the formation of silicon-oxide like molecular units (SiO_x) where a Si atom is surrounded by one or more electronegative oxygen atoms.

References

- 1) M. Itou et al., J. Appl. Opt. **28**, 146 (1989).
- 2) J. Stöhr et al., Phys. Rev. **B30**, 5571 (1984).
- 3) F. S. Himpel et al., Phys. Rev. **B38**, 6084 (1988).
- 4) M. Yanagihara et al., KEK-Report **84-17** (1984).
- 5) J. L. Dehmer, J. Chem. Phys. **56**, 4496 (1972).

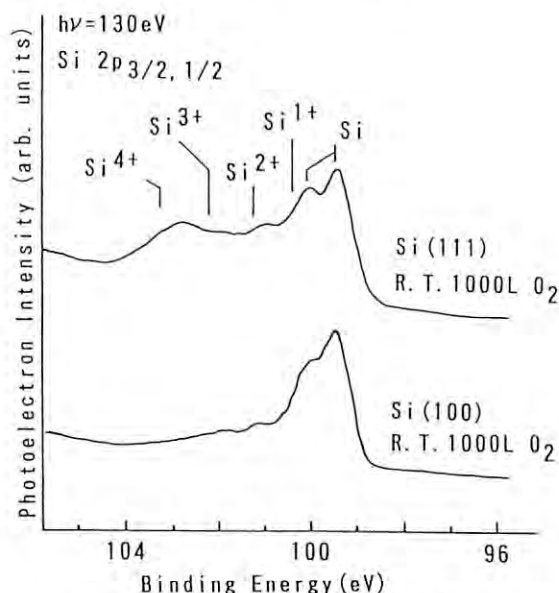


Fig.1 Si 2p XPS spectra ($h\nu=130\text{eV}$).

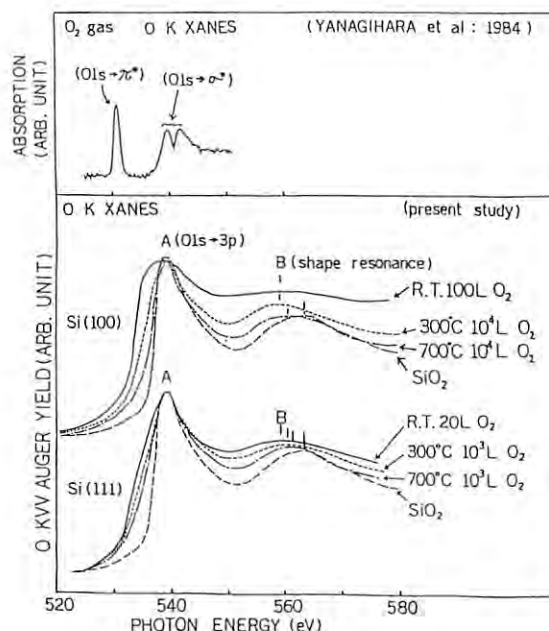


Fig.2 Oxygen K-XANES spectra.

Taro OGAWA, Kozo MOCHIJI, Yasunari SODA, and Takeshi KIMURA

Central Research Laboratory, Hitachi Ltd., Higashi-Koigakubo, Kokubunji, Tokyo 185

Introduction

In SR lithography, secondary electrons generated from the substrate material deteriorate its excellent resolution. In this study, the effects of secondary electrons from an Si substrate, which is the most important material for LSIs, on the resolution of SR lithography, is investigated both experimentally and theoretically.

Experimentals

The lithography instrument with an oscillating mirror at BL-8C was used for the experiments. Peak wavelengths of 0.5-0.8nm can be acquired by this instrument.

The new X-ray mask was prepared to estimate the resolution limit of SR lithography. This mask consisted of absorbing patterns at a width of 0.05 μ m by Si(110) anisotropic etching and the tantalum shadowing technique¹⁾.

Path of the electrons in the resist was simulated. In the simulation, the X-ray profile was calculated using Fresnel diffraction. A single photon absorption generated a pair of photo- and Auger electrons, and their yield corresponded to X-ray absorption. Angular distribution of Auger electron was treated as spherical, while asymmetry parameter β was given by 2 for photoelectrons. Rutherford and Bethe-Bloch models were used to calculate the energy loss of electrons in the resist, and the developed resist pattern shape was simulated using the ray-tracing model^{2,3)}.

Results and Discussions

In Figs.1(a) and 1(b), the SEM photographs of PMMA patterns on an Si and the polymer-coated Si substrate, exposed to an energy of 2J/cm² is shown. In Fig.1(a), an undercut was produced at the resist-substrate boundary by secondary electrons from the substrate, while no undercut

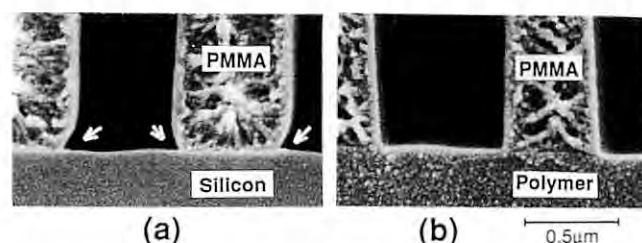


Fig.1 SEM photographs of replicated PMMA patterns, (a) on the Si substrate, (b) on the polymer-coated Si substrate.

Fig.2 SEM photograph of a replicated PMMA pattern at a width of 0.05 μ m. The proximity gap is 5 μ m.



was observed in Fig.1(b). Furthermore, on the polymer-coated Si substrate, as shown in Fig.2, a PMMA pattern at a width of 0.05 μ m could be fabricated using the mask mentioned above.

As the above exposing wavelengths include an Si 1s absorption edge of 1.84keV (\approx 0.675 nm), excitation of 1s, 2s/2p photoelectrons and the KLL Auger electron is possible. In these electrons, contribution of Auger electron is the highest, because it has both high kinetic energy and high yield, and the simulation mentioned above was applied to confirm whether this Auger electron produces an undercut on the developed pattern.

For the exposing X-ray, a monochromatic wavelength of 0.67nm was selected. This wavelength coincides with the Si 1s absorption edge, where the effects of Si KLL Auger electrons can be observed selectively. In Fig.3(a), simulated resist pattern on the Si substrate exposed to an energy of 2J/cm² is shown. An undercut was produced at the resist-substrate boundary, while no undercut was produced in the simulation of the polymer-coated Si substrate. This result coincides well with the above experiments. Therefore, this undercut is due mainly to Si KLL Auger electrons. Furthermore, in Fig.3(b), a simulated resist pattern on the Si substrate exposed to a monochromatic wavelength of 0.7nm, which cannot excite Si 1s electrons is shown. An undercut can also be eliminated by this approach, and this shows eliminating the wavelength which excites the Si 1s electron from the exposing SR beam is promising for fabricating deep submicron patterns on the Si and the Si compound substrate with SR lithography.

SR lithography was also confirmed to improve the resolution to lower than 0.1 μ m if secondary electrons from the substrate were effectively minimized.

References

- 1) N.Tsumita et al., J.Vac.Sci.Technol.19 (1981) 4, 1211.
- 2) P.Hagouel, Ph.D.dissertation, UCB,1976.
- 3) T.Matsuzawa et al,IEEE Electron Device Lett.6 (1985) 416.

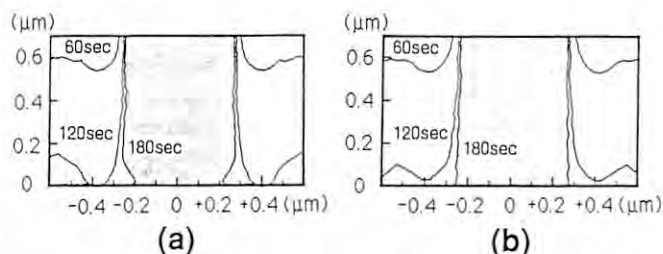


Fig.3 Simulated PMMA pattern profile. The pattern size is 0.6 μ m line/space, and the proximity gap is 20 μ m. The substrates are Si. Wavelengths are (a) 0.67nm, (b) 0.70nm. The profile reflects different development times, 60sec, 120sec, 180sec.

A MASK ALIGNMENT SYSTEM FOR SR X-RAY LITHOGRAPHY

Yoshiharu TANAKA, Eiichi KOUNO, Jouji IWATA, Kiyoshi FUJII and Katsumi SUZUKI

Production Engineering Development Laboratory, NEC Corporation
M3-484, Tsukagoshi, Saiwai-ku, Kawasaki 210
Fundamental Research Laboratories, NEC Corporation
34, Miyukigaoka, Tsukuba, Ibaraki 305

Introduction

SR X-ray lithography offers advantages in (1) resolution, (2) process latitude, and (3) throughput for the deep submicron ULSI fabrication use. The major issues for X-ray lithography are the overlay accuracy and the critical dimension control. The development of a useful X-ray mask aligner is thus, one of the most important subject for the SR X-ray lithography. This paper describes the new X-ray mask alignment system employing a simple projection linear fresnel zone plate (LFZP) method.

Mask Alignment System

The block diagram of the newly developed mask alignment system is shown in Fig.1. Both an X-ray mask and a wafer are set in the open air for suppressing the temperature rise during X-ray exposure process as well as for realizing high throughput. The alignment optics is installed in a He chamber, where He gas pressure is kept $1 \text{ atm} \pm 10 \text{ mm H}_2\text{O}$. The X-ray extraction window for the He chamber is made of a $1 \mu\text{m}$ thick SiN_x membrane, which is stable for the X-ray exposure in comparison with a polyimide film which is degraded by X-ray irradiation resulting in darkening and wrinkling due to scission of main chain of polymer.

Figure 2 shows the alignment optics for the projection LFZP method. The wafer mark consists of a $2 \mu\text{m}$ wide, $4 \mu\text{m}$ pitch grating, which yields high signal to noise ratio. An LFZP with $40 \mu\text{m}$ focal length is used for the mask mark. The focal length of the LFZP equals to the gap between the mask and the wafer. When a laser beam focused by the LFZP mark illuminates the wafer mark, the laser beam is diffracted by the wafer mark. The first order of diffracted laser beam is collimated through the LFZP mark on to

the photodetector. The focusing position of the collimated laser beam changes according to the relative position of the grating line with regard to the LFZP mark.

Overlay Accuracy

Figure 3 shows an alignment signal obtained with the projection LFZP alignment system. It is shown that the alignment signal has $8.9 \text{ V}/\mu\text{m}$ sensitivity and $2 \mu\text{m}$ capture range. An excellent linearity near the zero-cross point has been obtained. The noise level is only 80 mV peak to peak, which corresponds to better than $0.01 \mu\text{m}$ resolution for the alignment error detection.

The overlay error of this alignment system was measured by the double exposure technique, which employs two exposure processes using the same X-ray mask. The alignment data, thus, do not include the error due to the mask distortion. The overlay errors, measured by using vernier patterns, are shown in Fig. 4. The overlay errors were less than $0.1 \mu\text{m}$ in 3 sigma in both X and Y directions. This result shows the usefulness of this mask alignment system for sub-half micron feature size device fabrication.

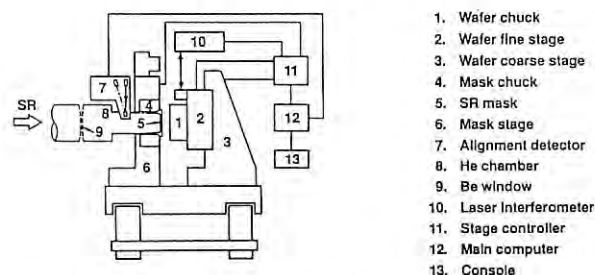


Fig.1 Block diagram for the X-ray mask alignment system.

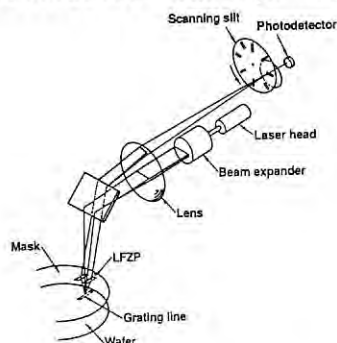


Fig.2 Schematic diagram of the alignment optics for projection LFZP method.

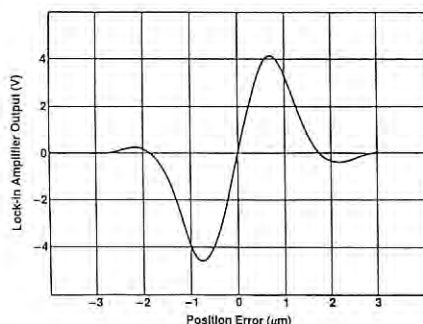


Fig.3 Typical alignment signal obtained from the projection LFZP alignment system.

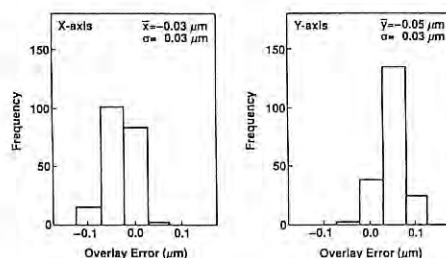


Fig.4 Overlay error measured by double exposure method using single mask.

X-ray absorption spectra of poly-p-phenylenes: localization of π^* orbitals

Toshihiko YOKOYAMA, Kazuhiko SEKI, Ikuo MORISADA, Kunishige EDAMATSU
and Toshiaki OHTA

Department of Materials Science, Faculty of Science, Hiroshima
University, Naka-ku, Hiroshima 730

Understanding of XANES spectra of molecules and solids is an attractive current subject. There remains several unsettled fundamental problems. One of them is that the oscillator strength of the transition to the upper-lying π^* orbital in conjugated π -electron systems is surprisingly smaller than that to the lower-lying one, and a simple MO consideration fails in explaining such anomaly. In this work, C K-edge XANES spectra of poly-p-phenylenes and polyacenes were measured, and in order to explain the observed $1s \rightarrow \pi^*$ features, empirical MO calculations based on the CNDO scheme were performed. Multi-layer films of π -conjugated hydrocarbons were prepared by evaporation onto polycrystalline Cu substrates. XANES measurements with the total electron yield mode were performed at the Grasshopper Monochromator Station BL 11A.

Figure 1 shows normal-incident XANES spectra of poly-p-phenylenes around π^* regions, together with a spectrum of gaseous benzene taken with EELS[1]. All the spectra give a similar trend that only one intense π^* resonance appears at nearly the same excitation energy. It is, however, expected from virtual π^* orbitals of their ground states and confirmed from electron transmission spectroscopy that the energy of the lowest π^* orbital(s) should gradually decrease with the extension of π conjugated system and that there should appear a greater number of strong bands in a larger molecule. The present MO calculation based on the equivalent core approximation significantly suppresses the relative intensity. The suppression of the transition probability to the higher-lying π^* orbital is interpreted in terms of the localization of π^* orbitals in the $1s$ -excited state. When a $1s$ core electron is excited or ionized, passive valence electrons experience a sudden enhancement of a Coulomb attractive potential as if the carbon nucleus were replaced with nitrogen. Since the $2p_z$ level of nitrogen is at a lower energy than the C $2p_z$ one, the lowest π^* orbital becomes concentrated at the excited atom, and the atomic orbitals of the unexcited carbon atoms compose higher π^* states. Since the peak intensity is essentially determined by the population of π^* orbitals of the excited atom, this leads to a significant sup-

pression of transition probabilities to higher-lying excited states. The experimentally obtained spectra of π^* region of poly-p-phenylenes resemble that of benzene, and the lowest-lying virtual π^* orbital dominates the spectral features, again exemplifying the rearrangement (localization) of their π^* orbitals.

[1] J.A.Horsley, J.Stohr, A.P.Hitchcock, D.C.Newbury, A.L.Johnson, and F.Sette, J.Chem.Phys. **83**, 6099 (1985).

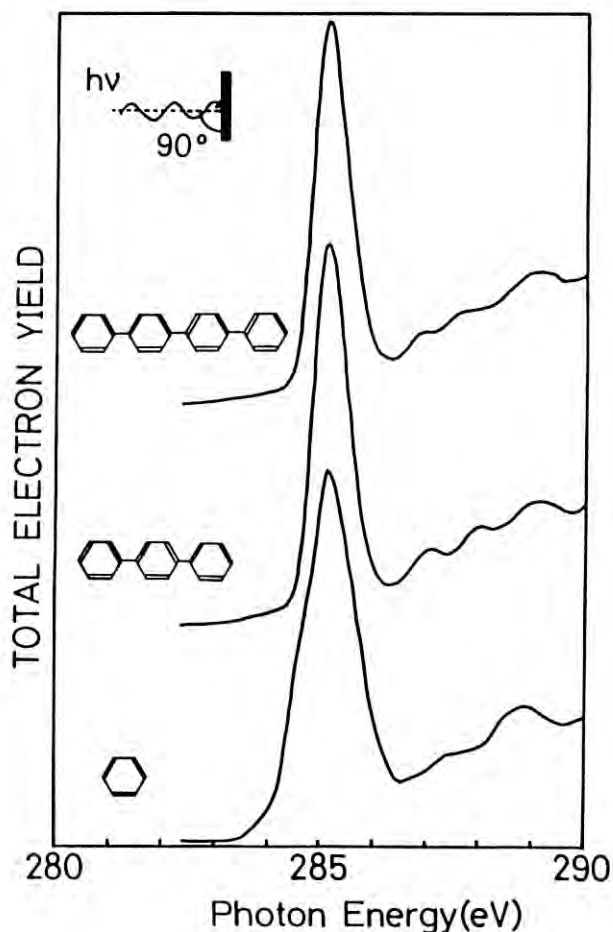


Fig.1. Normal-incident C K-edge XANES spectra in the vicinity of the $1s \rightarrow \pi^*$ region of poly-p-phenylenes. An EELS spectrum of gaseous benzene is inserted[1].

UV photopolymerization of long-chain diacetylene compounds
studied by Polarized XANES spectroscopy

Kazuhiko SEKI, Toshihiko YOKOYAMA, Ikuo MORISADA, Kunishige EDAMATSU,
Hiroshi TANAKA, Hiroshi YANAGI, and Toshiaki OHTA

Department of Materials Science, Faculty of Science, Hiroshima
University, Naka-ku Hiroshima 730

Hiroo NAKAHARA and Kiyoshige FUKUDA

Department of Chemistry, Faculty of Science, Saitama University,
Shimookubo, Urawa 338

Diacetylene compounds of general formula $RC\equiv C-C\equiv CR'$ polymerize e.g. by UV light, to form polydiacetylenes $\{RC-C\equiv C-CR'\}_n$. We already reported that the Cls XANES of a long-chain diacetylene tricoso-10,12-dienoic acid (TDA) ($R = CH_3(CH_2)_9$, $R' = (CH_2)_8COOH$) and its Cd salt, in the form of evaporated and Langmuir-Blodgett (LB) films, respectively, changes drastically on UV photopolymerization in the Cls $\rightarrow \pi^*$ excitation region [1]. Here we report further study of this change and its interpretation by MO calculations [2,3].

The samples were: (1) evaporated films of TDA, (2) LB films of TDA Cd salt polymerized after deposition on a NESA glass, and (3) TDA Cd salt polymerized in monolayer form on water and then deposited by LB method on a NESA glass. The XANES spectra were measured as the total-electron yield at the beamline 11A of Photon Factory with a grasshopper monochromator with resolution of 0.5-0.7 eV in the Cls region. UV photopolymerization was carried out using a D₂ lamp in and outside of the vacuum chamber.

The change of the XANES spectra of an evaporated film of TDA in the Cls $\rightarrow \pi^*$ region by UV polymerization is shown in Fig. 1. The peak at 285.1 eV of monomer (with a fine structure of 0.3 eV splitting) is split to two peaks at 284.4 and 285.7 eV. These features are interpreted by MO calculation using equivalent-core approximation [4]. The monomer peak is ascribed to the transition to the lower π^* levels resulting from the interaction of two pairs of π^* levels in diacetylene. The transition to the upper π^* levels has negligible transition probability. In polymer, two π^* systems are formed from the C2p orbitals in and normal to the molecular plane. The two features in Fig. 1 corresponds to the excitations to the bottom of these states.

The LB films of type (2) polymerized after deposition gave qualitatively similar change, but the degree of change was and not so extensive as that of evaporated films. This difference is ascribed to the disorder in the films

caused by the deposition on the NESA glass. To confirm this, the films of type (3) polymerized on the water surface showed similar spectra as those of evaporated films.

- [1] K. Seki et al., This Report, p.240 (1988).
- [2] K. Seki et al., Thin Solid Films, in press.
- [3] K. Seki et al., Phys. Scripta, in press.
- [4] T. Yokoyama et al., Phys. Scripta, in press.

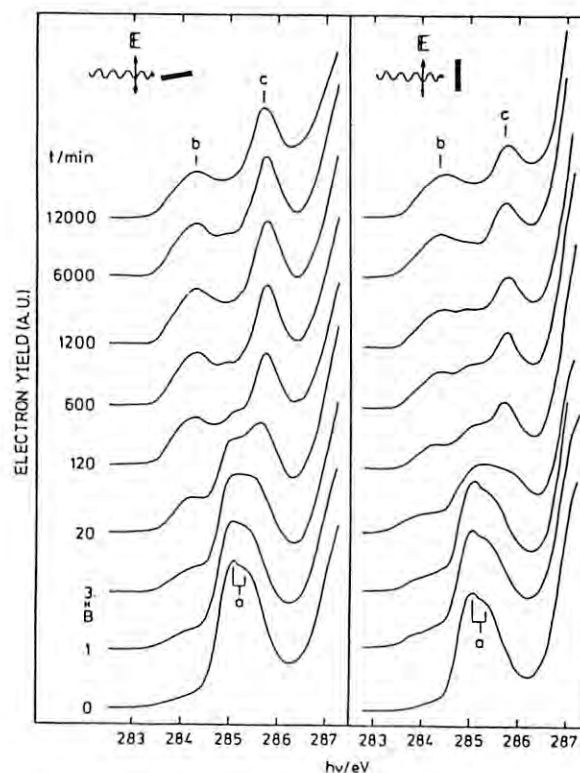


Fig. 1. Change of the XANES spectra in the π^* excitation region by UV polymerization for grazing (15°) incidence (left) and normal incidence (right) of synchrotron radiation. The time of UV irradiation (in min) are shown for each curve.

THRESHOLD PHOTOIONIZATION OF N_2 K SHELLTatsuji HAYAISHI, Akira YAGISHITA¹, Eigorou MURAKAMI² and Yumio MORIOKA³¹Institute of Applied Physics, University of Tsukuba, Tsukuba, Ibaraki 305, Japan²National Laboratory for High Energy Physics, Tsukuba, Ibaraki 305, Japan³Chiba Institute of Technology, Narashino, Chiba 275, Japan³Institute of Physics, University of Tsukuba, Tsukuba, Ibaraki 305, JapanIntroduction

In previous works¹⁻⁵), we have studied photodissociation of molecules in the VUV region using a threshold-electron photoion coincidence technique. The present study is an extension of the work into the soft X-ray region where excitation and ionization of a deeper inner-shell are possible. The inner-shell hole causes more various dissociation processes than valence-shell ionization. In this work, we report photo-dissociation from K 1s-shell excitation of N_2 .

Experimental

Experiments were carried out at BL-11A using a 2m grasshopper monochromator. The mass spectrometer used was of time-of-flight (TOF) type accompanied with a threshold-electron energy analyzer²⁾. The resolution of the electron energy analyzer is estimated to be about 0.03 eV from a measurement for Kr 4p photoelectrons.

Results and Discussion

Figure 1 shows an example of TOF spectra obtained in the threshold-electron photoion coincidence measurements. The photon energy at 401 eV corresponds to N_2 K 1s \rightarrow 2p π excitation. One can see three peaks; A, B and C. The peak A is due to the formation of N_2^+ parent ions and the peak B is that of N_2^{++} parent ions. It follows that kinetic energies of these ions are zero. The peak C is due to the formation of N^+ fragment ions with a dissociation energy. In general, the TOF spectrum of a fragment ion is composed of two peaks when the fragment ion has a dissociation energy. The two peaks correspond to ions generated with forward and backward initial velocities with respect to the axis of the TOF spectrometer. In the present work, however, the energetic ions with backward velocities escape from the detection cone of the TOF spectrometer because the low voltage of 10 eV is applied to an ion repeller. The low voltage is necessary to the high resolution of the threshold-electron energy analyzer. As a result, a peak alone corresponding to energetic ions with forward velocities was observed.

The K 1s-hole may be filled by Auger and/or Auger cascade transitions. The decay causes the formation of multiply charged parent-ions (ex, N_2^{++}). In succession, the parent ions dissociate to N^+ fragment ions. The present work is consistent with this fact. However, the N_2^+ parent ions are also observed in addition to N_2^{++} . This observation suggests that a radiative transition takes part in the decay from K 1s-shell excitation. Thus, the present technique is also useful to photodissociation of molecules in the soft X-ray region.

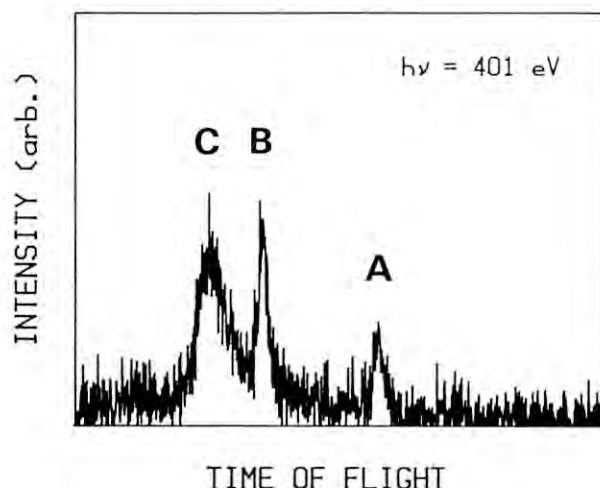


Figure 1. The TOF spectrum in coincidence with threshold electrons from N_2 K 1s \rightarrow 2p π excitation. The abscissa shows the TOF of ions which is directly related to the kinetic energy of the ions. Peaks A, B and C correspond to N_2^+ , N_2^{++} and N^+ ions produced by the excitation, respectively.

References

- 1) Y. Morioka, T. Akahori, M. Watanabe, M. Nakamura, T. Hayaishi and K. Ito, PF Activity Rep. No. 2 126 (1985)
- 2) Y. Morioka, T. Akahori, T. Hayaishi, T. Namioka, T. Sasaki and M. Nakamura, J. Phys. B **19**, 1075 (1986)
- 3) K. Ito, A. Yagishita, Y. Morioka and T. Hayaishi, J. Phys. B **19**, 3061 (1986)
- 4) T. Hayaishi, A. Yagishita, K. Ito, M. Kihara and Y. Morioka, J. Phys. B **20**, L207 (1987)
- 5) Y. Morioka, T. Matsumoto, T. Endow, T. Hayaishi, K. Tanaka and K. Ito, PF Activity Rep. No. 6 260 (1988)

X-RAY ABSORPTION SPECTROSCOPY OF $\text{Nd}_{2-x}\text{Ce}_x\text{CuO}_4$

Hiroyoshi MATSUYAMA¹, Takashi TAKAHASHI¹, Takanori WATANABE¹, Takayuki KASHIWAKURA¹, Takeo EJIMA¹, Hiroshi KATAYAMA-YOSHIDA¹, Shigeru SATO¹, Nobuhiro KOSUGI², Akira YAGISHITA³, Kenichiro TANAKA³, Shinichi SHAMOTO⁴, and Masatoshi SATO⁴

¹Department of Physics, Tohoku University, Sendai 980

²Division of Molecular Engineering, Kyoto University, Kyoto 606

³Photon Factory, KEK, Tsukuba 305

⁴Institute for Molecular Science, Okazaki 444

Recently Nücker et al.[1] reported an electron energy-loss spectroscopy on newly discovered "electron-doped" superconductor $\text{Nd}_{2-x}\text{Ce}_x\text{CuO}_4$ [2]. In the report the authors questioned n-type superconductivity in $\text{Nd}_{2-x}\text{Ce}_x\text{CuO}_4$ according to their oxygen-K absorption measurement. We examine this challenging report, since we have done a quite similar experiment but reached a different conclusion.

Figure 1 shows O-K absorption spectra obtained by a total-photoemission-yield-method for $\text{Nd}_{2-x}\text{Ce}_x\text{CuO}_4$ at $x=0.04$ (non-superconductor) and $x=0.15$ (superconductor with $T_c=23\text{K}$). The spectra are in good agreement with those reported by Nücker et al. [1]. We include in Fig. 1 an O-K absorption spectrum of $\text{Bi}_2\text{Sr}_2\text{CaCu}_2\text{O}_8$ ($T_c=85\text{K}$) measured with the same experimental setup for comparison. An inset in Fig. 1 shows x-ray photoemission spectra of the O 1s core level for $\text{Bi}_2(\text{Sr}, \text{Ca})_2\text{CuO}_8$ and $\text{Nd}_{1.8}\text{Ce}_{0.2}\text{CuO}_4$. In Fig. 1 we immediately find a considerable difference in energy between the O 1s core level and the O-K absorption edge for $\text{Bi}_2\text{Sr}_2\text{CaCu}_2\text{O}_8$; the absorption edge (peak A at 528 eV) has an energy about 1 eV smaller than that of the O 1s core level (529 eV). A similar discrepancy is also found for $\text{La}_{2-x}\text{Sr}_x\text{CuO}_4$ and $\text{YBa}_2\text{Cu}_3\text{O}_{7-\delta}$. We attribute this discrepancy to a kind of excitonic effect which lowers the absorption energy by the electron-hole Coulomb interaction.

The inset in Fig. 1 shows that the O 1s core level has almost the same binding energy (529 eV) between Bi- and Nd-system high- T_c superconductors. When we assume a similar excitonic effect in $\text{Nd}_{2-x}\text{Ce}_x\text{CuO}_4$, we should take 528 eV as an optical transition from the O 1s core level to the electronic states just at the Fermi level (E_F) also for $\text{Nd}_{2-x}\text{Ce}_x\text{CuO}_4$. This means that the absorption edge in $\text{Nd}_{2-x}\text{Ce}_x\text{CuO}_4$ (peak B) no longer corresponds to the Fermi level and instead the center of the first unoccupied states (peak B) is located 1 eV above E_F . This unoccupied electronic state would be $3d^{10}$ state (upper Hubbard band) because a strong hybridization between the Cu 3d and O 2p orbitals enables the appearance of the $3d^{10}$ state in an O-K absorption spectrum. This assignment explains reasonably the existence of peak B ($3d^{10}$) even for non-superconductors.

As shown in Fig. 1, the absorption edge (peak B) shows almost no change in the energy position or in the intensity with Ce-doping compared with a drastic change observed for $\text{La}_{2-x}\text{Sr}_x\text{CuO}_4$ and $\text{YBa}_2\text{Cu}_3\text{O}_{7-\delta}$. This static feature of peak B ($3d^{10}$ state) seems unfavorable to the d orbital as an acceptor of doped electrons, since if

electrons are doped in the d orbital the $3d^{10}$ state should be shifted toward the Fermi level and at the same time the intensity of the absorption spectrum should be reduced. Thus, the experimental results observed by Nücker et al. [1] and also in the present study suggest that doped electrons may be transferred to the other atomic orbital(s), for example Cu 4s. However, it seems very difficult at this point to finally determine the character of the atomic orbital which accommodates doped electrons and thereby drives the high- T_c superconductivity. Further experimental and theoretical studies are necessary.

1. N. Nücker, P. Adelman, M. Alexander, H. Romberg, S. Nakai, J. Fink, H. Rietschel, G. Roth, H. Schmidt, H. Spille, Z. Phys. B75, 421 (1989).
2. Y. Tokura, H. Takagi, S. Uchida, Nature 337, 345 (1989).

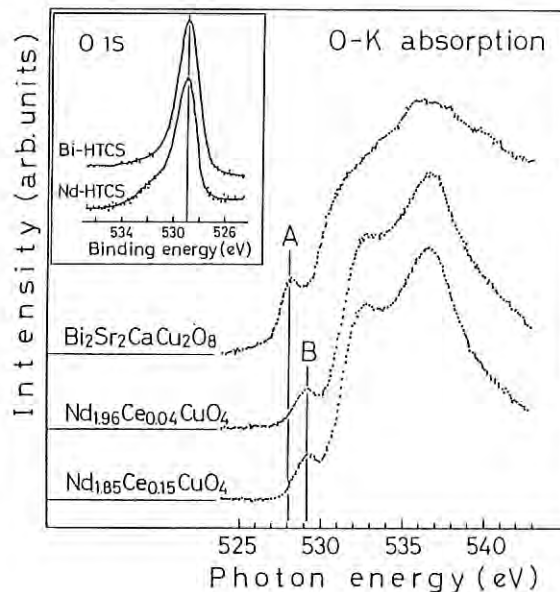


Fig. 1
Oxygen K absorption spectra of $\text{Nd}_{2-x}\text{Ce}_x\text{CuO}_4$ with $x=0.04$ (non-superconductor) and $x=0.15$ (superconductor with $T_c = 23\text{K}$) measured with the total-photoemission-yield-method, compared with that of $\text{Bi}_2\text{Sr}_2\text{CaCu}_2\text{O}_8$ (superconductor with $T_c=85\text{K}$). Note a difference in the energy of the absorption edge between the two classes of superconductors. The inset shows x-ray photoemission spectra of oxygen 1s core level for $\text{Bi}_2(\text{Sr}, \text{Ca})_2\text{CuO}_8$ (Bi-HTCS) and $\text{Nd}_{1.8}\text{Ce}_{0.2}\text{CuO}_4$ (Nd-HTCS). The O 1s core level shows almost the same binding energy between the two high- T_c superconductors.

POLARIZED X-RAY ABSORPTION SPECTROSCOPY OF $\text{Bi}_2\text{Sr}_2\text{CaCu}_2\text{O}_8$

Hiro Yoshi MATSUYAMA¹, Takashi TAKAHASHI¹, Takayuki KASHIWAKURA¹, Takanori WATANABE¹, Takeo EJIMA¹, Hiroshi KATAYAMA-YOSHIDA¹, Shigeru SATO¹, Nobuhiro KOSUGI², Akira YAGISHITA³, and Kenichiro TANAKA³

¹Department of Physics, Tohoku University, Sendai 980

²Division of Molecular Engineering, Kyoto University, Kyoto 606

³Photon Factory, KEK, Tsukuba 305

It has been gradually accepted that the Fermi-liquid states do exist in the high- T_c superconductor and play a central role in appearance of the high- T_c superconductivity [1]. The next step to approach the high- T_c mechanism is to elucidate the nature and origin of the Fermi-liquid states.

Samples of $\text{Bi}_2\text{Sr}_2\text{Ca}_{1-x}\text{Y}_x\text{Cu}_2\text{O}_8$ ($x=0.0$ to 1.0) were prepared by sintering^x mixtures of Bi_2O_3 , SrCO_3 , CaCO_3 , Y_2O_3 and CuO powders of 99.99 % purity with its respective composition. X-ray diffraction measurements confirmed that they are all single-phased except for the sample of $x=0.0$ which contains some impurity phases of less than a few percent volume fraction. The magnetic susceptibility measurements showed that T_c is 80 K for $x=0.0$ and gradually decreases as the content of Y and finally the sample with $x=1.0$ does not show superconductivity.

X-ray absorption measurement was performed at BL11A, with the total-photoemission-yield-method. In order to obtain a fresh and clean surface of the sample for measurements, we scraped the sample surface with a diamond file in the spectrometer just before the measurements and kept it at room temperature. No surface degradation was observed throughout the measurements.

Figure 1 shows oxygen K-absorption spectra of $\text{Bi}_2\text{Sr}_2\text{Ca}_{1-x}\text{Y}_x\text{Cu}_2\text{O}_8$ with $x=0.0$ to 1.0 . The K-absorption edge, which is a transition from the $01s$ level to the empty $02p$ state at E_F , corresponds to the photon energy of 528.2 eV. The spectrum for $x=0.0$ has a narrow and prominent peak just at the K-absorption edge, indicating the existence of substantial density of $02p$ states at E_F . The intensity of this narrow K-edge peak gradually decreases in accordance with the increase of Y content, namely the decrease of hole concentration, and finally the K-absorption edge disappears at $x=1.0$. This is a direct evidence for accommodation of doped holes in the $02p$ states at E_F .

The most remarkable feature in Fig. 1 is the static nature of absorption spectrum against the hole-doping. The absorption spectrum is not shifted as a whole with respect to E_F (528.2 eV) according to the hole concentration. The hole-doping causes the change only in the intensity of the K-absorption edge. This indicates that the change of electronic structure caused by hole-doping is not a shift of the Fermi level but is creation or annihilation of new electronic states at E_F .

Figure 2 shows the result of a polarized K-absorption measurement on a single crystal $\text{Bi}_2\text{Sr}_2\text{CaCu}_2\text{O}_8$. The intensity of K-absorption edge

at 528 eV decreases monotonously as the electric vector of the linearly-polarized incident light is aligned to the normal of the crystal surface (a-b plane). This indicates that the $02p$ orbital at E_F is almost perfectly oriented along the a-b plane.

Thus, the present x-ray absorption study on $\text{Bi}_2\text{Sr}_2\text{Ca}_{1-x}\text{Y}_x\text{Cu}_2\text{O}_8$ clearly shows that the Fermi-liquid state in the high- T_c superconductor is not a simple one-electron state predicted from band structure calculations. The experimental result that hole-doping does not necessarily cause a shift of E_F but produces new electronic states at E_F is in favor of a kind of impurity state or a Kondo-like state as an origin of the Fermi-liquid state. The possibility of a Kondo-like state, however, may be ruled out by the observed dominant $02p$ nature of the electronic states at E_F since a Kondo-like state should have a dominant $\text{Cu}3d$ nature.

1. T. Takahashi, H. Matsuyama, H. Katayama-Yoshida, Y. Okabe, S. Hosoya, K. Seki, H. Fujimoto, M. Sato and H. Inokuchi, Nature 334 (1988) 691; Phys. Rev. B 39 (1989) 6636.

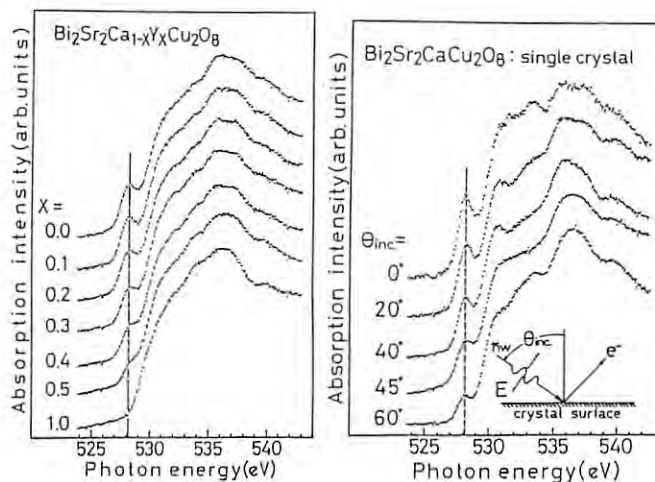


Fig. 1 (left)

Oxygen K-absorption spectra of $\text{Bi}_2\text{Sr}_2\text{Ca}_{1-x}\text{Y}_x\text{Cu}_2\text{O}_8$ with $x=0.0$ to 1.0 . Note a prominent K-absorption-edge peak at 528 eV for $x=0.0$ and its gradual decrease in intensity with decreasing the hole concentration by increasing Y content.

Fig. 2 (right)

Oxygen K-absorption spectra of single crystal $\text{Bi}_2\text{Sr}_2\text{CaCu}_2\text{O}_8$ measured with linearly-polarized light by changing the incident angle (θ_{inc}).

XANES study of diamond films synthesized by hot filament CVD

Y.Takata,K.Edamatsu,T.Yokoyama,K.Seki,M.Tohtan⁺,T.Okada⁺ and T.Ohta

Department of Materials Science, Faculty of Science, Hiroshima University, Naka-ku, Hiroshima 730

⁺Chemical Research Laboratory, TOSOH Corporation, Tonda, Shinnanyou, Yamaguchi, 736

Structures of synthesized diamond films have been studied by various methods such as scanning electron microscopy (SEM), X-ray and electron diffraction, and Raman spectroscopy. In the present study, we introduced a new method, XANES as the probe of searching local atomic structures of diamond films[1].

Diamond films were synthesized by the hot filament CVD method from methane diluted in hydrogen at three kinds of methane concentration: 1.0 % (film A), 4.0 % (film B) and 7.5 % (film C). From the SEM, Raman spectroscopy and X-ray diffraction experiments, it was confirmed that film A and B are composed of diamond crystals, while film C consists of ball-like particles without crystalline habits, as shown in Fig 1.

C K-XANES spectra of these samples were taken at BL 11A (Grasshopper monochromator station). A 1200 lines/mm holographic grating supplied by Astron Co. was used. The spectra were measured by means of the total electron yield detection mode. The collected data were normalized by the spectrum from an evaporated gold thin film to correct for energy-dependent structures on the monochromator transmission function. The normalized spectra of films A, B, C are shown in Fig.2, along with those of natural diamond and highly-oriented pyrolytic graphite (HOPG). The XANES spectral features of films A and B, both of which have been identified as diamond by X-ray diffraction and Raman spectroscopy, are quite similar to those of natural diamond. The peak at 285.2 eV is assigned to the transition to either the $\pi^*(C\equiv C)$ or $\pi^*(C=C)$ antibonding orbital.

It indicates the existence of unsaturated (sp^2 or sp) bonds as observed in HOPG. It is rather surprising that film

C, which was not identified as diamond, gives essentially the same XANES as that of natural diamond, as shown in Fig.2. Above results can be explained by a model whereby film C consists of diamond clusters having only short-range order. An average diameter of the clusters is estimated to be less than 40 Å from the fact that no sharp x-ray patterns were observed.

[1] Y.Takata, K.Edamatsu, T.Yokoyama, K.Seki, M.Tohtan, T.Okada and T.Ohta, Jpn. J. App. Phys. 28 (1989) L1282

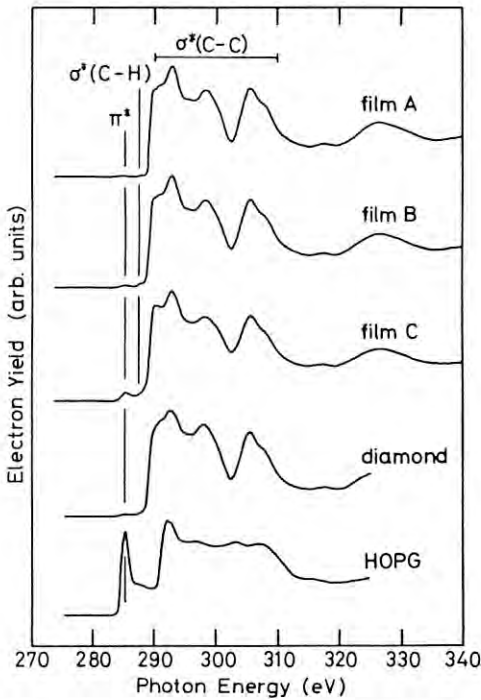


Fig.2 Carbon K-edge XANES spectra of films A, B and C, HOPG and natural diamond.

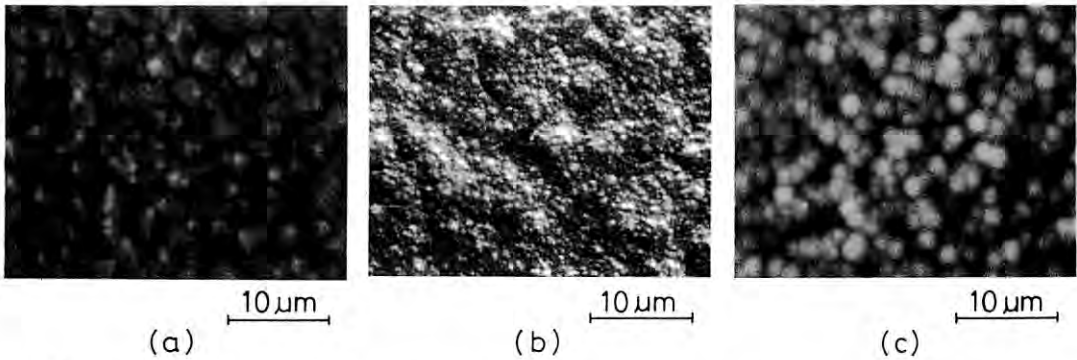


Fig.1 Scanning electron micrographs of polycrystalline diamond films grown at methane concentrations of (a) 1.0 % (film A), (b) 4.0 % (film B), and (c) 7.5 % (film C).

SURFACE EXAFS STUDIES OF SULPHUR ADSORBED ON STEPPED SURFACE; S/Ni(7 9 11)

Hideshi ISHII¹, Kiyotaka ASAKURA¹, Yoshinori KITAJIMA², Manabu FUNABASHI³, Yuji OKAWA¹, Hidetoshi NAMBA¹, Nobuhiro KOSUGI⁴, Toshiaki OHTA⁵ and Haruo KURODA^{1,3}

1. Department Chemistry and Research Center for Spectrochemistry, Faculty of Science, The University of Tokyo, Hongo, Tokyo, 113
2. Photon Factory, National Laboratory for High Energy Physics, Tsukuba, Ibaraki, 305
3. J.R.D.C, 5-9-4 Tokodai, Tsukuba, Ibaraki, 300-26
4. Division of Molecular Engineering, Kyoto University, Kyoto, 606
5. Department of Material Science, Faculty of Science, Hiroshima University, Hiroshima, 700

Introduction

The step on a metal surface is generally expected to play an important role in the initial stage of adsorption. In this connection, sulphur adsorbed on stepped surfaces is quite attractive for the structural study. They are investigated by LEED method and so on, but the local structure of sulphur in these systems have not been well elucidated yet. In this work, we investigated the structure of the S/Ni(7 9 11) systems by means of surface EXAFS.

Experimental

The Ni(7 9 11)=[5(111)x(101)] surface (7x7x2mm³) was cut out from a Ni single-crystal rod. The sample surface was cleaned by repeated cycles of annealing to 800°C and Ar⁺ bombardment. Hydrogen sulphide was dose at room temperature until the value of S_{LVV}(152eV)/Ni_{MVV}(60eV) peak-to-peak ratio was equal to 0.2 in the AES profiles. A (1x1) LEED pattern appeared. The sample was subsequently annealed at 600°C. This treatment gave a clearer (1x1) LEED pattern. No superstructure was found.

S K-edge EXAFS spectra were measured by fluorescence X-ray detection mode at BL-11B.

Results and Discussion

EXAFS spectra were measured for two different X-ray polarizations; one for E parallel to the [101] i.e. perpendicular to the step and one for parallel to the [121] i.e. parallel to the step. Fig.1 shows the Fourier transforms of the EXAFS oscillations measured at incident angles of 15°, 60° and 90° for each azimuthal-angles.

Bond length R and effective coordination number N*, corresponding to the nearest neighbor S-Ni bond, were obtained by the curve fitting analysis, using EXAFS data of Ni₃S₂ (R=2.28Å,

N=6) as the standard. From all the EXAFS data, R was estimated to be 2.25±0.03Å. This value is somewhat longer than that of the nearest neighbor S-Ni bond in the S overlayers formed on planar surfaces, such as p(2x2)S/Ni(111) (2.20Å)¹⁾ and (5√3x2)S/Ni(111) (2.22Å)²⁾.

Since effective coordination number N* depends on the azimuthal-angle, S atoms are not adsorbed on a high symmetry site, such as the 3-fold site. In order to determine the adsorption site the polarization dependance of the experimental N* was compared with the calculated ones for the several models. (Table and Fig.2)

As shown in Table 1, the polarization dependance of the step 4-fold site well agreed with the observation. This is the first observation of the local structure of sulphur adsorbed on the step site by surface EXAFS method.

We measured also the EXAFS spectra of (√3x√3)R30°S/Ni(7 9 11); the ratio of S_{LVV}/Ni_{MVV} peak-to-peak is equal to 0.6. This system was prepared by dosing hydrogen sulphide at room temperature after the measurements on (1x1)S/Ni(7 9 11) (S/Ni=0.2 ptp). The nearest neighbor S-Ni distance in this system was estimated to be 2.22±0.03 Å, which is closer to the values found for S/Ni (planar surface) systems.

This fact shows that sulphur is adsorbed on the step site, and then on the terrace site, growing from preadsorbed sulphur on the step site to form the (√3x√3)R30° structure. Further analyses are now in progress.

We thank Yasutaka Takata (KEK-PF, Hiroshima Univ.) for his help in this experiment.

References

- 1) T.Ohta et al, J. Phys. (Paris), **47**, C8-503(1986)
- 2) Y.Kitajima et al. Surf. Sci. **214**, L261 (1989)

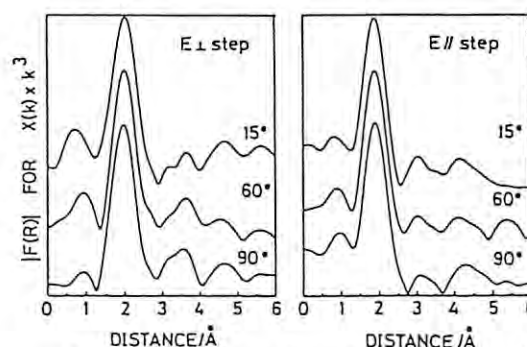


Fig.1 Fourier transformed spectra of S/Ni(7 9 11)

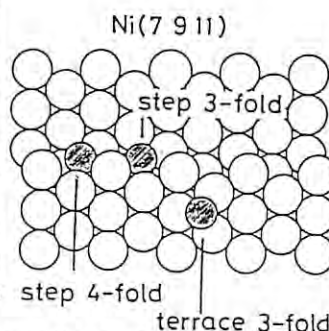


Fig.2 Models for adsorption sites of sulphur atoms

	Exp.	Step 4-fold	Step 3-fold	3-fold
E ⊥ step				
15°/60°	1.08	1.01	0.66	1.87
90°/60°	1.11	1.09	1.45	0.68
E // step				
15°/60°	0.89	1.01	0.97	1.87
90°/60°	0.95	0.94	1.32	0.68

Surface relaxation in c(2x2)Cl/Ni(100) determined by the soft x-ray standing-wave method combined with SEXAFS spectroscopy

Toshihiko YOKOYAMA[1], Yasutaka TAKATA[1], Masahiko YOSHIKI[1],
Toshiaki OHTA[1], Manabu Funabashi[2], Yoshinori KITAJIMA[3]
and Haruo KURODA[4]

- [1] Department of Materials Science, Faculty of Science, Hiroshima University, Naka-ku, Hiroshima 730, Japan
- [2] Research Development Corporation of Japan, Tokodai, Tsukuba, Ibaraki 300-26, Japan
- [3] Photon Factory, National Laboratory for High Energy Physics, Oho, Tsukuba, Ibaraki 305, Japan
- [4] Department of Chemistry, Faculty of Science, the University of Tokyo, Bunkyo-ku, Tokyo 113, Japan

The x-ray SW method is a powerful technique for determining the surface structure and a number of works by use of hard x-rays have been published so far. On the contrary, the soft x-ray SW method is less common because the light source of soft x-rays has been very limited. Recently, however, several facilities supplying tunable and intense soft x-rays have been developed by use of synchrotron radiation, and the utility of the soft x-ray SW method has been pointed out. In this report, we describe the application of this method and surface EXAFS to c(2x2)Cl/Ni(100) and discuss the detailed surface structure accompanied with surface relaxation.

Spectroscopic measurements were performed at the soft x-ray double-crystal monochromator station BL 11B. Bragg reflectivities from the Ni(200) lattice plane were measured by monitoring photoelectric current I_G from the Cu grid in front of a clean Ni(100) single crystal. Angular dependence of the reflectivity was studied at several angles. A Cl-K fluorescence yield spectrum (SW absorption profile) was recorded at the Bragg angle of 85.0° (nearly normal incidence) by use of a UHV-compatible gas-flow proportional counter. In order to obtain a SW profile from the substrate itself, total electron yield spectra were also taken simultaneously. Polarization-dependent Cl K-edge SEXAFS spectra were recorded at room temperature with varying the direction of the incident E vector of 90°, 45° and 15° with respect to the surface normal, by use of the same proportional counter.

The surface structure can be described by use of the SW and SEXAFS results. The SEXAFS results reveal that Cl locates at the 4-fold hollow site and the layer spacing between Cl and Ni is 1.60 ± 0.02 Å. This value is significantly different from the location of Cl (1.80 Å) relative to the bulk lattice plane, which is determined by the SW analysis. This deviation indicates that there exists outward relaxation of the first Ni layer. If we assume that only the first Ni layer relaxes and other layers are fixed with the bulk lattice spacing

of 1.76 Å, the surface layer spacing is estimated to be 1.96 ± 0.05 Å, which corresponds to the expansion of 0.20 ± 0.05 Å compared with the bulk value. The surface structure of the present system is consequently visualized as shown in Fig.1.

In this report, the usefulness of the soft x-ray SW method is emphasized. We can use the same optical system and the same UHV chamber with a fluorescence detector as surface EXAFS spectroscopy since the soft X-ray SW method requires neither the quite high resolution nor the high collimation of monochromatized X-rays. These two techniques provide complementary information; surface EXAFS spectroscopy gives local structures such as interatomic distances between adsorbates and substrate surfaces, while the SW method provides the displacement of adsorbates relative to the net plane of the bulk substrate. Combining these methods, we can elucidate the whole surface structure for adsorbate-substrate systems. Details of the present analysis are given elsewhere.

- [1] T.Yokoyama, Y.Takata, M.Yoshiki, T.Ohta, M.Funabashi, Y.Kitajima, and H.Kuroda, Jpn.J.Appl.Phys. 28 (1989) L1637.

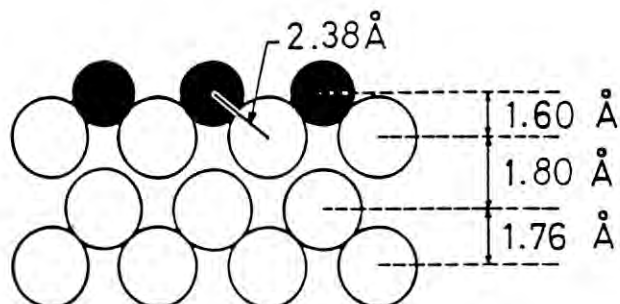


Fig.1. Surface structure (side view) of c(2x2)Cl/Ni(100).

THE USE OF A Si(Li) SOLID STATE DETECTOR FOR THE X-RAY STANDING-WAVE METHOD

Yasutaka TAKATA[1], Toshihiko YOKOYAMA[1], Masahiko YOSHIKI[1],
Yoshinori KITAJIMA[2], Manabu FUNABASHI[3], Haruo KURODA[3,4], and
Toshiaki OHTA[1]

[1] Dept. Materials Science, Fac. Science, Hiroshima Univ., Hiroshima 730, JAPAN.

[2] Photon Factory, KEK, Tsukuba, Ibaraki 305, JAPAN.

[3] Research Development Corp. Japan, Tokodai, Tsukuba, Ibaraki 300-26, JAPAN.

[4] Dept. Chemistry, Fac. Science, Univ. Tokyo, Hongo, Tokyo 113, JAPAN.

INTRODUCTION

Recently, the soft X-ray standing-wave (SW) method has been exploited using synchrotron radiation[1]. In order to determine the surface structure with accuracy by this method, it is essential to separate the signal of adsorbates from the undesirable background. We have used a UHV compatible gas-flow proportional counter (FPC)[2] to measure the SW profiles so far. In some cases, depending on the Bragg reflection energy and the elemental combination of adsorbates and substrates, it was hardly to isolate the fluorescence of adsorbates due to the poor energy resolution of FPC. Si(Li) solid state detector (SSD) has much higher energy resolution. In this study the SW profile of S-K fluorescence for $(5\sqrt{3}\times 2)\text{S}/\text{Ni}(111)$ was measured with Si(Li) SSD and compared with the previous one measured with FPC.

EXPERIMENTAL

The experiment was carried out at the soft X-ray double crystal monochromator station (BL-11B). A single crystal Ni(111) was cleaned by argon ion bombardment and annealing. The clean surface was dosed with H_2S and subsequently heated at about 600K. This treatment leads to clear $5\sqrt{3}\times 2$ complex LEED pattern which retains its sharpness for several days under the UHV condition.

The SW profiles associated with a normal-incidence Ni(111) Bragg reflection were measured with the energy-scanning mode. A Si(Li) SSD was used for the measurement of S-K fluorescence yield, whose energy resolution is about 140eV (FWHM) at 2308eV (S-K fluorescence).

RESULTS AND DISCUSSION

The pulse height spectrum for the soft X-ray yield from $(5\sqrt{3}\times 2)\text{S}/\text{Ni}(111)$ measured with SSD and FPC are shown in Fig.1 and Fig.2, respectively. The incident photon energy is 3060eV. In the spectrum from SSD, S-K fluorescence is completely isolated from the elastically scattered X-rays and Si-K fluorescence in contrast with that from FPC. Si-K fluorescence may originate from insulating materials or viewing ports. The SW profile of S-K fluorescence for $(5\sqrt{3}\times 2)\text{S}/\text{Ni}(111)$ associated with normal-incidence Ni(111) Bragg reflection is shown in Fig.3. This spectrum was recorded using a single channel analyzer to window the S-K fluorescence peak shown in Fig.1. The profile is different from that measured with FPC (see Fig.1 in Ref.3). As shown in Fig.2, we cannot separate S-K fluorescence completely with FPC.

So, in the previous study the background spectrum from the clean surface had to be subtracted in order to obtain the correct profile. The present profile (Fig.3) is almost the same with the background subtracted one (not shown).

By use of SSD, it will be possible to study surface structures including elements whose fluorescence cannot be resolved with FPC.

REFERENCES

- [1] T. Yokoyama et al. JJAP **28** (1989) L1637.
- [2] M. Funabashi et al. RSI **60** (1989) 2505.
- [3] T. Yokoyama et al. Photon Factory Activity Report #6 (1988) 243.

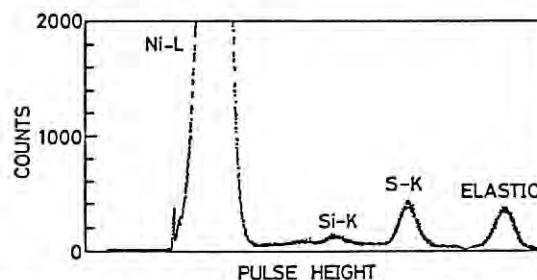


Fig.1. Pulse height spectrum from Si(Li) SSD for $(5\sqrt{3}\times 2)\text{S}/\text{Ni}(111)$.

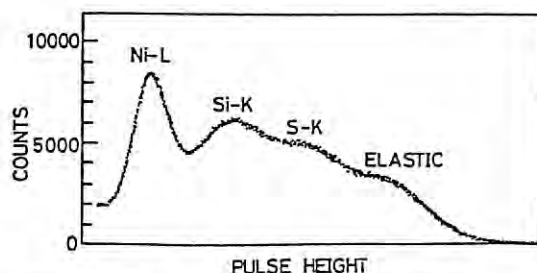


Fig.2. Pulse height spectrum from FPC.

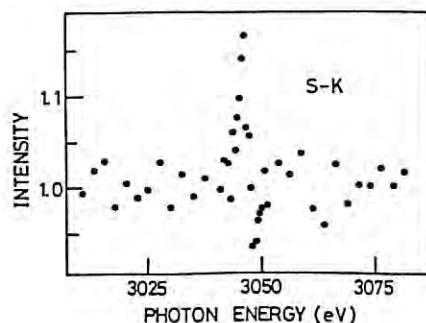


Fig.3. SW profile of S-K fluorescence for $(5\sqrt{3}\times 2)\text{S}/\text{Ni}(111)$.

SURFACE EXAFS STUDY OF $(\sqrt{7} \times \sqrt{7})R19.1^\circ\text{S}/\text{Cu}(111)$

Yoshinori KITAJIMA¹, Toshihiko YOKOYAMA², Yasutaka TAKATA^{1,2},
Masahiko YOSHIKI², Manabu FUNABASHI³, Haruo KURODA^{3,4}, and Toshiaki OHTA²

1. Photon Factory, National Lab. for High Energy Phys., Tsukuba, Ibaraki 305, Japan.
2. Dept. of Materials Sci., Fac. of Sci., Hiroshima Univ., Hiroshima 730, Japan.
3. Research Development Corp. of Japan, Tsukuba, Ibaraki 300-26, Japan.
4. Dept. of Chemistry, Fac. of Science, Univ. of Tokyo, Bunkyo, Tokyo 113, Japan.

INTRODUCTION

The surface EXAFS method is suitable for the study of the adsorption-induced surface reconstruction. We have investigated the $(5\sqrt{3} \times 2)\text{S}/\text{Ni}(111)$ system with this method and confirm the surface reconstruction into the pseudo- $c(2 \times 2)$ $\text{S}/\text{Ni}(100)$ structure¹. Here we report the surface EXAFS results for $\text{S}/\text{Cu}(111)$ system with $(\sqrt{7} \times \sqrt{7})R19.1^\circ$ LEED pattern.

EXPERIMENTAL

When a cleaned single-crystal $\text{Cu}(111)$ was dosed with $1 \times 10^{-4} \text{ Pa H}_2\text{S}$ for more than 20 seconds at room temperature, the $(\sqrt{7} \times \sqrt{7})R19.1^\circ$ LEED pattern was observed. The surface EXAFS measurements for this sample were carried out at the BL-11B soft x-ray double crystal monochromator station by monitoring sulfur K fluorescence yields with an ultrahigh vacuum compatible gas-flow proportional counter². The polar angle of incident x rays, θ , was changed from 15° (glancing incidence) to 45° and 90° (normal incidence).

RESULTS AND DISCUSSION

Figure 1 shows the sulfur K fluorescence yield spectra for the three different polarization angles. The periods of EXAFS oscillation are different from each other, and correspondingly the position of the

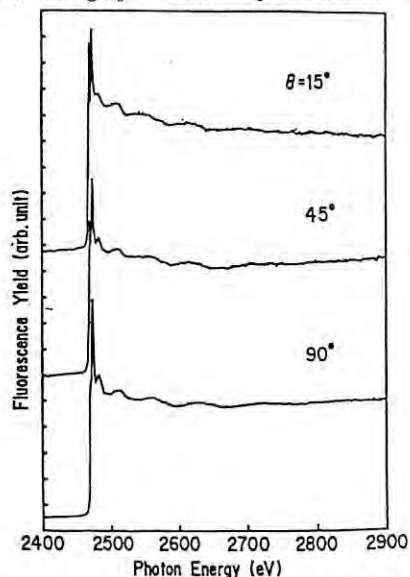


Fig. 1 S-K EXAFS spectra for $(\sqrt{7} \times \sqrt{7})R19.1^\circ\text{S}/\text{Cu}(111)$.

dominant peak in the Fourier transform moves with the polar angle. It means that there are two or more types of S-Cu bonds and the contribution of these components changes with the polar angle, leading to the apparent shift of bond length. Thus we performed the EXAFS spectral simulation for several structure models proposed by the LEED pattern and the qualitative feature of the EXAFS spectra.

The final model we propose is shown in Fig. 2, where the top layer of $\text{Cu}(111)$ is separated into two layers through both the vertical and lateral movements. Cu_1 (open solid circle) is located in the upper level, while Cu_2 (open dashed circle) is in the lower level. Sulfur atoms (full circles) are adsorbed at three types of sites. S_1 is at the 3-fold hollow site composed of Cu_1 , S_2 is at the other 3-fold hollow site composed of Cu_1 , and S_3 is at the 3-fold hollow site composed of Cu_2 . The structure parameters were obtained by the EXAFS simulation and summarized in Table. Although the vertical distance of Cu_1 - Cu_2 cannot be determined directly by this method, it should be larger than 1.15 \AA to avoid an unreasonable contraction of Cu_1 - Cu_2 distance.

REFERENCES

1. Y. Kitajima et al: Surface Sci. 214, L261 (1989).
2. M. Funabashi et al: Rev. Sci. Instrum. 60, 2505 (1989).

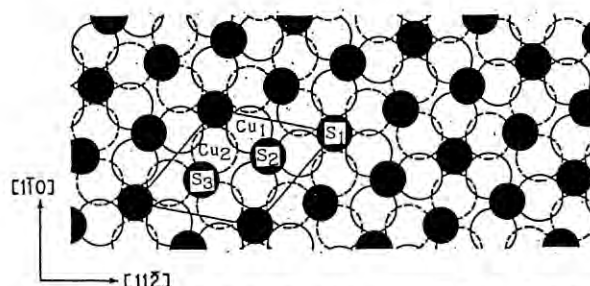


Fig. 2 Structure model for $(\sqrt{7} \times \sqrt{7})R19.1^\circ\text{S}/\text{Cu}(111)$

Table The structure parameters obtained by EXAFS simulation.

Lateral displacement (Å)		Vertical distance (Å)	
$x_1(\text{S}_1-\text{Cu}_1)$	0.34	$d_1(\text{S}_1-\text{Cu}_1)$	0.00
$x_2(\text{S}_1-\text{Cu}_2)$	0.21	$d_2(\text{S}_2-\text{Cu}_1)$	1.47
		$d_3(\text{S}_3-\text{Cu}_2)$	1.66
Bond distance (Å)		Bond declination angle (deg)	
$R_1(\text{S}_1-\text{Cu}_1)$	2.22	$\omega_1(\text{S}_1-\text{Cu}_1)$	0.0
$R_2(\text{S}_2-\text{Cu}_1)$	2.31	$\omega_2(\text{S}_2-\text{Cu}_1)$	39.6
$R_3(\text{S}_3-\text{Cu}_2)$	2.35	$\omega_3(\text{S}_3-\text{Cu}_2)$	45.0

STUDY ON S KLL AUGER ELECTRON SPECTRA BY X-RAY EXCITATION NEAR S K-EDGE
I. DEPENDENCE OF AUGER ELECTRON SPECTRA OF Na_2SO_4 AND $\text{Na}_2\text{S}_2\text{O}_3$ ON INCIDENT X-RAY ENERGY

Nobuyuki MATSUBAYASHI, Hiromichi SHIMADA, Isao KOJIMA, Masayasu KURAHASHI, Toshiaki Ohta*,
Yoshinori KITAJIMA**, Akio ITOH***, and Akio NISHIJIMA

National Chemical Laboratory for Industry, Tsukuba, Ibaraki 305

*Department of Physics, Faculty of Science, The University of Hiroshima,
Higashisenda-cho, Nakaku, Hiroshima 730

**Photon Factory, KEK, Oho, Tsukuba, Ibaraki 305

***Rigaku Industrial Corporation, 14-8, Akaohji-cyo, Takatsuki, Osaka 569

Introduction

Recent development in synchrotron radiation sources has made it possible to study resonance phenomena of Auger electrons. Auger shape-resonance phenomena were observed for C(KVV), O(KVV), and S(LVV) Auger processes in several gaseous samples.¹⁾ However, no reports have been made on resonance phenomena involving deep-core electrons of solid materials. During the course of the investigation on S(KLL) Auger spectra, the present authors found the analogous phenomena for solid samples containing S^{6+} .

Experimental

All the measurements were performed at the BL-11B in the Photon Factory. X-ray excited S(KLL) Auger spectra were taken using a newly constructed electrostatic hemispherical electron analyzer system (Rigaku Industrial Corp.) with high energy resolution up to 5000 eV.²⁾ The pass energy was set to 20 eV and the collection time was 0.5 s/ch. Powdered samples of MoS_2 , $\text{Al}_2(\text{SO}_4)_3$, and $\text{Na}_2\text{S}_2\text{O}_3$ were dispersed on Cu metal plates to restore conductivity of the samples.

Results and Discussion

S(KL_{2,3}L_{2,3}) Auger electron spectra for Na_2SO_4 excited by various incident X-ray energies (E_i) between 2476.5 and 2486 eV are shown in Fig.1. Kinetic energy-shift caused by charging up was corrected for each incident X-ray energy using the photoelectron energy of C 1s of contaminants. Two kinds of Auger decay processes were observed in Fig.1. One is the Auger peak at 2105 eV which has a maximum intensity when incident energy is 2482.0 eV. When the peak appears ($E_i=2476.5 - 2480.0$ eV) and disappears ($E_i=2484.0-2486.0$ eV), the kinetic energy of the peak shifts to higher energy side with the increase of incident X-ray energy. The other is the Auger peak at 2109 eV which appears when E_i is greater than 2481 eV. This phenomenon is contrastive to MoS_2 which a single peak was observed for.³⁾

Figure 2 shows S(KL_{2,3}L_{2,3}) Auger electron spectra for $\text{Na}_2\text{S}_2\text{O}_3$ excited by various incident X-ray energies (E_i) between 2468.0 and 2486 eV. In this case, four kinds of Auger decay processes were observed. First is the Auger peak at 2109 eV which has a maximum intensity when $E_i=2471.0$ eV. Second is the Auger peak at 2104 eV which has a maximum intensity when $E_i=2480$ eV. Third and fourth are the Auger peaks at 2100 and 2104 eV which appear E_i is greater than 2482 eV. The peak at 2104 eV is corresponding to the Auger electron

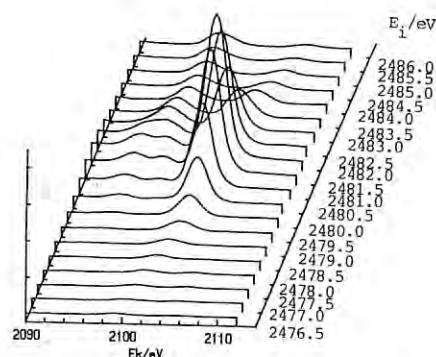


Fig.1 S(KLL) Auger electron spectra for Na_2SO_4 excited by various incident X-ray energies(E_i) between 2476.5 and 2486 eV.

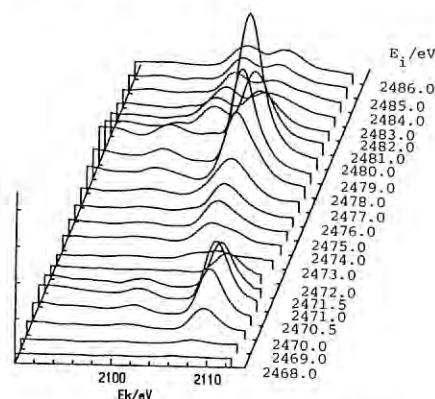


Fig.2 S(KLL) Auger electron spectra for $\text{Na}_2\text{S}_2\text{O}_3$ excited by various incident X-ray energies (E_i) between 2468.0 and 2486 eV.

due to S^{6+} . The peak at 2100 eV is corresponding to S^{2-} .

As shown above, there are differences in the behavior of S(KLL) Auger spectra among SO_4^{2-} , S^{2-} , and $\text{S}_2\text{O}_3^{2-}$. The most probable cause of the difference is the different structure of the valence band. Theoretical approaches are required for further discussion from this point of view.

References

- 1) U. Becker, T. Prescher, E. Schmidt, B. Sonntag, and H.-E. Wetzel: Phys. Rev. A33 (1986) 3891.
- 2) N. Matsubayashi, I. Kojima, M. Kurahashi, A. Nishijima, A. Itoh and T. Utaka: Rev. Sci. Instrum. 60 (1989) 2533.
- 3) N. Matsubayashi, H. Shimada, I. Kojima, M. Kurahashi, T. Ohta, A. Itoh, and A. Nishijima: Jpn. J. App. Phys. 28 (1989) L1051.

MEASUREMENT OF THE SOFT X-RAY ABSORPTION BY Al, Cr, AND Ni

Hisao Fujisaki, Nobuyuki Nakagiri, Hiroshi Nagata*, Naoto Kihara*,
Tsuneaki Miyahara**, and Akira Yagishita**

Yoshida Nano-Mechanism Project, JRDC, 5-9-9 Tohokodai, Tsukuba, Ibaraki 300-26

*Yoshida Nano-Mechanism Project, JRDC, 1-6-3 Nishi-Ohi, Shinagawa-ku, Tokyo 104

**Photon Factory, National Laboratory for High-Energy Physics, Tsukuba, Ibaraki 305

Introduction

We previously measured the x-ray reflection at the surfaces of metal films and, then, their refractive indices were determined by the least-squares fitting (1). The standard deviations of the imaginary part were somewhat large. We have, therefore, planned to determine independently the imaginary part of the refractive index, i. e., the absorption coefficient, of materials. As sample materials, Al, Cr, and Ni have been chosen: Cr and Ni are usable materials for optical elements used in the 2.4-4.3 nm wavelength region (2). Soft x-rays in this wavelength region (so-called "water window") are suitable for biological studies.

Experimental

X-Ray absorption measurements were done at the wavelength region of 1.25-6 nm at the beam line BL-11A. The incident beam was filtered by a 250-nm-thick copper foil (1.25-2.95 nm wavelength region) and a 350-nm-thick silver foil (2.95-6 nm wavelength region).

Each sample was deposited by electron beam evaporation onto a 400-nm-thick polycarbonate membrane substrate. The sample thickness was monitored by a quartz oscillator. The sample deposition and the x-ray absorption measurement were done alternatively in the same chamber without breaking the vacuum, by which the samples were prevented from being oxidized and polluted by air.

Results and Discussion

In Figs. 1-3, averaged mass absorption coefficients of Al, Cr, and Ni obtained by the present study are shown together with the values calculated from the atomic scattering factors of Henke et al. (3) for comparison. The average was carried out over 8 (for Al and Cr) or 10 (for Ni) data at each of 256 wavelength points.

Although the absorption edge of Ni agrees between both curves in Fig. 3 (1.45 nm), that of Cr does not agree in Fig. 2 (2.15 nm in our case and 2.07 nm in the case of Henke et al.). This remains a question.

Some large deviations from an expected smooth line are seen in Figs. 1-3. They are explained by the mixing of the second-order light. When the content of the second-order light is large, the value of mass absorption constant might be observed between the true value and the value for the second-order light. At 2.6-2.95 nm, the absorption of the first-order light by the Cu filter is higher than that of the second-order. At 5.8-6.2 nm, the Ag filter was not thick enough to reduce the second-order light sufficiently. The deviations at 4-4.3 nm might be caused by the carbon contained in the polycarbonate membrane: The relative content of the second-order light increases due to the absorption of the first-order light by the carbon in the membrane.

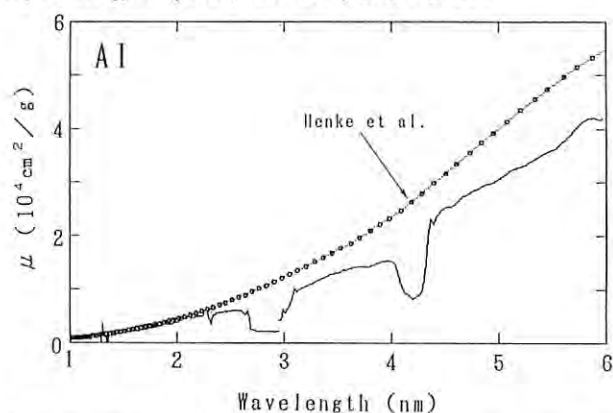


Fig. 1 Mass absorption coefficients of Al vs. wavelength.

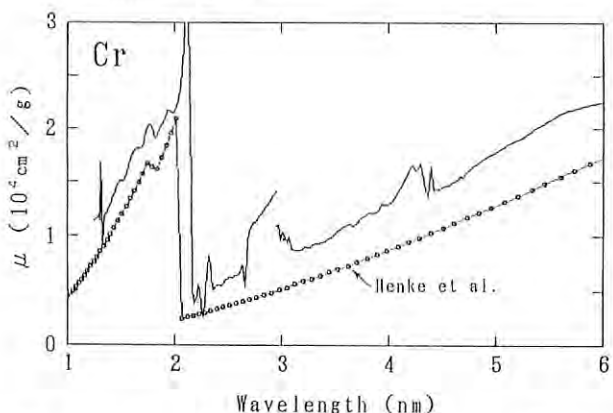


Fig. 2 Mass absorption coefficients of Cr vs. wavelength.

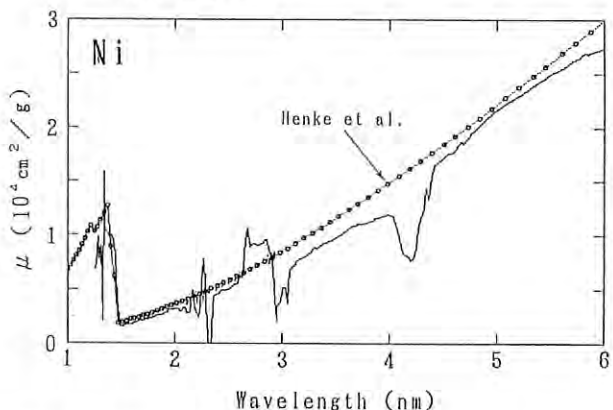


Fig. 3 Mass absorption coefficients of Ni vs. wavelength.

References

1. N. Kihara, H. Nagata, N. Nakagiri, H. Fujisaki, and T. Miyahara, *Rev. Sci. Instrum.* **60**, 2227 (1989)
2. H. Fujisaki, *Jap. J. Appl. Phys.* **27**, 1335 (1988)
3. B. L. Henke, P. Lee, T. J. Tanaka, R. L. Shimabukuro, and B. K. Fujikawa, *AIP Conf. Proc.* **75**, 340 (1981)

OPTICAL STUDY OF THE STOICHIOMETRY-DEPENDENT ELECTRONIC STRUCTURE OF TiCx , VCx AND NbCx

T. Koide, T. Shidara, H. Fukutani*, A. Fujimori**,
T. Miyahara, H. Kato, S. Otani*** and Y. Ishizawa***

Photon Factory, National Laboratory for High Energy Physics, Tsukuba, Ibaraki 305

* Institute of Physics, University of Tsukuba, Tsukuba, Ibaraki 305

** Department of Physics, Faculty of Science, University of Tokyo, Tokyo 113

*** National Institute for research in Inorganic Materials, Tsukuba, Ibaraki 305

The group-IVB and -VB transition-metal carbides and nitrides exhibit unique bonding properties. Their extreme hardness and high melting temperatures are typical of covalently bonded materials. These compounds also show metallic properties such as metallic color, good conductivity and, in some cases, superconductivity. In addition, they crystallize in the rock-salt structure typical for ionic crystals. Another remarkable property of this class of materials is their tendency to form nonstoichiometrically; they can accommodate up to 50% vacancies on the nonmetal sublattice while retaining the rock-salt phase. The vacancies have a strong influence on a variety of physical properties.

The stoichiometry-dependent bulk electronic structure has been studied by optical spectroscopy for single crystals of TiCx with $x=0.95$ and 0.70 , VCx with $x=0.86$ and 0.76 , and NbCx with $x=0.93$, 0.84 and 0.71 .¹⁾ The reflectance was measured in the photon energy range $0.5\text{--}40\text{ eV}$ for all the samples and measured up to 100 eV for $\text{TiC}_{0.95}$, $\text{VC}_{0.86}$, and $\text{NbC}_{0.93}$. By making a correction for the surface-roughness effect with use of measured roughness values, the data were Kramers-Kronig analyzed to obtain the dielectric function and related functions.

Figures 1-3 show the resultant optical conductivity spectra of TiCx , VCx and NbCx , respectively. The observed interband transitions, except for V, can be interpreted on the basis of existing calculations for the energy-band structure and partial density of states. Main peaks, D, E, and F, are assigned to transitions at and around the X and Q portions in the Brillouin zone. Their shifts to lower energy and reduced intensities with lowering carbon concentration can be explained by the concomitant changes in the p-d hybridization. Features, A and B, in three compounds and E' in NbCx are attributable to transitions involving initial or final states near the Fermi level. Their dramatic x-dependent behavior in VCx and NbCx provides clear experimental evidence that the Fermi level moves downward in these compounds with lowering carbon content. Structure V in VCx and NbCx , which remarkably develops in intensity as x decreases, cannot be identified in the band structures for $x=1$ and is ascribed to a transition between vacancy-induced states below and just above the Fermi level. No corresponding structure is observed in TiCx .

All the volume electron-energy-loss functions show the main volume plasmon peak which is close to the free-electron-gas plasmon energy and shifts to lower energy with lowering x.¹⁾ A small Drude plasma structure is observed at 2.7 eV in $\text{NbC}_{0.93}$, being rapidly attenuated with increasing carbon vacancies.

References

- 1) T. Koide et al. Phys Rev. B (submitted).

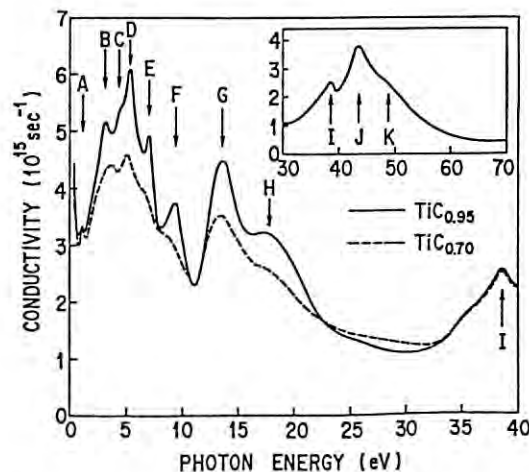


Fig. 1 Optical conductivity of TiCx .

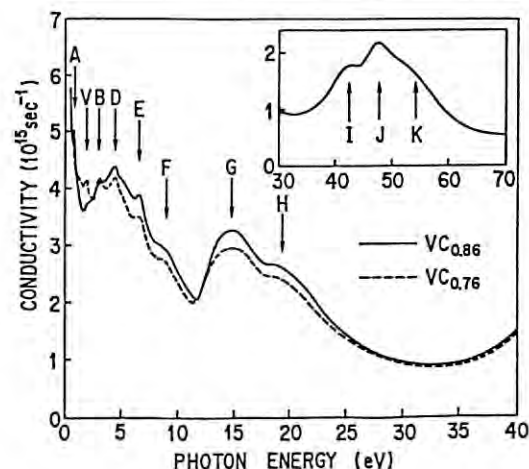


Fig. 2 Optical conductivity of VCx .

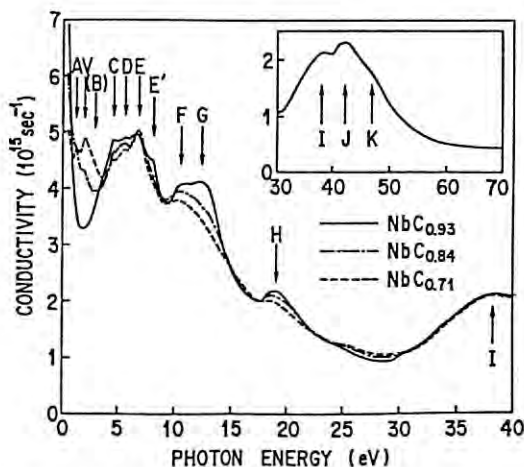


Fig. 3 Optical conductivity of NbCx .

DEVELOPMENT OF A VUV MAGNETO-OPTICAL APPARATUS AND MAGNETIC CIRCULAR DICHROISM OF EXCITONS IN ALKALI HALIDES

Tsuneharu KOIDE, Tetsuo SHIDARA, Masatada YURI*, and Hirohito FUKUTANI*

Photon Factory, National Laboratory for High Energy Physics, Tsukuba, Ibaraki 305

* Institute of Physics, University of Tsukuba, Tsukuba, Ibaraki 305

Introduction

Magneto optics is a powerful technique for spectroscopic studies of the magnetic properties of materials. In particular, magnetic circular dichroism (MCD) using circularly polarized light provides useful information about the spin-dependent electronic structure and has been widely used in the visible region. However, MCD studies have been severely limited in the VUV region because of experimental difficulties. For the past several years, we have developed a magneto-optical apparatus consisting mainly of a superconducting magnet in order to study MCD in the VUV region. A description of the apparatus is given here together with an example of results obtained so far.¹⁾

Apparatus

The magnet system satisfies the following specifications: (1) The superconducting magnet is a split-coil solenoid producing fields up to 5.8 T; (2) Its cryosystem has a double wall to make it bakable, i.e., UHV compatible; (3) The smaller magnet bore of the double wall is 4.8 cm in diameter, allowing MCD measurements in reflection as well as in transmission; (4) Field homogeneity at the sample position is better than 0.5% within a cube 1 cm in diameter. The whole system also meets the requirements: (5) It contains a component which can produce alternating left and right circularly polarized light; (6) The samples are interchanged without braking the vacuum; (7) The sample temperature is varied from liquid helium temperature to room temperature.

Figure 1 shows a schematic of the experimental setup. A calcium fluoride stress modulator is used for a quarter-wave retarder and linearly polarized synchrotron radiation from a Seya-Namioka monochromator is converted to 50-KHz left and right circularly polarized light. A lithium fluoride stress modulator will be used in near-future experiments. The detector is a sodium salicylate-coated photomultiplier specially designed for use under high magnetic fields. The d.c. component of an output of the photomultiplier is kept constant

by controlling a high voltage applied to the photomultiplier. The a.c. component, which is proportional to the MCD signal, is detected with a phase-sensitive technique.

Results

Figure 2 displays MCD (in reflection) and reflectance spectra of KI taken at room temperature in the region below 7.5 eV. Spectra of RbI are similar to those in Fig. 2. There are four exciton peaks, E_1 through E_4 and two shoulders, S_1 and S_2 , over this energy range, although E_2 and E_3 are not well resolved at room temperature. The MCD signal for each structure is proportional to the logarithmic derivative of reflectance, giving effective g values of 1.24, 1.22, ~ -0.8 and -0.76 for excitons E_1 , E_2 , E_3 and E_4 in KI, respectively. Effective g values for S_1 and S_2 are also determined to be 1.20 and ~ 1.3 . Similar results are obtained for RbI. Low-temperature measurements are required for a precise determination of g values for structures E_3 and S_2 .

The assignments of the structures deduced from the present g values are consistent with those determined from our previous piezoreflectance studies;²⁻³⁾ E_1 and E_2 are attributed to spin-orbit split Γ excitons, S_1 and S_2 to their interband thresholds, E_3 to an L exciton, and E_4 to a composite structure of L and X excitons. The finding that the measured g values for excitons, E_1 and E_2 , are nearly the same as those for the corresponding band-to-band transitions, S_1 and S_2 , indicates that the exchange interaction between the electron and hole has negligibly small effects on the MCD spectra of excitons in KI and RbI.

References

- 1) T. Koide et al., manuscript in preparation.
- 2) T. Koide et al., Solid State Commun. **32**, 547 (1979).
- 3) M. Miyabe et al., Solid State Commun. **60**, 281 (1986); J. Phys. Soc. Jpn. **56**, 378 (1987).

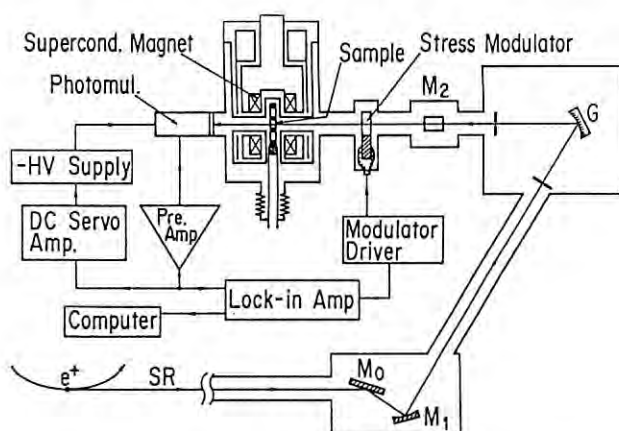


Fig. 1 Arrangement for MCD experiment.

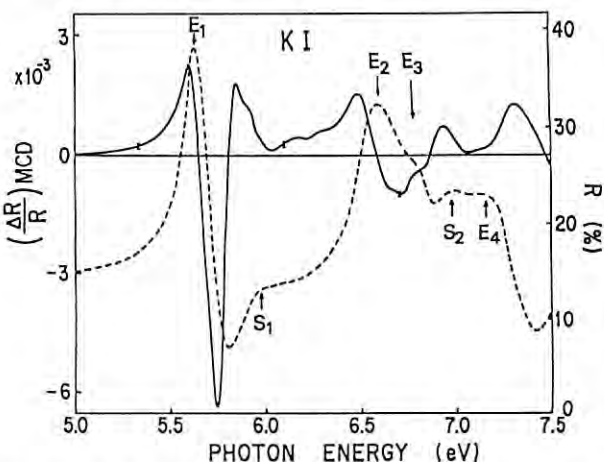


Fig. 2 MCD (solid line) and reflectance (dashed line) spectra of KI.

Adsorption kinetics of SiH_4 and Si_2H_6 on $\text{Si}(100)$ 0°off and 4°off surfaces

Yuji Takakuwa, Masafumi NOGAWA, Hirayuki ISHIDA, Fumihiko HIROSE,
Michio NIWANO, Hiroo KATO and Nobuo MIYAMOTO

Research Institute of Electrical Communication, Tohoku
University, Sendai 980

* Photon Factory, National Laboratory for High Energy Physics,
Tsukuba 305

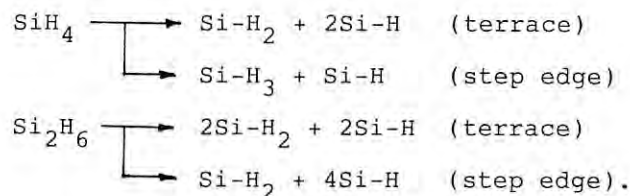
It is well known that the growth kinetics of Si epitaxial film indicates strong dependence upon the reactant-gas species and the substrate orientation. This means that the surface reactions such as adsorption of reactant gases and desorption of reaction products are severely affected by the crystal orientation. In this study, to clarify how surface atomic steps affect an adsorption kinetics of reactant gases we measured UPS spectra of SiH_4 - and Si_2H_6 -adsorbed $\text{Si}(100)$ 0°off and 4°off surfaces with synchrotron radiation.

The experiments were performed at beam line BL-11C. The substrates used were $\text{Si}(100)$ 0°off and 4°off wafers. The gas adsorption of SiH_4 and Si_2H_6 was done at room temperature and an amount of exposure was 36000 L.

Figure 1 shows UPS spectra of SiH_4 - and Si_2H_6 -adsorbed $\text{Si}(100)$ 0°off surface compared with that of H_2 -adsorbed surface. The photon energy is 30 eV. In the figure, the peak positions of monohydride, dihydride, and trihydride are indicated with arrows. From Fig.1, it is clearly seen that there is a lot of trihydride on the H_2 -adsorbed surface and monohydride and dihydride are dominant on the SiH_4 - and Si_2H_6 -adsorbed surfaces. A dip at 6 eV, corresponding to the structure due to trihydride, is deeper for Si_2H_6 than that for SiH_4 . This suggests that dissociative adsorption of Si_2H_6 leads to most of monohydride and dihydride.

This trend of adsorption kinetics for the reactant gas species can be seen more remarkably for the $\text{Si}(100)$ 4°off surface. A structure at 10 eV, corresponding to the peak due to trihydride, shows up clearly on the SiH_4 -adsorbed surface, but remains unchanged same as in Fig.1 for Si_2H_6 adsorption. In addition the dip structure at 6 eV becomes deeper for the latter. This indicates that surface steps change significantly a reaction path to increase Si-H_3 for SiH_4 and Si-H and Si-H_2 for Si_2H_6 .

We also measured UPS spectra with ultraviolet light of 23 eV and 15 eV. As a result, it is concluded that the dominant reaction kinetics of SiH_4 and



- 1) C.W.Pearce, VLSI Technology, ed. S.M.Sze (McGraw-Hill, New York, 1988) p.55.
- 2) R.Butz, E.M.Oellig, H.Ibach and H.Wagner: Surf. Sci. 147(1984)343.
- 3) K.C.Pandey, T.Sakurai and H.D.Hagstrom: Phys. Rev. Lett. 35(1975)1728.

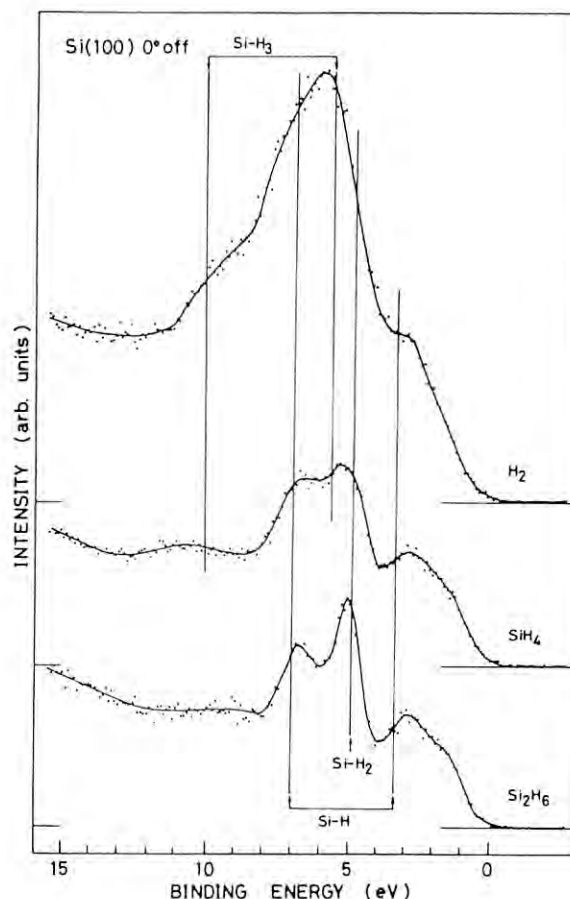


Fig.1 UPS spectra of H_2 -, SiH_4 - and Si_2H_6 -adsorbed $\text{Si}(100)$ 0°off surfaces.

Si_2H_6 adsorption on the terrace and step edge of $\text{Si}(100)$ surface is as follows;

Kinetics of photon-induced Si-H bond breaking reaction on SiH_4 -adsorbed Si(100) surface

Yuji TAKAKUWA, Masafumi NOGAWA, Hirayuki ISHIDA, Fumihiko HIROSE,
Michio NIWANO, Hiroo KATO and Nobuo MIYAMOTO

Research Institute of Electrical Communication, Tohoku
University, Sendai 980

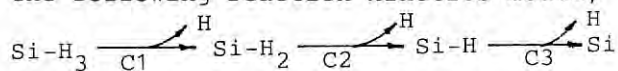
* Photon Factory, National Laboratory for High Energy Physics,
Tsukuba 305

It was reported that H_2 desorption from the crystal-growing surface is a rate-limiting reaction in Si crystal growth using SiH_4 gas at low temperatures.¹⁾ In order to establish a low-temperature process, we tried to break Si-H bonds on a SiH_4 -adsorbed Si(100) surface with synchrotron radiation. It was found that Si-H bond breaking takes place at a photon energy above 20 eV on this surface. Furthermore we clarified a reaction kinetics of the Si-H bond breaking by measuring ultraviolet photoelectron spectra with synchrotron radiation.

The experiments were performed at beam line BL-11C. The substrates were Si(100) 0° off surfaces. The SiH_4 adsorption was carried out at room temperature and its exposure was 36000 L.

Figure 1 shows a photon-stimulated desorption (PSD) spectrum of H^+ ion. It is seen that the H^+ -PSD yield increases at a photon energy above 20 eV and saturates at about 33 eV. This PSD yield spectrum is very different from that of a HF-passivated Si(111) surface, in which there is a maximum at 23 eV.²⁾ The Si-H bond configuration of hydrides on each surface is responsible for this difference.³⁾

To demonstrate clearly an irradiation-induced change in UPS spectral profile, we derived difference spectra with respect to that at $t=0$ min as shown in Fig.2. Unmonochromatized light was used for irradiation because of its strong intensity. Two peaks at 3 eV and 7 eV, corresponding to monohydride, do not decrease but increase with irradiation time. This means that the amount of monohydride increases in spite of Si-H bond breaking. On the other hand, from UPS spectra obtained with ultraviolet light of 15 eV it was seen that the amount of dihydride decrease significantly with irradiation time. These observed changes of each hydride can be explained in terms of the following reaction kinetics model;



where C_1 , C_2 and C_3 are the rate constants. In this model, breaking of the Si-H bond in dihydride leads to production of monohydride. Therefore if the value of the constant C_3 is

smaller than that of C_2 and the amount of trihydride is a little, the amounts of dihydride and monohydride would decrease and increase with time, respectively, as observed in this study.

- 1) F.Hirose, M.Suemitsu and N.Miyamoto: Jpn. J. Appl. Phys. 28(1989) in print.
- 2) Y.Takakuwa, M.Nogawa, M.Niwano, H.Katakura, S.Matsuyoshi, H.Ishida, H.Kato and N.Miyamoto: Jpn. J. Appl. Phys. 28(1989)L1274.
- 3) Y.Takakuwa et.al.: to be published.

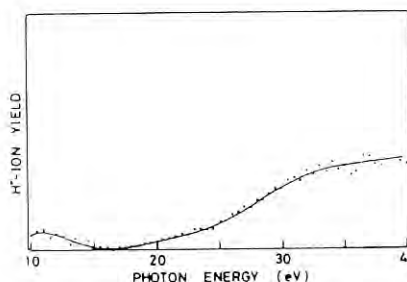


Fig.1 H^+ -PSD spectrum from the SiH_4 -adsorbed Si(100) surface.

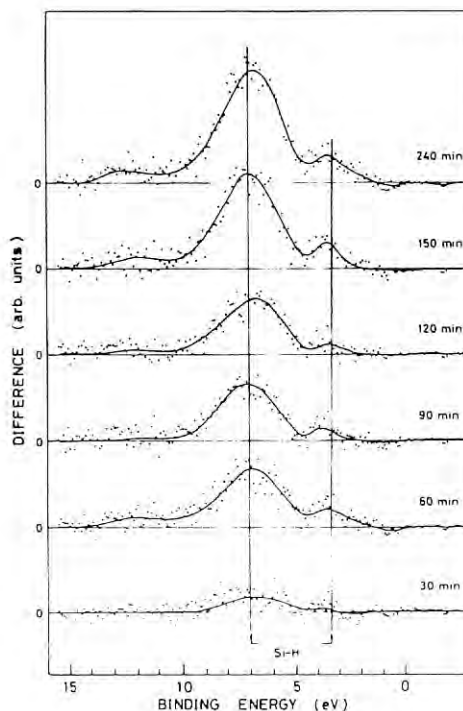


Fig.2 Difference UPS spectra of the SiH_4 -adsorbed Si(100) surface.

PIEZOREFLECTIVITY OF BaF₂ IN THE CORE EXCITATION REGION

Shintaro SATO, Masatada YURI, Hirohito FUKUTANI and Hiroo KATO*

Institute of Physics, University of Tsukuba, Ibaraki 305

*Photon Factory, National Laboratory for High Energy Physics, Ibaraki 305

BaF₂ has several sharp reflectivity peaks in the photon energy region from 16 to 21 eV. These peaks have been attributed to Ba²⁺ 5p-6s,5d core excitons, details of which, however, are not clear yet. Studies of stress effects are interesting for clarifying origins of these peaks. Piezorefectivity spectra of BaF₂ with non-normal incident geometry¹⁾ were measured at BL-11C using Seya-Namioka type monochromator. All measurements were made at room temperature.

Figure 1 shows the reflectivity spectrum of BaF₂. The spectrum is composed of four distinct peaks (B,C,E, and F) and two weak peaks (A and D). In figure 2, the cubic, tetragonal and trigonal piezorefectivity spectra, $(\Delta R/R)_{\text{cub}}$, $(\Delta R/R)_{\text{tet}}$ and $(\Delta R/R)_{\text{tri}}$, are shown. For comparison, the logarithmic energy derivative of the reflectivity spectrum, $(1/R)(dR/dE)$, is also shown. The line shape of each structure in the $(\Delta R/R)$ spectra is approximately proportional to that in the $(1/R)(dR/dE)$ spectrum. By comparing the peak-to-peak amplitude of each structure in the $(\Delta R/R)$ spectra with that in the $(1/R)(dR/dE)$ spectrum, one can obtain deformation potentials. These are listed in table 1. General tendency of the cubic deformation potentials - sign and magnitude - agrees with that of thermal shifts.

We interpret these origins in the atomic picture, while Rubloff assigned these structures in the band picture.²⁾ According to the point ion model, signs of deformation potentials for each excitation are predicted as shown in table 1. Comparing the signs of the deformation potentials with those by the point ion model, we assigned each structure as listed in table 1. The C and F structures are assigned to 5p-6s excitons. Their energy separation is 2.0 eV and this value is nearly equal to the S-0 splitting of free Ba²⁺ 5p states. In these assignments, some of the 5s-6d excitations are located at lower energy than the 5p-6s excitation, in good accord with the case in free Ba²⁺ ion. This result is different from that in Rb halides, where the structure appearing at the lowest energy in the core excitation region was assigned to the 4p-5s exciton.³⁾

It is concluded that the atomic picture explains well the core excitations in BaF₂ the same as in alkali halides.

References

1) Y.Aiura et al. : Photon Factory Activity Report 1986 #4 241.
2) G.W.Rubloff : Phys. Rev. B5 662 (1972).
3) C.Satoko et al. : J. Phys. Soc. Jpn. 34 701 (1973).

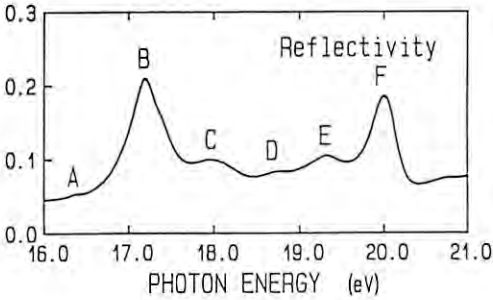


Fig.1

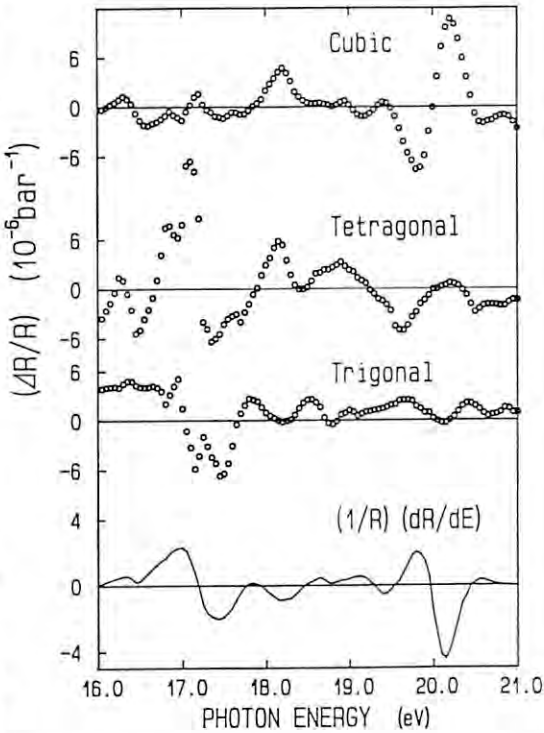


Fig.2

	Position (eV)	Deformation Potentials (eV)			Assignment
		Cubic	Tetragonal	Trigonal	
A	16.4	- 5.0 ± 0.7	- 1.4 ± 0.7	0.0 ± 0.1	5p → 5dγ
B	17.2	- -	- 0.3 ± 0.2	- 0.7 ± 0.1	5p → 5dε
C	18.0	2.6 ± 0.4	0.5 ± 0.3	- 0.8 ± 0.1	5p → 6s
D	18.7	negative	positive	negative	?
E	19.3	0.9 ± 0.1	- 0.2 ± 0.1	0.22 ± 0.04	5p → 5dε
F	20.0	1.7 ± 0.2	0.08 ± 0.04	- 0.12 ± 0.02	5p → 6s
5p → 6s		0	+	-	Table 1
5p → 5dε		+	-	?	
5p → 5dγ		-	?	+	

THE OPTICAL SPECTRA OF α - Al_2O_3 SINGLE CRYSTALS IN THE VUV REGION III

Tetsuhiko TOMIKI, Tohru SHIKENBARU, Yoshiiku GANAHA, Shintaro SATO*, Masatada YURI*,
Hirohito FUKUTANI*, Hiroo KATO** and Tsuneaki MIYAHARA**

Department of Physics, University of the Ryukyus, Nishihara, Okinawa 903-01.

* Department of Physics, University of Tsukuba, Tsukuba, Ibaraki 305.

** Photon Factory, National Laboratory for High Energy Physics (KEK), Tsukuba, Ibaraki 305.

The reflectivity spectra of α - Al_2O_3 single crystals measured with the plane polarized light have been reported by us in refs. 1) ~ 3). The spectrum in this report measured at BL-11C with no In-filter employed is dissimilar to each of the preceding results^{1~3)} in the relative magnitudes of the peaks found in the region up to 35 eV. The present spectral behaviour (full curve in Fig. 1) was obtained under the condition $I_o(\lambda)/I_o'(\lambda) = \text{const}$ of λ which ascertains that no appreciable changes in the incident light intensities occurred at each of λ 's during the passage of time in the measurement; here, $I_o(\lambda)$ and $I_o'(\lambda)$ are the reference light intensities at the wavelength λ before and after the run of the reflected light measurement, respectively. Thus, it appears probable that the present spectrum is more reliable. The dotted curve stands for the reflectivity spectrum calculated with the use of literature values of the refractive indices.

The spectrum of N_{eff} , which is Kramers-Kronig transformed from this reflectivity spectrum, is found to be consistent with the number of the valence band electrons. As regards the physical interpretation of the spectra of optical constants, no new materials are found at present to be added to the preceding publication³⁾.

References

- 1). T. Tomiki, T. Futemma, H. Kato, Y. Aiura, H. Fukutani and T. Miyahara: Photon Factory Activity Report #5 (1987) p. 289.
- 2). T. Tomiki, T. Futemma, H. Kato, T. Miyahara, Y. Aiura and H. Fukutani: Photon Factory Activity Report #6 (1988) p. 248.
- 3). T. Tomiki, T. Futemma, H. Kato, T. Miyahara, Y. Aiura, H. Fukutani and T. Shikenbaru: J. Phys. Soc. Jpn. 58 (1989) 1486.

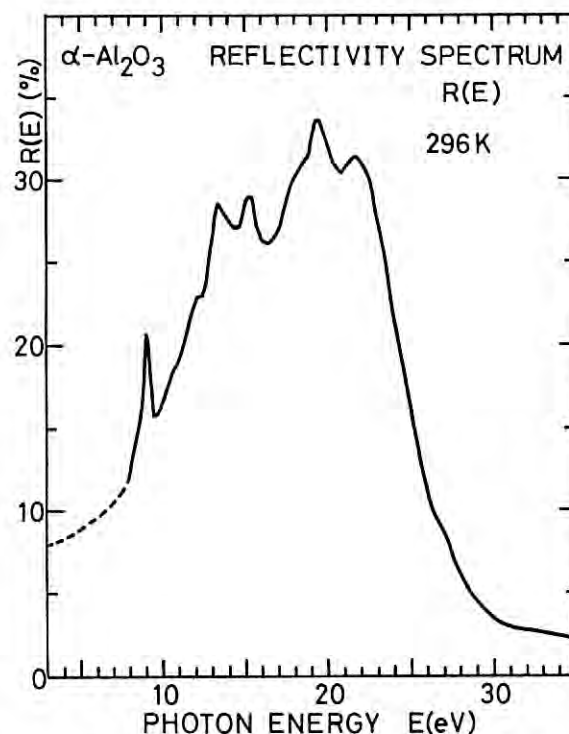


Fig. 1. The reflectivity spectrum of α - Al_2O_3 measured with the plane polarized light at BL-11C. The orientation of the specimen relative to \vec{E} , the field vector of the light, is the same as the preceding specification of $\langle c \rangle \perp \vec{E}$ in refs. 1) ~ 3). The crystallographic check is now being carried out.

ANGLE-RESOLVED PHOTOEMISSION STUDY OF THE BULK MAGNETIC PHASE TRANSITION IN Cr

Tadahiro KOMEDA, Yasuo SAKISAKA, Masaru ONCHI, Hiroo KATO*,
Shoji SUZUKI**, Kazuyuki EDAMOTO***, and Yoshihiro AIURA****

Department of Chemistry, Faculty of Science, Kyoto University, Kyoto 606,
Japan

* Photon Factory, National Laboratory for High Energy Physics, Tsukuba-shi,
Ibaraki 305, Japan

** Department of Physics, Faculty of Science, Tohoku University, Sendai 980,
Japan

*** Department of Chemistry, Faculty of Science, Tokyo Institute of Technology,
Ookayama, Tokyo 152, Japan

**** Institute of Physics, University of Tsukuba, Tsukuba-shi, Ibaraki 305,
Japan

Introduction

In addition to our previous results¹⁾, we report further photoemission evidence for the bulk anti-ferromagnetic (AF)-paramagnetic (PM) phase transition in Cr. An emission from the Σ_4 and Σ_1 bands unique to the AF phase was found to disappear at above the Neel temperature ($T_N = 312$ K).

Experimental

The ARUPS experiments were made on BL-11D. The clean Cr(110) was prepared by repeated Ar⁺ sputtering and annealing cycles. The working pressure was 1×10^{-10} Torr.

Results and discussion

Fig.1 shows normal-emission photoelectron spectra of the clean Cr(110) surface measured at 80 and 470 K: (a) $h\nu = 25$ eV and $\theta_i = 60^\circ$ from the surface normal and (b) $h\nu = 45$ eV and $\theta_i = 25^\circ$. The $T = 80$ K spectra show four features at ~ 0.3 , 1, 3, and 6 eV below E_F . Throughout this work, the surface component of the vector potential ($A_{||}$) of the incident light was at an angle of 55° with the [001] azimuth (see the inset of Fig.1), i.e., in the [111] azimuth ($A_{||}$ along [111]). The $h\nu$ dependence of the normal-emission spectra for $A_{||}$ parallel to the [001] azimuth have been reported previously¹⁾. According to Ref.1, the observed features at ~ 0.3 , 1, 3, and 6 eV in the $T = 80$ K spectra of Fig.1 are ascribed to the emission from the surface resonance (SR) state and 3d-like Σ_3 band, the 3d-like top Σ_1 bands, the middle Σ_1 bands, and the 4s-like lowest Σ_1 bands, respectively. For the $h\nu = 45$ eV spectrum [Fig.1(b)], the lowest Σ_1 band emission is superposed to an incoherent $M_{23}VV$ Auger emission with a fixed kinetic energy of 36-38 eV as referenced to E_F . Since $A_{||}$ along [111] has a component parallel to the [110] azimuth, an emission from the Σ_4 band can be excited. The position of the 3-eV feature determined from this study is plotted in Fig.2 (stars marked by arrows), which show all the experimental points (from Ref.1) plotted over the calculated bulk band structure (lines) of AF Cr²⁾ (circles are for the Σ_1 peaks and crosses for the Σ_3 peaks). There, we assume a free-electron-like final-state band with Σ_1 symmetry and with an inner potential $V_0 = 9.8$ eV for the case of Cr(110) [Ref. 1]. The Σ_4 -band emission may overlap the emission from the middle Σ_1 band at ~ 3 eV.

As has been discussed in Ref.1, the existence of the Σ_3 -band emission is possible at $20 \leq h\nu \leq 45$ eV for both the AF and PM phases, but the Σ_4 and middle Σ_1 bands unique to the bulk AF phase should disappear at above T_N . In fact, as seen in Fig.1, when increasing temperature from 80 K (below T_N) to 470 K (above T_N , $T = 1.5 T_N$), the ~ 3 -eV emission feature disappears, while other features are essentially unchanged.

References

- 1) Y. Sakisaka, T. Komeda, M. Onchi, H. Kato, K. Edamoto, and Y. Aiura, Phys. Rev. B **38**, 1131 (1988).
- 2) S. Asano and J. Yamashita, J. Phys. Soc. Jpn. **23**, 714 (1967).

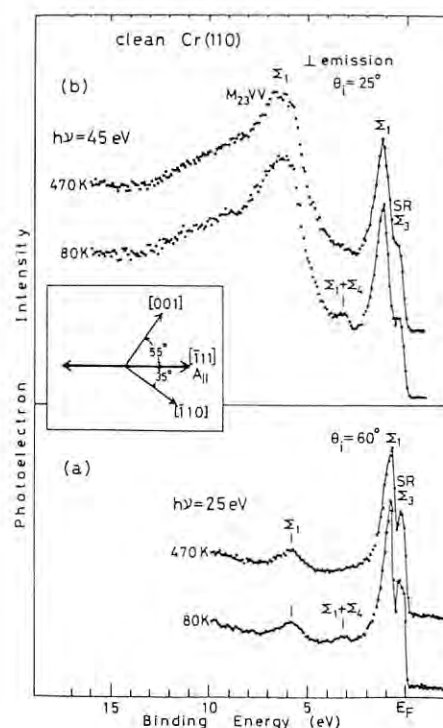


Fig. 1

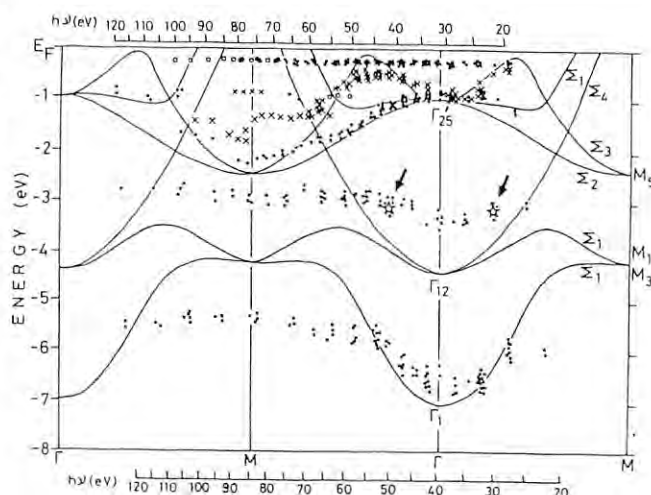


Fig. 2

ANGLE-RESOLVED PHOTOEMISSION OF Xe PHYSORBED ON Cr(110)

Tadahiro KOMEDA, Yasuo SAKISAKA, Masaru ONCHI, Hiroo KATO *,
Shoji SUZUKI**, Kazuyuki EDAMOTO***, Yoshihiro AIURA****

Department of Chemistry, Faculty of Science, Kyoto University, Kyoto 606,
Japan

* Photon Factory, National Laboratory for High Energy Physics, Tsukuba-shi,
Ibaraki 305, Japan

** Department of Physics, Faculty of Science, Tohoku University, Sendai 980,
Japan

*** Department of Chemistry, Faculty of Science, Tokyo Institute of Technology,
Ookayama, Tokyo 152, Japan

**** Institute of Physics, University of Tsukuba, Tsukuba-shi, Ibaraki 305,
Japan

Introduction

Two-dimensional band dispersion was studied by angle-resolved photoemission (ARUPS) for a $p(2 \times 2)$ -Xe overlayer on Cr(110) with a Xe-Xe nearest-neighbor distance of $d_{\text{Xe-Xe}} = 4.99 \text{ \AA}$, which is much larger than earlier reported ones. The Xe $5p_{1/2, 3/2}$ levels show $\sim 0.2 \text{ eV}$ dispersion, which confirms the theoretical prediction, or a simple exponential dependence of the bandwidth on $d_{\text{Xe-Xe}}$.

Experimental

The ARUPS experiments were made on BL-11D. The clean Cr(110) was prepared by repeated Ar⁺ sputtering and annealing cycles. With liquid-N₂ cooling, the sample could be cooled to $\sim 80 \text{ K}$. The working pressure was $1 \times 10^{-10} \text{ Torr}$.

Results and discussion

As the Cr(110) clean surface is exposed to Xe gas at 80 K, a $p(2 \times 2)$ LEED pattern is observed at $5 \times 10^{-6} \sim 2 \times 10^{-5} \text{ Torr Xe}$. For the $p(2 \times 2)$ Xe/Cr(110) overlayer, $d_{\text{Xe-Xe}}$ is 4.99 \AA , being 14% larger than the bulk value. Fig.1 shows off-normal UPS spectra along the $[001](\bar{\Gamma}-H)$ azimuth for the $p(2 \times 2)$ Xe surface ($h\nu = 30 \text{ eV}$, $\theta_i = 60^\circ$, 80 K). Both the Xe $5p_{3/2}$ and $5p_{1/2}$ peaks shift slightly to higher binding energies as the emission angle θ_e is increased until a surface Brillouin zone boundary is reached. Fig.2 shows measured dispersion of both Xe $5p$ bands for $p(2 \times 2)$ Xe/Cr(110). A compilation of the available experimental data, in a semilogarithmic plot, for the full Xe $5p$

$1/2$ bandwidth for ordered monolayers on various substrates as a function of $d_{\text{Xe-Xe}}$ is shown in Fig.3 (solid symbols)[see Ref.1]. Here, a simple exponential dependence of the bandwidth on $d_{\text{Xe-Xe}}$ is assumed, as can be expected if the bandwidth is determined by wave-function overlap. The three open circles connected by a straight line are the results given by the LRC band calculation for an unsupported Xe monolayer²⁾. As seen in Fig.3, except for Xe/Pt(111), the data obtained previously are concentrated on the narrow $d_{\text{Xe-Xe}}$ range between 4.3 and 4.5 \AA , and therefore it is not sufficient to prove the LRC calculation or the exponential dependence of the bandwidth on $d_{\text{Xe-Xe}}$. However, when our Xe/Cr(110) datum (denoted by a solid star) is included, we find the agreement between theory and experiment becomes good. That is to say, though the data in Fig.3 are somewhat scattered, the general trend of the data indicate that the bandwidth of the Xe $5p$ state seems to be determined by $d_{\text{Xe-Xe}}$. The Xe-substrate interaction might be relatively important for larger $d_{\text{Xe-Xe}}$, but our data indicate the Xe-substrate interaction is of minor importance as compared with the lateral Xe-Xe interaction.

References

- 1) T.Komeda, Y.Sakisaka, M.Onchi, H.Kato, S.Suzuki, K. Edamoto, and Y.Aiura, Phys.Rev.B40, 3344 (1989).
- 2) K.Hermann, J.Noffke, and K.Horn, Phys. Rev. B 22, 1022 (1980).

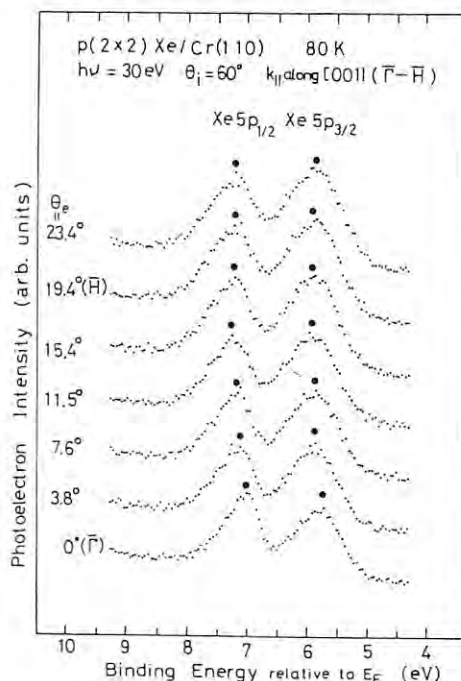


Fig. 1

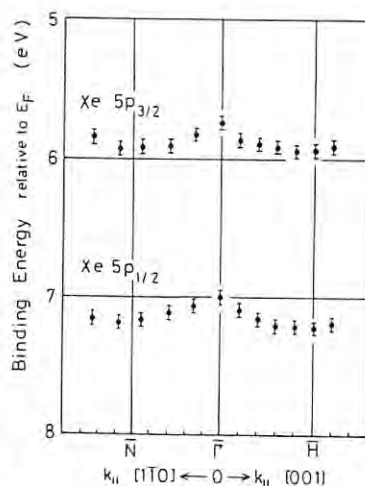


Fig. 2

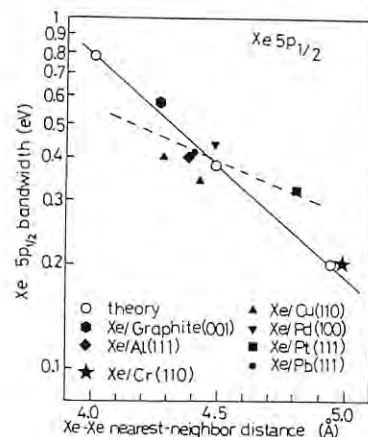


Fig. 3

ANGLE-RESOLVED PHOTOEMISSION STUDY OF Ag(111)

Kazuyuki EDAMOTO, Eizo MIYAZAKI and Hiroo KATO*

Department of Chemistry, Tokyo Institute of Technology, Tokyo 152

*Photon Factory, National Laboratory for High Energy Physics, Ibaraki 305

Introduction

The electronic structure of Ag is of considerable interest since its valence state consists of two different components, viz, localized d-states and free-electron like s,p-states. In this report, the electronic structure of Ag(111) is investigated by angle resolved photoemission spectroscopy.

Experimental

The measurements were conducted on BL-11D with a spherical analyzer. The clean Ag(111) surface was prepared by repeated Ar⁺ sputtering and annealing cycles. The base pressure was 1×10^{-10} Torr.

Results and Discussion

Figure 1 shows normal emission spectra for Ag(111). The intense band observed at 4 - 7.5 eV is composed of 4d bands. In this photon energy region, the density of state effect is dominant in the spectra,¹⁾ and thus the 4d bands appear in the overlapped form. We use the newly developed FIRO deconvolution method²⁾ to resolve the overlapped peaks. The resolved peak positions are used to map the energy band dispersions along Γ -L direction. Figure 2 shows the results together with the calculated band structure by Christensen.³⁾ The experimental bands are flat, but well reproduced by the flat parts of calculated bands. Besides the 4d bands, the plateau like emission is observed between E_F and 4d band (Fig. 1). In this region, only the s,p band is expected to exist, therefore, the plateau is associated with s,p band emitted via the indirect transition, which is probably due to thermally induced phonon-assisted process. Figure 3 shows a plot of the area intensities of the plateau as a function of photon energy. The emission is enhanced at $h\nu > 38$ eV where the emission comes from the region near the s,p band, and is weakened as the region separated from the s,p band (Fig. 2). These results suggest that the plateau arises from the s,p band and that the emission is broadened due to the phonon assisted process.

References

- 1) K. Edamoto, E. Miyazaki, K. Shimokoshi and H. Kato, *Physica Scripta*, in press.
- 2) K. Shimokoshi, K. Edamoto and E. Miyazaki, *J. Electron Spectrosc. Related Phenom.*, in press.
- 3) N. E. Christensen, *Phys. Stat. Sol.* 54, 551 (1972).

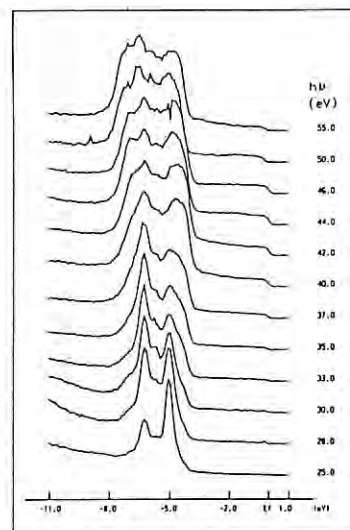


Fig. 1

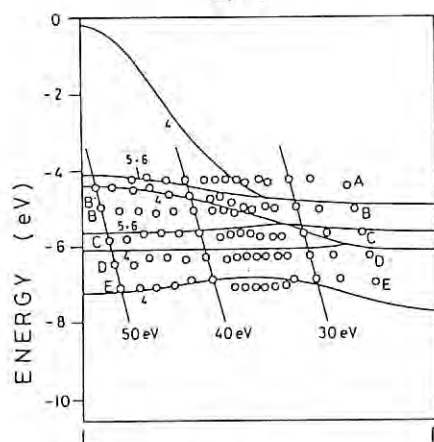


Fig. 2

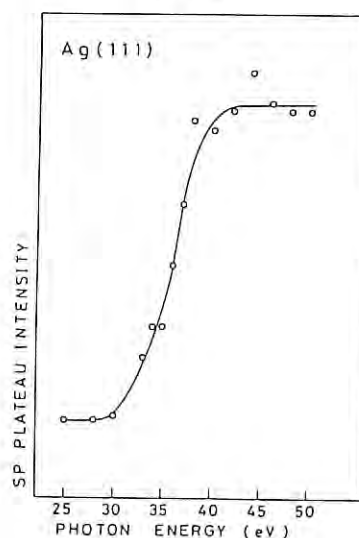


Fig. 3

PHOTOEMISSION FROM SmPd_3B_x

Hide nao SUGAWARA, Tomohiro KITAZUME, Hiromu ARAI^{a)}, Tsutomu MITSUISHI^{b)},
Tsuneaki MIYAHARA^{c)}, Hiroo KATO^{c)}, Shun-ichi NAKAI^{b)} and Mitsuo KASAYA^{a)}

Faculty of Education, Gunma University, Maebashi 371

a) Department of Physics, Faculty of Science, Tohoku University, Sendai 980

b) Faculty of Engineering, Utsunomiya University, Utsunomiya 321

c) Photon Factory, National Laboratory for High Energy Physics, Tsukuba 305

Introduction

Recently, it has been reported that the resistivity for SmPd_3B_x decreases with temperature when the concentration of boron is increased¹⁾. For SmPd_3B_x with high x-value, therefore, it is anticipated that the Sm 4f states are located near the Fermi level so that Kondo effect appears to occur.

We have performed photoemission measurements for samarium compounds of SmPd_3 , $\text{SmPd}_3\text{B}_{0.42}$ and $\text{SmPd}_3\text{B}_{1.0}$ in order to obtain detailed information about the electronic structure of these materials.

Experimental

Photoemission measurements were made for the valence band region in the photon energy range from 40 eV to 140 eV with use of an electron energy analyzer of a double pass cylindrical mirror type and a constant-deviation type monochromator at BL-11D. Constant-initial-state spectra (CIS's) were also measured for relevant materials in the photon energy ranges including the Pd 4p-4d and Sm 4d-4f thresholds which are located above 50 eV and 130 eV, respectively. Sample surfaces were prepared by scraping with diamond files in ultra high vacuum of 10^{-10} Torr.

Results and Discussion

Figure 1 shows valence band photoemission spectra of three samarium compounds which were taken at the photon energy of 40 eV. The intensities of these spectra were normalized with monitor signal measured for monochromatized light behind the exit slit of the monochromator. Gross feature of these spectra is similar to each other. They are characterized by prominent Pd 4d band appearing in the binding energy region from the Fermi level to 5 eV. However, they are different in the appearance of a step structure at the Fermi level with the addition of boron atoms. Moreover, the peak of the Pd 4d band of SmPd_3 at 2.5 eV is slightly shifted toward high binding energy with the content of boron, indicating the change of the electronic structure by adding boron atoms. It was found by analyzing the Pd 4d-4f resonance spectra that the Pd 4d band is about 2.4 eV in width and its peak is shifted from 1.8 eV for SmPd_3 to 2.4 eV for $\text{SmPd}_3\text{B}_{1.0}$ in the binding energy.

The electrical resistivity shows quite different temperature-dependence between samples with boron concentration below 0.25 and above 0.42 per unit cell¹⁾. This seems to be related to the feature of photoemission spectra that the spectrum of SmPd_3 has no step at the Fermi level, while those of $\text{SmPd}_3\text{B}_{0.42}$ and $\text{SmPd}_3\text{B}_{1.0}$ have conspicuous steps.

The CIS spectra of SmPd_3B_x which were observed at the initial-state-energy of 0.5 eV below the Fermi level, demonstrated resonant behavior above the Sm 4d-4f threshold. This

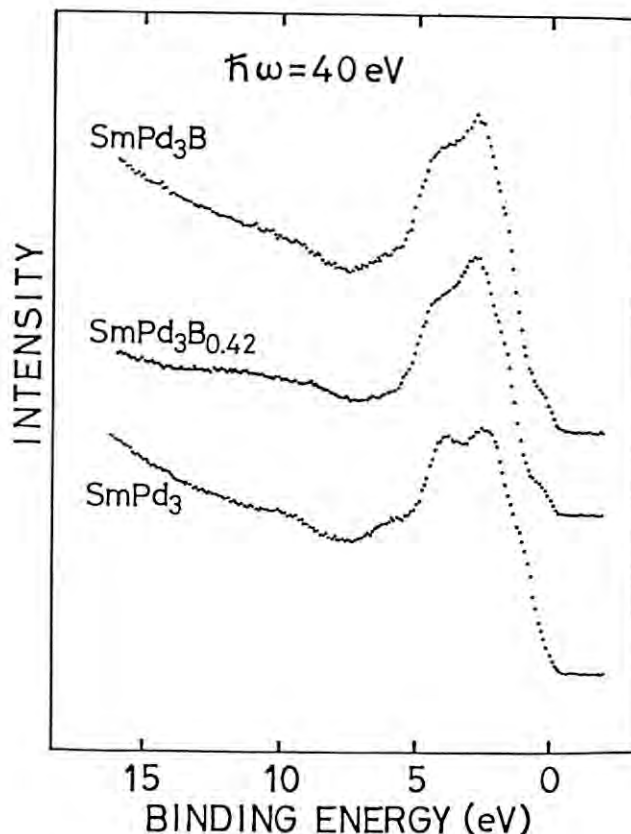


Fig. 1. Photoemission spectra of SmPd_3 , $\text{SmPd}_3\text{B}_{0.42}$ and $\text{SmPd}_3\text{B}_{1.0}$ which were taken with the photon energy of 40 eV.

suggests that Sm 4f states exist near the Fermi level, forming the step there. Photoemission spectra taken with the photon energy of 120 eV make contribution from the Sm 4f states dominant since the Cooper minimum for Pd 4d photoionization occurs around 120 eV. The 120-eV spectra for SmPd_3B_x seems to indicate that the Sm 4f states are distributed from the Fermi level down to about 11 eV. This fact is also consistent with Sm 4f spectra which were obtained by making difference spectra between on- and off-resonance spectra for Sm 4d-4f excitation above 130 eV.

Reference

- 1) B. Liu, "Magnetic and Transport Properties of the AuCu_3 -type Sm Compounds" (Thesis, Tohoku University, 1989), p.42.

ANGLE-RESOLVED PHOTOEMISSION STUDY OF NbC(111) SURFACE

Kazuyuki EDAMOTO, Yoshimi ABE, Tsuyoshi IKEDA, Norimasa ITO, Eizo MIYAZAKI, and Hiroo KATO*

Department of Chemistry, Tokyo Institute of Technology, Tokyo 152

*Photon Factory, National Laboratory for High Energy Physics, Ibaraki 305

Introduction

NbC possesses many interesting physical properties such as high melting point, ultrahardness, and superconductivity. These properties are closely related to the valence electronic structure.^{1,2)} We reported here the angle-resolved photoemission study on the electronic structure of NbC(111) single crystal.

Experimental

The measurements were conducted on BL-11D with a spherical sector type analyzer. The NbC(111) clean surface was prepared by flashing to about 1500°C in the vacuum chamber (the base pressure was 1×10^{-10} Torr).

Results and discussion

Fig. 1 shows normal-emission spectra for the NbC(111) surface taken at various photon energies (25 - 80 eV). At $h\nu > 35$ eV, the resonant emission is observed at just below E_F . This resonance has also been observed in the spectra for NbC(100)¹⁾ and is attributed to a Fano-type resonance corresponding to a $Nb\ 4p \rightarrow 4d$ excitation followed by a super Coster Kronig decay. A sharp peak is also observed at just below E_F (labelled A) at $h\nu = 27.5$ eV, which is ascribed to a surface induced state. Peaks B-F are the emissions from the bulk bands. According to the symmetry selection rules, polarization dependences shown in Fig. 1 show that the initial state symmetries are Δ_1 for peaks E-G and E', Δ_3 for peak D, and obscure for peaks B and C. With regard to the energy levels and symmetries, experimentally determined bands are well reproduced by the flat part of the theoretical bands.²⁾ The peaks B and C are both emitted from the flat parts of the bands at Γ point where the bands of different symmetries are degenerated, which is compatible with the results that the polarization dependences of these peaks are obscure.

It is known that a surface state is important for the surface reactivity. The surface reactivity of NbC(111) is much higher than that of (100).³⁾ This is considered to be due to the difference of surface electronic structure, thus the investigation of surface state on NbC(111) is well motivated. Fig. 2 shows the effect of O_2 adsorption on the spectra of NbC(111). It is shown that the peak A is very sensitive to adsorption relative to other peaks. Fig. 1 shows that the initial state symmetry of peak A is Δ_1 , while only the bulk bands of Δ_3 symmetry are expected to exist around E_F , theoretically. These results suggest that the peak A is attributed to a surface induced state. The dispersion of this peak plotted in the surface Brillouin zone²⁾ indicates that this level is half-filled metallic state, which may play an important role on the surface reaction.

References

- 1) K. Edamoto, S. Maehama, E. Miyazaki, and H. Kato, Phys. Rev. B39 (1989) 7461.
- 2) K. Edamoto, E. Miyazaki, and H. Kato, Vacuum, in press.
- 3) I. Kojima, M. Orita, E. Miyazaki, and S. Otani, Surface Sci. 160 (1985) 153.

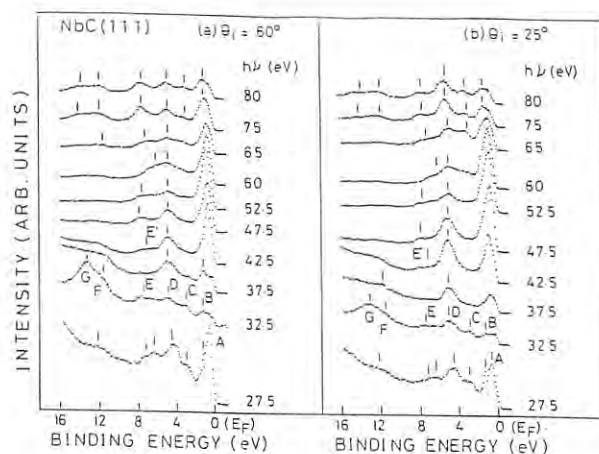


Fig. 1

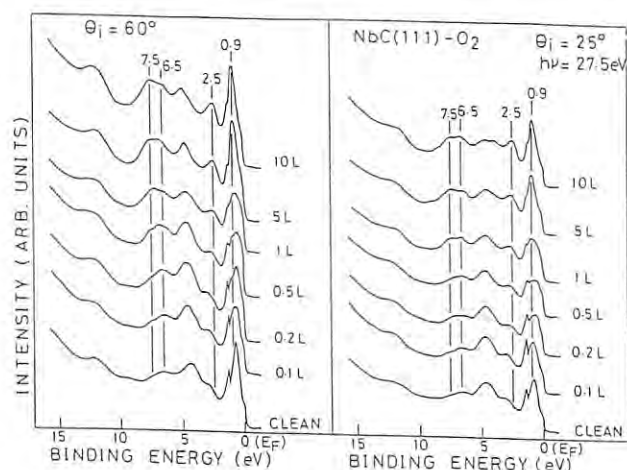


Fig. 2

Photoelectron Spectra of Molybdenum During Ion Bombardment

Masahiro KITAJIMA, Kazutaka NAKAMURA, Masakazu FUJITSUKA, Hitoshi SHINNO, Tetsuji NODA,
Hiroo KATOH* and Tsuneyuki MIYAHARA*

National Research Institute For Metals, Tsukuba Laboratories, Tsukuba, Ibaraki 305

**Photon Factory, National Laboratory for High Energy Physics, Tsukuba, Ibaraki 305*

INTRODUCTION

Ion bombardment onto the materials surface has become one of the most important subjects for forming new materials and analyzing the surface states. It causes the lattice damage, which may lead to various types of chemical effects on the surface through the change in electronic structure. We report here electron photoemission measurement of molybdenum under the argon ion bombardment in order to clarify the effect of the ion bombardment on electronic structure.

EXPERIMENTALS AND RESULTS

Photoelectron spectra were measured with a cylindrical mirror analyser at beam line 11D. The photon energy region was between 35 and 130eV. The system was evacuated by using two turbo pumps of 400l/s, and the working pressure was $(1-2) \times 10^{-7}$ Torr-Ar with ultimate impurity level of 6×10^{-11} Torr-H₂O. The clean Mo(110) was prepared by repeated

argon sputtering and annealing. The measurements were made during and after the ion bombardment(3keV) around 800C. Here, the heating of sample was done through an electron bombardment to the backside of the tantalum sample holder.

Figure 1 shows an example of emission spectra for the clean molybdenum at 820C with the histogram of density of state(DOS) obtained by the APW method[1]. The peak positions are in good agreement with the DOS calculation. Figure 2 shows the spectra with photon energy of 84-130eV during(b) and after(a) the argon ion bombardment. The spectrum peak C becomes weak during the ion bombardment, and the electronic structure disappeared.

- [1] D.D. Koelling, F.M. Mueller and B.W. Veal, Phys. Rev. B10, 1290 (1974).

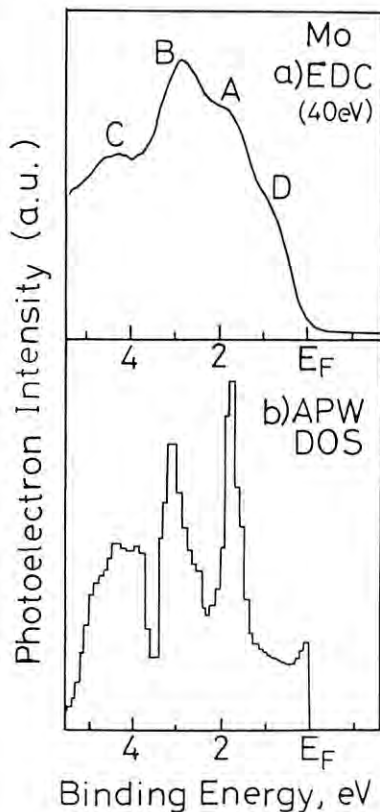


Fig. 1

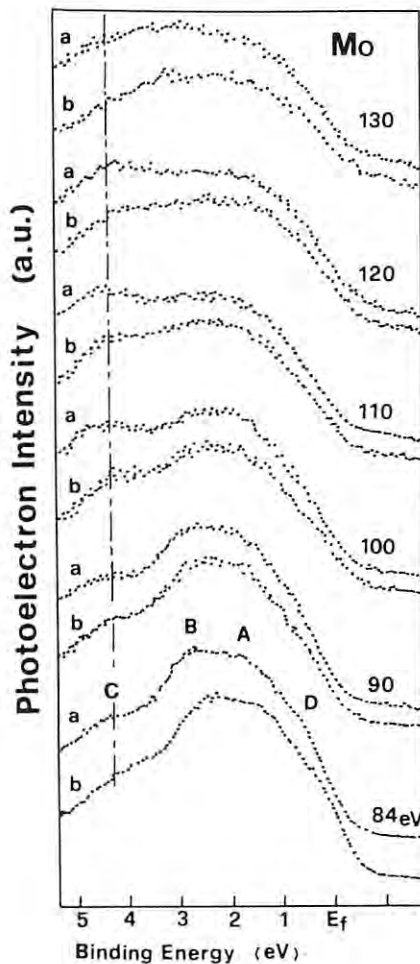


Fig. 2

ANGLE-RESOLVED PHOTOEMISSION STUDY OF RELATIVISTIC EFFECTS IN THE ELECTRONIC STRUCTURE OF Fe

Yasuo SAKISAKA, Takahiro MARUYAMA, Hiroo KATO *, Yoshihiro AIURA**
and Hiroyuki YANASHIMA

Department of Chemistry, Faculty of Science, Kyoto University, Kyoto 606,
Japan

* Photon Factory, National Laboratory for High Energy Physics, Tsukuba-shi,
Ibaraki 305, Japan

** Institute of Physics, University of Tsukuba, Tsukuba-shi, Ibaraki 305,
Japan

Introduction

The band structure of ferromagnet Fe, which is fundamental for understanding various physical phenomena, has been the subject of many angle-resolved photoemission spectroscopy (ARUPS) studies. Although spin-orbit coupling has an important effect on the electronic structure, until now there has been no report for the observation of such effects despite the extensive ARUPS work. Our ARUPS study of Fe(110) reveals spin-orbit splitting of the upper $\Gamma_{25'}$ state into two, separated by ~ 110 meV, being much larger than theoretical estimate (~ 45 meV).

Experimental

The ARUPS experiments were made on BL-11D. The clean Fe(110) was prepared by repeated Ar⁺ sputtering and annealing cycles. The base pressure in the system was $\sim 1 \times 10^{-10}$ Torr.

Results and discussion

Fig.1 shows the normal-emission spectra of clean Fe(110) between E_F and ~ 1 eV measured at $23 \leq h\nu \leq 40$ eV. Three features at ~ 0.2 , 0.4 , and 0.7 eV move as $h\nu$ is changed. If we assume a free-electron final band with Σ_1 symmetry and $V_o = 8.9$ eV for the case of Fe(110) as used successfully in Ref.1, we can map the binding energies of all the peaks in the normal-emission spectra onto points along the $[\Gamma 110]$ ($\Gamma \Sigma N$) direction in the bulk Brillouin zone. The results between E_F and ~ 1 eV are shown in Fig.2 (solid circles). The calculated non-relativistic band structure²⁾ is also shown (thin lines). There are some discrepancies between non-relativistic theory and experiment (the situation is aggravated if compared with the relativistic theory³⁾). Such discrepancies are considered to be partly due to the local density approximation to the exchange-correlation potential.

The most important finding is that the experimentally determined $\Sigma_{3\downarrow}$ and $\Sigma_{1\downarrow}$ bands are never merged into a $\Gamma_{25'\downarrow}$ state in contrast to a non-relativistic band structure²⁾, but are split into two components. This splitting is clearly relativistic (spin-orbit coupling) effects. The binding energies of the two components are $\Gamma_{7+\downarrow} = 0.27$ eV and $\Gamma_{8+\downarrow} = 0.39$ eV, separated by ~ 110 meV. This splitting is ~ 2.5 times as large as that (~ 45 meV) estimated by the relativistic band calculation³⁾. Fully relativistic band calculation of Fe with the inclusion of spin-orbit coupling in a more accurate way is desired.

References

- 1) Y. Sakisaka, T. Rhodin, and D. Mueller, Solid State Commun. 53, 793 (1985).
- 2) J. Callaway and C.S. Wang, Phys. Rev. B **16**, 2095 (1977).
- 3) M. Singh, C.S. Wang, and J. Callaway, Phys. Rev. B **11**, 287 (1975).

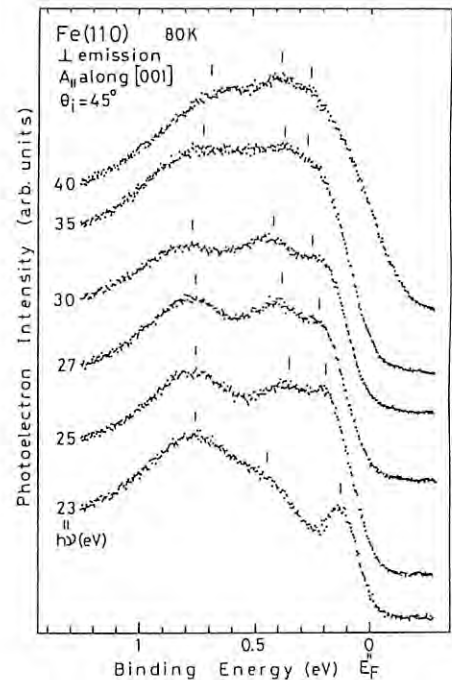


Fig. 1

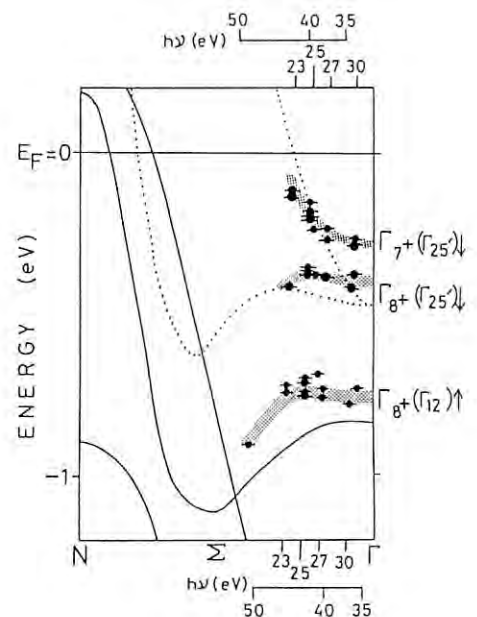


Fig. 2

ABSOLUTE CALIBRATION OF A NORMAL INCIDENCE VACUUM SPECTROMETER FOR FUSION PLASMA DIAGNOSTICS

Hirota Kubo, Akira Sakasai, Nobuhiro Nishino*, Yoshihiko Koide, Nobuo Akaoka, Makoto Hara, Shinichi Chiba, Tatsuo Sugie, Hiroshi Takeuchi, Hideaki Yokomizo, Naohiro Yamaguchi**, Kenichiro Tanaka***, Hideki Maezawa***, and Kenji Itoh***
 Japan Atomic Energy Research Institute, Naka-machi, Naka-gun, Ibaraki 311-01

* Hitachi Energy Research Laboratory, Hitachi-shi, Ibaraki 316

** Plasma Research Center, University of Tsukuba, Tennoudai, Tsukuba-shi, Ibaraki 305

***Photon Factory, National Laboratory for High Energy Physics, Oho, Tsukuba, Ibaraki 305

Introduction

In fusion research, absolute intensity calibration of the spectrometer is needed for measurements of impurity densities, radiative losses, and impurity transports. The present paper describes the method and the result of absolute calibration^{1,2)} carried out for a normal incidence VUV spectrometer over a wide wavelength region from 350 to 1250 Å by using a calibrated photodiode and synchrotron radiation for the purpose of impurity diagnostics in JT-60³⁾.

Normal Incidence Spectrometer

The spectrometer to be calibrated is a normal incidence vacuum spectrometer (Nikon, NU-1000) with a multichannel detector (Hamamatsu Photonics, C2321-02). The spectrometer-detector system covers a wavelength range of 687-1328 Å in the first order with a resolution of 1.4 Å. Figure 1 shows a sketch of the optical arrangement of the spectrometer and the experimental arrangement. The spectrometer was equipped with a 0.4 m, 2400 grooves/mm ruled concave grating with an Al+MgF₂ coating and a blaze angle of 6.9°. The detector⁴⁾ is a photodiode array with a pair of microchannel plates

Experimental

The normal incidence spectrometer was absolutely calibrated for light 700-1250 Å in the first order and 350-650 Å in the second order at the beam line 12A. As shown in Fig.1, synchrotron radiation was monochromatized by a 1 m Seya-Namioka monochromator, and the absolute intensity of the incident photon flux was measured with a windowless far-UV photodiode⁵⁾ calibrated at the National Institute of Standards and Technology, USA.

As the first step of the experiment, we measured the intensities of the first- and second-order light coming from the post focusing mirror. As the second step, we measured the signal of the test spectrometer and the signal of a standard photodiode for the light coming into the spectrometer. Then, the sensitivity of the spectrometer was calculated from the results measured in the previous two steps. The sensitivity in the wavelength region of 1050-1250 Å was also measured by cutting off the higher-order light with a LiF filter. The calibration experiment was performed in two cases: that the grooves of the grating were vertical and that they were horizontal. The result was averaged in order to compensate the effect of the polarization.

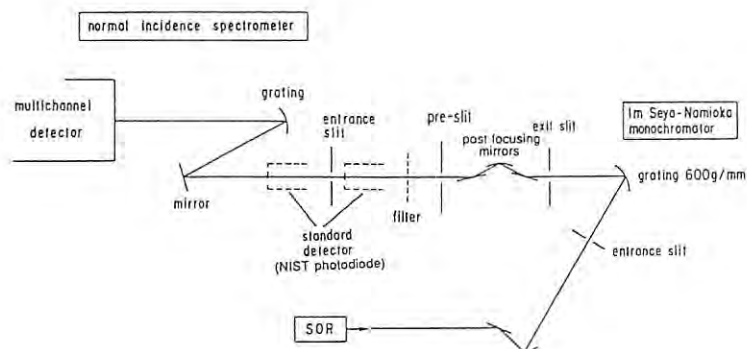


Fig.1 Optical arrangement of the normal incidence vacuum spectrometer and experimental arrangement of the calibration.

Result and Discussion

The result of the calibration experiment is shown in Fig.2, where the sensitivity refers to the output (V) of the spectrometer divided by the flux (photons/s) of the incident light. The figure shows the sensitivities for the first-order light of 700-1250 Å and the sensitivities for the second-order light of 350-650 Å. In the wavelength region longer than 1050 Å, the sensitivities obtained by two methods are shown. Open points show the sensitivities obtained by employing a LiF filter to cut off the higher-order light. Solid points show the sensitivities corrected by estimating the contribution of the second-order light to the signal. The results obtained by the two methods agreed typically within 20%. Therefore, it is expected that the contribution of second-order light was corrected well in the measurement without the LiF filter. The sensitivity for the first-order light was higher by an order of magnitude than the sensitivity for the second-order light. The sensitivity had a dip at the wavelength of 1120 Å. The dip would be due to the absorption edge of MgF₂⁶⁾. The error in the calibration is estimated to be 13-35%, and the sensitivity obtained by this method is greater than that obtained by other methods⁷⁾ using line emissions. Therefore, the result indicates that the present calibration would provide an accuracy needed for the measurement of impurity line intensities in tokamaks. The spectrometer is used to study impurity behaviors in the JT-60 tokamak.

References

- 1) H.Kubo, T.Sugie, A.Sakasai, et al., Rev.Sci.Instrum., **59** 1515 (1988).
- 2) H.Kubo, A.Sakasai, N.Nishino, et al., to be published in Jpn.J.Appl.Phys.
- 3) JT-60 team: Proc. 11th Int. Conf. on Plasma Physics and Controlled Nuclear Fusion Research, Kyoto, 1986 (IAEA, Vienna, 1987) Vol.1. p.11.
- 4) T.Sugie, H.Kubo, A.Sakasai, et al., KAKUYUGO KENKYU Special Supplement **59** 157 (1988).
- 5) L.R.Canfield, R.G.Johnson, and R.P.Madden: Appl.Opt. **12** 1611 (1973).
- 6) M.W.Williams, R.A.MacRae, and E.T.Arakawa, J.Appl.Phys. **15** 1701 (1967).
- 7) E.Hinnov: Phys.Rev. **A14** 1533 (1976).

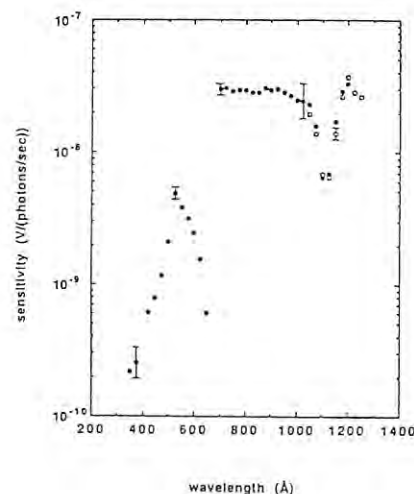


Fig.2. Calibration curves of the spectrometer.

AN ATTEMPT OF FLUORESCENCE LIFETIME MEASUREMENTS USING THE PULSE STRUCTURE OF PHOTON FACTORY

Masatoshi UKAI, Noriyuki KOUCHI, Kosei KAMETA, Ryo CHIBA, Kazunori NAGANO,
Kenichiro TANAKA* and Yoshihiko HATANO

Department of Chemistry, Tokyo Institute of Technology, Meguro-ku, Tokyo 152

*: Photon Factory, National Laboratory for High Energy Physics, Oho, Tsukuba 305

Introduction

One of the most fascinating opportunities in applications of synchrotron radiation to studies of the molecular superexcited states is to improve the SR pulse structure, especially its single-bunched character.¹⁾ Special attention was also acquired in studies of the dynamic processes of highly excited molecules.²⁾ The present group applied, for the first time, the single bunch character of SR to the study of binary collision process or gas-phase chemical reaction.³⁾ Fluorescence lifetimes of some fundamental saturated hydrocarbons in liquid phase were also examined with the aid of the single-bunched SR.⁴⁾ In those experiments, the SR pulse was employed from the ISSP-SOR ring. However, it has been of continuing considerable desire to apply the single bunched SR beam from Photon Factory in combination with other excellent features.

This is the first attempt to improve the single-bunched pulse from Photon Factory to studies of dynamic processes of highly excited molecules. We present measurements of the fluorescence lifetimes from some highly excited N_2 molecules.

Experimental

Time-resolved detection of the optical emission was carried out using a conventional delayed coincidence technique. The block diagram is shown by fig.1. Optical emissions of 115-200nm from N_2 gas excited by SR-photon impact passing through MgF_2 window was detected by a microchannel plate (MCP). Signal pulse was amplified and discriminated to form a start pulse into the time to amplitude converter. A RF pick off signal through a 1/312 divider was utilized as a stop pulse. Time profile of the incident beam was monitored with the same MCP and coincidence circuit using the reflected SR beam from the monochromator.

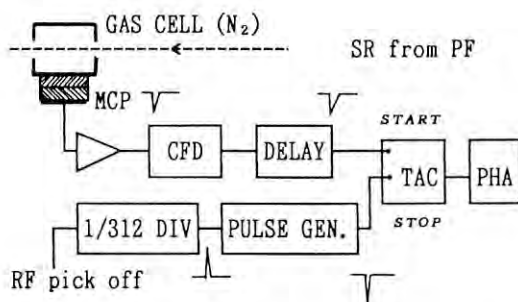


Fig.1 Block diagram of the time-resolved emission detection.

Results

Time resolved decay profiles of the optical emissions are presented in fig.2 at several excitation wavelengths. As can be seen, the decay of the

fluorescence was dependent on the excitation wavelength. In the present operation, however, elimination of the nearest neighboring pulses was not complete; the main pulse accompanied neighboring pulses with a few percent heights of the main one. The decay curves were analyzed by means of the moment method. The lifetimes obtained were shown in table 1, which are in good agreement with the previous measurements.^{5, 6)}

References

- 1) Y. Hatano & T. Ohta eds, *KEK Report*, 81-16(1981).
- 2) A. Ogata & S. Tagawa, *Rev. Sci. Instrum.*, **60**, 2197(1989)
- 3) Y. Hatano et al., *Chem. Phys. Lett.*, **84**, 454(1981).
- 4) K. Shinsaka et al., *J. Chem. Phys.*, **83**, 4405(1985).
- 5) H. Oertel et al., *Chem. Phys. Lett.*, **82**, 552(1981).
- 6) J. E. Hesser & K. Dressler, *J. Chem. Phys.*, **45**, 3149(1966).

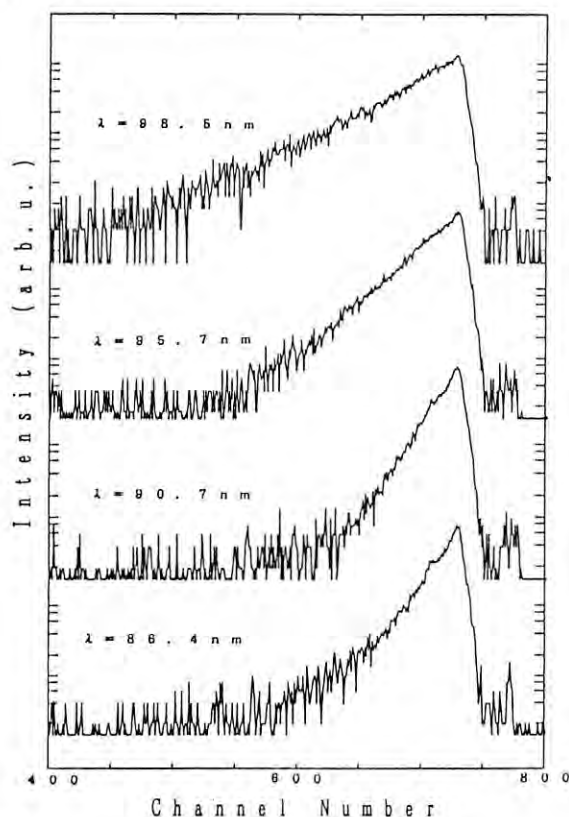


Fig.2 Fluorescence decay profiles from N_2 .

λ (nm)	Electronic State	Lifetime (ns)	
98.5	$b^1 \Pi_u, v'=1$	1.9	1.75 ^{ref. 5)}
95.7	$c^1 \Sigma_u, v'=0$	1.0	0.9 ⁶⁾
90.7	$b^1 \Sigma_u, v'=9$	0.6	0.71 ⁵⁾
86.4	$3 \sigma_g \rightarrow 5p \sigma_u$	0.7	0.6 ⁵⁾

Table.1. Fluorescence lifetimes from the highly excited N_2 molecules.

This work is financially supported in part by the Ministry of Education, Science, and Culture.

ABSOLUTE MEASUREMENTS OF PHOTOABSORPTION CROSS SECTION AND IONIZATION QUANTUM YIELD OF SiH_4 Kosei KAMETA, Masatoshi UKAI, Ryo CHIBA, Kazunori NAGANO, Noriyuki KOUCHI,
Kenichiro TANAKA* and Yoshihiko HATANO

Department of Chemistry, Tokyo Institute of Technology, Meguro-ku, Tokyo 152

*: Photon Factory, National Laboratory for High Energy Physics, Oho, Tsukuba 305

Introduction

Photoionization of group-V hydrides and their derivative molecules acquires an elementary interest to substantiate efficient energy deposition in gas-phase reactive plasmas. Recent experimental efforts were mainly devoted to inner shell ionization of SiH_4 molecules.¹⁻⁴⁾ However, according to electron scattering studies,⁵⁾ maximum photoabsorption was expected to exist in the extreme-UV region. A few quantitative works available were restricted below 105nm.^{6, 7)} Above 105 nm, a quantitative study, the measurement of the absolute photoabsorption or the photoionization cross section was not reported; only relative ionization cross sections were obtained previously.^{8, 9)}

We present, here, the first absolute measurements of the photoabsorption cross section and the photoionization quantum yield of SiH_4 in 30-97 nm region.

Experimental

Multipole statged ionization chamber employed in the present experiment was similar to those reported in the previous measurements.^{10, 11)} However, in order to remove the secondary artifacts and to increase collecting efficiency, a new chamber with a cylindrical fashion was used in this experiment. To eliminate higher order radiation and to avoid gas effusion into the optical path, Al-Te, Sn, or In foil filter was employed as the window of incoming SR beam.

Results and Discussion

Photoabsorption cross section obtained in the present experiment is shown in fig.1. The cross section of about 80Mb at around 90nm decreased gradually with the increase in the photon energy down to a few Mb at 30nm. A broad peak was observed with the peak maximum at 84nm. An oscillatory structure in 70-78nm was observed, which was interpreted as the $3s\sigma^*(1\sigma)^{-1}$ Rydberg series.^{5, 9)} The general feature of the cross section is in good agreement with the electron energy loss spectrum obtained in a small angle scattering experiment.⁵⁾ The cross section is also very similar to the higher energy side than 89nm of the total photoionization cross section obtained by Hayaishi et al.⁹⁾

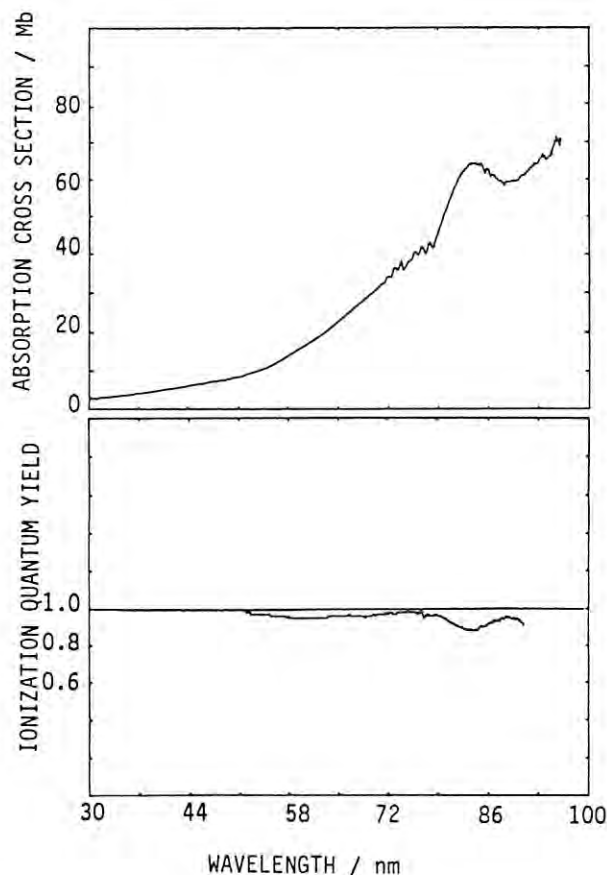
In fig.2, photoionization quantum yield is also shown. The wavelength region was limited to 50-92nm owing to the experimental difficulties. Very unfortunately, the increasing structure below 92nm from the ionization threshold, which explains the structural discrepancy between the ionization cross section by Hayaishi et al. and the present absorption cross section in this region, was not able to be obtained. The ionization quantum yield was very close to unity in this region. However, a broad minimum was observed centered at around 84nm. The minimum corresponds very well to the peak maximum in the photoabsorption cross section. The maximum was supposed due to electronic excitation in the inner valence $3s\sigma_1$ orbital into the σ^* valence

shell.^{5, 9)} The present observation well demonstrates the interpretation. By using the present absorption cross section and the ionization quantum yield in combination with the results by Hayaishi et al. the absolute ionization cross section of SiH_4 is calculated. The cross section is 64Mb at the peak maximum of 84nm.

References

- 1) W. Hayes & F. C. Brown, *Phys. Rev.*, **A6**, 21(1972).
- 2) A. Yagishita et al, *Chem. Phys. Lett.*, **132**, 437(1986).
- 3) E. Shigemasa et al, *Phys. Scripta.*, in press.
- 4) S. Bodeur et al, *Phys. Rev.*, **A39**, 5075(1989).
- 5) M. Dillon et al, *J. Chem. Phys.*, **82**, 2909(1985).
- 6) M. Suto & L. C. Lee, *J. Chem. Phys.*, **84**, 1160(1986).
- 7) U. Itoh et al, *J. Chem. Phys.*, **85**, 4857(1986).
- 8) J. Berkowitz et al, *J. Chem. Phys.*, **86**, 1235(1987).
- 9) T. Hayaishi et al, *Chem. Phys.*, **116**, 151(1987).
- 10) T. Koizumi et al, *J. Chem. Phys.*, **82**, 4856(1985); **85**, 4276(1986).
- 11) H. Koizumi et al, *Radiat. Phys. Chem.*, **32**, 111(1988).

This work is financially supported in part by the Ministry of Education, Science, and Culture.

Fig.1 Photoabsorption cross section of SiH_4 .Fig.2 Photoionization quantum yield of SiH_4 .

SYNCHROTRON RADIATION-ASSISTED ETCHING OF Si

Shingo Terakado, Osamu Kitamura, Masayoshi Ogura,
Mitsuaki Harada, Shigeo Suzuki and Kenichiro Tanaka*

SANYO Tsukuba Research Center, 2-1 Koyadai, Tsukuba, Ibaraki 305

*Photon Factory, National Laboratory for High Energy Physics, 1-1 Oho, Tsukuba, Ibaraki 305

Introduction

The photochemical etching of n-Si (100) by sulfur hexafluoride (SF_6) / Ar was investigated using SR. The purpose of the present experiment is to realize highly selective etching in the SR irradiated region.

We confirmed by a preliminary experiment that etching reaction of Si was not observed only by SR irradiation in the SF_6 / Ar environment. Therefore, we tried to use a 2.45 GHz microwave discharge together with SR. Microwave discharge is usually used to decompose the etching gas. It is well known that Si is etched by the decomposed products of SF_6 made from microwave discharge.¹⁾ Highly selective etching in the irradiated region was shown by N. Ueno et al. by the combined use of a capillary discharge lamp and microwave discharge.²⁾ The great increase of the etching rate in the SR irradiated region was realized in this work as expected.

Experimental

The zero-th order dispersion of the Seya-Namioka monochromator at the beamline 12A was used as an excitation source. The radiation which passed the monochromator was limited to $\lambda > 35\text{nm}$. A side view of the apparatus used for the experiment is schematically shown in Fig. 1. SR beam was led into the reaction chamber (RC) through two differential pumping chambers (DPC) and three cylinders set at the joint of the chambers. These cylinders are 6 mm in diameter and about 100 mm in length. The system was evacuated by turbo molecular pumps (TP). The base pressure of RC was 2×10^{-7} Torr. SF_6 and Ar used as the reactive gas were simultaneously fed into RC. The partial pressure of SF_6 was from 2 to 50 mTorr and that of Ar was from 250 to 750 mTorr. The flow rate of these gases were controlled by a needle valve in the gas inlet line, respectively. The reactive species, which were generated by 2.45 GHz microwave discharge of SF_6 / Ar, were transported to RC through a quartz tube. Microwave power was controlled from 10 to 45 W. The gate valve which was set between RC and its TP was closed while RC was filled with gas. Even when gas was fed into RC, the high vacuum of the monochromator was kept by the differential pumping system. For instance, when the pressure of RC was 750 mTorr, that of DPC-A was 3×10^{-7} Torr. The pressure (2×10^{-7} Torr) of the post-focusing mirror chamber between the monochromator and DPC-A was not changed by introducing the gas into RC.

Results and discussion

The experiments using SR together with microwave discharge were performed by changing the reactive gas pressure and microwave power. A typical surface profile of Si etched by SF_6 / Ar is shown in Fig. 2. In this experiment, partial pressure of SF_6 was 10 mTorr, that of Ar was 500 mTorr and microwave power was 15 W. The dose defined as the product of the real irradiation time and the average ring current was 15,000 min \times mA. A Ni mesh which has 10 μm line and 40 μm spacing was used as a mask and was put 0.3 mm apart from the Si substrate. From this figure it is found that the mask pattern was replicated in the

etching profile on the Si substrate. Many stripes appeared parallel to the edges of the mask in the irradiated square region. It is considered that this profile is possibly due to diffraction effect at the Ni mask. The surface profile measured by using surface profiler (DEKTA 3030) is shown in Fig. 3. The etched depth of the irradiated region was about 3,500 Å (mark A) and that of the non-irradiated region was about 400 Å (mark B). This result apparently shows that the etching rate is extremely enhanced by simultaneous use of SR irradiation and microwave discharge. Detailed studies are being carried out to elucidate the mechanism of etching process and to realize much more selective etching in the SR irradiated region.

References

- 1) S. Tachi et al., J. Vac. Sci. Technol. 4 (1986) 459
- 2) N. Ueno et al., Jpn. J. Appl. Phys. 27 (1988) 1723

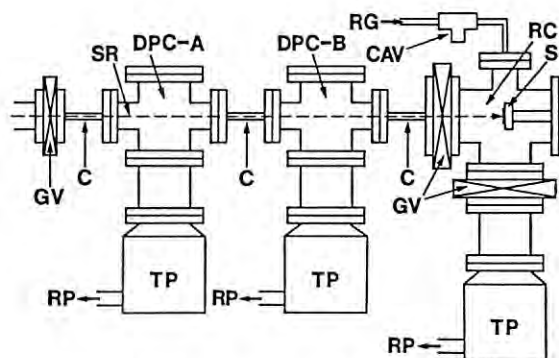


Fig. 1 Experimental apparatus used for SR-assisted etching

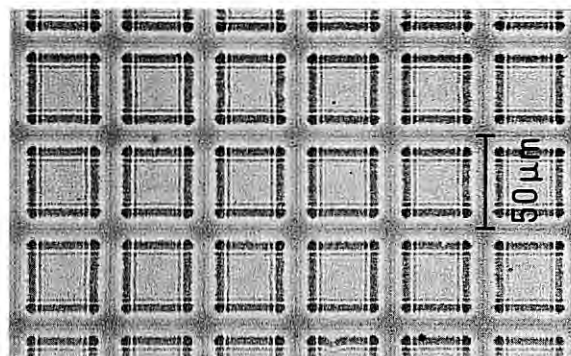


Fig. 2 Micrograph of Si surface etched by SF_6 / Ar

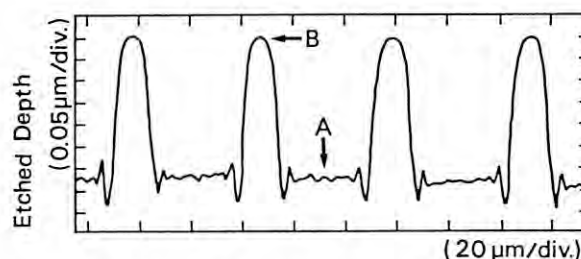


Fig. 3 The surface profile measured by DEKTA

PHOTOABSORPTION CROSS SECTIONS OF RARE GASES IN THEIR AUTOIONIZATION REGIONS

Kengo MAEDA¹, Kenji ITO², Kiyoshi UEDA³ and Takeshi NAMIOKA³

1) Faculty of Education, Kumamoto University, Kurokami, Kumamoto 860, Japan.

2) Photon Factory, National Laboratory for High Energy Physics, Oho, Tsukuba 305, Japan.

3) Research Institute for Scientific Measurements, Tohoku University, Katahira, Sendai 980, Japan.

INTRODUCTION

The photoabsorption cross sections for the rare-gas atoms, argon, krypton and xenon, in their autoionization regions have been measured photoelectrically with the highest resolution ever achieved in these wavelength regions. The cross sections can be described using the line-shape formula which is based on multichannel quantum-defect theory (MQDT) and has a form analogous to Fano's resonance formula /1/.

In this report, the results deduced from the line-shape fitting procedure are compared with those obtained from the ab-initio and semiempirical calculations.

EXPERIMENTAL

The present experiments were carried out using the focal plane scanning mode of the 6.65 m high resolution spectroscopic facility (6VOPE) installed at BL-12B of the Photon Factory. The 6.65 m, 1200 grooves/mm grating blazed for 5500 Å was used in the 6th spectral order. In this way, the resolving power was estimated to be $\geq 1.5 \times 10^5$ at ~ 887 Å with the entrance and exit slits of 10 μ m wide. The main spectrometer tank was used as an absorption cell and was filled with rare gas at a pressure of $1 - 4 \times 10^{-4}$ Torr. The uncertainty of the obtained photoabsorption cross sections was estimated to be less than 5 %.

RESULTS

The profiles of the photoabsorption cross sections were fitted to the resonance formula as follows /1/:

$$\sigma = \sigma_{as}(\epsilon_s + q_s)^2 / (1 + \epsilon_s^2) + \sigma_{ad}(\epsilon_d + q_d)^2 / (1 + \epsilon_d^2) + \sigma_b.$$

Here ϵ_ℓ is a periodic energy scale given by

$$\epsilon_\ell = \tan[\pi(v_{1/2} + \mu_\ell)] / W_\ell \text{ for } \ell = s \text{ and } d,$$

in which $v_{1/2} = [Ry / (I_{1/2} - E)]^{1/2}$ for the second ionization limit $I_{1/2}$, the energy of interest E and Rydberg constant Ry . The quantum defect μ_ℓ and the width parameter W_ℓ are related to the resonance energy $E_{n\ell}$ and the resonance width Γ_ℓ through the relations /1/:

$$I_{1/2} - E_{n\ell} = Ry / (n - \mu_\ell)^2 \text{ and } \Gamma_\ell / 2 = 2RyW_\ell / (n - \mu_\ell)^3.$$

The present photoabsorption cross sections of the 11s' and 9d' line pairs of argon atom (●) are shown in Fig.1 together with the curve (—) fitted by least square method. The fitted curve is in good agreement with the experimental points.

In Fig.2 and 3, the quantum defect μ_ℓ and the width parameter W_ℓ determined from the curve fittings are shown together with those calculated from the ab-initio (AI) eigenchannel parameters /2/ and the semiempirical (SE) eigenchannel parameters /3,4,5/. The circles, triangles and squares, which are open for s and solid for d,

denote the values obtained from the present work, the AI calculation and the SE calculation, respectively. It should be noted that the values of W_s are reduced by 1/10 times. The figures indicate that the observed parameters are in reasonable agreement with those deduced from the AI and SE calculations, although the agreement is not perfect. The abrupt increase at $n > 11$ in the observed W_s may be caused by the lack of instrumental resolving power.

REFERENCES

- /1/ K. Ueda, J. Opt. Soc. Am., B4, 227(1987).
- /2/ W. R. Johnson, K. T. Cheng, K.-N. Huang and M. Le Dourneuf, Phys. Rev., A22, 989(1980).
- /3/ C.-M. Lee and K. T. Lu, Phys. Rev., A8, 1241(1973).
- /4/ M. Aymar, O. Robaux and C. Thomas, J. Phys., B14, 4225(1981).
- /5/ J. Geiger, Z. Phys., A282, 129(1977).

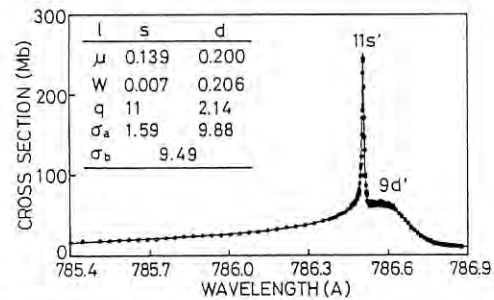


Fig.1 Photoabsorption cross sections of 11s' and 9d' line pairs of argon atom.

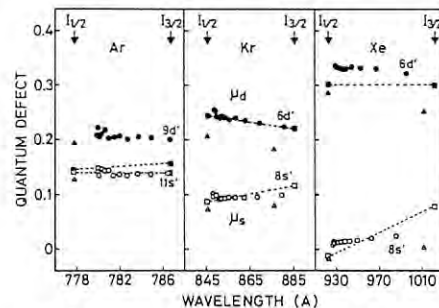


Fig.2 Quantum defects μ_s and μ_d .

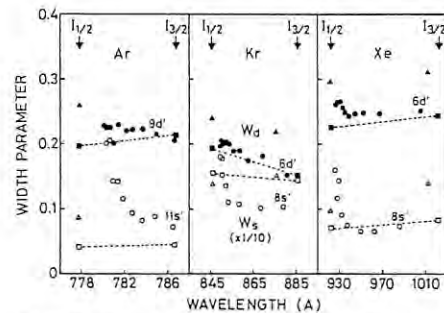


Fig.3 Width parameters W_s and W_d .

HIGH-RESOLUTION VUV ABSORPTION COEFFICIENTS FOR MOLECULES OF INTEREST TO ASTROPHYSICS

Kouichi YOSHINO¹, Peter L. SMITH¹, Kenji ITO², W. H. PARKINSON¹ & Glenn STARK³

1. Harvard-Smithsonian Center for Astrophysics, Cambridge, MA 02138, U.S.A.

2. Photon Factory, National Laboratory for High Energy Physics, Oho, Tsukuba, Ibaraki 305

3. Physics Department, Wellesley College, Wellesley, MA 02181, U.S.A.

1. Introduction

Molecules are found in a wide variety of astronomical objects: interstellar clouds, supernova remnants, circumstellar shells, stellar atmospheres (including that of the sun), planetary atmospheres, and comets. Knowledge of molecular parameters is necessary for interpretation of observed spectra and for modelling the photochemical processes that lead to observed abundances and excitations of the molecules in them. Rotational-line f -values are required for determination of column densities and abundances from observed absorption features, photoabsorption coefficients are needed to calculate rates for photodissociation--often a major molecular destruction mechanism, spectra of isotopic variants are required to predict isotopic fractionation, and high-resolution laboratory spectra are needed so that rotational analyses can be performed and, subsequently, the spectra at the peculiar conditions, *e.g.*, very low temperatures, in astronomical objects can be predicted.

2. Molecules in Diffuse Interstellar Clouds

Interstellar clouds are of interest to astronomers because they are regions of star formation. Dense clouds are opaque to light from the VUV through to the infrared and are studied by observing radio-wavelength emission from molecules; diffuse clouds are somewhat transparent, so that photochemistry affects the molecular abundances, and are studied by observing atomic and molecular absorption features in the spectra of stars imbedded in, or behind, the clouds. Although more molecular species are found in the dense clouds, study of diffuse clouds provides valuable information about the physical and chemical states of, and processes in, star-forming regions.

a) Carbon Monoxide: 91 - 100 nm

Carbon monoxide (CO) is believed to be the second most abundant interstellar molecule after H_2 , and, because it is readily observed, is used as a tracer of molecular material in interstellar clouds. However, abundances of CO are poorly determined observationally and not well understood theoretically. One of the major uncertainties is the rate of CO photodissociation by starlight, particularly that between 91.2 nm and the dissociation limit at 115 nm. Providing improved photoabsorption coefficient data for CO in this wavelength range has been a major focus of our research program in the past few years.

In November 1986, Yoshino, Smith, and Ito used the 6VOPE on BL-12B for high-resolution ($\lambda/\delta\lambda \geq 10^5$), photoelectric, measurements of a number of strong bands of CO between 93 and 100 nm. Our results were presented at International Astronomical Colloquium N° 102 and published in the proceedings thereof. In January, 1988, Yoshino, Parkinson, and Ito repeated some earlier measurements for which omissions, anomalies, and uncertainties were suspected. Every significant absorption feature between 91.2 nm and 100 nm was meas-

ured at several column densities. Absorption coefficients have been determined for the data and the results are being prepared for publication.

b) Carbon Monoxide: A-X, C-X, and E-X Bands

The bands of the $A(v')-X(0)$ system with $v' \geq 9$ (*i.e.*, with $\lambda < 130$ nm) are weak and, therefore, less likely to be saturated in interstellar cloud absorption spectra than the bands at longer wavelengths. Consequently, these bands are the optimum ones for observations with the *Hubble Space Telescope* and for subsequent determination of accurate CO column densities in clouds. Further, it is especially important to know the f -values for lines of the (14,0) band because there are accidental coincidences with the Ly- α line of atomic hydrogen that lead to fluorescence effects in astrophysical environments.

There is considerable discrepancy between sets of measured f -values for lines of the $C(v')-X(0)$ and $E(v')-X(0)$ bands of CO with $v'=0$ and 1, and theoretical values do not agree with the measurements. Determination of the correct f -values would provide benchmark data for assessment of the theoretical models of the CO molecule.

In order to provide improved f -values for some of the $A(v')-X(0)$, $C(v')-X(0)$, and $E(v')-X(0)$ bands of CO, we used 6VOPE to measure the absorption spectrum of CO at high resolution. Bands studied include $A(12)-X(0)$, $A(13)-X(0)$, $A(14)-X(0)$, $A(15)-X(0)$, $C(0)-X(0)$, $C(1)-X(0)$, $E(0)-X(0)$, and $E(1)-X(0)$. Analysis of these data will take place in the next year.

c) Other Interstellar Molecules: HCl

In 1980, we determined the f -values of the $C(0)-X(0)$ band of HCl using photographic techniques at the Center for Astrophysics. Our results were later questioned by others. Consequently, we remeasured the absorption coefficients using the photoelectric mode of 6VOPE. Data analysis is in progress.

3. Molecules in Planetary Atmospheres: C_2H_2

Acetylene (C_2H_2) features are prominent in the VUV albedos of the outer planets (Jupiter, Saturn, Uranus, and Neptune) and acetylene is expected to play major roles in the photochemistry of their atmospheres. Planetary atmosphere models that include acetylene features must incorporate photoabsorption cross section data that are accurate at the temperatures of planetary stratospheres, *i.e.*, 150 to 200 K. We have used the new low-temperature absorption cell on BL-12B to measure photoabsorption coefficients for C_2H_2 from ~140 nm to 174 nm at room-temperature and 195 K. Data analysis is in progress.

MEASUREMENT OF GAS-PHASE IONS GENERATED FROM SILANE BY SYNCHROTRON RADIATION EXCITATION*

Y. Nara, Y. Sugita, T. Ito, H. Kato* and K. Tanaka*

Fujitsu Laboratories LTD.

10-1 Morinosato-Wakamiya, Atsugi, Kanagawa, 243-01.

*Photon Factory, National Laboratory for High Energy Physics.

1-1 Oho, Tsukuba, Ibaraki, 305.

Introduction

Photochemical deposition by synchrotron radiation (SR) is a promising approach to the low-temperature semiconductor process, because the vacuum ultraviolet light can effectively excite the inner core energy level of source gas and generate highly-reactive ions. To investigate the SR induced photochemical process of silicon film deposition, we measured the gas-phase reactive ions from SiH_4 gas by SR excitation having the same energy and intensity as silicon film deposition experiments.

Experiments

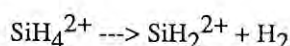
We used the beam line BL-12C. The SR reflected by Rh/C 21-layers multilayer mirror is quasi-monochromatic and it has the center photon energy of about 123 eV, which can excite L-core electrons of Si. Absorption cross-section of SiH_4 is about 6 Mb at 123 eV¹⁾. 5% SiH_4 gas diluted by He was introduced to the experimental chamber that is connected to the beam line through the differential pumping system. The total pressure was varied from 3×10^{-7} (base pressure of our system) to 1×10^{-5} Torr. Gas-phase ions are detected by photo-ionization quadrupole mass analyzer. By using photo-ionization method, SR excited ions are directly measured without fragmentation, that is commonly observed by electron-ionization method. SR passes through 10 mm diameter hole at the point of mass analyzer.

Results and discussions

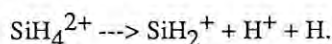
Figures 1 and 2 show the obtained mass spectrum at the mass number of 27-33 and 8-17, respectively. The pressure dependence of mass signal was also measured for each mass number and this indicates that the mass signals, except for mass number of 16, linearly increase as the SiH_4 partial pressure. Therefore the mass signals can be assigned as the molecule ions indicated in Figs. 1 and 2. Mass number of 16 is probably caused by O_2^{2+} or O^+ from the residual gas in the experimental chamber.

By absorbing the 123 eV light, SiH_4 was decomposed to produce a lot of univalent ions such as SiH_2^+ and SiH_3^+ . Bivalent ions such as Si^{2+} , SiH^{2+} and SiH_2^{2+} are also produced in the gas-phase. The amount of these bivalent ions was about 10% of that of univalent ions. Trivalent ions from SiH_4 , that are supposed to appear at the mass number 9.3-10.7, were not detected by our experimental system as shown in Fig.2.

L-core excitation of SiH_4 molecule by SR is assumed to produce transitional bivalent ion SiH_4^{2+} through the Auger process²⁾. SiH_4^{2+} ion is decomposed to produce bivalent ion as



and to produce a pair of univalent ions as



These processes are directly measured in the experiments.

In our experiment of growing silicon film, the contribution of gas-phase reactive species is smaller compared with that of surface excitation³⁾. However, the reactions described above are thought to occur between the surface SiH_4 adsorbates and incident SR.

- 1) W. Hayes and F.C. Brown, Physical Review A vol.6, No.1, p.21, 1972.
- 2) K. Ueda and Y. Sato, Hoshako, vol.1, No.2, p.1, 1988.
- 3) Y. Nara et al., PF Activity Report #6, p.270, 1988.

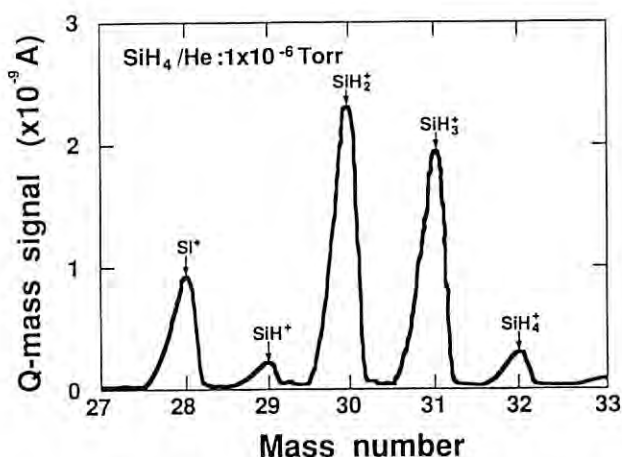


Fig.1 Mass spectrum from SiH_4 (Mass number = 27-33)

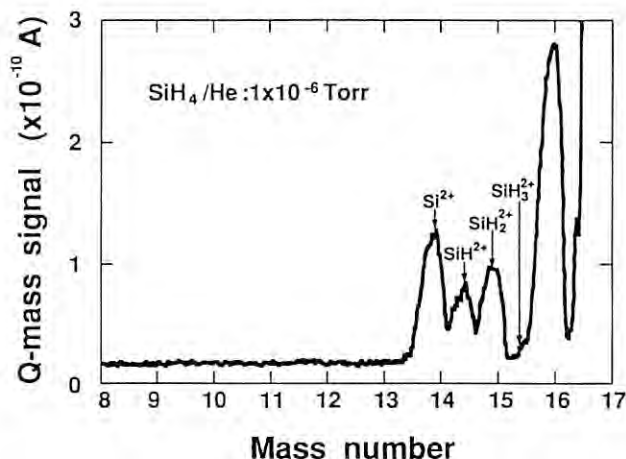


Fig.2 Mass spectrum from SiH_4 (Mass number = 8-17)

PHOTON ENERGY DEPENDENCE OF THE FILM QUALITY PREPARED BY
ADSORBED SiH_4 PHOTOLYSIS ON LOW-TEMPERATURE SURFACES

Y.Sugita, Y.Nara, T.Ito, H.Kato* and K.Tanaka*
Fujitsu Laboratories LTD.

10-1 Morinosato-Wakamiya, Atsugi, Kanagawa 243-01.

*Photon Factory, National Laboratory for High Energy Physics.
1-1 Oho, Tsukuba, Ibaraki 305.

INTRODUCTION

Surface reaction plays an important role in the deposition of semiconductor material by synchrotron radiation (SR).¹⁾

On the photo-chemical deposition of Si film, we have concentrated on the interaction between the surface adsorbed SiH_4 molecules and incident SR. We found that the irradiation of vacuum ultraviolet (VUV) light on a dense adsorbed surface causes the photolysis of adsorbed SiH_4 to produce amorphous silicon film and that the inner core excitation is an important factor.

EXPERIMENTS

The experiment was performed using BL-12C which has a multilayer monochromator and a differential pumping system. We used 5% SiH_4 diluted by He. In order to investigate surface adsorption effect of SiH_4 , the substrate temperature was lowered to -178°C by liquid N_2 .

To examine the effect of incident photon energy or inner core excitation of SiH_4 , we used two kinds of multilayer mirror. One is Rh/Si 27-layers mirror with center photon energy of 97 eV. The other is Rh/C 21-layers mirror with center photon energy of 123 eV. SiH_4 has a higher absorption cross-section at 123 eV than at 97 eV due to the L-core electron excitation of Si in SiH_4 .

Infrared absorption spectroscopy and Auger electron spectroscopy were used to examine the quality of the deposited films.

RESULTS AND DISCUSSIONS

Figure 1 shows the temperature dependence of the deposition rate. The deposition rate increases as the substrate temperature decreases due to the increased adsorbance of surface SiH_4 . By using a stencil mask with 5 micron open width, we found the deposition occurs only at the irradiated region. The mean free path of gas is about 100 micron, which is large enough compared with the open

width of the mask. This means that the surface reaction such as the photolysis of adsorbed SiH_4 is dominant.

Figure 2 shows the qualities of films deposited using photon energy of 97 and 123 eV at -178°C . The film deposited using 97 eV light contains SiH_3 and SiH_4 structure which suggests insufficient decomposition of surface SiH_4 adsorbates. The film deposited using 123 eV light is an amorphous silicon with structure of SiH_2 bonds. This film has no SiH_3 and SiH_4 bonds. From the Auger depth profile, the film deposited using 97 eV light has high oxygen incorporation into the deposited film. The oxygen concentration of the film using 123 eV light was very small and it was almost the same as the single crystal substrate.

The effect of substrate temperature and incident photon energy on the film quality is explained as follows. The coverage of adsorbed SiH_4 molecule is expected to be 1 below -150°C . Irradiation by VUV light that excites the inner core level of SiH_4 on a saturated adsorbed layer causes the interaction among the adsorbates and prevents oxygen incorporation. This process produces the amorphous silicon film with SiH_2 structure. If the light dose not excite the inner core level of SiH_4 as 97 eV, interaction among the adsorbates is not sufficient and this causes the film with SiH_4 and SiH_3 structure. Insufficient decomposition of the adsorbates causes the incorporation of oxygen probably from the residual gas such as water.

In conclusion, we deposited amorphous silicon film by the photolysis of adsorbed SiH_4 on the low-temperature surface. Inner core level excitation is important to bring about sufficient interaction among the adsorbates.

1) H.Kyuragi and T.Urisu, Appl.Phys.Lett. vol.50, p.1254, 1987

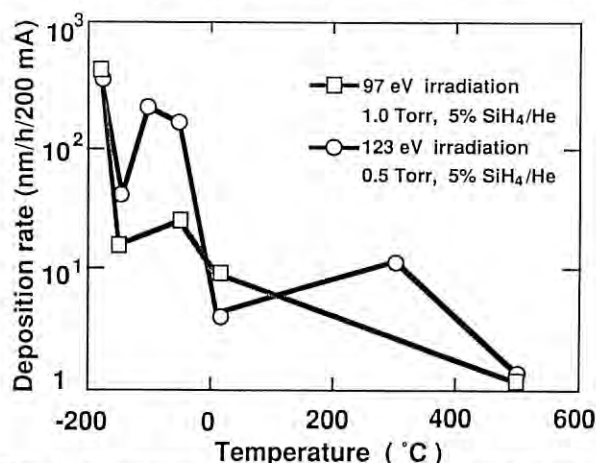


Fig. 1 Typical temperature dependence of deposition rate using 5% SiH_4/He

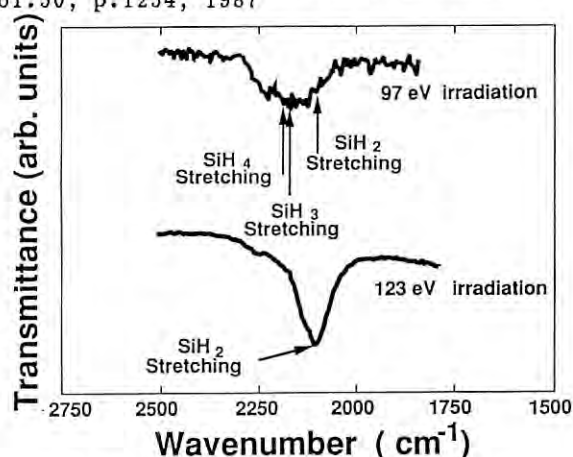


Fig. 2 FTIR spectra of films deposited at -178°C

RADIATION DAMAGE OF A Mo/C MULTILAYER FILM DUE TO SYNCHROTRON RADIATION

Haruki KOMANO, Yukiko KIKUTI, Masamitsu ITOH, Iwao HIGASHIKAWA,
Masaru HORI, Ichirou MORI and Kenichiro TANAKA*

ULSI Research Center, Toshiba Corp., Kawasaki, Kanagawa 210

*Photon Factory, National Laboratory for High Energy Physics, Tsukuba, Ibaraki 305

Introduction

A multilayer mirror for soft x-ray has a reflectivity of several tens percent at large glancing angles. The mirror is used for soft x-ray optical elements¹⁾, for example in a reflection-type demagnified optical system in which synchrotron radiation (SR) is generally used as the x-ray source. It is expected that such a mirror will be used more and more in experiments using SR. However, there are very few reports on damage due to SR irradiation on the mirror. The authors made multilayer films for soft x-ray and evaluated their reflectivities by calculations and experiments.

SR irradiation experiments were carried out using BL-12C. This reports the experimental results on SR irradiation damage of molybdenum and carbon multilayer films.

Experimental

Samples were molybdenum and carbon (Mo/C) multilayer films, which were made by evaporating molybdenum and carbon in turn on a silicon substrate. The thicknesses of the molybdenum and carbon layers were about 70 Å and 100 Å, respectively. The number of layers were 19. SR was irradiated on the samples in a vacuum chamber located in BL-12C. The vacuum pressure was less than 2×10^{-7} Torr under irradiation. The wavelength range of the irradiated SR was over 7 Å, which was achieved by inserting a SiC toroidal mirror in the beam line. The irradiated area was 10x20 mm. SR doses were 10^3 and 10^4 A sec.

The reflectivity of the samples were measured before and after the SR irradiation using the measurement system shown in Fig.1. The x-ray wavelength was 67.6 Å, which was generated by a boron target. An x-ray beam was collimated to a beam width of 50 µm. The x-ray detector was a proportional counter. The sample and the detector were turned against the incident x-ray

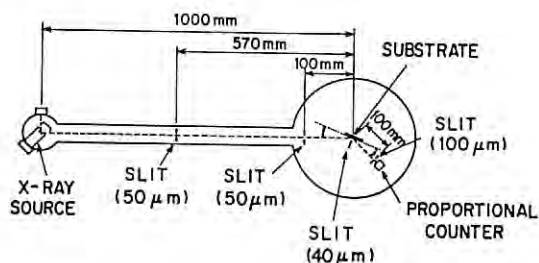


Fig.1 Schematic diagram of reflectivity measurement system

beam. Reflectivities of the samples were measured by changing the x-ray glancing angles from 0 to 16 degrees.

Results and discussion

No change in reflectivity was observed in the case of a 10^3 A·sec dose.

The results of reflectivity measurement before and after an SR irradiation of 10^4 A·sec is shown in Fig.2. The peaks near a 14 degree glancing angle show the reflection due to the multilayer films, and the other parts are due to surface reflection. The angle which showed the peak was changed towards a 0.5 degree lower angle after SR irradiation, though the reflectivities did not change so much before and after SR irradiation. Carbon adsorption to the surface was observed after SR irradiation. However, the adsorbed carbon did not cause an angle change because the film thickness was estimated to be less than 50 Å.

It has been reported that a similar angle change was observed after 1000 °C annealing in the case of a W/C multilayer film, and that the change was due to the thickness change of the carbon layers caused by the change of amorphous carbon to glassy carbon²⁾.

In the present experiments, the temperature rise of the sample under SR irradiation was estimated to be less than 100 °C from temperature measurements using a thermographic system (JEOL: THERMOVIEWER JTG-3200). Therefore, the temperature rise of the samples could be ignored. It is thought that there is possibility that amorphous carbon changed to glassy carbon by SR irradiation.

References

- 1) Troy W. Barbee, Jr.: Rev.Sci.Instrum.60(7), 1588(1989)
- 2) Zuimin Jiang, Xiaoming Jiang, Wenhan Liu, and Zigin Wu: J.Appl.Phys. 65(1), 196(1989)

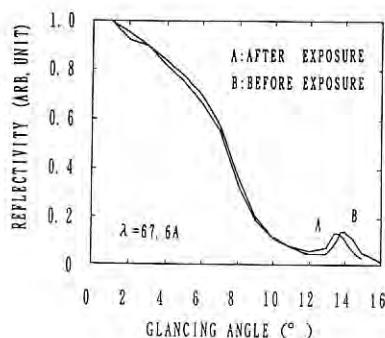


Fig.2 Reflectivity change of Mo/C mirror after SR irradiation

Performance of a double crystal monochromator at BL-17A

Yoshiaki TANIDA, Takashi SATO, Satoshi KOMIYA
Fujitsu Laboratories Ltd., 10-1 Morinosato-Wakamiya, Atsugi, 243-01

We constructed a beam line (BL-17A) which aims at (1) producing monochromatic X-rays in the 1800-13800 eV range with energy resolution within 1.0-2.5 eV, (2) yielding a spatially fixed beam at a sample position, and (3) making X-rays available in an UHV. These objectives reflect the use of this line for (E)XAFS and SEXAFS studies. One feature of our double-crystal monochromator is in situ interchangeability of monochromator crystals in an UHV. Users can select Si(111) or InSb(111) crystals according to the required energy range. The most important requirement for a double-crystal monochromator is the capability of changing the Bragg angles while keeping the two crystals parallel. While the monochromator is scanning, the Bragg angles of the two crystals have to remain aligned within 10 arc sec, which is the narrowest full width at half maximum height (fwhm) of the rocking curves. Thus, to keep the monochromator output photon intensity optimized, we tune the incidence angle of one of the crystals with a feedback system using a personal computer.

The monochromator operates in the nondispersive (1,-1) parallel mode. We set the second crystal at an angle corresponding to a specified photon energy, then we rocked the first crystal around the right Bragg angle through a parallel alignment to the second crystal. The outgoing monochromatized X-ray intensity was measured by an ionization chamber. The measurements for silicon(111) at photon wavelengths of 1.3 Å, 1.45 Å, and 2.5 Å are shown in Fig.1. The entrance vertical slit used was about 0.5 mm high. We measured the copper K edge absorption fine structure by means of the transmission method. Fig.2 shows the Cu K edge XANES spectrum taken from a 10 µm-thick copper foil. The resolution estimated from the absorption near edge is about 2.0 eV at a photon energy of 9020 eV. This value agrees closely with the rocking curve measurements.

In summary, we constructed a beam line and studied its energy resolution. An energy resolution of 2.0 eV was obtained at a photon energy of 9020 eV in an UHV.

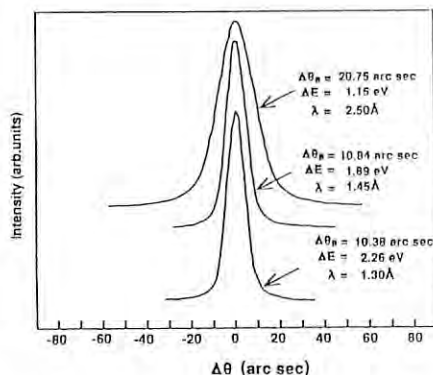


Fig.1. Double crystal rocking curves of Si(111).

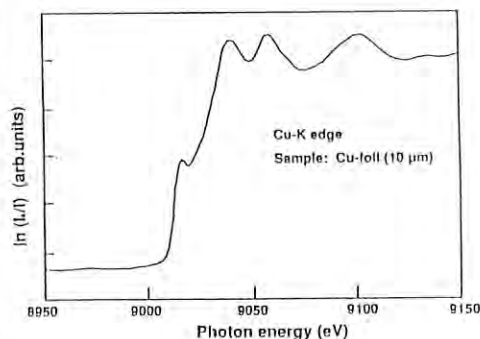


Fig.2. XANES spectrum above the Cu K edge.

Yoshimi YAMASHITA, Fumiaki KUMASAKA, Syunji GOTOH,
Hidetoshi ISHIWARI, Kei HORIUCHI, and Shinpei HIJIIYA
FUJITSU LABORATORIES LTD., 10-1 Morinosato-Wakamiya, Atsugi 243-01

Introduction

Soft X-ray lithography with synchrotron radiation (SR) is promising for quarter-micron pattern replication. We investigated how exposure conditions such as proximity gap and wavelength affect pattern replication.

This report describes relations between replicated resist pattern width (W_r) and mask pattern width (W_m) at different exposure dose.

Experiment

We conducted pattern replication tests using the beamline BL-17C¹⁾ which was equipped with double fused quartz mirrors (a pair of two parallel mirrors) and a 50 μm -thick Be window. The X-ray mask had a 0.65 μm -thick Ta absorber on the 2 μm -thick SiN membrane. The resist was 0.5 μm -thick positive EB resist (CMR) on the Si substrate. The resist was developed in MIBK at 23°C for 120 s. An X-ray mask and a wafer were spaced at a fixed proximity gap and mounted in an exposure chamber filled with He gas. The wavelength region was selected by the glancing angle of the two quartz mirrors. The SR spectra in this pattern replication test is shown in Fig. 1.

Pattern replication accuracy was evaluated by measuring the change in the pattern width for dose fluctuation²⁾ at different glancing angles (12 to 18 mrad) and proximity gaps (5 to 200 μm).

Results

We determined the relationship between W_m and W_r in detail at different doses with a glancing angle of 14 mrad and proximity gap of 32 μm (Fig. 2). The W_m - W_r plot has a slope of 1 with a parallel shift at different doses. The amount of shift is nearly proportional to logarithm of the dose difference. It can be approximated by the following equation

$$W_r = W_m - \alpha \cdot \log(D/D_0)$$

where D is the actual dose, D_0 the dose for $W_r = W_m$, and α is the coefficient of the pattern width fluctuation, representing process stability against dose fluctuation. We calculated α to be 0.3 in Figure 2.

α depends on exposure conditions: glancing angle of mirror (wavelength) and proximity gap (Fig. 3). The α decreases when the proximity gap decreases or the glancing angle increases. From this, $\alpha \leq 0.3$ at a gap of less than 30 μm and a glancing angle larger than 14 mrad. $\alpha = 0.3$ means a dose fluctuation $\Delta D/D = 0.17$ causes a pattern width fluctuation $\Delta W_r = -0.02 \mu\text{m}$.

The minimum line width we obtained was 0.15 μm . Figure 4 shows a 0.5 μm -thick, 0.15 μm line and 0.2 μm space CMR pattern, replicated at 14 mrad glancing angle and 8 μm proximity gap.

References

- 1) H. Ishiwari et al.: Photon Factory Activity Report, No. 6, p.77(1988).
- 2) Y. Yamashita et al.: Photon Factory Symposium, No. 6, p.55(1988).

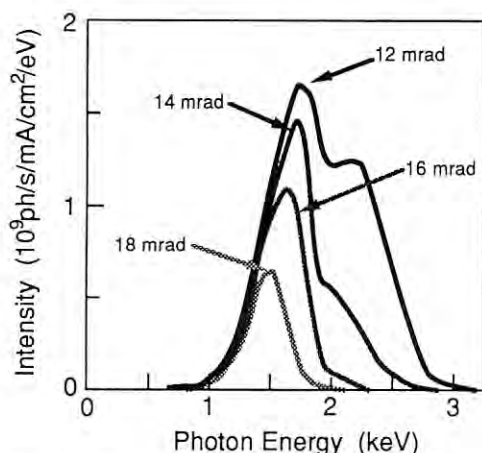


Figure 1. Spectra of SR reflected by two quartz mirrors and passed through 50 μm -thick Be window.

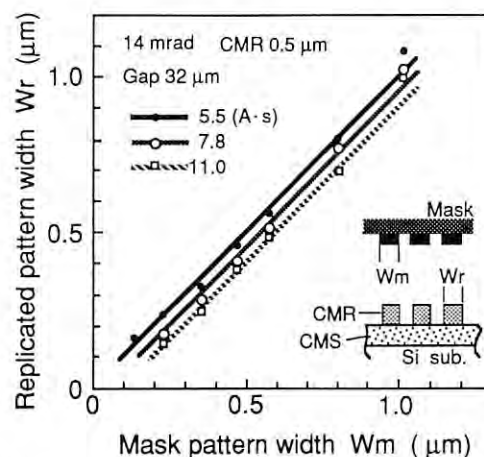


Figure 2. Replicated resist pattern width of 0.5 μm -thick CMR for various mask pattern width.

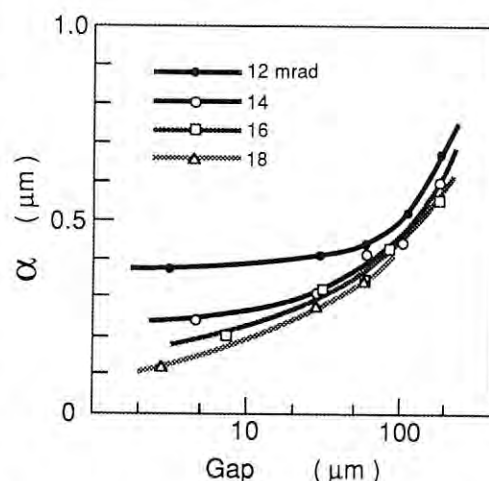


Figure 3. Gap dependence of α for different glancing angles.

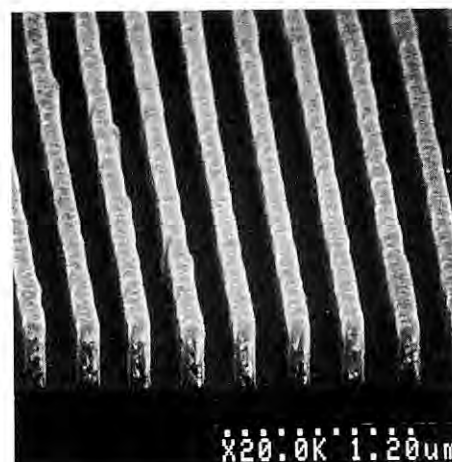


Figure 4. 0.15 μm line and 0.2 μm space pattern replicated into 0.5 μm -thick CMR under 14 mrad, 8 μm proximity gap.

Syunji GOTOH, Takao TAGUCHI, Shigeru OKAMURA, and Tokushige HISATSUGU
FUJITSU LABORATORIES LTD., 10-1 Morinosato-Wakamiya, Atsugi 243-01

INTRODUCTION

We designed a spectrometer using He gas scattering with a Si(Li) detector to measure the broadband spectra of synchrotron radiation (SR) in the soft X-ray region¹⁾.

To measure spectra accurately, we must take into account the response function of the Si(Li) detector²⁾. We measured the spectra of the SR passed through a 50- μ m-thick Be window at station BL-17C using the unfolding with the response function.

RESPONSE FUNCTION OF THE Si(Li) DETECTOR

We measured the response function of Si(Li) detector with AlK and SiK fluorescence and monochromatic X-rays between 2.2 keV and 10 keV obtained from a Si(111) double crystal monochromator at the station BL-17A. We fit the measured response function with HYPERMET function^{2,3)} and determined the photon energy dependence of the fitting parameters.

For example, the response function for 4.0-keV photons is shown in Fig. 1.

MEASUREMENT OF SR SPECTRA

We measured the direct beam spectrum passed through a 50- μ m-thick Be window and estimated the absolute intensity spectrum by correcting with the scattering cross section of He and the detection efficiency of the Si(Li) detector^{1,2)}.

To determine the detection efficiency, we took into account the transmittance of a 8- μ m-thick Be window and a 20-nm-thick Au contact layer of the detector.

The measured spectrum without unfolding, spectrum with unfolding and calculated spectrum of the direct beam are shown in Fig. 2. The measured spectrum with unfolding agreed with the calculated spectrum well.

We also measured the spectrum of the reflected beam from two fused quartz mirrors with a glancing angle of 8 mrad. The measured and calculated spectra are shown in Fig. 3. The mirror reflectivity was calculated by using the scattering factors⁴⁾, extrapolating the real part of the scattering factor by the Kramers-Kronig integral¹⁾. The agreement between calculated and measured spectra shows that the reflectivity can be accurately calculated using the real part of the scattering factor in our previous report.

CONCLUSION

We showed that we could accurately measure the broadband spectra of SR above 1 keV by our spectrometer using the unfolding with the response function of the Si(Li) detector.

REFERENCES

1) S. Gotoh, T. Taguchi, S. Okamura, and T.

Hisatsugu, Rev. Sci. Instrum. **60**, 2239 (1989).

2) M. Krumrey, E. Tegeler, and G. Ulm, Rev. Sci. Instrum. **60**, 2287 (1989).

3) Y. Inagaki, K. Shima, and H. Maezawa, Nucl. Instr. and Meth. **B27**, 353 (1987).

4) B. L. Henke, P. Lee, T. J. Tanaka, R. L. Shimabukuro, and B. K. Fujikawa, Atom. Data Nucl. Data Tables **27**, 1 (1982).

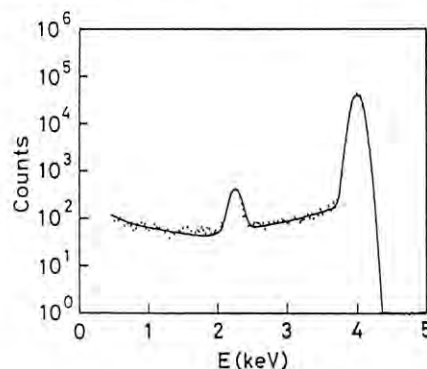


Fig. 1 Response function of Si(Li) detector for 4-keV photons.

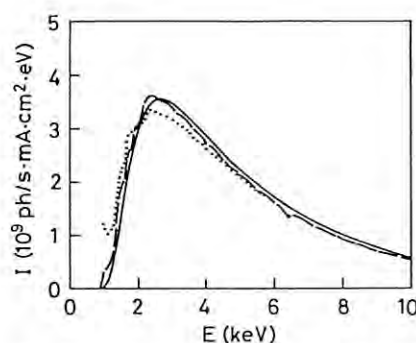


Fig. 2 Direct beam spectra. Solid line shows calculated spectrum, dotted line measured spectrum without unfolding and broken line measured spectrum with unfolding.

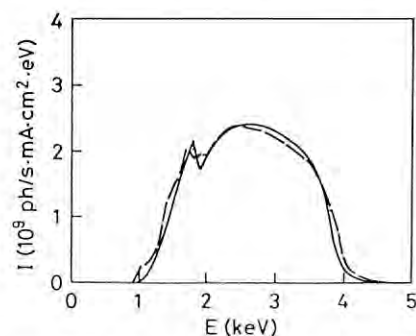


Fig. 3 Spectra of reflected beam from two fused quartz mirrors. Solid line shows calculated spectrum and broken line measured spectrum with unfolding.

EXAFS STUDY ON VANADIUM IN BLOOD CELLS (VANADOCYTES) OF ASCIDIANS

Hiromu SAKURAI^a, Hironobu MAEDA^b, Nobuyoshi ESAKI^c, Takatoshi MURATA^d,
Yuzuru HIIRAGI^c and Masaharu NOMURA^e

^a Faculty of Pharmaceutical Sciences, University of Tokushima, Tokushima 770,

^b Department of Chemistry, Faculty of Science, Okayama University, Okayama 700,

^c Institute for Chemical Research, Kyoto University, Uji, Kyoto 612,

^d Department of Physics, Kyoto University of Education, Kyoto 612,

^e Photon Factory, National Laboratory for High Energy Physics, Tsukuba, Ibaraki 305

Vanadium is found in blood cells of several species of ascidian¹. Although about 80 years have passed since the initial finding of vanadium in ascidian blood cells (vanadocytes)². The biological functions and the structure of this metal in ascidians are still unknown. Recently, on the basis of the results on EXAFS study of vanadocytes in an ascidian, *Ascidia ceratodes*, the oxidation state of vanadium and the structure around vanadium have been proposed³. Here, we report the results on XANES and EXAFS studies on a Japanese ascidian, *A. ahodori*, collected at Naruto of Tokushima.

Experimental

Each sample was ground to a fine powder. For fluorescence mode measurements, the samples were pressed into pellets of 13.0 mm in diameter and their spectra were obtained by Lytle detector^{4,5} which was set to be perpendicular to the incident beam using Ti filter. For transmission mode measurements, the samples were dusted onto Scotch tape until suitable edge jumps were obtained. The several vanadium complexes were measured. The X-ray absorption measurements were performed by using the synchrotron radiation from the Photon Factory at the National Laboratory for High Energy Physics^{6,7}. The V K-edges EXAFS spectra of vanadocytes were taken in both transmission and fluorescence modes at 10K, using a beam line BL-7C. A double-crystal monochromator was used with two Si(111) which detuned from parallel to pass only 50% of maximal intensity in order to reduce the harmonic content of the beam. The X-ray beam was focused on the specimen by means of sagittal focusing of the monochromator crystal. The photon energy, E , was calibrated with respect to Cu foil by assigning 8.9788 keV to the pre-edge peak on the absorption edge. The EXAFS oscillation $\chi(k)$ were extracted from the absorption spectra followed by the standard procedure⁸. In Fig. 1, the $k^3\chi(k)$ for V K-edge and its Fourier transformed radical structure function, $\phi(r)$, are shown. In the figure, one major peak in $\phi(r)$ is due to O atoms, where the peak position is shifted a few tenths of an angstrom from the actual interatomic distance because of the phase shift.

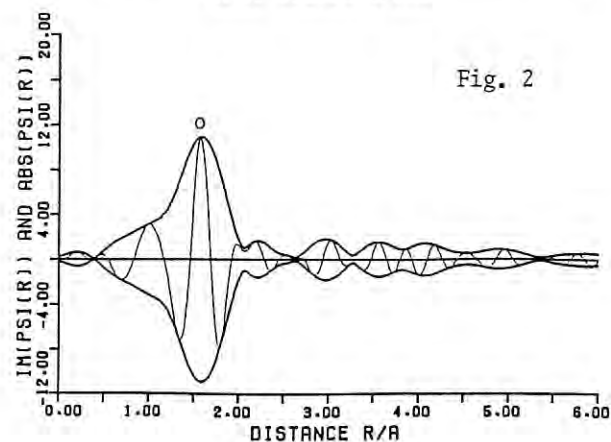
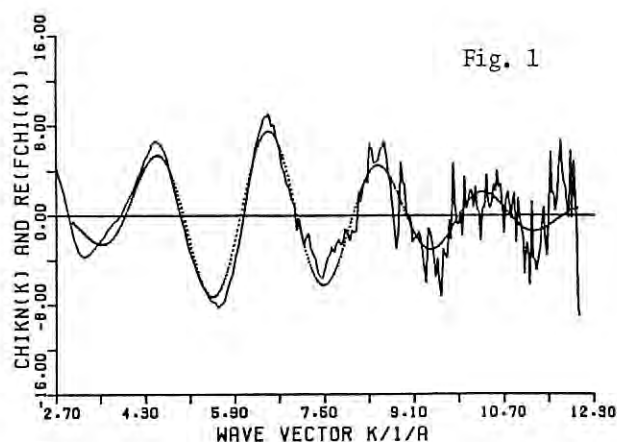
Results and Discussion

In the XANES spectra of several types of vanadium complexes in the +3 or +4 oxidation state, the intensity ratio of the pre-edge and edge peaks was found to be correlated on the oxidation state of the metal as well as the type of coordination structure of the complex. The ratios for V^{3+} complexes were 0-0.2, while those for VO^{2+} complexes distributed between 0.3 to 0.6. The ratio of vanadocytes was found to be 0.06, indicating that the oxidation state of vanadium is in the V^{3+} . Thus we analyzed the EXAFS spectra of vanadocytes and model complexes. The Fourier transforms and curve fits of

vanadocyte EXAFS are shown in Fig. 1 and 2, respectively. After the curve-fitting method using the EXAFS parameters of many vanadium complexes, the vanadium in vanadocytes was found to be in a symmetrical, single-shell coordination environment, providing that the vanadium coordinates with 6.2 oxygens in a distance at 2.006 Å. These results agree with the reported EXAFS data (coordination numbers, 5.4 and distance of V-O, 1.99 Å)³. The studies on the more precise structure of vanadium in the ascidian are now in progress.

References

1. H.Sakurai et al.: Biochem. Biophys. Res. Commun. 149 (1987) 411.
2. M.Henze: Hoppe-Seyler's Z. Physiol. Chem. 72 (1911) 494.
3. T.D.Tullius et al.: J. Am. Chem. Soc. 102 (1980) 5670.
4. The EXAFS Co., Seattle WA.
5. E.A.Stern and S.M.Heald: Rev. Sci. Instrum. 50 (1979) 1579.
6. H.Oyanagi et al.: KEK Report 83 (1984).
7. M.Nomura: KEK Report 83 (1986).
8. H.Maeda: J.Phys.Soc.Jpn. 56 (1987) 2777.



HIGH PRESSURE X-RAY STUDY USING SINTERED DIAMOND ANVILS

Osamu SHIMOMURA, Wataru UTSUMI*, Takashi TANIGUCHI,
Hisao KANDA, Minoru AKAISHI, Shinobu YAMAOKA, Takashi NAGASHIMA
Takumi KIKEGAWA**, Takumi KATO***, Kenichi YAOITA****

Nat. Inst. Res. in Inorganic Mater., Tsukuba, Ibaraki 305

* Inst. Solid State Physics, Univ. Tokyo, Roppongi, Tokyo 106

** Photon Factory, Nat. Lab. High Energy Physics, Tsukuba, Ibaraki 305

*** Dept. Mineralogy, Tohoku Univ., Aramaki, Sendai 223

****Dept. Physics, Keio Univ., Hiyoshi, Yokohama

Introduction

10 years has been passed since the planning of MAX80 has begun. Based on the experience using MAX80, a new X-ray apparatus for the experiments at higher pressure region utilizing synchrotron radiation from a multi-pole wiggler was constructed.

The basic concept of the new apparatus succeeds that of MAX80, hence it is named as MAX90. The characteristic of MAX90 is the use of sintered diamond as anvil material so that higher pressure can be attainable.

MAX90 is mainly used at BL13C with SR from a multi-pole(27poles) wiggler. Also, it is used at BL14C, a high field wiggler beam line, to perform a high energy experiments up to 120keV.

Apparatus

MAX90 consists of a 350 ton press, a cubic type (DIA10) high pressure vessel, a 4-axes table, a base, a goniometer, a machine control system, a data acquisition & treatment system. Total weight is about 10ton.

Figure 1 shows the anvil assembly with sintered diamond. The outer dimensions are compatible with that made of tungsten carbide, which has been so far used. The truncation of the anvil top is 4mm square.

Pressure and Temperature Generation

Pressure generation was confirmed by measuring the unit cell volume of NaCl. The experiments were done at BL14C. Pressure transmitting medium was a mixture of boron and epoxy-resin (4:1 in weight) with 6mm cube shape. Preformed gasket made of boron and epoxy-resin (1:1 in weight) were used. With this assembly, cracks were occurred nearly at the center of the anvil and spread linearly to the margin at the pres-

sure of 12 to 13 GPa. Then the maximum pressure is about 14GPa.

This pressure is quite lower than that is expected by the compressive strength of diamond. This may be caused by the large grain size of the diamond (average size is about 70micron). A cleavage may take place at certain single crystal by the local stress and spread to the margin. The use of boron as pressure transmitting medium may enhance this effect. Detail investigation on this point is now in progress. As for the temperature generation, graphite heater transforms to diamond at 1500C at 13GPa. The pressure and temperature region attainable with current system is shown in Fig.2, together with that realized by tungsten carbide anvils.

Preliminary Experiments

In this P-T rang, we investigated the phase stability of AlN and BN.

AlN, which crystallizes in the wurzite structure at normal pressure, was found to show no phase transition up to 12 GPa and 1500C.

Hexagonal BN transformed to wurzite type structure at about 10 GPa at room temperature, as well known. Single phase of wurzite type structure was obtained by raising the temperature at about 300C, and transition to cubic phase was found with further increase of temperature. These points are plotted also in Fig. 2. This is the first time for the direct observation of wurzite-cubic transition, though there have been many investigation by quenching method.

This work was supported by Special Coordination Funds for Promoting Science and Technology.

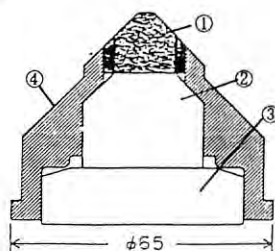


Figure 1. Assembly for sintered diamond anvil.
1: sintered diamond, 2: WC backup,
3: WC spacer, 4: steel ring

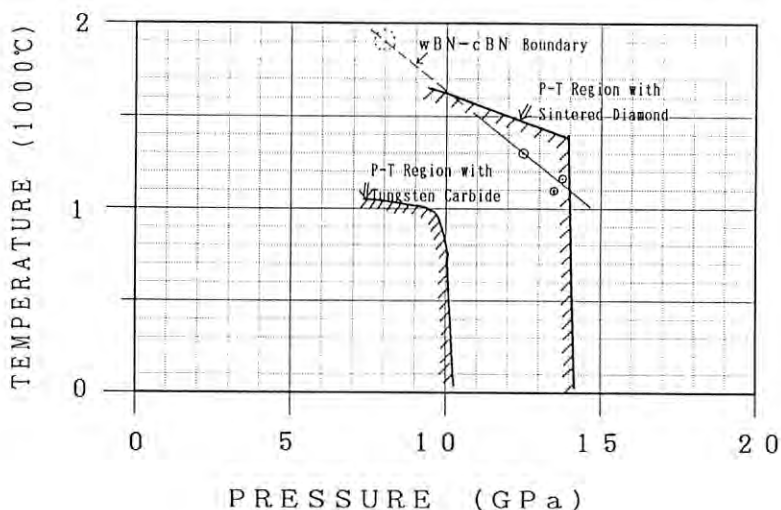


Figure 2. P-T region with sintered diamond and tungsten carbide. wBN-cBN boundary is also shown; are present result and is a quenching experiment.

BL-16 VUV/SOFT X-RAY MONOCHROMATOR FOR UNDULATOR RADIATION,
(1) SPECTRAL DISTRIBUTION OF UNDULATOR RADIATION USING THERMALLY
RESISTANT OPTICAL ELEMENTS

Yasuji MURAMATSU, Hideki MAEZAWA*, Hiroo KATO* and Tatsuo HARADA**

NTT Applied Electronics Laboratories, Musashino, Tokyo 180.

*Photon Factory, National Laboratory for High Energy Physics, Tsukuba,
Ibaraki 305.

**Hitachi Ltd. Central Research Laboratory, Kokubunji, Tokyo 185.

INTRODUCTION

A VUV/soft x-ray monochromator has been developed to utilize undulator radiation from a 26-period multipole wiggler/undulator at the Photon Factory¹⁾. The most critical problem of this entrance slit-less monochromator is heat load on optical elements. A conventional replicated grating is not suitable for this monochromator, because the surface of the grating is damaged by the high power density of the undulator radiation²⁾.

This problem was solved by developing thermally resistant optical elements made of SiC and mounting them on the monochromator. This paper describes spectral measurements of the undulator radiation using the SiC-optical elements and evaluates the the monochromator system.

EXPERIMENTAL

During spectral measurements, the magnetic gaps of the 26-period multipole wiggler/undulator were set to 100, 70 and 50 mm, corresponding to the K-parameter of 1.40, 3.21 and 5.75, respectively. The positron beam current of the Photon Factory storage ring was around 250 mA. Thermally resistant front mirrors and a master grating made of SiC were mounted on the monochromator. The mechanically ruled gold grating with SiC substrate was manufactured by Hitachi Ltd. It was a 2m radius cylindrical grating with a groove density of 1200 lines/mm. The size of this grating was 100mm^L x 36mm^W x 10mm^T. Spectral intensity was measured with a gold-mesh photocathode mounted after the rear focusing mirror.

RESULTS AND DISCUSSION

Figure 1 shows the spectral responses of the monochromator over the photon energy range from 40 eV to 300 eV with a 20 μ m slit. For K=5.75 (the photon energy of the first harmonic peak was 28.2 eV), higher order harmonics from the second to the ninth were clearly observed. The peak of the tenth harmonic was hidden by the K-absorption edge of carbon. The fractional bandwidth of the third peak was evaluated at 1/38. This figure shows that the monochromator was well aligned over the entire scanning photon energy range.

The shapes of these spectral responses were constant during more than 24 hours of irradiation

by undulator radiation. Therefore, the thermally resistant optical elements are well able to withstand the high power density of undulator radiation.

References

- 1)Y.Muramatsu and H.Maezawa; Rev.Sci.Instrum.,60 (7),2078(1989).
- 2)Y.Muramatsu and H.Maezawa; Photon Factory Activity Report,#6,265(1988).

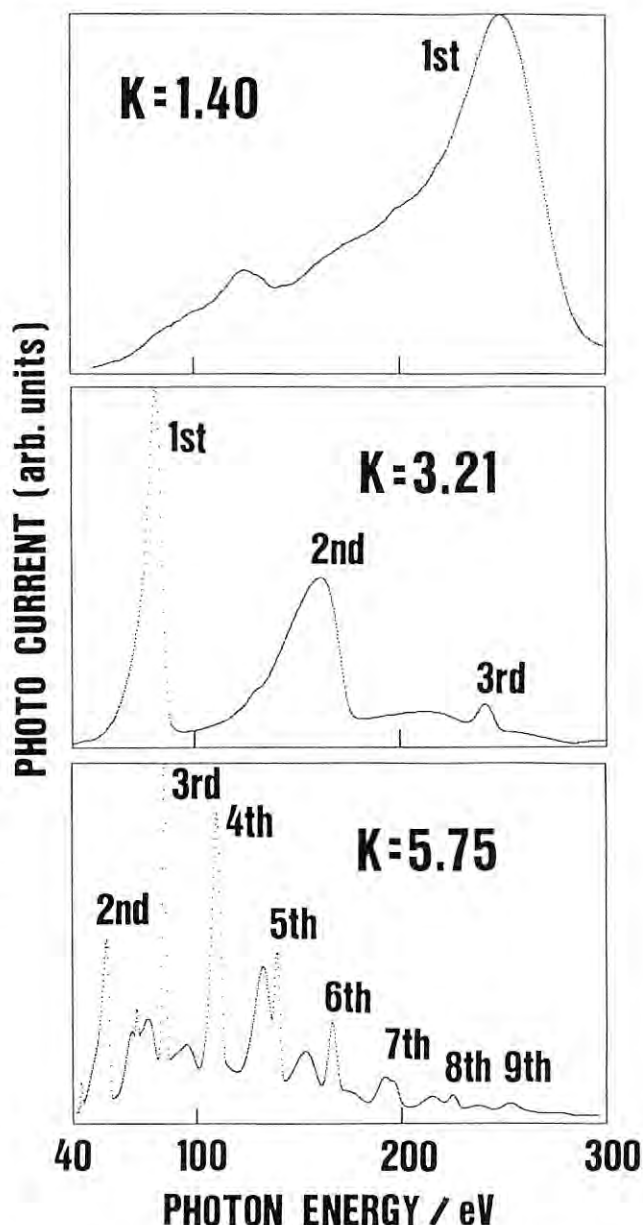


Fig.1 Spectral responses of the monochromator.

Author Index

	A
Abe, T.	101
Abe, Y.	274
Adachi, G.	30
Ago, H.	108
Aiura, Y.	270,271,276
Akai, T.	42,84,85
Akaishi, M.	290
Akaogi, M.	219
Akaoka, N.	277
Akeyama, K.	52,53
Akimoto, K.	184
Akisada, M.	139,179
Akiyama, M.	126
Amemiya, Y.	122,123,124,125,126,127 128,130,131,132,133,134 135,136,137,138,192,193 207
Ando, H.	46
Ando, M.	139,140,149,150,151,152 192,193,205,211,221,222 223,241,243,
Anno, I.	179
Aoki, S.	154,197,198,243
Arai, H.	273
Arakawa, H.	136
Arashi, H.	64
Asahi, T.	169
Asakura, K.	18,26,31,32,38,45,56,60 61,73,75,76,77,258
Ashida, T.	191
Ashida, T.	143,157,161
Ato, T.	219
	B
Ban, S.	206
Bando, K. K.	45
Bando, Y.	172
	C
Chaen, S.	138
Chakravarthy, S.	112
Chamberod, A.	168
Chiba, E.	86
Chiba, R.	278,279
Chiba, S.	277
Chijimatsu, T.	215
Cho, T.	197,198
Corbin, D. R.	47
	D
Domen, K.	56
	E
Edamatsu, K.	252,253,257
Edamoto, K.	270,271,272,274
Egi, T.	35
Einspahr, H. M.	114
Ejima, T.	255,256
Ejima, Y.	91
Emura, S.	28,39,50
Endo, H.	49,203,224,226

Endo, S.	149
Esaki, N.	289
	F
Finzel B. C.	114
Fujihisa, H.	174
Fujii, K.	251
Fujii, Y.	172,174,178
Fujimori, A.	264
Fujimori, H.	168
Fujimoto, T.	21,27,33
Fujinaga, Y.	168,220
Fujioka, M.	240
Fujisaki, H.	263
Fujita, M.	48,59,211
Fujitsuka, M.	275
Fujiwara, S.	241
Fukagawa, H.	139
Fukamachi, T.	175
Fukase, T.	230
Fukuda, K.	253
Fukuda, M.	98
Fukuda, Y.	200
Fukunaga, T.	55,63,156
Fukuoka, A.	21,27,33
Fukushima, T.	67
Fukutani, H.	264,265,268,269
Fukuyama, K.	101,107
Funabashi, M.	258,259,260,261
Funabiki, T.	62
Funaki, M.	181,182
Funasaki, N.	102
Furubayashi, E.	180
Furukawa, H.	31
Fushimi, T.	202
	G
Ganaha, Y.	269
Gatto, T.	121
Gohshi, Y.	144,145,154
Goto, A.	209,210
Goto, M.	170
Goto, T.	241
Gotoh, S.	287,288
Gu, C.	204
	H
Hagihara, H.	36
Hagiya, K.	187
Hamada, H.	181
Hamanaka, T.	131,133,134
Hamaya, N.	174
Hanada, S.	185
Hara, M.	277
Harada, J.	164,165,171,185
Harada, M.	77
Harada, M.	241,280
Harada, T.	291
Hase, K.	174
Hasebe, K.	169
Hasegawa, S.	139,140
Hashimoto, S.	168,186,199,220
Hashizume, H.	201,229
Hata, T.	102
Hata, Y.	109
Hatta, I.	130
Hattori, H.	74

Hayaishi, T.	238,239,254	Inukai, J.	18,26
Hayakawa, K.	181,182	Inumaru, K.	37
Hayakawa, S.	154	Irie, T.	149
Hayakawa, T.	118	Ishibashi, N.	192
Hayashi, S.	117	Ishida, H.	266,267
Hida, M.	34	Ishigame, M.	64
Hidaka, O.	146	Ishiguro, K.	98
Hidaka, Y.	233	Ishihara, M.	98
Hieda, K.	93,95	Ishii, H.	258
Higashikawa, I.	285	Ishii, T.	69
Higuchi, T.	58	Ishikawa, M.	148
Higuchi, Y.	104,105	Ishikawa, M.	95
Hijiya, S.	287	Ishikawa, T.	194,200,212,213,214,215
Hikita, T.	56		216
Hiraga, T.	192	Ishiwari, H.	287
Hiragi, Y.	116,119,196,289	Ishizaka, S.	92,94
Hirai, M.	117	Ishizawa, Y.	264
Hirai, T.	117	Itakura, M.	20
Hirai, Y.	183,246,247,248	Itikawa, Y.	239
Hirano, K.	200	Ito, A.	96,100
Hirano, T.	180,181,182	Ito, H.	28,35
Hirata, M.	197,198	Ito, K.	227,277,281,282
Hirayama, H.	206	Ito, M.	72,221,222,223
Hirobe, M.	58	Ito, N.	274
Hiroi, Z.	35,172	Ito, T.	98
Hirosawa, I.	184	Ito, T.	283,284
Hirose, F.	266,267	Itoh, A.	262
Hisatsugu, T.	288	Itoh, F.	55,63,156,221,222,223
Honda, K.	58,170	Itoh, M.	285
Honda, T.	207	Itoh, Y.	239
Hondoh, T.	209,210	Iwamoto, H.	132,133
Honma, S.	97	Iwasaki, H.	180,186,199,220
Hori, M.	285	Iwasawa, Y.	18,26,31,38,45,60,61,73
Horiuchi, K.	287		75,77
Horiuti, K.	123,124	Iwata, J.	251
Hoshi, R.	209,210	Iwata, S.	110
Hoshi, S.	56	Iwazumi, T.	221,222,223
Hoshino, H.	49	Izawa, G.	148,240
Hosokawa, S.	49	Izumi, K.	141,142,200
Hosur, M. V.	111	Izumi, Y.	189
Hyodo, K.	139,140		

K

I			
Ichikawa, M.	21,27,33	Kagawa, S.	31
Ichikuni, N.	60	Kagoshima, Y.	243
Ichimura, K.	137	Kaimai, A.	64
Igarashi, Y.	137	Kajita, A.	137
Iguchi, Y.	242	Kajiwara, K.	116,119,196
Ihara, H.	162	Kakihana, M.	139
Iida, A.	97,144,145,146,147,148	Kakuchi, M.	243
	149,150,151,152,154,155	Kameta, K.	278,279
	217	Kamigaki, K.	166
Iida, S.	204	Kanai, H.	19,30
Ikai, A.	136	Kanazawa, K.	227
Ikeda, K.	193	Kanda, H.	290
Ikeda, K.	165	Kaneda, K.	241
Ikeda, S.	15	Kannan, K. K.	111,112
Ikeda, T.	274	Kasagi, N.	204
Ikeda, Y.	35	Kasano, H.	166,169
Imada, A.	70	Kasatani, H.	166
Imai, H.	152	Kasaya, M.	273
Imai, M.	176,203,224,225,226	Kashihara, Y.	165,171
Imai, Y.	180	Kashino, S.	39,69
Imazeki, S.	247	Kashiwagura, N.	171
Inagaki, Y.	240	Kashiwakura, T.	255,256
Inoko, Y.	120,121	Kataoka, M.	122,125
Inoue, H.	196	Katayama, Y.	49
Inoue, M.	79	Kato, H.	109
Inui, M.	49	Kato, H.	264,266,267,268,269,270
			271,272,273,274,275,276

	283,284,291	Koto, K.	43,50,69
Kato, K.	190,208	Kouchi, N.	227,278,279
Kato, M.	185	Kouno, E.	251
Kato, S.	130	Koyama, A.	87
Kato, T.	290	Kozai, T.	139
Katsube, Y.	102,105,108,109	Kubo, H.	277
Katsui, A.	90	Kubota, M.	228
Katsuragawa, T.	86	Kumar, V.	112
Kawado, S.	215,216	Kumasaka, F.	287
Kawamoto, I.	201	Kunishima, N.	107
Kawamoto, Y.	57	Kurahashi, M.	170,262
Kawamura, N.	234,236	Kurata, Y.	230
Kawamura, T.	141,142,200,228,229,230	Kurihara, H.	103
	235,237	Kurihara, S.	129
Kawano, S.	152,192,193	Kuroda, H.	21,27,33,52,53,76,244
Kawasaki, S.	157		245,258,259,260,261
Kawase, S.	249	Kuroda, M.	128
Kawashima T.	16,17,23,40,66,97	Kuroda, S.	217
Kawata, H.	149,150,151,204,205,211	Kuroiwa, Y.	167
	221,222,223	Kusaba, K.	219,220
Kihara, H.	127,128,136,137	Kusunoki, M.	108
Kihara, K.	46,143	Kuwano, N.	20
Kihara, N.	263	Kyushiki, H.	136
Kikegawa, T.	218,219,220,225,226,290		
Kikuchi, S.	96		L
Kikuta, S.	141,142,194,200,215	Leinenweber, K.	218
Kikutu, Y.	285	Lim, W-Y	34
Kim, C. W.	205	Lin, Z.	106
Kim, D. S.	80		
Kim, E.	119		M
Kimura, A.	109		
Kimura, H.	48,59	Maeda, F.	142,229,233
Kimura, K.	127,137	Maeda, H.	28,34,35,39,48,59,69,211
Kimura, M.	39		289
Kimura, T.	250	Maeda, K.	281
Kimura, T.	21,27,33	Maeta, H.	167
Kinjo, Y.	96	Maeyama, S.	89,90,141,229,235,237
Kishimoto, S.	144,169,240	Maezawa, H.	91,93,95
Kitagawa, Y.	102,108	Maezawa, H.	96,197,198,240,241,242,243
Kitaguchi, H.	35		277,291
Kitajima, M.	275	Maki, T.	42
Kitajima, Y.	258,259,260,261,262	Marumo, F.	24,57,158
Kitamura, O.	241,280	Maruo, T.	235
Kitano, T.	213,214	Maruo, Y. Y.	141,142,228,229
Kitazume, T.	273	Maruyama, H.	48,59,211
Kito, Y.	131	Maruyama, K.	49
Klausner, R.	228	Maruyama, N.	58
Kobayashi, K.	91,92,93,94,95,96,98,99	Maruyama, T.	276
	100,119,120,121,192,193	Mashiyama, H.	169
Kobayashi, S.	241	Masuda, C.	180
Kobayashi, T.	133,138	Masujima, T.	149,150,151,152,192,193
Koga, K.	167	Matsubara, E.	173
Koide, T.	264,265	Matsubara, H.	101
Koide, Y.	277	Matsubara, I.	123,124,129
Koike, Y.	42,84,85	Matsubayashi, N.	36,37,80,262
Koizumi, A.	48,59,211	Matsuda, A.	89
Koizumi, T.	238,239	Matsui, J.	184,213,214,
Kojima, H.	62	Matsui, M.	219
Kojima, I.	58,262	Matsumoto, T.	46,78,143
Kojima, S.	215,216	Matsuo, T.	238,239
Komano, H.	285	Matsuo, Y.	199
Komeda, T.	270	Matsuoka, T.	49
Komeda, T.	271	Matsushima, N.	189
Komiya, S.	286	Matsushita, T.	178,217
Kondo, Y.	118	Matsuura, Y.	108
Kondoh, H.	52,53	Matsuyama, H.	255,256
Kondoh, T.	197,198	Matsuyama, N.	42
Kosaka, H.	48,59	Matuoka, S.	130
Kosugi, N.	21,27,33,51,52,53,76	Metoki, N.	178
	188,255,256,258		

Minegishi, K.	234,236	Nakamura, N.	32
Mino, M.	48,59	Nakamura, T.	146
Minowa, T.	110	Nakanishi, H.	149
Misono, M.	37	Nakanishi, K.	98
Mitamura, T.	176,225,226	Nakano, A.	43,44
Mitsudo, S.	48,59	Nakano, H.	96
Mitsui, T.	133,134	Nakasako, M.	122,125
Mitsui, Y.	103	Nakashima, H.	206
Mitsuishi, T.	273	Nakatani, H.	119
Miura, K.	42,84,85	Nakatani, S.	194
Miura, Y.	35	Nakayama, N.	172
Miyahara, T.	228,263,264,269,273,275	Nakazawa, M.	249
Miyake, K.	88	Namba, H.	244,245,258
Miyamoto, N.	266,267	Namikawa, K.	211,242
Miyanaga, T.	15	Namioka, T.	281
Miyata, Y.	16	Nanao, S.	205,221,222,223
Miyawaki, R.	153	Nannichi, Y.	230,231,232
Miyazaki, E.	272,274	Nara, Y.	283,284
Miyoshi, N.	98	Nariyama, N.	206
Miyoshi, S.	197,198	Nasu, T.	55,63,156
Mizuki, J.	184	Negishi, H.	79
Mizutani, U.	72	Neya, S.	102
Mochiji, K.	250	Nie, H. Y.	230
Momose, A.	246,247,248	Niki, R.	116
Moody, M. F.	127	Nishi, K.	68
Mori, I.	285	Nishihata, Y.	166
Mori, K.	211,242	Nishijima, A.	36,37,80,262
Morigami, M.	241	Nishimura, K.	139,140
Morikawa, H.	24,57,158	Nishimura, Y.	19
Morimoto, Y.	104	Nishino, N.	277
Morinaga, M.	185	Nishioka, T.	109
Morioka, Y.	254	Nitani, S.	120
Morisada, I.	252,253	Nittoono, O.	202
Morita, H.	168	Niwano, M.	266,267
Motai, K.	168,220	Noda, T.	275
Motoyama, T.	46	Nogawa, M.	266,267
Motoyama, T.	143	Nojima, S.	191
Mukoyama, T.	240	Nomachi, I.	17,23
Munakata, N.	93	Nomata, H.	205
Murakami, E.	254	Nomura, M.	28,39,41,81,82,87,289
Murakami, K.	114	Nose, T.	191
Murakami, Y.	178	Nukui, A.	158
Muramatsu, Y.	291		
Murata, T.	28,39,289		0
Murata, Y.	228		
Muroga, Y.	118		
	N		
Nagano, K.	278,279	Oda, J.	109
Nagaoka, K.	55,63,156	Oda, K.	35
Nagashima, T.	290	Ogata, A.	227
Nagata, H.	263	Ogata, K.	43,44
Nagata, T.	181	Ogawa, T.	250
Nagata, T.	239	Ogino, Y.	207
Nagy, L.	41,81,82	Ogura, M.	241,280
Naitoh, H.	64	Ohara, S.	79
Nakae, H.	143	Ohashi, K.	144
Nakagawa, A.	101,105,107	Ohishi, Y.	172,174,178
Nakagiri, N.	263	Ohkoshi, K.	148
Nakahara, H.	253	Ohmachi, Y.	200
Nakahata, T.	229	Ohmasa, M.	187
Nakai, I.	16,17,23,40,47,66,97	Ohshima, K.	164,167,185,199
	153	Ohsumi, K.	156,158,159,161
Nakai, S.	273	Ohta, T.	110
Nakajima, T.	179	Ohta, T.	54,70,71,88,252,253,257
Nakajima, T.	174,175,177		258,259,260,261,262
Nakajima, H.	169	Ohtaka, O.	157,161
Nakamura, H.	275	Ohtake, H.	58
Nakamura, K.	103	Ohtaki, H.	82
Nakamura, K. T.		Ohtuka, S.	139
		Oigawa, H.	231,232
		Oishi, K.	147
		Okabe, K.	36

Okada, M.	191	Sano, Y.	119,196
Okada, T.	257	Sasaki, M. S.	91
Okamoto, N.	194	Sasaki, S.	185,186,187
Okamoto, T.	104	Sato, H.	146
Okamura, S.	288	Sato, K.	154
Okawa, Y.	244,258	Sato, M.	255
Okazaki, A.	186	Sato, N.	83
Oki, K.	20	Sato, S.	255,256
Okitsu, K.	204	Sato, S.	268,269
Okudera, H.	46,143	Sato, T.	102
Okuhara, T.	37	Sato, T.	286
Okuno, M.	46,78,143	Sato, T.	36
Okutani, H.	166	Sato, T.	15
Omori, T.	240	Satow, Y.	89,90
Omura, K.	218	Satsukawa, T.	71
Onchi, M.	270,271	Satyamurthi, P.	112
Onishi, T.	56	Segawa, K.	80
Ono, T.	210	Seidou, M.	131
Ooigawa, H.	230	Seki, K.	88,252,253,257
Ooiwa, K.	138	Sekiuchi, T.	55
Osaka, A.	35	Sekiyama, H.	249
Oshima, K.	48	Sera, K.	240
Oshima, M.	89,90,141,142,200,228 229,230,231,232,233,234 235,236,237	Seri, H.	30
Otani, S.	264	Shamoto, S.	255
Oyanagi, H.	162,163,217	Shibata, H.	227
Ozawa, H.	159,160	Shidara, T.	264,265
Ozutsumi, K.	16,17,23,40,66	Shigekawa, H.	230,231,232
	P	Shikenbaru, T.	269
Parise, J. B.	47	Shima, K.	238,240
Parkinson, W. H.	282	Shima, M.	68
Pimienta, P.	210	Shimada, H.	36,37,80,262
	R	Shimizu, R.	241
Reedy, M. C.	132	Shimizu, Y.	158
Reedy, M. K.	132	Shimojou, N.	97
	S	Shimomura, O.	174,203,224,225,226,290
Saeki, Y.	129	Shimomura, T.	162
Saigusa, S.	91	Shimura, T.	171
Sainis, J. K.	111	Shingaki, N.	172
Saito, J.	146	Shinjo, T.	172
Saito, S.	187	Shinno, H.	275
Saito, Y.	20	Shinohara, K.	96,100
Saitoh, K.	217	Shiota, I.	180
Saitoh, K.	147	Shiotani, N.	221,222,223
Sakabe, N.	110	Shirai, M.	73
Sakaguchi, H.	30	Shiwaku, H.	140,149,150,151,152,192
Sakai, N.	221,223		193
Sakakibara, A.	34	Shoda, A.	114
Sakamoto, K.	163	Smith, P. L.	282
Sakamoto, M.	169	Soda, Y.	250
Sakamoto, T.	163	Soeya, T.	80
Sakane, H.	29	Sone, T.	19
Sakasai, A.	277	Stark, G.	282
Sakata, M.	164,171	Stevenson, A. W.	164
Sakata, O.	201,229	Suda, N.	129
Sakisaka, Y.	270,271,276	Suematsu, H.	178
Sakuma, H.	201,229	Sugahara, H.	230,231,232,234,236
Sakurai, H.	289	Sugawara, H.	273
Sakurai, K.	72,155	Sugaya, H.	46
Sakurai, M.	55,63,156	Sugi, H.	132,133,138,217
Sakurai, Y.	205,221,222,223	Sugie, T.	277
Salama, T. M.	25	Sugise, R.	162
Sano, T.	127	Sugishita, Y.	139
		Sugita, Y.	283,284
		Sugita, Y.	204
		Sugitani, Y.	190,208
		Sugiyama, H.	202
		Sugiyama, K.	173
		Sugiyama, M.	201
		Sumiyama, K.	68
		Susaki, J.	219

Suzuki, H.	177	Taniguchi, T.	290
Suzuki, H.	218	Taniguchi, T.	78
Suzuki, K.	251	Tanokura, A.	242
Suzuki, K.	55,63,156	Tatsumi, T.	184
Suzuki, K.	99	Tauc, P.	127
Suzuki, M.	99	Tawara, H.	238
Suzuki, S.	241,280	Tenchov, B. G.	130
Suzuki, S.	270,271	Terakado, S.	241,280
Suzuki, T.	242	Teraoka, Y.	31
Suzuki, Y.	139	Terauchi, H.	166
Suzuki, Y.	183	Tohji, K.	195
Syono, Y.	220	Tohnan, M.	257
	T	Tokita, M.	116
Tabira, Y.	24	Tokunaga, F.	122,125
Tagawa, H.	118	Tokura, Y.	51,188
Tagawa, S.	227	Tomiki, T.	269
Taguchi, I.	181,182	Tomiooka, Y.	247
Taguchi, T.	288	Tomita, A.	22,65
Tai, C.	31	Tonuma, T.	238
Tajima, H.	52,53	Toshima, N.	77
Tajima, Y.	135	Toyoda, T.	149,150,151,152,192
Takada, J.	35	Toyofuku, F.	139
Takada, Y.	79	Tregear, R. T.	132
Takagi, H.	51,188	Tsou, C.	106
Takahara, S.	61	Tsuchiyama, A.	43,153
Takahashi, E.	197,198	Tsuda, O.	205
Takahashi, H.	174	Tsuji, K.	174,176,203,224,225,226
Takahashi, M.	144,145	Tsuji, T.	30
Takahashi, M.	191	Tsuji, T.	107
Takahashi, T.	255,256	Tsukihara, T.	101
Takahashi, T.	194,215	Tsuruta, H.	127,128,136,137
Takakura, K.	95	Tsutsumi, K.	177
Takakuwa, Y.	266,267	Tzou, M-S	76
Takamatsu, F.	70,88		U
Takano, M.	35	Uchida, F.	183,248
Takata, M.	171	Uchida, S.	51,188
Takata, Y.	88,257,259,260,261	Udagawa, Y.	195
Takeda, H.	146	Ueda, K.	204
Takeda, S.	173	Ueda, K.	179
Takeda, T.	139,179	Ueda, K.	281
Takemori, S.	123,124	Ueki, K.	220
Takemoto, Y.	34	Ueki, T.	117,120,121
Takemura, K.	174	Ukai, M.	278,279
Takenaka, A.	102	Umazume, Y.	123,124
Takenaka, H.	229	Umeki, T.	74
Takesue, N.	185	Umeo, K.	20
Takeuchi, H.	277	Umetani, K.	179
Takizawa, Y.	239	Umetani, Y.	57
Tamai, G.	152	Uno, R.	159,160
Tamura, K.	49,203	Urai, T.	223
Tamura, M.	52,53	Urakawa, H.	116,196
Tanabe, K.	25	Uruga, T.	134
Tanaka, H.	132,133,138	Usami, K.	180,181,182
Tanaka, H.	253	Usami, N.	92,94,99
Tanaka, K.	68	Ushikuba, T.	42,84,85
Tanaka, K.	255,256,277,278,279	Utsumi, W.	218,290
	280,283,284,285	Uzu, S.	58
Tanaka, M.	44		V
Tanaka, N.	102	Vachette, P.	127
Tanaka, S.	206		W
Tanaka, T.	19,25,62,74	Wada, I.	193
Tanaka, Y.	251	Wada, K.	42,84,85
Tanaka, Y.	180	Wakabayashi, K.	127,131,132,133,134,136
Tanaka, Y.	205,221		137,138
Tani, K.	86		
Tani, T.	88		
Tanida, Y.	286		
Taniguchi, M.	79		

Waki, I. 246,247,248
 Wakita, H. 20,41,81
 Wakita, M. 189
 Wang, E-Z. 133
 Waseda, Y. 173
 Watanabe, I. 15,29
 Watanabe, K. 99
 Watanabe, M. 96
 Watanabe, M. 99
 Watanabe, M. 123,124
 Watanabe, R. 95
 Watanabe, T. 255,256
 Watanabe, Y. 205
 Watenpaugh, K. D. 114
 Wilkins, S. W. 164

Y

Yabumoto, N. 234,236
 Yagi, N. 123,124,129
 Yagi, T. 218,219
 Yagi, T. 105
 Yagi, T. 161
 Yagishita, A. 197,198,238,239,254,255
 256,263
 Yamada, H. 126
 Yamada, M. 68
 Yamada, Y. 72
 Yamagami, H. 209
 Yamaguchi, A. 146
 Yamaguchi, H. 109
 Yamaguchi, H. 162,163
 Yamaguchi, N. 197,198,277
 Yamaguchi, T. 20,41,81,82
 Yamaguchi, T. 25
 Yamaji, A. 233
 Yamamura, T. 32
 Yamanaka, T. 143,157,161
 Yamaoka, S. 290
 Yamasaki, T. 207
 Yamashita, H. 22,65
 Yamashita, S. 20,41,81
 Yamashita, Y. 287
 Yamazaki, H. 48,59,211
 Yanagi, H. 253
 Yanai, H. 85
 Yanashima, H. 276
 Yao, H. 130
 Yao, M. 49
 Yao, S. 227
 Yao, T. 163
 Yaoita, K. 176,203,224,225,226,290
 Yasuda, H. 68
 Yasumi, S. 240
 Yasuoka, N. 104,105
 Yokomizo, H. 277
 Yokota, Y. 101,107
 Yokoya, A. 92,94,99
 Yokoyama, T. 42
 Yokoyama, T. 54,70,71,79,88,252
 Yokoyama, T. 253,257,259,260,261
 Yokoyama, Y. 29
 Yoshiasa, A. 50,69
 Yoshida, H. K. 255,256
 Yoshida, S. 19,22,30,62
 Yoshida, Y. 227
 Yoshiki, M. 70,88,259,260,261
 Yoshimura, J. 56
 Yoshimura, J. 212
 Yoshimura, Y. 36

Yoshino, H. 189
 Yoshino, K. 282
 Yoshino, M. 239
 Yoshitake, H. 38
 Yoshizawa, M. 175
 Yoshizawa, M. 206
 Yukawa, N. 185
 Yukino, K. 160
 Yuri, M. 265,268,269
 Yusa, H. 219

Z

Zhang, F. 106

Subject Index

2-dimensional crystal 125
 3d transition metal complex 29
 2,3-butanedione-2-monoxime 124
 α -FeOOH 187
 α -helix 125
 α -PbO₂ 219
 α_2 -macroglobulin 136
 A
 Absolute calibration 277
 Absolute photoabsorption 279
 cross section
 Actin polymerization 128
 Action spectra 93
 Adenosine 82
 Adsorption 261,266
 Ag 194
 Ag(111) 272
 Ag₃AsS₃ glass 46
 Alanin 206
 AlAs 165
 Alcohol 27
 Alignment 251
 Alkali halide 28
 Alkali-halide 228
 Allende 146,181
 Allosteric transition 127
 Amino acid analysis 92
 Aminocarboxylato 16
 Amorphization 157
 Amorphous 30,43,44
 47,68,207
 Amorphous alloy 55,72,156
 Amorphous semiconductor 176
 Amorphous silicon 284
 Amylase 108
 Amylose 117
 An equilibrium adsorption method 80
 Analytical 23
 Angiography 139,140
 Angle-resolved photoemission 270,271,272
 274,276
 Angle-resolved topography 213
 Anharmonic vibration 69
 Anharmonicity 15,71
 Animal experiment 179

DPPC	130	Ga-S bond	230
Drickamer anvil	218	GaAs	200, 213, 214
dUMP	95		228, 230, 231
Dynamic process	278		232, 237
Dynamic spectroscopy	45	Gallium	224
Dynamical diffraction	201	GAPDH	106
		Gasification	22, 65
E		Ge	215
E-scan	160	Ge(100)	245
Earthworm hemoglobin	137	Ge/Si superlattice	163
Edta	40	Gel	47
Effective g factor	265	GeO ₂ -P ₂ O ₅ glass	158
Electron capture in ¹⁶³ Ho	240	Glass	24, 78
Electron neutrino mass	240	Glutathione synthetase	109
Electronic structure	223, 253, 255	Glycerinated fiber	138
	256, 264	Glycolipid	126
EMPW	223	Gold	77
Energy subtraction	140	Graphite	178, 195
Enterotoxin	107	Grazing incidence	155, 201
Epitaxial multilayer	165	Grazing incidence diffraction	217
Equatorial reflection	138		
Equi-lattice-spacing mapping	214	H	
topography		Hard X-ray	147
Etching	280	HeLa cells	100
EXAFS	15, 16, 17, 18	Helicity	175
	19, 22, 23, 24	Heterostructure	165
	26, 29, 30, 31	High dispersion	19
	32, 35, 36, 39	High pressure	157, 172, 174
	40, 41, 42, 43		176, 186, 203
	44, 45, 46, 47		209, 218, 219
	49, 54, 55, 58		220, 224, 225
	60, 61, 62, 63		226, 290
	65, 66, 68, 69	High Tc superconductor	35, 48, 51, 52
	70, 71, 72, 73		53, 188
	75, 76, 77, 78	High-order reflection	204
	79, 81, 82, 83	High-resolution diffraction	216
	84, 85, 86, 87	profile	
	88, 150, 151	High-resolution VUV spectroscopy	282
	152, 195, 289	High-Tc	255, 256
EXAFS analysis	48, 59	High-temperature X-ray	143
Excitons	265	experiment	
Extended X-ray absorption	162	Higher order	87
fine structure (EXAFS)		Higher-harmonics suppressor	246
Extreme-UV region	279	Highly excited molecules	278
		Histone	121
F		Hopeite crystal	83
Fe	74	Hot filament CVD	257
Fe(110)	276	HPLC	95
Fe-B-Si alloy	207	Human body	97
Fe-Ni	168	Human chromosome fiber	96
Fe-Ni alloy	59	Hydride	30
Fe-Ti-H alloys	68	Hydrocarbon	33
Ferromagnetic Fe	222	Hydrogen evolution	56
Ferromagnetic Ni	221	Hydrogenase	32, 104
Fibonacci lattice	166	Hydrogenation	27, 68
First order transition	178	Hydroxylation	33
Fish vertebra	148		
Fluorescence EXAFS	28	I	
Fluorescence lifetime	278	Ice	209, 210
Fluorescence M X-rays of Dy	240	Icosahedral phase	205
Fluoride glass	57	Image processing	139
Fourier transform	83	Imaging	97, 145, 153
Free air ionization chamber	206		192, 193, 208
Fusion plasma	277	Imaging plate	168, 171, 199
			223
G		Imbar alloy	168
		Immiscible system	72
		Impurity	51, 188

Offset	87	Protein structure	105
Oligomeric protein	120	Proton	245
Omega phase	185	Proton pump	122
Optical element	291	PSD	245, 267
Oxidation	234	Pt particle	26
Oxidative disruption	67	Pulse radiolysis	227
Oxide superconductor	162	Pulse structure	278
		Purple membrane	122, 125, 134
		Pyridine	66
P			
p-PDM	138	Q	
p.A scattering	242		
Pair distribution function	205	Quartz powder	164
Palladium	77		
Pattern replication	287	R	
Pb-Sr-Ca-Cu-D system	35		
Pd-Ce	20	R ₂ Fe ₁₄ B compound	211
Pd-M/C	84	Radial distribution function	173
Pd-Si alloy	63	Radiation products	92
Performance	87	Radiosensitization	100
Phase	152	Rare earth	20
Phase diagram	168	Rare gas	281
Phase separation	191	RDF	86
Phase transition	126, 130, 172	Reaction kinetics	267
	176, 186, 199	Reconstitution	196
	219	Reduction	74
Phodium	67	Refinement	108
Phosphorus	94	Reflectance	264
Phosphorus K edge	91	Reflection	247
Photoabsorption cross section	281	Reflectivity spectra of Al ₂ O ₃	269
Photoacoustic	149, 150, 151	in VUV	
	152, 190, 208	Reflectometer	248
Photoacoustic method	192, 193	Relativistic effects	276
Photocatalysis	75	Renin	114
Photocatalyst	56	Resolution	251
Photocycle	122	Resolution limit	250
Photodissociation	254	Resonance absorption	92, 94
Photoelectric effect	100	Resonance magnetic scattering	211
Photoemission	228, 230, 231	Response function	288
	232, 273	Reversible activity enhancement	26
Photoemission spectroscopy	236	Rh dimer	45
Photographic grain	161	Ribonuclease	103, 119
Photoionization	235, 238, 239	Ring distortions	21
Photolysis	284	Rock	154
Photopolymerization	253	Rotatory polarization	175
Phthalocyanine	21, 33	Ruthenium	58, 146
Piezorefectivity	268	Rutile	219
Plasma diagnostics	197, 198		
Plastic deformation	156	S	
Poly(2-chlorostyrene)	191		
Poly-N ⁵ -(2-hydroxyethyl)-L-glutamine	118	S-treatment	230
Polyaromatic hydrocarbon	252	Satellite reflection	169
Polymer blend	191	Satellites	187
Polymorphism	103	SAXS	116, 119
Polystyrene	191	Scattering	191
Porous silicon	202	Schottky barrier	231, 232
Porphyrin	58	Schottky barrier height	230
Position sensitive detector	144	Se	49
Powder	190	Se _{1-x} Te _x	86
Powder diffraction	143, 170	Secondary electrons	250
Powder diffractometry	159	Section topography	204
Precipitate	23	Selenium	17, 203
Precursive phenomena	167	Self-similarity	166
Preferred orientation	160	Semi-pulse	192
Profile analysis	161	Semiconductor	283
Protein	108	SEXAFS	258, 259
Protein crystal structure	114	Si	43, 44, 216
Protein crystallography	109	Si oxidation	234, 280
			249

Si surface	236		255, 256
Si(111)	194	Superexcited state	279
Si(Li) detector	288	Superlattice	172
Si(Li)SSD	260	Supported catalyst	80
Si ₂ H ₆	266	Surface	171, 228, 231
SiH ₄	266, 267, 279		234, 244, 272
Silane	283, 284		274
Silica	67	Surface analysis	155
Silicon	184, 200, 204	Surface EXAFS	260, 261
Silicon di oxide	184	Surface reconstruction	259, 261
Silicon substrate	250	Surface structure	194, 260
Silicon surface barrier detector	197	Surface-sensitive EXAFS	163
Silver halide	88, 161	Synchrotron radiation	132, 179, 182
SiN	44		207, 250, 285
Single bunch	278		287
Sintered diamond	290		
Sinusoidal length change	133	T	
SiO ₂	85		
Size effect	160	Ta	85
Sm compound	273	Temper embrittlement	207
Small angle X-ray scattering	118, 191, 207	Terbium	64
Small-angle scattering	121	Thermal expansion	54
Small-angle X-ray diffraction	134	Thickness	247
Soft X-ray	237, 247	Thin film	30, 37, 200
Soft X-ray absorption measurement	260	Thin layer catalyst	73
Soft X-ray microscope	243	Thin-filament	123
Soft X-ray spectra	288	Thiourea	169
Soft X-rays	246	Three-dimensional measurement	182
Solid solution	88	Threshold electron	254
Solid state amorphization	63	Ti	25
Solution	17	Time-resolved diffraction	215
Solution X-ray scattering	189	Time-resolved measurement	199
SOR	180	Time-resolved X-ray diffraction	130
SOR soft X-ray	242	Tin	34
Spectroscopy	190	TiO ₂	18, 219
Spin-orbit splitting	276	Titanium alloy	185
Spore	93	Tl-Ba-Ca-Cu-O	162
Sputtering	235	TLD	206
Squid retina	131	TMV	196
SR scanning	148	TMV-RNA	196
SrCaSi ₂ O ₆	78	TMVP	196
Standing wave	141, 142, 200	Tobacco necrosis	101
	237	Topography	177
Standing-wave	229, 260	Topotaxy	187
State analysis	153	Total reflection	155
Step	244	Trace elements	148
Stepped surface	258	Transferability	34
Stoichiometry	264	Transforming effects	99
Stopped-flow	127, 137	Transition	157
Strong gel	116	Transition-metal carbides	264
Strontium	65	Tridymite	143
Structural analysis	83	Trimer	125
Structural change	136	Two electron excitation	245
Structure	17, 41, 46, 47		
	101, 108, 176	U	
Structure analysis	143, 170		
Structure factor	156	Ultra clean	236
Structure transition	143	Undulator	291
Subtraction imaging	193	Undulator radiation	243
Subunit	120	Uniformity	247
Sugar	41	UPS	266, 267, 275
Sulfide	231, 232		
Sulfur	92, 258, 261	V	
	262		
Sulfur hexafluoride	280	V ₂ O ₅	19, 37
Super-thin layer	18	Vacuum	237
Superbead	96	Vacuum ultraviolet	277, 283, 284
Superconducting magnet	265	Vacuum UV	280
Superconductor	89, 90, 233	Valence	52, 53, 58

Valence band	233	Zr	25
Vanadium	289	Zr-EXAFS	57
Vanadocytes	289	ZrO ₂	42
Very low temperature	177		
Virus	101		
Visible light	56		

W

Weak gel	116
----------	-----

X

X ray	181
X ray CT	180
X-ray	101,109,200
X-ray absorption	150,151,255
	256,263
X-ray absorption near-edge structure (XANES)	162
X-ray computed tomography	182
X-ray crystal structure analysis	106,111,112
X-ray crystallography	103
X-ray detector	197,198
X-ray diffraction	104,105,131
	132,133,168
	177,194,203
	205,225,226
X-ray diffraction liquid	224
X-ray diffraction study	107
X-ray fluorescence	97,144,153
	155
X-ray fluorescence analysis	145
X-ray lithography	250,287
X-ray microprobe	183
X-ray microscopy	96,183
X-ray multiple-crystal diffractometry	202
X-ray optics	145,212
X-ray Raman	195
X-ray scattering	127,137
X-ray sensing pickup tube	182
X-ray standing wave	259
X-ray topography	209,210,212
XAFS	25
XANES	17,19,20,23
	31,32,36,38
	42,51,52,53
	58,62,64,74
	79,81,82,84
	85,89,90,149
	150,151,188
	249,252,253
	257,289
XAS	43,44
Xe physisorption	271
XPS	249
XRF	146

Y

Y-Ba-Cu-O system	48
Yeast	94

Z

Zeolite	21,31,33,36
	47,76
Zirconium fluoride	57
Zone plate	147,243

VIII. LIST OF PUBLISHED PAPERS

(Continued from the publication list in Photon Factory Activity Report 88)

1988

En-Zhong Wang, K.Wakabayashi, H.Tanaka, H.Iwamoto, T.Kobayashi, T.Hamanaka, Y.Amemiya, H.Sugi and T.Mitsui
Time-Resolved Synchrotron X-Ray Diffraction Studies of Effects of Sinusoidal Length Changes on the Intensities of the Myosin Meridional and Equatorial Reflections from Tetanized Frog Skeletal Muscles

Book of Abstracts Second Japan-China Bilateral Symposium on Biophysics, (1988) 305.

Y.Amemiya and K.Wakabayashi
Mechanism of Muscle Contraction Probed by Synchrotron Radiation
Iden, 42 (1988) 70. (in Japanese).

Y.Amemiya and J.Miyahara
Imaging Plate Illuminates Many Fields
Nature, 336 (1988) 89.

Y.Amemiya, H.Iwamoto, T.Kobayashi, H.Sugi, H.Tanaka and K.Wakabayashi
Time-Resolved X-Ray Diffraction Studies on the Effect of Slow Length Changes on Tetanized Frog Skeletal Muscle
J. Physiol., 407 (1988) 231.

Y.Amemiya, T.Matsushita, A.Nakagawa, Y.Satow, J.Miyahara and J.Chikawa
Design and Performance of an Imaging Plate System for X-Ray Diffraction Study
Nucl. Instrum. Methods, A266 (1988) 645.

Y.Amemiya, Y.Satow, T.Matsushita, J.Chikawa, K.Wakabayashi and J.Miyahara
A Storage Phosphor Detector and Its Application to Diffraction Studies Using Synchrotron Radiation
Topics in Current Chem., 147 (1988) 121.

H.Arashi, O.Shimomura, T.Yagi, S.Akimoto and Y.Kudoh
P-T Phase Diagram of ZnO₂ Determined by in Situ X-Ray Diffraction Measurements at High Pressures and High Temperatures
Advances in Ceramics, 24 (1988) 493.

K.Asakura and Y.Iwasawa
A Structure Model as the Origin of Catalytic Properties of Metal-Doped MgO Systems
Materials Chemistry and Physics, 18 (1988) 499.

K.Asakura and Y.Iwasawa
New Reversible Enhancement/Repression Phenomenon on Catalysis of Platinum Supported on One-Atomic Layer Niobium Oxide for Ethene Hydrogenation
Chem. Lett., (1988) 663.

K.Asakura, M.Aoki and Y.Iwasawa
Selective Isopenta Formation from CH₃OH on a New One-Atomic Layer ZrO₂/ZSM-5 Hybrid Catalyst
Catalysis Lett., 1 (1988) 395.

K.Asakura, Y.Iwasawa
Structures and Synergistic Catalyses of FeRu/Al₂O₃ np(3%) Catalysts Derived from FeRu₃-x(CO)₁₂(x=0,1,2,3) Part I
J. Chem. Soc., Faraday Trans. I, 84 (1988) 2445.

K.Asakura, Y.Iwasawa and M.Yamada
Structures and Synergistic Catalyses of FeRu/Al₂O₃ Catalysts Derived from FeRu₃-x(CO)₁₂(x=0,1,2,3) Part II
J.Chem. Soc., Faraday Trans. I, 84 (1988) 2457.

K.Asakura, Y.Iwasawa and H.Kuroda
A New TiO₂-Supported Rhodium Metal Catalyst. Catalyst Characterization and Non-SMSI Behavior
J. Chem. Soc., Faraday Trans., I, 84 (1988) 1329.

T.Cho, N.Yamaguchi, T.Kondoh, M.Hirata, S.Miyoshi, S.Aoki, H.Maezawa and M.Nomura
Quantum Efficiency of Gold Photocathodes(2-8keV) and EXAFS in Its Secondary Electron Yield and in the Detection Currents of a Microchannel Plate and a Silicon Surface Barrier Detector
Rev. Sci. Instrum., 59 (1988) 2453.

A.Fukuoka, L.Rao and M.Ichikawa
Structural Characterization of Zeolite-entrapped Rh₆ and RhFe Bimetallic Clusters and Their Catalysis in CO Hydrogenation Reaction
Kagaku to Kogyo ., (1988) 561. (in Japanese).

A.Fukuoka, T.Kimura and M.Ichikawa
Selective Hydrogenation of CO into C₁ and C₂ Alcohols by SiO₂-Supported RhFe, PtFe, and PdFe Bimetallic Cluster-Derived Catalysts
J. Chem. Soc., Chem. Commun., (1988) 428.

Y.Furusawa, H.Maezawa, K.Suzuki, K.Kobayashi, K.Hieda and T.Ito
Effect of Monochromatic X-Rays Having Energy at Around K-Shell Absorption Edge of Phosphorus on Bacteriophage T1.
J. Radiat. Res., 29 (1988) 43.

T.Hamanaka, Y.Kito, K.Hiraki, K.Wakabayashi, T.Mitsui and Y.Amemiya
Aggregation of Detergent-Solubilized Bovine Rhodopsin upon Light Illumination Studied by Synchrotron Radiation
Molecular Physiology of Retinal Proteins, (1988) 387.

Y.Hatano
Primary Processes of Radiation Interactions with Matters as Studied by Means of Synchrotron Radiation
J. Radiat. Res., 29 (1988) 10.

Y.Hiragi, H.Inoue, Y.Sano, K.Kajiwar, T.Ueki, M.Kataoka, H.Tagawa, Y.Izumi, Y.Muroga and Y.Amemiya
Temperature Dependence of the Structure of Aggregates of Tobacco Mosaic Virus Protein at pH7.2. Static Synchrotron Small-Angle X-Ray Scattering
J. Mol. Biol., 204 (1988) 129.

F.Itoh, T.Sekiuchi, M.Sakurai, T.Fukunaga, K.Suzuki
A Structural Study on Solid State Amorphization of Ni-Zr Alloys by Ball Milling

Proceedings of JIMIS-5, 29 (1988) 127.

M.Kataoka, M.Nakasako and F.Tokunaga
Structural Information on Proteins from
Small-Angle X-Ray Scattering with Heavy-Atom
Labeling. Application to Solubilized
Bacteriorhodopsin
J. Appl. Crystallography, 21 (1988) 355.

T.Koide, T.Shidara, M.Yanagihara and S.Sato
Resuscitation of Carbon-Contaminated Mirrors and
Gratings by Oxygen-Discharge Cleaning. 2:
Efficiency Recovery in the 100-1000eV Range
Appl. Opt., 27 (1988) 4305.

N.Kosugi
XANES and Molecular Orbital Picture. 3d
Transition Metal Compounds
Springer Series in Solid-State Science, 81 (1988)
203.

T.Koyano, Y.Kuroiwa, E.Kita, N.Saegusa, K.Ohshima
and A.Tasaki
The Enhanced Magnetic Moment and Structural Study
of Fe/MgO Multilayered Films
J. Appl. Phys., 64 (1988) 5763.

H.Maezawa, K.Hieda, K.Kobayashi and T.Ito
Effects of Auger Cascades of Bromine Induced by
K-Shell Photoionization on Plasmid DNA,
Bacteriophage, E.coli and Yeast Cells
DNA Damage by Auger Emitters, Taylor & Francis,
(1988) 135.

T.Masujima
Photoacoustic X-Ray Absorption Spectroscopy
Topics in Current Chemistry, 147 (1988) 145.

T.Masujima, H.Kawata and M.Ando
X-Ray Photoacoustic Spectroscopy
Isotope News, (1988) 2. (in Japanese).

T.Masujima, H.Kawata and M.Ando
X-Ray Photoacoustic Spectroscopy
Houshakou, 1 (1988) 27. (in Japanese).

T.Masujima, H.Kawata and M.Ando
X-Ray Photoacoustic Spectroscopy
Bunseki, (1988) 865. (in Japanese).

E.Matsubara and Y.Waseda
A few Topics of the Method for Structural
Characterization of Thin Films X-Ray Diffraction
MAC Science Journal, 2 (1988) 1. (in Japanese).

E.Matsubara and Y.Waseda
Structural Analysis of High-T_c Superconductor Film
by X-Ray Total-Reflection-Seemann-Bohlin Method
Nihon Kinzokugakukai Kaihou, 27 (1988) 461. (in
Japanese).

E.Matsubara, Y.Waseda, M.Mitera and T.Masumoto
A New Quantitative Anomalous X-Ray Scattering
Method for the Structural Analysis of Amorphous
Thin Films
Trans. Jpn. Inst. Metal., 29 (1988) 697.

E.Matsubara, K.Harada, Y.Waseda, A.Inoue, Y.Bizen
and T.Masumoto
X-Ray Diffraction Study of an Amorphous Al₆₀Ge₃₀
Ni₁₀ Alloy

J. Material Sci., 23 (1988) 3485.

Y.Matsuo, K.Ohshima, H.Iwasaki, Y.Kuroiwa,
H.Maeta and K.Haruna
X-Ray Diffuse Scattering from β' -AgZn Alloy
J. Phys. F., 18 (1988) 2505.

T.Mitsui and K.Wakabayashi
Time-Resolved X-Ray Diffraction Study of Muscle
Contraction by Using Synchrotron Radiation
Proceedings of 3rd Asia Pacific Physics
Conference, (1988) 327.

T.Mitsui and H.Ohshima
A Self-Induced Translation Model of Myosin Head
Motion in Contracting Muscle I. Force-velocity
Relation and Energy liberation
J. Muscle Research & Cell Motility, 9 (1988) 248.

N.Nakayama, I.Moritani, T.Shinjo, Y.Fujii and
S.Sasaki
Anomalous X-Ray Scattering Study of Composition
Profile in Fe/Mn Superlattice films
J. Phys. F, 18 (1988) 429.

M.Nishimura, K.Asakura and Y.Iwasawa
Self-Assisted Dehydrogenation of Ethanol on
Inorganic Oxide-Attached Nb-Monomer Catalysts
Proceedings of 9th. International Congress on
Catalysis, (1988) 1842.

K.Ohshima, J.Harada, M.Morinaga, F.Georgopoulos
and J.B.Cohen
Vacancy Arrangements in NbC_x
Materials Sci. Engineering, A105/106 (1988) 29.

H.Okuda, K.Osamura, Y.Amemiya and H.Hashizume
Synchrotron Radiation Small-Angle X-Ray
Scattering Study on Reversion Process of G.P.
Zones in Al-Zn Binary Alloys
J. Jpn. Inst. Metals, 52 (1988) 375. (in
Japanese).

K.Osamura, H.Okuda, Y.Amemiya and H.Hashizume
Growth and Coarsening of G.P. Zones in Al-Zn
Alloys
Metallurgical Transactions, 19a (1988) 1973.

M.Oshima, T.Kawamura, S.Maeyama and T.Miyahara
Combined Surface Analysis by Synchrotron Radiation
Photoemission Spectroscopy and Surface Extended
X-Ray Absorption Fine Structure of Oxidation
Features of Metal-Deposited GaAs
J. Vac. Sci. Technol., A6 (1988) 1451.

M.Oshima, Y.Yamada, T.Kawamura, S.Maeyama,
K.Hohkawa, Y.Tazoh and T.Miyahara
Synchrotron Radiation PES Studies of High T_c
Superconductor Surfaces and Interface for Contact
and Junction Formation
Ext. Abstract 20th Conf. SSDM, (1988) 447.

M.Oshima, Y.Kobayashi, T.Kawamura, S.Maeyama,
Y.Shinoda and T.Miyahara
Synchrotron Radiation Photoemission Spectroscopy
of Ga-Insulator Interfaces for GaAs Lateral
Epitaxial Growth
Appl. Surf. Sci., 33/34 (1988) 1168.

M.Oshima, Y.Yamada, T.Kawamura, S.Maeyama,
K.Hohkawa, Y.Tazoh and T.Miyahara

- Surfaces and Interfaces of High-Tc Superconductors for Contact and Junction Formation Studied with Synchrotron Radiation Photoemission Spectroscopy
Jpn. J. Appl. Phys., 27 (1988) 243.
- H.Oyanagi
Characterization of Hetero-Interfaces by Surface-Sensitive EXAFS
Hyomen Kagaku, 9 (1988) 582. (in Japanese).
- H.Oyanagi, H.Ihara, R.Sugise, M.Hirabayashi, T.Matsushita, M.Tokumoto, K.Murata, Y.Nishihara and Y.Kimura
Local Structure and Valence States in $\text{Ba}_2\text{YCu}_3\text{O}_y$ Studied by X-Ray Absorption Fine Structure
Physica C, 153-155 (1988) 982.
- H.Oyanagi, M.Yoneyama, K.Ikegami, M.Sugi, S.Kuroda, T.Ishiguro and T.Matsushita
Langmuir-Blodgett Monolayers Studied by Surface-Sensitive X-Ray Absorption Fine Structure Thin Solid Films, 159 (1988) 435.
- H.Oyanagi, Y.Takeda, Y.Matsushita, T.Ishiguro, T.Yao and A.Sasaki
Local Structure around Ga and As Doped in InP Studied by Fluorescence-Detected EXAFS
Solid State Commun., 4 (1988) 413.
- H.Oyanagi, Y.Takeda, T.Matsushita, T.Ishiguro, T.Yao and A.Sasaki
Structural Studies of (Ga,In)(As,P) Alloys and $(\text{InAs})_m(\text{GaAs})_n$ Strained-Layer Superlattices by Fluorescence-Detected EXAFS
Superlattices and Microstructure, 4 (1988) 413.
- T.K.Sham, T.Ohta, T.Yokoyama, Y.Kitajima, M.Funabashi, N.Kosugi, and H.Kuroda
Ru L Edge X-Ray Absorption Studies of the Electronic Structure of $\text{Ru}_3(\text{CO})_{12}$ Adsorption and the Formation of Ru-Cu Bimetallics on Cu(111)
J. Chem. Phys., 88 (1988) 475.
- K.Shinohara, H.Nakano, M.Watanabe, Y.Kinjo, S.Kikuchi, Y.Kagoshima, K.Kobayashi and H.Maezawa
X-Ray Contact Microscopy of Human Chromosomes and Human Fibroblasts
X-Ray Microscopy 2 (1988) 429.
- K.Sugiyama, E.Matsubara, Y.Waseda, A.Inoue and T.Masumoto
Direct Estimation of Local Environmental Structure around Superconducting Oxides of $\text{Ba}_2\text{YCu}_3\text{O}_{7-x}$
J. Mat. Sci., 7 (1988) 450.
- A.Suwa, H.Fukagawa, K.Suzuki, S.Hasegawa, M.Ando, K.Hyodo, M.Akisada, K.Nishimura, K.Konishi, F.Toyofuku and E.Takenaka
X-Ray K-Edge Subtraction Television System
Jpn. J. Appl. Phys., 27 (1988) 1989.
- T.Suzuki, N.Saitoh, H.Nomura and Y.Gohshi
X-Ray Fluorescence Analysis of Twins' Hair Using Synchrotron Radiation Excitation
Proceedings of 10th Australian Forensic Science, (1988)
- M.Suzuki, T.Hayashi, M.Oshima, M.Wada and J.Nakano
Photoemission Study of Schottky Barriers Formed on PbIn Alloys by Plasma Oxidation
Appl. Surf. Sci., 33/34 (1988) 1051.
- T.Takahashi, S.Nakatani, N.Okamoto, T.Ishikawa and S.Kikuta
Studies on Si(111) $\sqrt{3} \times \sqrt{3}$ -Ag Surface Structure by X-Ray Diffraction
Jpn. J. Appl. Phys., 27 (1988) L753.
- T.Takizawa, H.Ohwada, H.Kobayashi, K.Kanbara, T.Irie, S.Endo, H.Nakanishi, H.Kato and H.Fukutani
VUV Reflection Spectra and Fundamental Optical Constants of CdIn_2S_4 , CdInGaS_4 , $\text{Cd}_3\text{InGaS}_6$ Single Crystals
Solid State Commun., 67 (1988) 739.
- T.Tanaka, H.Yamashita, R.Tsuchitani, T.Funabiki and S.Yoshida
X-Ray Absorption (EXAFS/XANES) Study of supported Vanadium Oxide Catalysts: Structure of Surface Vanadium Oxide Species in Silica and γ -alumina at a Low Level of Vanadium Loading
J. Chem. Soc., Faraday Trans. 1, 84 (1988) 2987.
- T.Tanase, F.Shimizu, M.Kuse, S.Yano, M.Hidai and S.Yoshikawa
Novel C-2 Epimerization of Aldoses Promoted by Nickel(II) Diamine Complexes Involving a Stereospecific Pinacol-Type 1,2-Carbon Shift
Inorg. Chem., 27 (1988) 4085.
- H.Terauchi, Y.Noda, K.Kamigaki, S.Matsunaka, M.Nakayama, H.Kato, N.Sano and Y.Yamada
X-Ray Diffraction Patterns of Configurational Fibonacci Lattices
J. Phys. Soc. Jpn, 57 (1988) 2416.
- K.Toriumi, T.Kanao, Y.Umetsu, A.Oyoshi, M.Yamashita and T.Ito
Structural Study of Bromo-Bridged One-dimensional Nickel(II)-Nickel(IV) Mixed Valence Complexes by Means of EXAFS
J. Coord. Chem., 19 (1988) 209.
- Y.Udagawa and K.Tohji
Observation of X-Ray Resonant Raman Scattering and Transition to Resonance Fluorescence
Chem. Phys. Lett., 148 (1988) 101.
- K.Ueda and Y.Sato
Ionic Fragmentation Following Inner-Core Level Excitation of Polyatomic Molecules SiH_4 and $\text{Sn}(\text{CH}_3)_4$
Houshakou, 1 (1988) 1-11. (in Japanese).
- Y.Waseda, E.Matsubara and H.Ohta
X-Ray Absorption Edge for Rare Metals (Lanthanoid and Actinoid) Estimated by Calculating the Energy Dependence of the Anomalous Dispersion Factors
High Temperature Materials and Processes, 8 (1988) 61.
- Y.Yamada, M.Oshima, T.Waho, T.Kawamura, S.Maeyama and T.Miyahara
Structure and Bonding at the $\text{GaF}_2/\text{GaAs}(111)$ Interface
Jpn. J. Appl. Phys., 27 (1988) L1196.
- Y.Yamada, M.Oshima, S.Maeyama, T.Kawamura and T.Miyahara
Determination of Ca-As Bonding at the CaF_2/GaAs Interface
Appl. Surf. Sci., 33/34 (1988) 1073.

M.Yamamoto, S.Nakayama and T.Namioka
Optimum Design Method of Multilayer Elements
Proc. SPIE, 984 (1988) 160.

M.Yanagihara, M.Yamamoto, A.Arai, J.Cao and T.Namioka
Multilayer Reflection Filters for Soft X-Rays
Proc. SPIE, 984 (1988) 228.

S.Yoshida, T.Tanaka, Y.Nishimura, H.Mizutani and T.Funabiki
The Local Structure of Vanadium Oxide on Silica and γ -Alumina Studied by X-Ray Absorption (XANES/EXAFS) Spectroscopy -the Effect of Hydration
Catalysis: Theory and Practice, 3 (1988) 1473.

1989

K.Asakura and Y.Iwasawa
Extended X-Ray Absorption Fine Structure Studies on the Structure Change of the Al_2O_3 -attached $(Co)_4$ Catalyst during a CO Oxidation Reaction.
J. Phys. Chem., 93 (1989) 4213.

Zhi-Xin Wang, H.Tsuruta, Y.Honda, Y.Tachi-iri, K.Wakabayashi, Y.Amemiya and H.Kihara
Kinetic Study on the Dimer-Tetramer Interconversion Phosphorylase b by a Stopped-Flow X-Ray Scattering method
Biophys. Chem., 33 (1989) 153.

Y.Amemiya, S.Kishimoto, T.Matsushita, Y.Satow and M.Ando
Imaging Plate for Time-Resolved X-Ray Measurements
Rev. Sci. Instrum., 60 (1989) 1552.

K.Asakura, M.Nishimura and Y.Iwasawa
Spectroscopic Evidence for a Surface Nb Carbene in a New SiO_2 -Attached Nb Catalyst Active for Propene Metathesis
J. Mol. Catalysis, 55 (1989) 159.

K.Asakura
Dynamic Structure Analysis of Solid Surface by Means of EXAFS Spectroscopy
Shokubai, 31 (1989) 290. (in Japanese).

K.Asakura and Y.Iwasawa
EXAFS Studies on Molecular Phenomena on Solid Catalysts in a Working State
Physica B, 158 (1989) 142.

K.Asakura and Y.Iwasawa
EXAFS Studies about the Mechanism of the CO Oxidation Reaction on the Co Tetramer Catalyst
Physica B, 158 (1989) 152.

K.Asakura, K.Bando, Y.Iwasawa, H.Arakawa and K.Isobe
Dynamic Structure of the Active Sites on Solid Surface Determined by in-situ Spectroscopic Techniques
Shokubai, 2 (1989) 92. (in Japanese).

A.Bianconi, T.Miyahara, A.Kotani, Y.Kitajima, T.Yokoyama, H.Kuroda, M.Funabashi, H.Arai and T.Ohta

Correlation Satellites in Deep Metal 3p Core X-Ray Photoemission of Tetravalent Oxides MO_2 (M=Ce, Pr, Tb, Hf) and LaF_3
Phys. Rev., B39 (1989) 3380.

T.Cho, N.Yamaguchi, T.Kondoh, M.Hirata, S.Miyoshi, S.Aoki, H.Maezawa and M.Nomura
Detection Characteristics of Microchannel Plates and Gold (Near the Absorption edges (2.8)KeV)
Rev. Sci. Instrum., 60 (1989) 2337.

K.Edamoto, S.Maehama, E.Miyazaki, H.Kato and S.Otani
Oxygen Adsorption on a NbC(100) Surface: Angle-Resolved Photoemission Study
Surf. Sci., 223 (1989) 56.

S.Emura, K.Koto, A.Yoshiasa, H.Ito, S.Gonda and S.Mukai
Effect of Structural Disorder to Photoelectron in Pentanary Alloy Semiconductor $AlGaInPAs$
J. Material Sci. Lett., 8 (1989) 1236.

Y.Fujii, K.Hase, Y.Ohishi, H.Fujihisa, M.Hamaya, K.Takemura, O.Shimomura, T.Kikegawa, Y.Amemiya and T.Matsushita
Evidence for Molecular Dissociation in Bromine near 80 GPa
Phys. Rev. Lett., 63 (1989) 536.

T.Fujimura, H.Iwasaki, T.Kikegawa, Y.Tsuchida, O.Terasaki and O.Shimomura
Structure Changes in Vacancy-Rich Titanium Monoxide at High Temperatures
High Pressure Research, 1 (1989) 213.

T.Fujisawa, T.Ueki and S.Iida
Structural Change of the Troponin C Molecule upon Ca^{2+} Binding Measured in Solution by the X-Ray Scattering Technique
J. Biochem., 105 (1989) 377.

S.Fujiwara, Y.Inoko and T.Ueki
Synchrotron X-Ray Scattering Study of Chromatin Condensation Induced by Monovalent Salt: Analysis of the Small-Angle Data
J. Biochem., 106 (1989) 119.

M.Funabashi, Y.Kitajima, T.Yokoyama, T.Ohta and H.Kuroda
Study of Surface EXAFS and X-Ray Standing-Wave Absorption Profiles for $(3 \times 3)R30$ $Cl/Ni(111)$
Physica B, 158 (1989) 664.

M.Funabashi, T.Ohta, T.Yokoyama, Y.Kitajima and H.Kuroda
Compact Fluorescence Detector for Surface EXAFS and X-Ray Standing-Wave Measurements
Rev. Sci. Instrum., 60 (1989) 2505.

M.Funabashi, M.Nomura, Y.Kitajima, T.Yokoyama, T.Ohta and H.Kuroda
Performance of the Cooling System for the Soft X-Ray Double-Crystal Monochromator at the Photon Factory
Rev. Sci. Instrum., 60 (1989) 1983.

Y.Furusawa, H.Maezawa, K.Suzuki, K.Kobayashi, K.Hieda and T.Ito
Radiolysis of Bromodeoxyuridine with Monoenergetic X-Rays at Br-K-Shell Absorption

- Energy.
J. Radiat. Res., 30 (1989) 58.
- M.Fuseya, K.Ichimura, T.Yamamura, Y.Tachi-iri, K.Satake, Y.Amemiya and H.Kihara
Dissociation and Auto-Oxidation of Hemerythrin Induced by SH-Modification. Kinetic Study
J. Biochem., 105 (1989) 293.
- S.Hayakawa, A.Iida, S.Aoki and Y.Gohshi
Development of a Scanning X-Ray Microprobe with Synchrotron Radiation
Rev. Sci. Instrum., 60 (1989) 2452.
- S.Hayakawa, A.Iida, S.Aoki and Y.Gohshi
Micro X-Ray Fluorescence Analysis with Synchrotron Radiation
Adv. X-Ray Anal., 32 (1989) 141.
- K.Honma K.Tanaka S.Suzuki and I.Koyano
A TPEPICO Study of Dissociative Photoionization of C₂H₂D₂ Isomers
Int. J. Mass Spectrom. Ion Proc., 93 (1989) 1.
- K.Huke
Low Emittance and Positron Storage Operation at the Photon Factory
Rev. Sci. Instrum., 60 (1989) 1382.
- A.Iida, M.Takahashi, K.Sakurai and Y.Gohshi
SR X-Ray Fluorescence Imaging by Image Reconstruction Technique
Rev. Sci. Instrum., 60 (1989) 2458.
- T.Ishikawa
X-Ray Topography with Highly Collimated Beam at Photon Factory
Rev. Sci. Instrum., 60 (1989) 2490.
- T.Ishikawa
X-Ray Monochromators for Circularly Polarized Incident Radiation
Rev. Sci. Instrum., 60 (1989) 2058.
- G.Isoyama, S.Yamamoto, T.Shioya, H.Ohkuma, S.Sasaki, T.Mitsuhashi, T.Yamakawa and H.Kitamura
Construction of a Multiundulator, Revolver No. 19, at the Photon Factory
Rev. Sci. Instrum., 60 (1989) 1863.
- K.Ito and T.Namioka
High-resolution VUV Absorption Spectroscopy with the 6-VOPE Facility
Rev. Sci. Instrum., 60 (1989) 1573.
- K.Ito, K.Maeda, Y.Morioka and T.Namioka
Performance of the 6VOPE High Resolution VUV Spectroscopic Facility in the Photoelectric Detection Mode
Appl. Opt., 28 (1989) 1813.
- F.Ito, M.Sakurai, T.Sugawa, K.Suzuki, N.Sakai, M.Ito, O.Mao, N.Shiotani, Y.Tanaka, Y.Sakurai, S.Nanao, H.Kawata, Y.Amemiya and M.Ando
A High Resolution Compton Profile Spectrometer for 29.5 keV X-Rays with a Combination of Crystal Analyzer and Imaging Plate
Rev. Sci. Instrum., 60 (1989) 2402.
- Y.Iwasawa
Acid-Base Catalysis Structure of Acid-Base Design Surfaces and Their Catalysis
Acid-Base Catalysis, (1989) 267.
- Y.Iwasawa
Fine Particles, Ultrafine Particles
Hyomen Kagaku, 10 (1989) 824. (in Japanese).
- Y.Iwasawa
Catalysis by Inorganic Oxide-Attached Metal-Dimer
Catalysis Today, 6 (1989) 27.
- Y.Izumi, N.Matsushita and H.Yoshino
Expression of Calmodulin Function Revealed from X-Ray Solution Scattering: A Model of the Calmoduline-Mastoparan Complex
Houshakou, 2 (1989) 23.
- H.Kageyama, N.Kamijo, T.Kobayashi and M.Haruta
EXAFS Studies of Ultra-Fine Gold Catalysts Supported on Hematite Prepared from Coprecipitated Precursors.
Physica B, 158 (1989) 183.
- N.Kanaya, S.Sato, S.Asaoka, K.Nakajima, S.Hayashi and S.Kurita
Pneumatic Fast-Closing Valve for Synchrotron Radiation Beam Lines at the Photon Factory
IEEE Trans. Nucl. Sci., 36 (1989) 1391.
- Y.Kashihara, S.Kimura and J.Harada
X-Ray Measurements of the Crystal Truncation Rod Scattering from Cleavage Surfaces of Ionic Crystals
Surf. Sci., 214 (1989) 477.
- Y.Kashiwase, M.Mori, M.Kogiso, K.Ushida, M.Minoura, T.Ishikawa and S.Sasaki
Anomalous Transmission of X-Rays Scattered by Phonons in a Germanium Crystal
Phys. Rev. Lett., 62 (1989) 925.
- K.Kato and Y.Sugitani
Simultaneous Detection of X-Ray Photoacoustic and Fluorescence Signals as Applied to Characterization of Layered Materials
Analytical Sci., 5 (1989) 545.
- S.Kawado, S.Kojima, T.Ishikawa, T.Takahashi and S.Kikuta
Time-Resolved X-Ray Measurement System for Studying the Lattice Deformation of Semiconductor Crystals Under Laser Irradiation
Rev. Sci. Instrum., 60 (1989) 2342.
- T.Kawamura, S.Maeyama, M.Oshima, Y.Ishii and T.Miyahara
Solid Surface Analysis Beamline BL-1A at the Photon Factory
Rev. Sci. Instrum., 60 (1989) 1928.
- T.Kawamura, S.Maeyama, M.Oshima, Y.Ishii and T.Miyahara
Solid Surface Analysis Beamline with a Grating/Crystal Monochromator at the Photon Factory
Nucl. Instr. Methods, A275 (1989) 462.
- H.Kawata, T.Miyahara, S.Yamamoto, T.Shioya, H.Kitamura, S.Sato, S.Asaoka, N.Kanaya, A.Iida, A.Mikuni, M.Sato, T.Iwazumi, Y.Kitajima and M.Ando
Design and Construction of Beam Line-NE1 for

- Circularly Polarized Synchrotron Radiation from the 6 GeV TRISTAN Accumulation Ring
Rev. Sci. Instrum., 60 (1989) 1885.
- T.Kikegawa, O.Shimomura, H.Iwasaki, S.Sato, A.Mikuni, A.Iida and N.Kamiya
High Pressure-High Temperature Research Using High Energy Synchrotron Radiation at the TRISTAN Accumulation Ring
Rev. Sci. Instrum., 60 (1989) 1527.
- M.Kimura, M.Matsuo, M.Murakami, K.Sawano and S.Matsuda
Characterization of Oxide Superconductor by Means of X-Ray Diffractometry and X-Ray Absorption Near Edge Structure
ISIJ International, 29 (1989) 213.
- H.Kitamura, S.Yamamoto and S.Kamada
Insertion Devices at the Photon Factory: Present Status and Future Development
Rev. Sci. Instrum., 60 (1989) 1407.
- R.Klauser, M.Kubota, Y.Murata, M.Oshima, Y.Yamada, T.Kawamura and T.Miyahara
Photoemission Study of NaF and KF Overlayers on GaAs Surfaces
Surf. Sci., 211 (1989) 759.
- R.Klauser, M.Kubota, Y.Muyata, M.Oshima, Y.Yamada-Maruo, T.Kawamura and T.Miyahara
Electronic Properties of Ionic Insulators on Semiconductor Surfaces: Alkali Fluorides on GaAs(100)
Phys. Rev. B, 40 (1989) 3301.
- H.Kobayakawa and K.Huke
Worldwide Census of Synchrotron Radiation Facilities
Rev. Sci. Instrum., 60 (1989) 2548.
- T.Koide, S.Sato, N.Kanaya and S.Asaoka
Design and Construction of the Front End of the 53-pole Wiggler/Undulator Beamline
Rev. Sci. Instrum., 60 (1989) 1877.
- T.Koide, T.Shidara, K.Tanaka, A.Yagishita and S.Sato
In situ DC Oxygen-Discharge Cleaning System for Optical Elements
Rev. Sci. Instrum., 60 (1989) 2034.
- A.Koizumi, H.Maeda, N.Bamba, H.Murayama, E.Takayama-Muromachi, J.Shi, K.Shimizu, M.Mino and H.Yamazaki
EXAFS Study on Fe-Doped $\text{YBa}_2\text{Cu}_3\text{O}_y$.
Jpn. J. Appl. Phys., 28 (1989) L203.
- T.Koizumi, T.Hayaishi, T.Matsuo, K.Shima, H.Tawara, T.Tonuma and A.Yagishita
Photoionization Cross Sections of Xenon in the L-edge Region
J. Phys. Soc. Jpn., 58 (1989) 13.
- T.Komeda, Y.Sakisaka, M.Onchi, H.Kato, S.Suzuki, K.Edamoto and Y.Aiura
Electronic Structure of a $\text{NbC}_{0.9}(100)$ Surface: Angle-Resolved Photoemission Study
Phys. Rev. B, 39 (1989) 7461.
- T.Komeda, Y.Sakisaka, M.Onchi, H.Kato, S.Suzuki, K.Edamoto and Y.Aiura
Photoemission Study of the Bulk Magnetic Phase Transition in Cr
Phys. Rev. B, 39 (1989) 6198.
- T.Komeda, Y.Sakisaka, M.Onchi, H.Kato, S.Suzuki, K.Edamoto and Y.Aiura
Photoemission of Xe on Cr(110): Evidence for Exponential Dependence of the Band Dispersion on the Interatomic Spacing
Phys. Rev. B, 40 (1989) 3344.
- N.Kosugi, H.Kondoh, H.Tajima and H.Kuroda
Cu K-Edge XANES of $\text{YBa}_2\text{Cu}_3\text{O}_y$. The Valence and Structure of Different Cu Sites
Physica B, 158 (1989) 450.
- N.Kosugi, H.Kondoh, H.Tajima and H.Kuroda
Cu K-Edge XANES of $(\text{La}_{1-x})_2\text{CuO}_4$, $\text{YBa}_2\text{Cu}_3\text{O}_y$ and Related Cu Oxides. Valence, Structure and Final-State Effects on $1s-4p\pi$ and $1s-4p\sigma$ Absorption
Chem. Phys., 135 (1989) 149.
- A.Koyama, S.Sasaki and T.Ishikawa
Closed Feedback System on the Vertical Beam Position
Rev. Sci. Instrum., 60 (1989) 1953.
- T.Koyano, Y.Kuroiwa, E.Kita, N.Saegusa, K.Ohshima and A.Tasaki
Magnetic Properties and Structural Study of Fe/MgO Multilayered Films
MRS Int'l. Mtg. on Adv. Mats., 10 (1989) 3493.
- Y.Kuroda, H.Maeda, H.Moriwaki, N.Bamba and T.Morimoto
Local Crystal Structure of Exchanged Ions in Zeolite
Physica B, 158 (1989) 185.
- N.Kuwano, Y.Saito, K.Umeo, M.Itakura and K.Oki
Measurements of Mixed Valences of Ce by L_3 -XANES Analysis
Engineering Sci. Rep. Kyushu Univ., 11 (1989) 195. (in Japanese).
- Y.Kitajima, T.Yokoyama, M.Funabashi, T.Ohta, and H.Kuroda
Surface EXAFS and XANES Study of $5\sqrt{3}\times 2\text{ S/Ni}(111)$: a Pseudo- $c(2\text{ TIMES } 2)\text{S/Ni}(100)$ Model with Surface Reconstruction
Physica B, 158 (1989) 668.
- Y.Kitajima, T.Yokoyama, T.Ohta, M.Funabashi, N.Kosugi and H.Kuroda
Surface EXAFS and XANES Study of $5\sqrt{3}\times 2\text{ S/Ni}(111)$: a Pseudo- $c(2\text{ TIMES } 2)\text{S/Ni}(100)$ Model with Surface Reconstruction
Surf. Sci., 214 (1989) L261.
- H.Maeda, A.Koizumi, N.Bamba, E.Takayama-Muromachi, F.Izumi, H.Asano, K.Shimizu, H.Moriwaki, H.Maruyama, Y.Kuroda and H.Yamazaki
EXAFS and Neutron Diffraction Studies of Local and Average Structures for $\text{YBa}_2\text{Cu}_{2.8}\text{Zn}_{0.2}\text{O}_{7-8}$.
Physica C, 157 (1989) 483.
- F.Maeda, T.Kawamura, M.Oshima, Y.Hidaka and A.Yamaji

- Synchrotron Radiation Photoelectron Spectroscopy of High Tc Bi-Sr-Ca-Cu-O Single Crystal
Jpn. J. Appl. Phys., 28 (1989) L361.
- S.Maeyama, T.Kawamura and M.Oshima
EXAFS Measurement of Oxygen in Thin Films
X-sen Bunseki no Shinpo, 20 (1989) 133. (in Japanese).
- S.Maeyama, T.Kawamura, M.Oshima, H.Takenaka and Y.Ishii
Application of Multi-Layer Mirror to Soft X-Ray Spectroscopy
Shinku, 32 (1989) 845. (in Japanese).
- S.Maeyama, Y.Satow, M.Oshima and A.Katsui
Barium K-Edge Polarized EXAFS of High-Tc Superconducting Single-Crystal $\text{YBa}_2\text{Cu}_3\text{O}_y$
Physica B, 158 (1989) 473.
- T.Masujima, H.Imai, H.Shiwaku, H.Yoshida, T.Sano, Y.Amemiya, H.Kawata, M.Kataoka, M.Hoshi, C.Nagoshi, S.Uehara and M.Ando
Instrumentation for X-Ray Photoacoustic Imaging and Depth Profiling
Rev. Sci. Instrum., 60 (1989) 2468.
- T.Masujima, H.Kawata, Y.Amemiya, T.Katsura, M.Ando, T.Nanba, K.Fukui and M.Watanabe
Photoacoustic Detector for Synchrotron Radiation Research
Rev. Sci. Instrum., 60 (1989) 2318.
- T.Masujima, H.Shiwaku, H.Yoshida, M.Kataoka, M.Reichling, H.Imai, H.Kawata, A.Iida, A.Koyama and M.Ando
Photoacoustic EXAFS of Solid Phase
Jpn. J. Appl. Phys., 28 (1989) L513.
- E.Matsubara and Y.Waseda
Structural Study of a $\text{YBa}_2\text{Cu}_3\text{O}_{7-x}$ Superconductor by Anomalous X-Ray Scattering
Materials Trans., JIM., 30 (1989) 235.
- E.Matsubara and Y.Waseda
Anomalous X-Ray Scattering on Amorphous $\text{Al}_{87}\text{Y}_8\text{Ni}_5$ and $\text{Al}_{90}\text{Y}_{10}$ Alloys
Z. Naturforsch., 44a (1989) 814.
- E.Matsubara and Y.Waseda
An Anomalous X-Ray Scattering Study of an Aqueous Solution of ZnCl_2
J. Phys.:Condensed Matter, 1 (1989) 8575.
- E.Matsubara, Y.Waseda, M.Mitera and T.Nasumoto
Structural Study of an Amorphous Bi-Fe-Ca-O Thin Film by the Anomalous X-Ray Scattering
Sci. Rep. Res. Inst. Tohoku Univ. Series A, 34A (1989) 155.
- E.Matsubara, Y.Waseda, K.Inomata and S.Hashimoto
X-Ray Structural Study of Ferromagnetic Vitreous $0.5\text{La}_{0.7}\text{Sr}_{0.3}\text{MnO}_3 \cdot 0.5\text{B}_2\text{O}_3$
Z. Naturforsch., 44a (1989) 723.
- I.Matsubara, N.Yagi, D.W.Moughan, Y.Saeki and Y.Amemiya
X-Ray Diffraction Study on Heart Muscle During Contraction
Muscle Energetics, (1989) 481.
- N.Matsubayashi, H.Shimada, I.Kojima, M.Kurahashi, T.Ohta, A.Itoh and A.Nishijima
S(KLL) Auger Resonancelike Phenomena for Solid Samples
Jpn. J. Appl. Phys., 28 (1989) L1051.
- H.Matsuyama, T.Takahashi, H.Katayama-Yoshida, T.Kashiwakura, Y.Okabe, S.Sato, N.Kosugi, A.Yagishita, K.Tanaka, H.Fujimoto and H.Inokuchi
Impurity-State-Like Nature of Fermi-Liquid Status in $\text{Ba}_2\text{Sr}_2\text{CaCu}_2\text{O}_8$ Observed by Photoemission and X-Ray Absorption
Physica C, 160 (1989) 567.
- N.Metoki, H.Suematsu, Y.Murakami, Y.Ohishi and Y.Fujii
Kinetics of the First-Order Transition in Stage 1 Rubidium Graphite Intercalation Compound
Synthetic Metals, 28 (1989) 3344.
- S.Mitani, T.Namioka, M.Yanagihara, K.Yamashita, J.Fujita, S.Morita, T.Harada, T.Sasaki, S.Sato, T.Miyahara, T.Koide, A.Mikuni, W.Okamoto and H.Maezawa
Apparatus for Characterizing the VUV and Soft X-Ray Optical Elements at the Photon Factory
Rev. Sci. Instrum., 60 (1989) 2216.
- T.Miyahara
Geometrical and Wave-Optical Phase-Space Matching between Undulator Radiation and Grating Monochromators
Rev. Sci. Instrum., 60 (1989) 2068.
- T.Miyanaga, T.Fujikawa, N.Matsubayashi, T.Fukumoto, K.Yokoi, I.Watanabe and S.Ikeda
Anomalous Peak Intensities in the EXAFS of Polynuclear Molybdenum Compounds
Bull. Chem. Soc. Jpn., 62 (1989) 1791.
- T.Murata, S.Emura, H.Ito and H.Maeda
EXAFS Study of Relaxation of Cu^+ Impurities in Alkali Halide
Physica B, 158 (1989) 613.
- S.Nagaoka, I.Koyano, K.Ueda, E.Shigemasa, Y.Sato, A.Yagishita T.Nagata and T.Hayaishi
Site-Specific Fragmentation Following Inter-Core Level Excitation of $\text{Pb}(\text{CH}_3)_4$ in the Vapor Phase
Chem. Phys. Lett., 154 (1989) 363.
- L.Nagy, H.Ohtaki, T.Yamaguchi and M.Nomura
EXAFS Study of Iron(III) Complexes of Sugartype Ligands
Inorg. Chim. Acta, 159 (1989) 201.
- T.Nakahata, H.Hashizume, M.Oshima and T.Kawamura
X-Ray Diffraction Curves from Mosaic Crystals at Near-Normal Incidence Angles
Jpn. J. Appl. Phys., 28 (1989) L1300.
- Y.Ohishi, Y.Fujii, N.Nakayama, T.Shinjo, T.Matsushita and J.Fujita
Synchrotron X-Ray Diffraction Study of Supermodulus Effect in Ni/Mo Superlattices under High Pressure
Multilayers, 10 (1989) 569.
- K.Ohno, H.Harada, T.Yamagata, M.Yamazaki and K.Ohsumi
X-Ray Diffractometric Determination of Lattice

- Misfit between γ and γ' Phases in Ni-base Superalloys -Conventional X-Ray Source vs. Synchrotron Radiation-
Advances in X-Ray Analysis, **32** (1989) 363.
- E.Ohtani, N.Kagawa, O.Shimomura, M.Togaya, K.Suito, A.Onodera, H.Sawamoto, M.Yoneda, S.Tanaka, W.Utsumi, E.Ito, A.Matsumura and T.Kikegawa
High-Pressure Generation by Anvil System with Sintered Diamond Anvils
Rev. Sci. Instrum., **60** (1989) 922.
- B.Okai, K.J.Takano, J.Yoshimoto, H.Takahashi, A.Izawa and K.Tsuji
Intensity of X-Ray (222) Line in InSb at 77 K under Pressure
Modern Phys. Lett. B, **3** (1989) 1101.
- H.Okuda, K.Osamura, Y.Amemiya and H.Hashizume
Synchrotron Radiation Small-Angle Scattering Study on the Reversion Process of G.P. Zones below Miscibility Gap in Al-Zn Binary Alloy
Materials Transactions, JIM, **30** (1989) 886.
- M.Oshima, Y.Yamada-Maruo and R.Klauser
Synchrotron Radiation Photoemission Spectroscopy of Epitaxially-Grown Fluoride Films/GaAs Interfaces
Ext. Abstract. 21st Conf. SSDM, (1989) 517.
- N.Sakai, N.Shiotani, M.Ito, F.Itoh, H.Kawata, Y.Amemiya, M.Ando, S.Yamamoto and H.Kitamura
Challenge to Precise Magnetic Compton-Profile Measurements
Rev. Sci. Instrum., **60** (1989) 1666.
- N.Sakai, N.Shiotani, F.Itoh, O.Mao, M.Ito, H.Kawata, Y.Amemiya and M.Ando
High-Resolution Compton Profile of Si Using 29.5keV Synchrotron-Radiation X-Rays
J. Phys. Soc. Jpn., **58** (1989) 3270.
- Y.Sakisaka, T.Komeda, T.Maruyama, M.Onchi, H.Kato, Y.Aiura, H.Yanashima, T.Terashima, Y.Bando, K.Iijima, K.Yamamoto and K.Hirata
Angle-Resolved Photoemission from Epitaxial $\text{YBa}_2\text{Cu}_3\text{O}_{7-x}$ (001) Films
Phys. Rev. B, **39** (1989) 2304.
- Y.Sakisaka, T.Komeda, T.Maruyama, M.Onchi, H.Kato, Y.Aiura, H.Yanashima, T.Terashima, Y.Bando, K.Iijima, K.Yamamoto and K.Hirata
Angle-Resolved Photoemission Investigation of the Electronic Band Properties of $\text{YBa}_2\text{Cu}_3\text{O}_{7-x}$ (001)
Phys. Rev. B, **39** (1989) 9080.
- T.Sakuma, K.Sugiyama and Y.Waseda
Structural Characterization of Crystalline Materials by the Anomalous X-Ray Scattering
Bull. Jpn. Inst. Metals, **28** (1989) 195. (in Japanese).
- T.Sakuma, K.Sugiyama, E.Matsubara and Y.Waseda
Determination of the Crystal Structure of Superionic Phase of Cu_2Se
Materials Trans., JIM., **30** (1989) 365.
- K.Sakurai, A.Iida and Y.Gohshi
Chemical State Analysis by X-Ray Fluorescence Using Absorption Edge Shifts
Adv. X-Ray Anal., **32** (1989) 167.
- S.Sasaki
Anomalous Scattering Studies with a Four-Circle Diffractometer at BL-10A
Rev. Sci. Instrum., **60** (1989) 2417.
- M.S.Sasaki, K.Kobayashi, K.Hieda, T.Yamada, Y.Ejima, H.Maezawa, Y.Furusawa, T.Ito and S.Okada
Induction of Chromosome Aberrations in Human Lymphocytes by Monochromatic X-Rays of Quantum Energy between 4.8 and 14.6 keV
Int. J. Radiat. Biol., **56** (1989) 975.
- S.Sasaki, S.Yamamoto, T.Shioya and H.Kitamura
Construction of a Multipole Wiggler, MPW 13, at the Photon Factory
Rev. Sci. Instrum., **60** (1989) 1859.
- S.Sato, A.Iijima, S.Takeda, M.Yanagihara, T.Miyahara, A.Yagishita, T.Koide and H.Maezawa
SIC Mirror Development at the Photon Factory
Rev. Sci. Instrum., **60** (1989) 1479.
- K.Seki, I.Morisada, H.Tanaka, K.Edamatsu, M.Yoshiki, Y.Takata, T.Yokoyama, T.Ohta, S.Asada, H.Inokuchi, H.Nakahara and K.Fukuda
Photopolymerization of Long-Chain Diacetylene Monocarboxylic Acid and in Langmuir-Blodgett Films Studied by Photoelectron Spectroscopy and X-Ray Absorption Near-Edge Structure
Thin Solid Films, **179** (1989) 15.
- T.K.Sham, T.Ohta, T.Yokoyama, Y.Takata, Y.Kitajima, M.Funabashi and H.Kuroda
Ru L-Edge X-Ray Absorption Studies of the Formation of Ru-Cu Bimetallics on Cu(111) and Cu(100)
Physica B, **158** (1989) 698.
- N.Shiotani, N.Sakai, M.Ito, O.Mao, F.Itoh, H.Kawata, Y.Amemiya and M.Ando
Compton Profiles of Aluminum and Silicon
J. Phys. Condensed Matter, **1** (1989) SA27.
- N.Shiotani, N.Sakai, F.Itoh, M.Sakurai, H.Kawata, Y.Amemiya and M.Ando
An X-Ray Spectrometer for Compton Scattering Experiments with Synchrotron Radiation
Nucl. Instr. Methods, **A275** (1989) 447.
- T.Shioya, S.Yamamoto, S.Sasaki, M.Katoh, Y.Kamiya and H.Kitamura
Construction and Operation of the Multipole Wiggler, MPW 16, at the Photon Factory
Rev. Sci. Instrum., **60** (1989) 1855.
- H.Sugahara, M.Oshima, H.Oigawa, H.Shigehara and Y.Nannichi
Synchrotron Radiation Photoemission Study on $(\text{NH}_4)_2\text{S}_x$ -Treated n-GaAs
Ext. Abstract. 21st Conf. SSDM, (1989) 547.
- Y.Tajima, K.Okada, O.Yoshida, T.Seto and Y.Amemiya
Rapid Small-Angle X-Ray Diffraction of a Tonically-Contracting Smooth Muscle Recorded with Imaging Plates
J. Appl. Crystal., **22** (1989) 72.
- T.Takahashi
X-Ray Surface Diffraction

- Bull. Jpn. Inst. Metals, 28 (1989) 203. (in Japanese).
- T.Takahashi, S.Nakatani, N.Okamoto, T.Ishikawa and S.Kikuta
Structure Analysis of Si(III) $\sqrt{3}$ TIMES $\sqrt{3}$ -Ag Surface by X-Ray Diffraction
Houshakou, 2 (1989) 55. (in Japanese).
- T.Takahashi, S.Nakatani, N.Okamoto, T.Ishikawa and S.Kikuta
Studies on Si(III) $\sqrt{3}$ TIMES $\sqrt{3}$ -Bi and -Ag Surface by X-Ray Diffraction under Nearly Normal Incidence
Rev. Sci. Instrum., 60 (1989) 2365.
- K.Takakura
Auger effects on Bromo-Deoxyuridine-Monophosphate Irradiated with Monochromatic X-Rays around Bromine K-absorption Edge
Radiat. Environ. Biophys., 28 (1989) 177.
- Y.Takakuwa, M.Niwano, M.Nogawa, H.Katakura, S.Matsuyoshi, H.Ishida, H.Kato and N.Miyamoto
Photon-Stimulated Desorption of H⁺ Ions from Oxidized Si(111) Surfaces
Jpn. J. Appl. Phys., 28 (1989) 2581.
- Y.Takakuwa, N.Nogawa, M.Niwano, H.Katakura, S.Matsuyoshi, H.Ishida, H.Kato and N.Miyamoto
Low-temperature Cleaning of HF-Passivated Si(111) Surface with VUV Light
Jpn. J. Appl. Phys., 28 (1989) L1274.
- Y.Takata, K.Edamatsu, T.Yokoyama, K.Seki, M.Tohnan, T.Okada and T.Ohta
XANES and Raman Spectroscopic Studies of Diamond Films Synthesized by Hot Filament CDV
Jpn. J. Appl. Phys., 28 (1989) L1282.
- T.Takizawa, H.Ohwada, H.Kato and H.Fukutani
VUV Reflection Spectra and Fundamental Optical Constants of Paratellurite, TeO₂
J. Phys. Soc. Jpn., 58 (1989) 2167.
- Y.Tazoh, K.Aihara, K.Miyabara, K.Hohkawa and M.Oshima
Low Resistance Ohmic Contacts to High Tc Superconducting Thin Films
IEEE Trans. on MAG, 25 (1989) 2049.
- K.Tohji and Y.Udagawa
X-Ray Raman Scattering as a Substitute for Soft X-Ray EXAFS
Phys. Rev., 148 (1989) 101.
- M.Tokushige, N.Tsujimoto, T.Oda, T.Honda, N.Yumoto, S.Ito, M.Yamamoto, Yui Ho Kim and Y.Hiragi
Role of Cysteine Residues in Tryptophanase for Monovalent Cation-Induced Activation
Biochemie, 71 (1989) 711.
- S.Tokutomi, M.Nakasako, J.Sakai, M.Kataoka, K.T.Yamamoto, M.Wada, F.Tokunaga and M.Furuya
A Model for Dimeric Molecular Structure of Phytochrome Based on Small-Angle X-Ray Scattering
FEBS Letters, 247 (1989) 139.
- T.Tomiki, T.Futemma, H.Kato, T.Miyahara, Y.Aiura, H.Fukutani and T.Shikenbaru
The Optical Spectra of α -Al₂O₃ Single Crystals in the Vacuum Ultraviolet Region
J. Phys. Soc. Jpn., 58 (1989) 1486.
- K.Tsuji, K.Yaoita, M.Imai, O.Shimomura and T.Kikegawa
Measurements of X-Ray Diffraction for Liquid Metals under High Pressure
Rev. Sci. Instrum., 60 (1989) 2425.
- K.Tsunetomo, T.Sugishima, T.Imura and Y.Osaka
Te-K EXAFS Study on the Local Structure of Amorphous Te₂C_{1-x} Alloys
Jpn. J. Appl. Phys., 28 (1989) 1061.
- H.Tsuruta, T.Nagamura, K.Kimura, Y.Igarashi, A.Kajita, Z.Wang, K.Wakabayashi, Y.Amemiya and H.Kihara
Stopped-Flow Apparatus for X-Ray Scattering at Subzero Temperature
Rev. Sci. Instrum., 60 (1989) 2356.
- K.Ueda, E.Shigemasa, Y.Sato, S.Nagaoka, A.Yagishita, T.Nagata and T.Hayaishi
Ionic Fragmentation Following the 3d Core Excitation of Sn(CH₃)₄ by Soft X-Rays
Chem. Phys. Letters, 154 (1989) 357.
- N.Ueno, T.Mitsuhata, K.Sugita and K.Tanaka
Mechanism of UV- and VUV-Induced Etching of Poly (Methyl Methacrylate): Evidence for an Energy-Dependent Reaction
ACS Symp. Ser., 412 (1989) 424.
- M.Ukai
Autoionization of Highly Excited Molecules -Photoionization and Penning Ionization
Kagaku to Kougyou, 42 (1989) 215. (in Japanese).
- T.Urisu, H.Kyuragi, Y.Utsumi, J.Takahashi and M.Kitamura
Synchrotron Radiation Stimulated Semiconductor Processes -Chemical Vapor Deposition and Etching-
Rev. Sci. Instrum., 60 (1989) 2157.
- Y.Utsumi, T.Urisu, J.Takahashi and H.Maezawa
Soft X-Ray W/Be Multilayer and Its Application to a Diffraction Grating
Rev. Sci. Instrum., 60 (1989) 2024.
- I.Waki and Y.Hirai
The Silicon L-edge Photoabsorption Spectrum of Silicon Carbide
J. Phys.:Condensed Matter, 1 (1989) 6755.
- Y.Waseda
Structural Characterization of Non-crystalline Materials by the Anomalous X-Ray Scattering (AXS) Method
ISIJ International, 29 (1989) 193.
- N.Watanabe, K.Sakabe, N.Sakabe, T.Higashi, K.Sasaki, S.Aibara, Y.Morita, K.Yonaha, S.Toyama and H.Fukutani
Crystal Structure Analysis of ω -Amino Acid: Pyruvate Aminotransferase with a Newly Developed Weissenberg Camera and an Imaging Plate Using Synchrotron Radiation
J. Biochem.(Tokyo), 105 (1989) 1-3.
- K.Yakushi, H.Yamakado, M.Yoshitake, N.Kosugi and

- H.Kuroda
Electrochemical Preparation and Characterization of the Radical Salts of (Phthalocyaninato)Nickel, $\text{NiPc}(\text{SbF}_6)_{0.5}$
Bull. Chem. Soc. Jpn., 62 (1989) 687.
- Y.Yamada-Maruo, M.Oshima, T.Waho, T.Kawamura, S.Maeyama and T.Miyahara
Photoemission Studies of Bonding Properties at the MBE-grown CaF_2/GaAs Interface
Appl. Surf. Sci., 41/42 (1989) 647.
- Y.Yamada, M.Oshima, T.Waho and T.Kawamura
Photoemission and RHEED Studies of Structure and Bonding Properties at the $\text{CaF}_2/\text{GaAs}(001)$ Interface
Jpn. J. Appl. Phys., 28 (1989) L299.
- N.Yamaguchi, T.Cho, T.Kondoh, M.Hirata, S.Miyoshi, S.Aoki, H.Maezawa and M.Nomura
X-Ray Detection Characteristics of Microchannel Plates in the Energy Range from 1.8 to 8 KeV
Rev. Sci. Instrum., 60 (1989) 368.
- N.Yamaguchi, T.Cho, T.Kondoh, M.Hirata, S.Miyoshi, S.Aoki, H.Maezawa, M.Nomura and Y.Satow
Characterization of Microchannel Plates for Plasma X-Ray Diagnostics in the 0.6–82KeV Energy Region
Rev. Sci. Instrum., 60 (1989) 2307.
- S.Yamamoto, T.Shioya, S.Sasaki and H.Kitamura
Construction of Insertion Devices for Elliptically Polarized Synchrotron Radiation
Rev. Sci. Instrum., 60 (1989) 1834.
- T.Yamasaki, Y.Ogino, T.Honda and Y.Amemiya
Two-Stage Temper Embrittlement of Amorphous Fe-B-Si Alloys and Structural Changes Examined by SR-Small Angle X-Ray Scattering
Scripta Metallurgica, 23 (1989) 1963.
- H.Yamashita, Y.Ohtsuka, S.Yoshida and A.Tomita
Local Structures of Metal Dispersed on Coal. 1. Change of Local Structure of Iron Species on Brown Coal during Heat Treatment
Energy & Fuels, 3 (1989) 686.
- H.Yamashita, Y.Ohshita, S.Yoshida and A.Tomita
Change of Local Structure of Iron Compounds on Brown Coal During Devolatilization and Gasification
Shokubai, 31 (1989) 88. (in Japanese).
- T.Yamazaki, Y.Ogino, T.Honda and Y.Amemiya
Two-Stage Temper Embrittlement of Amorphous Fe-B-Si Alloys and Structural Changes Examined by SR-Small Angle X-Ray Scattering
Scripta Metallurgica, 23 (1989) 1963.
- M.Yanagihara, S.Sato, T.Koide, S.Takeda and A.Iijima
Optical Constants of CVD-SiC Mirrors Produced by Different Processes from 200 to 1000 eV
Jpn. J. Appl. Phys., 28 (1989) 128.
- M.Yanagihara, J.Cao, M.Yamamoto, T.Namioka, S.Sato, T.Koide, S.Takeda and A.Iijima
Optical Constants of SiC Mirrors Produced by Different Methods for Photons of 60–1000 eV
Rev. Sci. Instrum., 60 (1989) 2030.
- M.Yanagihara, J.Cao, M.Yamamoto, A.Arai, S.Nakayama, T.Mizuide and T.Namioka
Optical Constants of Superthin Gold Films for Soft X-Rays
Rev. Sci. Instrum., 60 (1989) 2014.
- T.Yokohama, T.Satsukawa and T.Ohta
Anharmonic Interatomic Potentials of Metals and Metal Bromides Determined by EXAFS
Jpn. J. Appl. Phys., 28 (1989) 1905.
- K.Yokoi, N.Matsubayashi, T.Miyanaga, I.Watanabe, S.Ikeda and K.Murata
Studies on the Structure of the Paramagnetic μ -oxo Dimer of Molybdenum(V) in Hydrochloric Acid Solutions by EXAFS
Polyhedron, 8 (1989) 45.
- T.Yokoyama, S.Kimoto and T.Ohta
Temperature-Dependent EXAFS Study on Silica-Supported Small Silver and Palladium Clusters
Physica B, 158 (1989) 255.
- T.Yokoyama, K.Asakura, Y.Iwasawa and H.Kuroda
Temperature Dependence of Extended X-Ray Absorption Fine Structure Spectra of Rh and Pd Catalysts in the Strong Metal-Support Interaction State
J. Phys. Chem., 93 (1989) 8323.
- T.Yokoyama, S.Kimoto and T.Ohta
Temperature-Dependent EXAFS Study on Supported Silver and Palladium Clusters
Jpn. J. Appl. Phys., 28 (1989) L851.
- T.Yokoyama, T.Satsukawa and T.Ohta
Anharmonic Interatomic Potentials of Metals and Metal Bromides Determined by EXAFS
Jpn. J. Appl. Phys., 28 (1989) 1905.
- T.Yokoyama, M.Funabashi, Y.Kitajima, T.Ohta and H.Kuroda
Study of Surface EXAFS and X-Ray Standing-Wave Absorption Profiles for $\text{p}(2 \times 2)\text{S}/\text{Ni}(111)$
Physica B, 158 (1989) 643.
- T.Yokoyama, Y.Takata, M.Yoshiki, T.Ohta, M.Funabashi, Y.Kitajima and H.Kuroda
Applicability of the Soft X-Ray Standing-Wave Method to Surface Structure Determination
Jpn. J. Appl. Phys., 28 (1989) L1637.
- K.Yoshihara, H.Kaji, T.Sekine, T.Nakajima and T.Mukoyama
Photonuclear Excitation of ^{103}Rh by Synchrotron Radiation
Appl. Radiat. Isot., 40 (1989) 491.

